OCS Study
BOEM 2018-041

Simulation Modeling of Ocean Circulation and Oil Spills in the Gulf of Mexico
Volume III: Data Collection, Analysis and Model Validation

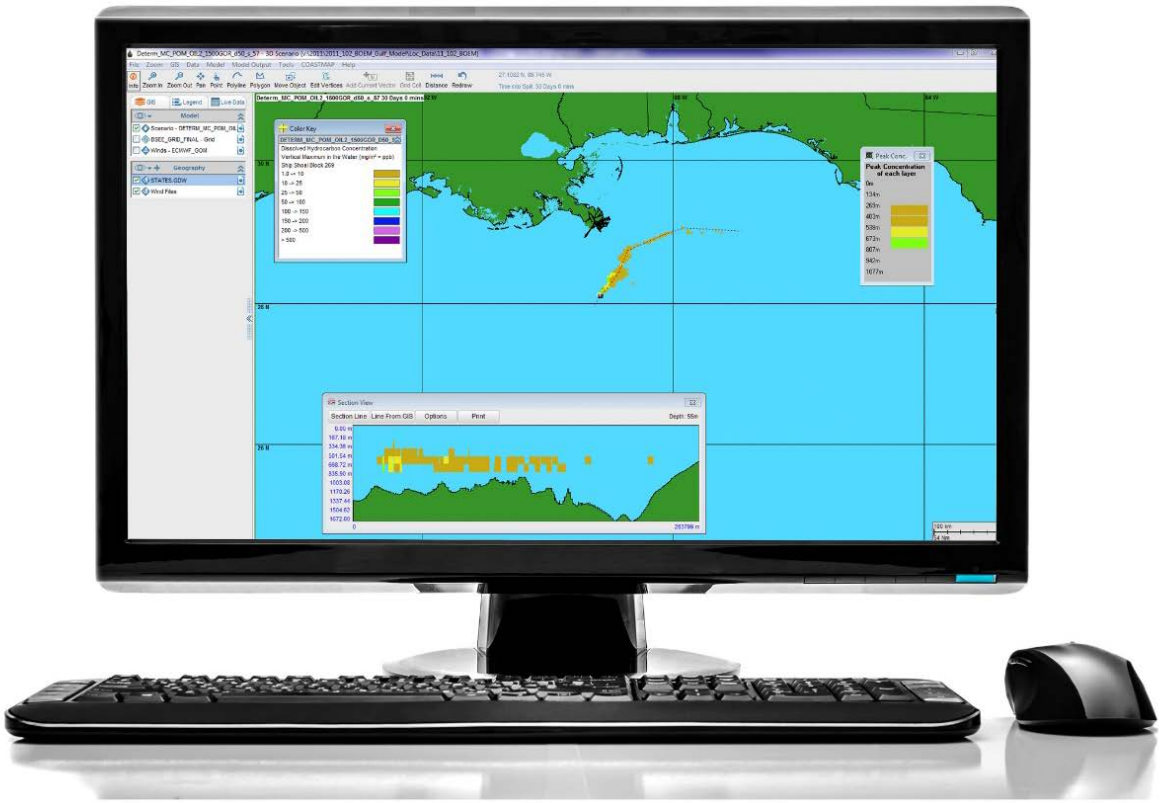

U.S. Department of the Interior
Bureau of Ocean Energy Management
Gulf of Mexico OCS Region

BOEM
Bureau of Ocean Energy Management

OCS Study
BOEM 2018-041

Simulation Modeling of Ocean Circulation and Oil Spills in the Gulf of Mexico
Volume III: Data Collection, Analysis and Model Validation

Editors:
Chris Galagan
Deborah French McCay
Jill Rowe
Lisa McStay

Authors:
Deborah French McCay
Matthew Horn
Zhengkai Li
Deborah Crowley
Malcolm Spaulding
Daniel Mendelsohn
Katherine Jayko
Yong Kim
Tatsu Isaji
Jeremy Fontenault
Rachel Shmookler
Jill Rowe

Prepared under BOEM Contract M11PC00028
By
RPS ASA
55 Village Square Drive
South Kingstown, RI 02879

Published by

U.S. Department of the Interior
Bureau of Ocean Energy Management
Gulf of Mexico OCS Region

New Orleans, LA
August 2018

Disclaimer

This report was prepared under contract between the Bureau of Ocean Energy Management (BOEM) and RPS ASA. This report has been technically reviewed by BOEM, and it has been approved for publication. Approval does not necessarily signify that the contents reflect the views and policies of BOEM, nor does mention of trade names or commercial products constitute endorsement or recommendation for use.

Report Availability

To download a PDF file of this Gulf of Mexico OCS Region report, go to the U.S. Department of the Interior, Bureau of Ocean Energy Management, Environmental Studies Program Information System website and search on OCS Study BOEM 2018-041.

This report can be viewed at select Federal Depository Libraries. It can also be obtained from the National Technical Information Service; the contact information is below.

U.S. Department of Commerce
National Technical Information Service
5301 Shawnee Rd.
Springfield, Virginia 22312
Phone: (703) 605-6000, 1(800)553-6847
Fax: (703) 605-6900
Website: http://www.ntis.gov/

Citation

French McCay, D., M. Horn, Z. Li, D. Crowley, M. Spaulding, D. Mendelsohn, K. Jayko, Y. Kim, T. Isaji, J. Fontenault, R. Shmookler, and J. Rowe. 2018. Simulation Modeling of Ocean Circulation and Oil Spills in the Gulf of Mexico, Volume III: Data Collection, Analysis and Model Validation. US Department of the Interior, Bureau of Ocean Energy Management, Gulf of Mexico OCS Region, New Orleans, LA. OCS Study BOEM 2018-041; 313 p.

Acknowledgements

Dr. Rebecca Green, the BOEM Project Manager, made significant contributions to the project documentation and to the overall success of the project. Dr. Walter Johnson of BOEM contributed insight and guidance at key decision points throughout the project. Members of the Science Review Group contributed considerable technical expertise and shared their years of experience to make the project a success. They include: Dr. Jim Payne, Dr. Jerry Galt, Dr. Rich Patchen and Dr. Steve Masutani.

Contents

List of Figures

List of Tables

Abbreviations, Acronyms, & Units

°C	Degrees Celsius
ADCP	Acoustic Doppler Current Profiler
AL1, AL2…	Aliphatic pseudo-components that are volatile or semi-volatile
AR1, AR2…	Aromatic and aliphatic pseudo-components that are soluble or semi-soluble
AT	AquaTracka
AVIRIS	Airborne visible infrared imaging spectrometer
BAOAC	Bonn Agreement Oil Appearance Code
bbl	Barrel(s) (42 US gallons)
BOEM	US Department of Interior, Bureau of Ocean Energy Management
BOD	Biological oxygen demand
BOP	Blowout preventer
BP	Boiling point
BTEX	Benzene + toluene + ethylbenzene + xylene
CDOM	Colored dissolved organic matter
cP	Centipoise
CSDL	NOAA/NOS Coast Survey Development Laboratory
cSt	Centistokes
CFSR	Climate forecast system reanalysis
CTD	Conductivity-temperature-depth
DO	Dissolved oxygen
DOR	Dispersant-to-oil ratio
DOSS	Dioctyl sodium sulfosuccinate
DWHOS	*Deepwater Horizon* oil spill
EPA	Environmental Protection Agency
ESI	Environmental Sensitivity Index
ERMA	Environmental response management application
FRTG	Flow Rate Technical Group
FSU	Florida State University
g/cm^3	Grams per cubic centimeter
g/m^3	Grams per cubic meter
GIS	Geographic information system
GOM	Gulf of Mexico
GRIB	Gridded binary data format
HC	Hydrocarbon
HYCOM	Hybrid Coordinate Ocean Model
IAS ROMS	Intra-Americas Sea Regional Ocean Modeling System
K_{ow}	Octanol-water partition coefficient
kt	Knot
LE	Lagrangian Element
LISST	Laser in-situ scattering and transmissometry

m	Meters
m^2/s	Square meters per second
m^3/hr	Cubic meters per hour
µm	Micron
mb	Millibar
MT	Metric tonnes
mg/L	Milligrams per liter
mN/m	Millinewton per meter
MAH	Monoaromatic hydrocarbon
MODIS	Moderate resolution imaging spectroradiometer
MTIR	MODIS thermal infrared
MVIS	MODIS visible
NAM	North American Mesoscale Forecast System
NARR	North American Regional Reanalysis
NCEP	National Centers for Environmental Prediction
NCOM	Navy Coastal Ocean Model
NDBC	National Data Buoy Center
NetCDF	Network common data form
NGDC	National Geophysical Data Center
NGOM	Northern Gulf of Mexico model
NIR	Near infrared
NOAA	National Oceanic and Atmospheric Administration
NODC	National Oceanographic Data Center
NOGAPS	Navy Operational Global Atmospheric Prediction System
NRDA	Natural Resource Damage Assessment
NRL	Naval Research Laboratory
OBC	Oil budget calculator
OCR	Observable chemistry regimes
OEDA	Oil emulsion detection algorithm
OPA	Oil Pollution Act
PAH	Polycyclic aromatic hydrocarbons
RITT	Riser insertion tube and top hat
RMSE	Root mean square error
SABGOM	South Atlantic Bight Gulf of Mexico
SAR	Synthetic aperture radar
SCAT	Shoreline cleanup and assessment
SIMAP	Spill Impact Model Application Package
SPC	Small particle concentrations
SPM	Suspended particulate matter
SSDI	SubSea Dispersant Injection
sTPH	Speciated total petroleum hydrocarbon
TCNNA	Texture classifying neural network algorithm
TM	Thematic mapper
TPH	Total petroleum hydrocarbon

tVOA	Total volatile organic analysis
TSS	Total suspended solids
USGS	U.S. Geological Survey
VOA	Volatile organic analysis
WAF	Water accommodated fraction

1. Introduction

1.1 Objectives and Scope

The objectives of this report are to describe validation of the Spill Impact Model Application Package (SIMAP) oil fate model for deep water oil releases. The SIMAP model has been developed over 30 years, and has undergone several peer reviews. The model originated from the Natural Resource Damage Assessment Model for Coastal and Marine Environments (NRDAM/CME) that ASA developed for the US Department of the Interior for use in Natural Resource Damage Assessment (NRDA) regulations (French et al. 1996). As part of the NRDA regulatory process for the NRDAM/CME, the model was extensively peer-reviewed. There was also a public review process, during which industry groups and state trustees reviewed the model and commented. Those comments were addressed in the Final Rule (Federal Register, May 7, 1996, Vol. 61, No. 89, p. 20559–20614). The NRDAM/CME was also used for development of the Oil Pollution Act (OPA) of 1990 NRDA regulations lead by National Oceanic and Atmospheric Administration (NOAA), undergoing additional peer review as part of that process. SIMAP was developed from the NRDAM/CME in the 1990s and has been used for many government-supported projects, many of which involved peer review (e.g., French McCay et al. 2004; French McCay et al 2005a, b).

Previously, the model has been validated with more than 20 case histories, including the *Exxon Valdez* and other large spills (French and Rines 1997, French McCay 2002, 2003, 2004, French McCay and Rowe 2004) as well as test spills designed to verify the model (French et al. 1997). For most of the case histories, observational data were available for surface oil impacts, as field observations after spills focus on these effects. The validation studies show that the model is capable of hindcasting the oil trajectory and shoreline oiling, given: (1) accurate observed wind data following the spill, and (2) a reasonable depiction of surface currents, both tidal and background. As winds and currents are the primary forcing variables on oil fate, obtaining accurate data for these is very important to the accuracy of any simulation.

For the North Cape oil spill of January 1996 in Rhode Island, field observations were available for both surface and subsurface oil fate. The model's prediction of the oil's fate agreed with observations of surface oil movements and measurements of total hydrocarbons and soluble-semi-soluble aromatic concentrations in the water. The model estimate of birds oiled in the area swept by oil was 2,200–4,400, depending on the pre-spill abundance data assumed. The mid-point of this range is 8.5 times the number of birds collected on beaches, in agreement with estimates for other spills. (The negotiated settlement used a factor of six for this spill.) Impacts on water column organisms were validated by comparison of the model estimate to the field sampling-based estimate of the

lobsters killed (8.3 million and 9 million, respectively). The model estimates of impacts to other marine species were used in the government's natural resource damage claim to the responsible party. This claim was settled based on these estimates of injury.

SIMAP has undergone extensive testing and code verification many times. The evaluations included testing the transport algorithms against simple cases for advective and dispersive transport and dye studies (French McCay et al. 2007). The most recent was a thorough evaluation and testing of the algorithms to ensure each algorithm is operating as expected and is consistent with the underlying theoretical framework. This was undertaken as part of the support to NOAA and the *Deepwater Horizon* (DWHOS) Trustees (DWHOS Trustees 2016) as part of the NRDA for the DWHOS (French McCay et al. 2015).

With respect to deep water blowouts, only one has been studied in enough detail where sufficient comparison data are available for validation: the DWHOS. Thus, this is the focus of this Volume III. The steps are outlined below.

1. Collate the data available for use as input to the model.
2. Evaluate the data available for validation of model results.
3. Apply model to DWHOS focusing first on the blowout simulations, next on the subsurface transport and finally on the surface transport and shoreline oiling.
4. Compare model predictions to publicly-available observations including trapping depth, oil particle size distribution and rise velocities, oil and gas-hydrates concentrations in the water column, surface oil patterns, and shoreline oiling.
5. Compare model predicted mass balance at the end of the spill to the NOAA Oil Budget Calculator (OBC) and other studies
6. Perform sensitivity (uncertainty) studies with a focus on the key environmental input data sets (currents, winds and waves) and the spill model algorithms.

Appendix II of Volume II of this report describes the SIMAP model, algorithms, needed input data, oil component properties and degradation rates. Thus, the modeled processes are only briefly summarized here (Section 1).

Following introductory information in this section, the remainder of this Volume III describes simulations of the DWHOS using the SIMAP oil trajectory and fate model. Model inputs are described in Section 2. Annex A provides additional information on the model inputs: maps displaying the gridded water temperature and salinity data used in the simulations, and data used to quantify response activities (i.e., *in situ* burning and aerial dispersant operations). Section 3 summarizes the observational data, with further detail provided in Annex B. The results are presented in Section 4. Annex C to Annex F contain maps and other figures depicting the model results and comparisons to observational data.

Because of the large extent of the spill and the complexity of the model results, many figures were needed to display the results. For convenience, these figures are assembled in groups in attachments to each annex, as described in Section 4. Comparisons of the model results to literature reports and data collected during the DWHOS Response and NRDA are in Section 5. Section 6 contains complete citations for references cited in the text.

1.2 Brief Description of the Model System

The oil fate model in SIMAP estimates the distribution and mass of oil in the water column, on the water surface, on shorelines, and in the sediments through time. Processes simulated in the physical fates model include oil droplet and surface oil transport and randomized dispersion, oil surfacing, surface oil spreading, evaporation of volatiles from surface oil to the atmosphere, stranding of oil on shorelines, emulsification of oil, entrainment of oil as droplets into the water column (natural and facilitated by dispersant), re-surfacing of oil, dissolution of soluble components into the water column, volatilization from the water column to the atmosphere, adherence of oil droplets to suspended particulate matter (SPM), adsorption of soluble and semi-soluble hydrocarbons to SPM, sedimentation, and degradation. The model results provide estimates of water volumes exposed above various thresholds, such as water quality or other criteria. The output of the fate model includes the location and dimensions of floating oil, concentrations of hydrocarbon constituents in water, loading of oil onto shorelines, and fluxes of hydrocarbons to air and sediment over time. Concentrations of particulate (oil droplet) and dissolved hydrocarbon concentrations are saved to files for later viewing and calculations.

The blowout model (described in Appendix III of this report) evaluates the jet and buoyant plume of the oil and gas near the release location(s). This “near field” model follows the movements of the oil and gas as it comes out of aperture(s), entrains surrounding sea water and rises as a buoyant oil-gas-water plume until the plume reaches neutral buoyancy. At this point, the density of the oil-gas-water plume has increased enough to match the surrounding seawater. At the neutral-buoyancy depth, the oil droplets separate from the buoyant plume and are transported horizontally by currents and vertically by their individual buoyancies. At this stage the blowout model outputs the locations, volumes, and droplet sizes of the released oil droplets. These are then used as inputs to the far field SIMAP oil transport and fate model.

In addition to the initial conditions provided by the blowout model, the oil fate model requires winds, waves, and currents as inputs. Wind data and well-developed wind models inclusive of the Gulf of Mexico (GOM) are publicly available from government websites (see Section 3 of Appendix V Data Manual). Current data are available for the offshore continental slope area of the northern GOM from Acoustic Doppler Current Profilers

(ADCPs) that are moored or attached to offshore platforms and are included in NOAA's online data sets. Hydrodynamic model outputs (i.e., currents, temperature, salinity, water levels) are also publicly available from government websites and were developed as part of this project (see Appendix V, Section 2).

1.3 Compound Groups Tracked by the SIMAP Oil Fate Model

As described in Appendix II, the SIMAP fates model tracks lower molecular weight soluble and semi-soluble hydrocarbons in oil divided into chemical groups (pseudo-components) based on volatility, solubility, and hydrophobicity (Table 1-1). All but the residual oil pseudo-component (representing non-volatile and insoluble aromatics and aliphatics) evaporate at rates specific to the pseudo-component. Solubility is strongly correlated with volatility, and the solubility of aromatics is higher than aliphatics of the same volatility. Of the aromatics, the MAHs are the most soluble, the 2-ring PAHs are less soluble, and the 3-ring PAHs slightly soluble (Mackay et al. 1992, 2006a, b). Both the solubility and toxicity of the aliphatic hydrocarbons are much less than for the aromatics of similar molecular weight. Dissolved concentrations are calculated in the model for each of the soluble and semi-soluble hydrocarbons pseudo-components (named AR1 to AR9). Note that non-aromatic compounds that are soluble (i.e., C1-C10 n-alkanes, isoalkanes and cycloalkanes) are included in "AR9" and tracked by the model.

Table 1-1. Code designations and included compounds for the 19 pseudo-components.

Code	Group	Includes
AR1	BTEX	BTEX, styrene
AR2	C3-benzenes	C3-benzenes
AR3	C4-benzenes	C4-benzenes
AR4	Decalins	cis/trans decalin to C4-decalin
AR5	C0-C2 Naphthalenes	C0-C2 Naphthalenes, C0-C2 Benzothiophenes, biphenyl, acenaphthene, acenaphthylene
AR6	C3-C4 Naphthalenes	C3-C4 Naphthalenes, C3-C4 Benzothiophenes, dibenzofuran
AR7	Fluorenes & C0-C2 3-ring PAHs	C0-C3 Fluorenes, C0-C1 dibenzothiophenes, C0-C1 phenanthrenes
AR8	4-ring PAHs & C2-C3 3-ring PAHs	C0-C2 pyrenes & fluoranthenes, C2-C3 dibenzothiophenes, C2-C3 phenanthrenes, chrysene
AR9	Soluble alkanes	Low mol. wt. Alkanes, Isoalkanes, Cycloalkanes
AL1	Aliphatics: BP < 150	(unmeasured compounds)
AL2	Aliphatics: BP 150-180	(unmeasured compounds)
AL3	Aliphatics: BP 180-200	C11 Alkanes
AL4	Aliphatics: BP 200-230	C12 Alkanes
AL5	Aliphatics: BP 230-280	C13-C16 Alkanes

Code	Group	Includes
AL6	Aliphatics: BP 280-300	C17-C18 Alkanes
AL7	Aliphatics: BP 300-350	C19-C20 Alkanes
AL8	Aliphatics: BP 350-380	C21-C23 Alkanes
AL9	Dispersant indicator(s)	(dispersant indicator(s) on oil droplets)
Residual	Residual	Other non-volatile, non-soluble hydrocarbons

The initial (at the point of release to the water column) mass concentrations of the eight aromatic pseudo-components (AR1-AR8) and the soluble aliphatic pseudo-component (AR9) are computed using measured source oil sample concentrations. The mass concentrations of the eight non-soluble aliphatic pseudo-components (AL1-AL8) were based on measured weight fractions of a boiling curve for fresh source oil, using the boiling point ranges listed in Table 1-1. For pseudo-components AL1 and AL2, all of the compounds typically measured by standard laboratory methods are soluble, and so their mass concentrations are included in pseudo-component AR9. Thus, AL1 and AL2 represent unmeasured compounds in their respective boiling ranges (where solubility is unknown and not considered in the model). Pseudo-component AL9 is reserved for tracking dispersant component(s) or other contaminants. Each of the pseudo-components (or "components") is tracked in both the whole oil (droplets and floating) and dissolved phases.

This number (19) of pseudo-components provides sufficient accuracy for the evaporation and dissolution calculations, particularly given the time frame (minutes) over which these processes occur. The model has been validated in predicting dissolved concentrations, supporting the adequacy of the use of this number of pseudo-components (French McCay 2003).

1.4 The *Deepwater Horizon* Oil Spill

The scope of the *Deepwater Horizon* oil spill (DWHOS) was extensive, with areas potentially affected including the entire northeastern GOM. MC252 oil released from the broken riser of the DWHOS from April 22 to July 15 of 2010 both dispersed at depth and rose through nearly a mile of water column. The composition of the released gas-liquid mixture changed over time and space as the result of dilution, changes in pressure, dissolution, and the addition of other constituents such as dispersants. Of oil that made it to the water surface, some volatilized in the air, entrained water forming mousse, was dispersed into the water column naturally and by application of dispersants, and was removed mechanically or by *in situ* burning. Floating oil, oil droplets, and dissolved components were transported large distances at various levels of the water column. Oil also picked up sediments and other particulate matter, some of which became neutrally or negatively buoyant, sinking to

various depths. The oil dispersed at the wellhead (both via turbulence and by injection of dispersants) and was transported by currents that varied in time and space. This yields a complex pathway of subsurface oil contamination that affected abyssal, bathypelagic, and mesopelagic waters of the GOM.

In addition, there were logistical constraints in obtaining sufficient field sample data to completely characterize the contamination in space and time over and after the 87 days of oil and gas release. For these reasons, as part of the NRDA and at the direction of the DWHOS Trustees (2016), a modeling effort was undertaken to analyze the blowout, deep water oil plume, rising oil droplets and fate of the spilled oil during its journey through the water column to just below the water surface. The SIMAP oil fate model (described herein) was used to evaluate concentrations of oil and components in the water column encompassing the deep-water plume and rising oil resulting from the spill. Surface oil and processes in the upper 20m of the water column were not included in the DWHOS Trustees (2016) analyses of the spill.

The DWHOS Trustees published their *Deepwater Horizon* Oil Spill Final Programmatic Damage Assessment and Restoration Plan and Final Programmatic Environmental Impact Statement in February of 2016. (PDARP/PEIS; DWHOS Trustees, 2016.) Attached to this PDARP/PEIS were a series of technical reports detailing the findings upon which the trustees relied. The SIMAP modeling analysis was described in one of these technical reports (French McCay et al., 2015), as was the blowout modeling described in a technical report by Spaulding et al. (2015). These may be downloaded from public websites (see urls in reference citations, Section 6).

Considerable data were developed from sampling and sensor measurements during the NRDA analyses. The data were compiled and published by the DWHOS Trustees on the NOAA GOM ERMA website (ERMA, 2016). Data used for input to or verification of the modeling described herein, as well as a review of the literature and findings based on the data collections, are contained in this Volume II to the overall project report.

2. Model Input Data

2.1 Geographical and Model Grid

SIMAP uses a rectilinear grid to designate the location of the shoreline, the water depth (bathymetry), shore type or another habitat type. Appendix V in Volume II describes the sources of data used to develop depth and habitat grids. Grids used for modeling the DWHOS are described below.

2.1.1 Habitat Mapping

Digital shoreline data were mapped from Environmental Sensitivity Indices (ESI) coverages in Environmental Sensitivity Atlas Geographical Information System (GIS) for the GOM coast. ESI codes, which identify the shoreline substrate type and sediment grain size, were translated to equivalent habitat codes for SIMAP (see Appendix V for details). The subtidal habitats in the roughly 600-m grid were all designated as open water types (subtidal sand bottom), as subtidal habitat type had little influence on oil fate for the DWHOS in the deep water GOM.

Below is a summary of the resolution of the grid used for modeling.

- Origin longitude, latitude: -95.0°, 25.0°
- Number of cells W-E, S-N: 2000, 1000
- Cell size W-E, S-N: 0.006°, 0.006°
- Cell size (meters) W-E, S-N: 605.36 m x 667.94 m

The 600-m resolution grid (95TO83W-NOF25-ALLOPEN_GT200M-SWD_600m-2.HAB) is shown in Figure 2-1. The DWHOS well site is depicted on the map as the circled cross. This grid contains shoreline (intertidal) cells that define the areas and lengths of shore, by type, listed in Table 2-1.

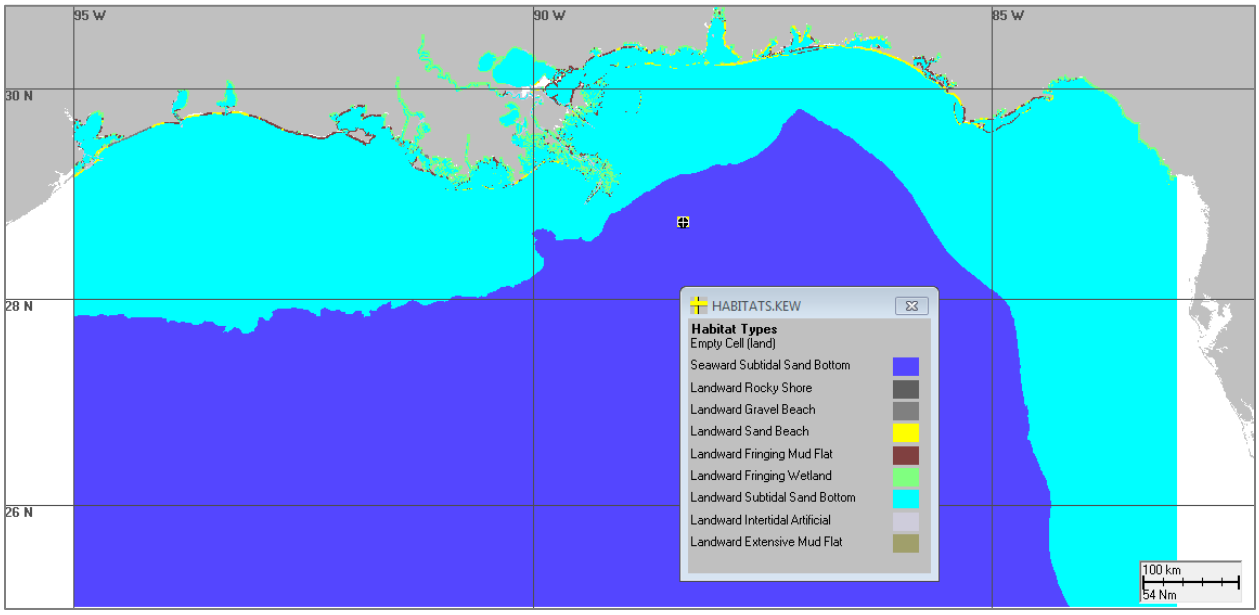

Figure 2-1 Map of the 600-m resolution habitat grid.

Table 2-1. Areas, lengths and widths of shoreline (intertidal) cells in the 600-m grid.

Habitat Name	Area (km^2)	Shore Length (km)	Shore Width (m)
Rocky Shore	0.0585	58.5	1
Gravel Beach	0.5490	275	2
Sand Beach	12.2000	1,222	10
Fringing Mud Flat	44.3000	2,217	20
Fringing Wetland	294.0000	5,873	50
Intertidal Artificial	0.1190	1,187	0.1

2.1.2 Bathymetry

A depth grid was created matching the extent and resolution of the habitat grid, as shown in Figure 2-2. Bathymetry for the GOM was obtained from NOAA's National Geophysical Data Center (NGDC) as described in Appendix V.

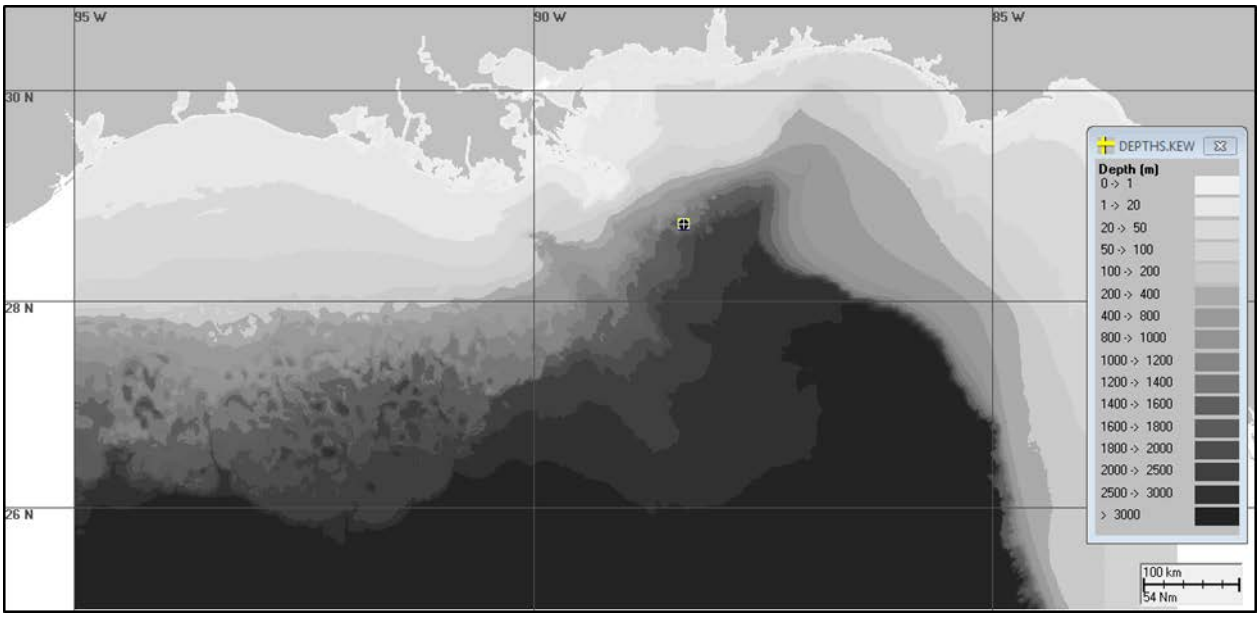

Figure 2-2. Map of the 600-m resolution depth grid.
(Circled cross is the DWHOS well site.)

2.2 Environmental Data

2.2.1 Water Temperature and Salinity

Water temperature and salinity data used for model inputs vary spatially, with depth, and by month. Climatic monthly mean water temperature and salinity data were obtained from the National Oceanographic Data Center (NODC) Ocean Climate Laboratory's Monthly Climatology data set for the GOM (Boyer et al. 2005, 2009, Locarnini et al. 2009, Garcia et al. 2010a, b; Antonov et al. 2010). This NODC analysis uses all data for the region that had been collated in the World's Ocean Database to provide gridded monthly-mean climatological data. The most recent version of the NODC database contains data through 2013, gridded on a ¼° grid. The data source and development of input files for SIMAP are described in Section 4 of Appendix V. Figures displaying the temperature and salinity grids used to model the DWHOS are in Annex A to this Volume III.

The vertical temperature profiles measured by Brooks McCall and other cruises in summer of 2010 were consistent with the climatology (Grennan et al. 2015). Typical temperatures in the upper mixed layer were 20–31°C, in the thermocline below the mixed layer 7–20°C, and in deep water (>800 m) 4–7°C. Additional description of the data is in Grennan et al. (2015) and French McCay et al. (2015). Figures showing the climatic mean surface water temperature and salinity data for April–September 2010 that were used for modeling are in Annex A.

The air immediately above the water is assumed to have the same temperature as the water surface. This is a reasonable estimate of air temperature in contact with the water and floating oil.

Water density was calculated from temperature and salinity using the algorithm of Bryden (1973). As summarized by Grennan et al. (2015), in areas influenced by the Mississippi plume, there is a strong pycnocline in the upper 30 or 50 m. However, outside the Mississippi plume, the upper 50 m often shows little density gradient. The mixed layer depth varies in space and time, and in some cases the upper 50m can be quite stratified. Below 200 m, there is only a small change in water density with depth.

2.2.2 Winds

The model uses time-varying wind speed and direction for the time of the spill and simulation. Thus, several observational and modeled wind data sets for April to September of 2010 were compiled.

2.2.2.1 Observational Data

Standard meteorological data were acquired from the National Data Buoy Center (NDBC 2013) for the six nearest NDBC buoy stations to the spill site (stations 42012, 42039, 42040, 42363, BURL1, and DPIA1). These observational data show generally light winds typical of summers in the northern GOM, and several storm periods. The station data also document spatial variation in the winds over the large area encompassed by the spill.

There were several tropical cyclone events between April and September of 2010: Hurricane Alex (June 25–July 2, 2010), Tropical Depression Two (July 8–9, 2010), and Tropical Storm Bonnie (July 22–24, 2010). Winds in the northeast GOM were higher than average during these periods, as well as during late April, May 9–15, and August 11–22, 2010. At wind speeds above about 10–12 knots, breaking waves form and increasingly more oil is entrained into the water column. Winds exceeding 10 knots averaged over the prior 24 hours occurred in late April, May 9–15, June 6, June 23, June 30–July 7, July 11–13, July 22, July 25, July 30, August 11–23, and August 28–31, 2010 Figure 2–3 shows the wind speed data from buoy 42040 located closest to and north of the DWHOS wellhead site at 88.207°W, 29.212°N.

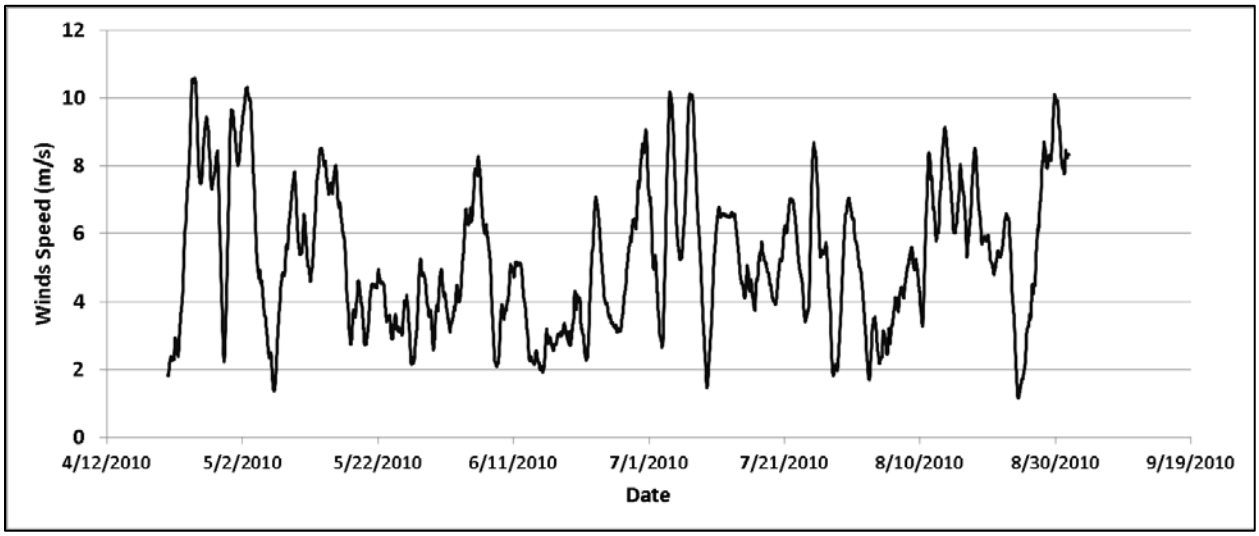

Figure 2-3. Wind speeds (m/s), averaged for the prior 24 hours, at NOAA buoy 42040.

2.2.2.2 Wind Models

Wind reanalysis products covering the northeastern GOM were obtained from NOAA and U.S. Navy government websites. See section 3 of Appendix V for further description of wind products available.

NOAA and NCEP NAM

The North American Mesoscale Forecast System (NAM) is provided by NOAA NCEP. The regional domain covers 16.85–31.64°N and 79.42–98.41°W with 614 x 428 grid cells, which is approximately 12 km resolution. The data are available at 1-hour resolution. The NAM data for year 2010 were downloaded as GRIB format, and then converted into NetCDF format.

NOAA and NCEP NARR

NOAA National Center for Environmental Prediction (NCEP) provides high resolution combined model and assimilated datasets for meteorological conditions, including wind fields for the North American region called North American Regional Reanalysis (NARR). The data are available at 3-hour resolution. The regional domain covers 12.2–57.3°N and 152.9–49.4°W, with 349 x 277 grid cells which is approximately 0.3° (32 km) resolution at the lowest latitude. The data for 2010 were downloaded as GRD format, and then converted into NetCDF format.

NOAA and NCEP Climate Forecast System Reanalysis (CFSR)

CFSR data are developed by NOAA's National Centers for Environmental Prediction (NCEP). CFSR provides a global reanalysis (a best estimate of the observed state of the atmosphere)

of past weather from January 1979 through March 2011 at a horizontal resolution of 0.5° (NCEI 2013).

US Navy NOGAPS

The US Navy operates a global atmospheric prediction system, called Navy Operational Global Atmospheric Prediction System (NOGAPS). The integration domain is global and the horizontal resolution is 0.5° on the Gaussian computational grid. The model uses a total of 30 sigma levels (based on pressure) in the vertical, with approximately 6 sigma levels below 850mb. The forecast time interval is every 6 hours (FNMOC 2013).

2.2.3 Currents

Oceanographic and tidal currents are variable in space and time at a range of scales as short as a few hours to seasonally. River discharge may vary by an order of magnitude or more over the course of the year, which in turn affects water velocity in coastal waters and in the area of the Mississippi River discharge into the offshore region. Several current data sets were available for the period and entire area of interest, and therefore were used in model runs using SIMAP. See Section 2 of Appendix V for further description of publicly-available hydrodynamic products available.

2.2.3.1 Observational Data

An ADCP is a hydro-acoustic current meter to measure water current velocities over a depth range using the Doppler effect. They are mounted on a buoy, rig, or drilling platform (i.e., structures located at the water surface) looking downward or mounted at the bottom looking upward. ADCPs were moored in place along the continental slope of the Northeastern GOM (Figure 2-4), measuring currents during 2010 before and during the spill period. In addition, ADCPs were deployed near the MC252 wellhead site, including a pair sampling the upper water column and waters deeper than 1000 m set out by a cooperative NRDA plan (Mulcahy 2010). The ADCP station closest to the DWHOS well is number '42916', which was installed on the Development Driller 3 that operated one of the relief wells within 1 km of the DWHOS wellhead. During the period from April–July 2010, the temporally-averaged current velocity at that station was 2.2 cm/s (0.04 kt) to the northeast and 3.9 cm/s (0.08 kt) to the southwest at 64 and 1,087 m below the water surface, respectively. The maximum current was 51 cm/s in the surface layer.

ADCP data from 60 stations in the northern GOM were downloaded from the NDBC data archive NDBC 2011). Of the ADCPs from these 60 stations, 18 ADCPs at 17 stations (locations) met the criteria for inclusion in the set used for modeling:

- Located within the area potentially most affected by the spill (~26.5–30°N, ~87.5–93°W).

- The metadata were corroborated (e.g., records without obvious errors, change or inconsistencies in the locations).
- Data quality checks eliminated station data where:
    1) The original data sets came with quality flags generated by NDBC, such that the data failed in their quality tests.
    2) Depth bins with data gaps exceeded 50% of the period of interest, April 1–September 30, 2010.
    3) Depth bins consisted of more than 10% of data points showing unreasonably large (e.g., the current speed larger than 1 m/s) or inconsistent values when compared to the layers (bins) above and/or below.
    4) A coherency check among the stations within 50 km distance failed. In cases where the correlation coefficient (r-square value) was less than 0.7 for more than two nearby sets, the time series of the ADCP station was investigated more carefully (e.g., #42365).

After meeting the quality checks based on the criteria listed above, the stations and bins identified as acceptable are listed in Table 2-2 and shown in Figure 2-4.

Table 2-2. List of 18 ADCPs and bins selected for use in modeling.

ADCP	Lon (°)	Lat (°)	Start Date in 2010	End Date in 2010	Water Depth (m)	ADCP Start Depth	ADCP End Depth	Bin dz (m)	Total # Bins	# Bins with Data	Start Bin-Met QA/ QC	End Bin-Met QA/ QC	Owner	Description
42361	-92.490	27.550	4/1	9/30	872	51	803	16	48	48	1	32	Shell	Auger-Garden Banks 426
42362	-90.670	27.800	4/1	9/30	910	80	848	16	60	49	1	47	Shell	Brutus-Green Canyon 158
42363	-89.220	28.160	4/1	9/30	894	53	885	16	60	53	1	42	Shell	Mars-Mississippi Canyon 807
42364	-88.090	29.060	4/1	9/30	980	51	995	16	60	60	1	57	Shell	Ram-Powell-Viosca Knoll 936
42368	-92.203	27.204	5/15	9/30	1,424	67	1,123	32	34	34	1	34	Conoco-Phillips	Magnolia-Garden Banks 783
42370	-90.536	27.321	4/1	9/30	1,311	62	991 or 1,315.5	30	64	45	1	45	BP	Holstein-Green Canyon 645
42377	-90.968	27.293	4/1	9/30	1,524	71	999	32	32	30	1	30	Kerr-McGee	Constitution-Green Canyon 680
42383	-89.924	27.370	4/1	9/30	1,290	77	685	32	32	20	1	20	BHP Billiton	Neptune-Green Canyon 613
42385	-88.266	28.340	4/1	8/1	1,975	79	751	32	32	22	1	22	Chevron	Blind Faith-Mississippi Canyon 696
42386	-90.714	27.326	4/1	9/30	1,219	97	865	32	32	25	1	24	Chevron	Tahiti-Green Canyon 641
42391	-89.101	28.034	5/4	9/30	1,250	119	1,047	32	40	30	1	13	ATP	Titan-Mississippi Canyon 941
42868	-88.356	28.745	5/11	9/18	1,508	78	1,166	32	35	35	1	34	BP	Discoverer Enterprise-Mississippi Canyon 822
42887	-88.496	28.191	4/1	9/30	1,844	73	1,001	32	30	27	1	27	BP	Thunder Horse-Mississippi Canyon 778
42889	-89.465	28.394	4/1	9/30	678	117	627	30	18	18	1	14	Murphy	Medusa-Mississippi Canyon 582
42904	-87.986	28.085	5/1	9/30	2,438	80	1,072	32	32	32	1	22	Anadarko	Independence Hub-Mississippi Canyon 920
42916	-88.363	28.731	5/1	9/28	1,521	65	993	32	36	36	1	33	BP	Development Driller 3-Grand Island
NRDA ADCP bottom	-88.434	28.742	6/16	9/30	1,485	1,020	1,484	16	31	30	1	30	BP	Deployed as part of cooperative work plan

ADCP	Lon (°)	Lat (°)	Start Date in 2010	End Date in 2010	Water Depth (m)	ADCP Start Depth	ADCP End Depth	Bin dz (m)	Total # Bins	# Bins with Data	Start Bin-Met QA/ QC	End Bin-Met QA/ QC	Owner	Description
NRDA ADCP surface	-88.434	28.742	6/16	9/30	1,485	25	89	18	27	9	1	9	BP	Deployed as part of cooperative work plan

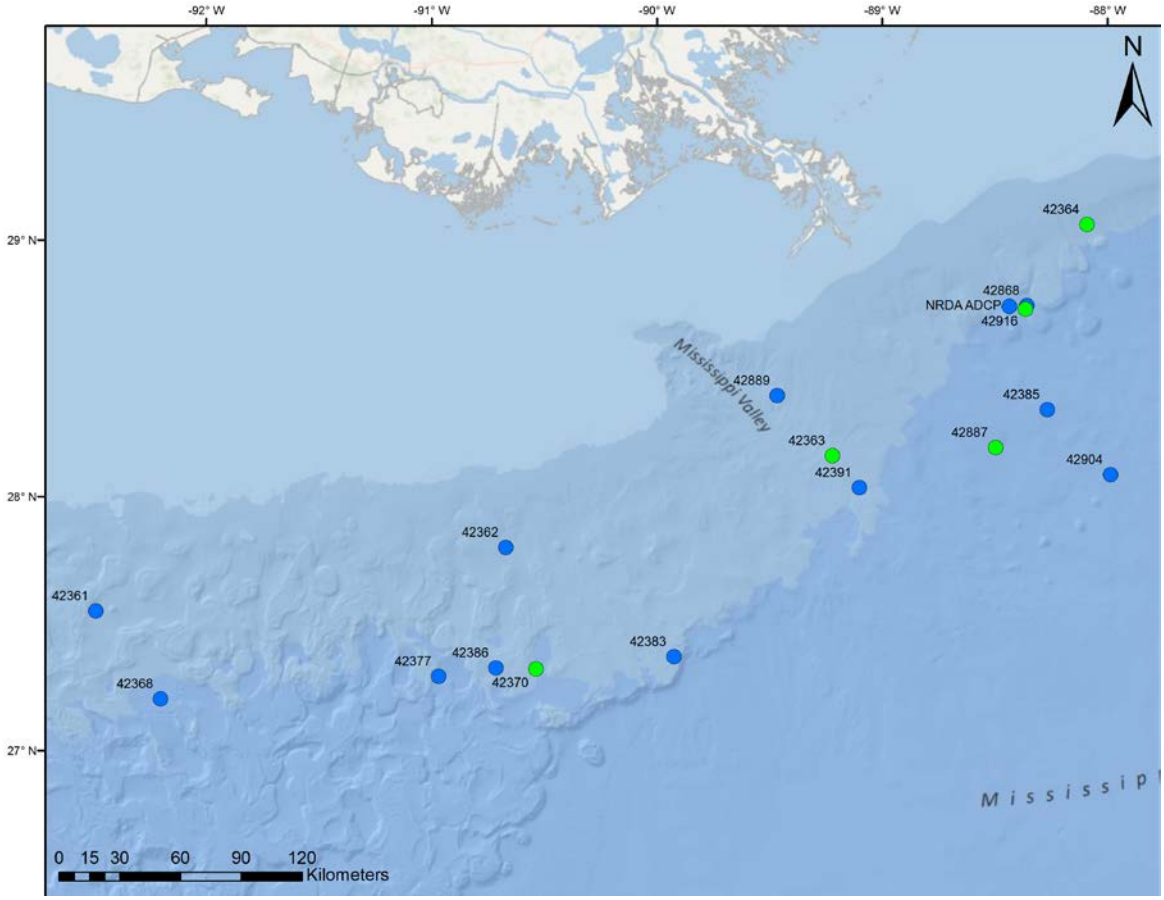

Figure 2-4. Locations of 18 ADCPs at 17 stations where sufficient data were available for 2010.

ADCP data meeting the quality criteria were used in SIMAP model simulations for comparison with simulations run with hydrodynamic model results. The data for these 18 ADCPs at 17 stations were interpolated to develop three-dimensional and time-varying current fields using an inverse distance-weighted scheme employing all sensors. This provided a three-dimensional and time-varying current field that could be used for transport calculations.

The following steps were used in preparing and interpolating the ADCP data to develop the four-dimensional current field:

1. *Vertical registration*: The original ADCP data sets were first mapped to the same vertical locations (*bins*) extending from the top- to bottom-most data.
2. *Time registration*: All data sets were linearly interpolated in time so that all data were available at prescribed times and at fixed intervals of time (10 min).

3. *Spatial interpolation:* As is clear from Figure 2-4, the ADCPs covered a limited portion of the spill-affected area horizontally. The vertical extent of the data was typically from depths between 50 and 1,200 meters. Few data were available near the surface (0 to 50 m) and from 1,200 m to the bottom, the only such data being those from the NRDA ADCPs near the wellhead. This necessitated a process to extrapolate or interpolate the data to locations where it was needed. The methods used in both the vertical and horizontal interpolation are summarized below. This interpolation was implemented for each spillet at each time step in the spill model simulation.
4. *Horizontal interpolation and extrapolation:* At the horizontal (latitude, longitude) location of the spillet, the currents are determined by inverse square distance weighting using the five closest horizontal neighbors.
5. *Vertical interpolation and extrapolation:* If current observations were available both above and below the spillet location, then linear interpolation using the five nearest vertical neighbors was used to estimate the current vector. Above the shallowest bin where data were available, the closest vertical value was used. Based on coherence analysis, ADCP stations were grouped into five clusters (vicinity of the well and NE, S, SW, and distant SW of the well). A representative station in each cluster (green dots in Figure 2-4) was selected to extrapolate values in the bottom-most bin to the seabed. The core assumptions are that currents are constant with depth above the shallowest and below the deepest observation (no or very weak vertical structure).

Note that the ADCP data coverage extends along the continental slope in the area of concern. There are no data on the shelf. Thus, due to the inverse distance weighting scheme used, currents on the shelf are weak and have little influence on transport in simulations employing ADCP data. In addition, the interpolation provides a smoothed surface current field, and does not resolve smaller scale features and shear less than the scale of the distance between ADCP moorings (order of 30–100 km). Also, ADCPs do not provide estimates of surface currents. Thus, simulations using ADCPs were only performed for oil transport below the 40m mixed layer.

2.2.3.2 Hydrodynamic Models

In addition to the North Carolina State University (NCSU) SABGOM and the Florida State University (FSU) HYbrid Coordinate Ocean Model (HYCOM) hydrodynamic model datasets developed for the risk assessment modeling (see Appendix V), several publicly-available hydrodynamic model simulations of currents in the north-eastern GOM were used in model simulations. Available model products are briefly described below.

<u>SABGOM (Principal Investigator: Ruoying He, NCSU)</u>

SABGOM is a ROMS application for the GOM developed by NCSU. The model domain of SABGOM ROMS encompasses the entire GOM and South Atlantic Bight (Hyun and He 2010; Xue et al. 2013). SABGOM ROMS uses a mesh with a horizontal resolution of ~5 km and 36 terrain-following vertical layers used to resolve the water column. This implementation of SABGOM was forced with NARR winds. Current predictions were provided every 3 hours. See Section 2.2 of Appendix V for further details.

HYCOM-FSU (Principal Investigator: Eric Chassignet, FSU)

The FSU HYCOM uses a hybrid coordinate system, advantageous for resolving water bodies with large ranges of bathymetry (Chassignet et al. 2009, 2015). The hydrodynamic simulation was forced with NARR winds. FSU's HYCOM has a 3–4 km horizontal resolution, 20 hybrid layers in the vertical, and provides current predictions every 3 hours. See Section 2.3 of Appendix V for further details.

NGOM (NOAA and NOS and OCS; Principal Investigator: Richard Patchen)

The NOS Gulf of Mexico Nowcast and Forecast Model (NGOM) is the NOAA and NOS Coast Survey Development Laboratory (CSDL) GOM implementation of the Princeton Ocean Model (POM, developed by Dynalysis of Princeton). NGOM was run as a nowcast in real time for 2010, forced with winds and river discharges. NOAA's surface winds (12 km resolution) and atmospheric forecasts from the NAM model were used. Synoptic river flow discharges are specified from 36 rivers at 29 discharge model locations along the U. S. coastline, based on USGS and USACE gages. The resolution of NGOM is 2–3 km in the north-western GOM, 5–6km in the north-eastern and central basin, with 37 levels in the vertical. Predictions are provided every 3 hours.

GLOBAL HYbrid Coordinate Ocean Model (HYCOM; US Navy; HYCOM-NRL, Real-time)

The US Naval Research Lab (NRL) provides its real-time operational forecast GLOBAL HYbrid Coordinate Ocean Model (HYCOM) simulations on its government website, and many transport modelers download and use these data products. The model is forced with NOGAPS winds. Model resolution is 1/25° (~3.5 km) in the horizontal, with 20 vertical layers. Data for the GOM during 2010 were downloaded and formatted in NetCDF files for use as input to SIMAP.

NRL Navy Coastal Ocean Model (NCOM Real Time, 3D; US Navy)

The Global NCOM was an ocean prediction system run (through 2013) by the Naval Oceanographic Office (NAVOCEANO) as the Navy's real-time operational global nowcast and forecast system. The Naval Research Laboratory developed NCOM based on the Princeton Ocean Model with time invariant hybrid (sigma over Z) vertical coordinates. See the Navy's NCOM Publications Web page for additional information. For distribution,

NAVOCEANO interpolates the output onto a regular latitude-longitude grid in the horizontal and a series of standard depths in the vertical, and parses the global domain into 13 regions. This site provides access to regions around the U.S. and its territorial waters.

NRL HYCOM+NCODA GOM (HYCOM-NRL Reanalysis)

NRL also has publicly provided a 3-D reanalysis product produced using the NRL's version of HYCOM, which uses CFSR winds as forcing. HYCOM-NRL reanalysis product hydrodynamic data were downloaded in March 2015. The NRL's HYCOM + NCODA Gulf of Mexico 1/25° Reanalysis product GOMu0.04/expt_50.1 uses the Navy Coupled Ocean Data Assimilation (NCODA) system (Cummings 2005; Cummings and Smedstad 2013) for data assimilation. The GOM model has 1/25° equatorial resolution and latitudinal resolution of 1/25° cos(lat) or ~3.5 km for each variable at mid-latitudes. This version has 36 coordinate surfaces in the vertical. Wind data used to force the hydrodynamics and oil spill modeling were the NOAA NCEP CFSR Selected Hourly Time-Series Products, January 1979 to December 2010 (Saha et al. 2010).

IAS ROMS (Principal Investigator: Yi Chao, UCLA)

Intra-Americas Sea Regional Ocean Modeling System (IAS ROMS) is a ROMS application that consists of a single domain covering the entire GOM and much of the western Atlantic Ocean (between the equator and 40˚N). SABGOM is the predecessor of IAS ROMS. The model has a grid resolution of ~6 km in the horizontal, with 30 levels in the vertical. The lateral boundary conditions for the model domain are provided by real-time global 1/12˚ HYCOM currents (Chassignet et al. 2009). Outputs were generated by the NRL at Stennis Space Center and distributed by FSU. Every 12 hours, IAS ROMS assimilated observational data (e.g., temperature, salinity, sea surface height, and the ADCP data described in Section 2.2.3.1) using its 3-D variational (3DVAR) data assimilation algorithm (Li et al. 2008a, b). Twelve-hourly data were used as a direct input to SIMAP, as were hourly predictions between these 12-hour steps. The hourly results are a combination of the observational data and the model first-guess field, which is the 12-hour IAS ROMS forecast (without data assimilation) initialized from the previous nowcast. An IAS ROMS simulation (version "4C") for 2010, that included a 2-km nested grid within the larger IAS ROMS domain, was run as part of the trustees' NRDA program and provided by Chao et al. (2014) in April 2014 (model described in Chao et al. 2009). This simulation was forced with NAM winds.

2.2.4 Suspended Particulate Matter

Suspended particulate matter (SPM) includes minerals, referred to as total suspended sediments (TSS) and organic particulates (matter). Oil can adhere to SPM and be transported in the water column in accordance to the density, shape, and size of the combined oil-sediment particulates. Typically, sedimentation of oil and PAHs, via mineral-

SPM interactions, becomes significant above suspended sediment concentrations of about 100 mg/L (Payne et al. 1984, 1987; French et al. 1996; French McCay et al. 2004, 2005). MC252 oil from the spill was identified on the sediments in the offshore area surrounding and down-stream of the well site (Montagna et al. 2013; Valentine et al. 2014). Thus, there is evidence that there was a flux of spilled oil to the sediments. Because mineral SPM concentrations are typically very low in the offshore GOM near the wellhead (D'Sa et al. 2007, 2008; Salisbury et al. 2004), the transport flux to the seafloor likely resulted from oil droplets becoming less buoyant after weathering and biodegradation, facilitated by droplet adherence to organic matter and settling of marine snow (Passow et al. 2012; Passow 2014), as well as the unsuccessful Top Kill activities (i.e., injection of heavy drilling mud into the well) where considerable oil and SPM was released from the well into the water column. Given the large volume of oil and sediments released by the failed Top Kills, the density of the Top Kill sediments (as opposed to near-neutral density of marine snow), and the majority of the oil in the footprint of contamination being focused very near the DWHOS wellsite (Valentine et al. 2014; Stout, 2015d; Stout et al. 2015), the Top Kill material likely accounted for the majority of the oil flux to the sediments near the wellsite. Indeed, Stout et al. (2016a) and Stout and Payne (2017) have shown that a large fraction of the sedimented oil close to the wellhead was associated with synthetic drilling mud lost during the blowout or introduced into the oil within the drill pipe during the failed Top Kill operations. The Top Kill operation was not included in the modeling reported herein, and oil sedimentation was only mediated by baseline ambient SPM.

Water quality data were evaluated to estimate baseline total suspended sediment (mineral) concentrations for use in model inputs. In the north-eastern GOM, suspended sediment concentrations are generally very low in offshore waters and the outer shelf areas affected by the DWHOS. Based on a review of the surface SPM distribution in the northern GOM, the mean total suspended sediment concentration in the is 3 mg/L (D'Sa et al. 2007, 2008; Salisbury et al. 2004). See Appendix V, Section 6 for a description of the SPM data set used for modeling the DWHOS spill.

Estimates of organic matter concentrations in the area at the time of the spill were not identified. Therefore, adherence of oil to varying amounts of organic matter was not included in the modeling of the spill. This may result in an underestimated flux of oil to the sediments.

2.2.5 Horizontal and Vertical Dispersion Coefficients

2.2.5.1 Subsurface Oil

For subsurface oil droplet and dissolved spillets, two scales of dispersion are modeled: advective and spreading. Spillets undergo a random walk, along with the transport by currents, as described in Annex A of Volume II. The horizontal and vertical dispersion

coefficients used for the random-walk portion of the advection of subsurface spillet centers are also used for spreading dispersion within subsurface spillets.

Dispersion coefficients used in all locations are as follows.

- Horizontal dispersion coefficients
    - 2 m^2/s in the upper 40 m of the water column (above the pycnocline).
    - 0.1 m^2/s in the water column below 40 m.
- Vertical dispersion coefficients
    - 10 cm^2/s in the upper 40 m of the water column.
    - 0.1 cm^2/s in the water column below 40 m.

These dispersion values are reasonable for offshore waters based on empirical data (Okubo and Ozmidov 1970; Okubo 1971; Csanady 1973 Socolofsky and Jirka 2005), consistent with the various hydrodynamic models used and modeling experience based on dye studies (French et al. 1997; French McCay et al. 2007).

2.2.5.2 Floating Oil

Sharma et al. (2010) used sets of drifters to identify potential transport paths of floating oil resulting from wind, waves, and surface water currents. They calculated drifter dispersion rates when 6 drifters, drogued at 5 m, were deployed in a cluster in early May of 2010. Several drifters were entrained in a southeasterly current; however, two moved to the coast. This caused a rapid separation of the drifters, and inferred a very large effective dispersion rate of 254 m^2/s. This value clearly reflects the action of velocity shear, and is not typical for turbulent dispersion. However, when using current data that do not capture fine scale shear (i.e., that vary at finer resolution than the current data grid), higher effective dispersion rates may be applied. A range of estimates from 10 to 200 m^2/s were explored in sensitivity analyses. Based on comparison to remote sensing data interpreted to depict floating oil (section 4.2.4), the horizontal dispersion coefficient for the random walk transport calculation (randomized mixing) was assumed to be 100 m^2/s for model runs.

2.3 Oil Properties

Annex B of Appendix II describes the bulk oil property inputs needed for modeling, as well as the values and sources of physical-chemical properties used for the modeled pseudo-components. Table 2-3 provides the bulk oil properties of MC252 oil used in the modeling (based on Stout 2015b; sample ID GU2988-A0521-09805).

Table 2-3. Bulk oil properties of MC252 oil.

Physical Parameters	MC252 Oil
Oil Type	Light Crude Oil
Surface tension (mN/m) at 20°C	3.43
Interfacial tension (mN/m) at 20°C	19.63
Pour Point (°C)	-28
Oil density at 30°C (g/cm3)	0.8372
Oil density at 15°C (g/cm3)	0.8483
Oil density at 5°C (g/cm3)	0.8560
Dynamic Viscosity (cP) @ 30°C	4.503
Dynamic Viscosity (cP) @ 15°C	7.145
Dynamic Viscosity (cP) @ 5°C	10.93
Maximum percentage of water in emulsified oil (mousse)	64
Resin Content (weight %)	10.1
Asphaltene Content (weight %)	0.27

The oil's contents of volatile and semi-volatile aliphatics and aromatics (Tables 2-4 and 2-5) were calculated from data provided by Stout (2015a). The 1- to 4-ring aromatics, as well as cyclic hydrocarbons and alkanes that are soluble or semi-soluble are listed in Annex B of Appendix II with their assigned pseudo-component. The sum of AR and AL pseudo-components totals approximately 61% of the whole oil. The remaining 39% is treated as an insoluble and non-volatile "residual" fraction.

Table 2-4. Fractional composition of whole MC252 source oil by pseudo-component group: soluble and semi-soluble components where measured concentrations in the oil were summed.

Code	Hydrocarbon Pseudo-component	Fraction in Oil (g g^{-1} oil)
AR1	BTEX	0.0191
AR2	C3-benzenes	0.00784
AR3	C4-benzenes	0.00467
AR4	Decalins	0.00379
AR5	C0-C2 Naphthalenes	0.00563
AR6	C3-C4 Naphthalenes	0.00243
AR7	Fluorenes & C0-C1 3-ring PAHs	0.00234
AR8	4-ring PAHs & C2-C3 3-ring PAHs	0.00167
AR9	Soluble alkanes	0.133

Table 2-5. Fractional composition of whole MC252 source oil by pseudo-component group: insoluble components where concentrations in the oil were based on boiling curve cuts.

Code	Hydrocarbon Pseudo-component	Fraction in Oil (g g^{-1} oil)
AL1	Aliphatics: BP < 150	0.00692
AL2	Aliphatics: BP 150-180	0.0609
AL3	Aliphatics: BP 180-200 (C11)	0.0343
AL4	Aliphatics: BP 200-230 (C12)	0.0538
AL5	Aliphatics: BP 230-280 (C13-C16)	0.0951
AL6	Aliphatics: BP 280-300 (C17-C18)	0.0363
AL7	Aliphatics: BP 300-350 (C19-C20)	0.0929
AL8	Aliphatics: BP 350-380 (C21-C23)	0.0495
∑ AR#s + ∑ AL#s	Total volatiles and semi-volatiles	0.610

2.4 Oil Hydrocarbon Degradation Rates

Degradation rates for each pseudo-component and compartment are developed and summarized in Annex C of Appendix II. The rates are based on data obtained from literature reviews that included estimates for compounds and/or components of MC252 oil and crude oil generally.

2.5 Shoreline Oil Retention

Retention of oil on a shoreline depends on the shoreline type, width and angle of the shoreline, viscosity of the oil, the tidal amplitude, and the wave energy. Shoreline holding capacities (maximum oil thickness retained on shore) and shore widths potentially oiled that were used for modeling are as described in Section 4.5 of Appendix II.

2.6 Surface Wind Drift

As discussed in Section 4.6 of Appendix II, hydrodynamic models do not resolve all of the transport in the upper centimeters of the ocean, where floating oil is present. Local wind-driven surface currents are calculated within the SIMAP oil fate model based on local wind speed and direction. Surface wind drift of oil has been observed in the field to be 1–6% (average 3–4%) of wind speed, in a direction 0–30° to the right (in the northern hemisphere) of the down-wind direction (ASCE 1996). In restricted or near shore waters with little fetch, or when wind changes directions within a few hours of the time of drift, the angle tends to be near zero. In open waters, the angle develops over time (hours) to be 20º–30º to the right of the downwind direction. A sensitivity study was performed to evaluate these ranges of wind drift speed and angle. In addition, simulations were run using the wind drift model for a fully-developed sea (Youssef 1993, Youssef and Spaulding 1993, 1994) applied to the latitude of the GOM; see Annex A of Appendix II).

2.7 Response Activities

Quantitative measurements of oil volume or mass held by booms and/or mechanically removed are not available. Thus, mechanical cleanup was not included in the model simulations. Inclusion of shoreline cleanup would have no effect on the model results, since in the oil fate model, oil accumulates on shorelines to a maximum capacity (see Annex A of Appendix II) and is not resuspended after stranding. In situ burning and surface applications of dispersants were included in the modeling.

2.7.1 In Situ Burning

Quantitative estimates of oil volume removed by in situ burns were obtained from the Response After-Action Report by Mabile and Allen (2010, also summarized by Lehr et al., 2010). Minimum and maximum burn estimates were provided, and daily totals were developed for model input (Figure 2-5). The mean (midpoint) of the range was used for model runs, except for sensitivity analyses where the range was examined. Time ranges for each burn on each given day were composited into a daily burn time window. Annex A, Section 2, describes the assumptions and summarizes the model inputs for use in SIMAP simulations.

Daily burn volume totals, within the time window of burning each day, were input to the model. The model removes oil mass within each time window up to a maximum daily volume prescribed by the model input. Additionally, the following assumptions were made regarding constraints for floating oil that could be removed by burning in the model.

- Minimum oil thickness: 13 µm (0.0005 inch), based on the thickness threshold for skimming operations by API et al. (2001), since oil was collected by booms for burning
- Maximum wave height: 1 m (API et al. 2001)

If insufficient floating oil volume, meeting the constraints, is available within a specified time window, the model removes only that oil mass floating and available. It is also assumed that the freshest oil was targeted first. Thus, the model removes oil first from the most-recently released surface oil spillet, proceeding to older oil spillets, as needed for the time window until the specified volume is removed or there is no more surface oil.

Oil "removed" by burning is totaled in the mass balance and not tracked further by the model. Burn efficiency was estimated as 90–95% (Mabile and Allen 2010), with the unburned material presumably remaining in the environment. Stout and Payne (2016b) reported that burn residue was collected at the sediment-water interface, indicating that at least some of the unburned material sank to the sea floor.

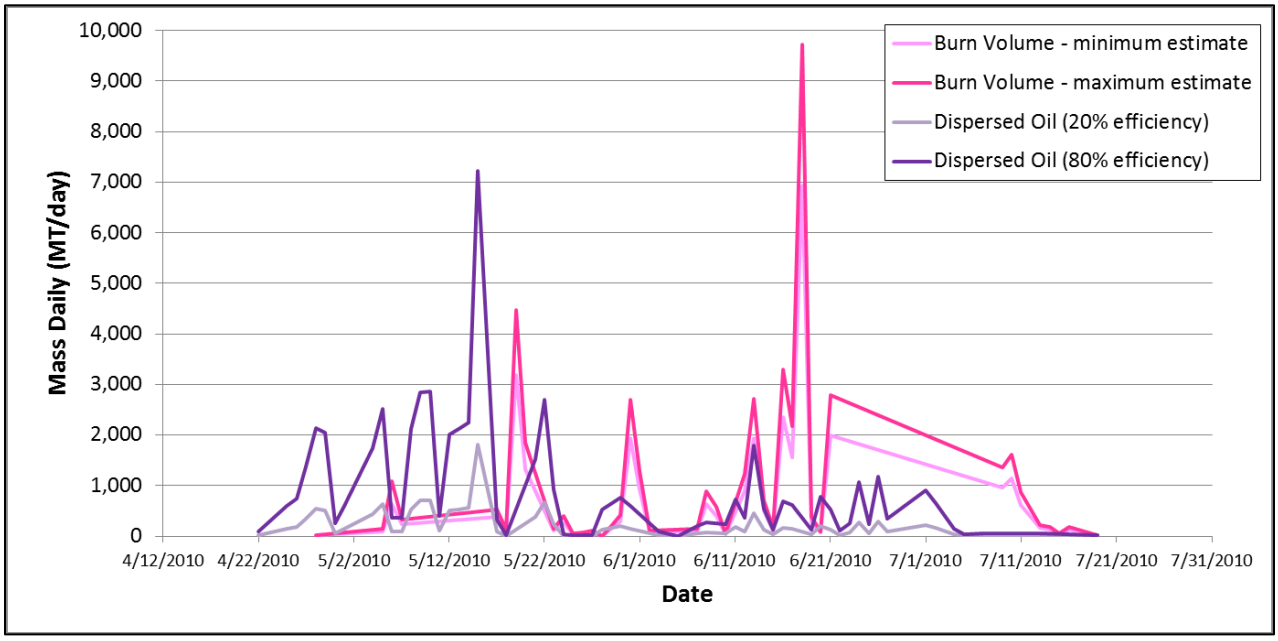

Figure 2-5. Daily burn volumes (translated to MT) and daily estimates of surface oil dispersed.

2.7.2. Surface Applications of Dispersants

Figure 2-6 summarizes the dispersant volumes applied at the water surface and subsea at the oil release points over the period of the spill in 2010 (based on data in Lehr et al. 2010). The subsea dispersant applications are accounted for in the nearfield blowout modeling (see Spaulding et al. 2015 for details).

Aerial and ship-board dispersant applications aimed at floating oil at the water surface may have increased effectiveness of natural dispersion processes by breaking waves. The MC252 oil is easily entrained naturally, and experiments by Belore et al. (2011) demonstrated that dispersant applications likely facilitated entrainment from the water surface.

Daily dispersant application rates were obtained from Response (Annex A, Section 2.2), but effectiveness estimates are not available. The volume of oil treated per dispersant volume applied (i.e., DOR, the dispersant-to-oil ratio) was based on assumptions in Lehr et al. (2010), who assumed that the minimum, median, and maximum ratios were 5, 10 and 20 by weight of oil, not including the water in mousse (i.e., MT/MT). For most model runs (except sensitivity analyses on this input) DOR was assumed 10. The model treated 10 (or 5 or 20) times as much oil as the dispersant volume applied during the daily time window for operations, if sufficient floating oil was present and if environmental conditions were within the constraints described below. The entrainment algorithm determined the fraction of oil dispersed into the water column based on the assumed DOR and resulting interfacial tension (see Annex A of Appendix II, for the description of the entrainment algorithm). Figure A.2.2 in Annex A shows the locations of the daily dispersant operations simulated.

Allowable environmental conditions for dispersant use were based on API et al. (2001) and NOAA (2010):

- Minimum wind speed = 3 knots
- Maximum wind speed = 27 knots
- Minimum water depth for dispersant application = 10m (based on typical government approval practices)

API et al. (2001) recommends oil >13 μm (0.005 inch) be targeted for dispersant applications. Thus, the model input for minimum thickness for dispersant to be assumed effective is 13 μm.

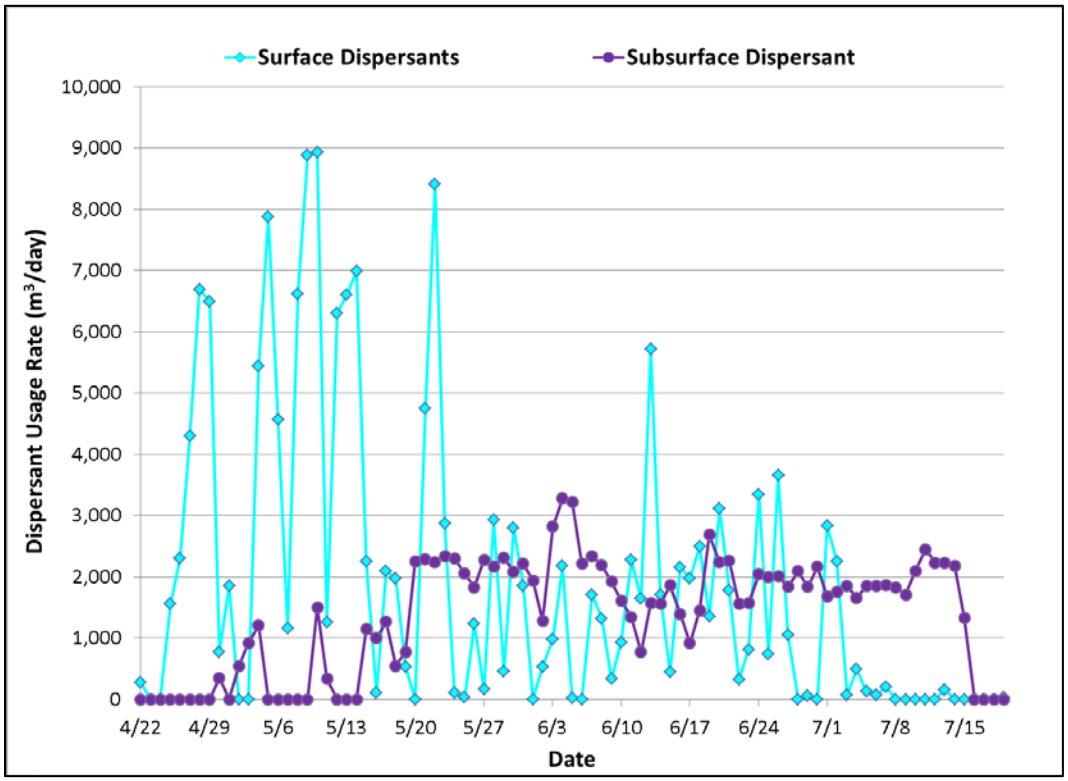

Figure 2-6. Summary of dispersant application rates from April 22 to July 15, 2010.
Data from Lehr et al., 2010.

2.8 Scenario Specifications

2.8.1 Time Line of Events

The release of oil and gas to the water column varied in amount released per day, location, and the amount treated with dispersant throughout the spill event. Early in the spill event, oil and gas was only released from the end of the broken riser. After approximately six days, it was discovered that oil and gas were flowing from multiple locations, the end of the broken riser and from a cluster of holes in the riser, where a kink formed when the rig sunk and the riser collapsed. This division of flow between the riser and kink holes varied over time, with the kink release increasing with time due to the evolution of more kink holes. As the number of holes increased, the larger cross-sectional area of the exit openings allowed more flow through. The kink flow occurred for 34 days, after which time the riser was cut just above the Blowout Preventer (BOP) (i.e., on June 3rd). Thus, from that point on, all oil and gas was released from the cut riser at the wellhead. Throughout the spill event, there were various levels of collection and dispersant treatment. Though the periods of time pre-cut and post-cut was the same (42 days each), the resulting mass of oil released to the

water column during pre-cut and post-cut was 60% and 40%, respectively, based on the analysis by the Flow Rate Technical Group (FRTG) (McNutt et al. 2011).

Table 2-6 summarizes the timeline of events (i.e., collections removing oil from the environment and subsea dispersant applications at the source), consistent with the Phase II Court findings (USDC 2015). See Spaulding et al. (2015) for a detailed discussion of the time line and sources of the information. Oil collection at the release points, i.e., the Riser Insertion Tube (RITT) and the Top Hat, was assumed to not have entered the environment, and is not tracked in the modeling of oil fate. These events are important to what was modeled and have been considered in the evaluation of the model results.

Table 2-6. DWHOS event timeline condensed into broad date intervals indicating release configurations and operations.

Start Date (mm/dd/ yyyy) (HH:MM)	End Date (mm/dd/ yyyy) (HH:MM)	Days	Description	Operational: Collection Rates	Operational: Subsea Dispersant Applications
4/22/2010 10:30	4/28/2010 15:33	6	Leak from end of broken riser only	-	-
4/28/2010 15:33	5/26/2010	28	Release from end of broken riser and kink	RITT collection small volumes, typically <5,000 bbl/day	highly variable use and volume, low effectiveness
5/26/2010	5/29/2010	3	Release from broken riser and kink. Top Kill.	-	-
5/29/2010	6/3/2010 9:05	5	Release from broken riser and kink. Cutting operations.	-	consistent use, variable volumes, low effectiveness
6/3/2010 9:05	6/4/2010	1	Riser flow only, post riser cut	-	-
6/4/2010	6/6/2010	2	Riser flow only, post cut, with Top Hat #4	consistent use, volume ramped up to ~11,000 bbl/day	consistent use, variable large volumes, low effectiveness
6/6/2010	6/13/2010	7	Riser flow only, post cut, with Top Hat #4	consistent use, at ~15,000 bbl oil/day	highly variable volumes, low effectiveness
6/13/2010	7/10/2010 12:35	27	Riser Flow only, post cut, with Top Hat #4	steady, increases to ~22,000 bbl/day	consistent use & volumes, moderate effectiveness
7/10/2010 12:35	7/14/10 17:00	4	Riser Flow only, post cut. Top Hat removed. Operations to set up capping stack.	~8,000 to ~16,000 bbl/day	dispersant volume high, moderate effectiveness

Start Date (mm/dd/yyyy) (HH:MM)	End Date (mm/dd/yyyy) (HH:MM)	Days	Description	Operational: Collection Rates	Operational: Subsea Dispersant Applications
7/14/10 17:00	7/15/2010 14:27	1	Riser Flow only, post cut. Capping stack in place	-	-

2.8.2 Oil Volume Released to the Water Column

The amount of oil released to the environment was assumed to be ~559 thousand metric tons (4.26 million bbl), based on information provided in the FRTG report developed during the Response phase of the spill (McNutt et al. 2011), as summarized in the Oil Budget Calculator (OBC) report, and including consideration of oil recovered at the release site and therefore not released to the environment (Lehr et al. 2010). The DWHOS Phase II Court findings (USDC 2015) were that 4.0 million bbl of oil were released from the reservoir and 3.19 million bbl of oil were discharged to the GOM, a total release to the environment that was 22% less than the OBC estimate used herein. In modeling performed for the NRDA, as described in French McCay et al. (2015, 2016), the OBC estimates of the daily release volumes (April 22–July 15 of 2010) made by the FRTG (McNutt et al. 2011) were proportionately reduced by 22% on each day of release, to match the Court's finding of the total discharge volume to the GOM.

Oil was released in one of two different configurations. The first configuration had varying percentages of the total release from two primary locations:

(1) Before June 3, at the end of the riser (which was lying on the sea floor), and from up to six small holes in the vicinity of a kink that developed in the riser pipe immediately above the BOP, and
(2) After June 3, flow only from the cut riser pipe immediately above the BOP.

Figure 2-7 depicts the total oil release rate as estimated by the FRTG (data from Lehr et al. 2010). Based on the OBC and McNutt et al. (2011), the release rate from the reservoir decreased from just over 60,000 bbl/day at the start of the spill to about 55,000 bbl/day by the time the release stopped. After the riser was cut on June 3 (day 42 of the release), the Top Hat was installed and a portion of the oil released from the well was recovered, accounting for the substantial decrease in the total discharge rate after day 42. The amount recovered was measured by BP and Response on a daily basis. The amount released to the environment was estimated by taking the difference between the amounts released and recovered.

Figure 2-7 shows the release rate from each of the kink holes and the end of the riser before June 3. These estimates were based on observations of the release using remotely operated underwater vehicle (ROV) video and application of the pipeline release model described in Spaulding et al. (2015). The riser release started on April 22, with the kink release beginning on April 28. The discrete stepping of the kink release is a result of the increase in the number of holes at the kink. An in-depth review of the available ROV video imagery indicated that the number of holes at the kink, as well as their sizes, increased with time from 2 beginning on April 28, 2010 to 6 just before the riser was cut. Both releases were present through June 3, at which point the riser pipe was cut above the BOP, thereby eliminating the kink releases.

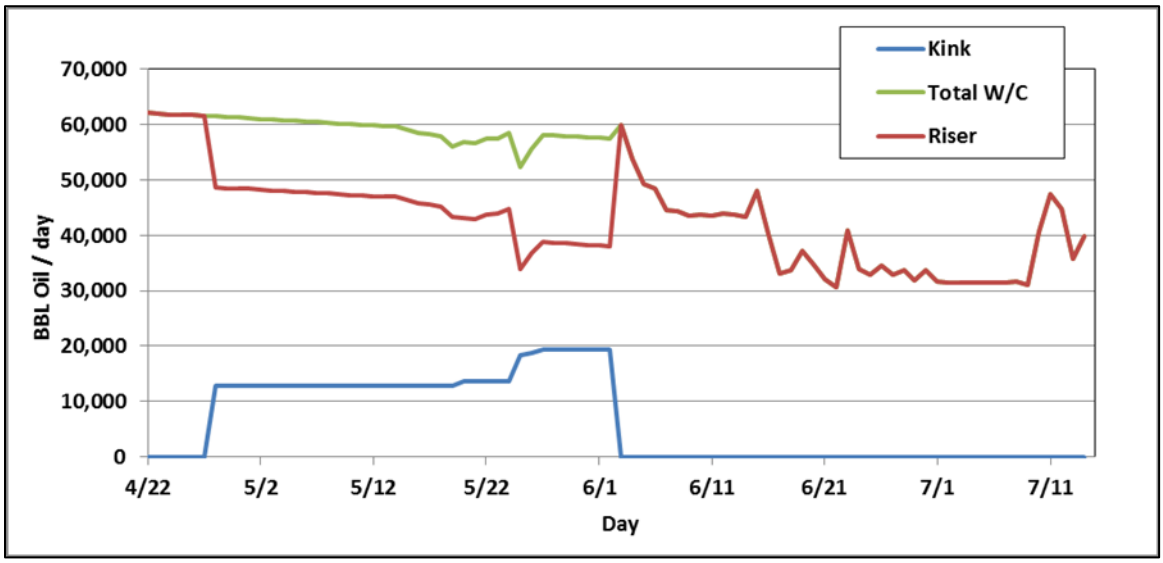

Figure 2-7. Estimated amount of oil released daily to the water column from the riser and kink for the period when both release locations were active, and from the riser after June 3rd (day 42).

2.8.3 Nearfield Modeling of the Blowout

III.2.8.3.1 Trap Height of Buoyant Plume

The main objective of the blowout modeling (Spaulding et al. 2015) was to determine the blowout plume characteristics, namely the trap height of the oil above the release points. At this trap-height depth, the buoyancy of the plume became negligible due to entrainment of seawater and the amount of mass released via out-gassing and individual droplets. A daily estimate of flow from each release type (kink, riser pre-cut and riser post-cut) was made by Spaulding et al. (2015) based on total flow released from the reservoir, the amount collected, and the amount released from the kink holes, using a pipeline release model to determine the flow split between the kink holes and the riser outlet. The riser and kink releases were simulated in the blowout plume model to estimate the resulting trap height

(which is sensitive to oil flow rate) from these locations. The trap heights were then used to initialize the oil release in the (far field) oil fate model (SIMAP).

Figure 2-8 shows the time series of trap heights for plumes from the riser and kink holes, estimated by the blowout model on a daily basis. Table 2-7 summarizes the locations of the release points. The mean trap height of releases for the broken riser is for the average of April 22–June 3, and for the cut riser the mean is for June 4–July 15.

The release from the kink was trapped at about 1,280–1,310m, whereas the (larger flow rate) release from the end of the riser trapped between 1,150m and 1,220m. The lower volume release rate in the court specified volume leads to a reduction in the trap height of about 40 m (12% of the OBC estimate; Spaulding et al. 2015; French McCay et al. 2015). This is within the uncertainty of the analysis of field fluorometry data used to estimate the trap height in the field (Grennan et al. 2015) and the uncertainty of the blowout modeling approach (Spaulding et al. 2015).

The daily trap heights in Figure 2-8 were used as vertical positions for initiating the oil mass released in the SIMAP model runs. Random lateral positioning of the released droplets within a specified radius at the trap height was implemented for initializing the oil droplets within the water column. Droplets were positioned within a 130-m radius from the kink and 180 m radius from the riser. These radii were based on estimates of the dimensions of the nearfield intrusion layer (Spaulding et al. 2015).

Table 2-7. Trap heights and coordinates of release locations used in the spill simulations.

Location	Latitude (N)	Longitude (W)	Water Column Depth (m)	Mean Trap Height (m)
Well	28.73814°	88.3659453°	1,523	(N/A)
Kink-Above BOP	28.73814°	88.3659453°	1,503	1,308
End of Broken Riser	28.74002°	88.3668618°	1,509	1,174
Cut Riser	28.73814°	88.3659453°	1,505	1,200

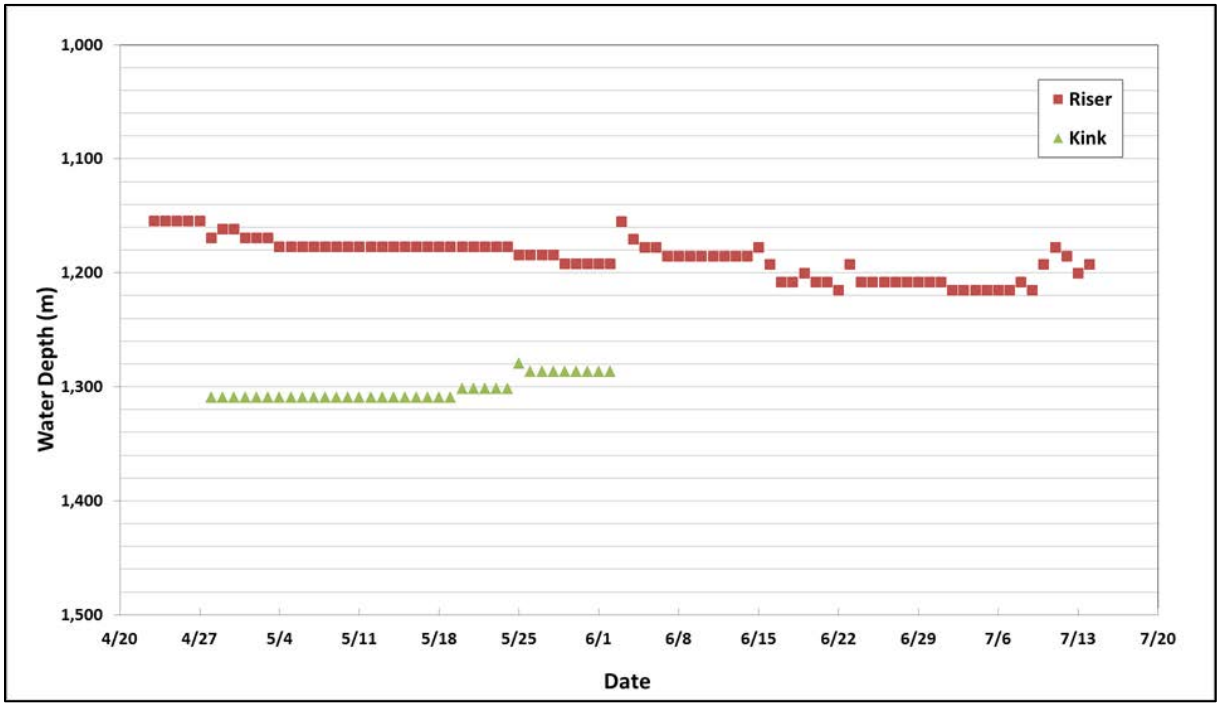

Figure 2-8. Time series of trap heights for plumes from the riser and kink holes estimated by the blowout model.

III.2.8.3.2 Oil Droplet Size Distribution Released to Far-Field Model

The droplet size distribution of the daily oil releases was applied to the daily release rate of oil mass, based on the following. Spaulding et al. (2015) estimated the fraction of the riser release effectively treated by dispersant, based on estimated circumference of the blowout plume treated using in situ videos taken of the release, which was then used to estimate the daily oil volume treated, since the release rate to the water column from the riser was not constant. This oil volume was then used along with the volume of dispersant applied on the same day to calculate the dispersant to oil ratio (DOR). The DOR is used to adjust the oil-water interfacial tension for the fraction treated; this being of significance for calculating the droplet sizes within the fraction treated, as a lowered oil-water interfacial tension with dispersant application allows for the formation of smaller droplets. There were different

DORs and fractions of riser release treated on each day. The DOR increased as a fraction of the oil treated decreased and vice versa, because the dispersant volume was known. Therefore, varying dispersant treatment effectiveness (i.e., fraction treated and thus the DOR) changed the resulting estimate of fraction of oil mass in smaller (dispersed) droplet sizes and the estimated size of these dispersed droplets.

Spaulding et al. (2015) simulated each of three different release types: Riser No Dispersant (RND), Riser Dispersant (RD), and Kink (K) with the droplet size model (varying mainly exit velocity by release type and oil-water interfacial tension) to estimate the resulting droplet size distributions from each source. The droplet size model is described in Spaulding et al. (2015) and Li et al. (2017a). Before April 28, only the RND release type applied; between April 28 and June 3, RND, RD and K release types applied; and after June 3, two release types applied (RND and RD). These sets of droplet size distribution results were combined to generate the far-field model input of the mass of oil released in different droplet sizes, initialized at different locations (end of broken riser, kink, cut riser), and at different heights in the water column (trap height).

Beginning on April 22, 2010 at 10:30AM (local time), oil was released from the end of the riser. Because the initial release was through a large pipe orifice, the oil droplets sizes were large (>800 μm). On April 28, 2010, the riser pipe just above the BOP began to leak at a point where the pipe had been severely kinked during the collapse. Between April 28 and June 3, 2010, the number of holes in the kink area increased from the initial two up to six holes. As the release continued, the holes in the kinked riser also increased in size. Together, they released a large amount of oil and gas that might otherwise have travelled the length of the riser to the severed end of the pipe several hundred meters away. The oil and gas released through the kink holes was under considerable pressure and was forced through fairly small holes, creating high velocity oil and gas jets. The exiting oil and gas mixture was therefore driven by far greater energy than if it had exited from the much larger riser pipe outlet. The increased energy has the effect of shifting the droplet size distribution to smaller sizes, increasing the amount of oil becoming trapped in the lower water column. This changed the overall oil mass balance, reducing the mass surfacing and increasing the amount remaining at depth. (See Spaulding et al. 2015, for further details.)

The analysis of the releases from the riser (pre- or post-cut on June 3) indicates that if all of the oil was effectively treated with dispersant, then the droplet size would range from 20 to 500 μm; if all the oil was untreated the range would be from 1,000 to 10,000 μm. More than 99% of the dispersant treated oil droplets would have diameters, d, ≤ 500 μm, whereas more than 99% of non-treated oil droplets would have d ≥ 1,000 μm. Because the droplets with d ≥ 1,000 μm would surface after a few hours from ~1,500 m, the droplet size

distribution remaining in the water column would be dominated by dispersant-treated oil (Spaulding et al. 2015).

Table 2-8 summarizes the predicted droplet size distributions for the different kink and riser release scenarios examined by Spaulding et al. (2015). The median droplet diameters of the riser flows are significantly larger than those predicted from the kink release, due to the much higher release velocity from the kink relative to the larger diameter riser. These large droplets are expected to ascend in the immediate vicinity of the riser release location due to their large size and buoyancy. For example, a droplet of fresh oil 2,000 μm in diameter rises at a terminal velocity of ~7 cm/s, and travels from a buoyant plume trap depth of 1,100 m to the surface in ~5 hours. In comparison, a droplet of 500 μm, rises at ~1.7 cm/s and takes ~20 hours to reach the surface; a droplet of 200 μm, rises at ~0.4 cm/s and takes ~96 hours to reach the surface; and a droplet of 100 μm, rises at ~0.1 cm/s and takes ~370 hours to reach the surface.

Table 2-8. Predictions of the volume median diameter of droplet size distribution for release scenarios occurring over the period of the spill.

Scenario	Release description	Release opening diameter (cm)	Volume median diameter (VD_{50}, μm)
A	Kink release, Stage I	2.0	328
B	Kink release, Stage II	2.2	356
C	Kink release, Stage III	2.6	361
D	Riser release, end of pipe, prior to kink onset	50	2,260
E	Riser release, end of pipe, split with kink release at stage II	50	2,970
F	Riser release, LMRP, post-cut, without dispersant	25	2,740

The analysis by Spaulding et al. (2015) indicates that during the pre-riser cut time period (before June 3), oil dispersion (formation of smaller droplets) was a result of mechanical processes (e.g., high exit velocities) at the kink holes and, to a more limited extent, dispersant application of low effectiveness (i.e., a small fraction of the release was treated) at the end of the riser. During the post-cut period, oil dispersion appeared to be primarily due to more effective dispersant treatment above the BOP.

Because of the SIMAP oil trajectory and fate model sensitivity to the released droplet size distribution with respect to the overall mass balance and oil constituent concentrations, Spaulding et al. (2015) evaluated four cases of varying Subsea Dispersant Injection (SSDI) assumptions with the dispersant treatment model. One case is the most realistic, based on the analyses, while the others bound the droplet size distributions that could have been released at the trap height.

- Most Realistic (Best) Case: Dispersants were applied based on predictions of the dispersant treatment model. The dispersant treatment model assumptions were that: 1) the dispersant was applied to part of the plume flow from the end of the riser by single wand (8.1% of the oil treated) pre-riser cut (pre-June 3rd) and by trident (30% of the oil treated) post riser cut, 2) the dispersant (contact) effectiveness was 80%, and 3) the DOR was estimated at end of the zone of flow establishment (i.e., a distance 6 times the diameters of the hole or pipe end). (See Spaulding et al. 2015, for further details).
- High Treatment Case: Same as for the best case, except that dispersants were assumed to completely mix in the plume within 6 diameters of the release location and 100% effectiveness is assumed. This assumption of complete mixing is based on visual observations of dispersant application in small-scale experiments performed by SINTEF in their deep-water laboratory test tank (Brandvik et al. 2013). The DOR is calculated on a daily basis using the ratio of dispersant application rate to oil release rate (e.g., 1 part dispersant to 100 parts oil yields DOR = 1:100).
- Low Treatment Case: Same as for the most realistic case, except that dispersants were assumed to completely mix in the plume within 6 diameters of the release location and 50% effectiveness is assumed. The DOR is calculated on a daily basis using the ratio of dispersant application rate to oil release rate, modified by dispersant effectiveness (e.g., 1 part dispersant to 100 parts oil yields DOR = 1:200).
- No Treatment Case: The subsea dispersant applications are assumed ineffective in this case; all the released oil is assumed untreated.

Figure 2-9 shows the DOR assuming all of the riser flow was treated (high treatment case; for the low treatment case the DOR estimates were twice these values), as compared to the DOR for the fraction of the riser plume estimated as treated for the best (most realistic) estimate case, over the entire 84-day period where oil was released to the environment. Table 2-9 summarizes the predicted cumulative droplet size distributions for all four treatment cases. Note the considerable differences in the fraction of oil represented by <500 μm droplets between cases where differing dispersant treatments (including no dispersant effectiveness) are assumed.

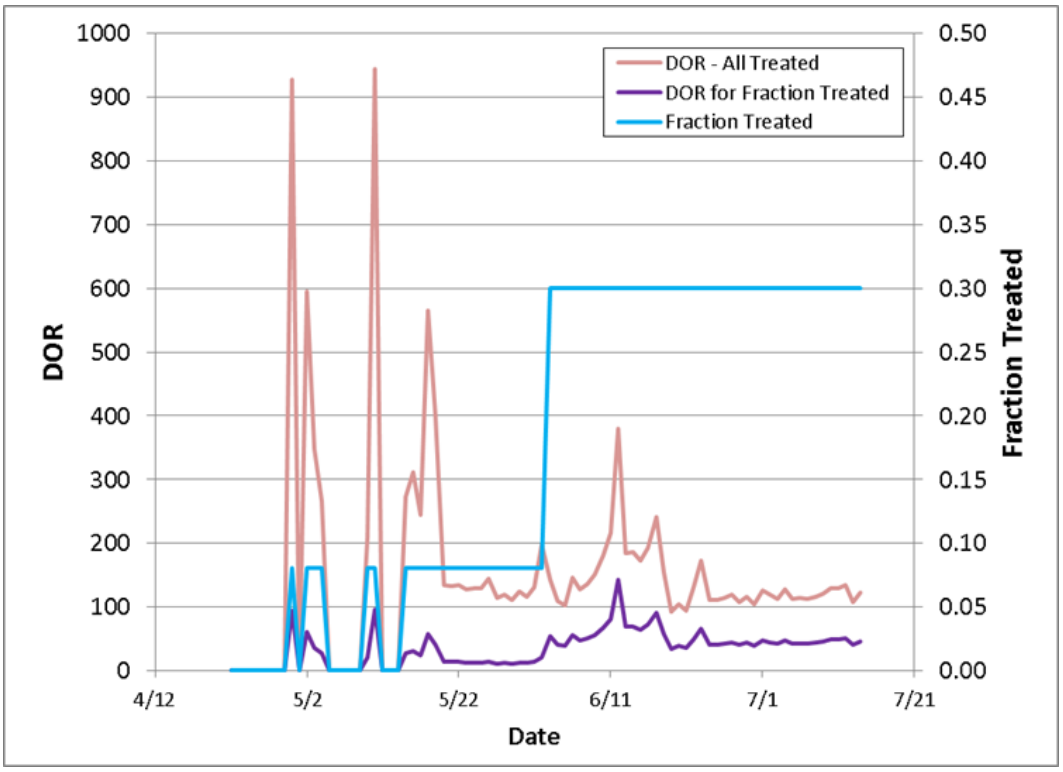

Figure 2-9. DOR assuming the entire riser outflow treated (high treatment case), and fraction treated and associated DOR for the best estimate case.

Table 2-9. Predicted cumulative droplet size distributions over the entire spill for the four treatment cases.

Diameter (µm)	Average Fraction of Daily Release			
	Best Case	Low Case	High Case	No Treatment Case
<100	0.04	0.00	0.01	0.00
<200	0.14	0.04	0.13	0.03
<300	0.20	0.09	0.30	0.07
<400	0.24	0.16	0.44	0.10
<500	0.26	0.25	0.56	0.13
<1,000	0.39	0.58	0.73	0.29
<2,000	0.69	0.82	0.87	0.64
<5,000	0.96	0.98	0.99	0.96
<10,000	1.00	1.00	1.00	1.00

The time histories of mass distribution in the varying droplet size bins are presented in Figures 2-10 to 2-13 for the no treatment, low treatment, high treatment, and the best estimate of dispersant treatment cases, respectively. Figures 2-14 to 2-21 show cumulative

droplet size distributions for the daily release on selected dates. Figure 2-14 depicts droplet size distributions when there were no kink holes and no subsea dispersant applied. Figure 2-15 depicts droplet size distributions when there were two kink holes and on a day when no subsea dispersant was applied. The droplet size distribution shown in Figure 2-16 is from the period when there were two kink holes and subsea dispersant was applied using the wand, which treated only part of the release. Figure 2-17 shows droplet size distributions when there were 4–6 kink holes and subsea dispersant was applied using the wand (which treated only part of the release). Figure 2-18 shows droplet size distributions during the time subsea dispersant was applied using the trident or similar highly effective techniques. The maximum amount of dispersant for any given date was applied at the riser on June 5. Figure 2-19 shows droplet size distributions for a period when subsea dispersant was applied using the trident or similar highly effective techniques. Subsea dispersant volumes applied were about 150–250 bbl/day. Figure 2-20 shows droplet size distributions for the period when subsea dispersant was applied using the trident or similar highly effective techniques and dispersant applied at about 250–300 bbl/day. Figure 2-21 depicts droplet size distributions when subsea dispersant was applied using highly effective techniques, but oil volume flow increased after the Top Hat was removed and the capping stack was being set in place. Subsea dispersant volumes applied were about 350 bbl/day.

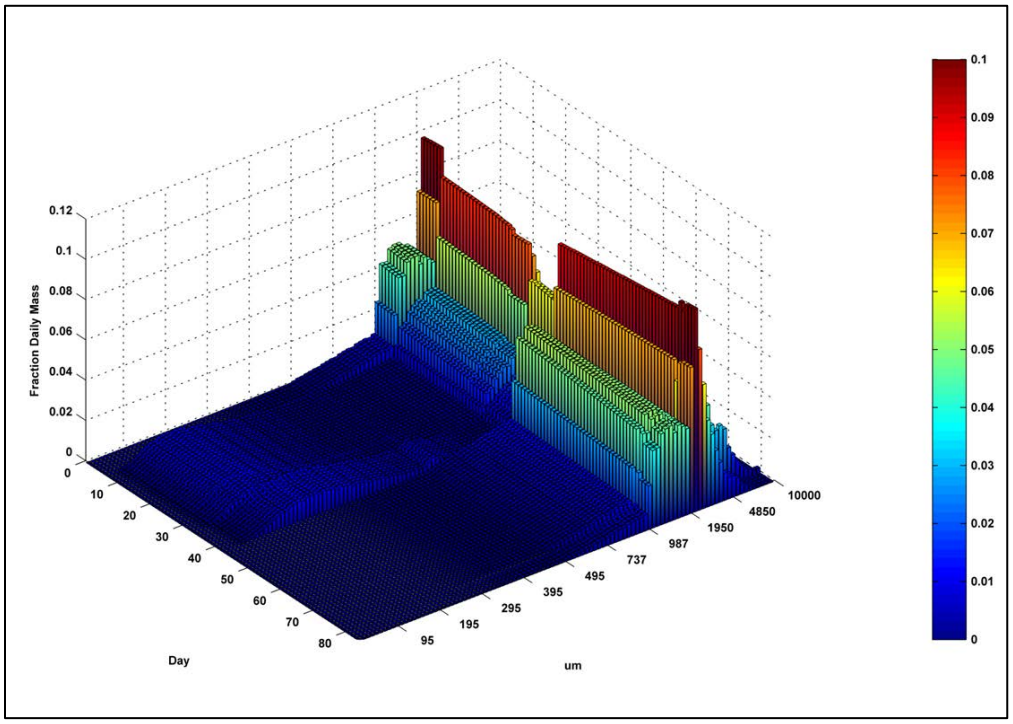

Figure 2-10. Daily distribution of mass in various sizes bins (µm) throughout the release for the no treatment case.

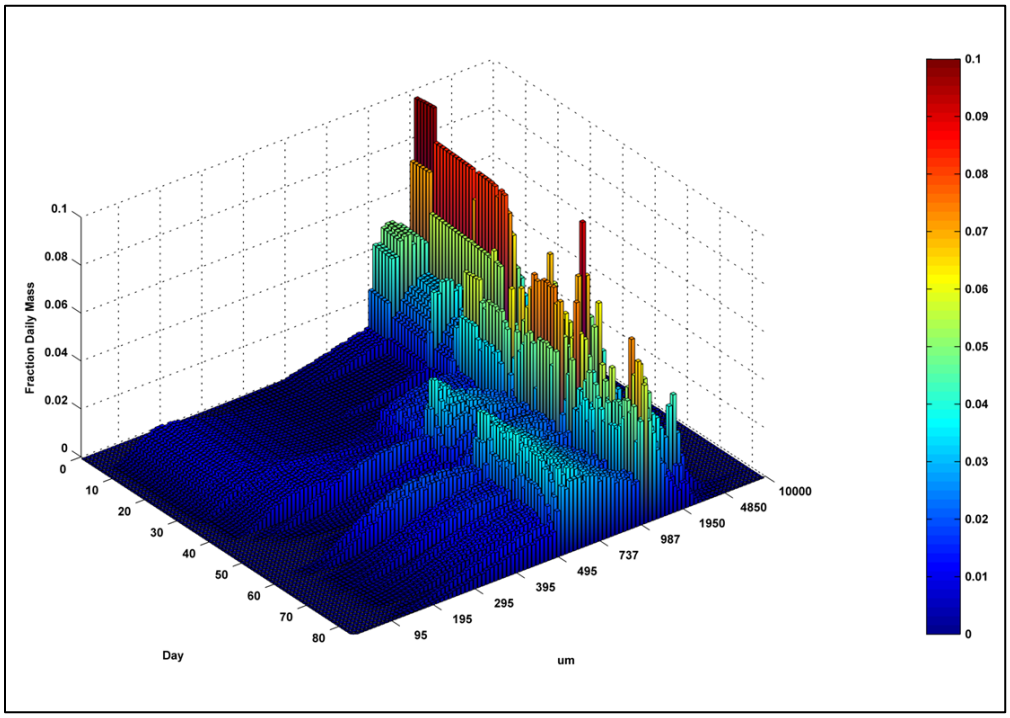

Figure 2-11. Daily distribution of mass in various sizes bins (µm) throughout the release for the low treatment case.

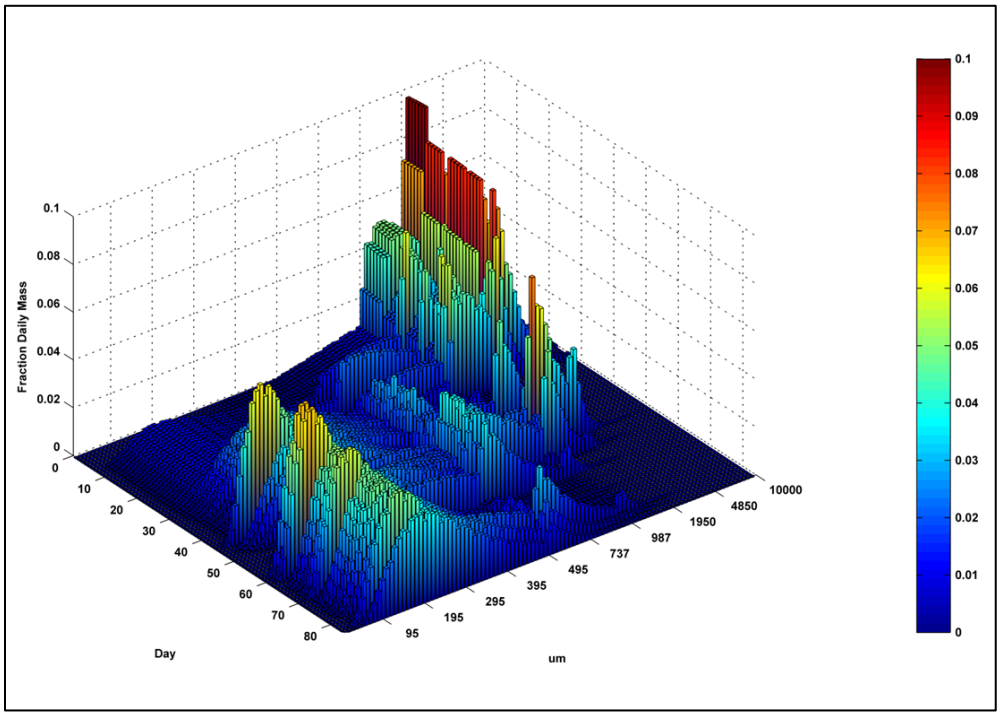

Figure 2-12. Daily distribution of mass in various sizes bins (µm) throughout the release for the high treatment case.

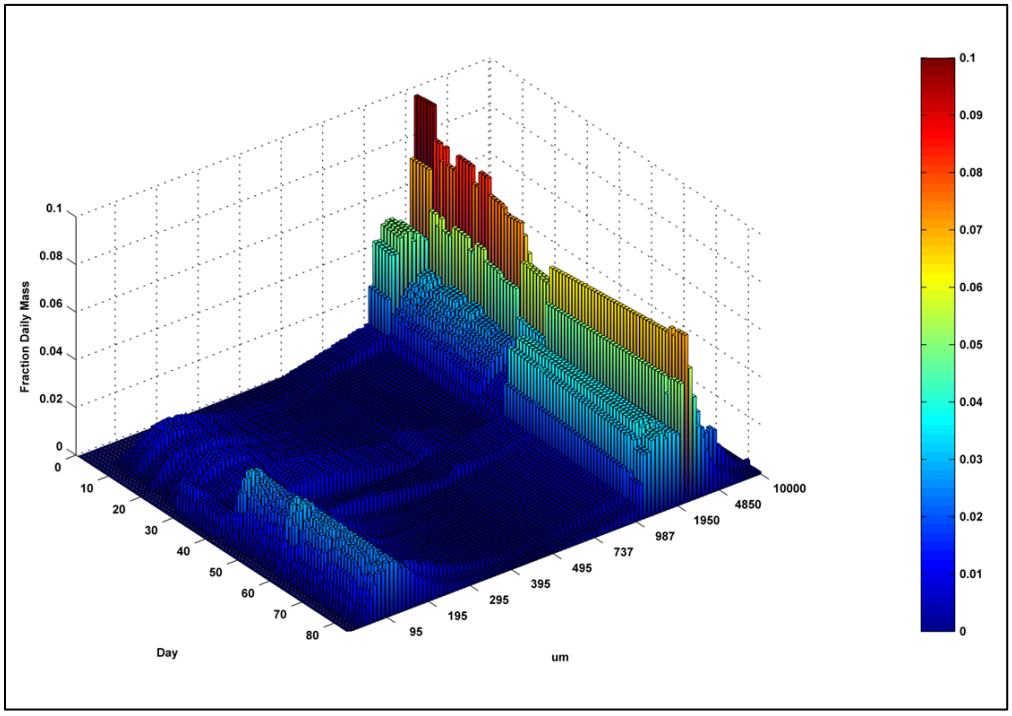

Figure 2-13. Daily distribution of mass in various sizes bins (µm) throughout the release for the best estimate case.

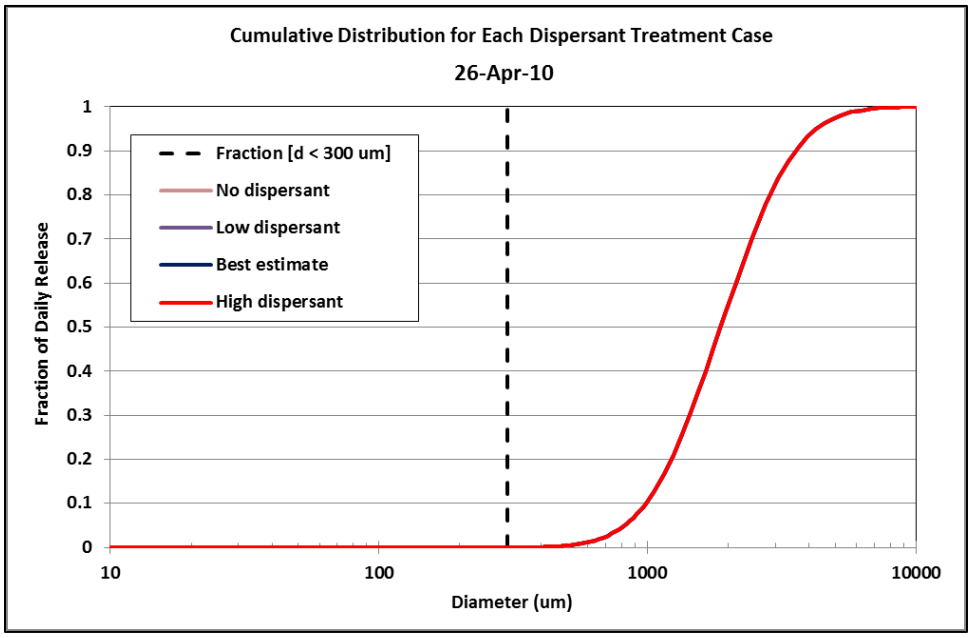

Figure 2-14. Cumulative droplet size distribution for the four treatment cases typical of April 22–28.

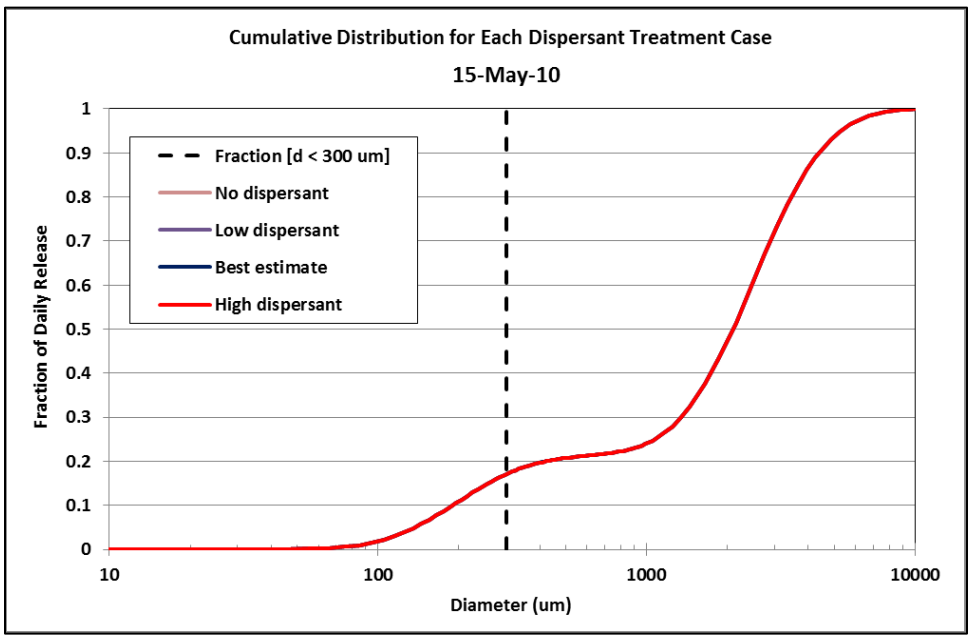

Figure 2-15. Cumulative droplet size distribution for the four treatment cases typical of April 29–May 20.

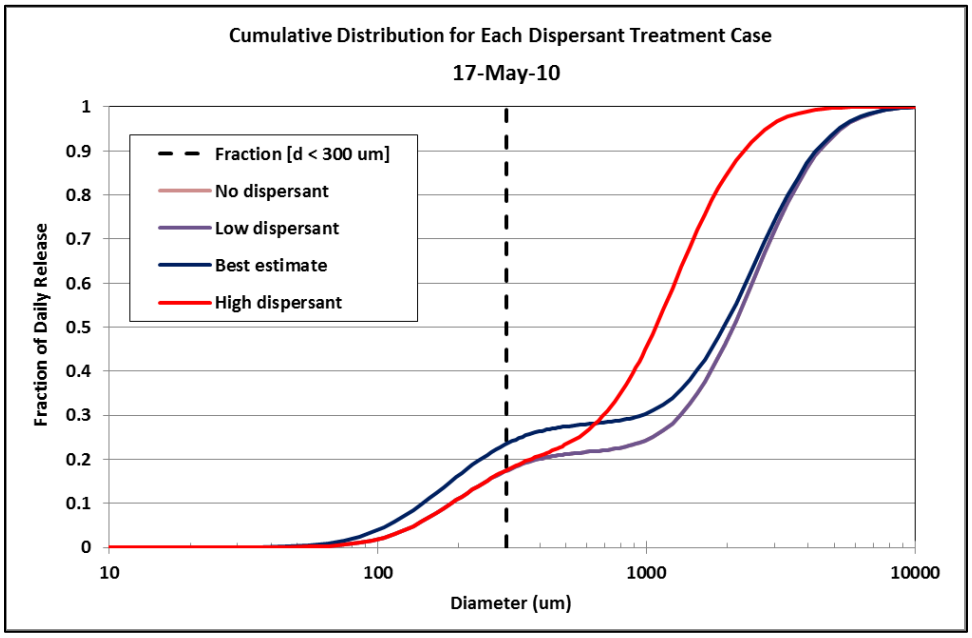

Figure 2-16. Cumulative droplet size distribution for the four treatment cases typical of April 29–May 20.

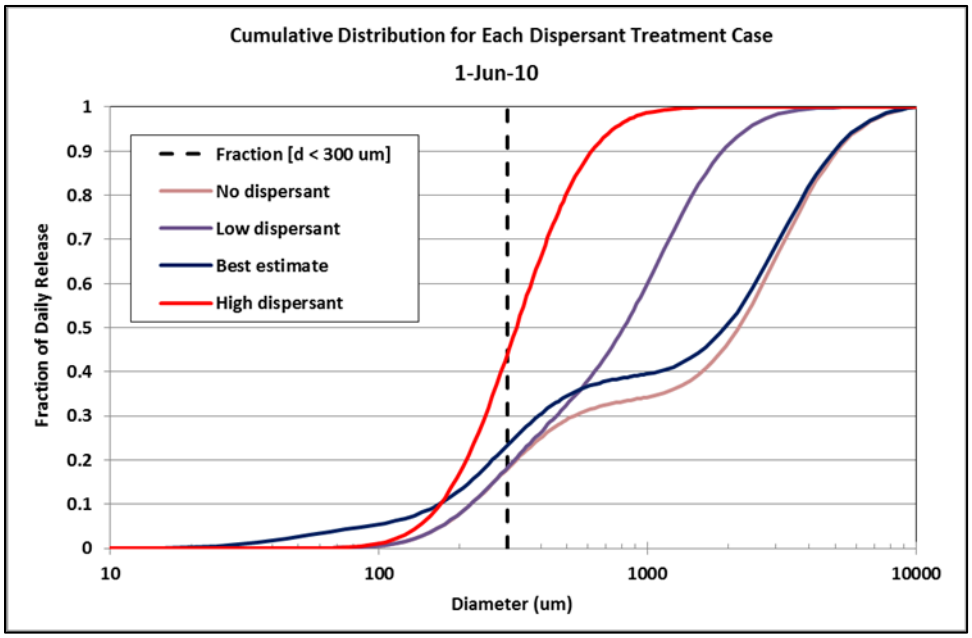

Figure 2-17. Cumulative droplet size distribution for the four treatment cases typical of May 21–June 3.

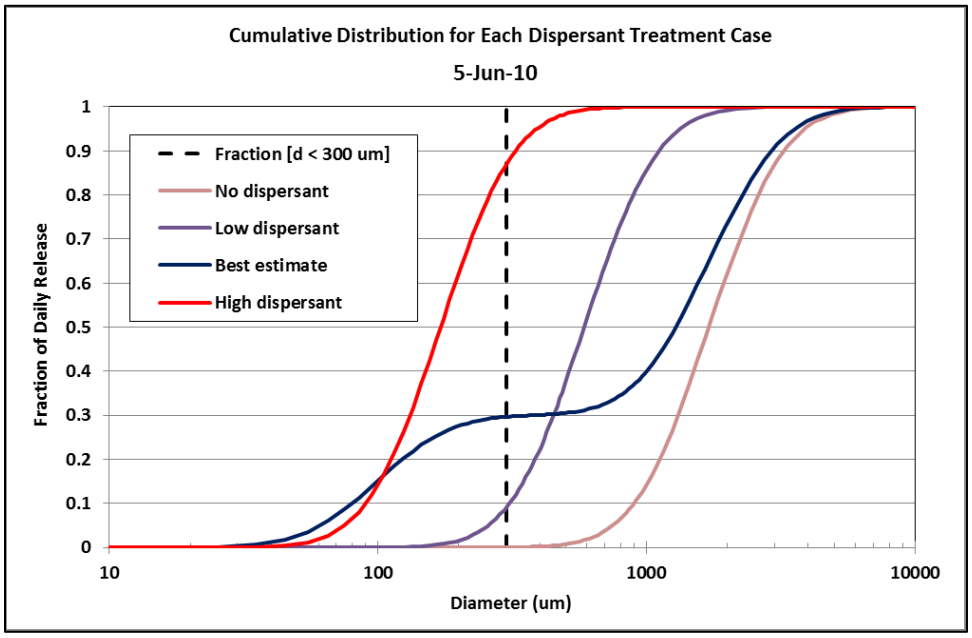

Figure 2-18. Cumulative droplet size distribution for the four treatment cases on June 5 after the riser was cut.

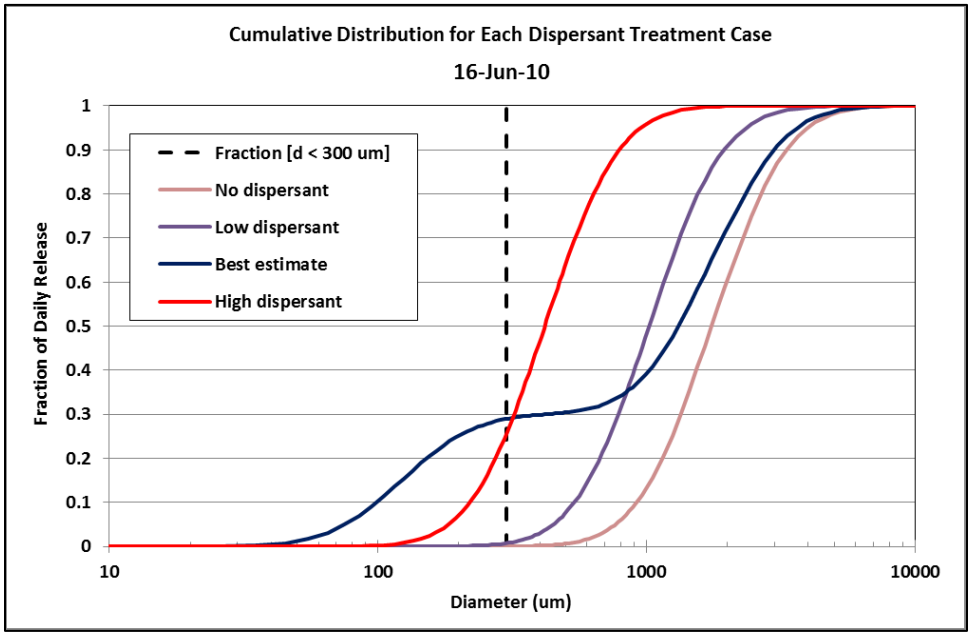

Figure 2-19. Cumulative droplet size distribution for the four treatment cases typical of June 7–June 19 after the riser was cut.

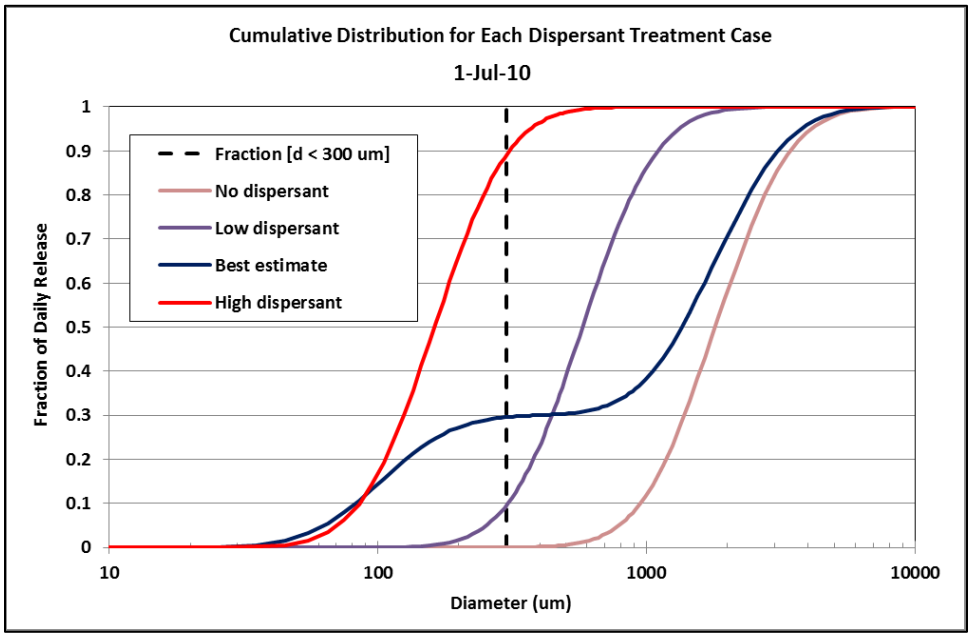

Figure 2-20. Cumulative droplet size distribution for the four treatment cases typical of June 20–July 10 after the riser was cut.

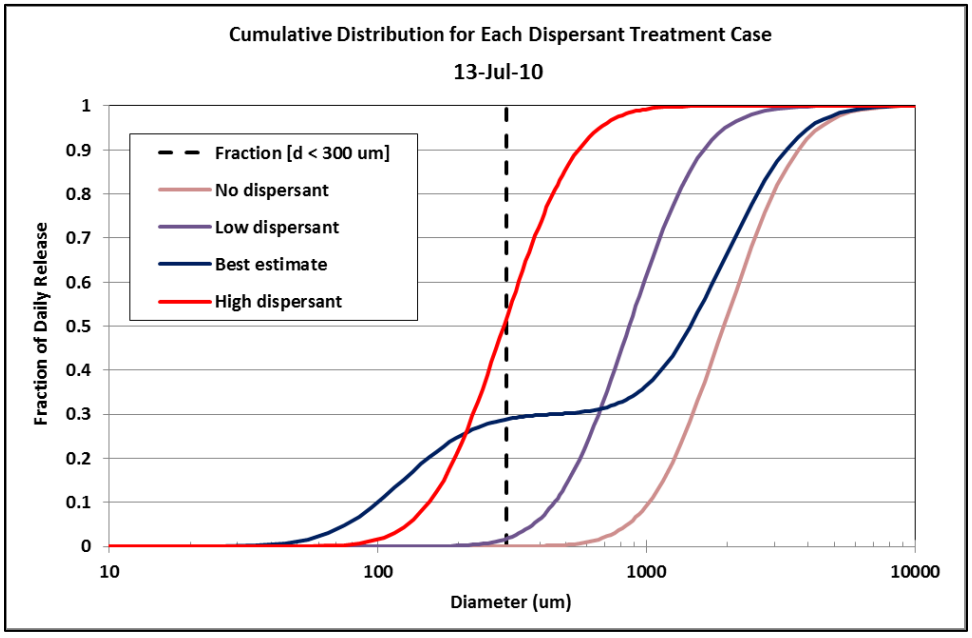

Figure 2-21. Cumulative droplet size distribution for the four treatment cases typical of July 11–July 15.

The results of these analyses serve as inputs to the SIMAP oil fate model to specify the initial oil mass, locations (x,y,z), and the droplet size distributions for the released mass.

The daily release volumes were divided into 48 half-hour increments and incremental masses were tabulated with locations and identified droplet sizes (based on the results summarized in Figures 2-8 to 2-11) to create input files for the far-field model runs.

2.9 Model Parameters

The start of the oil release is simulated as April 22, 2010 at 10:30AM CDT (local time). The release duration is assumed 2015 hours (84 days), i.e., until July 15, 2010 at 14:30 CDT.

Below is a summary of model input parameters defining the model resolution:

- Number of spillets (Lagrangian elements):
    - Surface or subsurface oil: ~100,000
    - Dissolved hydrocarbons: ~400,000
- Simulation Time Step: 0.5 hr
- Length of the Simulation: 161 days (until September 30, 2010)

To obtain sufficient resolution of modeled concentrations, concentration mapping was performed using a 500-m resolution horizontal grid at 20-m depth intervals throughout the water column (0–1400 m). The number of spillets, the time step, and the concentration gridding resolution are all model inputs and are adjusted in accordance with the resolution desired.

3. Observational Data Related to the DWHOS

3.1 Subsurface Oil Concentrations and Sensor Responses

3.1.1 Literature Studies on DWHOS Oil Contamination in Deep Water

Annex B of this Volume II provides a review of DWHOS observational data from offshore waters reported in published literature that were used for model validation, including water column chemistry and oil particle size information. When considered alongside the NRDA QA/QC'd data summarized below, in Annex B and in more detail in the reports by Horn et al. (2015a, b) and Payne and Driskell (2015a, b, c), a more complete understanding of the DWHOS becomes apparent, illustrating the transport, fate, and behavior of the oil and gas mixture that was released into the environment.

After the oil and gas were released from the blowout near the seafloor, the jets and subsequently buoyant plumes of oil and gas mixture quickly rose through the water column, entraining ambient seawater until the plume reached neutral buoyancy due to the balance of densities from the increasing density of the plumes (from entrained colder water along with gas dissolution) and the decreasing density of ambient seawater (i.e., at the trap height). During this fast-rising stage, little oil and gas would escape laterally from the rising plume as the deep-water currents were too weak to compete with the upward movement. Once the trap height of the initially ascending plume was reached, transport of oil and gas and dispersant became more complex, potentially resulting in different pathways due to the variable currents at the trap height as measured by ADCP instrumentation near the wellhead (Spaulding et al. 2015).

By the time the trapped plume reached the trap height, a considerable amount of oil remained entrained within the plume as additional (larger) oil droplets continued to be released into the water column above the plume. Specifically, the smaller droplets remained in the water column for an extended period of time due to their slow rise velocities, while larger droplets rose to the surface on the timescale of hours. The data and studies reviewed herein support the conceptual model that large droplets rose quickly in the immediate vicinity of the leaking wellhead, forming surface oil slicks in a relatively confined area near the wellhead (Ryerson et al. 2012). Intermediate-sized droplets extended further afield in the mid water column as they continued to rise through the water column, and a number of small droplets remained suspended within the plume in the deep-water column intrusion layer.

Hydrocarbons were repeatedly detected in the deep-water intrusion layer plume. Camilli et al. (2010) confirmed a large plume at ~1,000- to 1,200-m depth and in some areas >2km wide at ~ 4 km from the leak source during 23–27 June 2010. Their Sentry's methane *m/z* signal at 35km from the source was only 53% less than that at 5.8km, suggesting that the

plume extended considerably beyond the 35km survey bound at that time. Gas chromatography (GC) analysis focused on mono-aromatic hydrocarbons confirmed the presence of BTEX (50 µg/L) within the plume at 16 km downrange from the wellhead, suggesting a mechanism existed for direct hydrocarbon transfer (i.e., dissolution) within the deep plume.

The larger droplets continued rising to the upper layer and the surface, in a volume described as a rising cone (e.g., Ryerson et al. 2011; 2012; Spier et al. 2013), due to the buoyancy of larger droplets relative to the ambient seawater. Due to ADCP-documented current shear and varying rise rates for different diameter droplets, "plumes" of rising oil droplets clearly would have followed different trajectories during their ascent toward the surface.

In addition, while rising in the cone, the intermediate-sized droplets lost some of their relative buoyancy due to weathering (dissolution and degradation of the lighter hydrocarbons, fully-weathered oil having a density of >920 kg/m^3 versus ~856 kg/m^3 for fresh oil at 5^o C; Stout 2015a), as well as potentially combining with SPM in the water column. Meanwhile, the ambient current higher in the upper water column is increasingly stronger than in deep water (Hyun and He 2010), possibly causing separation of these intermediate-sized droplets such that they left the cone and formed "multiple plumes" of slowly rising droplets in the upper layers mimicking the deep-water plume.

Fluorescence anomalies (peaks) and water column hydrocarbon chemistry data (Spier et al. 2013, Camilli et al. 2010, Valentine et al. 2010, as well as NRDA data; Annex B) show relatively high concentrations of hydrocarbons in finite "clouds" of particulate- and dissolved-phase oil at various depths above the trap height of ~1,100–1,200 m (i.e., the deep plume). This phenomenon is in agreement with the theoretical prediction of a multiphase flow plume model (Socolofsky et al. 2011), although the mechanism proposed by these authors differs from the model of rising independent droplets, and the possibility that some of the oil droplets alone, or in combination with SPM, marine snow, or attached bacteria, became neutrally buoyant. If multiphase flow plumes occurred, one would expect similar fresh-oil chemistry signatures at the multiple depths, as opposed to more weathered oil signatures higher in the water column. With oil droplets rising through currents that are highly variable in direction vertically and over time, those shallower peaks (i.e., plumes or discrete clouds of oil droplets) may reflect different oil released at different times. We have not identified a vertical profile of samples containing similar fresh-oil chemistry signatures at the deep plume trap height and shallower depths. Instead, there is clear evidence of dissolution weathering as the oil roses through the water column. As a caveat, however, safety constraints precluded collecting sample profiles within 1–2 km of the release point. Samples taken from stations with vertical profiles having peaks at

multiple depths further from the wellhead show complex and differing chemistry (Payne and Driskell 2015a,b,c; Horn et al. 2015b).

Camilli et al. (2010) identified a "more diffuse plume" existing between 50- and 500-m depth in addition to the deep-water plume, based on their mass spectrometric and fluorescence data. Brown et al. (2011) and Boehm et al. (2012) have described chemistry results from the DWHOS spill response. Spier et al. (2013) compared hydrocarbon concentrations in two broad regions, indicating that Region 1 (i.e., the deep-water intrusion layer plume plus the confined rising cone) had the highest concentrations of hydrocarbons, whereas Region 2 (i.e., the rest of the water column of 45 km radius surrounding the wellhead) also contained substantial concentrations of hydrocarbons, mainly at shallower depths of 25 m, 265 m, and 865 m. After Top Hat #4 became operational (i.e., after June 3, post riser cut), both the sample concentrations and the percentage of detectable results decreased for the 865 and 1,175 m plumes. In addition, there was a significant increase in the frequency of detections and sample concentrations with high dispersant indicator concentrations typically associated with less water-soluble compounds, including di- and poly-cyclic aromatics, alkylated aromatics, and alkanes >C8, which is consistent with wider dispersion of reduced oil droplet sizes with application of subsea dispersants (Chan et al. 2014).

Changes in chemical composition with depth also support the preceding description of the transport of dissolved compounds, dispersed oil, and larger droplets. Most water soluble compounds such as benzene, alkylated mono-aromatics, and soluble C5–C10 alkanes were enriched in the deep plume (Payne and Driskell, 2015a). Less water soluble compounds were present both in the deep water plumes and in the upper water column: C13–C22 PAHs and C11–C22 alkanes were found at 1,175 m and 865 m, as well as even deeper water and near the surface; C23–C40 alkanes were found at 1175 m and 265 m, in surface waters, and also at lower concentrations in the 865 m plume (see Horn et al. 2015b, for details). These vertical changes in measured chemical composition, as well as the detailed forensic analyses by Payne and Driskell (2015a, b), indicate that dissolved hydrocarbons and (likely the smallest) droplets were concentrated in the intrusion layer plume.

Chemistry changes over the time of the release were also noted. Microbial community shift was reported by Dubinsky et al. (2013). Coincident with the date where partial capture at the wellhead began (i.e., after June 3), the plume microbial community structure changed significantly. The dominant species changed from alkane-degraders to aromatics-degraders, which was associated with a sharp decline in aliphatic hydrocarbons, and an increase in the relative amount of BTEX and other soluble hydrocarbons in the plume. However, the chemistry sampling was less focused on the area near the wellhead after June 3rd, which may have biased the average concentrations of aliphatic and soluble aromatic

hydrocarbons, as well as the characterization of the microbial communities, towards the observed patterns.

Water column dispersant chemistry data are reviewed in Annex B of this Volume II. For instance, Kujawinski et al. (2011) reported that the dispersant constituent dioctyl sodium sulfosuccinate (DOSS) was in general sequestered in deep water hydrocarbon plumes at 1,000–1,200 m water depth; although, in Cast 07 of their study, DOSS occurred at higher concentrations at shallower depths (850–900m), where it did NOT correlate with peaks in fluorescence or methane concentration. However, DOSS is an ingredient of cleaning products used during the sampling; thus, some observations of DOSS may be the result of contamination from cleaning the sampling gear. On the other hand, DOSS was frequently observed in deep water samples concurrent with fluorescence peaks, suggesting dispersant was associated with trapped oil droplets. Based solely on dispersant indicators, fluorescence and DO features, the presence of the deep plume was detected 412 km from the wellhead. Payne and Driskell (2015c) documented that dispersant indicators, measured for the first time in field-collected, particulate-phase oil samples at depth, demonstrate the effectiveness of dispersant injections at the wellhead. In addition, they found that dispersant application at depth resulted in significantly enhanced dissolution of lower-and intermediate-molecular weight PAH contributing to enhanced bioavailability to both benthic and pelagic organisms.

Valentine et al. (2010) focused on gas distribution and fate in the water column. They found that propane, ethane, and methane were most abundant at depths greater than 799 m and formed plume structures with dissolved concentrations as high as 8 μM, 16 μM, and 180 μM for the three gases, respectively. Concentrations were orders of magnitude lower at shallower depths. The persistent plume at 1,000- to 1,200-m depth was located to the southwest of the spill site, consistent with other reports (Camilli et al. 2010; Hazen et al. 2010). Separate plumes were also identified by Valentine et al. (2010) at similar depths to the north and to the east. A distinctive shallower plume was observed at 800- to 1000-m depth located to the east. Spier et al. (2013) calculated frequencies in each of 8 cardinal directions of detectable hydrocarbon concentrations in samples taken at various depths and within 45 km of the wellhead, finding the highest frequency of detectable results to the southwest, but also detections in the other directions. These findings, as well as other data sets compiled by the NRDA program, suggest that multiple plumes moved in varying and sometimes opposite directions, presumably originated at different times and indicative of complex current patterns in the area before sampling.

Dissolved oxygen profiles are shown and discussed in Grennan et al. (2015). Propane and ethane were identified by Valentine et al. (2010) as the primary drivers of microbial respiration, accounting for up to 70% of the observed oxygen depletion in fresh plumes.

The sum of these values, ~1.5 × 10^{12} g of O_2, provides an estimate of the maximum integrated deep-water O_2 anomaly expected from this event, with ~15% of the oxygen loss occurring in fresh plumes from respiration of propane and ethane, and ~two-thirds of the ultimate microbial productivity in deep plumes arising from metabolism of natural gases. The remaining oxygen loss would have been due to oil hydrocarbon degradation.

Davis and Loomis (2014) made measurements of the oil droplet size distribution using a Holocam during the M/V *Jack Fitz* (JF) 3 cruise. The average volume median droplet diameter from the JF3 cruise was 128 μm, with values ranging from 86 to 176 μm. Thus, the Holocam data provides evidence of small (volume mean diameter <300 μm) chemically-dispersed oil droplets in deep water and intermediate waters. Further discussions of the Holocam and other particle size data are in Annex B of this Volume II and in Li et al. (2015, 2017a).

Model simulations employing the well-known Stoke's Law (according to which rise rate increases with droplet diameter) provide additional evidence for the separation of small droplets (in the intrusion layer) from intermediate and large droplets (slowly or rapidly rising to the surface, respectively). For example, sensitivity analyses by North et al. (2011, 2015) showed that droplets with diameters of 10–50 μm would form distinct subsurface plumes that would be transported horizontally and remain in the subsurface for >1 month. Droplets with diameters ≥90 μm would rise more rapidly to the surface. Assumptions in this study included complete dispersant treatment of all released oil, assuming unlimited dispersant volume and complete mixing with the oil, corresponding to a DOR of 1:50 to 1:25. However, during the actual DWHOS spill response, the subsurface dispersant application volume varied along with oil flow rates, such that on average the actual DOR was only about 1:186 during the riser release pre-cut period (15 May–02 June 2010) and approximately 1:140 for the post-cut BOP riser flow period after 03 June 2010. Therefore, the actual oil mass of droplets d≤50 μm would have been much lower than those presented in North et al. (2011, 2015), and the droplet size distribution would have included larger droplet diameters.

The Paris et al. (2012) estimate of droplet size distribution is based on the assumption of a single size mode in the range between 20 and 100 μm. A similar approach was conducted in their follow-up work (Lindo-Atichati et al. 2014; Aman et al., 2013, 2015). However, their prediction of very small untreated oil droplet sizes (< 100 μm) is questionable and unlikely close to the DWHOS blowout release conditions because of the unrepresentative long period of high turbulence used in the laboratory experiments they depended upon for their theoretical droplet size distribution. Indeed, droplets of <100 μm have such slow rise velocities that it would require more than two weeks (unweathered, oil density 840 kg/m^3) to two months (fully weathered, oil density >920 kg/m^3) for the droplets to rise from the

trap height of the intrusion layer (~ 1200 m deep) to the surface. This is in conflict with observed field data (e.g., Ryerson et al. 2011; Ryerson et al. 2012; Reddy et al 2011; Spier et al. 2013), which showed that a significant amount of oil reached the surface within a relatively short time (3–10 h), constraining the (untreated oil) droplet diameters to include a large fraction in the range of 1–10 mm. Adams et al. (2013) commented on their droplet size assumptions, noting that the distribution of untreated oil droplets would likely fall in the 1–10 mm range, as opposed to their assumed diameters of <100 μm.

3.1.2 Summary of Water Column Chemistry and Sensor Data

During the DWHOS blowout and resulting spill, a variety of environmental data were collected by Response, academic, and NRDA sampling aboard numerous ships. Discrete surface and water column samples were collected, sub-sampled, and analyzed from various vessels using NRDA protocols. Though similar sampling protocols were followed, each vessel had slightly different objectives and sampling equipment. In addition to the collected chemical and forensic data, concurrent and continuous measurements of dissolved oxygen and UV fluorescence were recorded.

Because of the QA/QC procedures used to verify the chemistry data in the NRDA program, the NRDA data are used in this study for comparison with model results. A detailed description of the NRDA chemistry data used for validating the model may be found in Horn et al. (2015a,b). A detailed description of forensic findings may be found in reports by Payne and Driskell (2015a,b,c). Physical findings are described in Grennan et al. (2015). Summary figures and discussion are in Annex B of this Volume II.

Considerable spatial heterogeneity was evident in the distribution of hydrocarbons at various depths and as a function of distance from the wellhead. These resulted from variations in the oil release rate and subsea dispersant applications over time (changing droplet size distributions of the oil over time, see Section 2.8), spatially- and temporally-varying currents (both horizontally and vertically), dissolution, dispersion, and degradation of hydrocarbon constituents, as well as irregularly positioned sampling stations and different sampled depths. The multiple plumes observed moving in opposing directions presumably originated at different times, and indicated the complex current patterns in the area before sampling.

The spatial and temporal patterns of chemical sampling events may have partly driven the observed trends discussed below and in Annex B, and they do not lend themselves to decisively determining the complete distribution of hydrocarbons throughout the GOM. The large gaps between sampling locations in space and time render much uncertainty for any interpolation of the results in this dynamic environment. Furthermore, the sampling efforts to depict hydrocarbon distributions throughout the water column may be

complicated by the unavoidable heterogeneity within the water column. For these reasons, sampling gaps in space and time can be quite difficult to interpret conclusively as evidence of either the presence or absence of oil in regions not sampled. Sparse sampling requires systematic compiling and synthesis of all available field data, in combination with modeling analyses, in order to expand the scope of our understanding of spill impact.

Hydrocarbon concentrations, fluorescence, and dissolved oxygen varied at several scales ranging from factors to orders-of-magnitude in both space and time. Based on the analysis of the water column chemical and physical data, as well as the consideration of major events during response, four distinct periods of time are identifiable during the spill period in 2010. These are described as separate Observable Chemistry Regimes (OCR):

- OCR 1: Before Top Kill operations (Apr 20 to May 26)
- OCR 2: Top kill, riser-cutting, and initial Top Hat operations (May 26 to June 6)
- OCR 3: Post-cut and collection (June 6 to July 15)
- OCR 4: Post-cap (after July 15) phase

Sampling of the active release of oil and gas during the three phases (OCR 1–3) was focused around the wellhead (<20 km), while more extensive and broad-scale sampling into the far-field (focused to the south and southwest) did not commence until after the well shut-in was completed (OCR 4). (See Figures B.2-3 to B.2-7 in Annex B of this Volume II.) In-water concentrations remained elevated during the blowout and the released hydrocarbons began to dissipate just after the well was contained and eventually capped.

In April and May, oil was released from the broken riser (at 1,509 m deep) and from holes that developed at the kink in the riser pipe (at 1,503 m deep). The fluorescence and DO anomalies, chemical concentrations, and blowout models (Socolofsky et al. 2011; Spaulding et al. 2015) indicate that a considerable portion of the released oil rose from the depth of release to several hundred meters above the release depth as part of the buoyant plume. Several times during May 26–28, the spill responders attempted to fill the riser pipe with heavy drilling mud and bridging material, but the procedures did not stop the release and the mud and "junk" were forced out of the riser. Relatively high hydrocarbon concentrations and fluorescence anomalies were observed during this period. During June 1-3, while the riser pipe was being cut, oil flowed freely from the riser, and this is evident in the data as elevated fluorescence peaks and hydrocarbon concentrations between 1,000 and 1,300m compared to periods prior to and after this event. In OCR 3, oil was released from the BOP at a depth of 1,506 m from the opening of the Top Hat oil recovery installation or the gap between the Top Hat and the BOP. During OCR 4, after the release

was stopped on July 15, in-water hydrocarbon concentrations decreased with increasing time and space.

As may be seen in summary figures in Annex B, the maximum hydrocarbon and dispersant concentrations occurred at the surface (<40 m) and at depths between roughly 1,100 and 1,300 m deep (Figure B.2-8 and Figure B.2-10). The subsurface maximum in hydrocarbon and dispersant concentrations was the result of the high-energy discharge of oil from the kink and riser. Small droplets of oil were produced under high-pressure flows and made even smaller with the application of dispersant (Spaulding et al. 2015). With slow rise rates, these small droplets were trapped below 1,100 m, where both whole oil and dissolved phase hydrocarbons were found alongside dispersants. Elevated dispersant concentrations were identified between 1,000–1,300 m near the wellhead and between 1,100–1,200 m to out beyond 150 km.

Forensically-identified MC252 oil was commonly observed radially within roughly 50 km of the wellhead (Figure B.2-8 and Figure B.2-10 in Annex B). In addition, an extensive deep-water oil plume between 1000 and 1,400 m was evident advecting predominantly to the southwest with occasional shallower lenses (Payne and Driskell, 2015a). Effects of dispersant treatments were seen in the forensic profiles of both subsurface and surface samples, indicative of enhanced weathering including increased dissolution, implying dispersants were effective in reducing droplet sizes at depth and enhancing entrainment at the surface (Payne and Driskell, 2015c). Near surface samples showed evidence of substantial dissolution weathering as oil droplets rose through the water column (Payne and Driskell, 2015a). See Payne and Driskell (2015a) for a full description of forensically identified MC252 oil in subsurface water samples, including as particulate- and dissolved-phase hydrocarbons.

Elevated hydrocarbon concentrations at depth were observed in each of the investigated groupings ranging from BTEX (AR1) through to the soluble alkanes (AR9). The highest concentrations at depth were of the BTEX group and soluble alkanes (Figure B.2-8 in Annex B). When considered together, the total soluble compounds, the total investigated compounds, and PAH groups (AR 5 to 8) all had highest observed concentrations between 1,000–1,300 m. The highest measurements of total investigated compounds in the deep plume were >100–700 µg/L, with concentrations up to ~80 µg/L between 200–1,000 m. When considered individually, soluble alkanes (AR9) typically had the highest concentrations between 1,000–1,300 m with values of >100–400 µg/L, while BTEX (AR1) were typically >100–200 µg/L, and PAH50 were typically <120 µg/L.

Though most attention has been focused on hydrocarbon concentrations in near surface waters and the region between 1,000–1,300 m, it is important to note that elevated

concentrations in excess of the method detection limits were identified throughout the water column beyond 150 km (groups AR1 and AR9 in Figure B.2-9 in Annex B). However, sampling in the depth range between 100–1,000 m was much more sporadic than at the surface. The highest concentrations at depth in this region were for the BTEX group and soluble alkanes (Figure B.2-11, Annex B). The spatial extent in these intermediate waters is slightly greater proximal to the wellhead, with highest concentrations observed typically within 25 km of the wellhead.

There were consistently observed fluorescence anomalies, as relative high values or "peaks" at depths between approximately 1,000–1,300 m. Figures B.1-3 to B.1-6 in Annex B summarize the observed fluorescence anomalies. Maximum anomalies occurred between roughly 1,100–1,200 m. The highest values were observed near the wellhead; the anomalies decreased as distance from the wellhead increased. Anomalies of high fluorescence values at depths of 1,000–1,300 m were typically associated with elevated hydrocarbon concentrations in the water column, when water samples were collected concurrently with fluorescence measurements. These fluorescence peaks were observed mainly to the southwest of the wellhead. Although maximum fluorescence peaks were identified within a narrow range at depth, significantly elevated fluorescence values were noted throughout large portions of profiles. Peak fluorescence values at depth typically tapered to lower values in shallower waters. It was very common to observe significantly elevated fluorescence values as shallow as 600 m and occasionally shallower.

There were consistent anomalous dissolved oxygen "sags" (i.e., relatively low values of dissolved oxygen in vertical profiles when compared to baseline profiles) at depths between approximately 700–1,300 m. Figures B.1-7 and B.1-8 in Annex B summarize the dissolved oxygen anomalies. The maximum anomalies occurred between ~1,100 and 1,200 m deep. As distance from the wellhead increased, dissolved oxygen anomalies first increased and then decreased. As sags decreased in magnitude, they frequently became slightly broader, covering larger depth ranges. These observations are indicative of microbial degradation (i.e., hydrocarbon consumption) at depth followed by dispersion and mixing with surrounding waters above and below the plume.

The various chemical and physical observations depicted relatively consistent anomalies between 1,000–1,400 m that were generally observed as enhanced chemical concentrations, increased fluorescence, and decreased dissolved oxygen. A consistent pattern of observed anomalies at depth supports the assessment of trapping the buoyant oil and gas plume between 1,000–1,400 m. This subsurface region of hydrocarbon contamination contained trapped oil, dissolved hydrocarbons (primarily BTEX, semi-soluble PAHs, and soluble alkanes), and dispersants, which were slowly dispersed and consumed at depth. Results from chemical and physical measurements suggest that in

general, before about July 1 hydrocarbons in this “deep plume” were advected in various directions and after July 1 the plume predominantly moved to the southwest. The southwestward movement of the deep-water contamination, as well as neutrally-buoyant subsurface drifters deployed on NRDA cruises to track it, continued throughout the fall of 2010. Deep ocean currents in the region are dominated by cyclonic flows along the isobaths, which near the spill site are generally to the southwest (Schmitz et al. 2005). Therefore, the chemistry and sensor indicators are consistent with understanding of the circulation in the area.

When investigated alone, each sensor and measurement provides some evidence of contamination from MC252 oil. It is highly likely that hydrocarbons extended into regions that were not sampled or summarized in the data presented here. Furthermore, there were numerous compounds in MC252 oil that were not quantified (McKenna et al. 2013).

3.2 Oil Settled to Offshore Sediments

MC252 oil from the spill was identified in the sediments in the offshore area surrounding and down-stream of the well site (Joye et al. 2011; Montagna et al. 2013; Valentine et al. 2014). Valentine et al. (2014) estimated 4–31% of the released oil was sequestered in the deep sea. They noted that the pattern of contamination indicates deep-ocean intrusion layers as the source, consistent with deposition of a “bathtub ring” formed from an oil-rich layer of water impinging laterally upon the continental slope (at a depth of ~900–1,300 m) and a higher-flux “fallout plume” where oil-SPM aggregates sank to underlying sediment (at a depth of ~1,300–1,700 m). Stout (2015d), Stout et al. (2015), Stout and Payne (2016a), and Stout et al. (2016b) estimated the extent of Macondo oil from the DWHOS in benthic sediments using a combination of chemical fingerprinting and a geostatistical interpolation method of kriging for 2,397 sediment samples from 875 cores collected in 2010–2011 and 2014. Their conservative estimate was that the settled oil surrounding the wellhead was about 6.9–7.7% of the released oil mass.

Thus, there is evidence that there was a significant flux of spilled oil to the sediments. One additional mechanism of transport of oil to the sediments was as part of a rain of oiled olefin-based drilling muds ejected from the wellhead early in the blowout and after several attempts to plug the well with additional mud were made between May 26 and May 28 (i.e., the so-called “junk shot”, noted above). However, additional flux of oil to the sediments from more natural phenomenon may also have been significant. Because mineral SPM concentrations are typically very low in the offshore GOM near the wellhead, this additional transport flux to the seafloor was more likely due to oil adherence to organic matter, rather than mineral sediments. Indeed, Passow et al. (2012) and Passow (2014) measured

considerable sedimentation of organic marine snow in the offshore area near the wellhead in 2010–2011.

The carbon-flux in oil-contaminated surface water near the spill site was greatly affected by activities of microbes associated with macroscopic oil aggregates (Ziervogel et al. 2012). Roller bottles incubated with oil-amended water for 21 days showed rapid formation of oil aggregates that were similar in size and appearance compared to oil aggregates observed in surface waters near the spill site. Formation of oil aggregates following the Ixtoc oil spill in shallow (and relatively turbid) waters of the GOM has been reported previously (Patton et al. 1981), causing a major fraction of spilled oil to settle on the seabed (Jernelov and Linden 1981; Lehr et al. 2010). In the DWHOS, visual observations of sinking oil and/or mucus strings out to 9 km (Payne and Driskell 2015d) and chemical analysis of sediments in the vicinity of the wellhead (discussed above) also indicated oil-SPM sedimentation. Sinking of oil aggregates near the well head was observed throughout the water column in the second half of May 2010 (observations by Diercks al. 2010, cited by Ziervogel et al. 2012). Sinking oil aggregates likely transferred oil and organic carbon from the surface (Ziervogel et al. 2012) and the deep water plume (Ziervogel and Arnosti 2016) onto the sea floor. In addition, Stout and Payne (2016b) identified sedimented burn residues from *in situ* burning of Macondo oil. No attempt was made to recover residues from incomplete burning on the water surface, and this material also eventually settled to the bottom. However, sufficient quantitative data with which to model organic SPM-oil or burn residue flux to sediments were not available for this modeling effort.

3.3 Floating Oil

3.3.1 Remote Sensing Data

Remote sensing (satellite imagery) data may be used to: (1) indicate where oil surfaced, which is useful for evaluating the model's predictions of the net transport of oil droplets to the surface (i.e., rise rates of various droplet sizes and subsurface movements), (2) evaluate the transport of surface oil, and (3) estimate the amount of oil floating for comparison to the model's mass balance predictions that are functions of weathering and entrainment processes.

Several reviews of remote sensing applications to oil spills and evaluations of floating oil in the GOM are available (Garcia-Pineda et al. 2009, 2013a, b; Hu et al. 2009; Leifer et al. 2012; Svejkovsky et al., 2012, 2016; Marghany 2014; MacDonald et al. 2015). Remote sensing data indicating the extent of surface oil contamination are available for April to August 2010. Satellite Synthetic Aperture Radar (SAR) images were analyzed by DWHOS Trustees (2016) using the Texture Classifying Neural Network Algorithm (TCNNA, Garcia-Pineda et

al. 2010; Garcia-Pineda et al. 2013b; Garcia-Pineda et al. 2009). Figure 3-1 shows the cumulative footprint of floating oil coverage and the days oil cover was observed using the TCNNA (Environmental Response Management Application, ERMA 2016).

MacDonald et al. (2015) used neural network analysis of SAR images to quantify the magnitude and distribution of surface oil in the GOM from persistent, natural seeps and from the DWHOS discharge. To quantify the distribution of floating oil during the discharge from the DWHOS, MacDonald et al. (2015) analyzed 166 SAR images collected by Radarsat-1, Radarsat-2, TerraSAR-X, CosmoSKY-MED 1-2-3-4, ENVISAT, ALOS-1, and ERS-2 satellites between 23 April and 2 August 2010. SAR images were analyzed for presence of floating oil with use of the TCNNA. To estimate the contribution of thicker patches of floating oil to the aggregated volume, a subset of 60 of the SAR images collected during the DWHOS discharge was additionally analyzed to detect small SAR image anomalies caused by thicker patches of emulsion within overall regions of floating oil with use of the Oil Emulsion Detection Algorithm (OEDA) (Garcia-Pineda et al. 2013a). MacDonald et al. (2015) derived an estimate of ~70 μm thickness for oil anomaly pixels identified by OEDA (Garcia-Pineda et al. 2013a). All other oil-covered regions were classified as sheen, assumed to be ~1 μm thick following published guidance (ASTM International 2006; NOAA 2016).

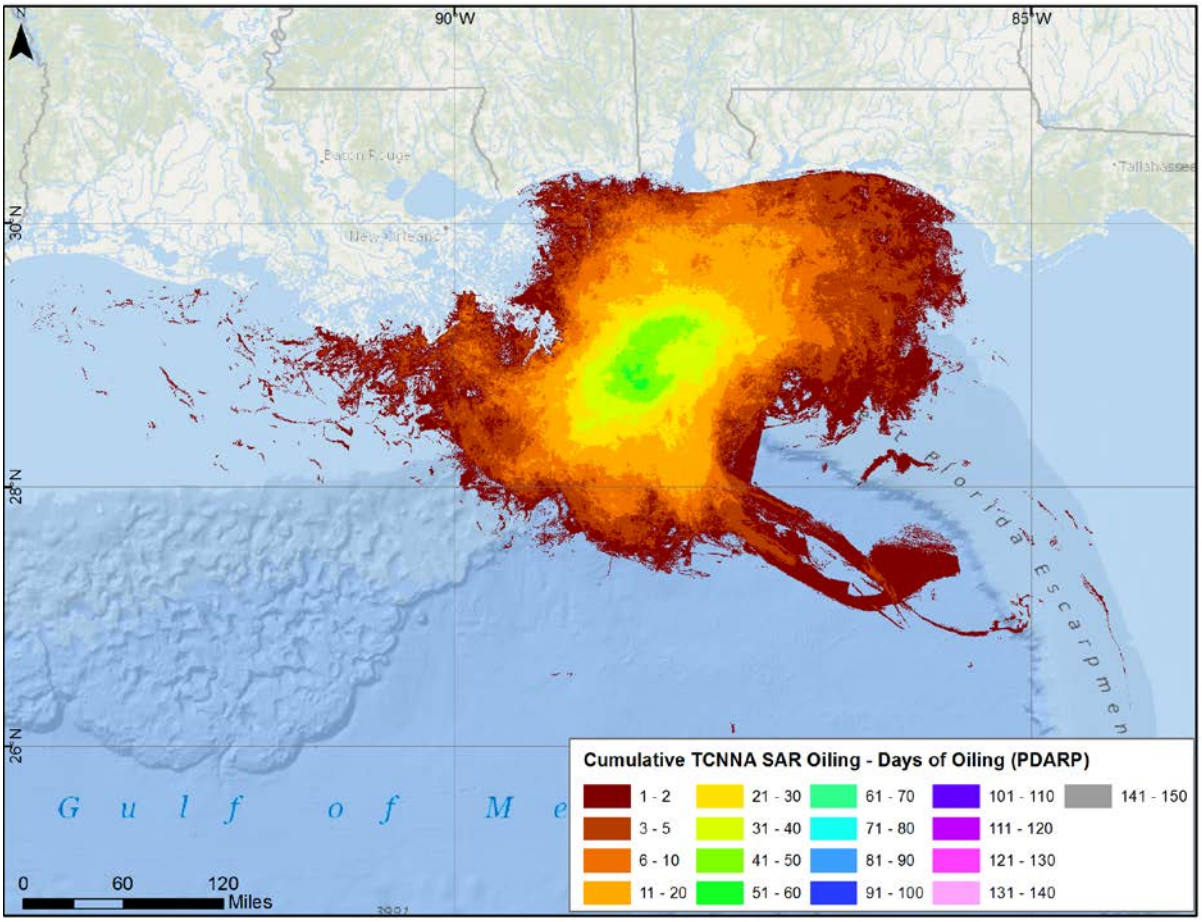

Figure 3-1. Cumulative days of oil presence on the water surface, based on SAR analysis using TCNNA.
(Data from ERMA 2016.)

SAR images from 2010, projected onto a 5 km x 5 km grid, showed that the 87-day DWHOS discharge produced a surface-oil footprint fundamentally different from background seepage, with an average ocean area of 11,200 km^2 (standard deviation, SD, of 5,028 km^2; maximum area of 28,400 km^2) and a volume of 22,600 m^3 (SD: 5,411 m^3). Combining all results during the 24 April to 3 August 2010 interval, the aggregated floating oil and oil emulsion footprints extended over an area of 149,000 km^2, from offshore Louisiana west of the Mississippi River Delta to the Florida Panhandle (Figure 3-2). Peak magnitudes of oil were detected during equivalent, ~14-day intervals around 23 May and 18 June, when wind speeds remained <5 m s^{-1}. The peak magnitudes of surface oil observed on 23 May and 18 June corresponded to two equivalent phases of about 14 days, when wind speeds were ideal for detecting surface oil using SAR. These phases were bookended by episodes

of higher winds. Over this interval, the aggregated volume of floating oil decreased by 21% and area covered increased by 49% ($p < 0.1$) (MacDonald et al. 2015).

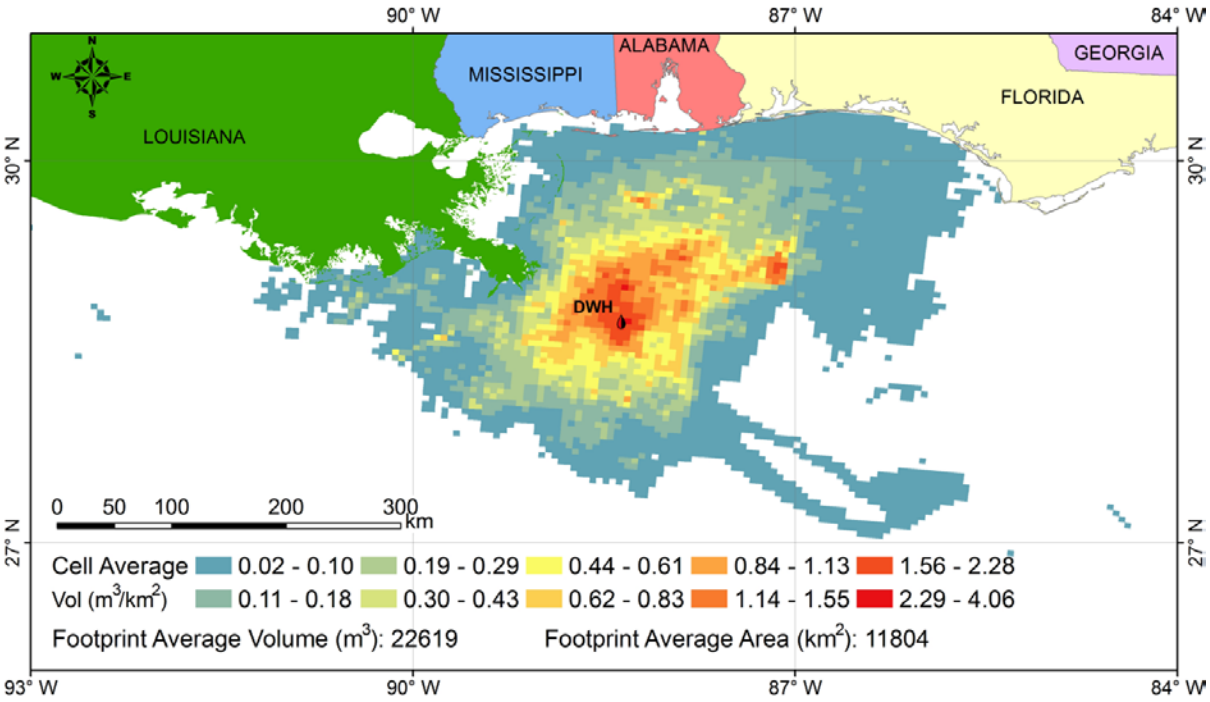

Figure 3-2. Time-averaged volume (m^3/km^2) of oil present on the water surface, based on SAR analysis.
(MacDonald et al. 2015)

The spatial distribution of floating oil and oil emulsion, relative to the DWHOS discharge point, was expressed by MacDonald et al. (2015) as its average daily volume ($m^3\ d^{-1}$) at progressive increments of distance and as its average daily concentration ($m^3\ d^{-1}\ km^{-2}$) in the geometrically increasing areas that these distance increments represent. The average daily volume increased out to distances of ~50 km from the well and then declined, while the average concentration steadily declined as oil was distributed over an ever-increasing area. The increase in volume with distance from the DWHOS discharge point out to ~50 km suggests the range over which recently discharged oil surfaced and drifted across the ocean after traveling from depth.

Remote sensing data, developed as part of the trustees' NRDA program in support of the Deepwater PDARP/PEIS (DWHOS Trustees 2016) were downloaded from the NOAA GOM ERMA website on 27 January 2016 (ERMA 2016). Data from four sensors were available:

SAR, MODIS Visible (MVIS), MODIS Thermal IR Sensor data (MTIR), and Landsat Thematic Mapper (TM). The following metadata were provided with the ERMA download:

- SAR images available in 2010 had resolutions ranging from 25 m to 100 m per pixel, with a few images with resolutions as fine as 6 m. There were 60 SAR images with good signal to noise ratios, where OEDA was used to classify areas of thick emulsified oil and TCNNA identified thin oil.
- Usable MODIS visible data were available for 18 days of surface oiling, at a pixel resolution of 250 m or 500 m, depending on the spectral band. Experts at the University of South Florida (USF) developed an algorithm to calibrate the MODIS visible and NIR data based on a USGS analysis of high-resolution airborne AVIRIS data collected concurrently with MODIS. Clouds in the MODIS images were masked using a probability density function algorithm. The images were then classified into three oil thickness classes based on the AVIRIS data. The three classes include a thin oil class (primarily silver sheen and rainbow, using NOAA [2016] Job Aid/Bonn Agreement Oil Appearance Code [BAOAC]; Table 3-3), a thick oil class (transitional dark to dark color), and a moderately thick oil class (metallic sheen) that falls between the other two classes.
- MTIR data were available for 25 days during the spill. MTIR was classified into a thin oil class (primarily silver sheen and rainbow, using NOAA (2016) nomenclature, Figure 3-2), a thick oil class (transitional dark to dark color), and a moderately thick oil class that falls between the other two classes.
- Useful Landsat TM data were available over a spatially limited area on 8 days when DWHOS oil was on the surface of the northern GOM. Ocean Imaging (OI) estimated the areal coverage per pixel of three oil thickness classes: a very thick class comprising heavy emulsions, a moderately thick class of dark-opaque oil, and a thin oil category that is thicker than sheen but thinner than dark-opaque oil. The Landsat TM oil thickness analyses did not classify oil sheens.

The DWHOS Trustees (2016) developed a gridded model of surface oil coverage each day (April–August 2010) using methods similar to MacDonald et al. (2015), except all four remote sensing products were used. The grid resolution was 5 km by 5 km, and the fraction of the grid cell covered by different thickness categories of oil was estimated. The methods are described in Graettinger et al. (2015). Figure 3-3 shows the cumulative footprint of floating oil coverage and estimated days of oil cover based on this gridded product (ERMA, 2016).

For comparisons with model results, floating oil distributions from 84 dates and times were used, these being times where the image was judged sufficiently synoptic of the area

of the floating oil. These included 34 SAR OEDA, 18 MVIS, 25 MTIR and 7 Landsat TM images analyzed by the DWHOS Trustees (2016; ERMA 2016).

Estimates of average oil thickness were also made so that surface oil volumes could be calculated and compared with the model results. MacDonald et al. (2015) estimated a representative thickness for each of the two SAR classes, 1 μm for thin oil (sheen) and 70 μm for thick oil (areas where emulsions are present). The NOAA Open Water Oil Identification Job Aid (NOAA 2016) reporting the Bonn Agreement Oil Appearance Code (BAOAC, Bonn Agreement 2009) indicates emulsions would be >200 μm (if continuous). However, the 70 μm "thickness" is based on the non-continuous cover of emulsions in these areas.

MODIS (MVIS and MTIR) and Landsat TM sensor data were classified into 3 classes, including a thin oil class, a moderately thick oil class and a very thick or thick emulsified oil class, with varying descriptions (Table 3-1 summarizes descriptions in ERMA 2016). Using the thickness ranges in the NOAA Open Water Oil Identification Job Aid (2016; Table 3-3), and assumptions described in Graettinger et al. (2015) and ERMA (2016), estimates were made of representative thicknesses for each class considering that oil of the nominal appearance thickness would be discontinuous in each pixel (Table 3-2). Graettinger et al. (2015) considered "thin oil" to have an average thickness of about 1 μm. Thicker oil characteristics range by orders of magnitude, varying both in thickness of oil and in percent oil in an emulsion. Across this broad spectrum, Graettinger et al. (2015) estimated that oil classified as "thick oil" corresponds to a volume of oil that would have an average thickness of no less than 10 μm. Figure 3-4 shows estimates of the volume of oil floating over time based on interpretation of thicknesses for categories of the remote sensing data. The SAR estimates are available at a frequency warranting interpolation, although it should be recognized that wind and wave conditions between the estimates could have been much different such that linear interpolation would not be representative of the conditions at those times.

Table 3-1. Summary of oil appearances for the remote sensor classifications.

Category	SAR	MVIS	MTIR	Landsat TM
Thin oil	sheen	silver and rainbow sheen	silver and rainbow sheen	thicker than sheen but thinner than dark-opaque oil
Moderately thick oil	(not applicable)	thicker than sheen but thinner than transitional dark to dark color	thicker than sheen but thinner than transitional dark to dark color	Dark-opaque oil
Thick oil	thick oil and emulsified oil	transitional dark to dark color	transitional dark to dark color	heavy emulsions
Reference	MacDonald et al. (2015)	ERMA (2016)	ERMA (2016)	ERMA (2016)

Table 3-2. Estimated thickness range and nominal thickness in brackets, based on reported oil appearances for the remote sensor classifications and estimates in Table 3-3.

Category	SAR	MVIS	MTIR	Landsat TM
Thin oil	1 µm	0.04–5.0 µm [1µm]	0.04–5.0 µm [1µm]	0.3–50 µm [1µm]
Moderately thick oil	(not applicable)	5–50 µm [10µm]	5–50 µm [10µm]	50–200 µm [10µm]
Thick oil	70 µm (to >200 µm)	>50 µm [50µm]	>50 µm [50µm]	>200 µm [50µm]

Table 3-3. Oil appearances based on NOAA Job Aid (2016) and BAOAC.

Code	Description	Layer-Thickness		Concentration	
		(µm)	(in)	m3/km2	bbl/acre
S	Silver Sheen	0.04–0.30	1.6 x 10-6– 1.2 x 10 -5	0.04-0.30	1 x 10 -3 – 7.8 x 10-3
R	Rainbow Sheen	0.30–5.0	1.2 x 10-5– 2.0 x 10 -4	0.3–5.0	7.8 x 10-3 – 1.28 x 10-1
M	Metallic Sheen	5.0–50	2.0 x 10-4– 2.0 x 10-3	5.0–50	1.28 x 10-1 – 1.28
T	Transitional Dark (or true) Color	50–200	2.0 x 10-3– 8 x 10-3	50–200	1.28–5.1
D	Dark (or true) Color	> 200	> 8 x 10-3	> 200	> 5.1
E	Emulsified	Thickness range is very similar to dark oil			

Chart from Bonn Agreement Oil Appearance Code (BAOAC) of May 2, 2006, as modified by A. Allen.

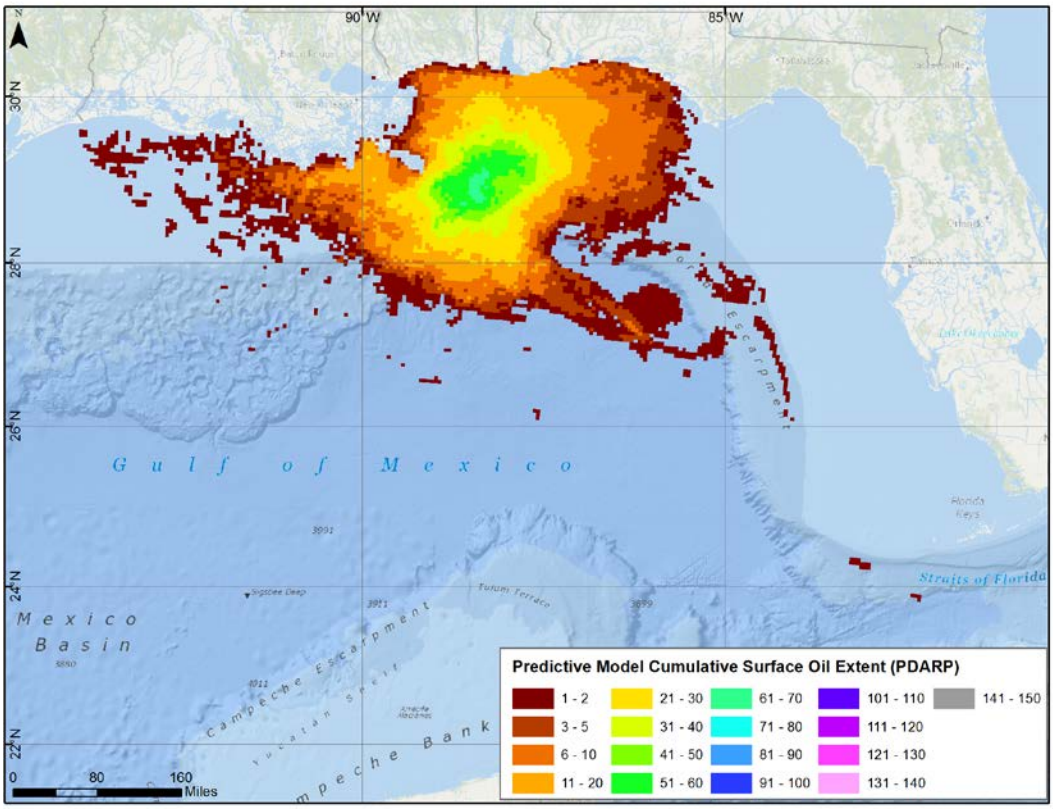

Figure 3-3. Cumulative footprint of floating oil coverage and estimated days of oil cover based on DWHOS Trustees' (2016) gridded model using data from four sensors.
(Data from ERMA 2016.)

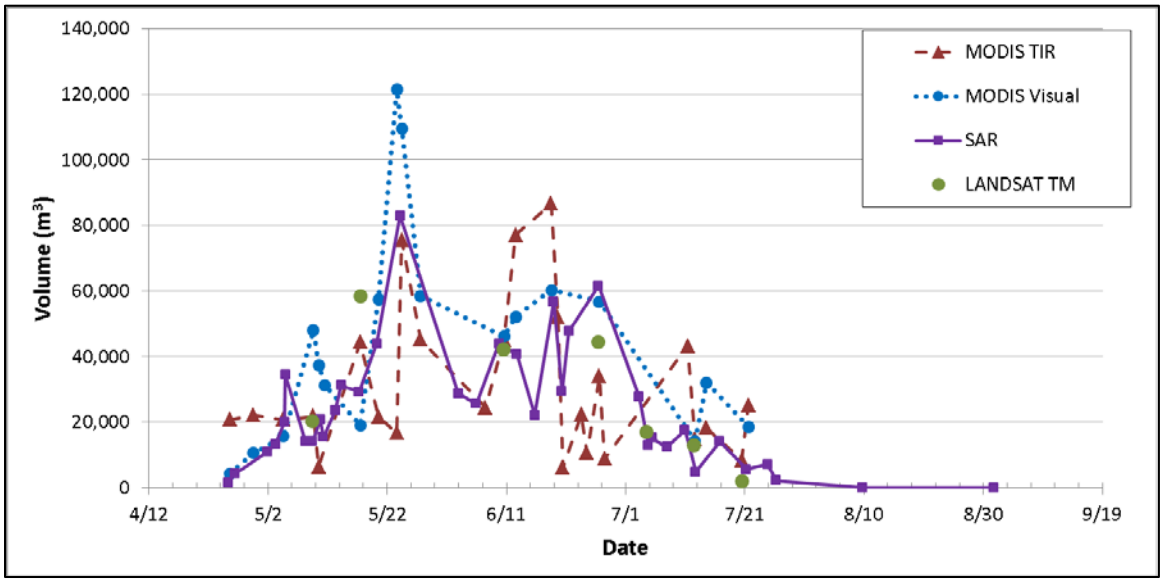

Figure 3-4. Estimated volume (m^3) of floating oil over time based on remote sensing.

3.3.2 Degree of Weathering of Floating Oil

The boiling cut curve of MC252 source oil indicated 61% of the mass was volatile and semi-volatile (Stout 2015a). SL Ross (Belore et al. 2011) concluded that the majority of the oil emulsion samples collected in the field had parent oil densities that would indicate that in excess of 55% of the initial oil volume had been lost through dissolution or evaporation before the sampling. SINTEF's (2010) field samples of emulsions were estimated to have 44–50% evaporative or dissolution loss. The field samples in the SINTEF study were collected 18.5–31.5 km from the wellhead. In the SL Ross and SINTEF studies, degree of weathering was not evaluated for oil samples taken close to the wellhead above the rising oil that might indicate the degree of loss through dissolution alone.

Daling et al. (2014), based on reviewed literature, concluded that MC252 crude oil droplets arriving on the sea surface would have already lost some of the original oil components through dissolution into the water column during the ascent from 1,500 m water depth. They estimated this loss as ~15% before the oil reached the surface. The lost fraction was comprised of saturates up to C7, BTEX, and C-3-Benzenes. Additionally, Brown et al. (2011) estimated that approximately 18% of the total PAHs were lost to the water before the oil surfaced.

Faksness et al. (2015) prepared Water Accommodated Fractions (WAFs) of two source oil samples and two field-weathered oils (collected from the surface) to evaluate the impact of weathering on chemical composition. Results indicated that the two source oils contained a large fraction of soluble and bioavailable components (such as BTEX and naphthalene). The two field residual oils taken from the water surface were depleted of these compounds via dissolution and evaporation.

Chemical measurements of floating oil and surface waters indicate that some of the PAHs remained in the larger oil droplets when they reached the surface; floating oil and surface water samples were observed to be enriched with 3- and 4-ring PAH's (Diercks et al. 2010; Spier et al. 2013; Stout 2015c, Payne and Driskell 2015a, b; Stout et al. 2016a). Analysis of 62 floating Macondo oil samples collected from the northern GOM sea surface during the DWHOS showed weathering of the oil droplets had occurred while the oil rose to the surface (Stout et al. 2016a).

Oil collected on June 16 with a Teflon net immediately upon reaching the sea surface during the *Jack Fitz* III cruise (Sample JF3-2km-onet-2010616-surf-N143) had already lost most mass below n-C8 from dissolution of soluble aliphatics, monoaromatics, and naphthalenes during the oil's ascent. Stout et al. (2016a) estimated that 20–25% by weight of the oil was lost to dissolution, with further reductions extending up to n-C13 due to the onset of evaporation. With additional time, weathering of floating oil samples advanced

with total PAH (TPAH) depletions averaging 69±23%, caused by the combined effects of evaporation, dissolution, and photo-oxidation. Floating oil samples collected less than 10 km from the wellhead exhibited a wide range of PAH depletion (12 to 91%, average 54 ± 20%), indicating a mix of freshly-surfaced and more weathered oil. PAHs were rapidly reduced by evaporation, imparting the wide range observed within relatively short distances from the well. Floating oils collected 10 to 75 km from the well exhibited 85 ± 14% depletion of PAH, on average, indicating that weathering of the floating oil quickly advanced as the oil moved away from the well. Even though evaporative losses beyond n-C20 are rarely recognized in oil spills, in this instance it is reasonable that the high air temperatures (28–30 °C) and high insolation in the northern GOM during the DWHOS allowed for severe evaporation in the floating oils (Stout et al. 2016a).

Biodegradation was not evident among the coalesced floating oils studied. However, considerable degrees of photo-oxidation were evident in the depletion patterns of the relative PAH concentrations in floating oil samples (Stout et al. 2016a).

3.4 Shoreline Oiling

Approximately 2,000 km of beaches and coastal wetlands were exposed to MC252 oil in 2010 (DWHOS Trustees 2016; Nixon et al. 2015). The oil was documented by shoreline assessment teams as stranding on 1,773 km of shoreline. Beaches comprised 50.8%, marshes 44.9%, and other shoreline types (mostly human-made) 4.3% of the oiled shoreline (Michel et al. 2013). Lengths of oiled shoreline by category and state, as determined by the DWHOS Trustees (2016) are listed in Table 3-4 (Nixon et al. 2015).

Oil was transported by wind and currents for 80–300 km before reaching the shoreline. The oil that eventually stranded on the shoreline was in the form of a thick, viscous emulsion, containing up to 60% water, as opposed to fresh, liquid oil. In most cases this emulsified oil stranded as discrete patches, rather than a continuous slick (Michel et al. 2013).

Table 3-4. Estimates of shore lengths (km) oiled.

Category	Beaches	Wetlands	Other	Total
Lighter oiling	248	754	36	1,038
Lighter persistent oiling	337	–	–	337
Heavier oiling	16	278	5	299
Heavier-Lighter persistent oiling	258	–	–	258
Heavier persistent oiling	105	73	2	180
Total	964	1,105	43	2,112

(Nixon et al. 2015)

Figures 3-5 to 3-10 summarize the best estimates of degree of shoreline oiling, as compiled and interpreted by the DWHOS Trustees (2016; ERMA, 2016). Data in Figures 3-5 to 3-10

were obtained from ERMA (2016). DWHOS Trustees (2016) mapped maximum observed oiling, categorized as not surveyed, no oil seen, or various degrees of oiling. Note that separate categorization schemes were used for beaches and for wetlands. Also, note the areas that were not surveyed, as they include much of Mobile Bay and considerable areas of wetlands in Louisiana.

With respect to the timing of when oil came ashore, available data consist of maps of where oil was first observed on various shoreline segments and assessments by the Shoreline Cleanup and Assessment (SCAT) program during Response. The shorelines were not searched synoptically, and areas were not visited for days or weeks; thus, the time oil was first observed could have been a considerable time after the actual initial oiling. Annex D contains figures mapping shoreline oiling based on SCAT data (based on shape files downloaded from ERMA) for 10-day intervals (April 22–September 30, 2010).

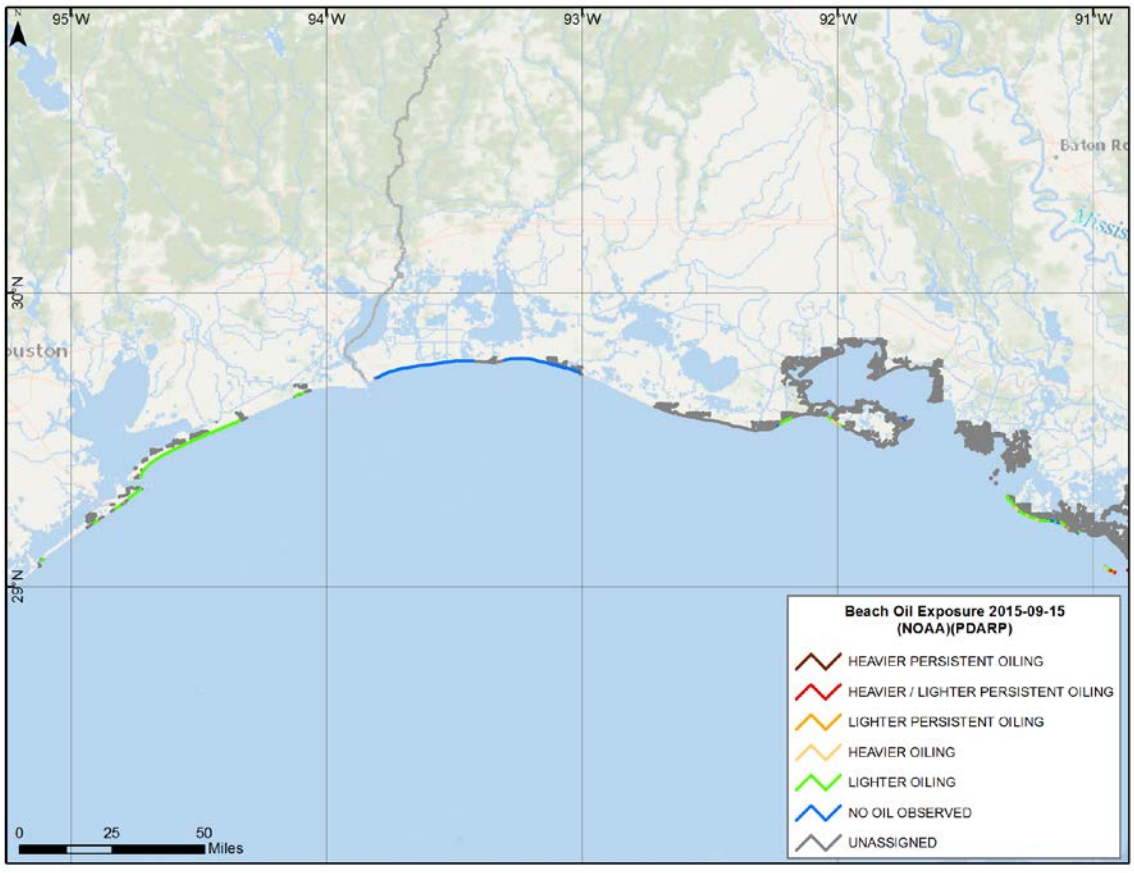

Figure 3-5. Summary of observed oiling on beaches (western GOM), as compiled and interpreted by the DWHOS Trustees (2016).

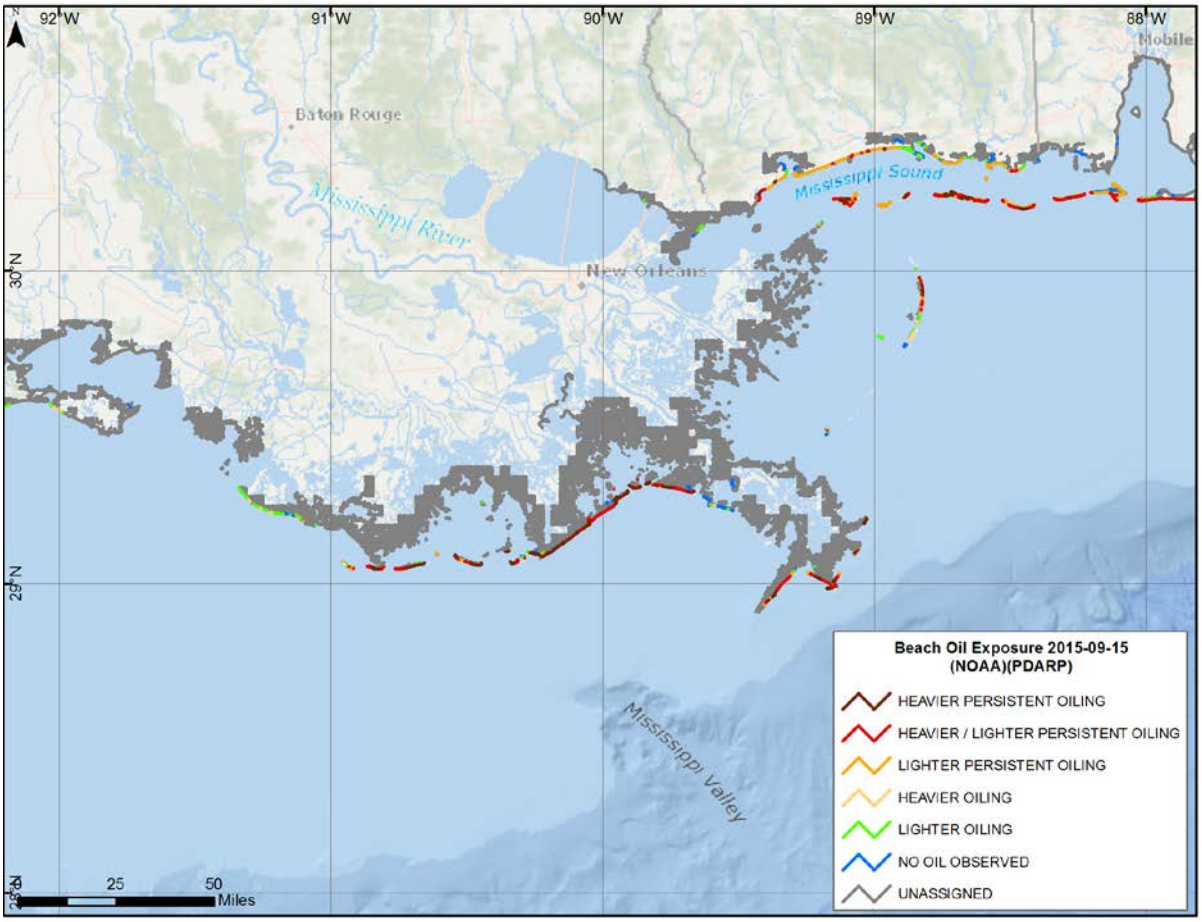

Figure 3-6. Summary of observed oiling on beaches (central GOM), as compiled and interpreted by the DWHOS Trustees (2016).

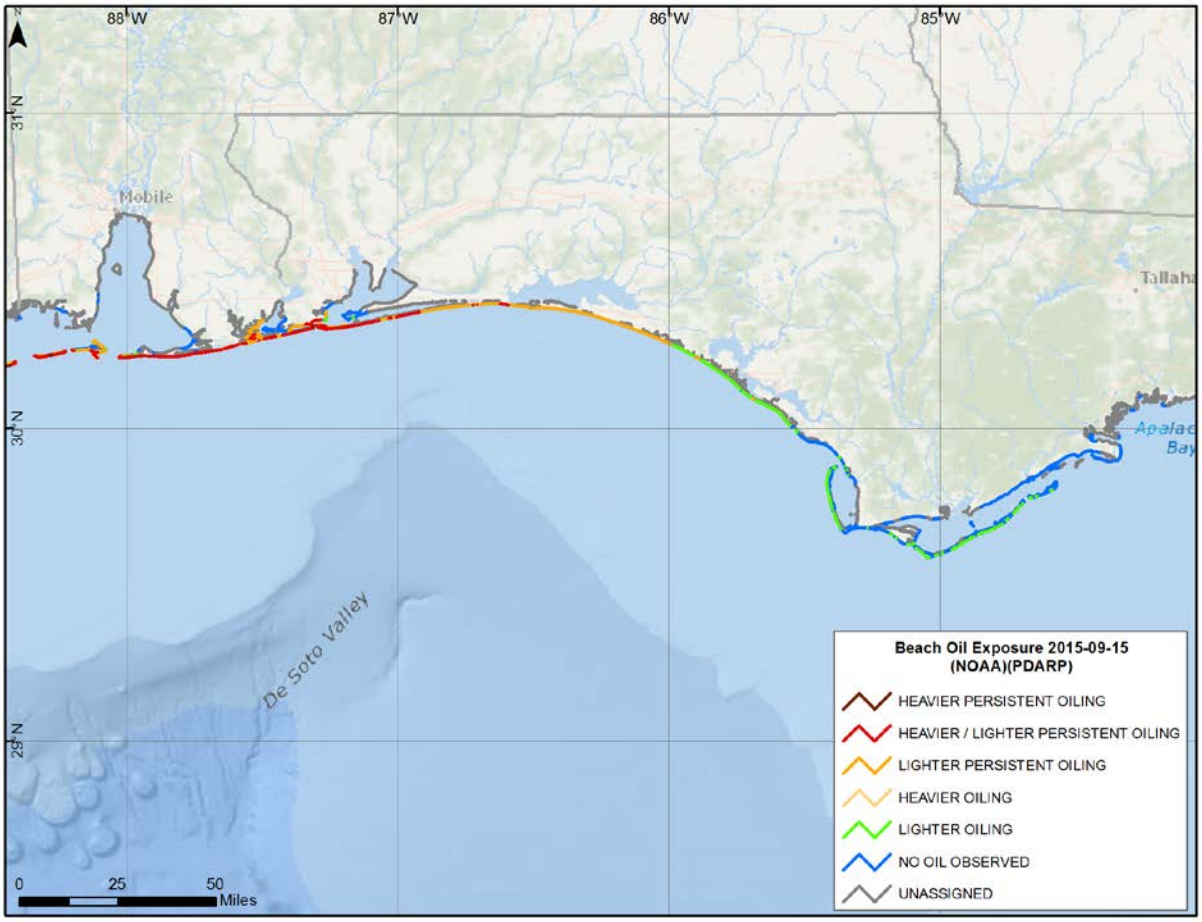

Figure 3-7. Summary of observed oiling on beaches (eastern GOM), as compiled and interpreted by the DWHOS Trustees (2016).

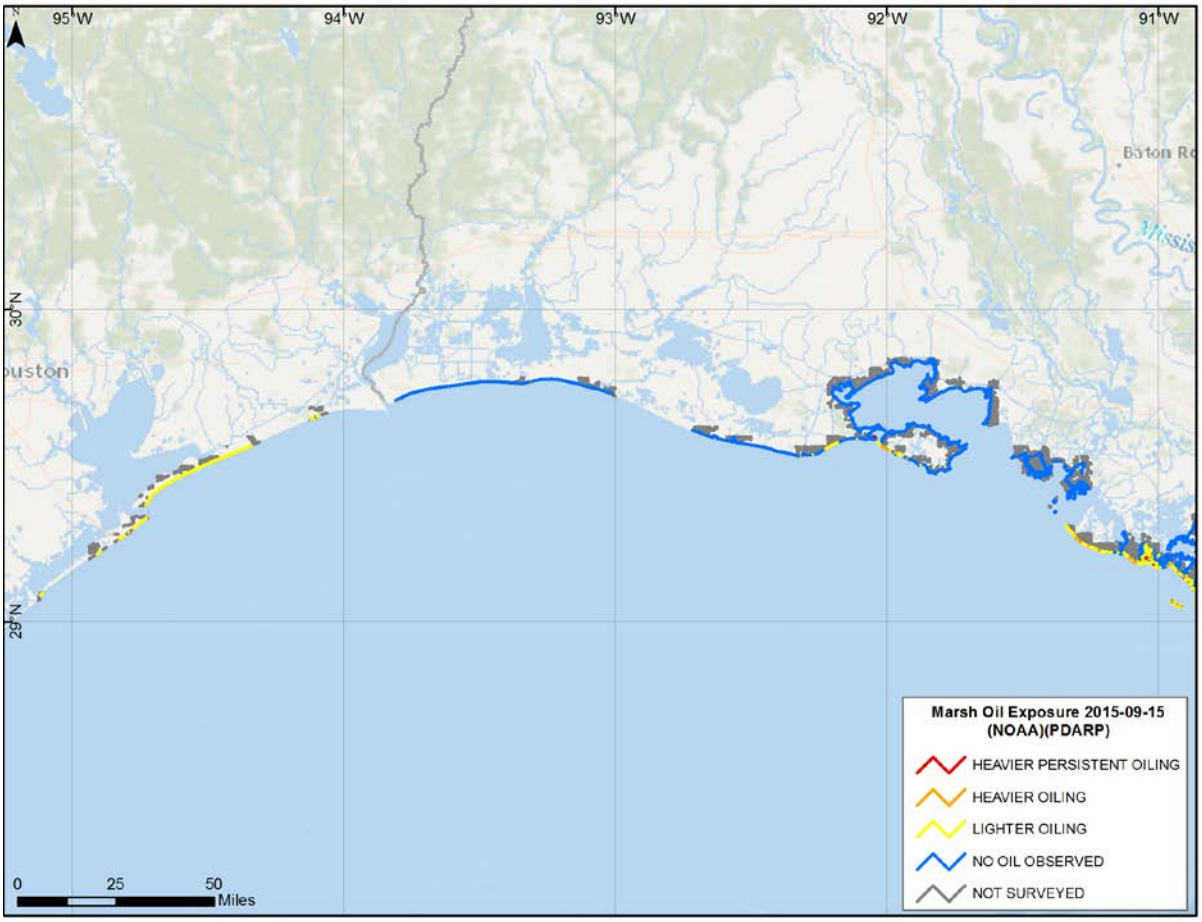

Figure 3-8. Summary of observed oiling in marshes (western GOM), as compiled and interpreted by the DWHOS Trustees (2016).

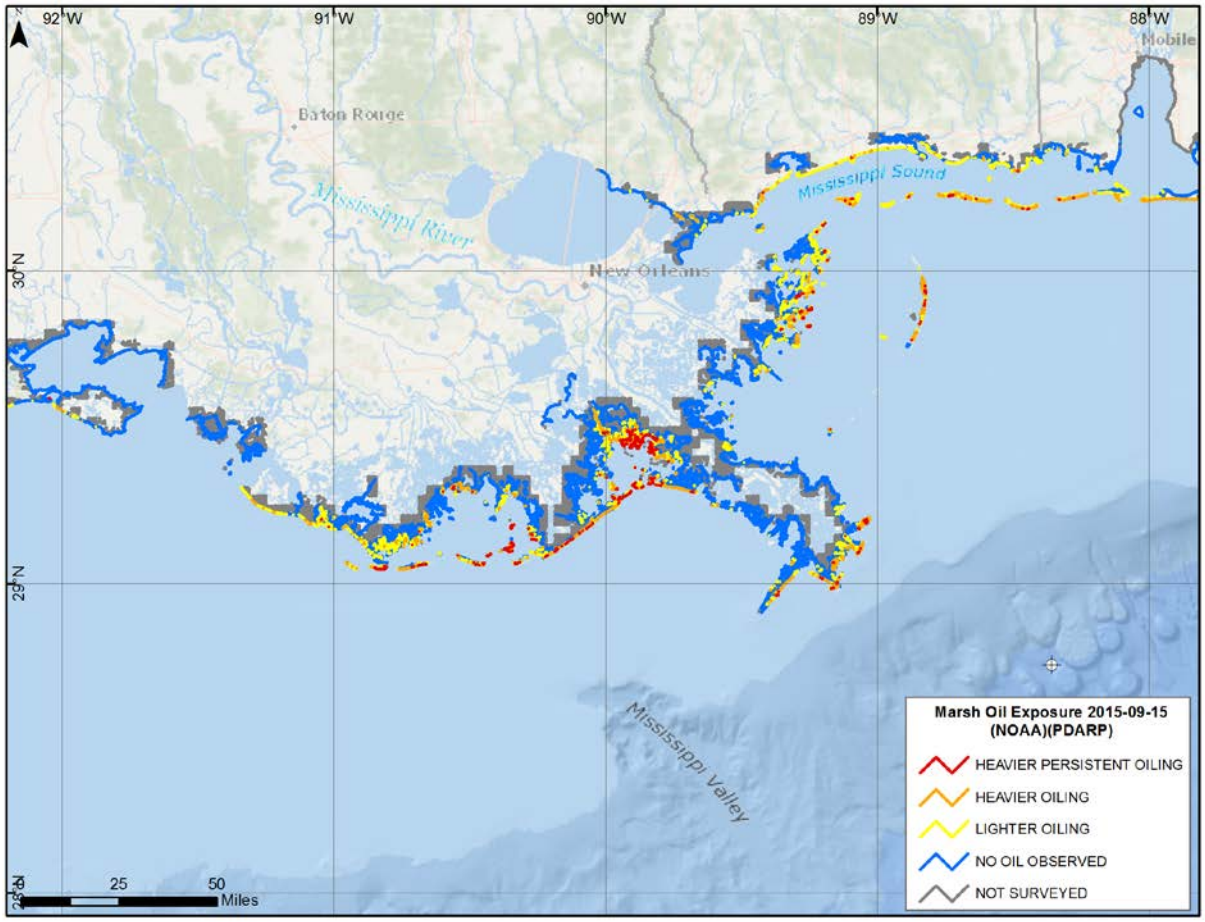

Figure 3-9. Summary of observed oiling in marshes (central GOM), as compiled and interpreted by the DWHOS Trustees (2016).

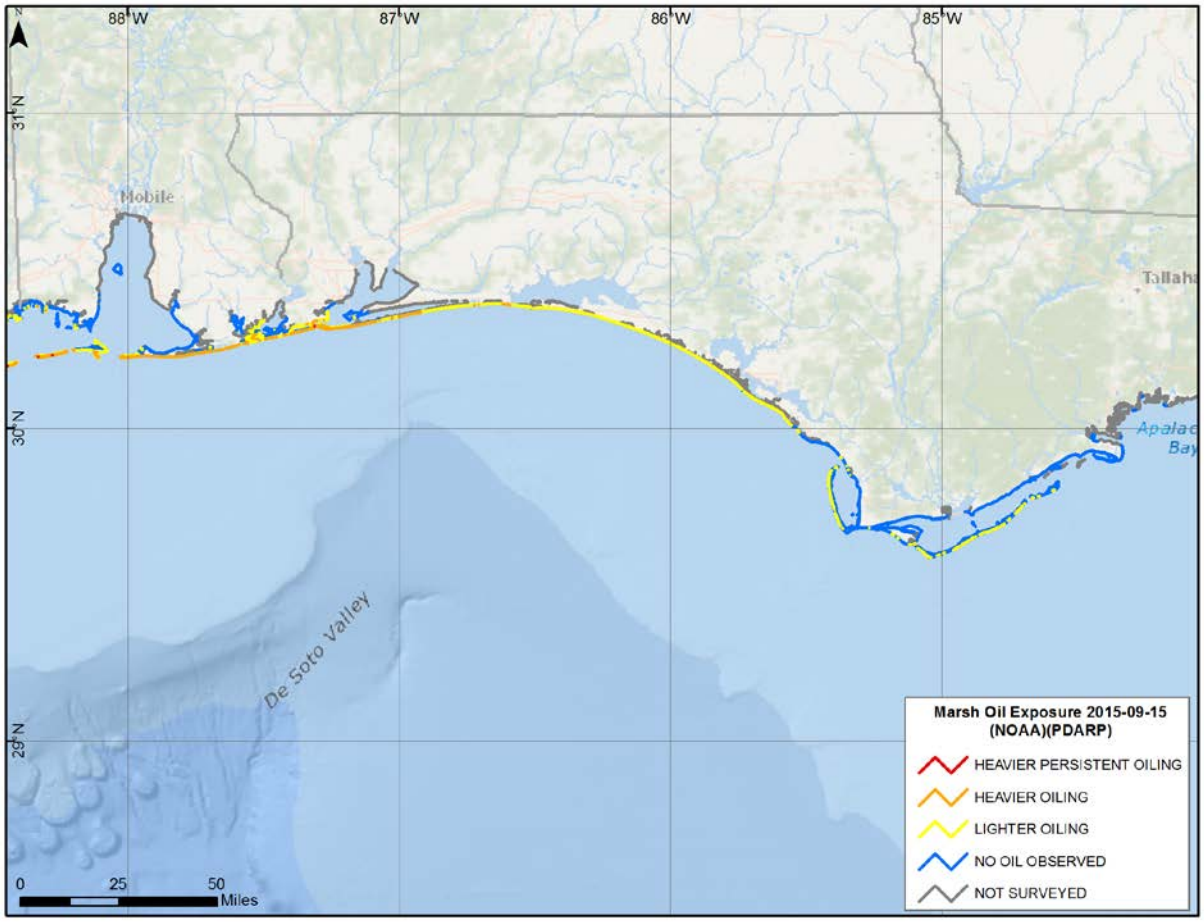

Figure 3-10. Summary of observed oiling in marshes (eastern GOM), as compiled and interpreted by the DWHOS Trustees (2016).

4. Results

Modeling of the trajectory and fate of the released oil from the DWHOS was performed using SIMAP. The model was run for 161 days, beginning April 22, 2010 at 10:30 AM local time (CDT), during which time the oil came ashore, settled to sediments, evaporated, degraded or dispersed at sea. The model conserves oil mass, estimates losses to evaporation and degradation, and estimates the amount and distribution of the spilled oil mass floating on the water, as well as dispersed in the surface waters and at various levels in the water column, at any given time. The SIMAP model quantifies, in space and over time:

- The spatial distribution of oil mass and volume on water surface over time;
- Oil mass, volume and thickness on shorelines over time;
- Subsurface oil droplet concentrations, as total hydrocarbons and by component, in three dimensions over time;
- Dissolved hydrocarbon concentrations for each of the modeled components in three dimensions over time; and
- Total hydrocarbons and semi-soluble hydrocarbons sedimented to the sea floor over time.

The fates model output at each (30-min) time step includes:

- Oil thickness and mass loading (μm and g/m^2), as well as weathering state (content of each of the pseudo-components, viscosity, and water content) on water surface;
- Average oil thickness and mass loading (μm and g/m^2) on shorelines, by grid cell of the habitat grid;
- Subsurface oil droplet concentration (ppb), as total hydrocarbons and by component;
- Dissolved hydrocarbon component concentrations in water (ppb);
- Total hydrocarbon loading on sediments (g/m^2); and
- Soluble-semi-soluble hydrocarbon loading on sediments (g/m^2).

Several model inputs, for which there is considerable uncertainty and/or to which the model results are sensitive, were varied to determine which provided the best fit to the observations. These included:

- Currents
- Winds
- Horizontal turbulent dispersion coefficient for floating oil (1, 5, 10, 100, 200 m^2/s).
- Wind drift: Constant at 2, 3, 4.1, or 5% of wind speed and angles of 0°, 10° 15° or 20°, and calculated using the Youssef and Spaulding model (see Section 2.6).

Model runs were made using 3-D and time-varying currents from interpolated observational data as measured by ADCPs (Section 2.2.3.1) and hydrodynamic model hindcasts (Section 2.2.3.2). The wind product used to force the hydrodynamics was used in SIMAP model simulations as the wind input. Table 4-1 lists model simulations run and described in this report. The first set of simulations ("First Set" in Table 4-1) was run to evaluate sensitivity to the assumed floating oil horizontal dispersion coefficient. The primary set of runs to be described herein are those altering the currents and winds used for forcing, and using 100 m^2/s for the floating oil horizontal dispersion coefficient ("Primary Runs" in Table 4-1). Simulations run with alternative wind drift assumptions to those listed in Table 4-1 (i.e., 3% of wind speed, noted as "Runs with Varied Inputs", and other assumptions not presented herein) resulted in subtle differences in oil trajectories, but similar mass balance and concentration results. Simulations using no currents were also run to evaluate the influence of winds as opposed to currents on surface oil distributions. To examine mass balance and changes in surface floating oil distributions, runs were made assuming no SSDI, SSDI with low dispersant effectiveness, and SSDI with high dispersant effectiveness, as well as the best estimate (see Section 2.8.3 for details).

For simulations of subsurface oil below the mixed layer depth of 40m, simulations were run with the hydrodynamic models listed in black font in Table 4-1. In addition, simulations from the release depths to 40 m were made using the interpolated ADCP data (Section 2.2.3.1).

The base-case simulation was run with HYCOM-FSU currents, NOAA/NCEP's NARR model-predicted winds, horizontal dispersion coefficient for floating oil of 100 m^2/s, and modeled wind drift. These forcing data yielded the closest agreement of the modeled floating oil distribution to the remote sensing data sets (see Section 4.2). The results for the base case model simulation using HYCOM-FSU currents and NARR winds will be the focus of the discussion below. However, results for other primary case simulations are also available.

Table 4-1. Matrix of inputs for model simulations used to examine floating and shoreline oil.

"Primary Runs" are highlighted in yellow.

Simulation Set	SSDI Treatment Case	Currents	Winds	Wind Drift Model	Floating Oil Horizontal Dispersion Coefficient (m^2/s)
First Set	Best	SABGOM	NARR	Modeled	5
First Set	Best	SABGOM	NARR	Modeled	10
First Set	Best	SABGOM	NARR	Modeled	50
First Set	Best	SABGOM	NARR	Modeled	100
First Set	Best	SABGOM	NARR	Modeled	200
First Set	Best	HYCOM-FSU	NARR	Modeled	5
First Set	Best	HYCOM-FSU	NARR	Modeled	10
First Set	Best	HYCOM-FSU	NARR	Modeled	50
First Set	Best	HYCOM-FSU	NARR	Modeled	100
First Set	Best	HYCOM-FSU	NARR	Modeled	200
First Set–Varied SSDI	High	HYCOM-FSU	NARR	Modeled	100
First Set–Varied SSDI	Low	HYCOM-FSU	NARR	Modeled	100
First Set–Varied SSDI	None	HYCOM-FSU	NARR	Modeled	100
Primary Runs	Best	ADCPs	NARR	Modeled	100
Primary Runs	Best	HYCOM-NRL, Reanalysis	CFSR	Modeled	100
Primary Runs	Best	HYCOM-NRL, Real-time	NARR	Modeled	100
Primary Runs	Best	SABGOM	NARR	Modeled	100
Primary Runs	Best	NCOM Real-Time	NARR	Modeled	100
Primary Runs	Best	NGOM-NOAA, Real-time	NARR	Modeled	100
Primary Runs	Best	IAS ROMS-hourly	NAM	Modeled	100
Primary Runs	Best	IAS ROMS-12 hourly	NAM	Modeled	100
Runs with Varied Inputs	Best	HYCOM-FSU	NARR	3% wind speed	100
Runs with Varied Inputs	Best	HYCOM-NRL, Real-time	NARR	3% wind speed	100
Runs with Varied Inputs	Best	HYCOM-NRL, Real-time	NARR	3% wind speed	100

Simulation Set	SSDI Treatment Case	Currents	Winds	Wind Drift Model	Floating Oil Horizontal Dispersion Coefficient (m^2/s)
Runs with Varied Inputs	Best	SABGOM	NARR	3% wind speed	100
Runs with Varied Inputs	Best	NGOM-NOAA, Real-time	NARR	3% wind speed	100
Runs with Varied Inputs	Best	NGOM-NOAA, Real-time	NARR	3% wind speed	100
Runs with Varied Inputs	Best	none	NAM	Modeled	100
Runs with Varied Inputs	Best	none	NARR	Modeled	100
Runs with Varied Inputs	Best	none	NAM	3% wind speed	100
Runs with Varied Inputs	Best	none	NARR	3% wind speed	100
Runs with Varied Inputs	Best	none	NOGAPS	3% wind speed	100
Runs with Varied Inputs	Best	none	NOGAPS	Modeled	100

Results of these simulations are described in the sections below. Sections 4.2, 4.3 and 4.4 describe and discuss the trajectories and concentration results of the modeled scenarios. Figures summarizing the results are below and in Annex C (floating oil), Annex D (shoreline oiling), Annex E (subsurface oil) and Annex F (comparison of modeled water column concentrations with chemistry data). Note that the simulations using ADCP data are reported in Section 4.4 and Annexes E-F describing concentrations below 40 m. Since ADCP data were not available from shelf and nearshore waters, modeled transport in those shallow waters was purely wind-driven. The floating and shoreline oil results using ADCP data are very similar to those using no currents and the same winds.

4.1 Mass Balance

Figure 4-1 shows the modeled mass balance of oil over time for the base case using HYCOM-FSU currents and NARR winds, as the percent of total mass spilled that was on the water surface, in the water column, on shorelines, in the sediment, in the atmosphere, and degraded as of the date shown. Figure 4-2 shows the mass of oil (in metric tons, MT, where 1 MT = 1,000 kg) remaining on or in the water, on sediments or on shorelines for the same base case. The mass balance is similar for model runs using other currents and winds,

although the amount of oil coming ashore varies somewhat among model runs (Table 4-1). For example, Figure 4-3 shows the mass balance in MT for the primary simulation using SABGOM. Figure 4-4 shows that if no SSDI were used, the amount of surface oil and oil coming ashore would have been higher, and the amount degraded in the water column lower. Though the differences in the floating and shoreline oil amounts are subtle, the simulation including SSDI results in considerably more biodegradation in subsurface waters (facilitated by the smaller droplets and thus faster dissolution rates with SSDI) and less volatilization to the atmosphere, particularly in June–July 2010. Note that the effectiveness of the SSDI was limited by the amounts of dispersants applied such that the resulting DORs were typically lower than 1:100 (<1%, Figure 2-9).

The percentage of the oil floating at any given time results from a combination of the release rate to the environment, the fraction of the released oil that is in the form of large droplets, and the wind speed over the previous several to 24 hours. The floating oil (natural) entrainment rate into the water increases substantially with wind speed above 10 knots (5 m/s) and associated wave heights. Winds exceeding 10 knots averaged over 24 hours occurred in late April, May 9–15, June 6, June 23, June 30–July 7, July 11–13, July 22, July 25, July 30, August 11–23, and August 28–31, 2010 (Figure 4-5). The influence of wind and wave heights on the floating oil mass is evident in Figure 4-5. (Also, compare to these same time frames in Figure 4-2.)

Initially all of the oil was subsurface, but after 3 hours (on April 22) larger droplets began to surface. In April, most of the oil was released as large droplets that surfaced rapidly. Oil that surfaced was quickly entrained by waves (i.e., natural dispersion into the water column). In April and early May there were three calm-wind periods where the entrained (water column) oil resurfaced in substantial amounts. These calms were followed by windy periods where oil was again entrained. This high dispersion in April and early May reduced the opportunities for evaporation of volatiles to the atmosphere (Figure 4-1) during those periods. This increased the amount of dispersed oil in the water column (Figure 4-2) and concomitant dissolution, but this latter phenomenon wasn't large enough to affect the overall mass balance (dissolved components barely register in Figures 4-2 through 4-4).

During May, holes developed in the riser kink at depth and oil was released through relatively small holes such that the releases were highly turbulent. Thus, the droplet size distribution included increasing amounts of small droplets that remained dispersed in the deep water. Oil flow from the riser continued to mainly include large droplets that rapidly surfaced. (See Section 2.8.3 for more detail.) The surfaced oil re-entrained during the windy period of May 9–15, or in calmer periods, substantially remained floating where evaporative weathering could take place.

Beginning on May 20, the daily subsea application volumes of dispersant increased substantially, and the fraction of oil dispersed into the water column increased (Figure 4-1). On June 3, 2010 the riser was cut, and the percentage of oil dispersed into the water column increased rapidly. The application rates of dispersant (particularly at the surface) were also substantially higher June 3–5 (Figure 2-6), and there was a high wind event June 5-6 (Figure 4-5), putting more oil in the water column and, as a result, less hydrocarbon mass was floating or volatilized to the atmosphere (Figure 4-1). The oil release rate to the environment decreased throughout June and early July (due to subsea recovery beginning on Jun 5, Figure 2-7). There was a substantial decrease in the amount of oil floating June 30–July 7 during Tropical Storm Alex and July 11–13, much of it coming ashore due to southeast winds or being entrained into surface waters (Figures 4-2 to 4-5).

Although it isn't clear in the overall mass balance figures, dissolution of the highly soluble aromatics (substituted benzenes, AR1-AR3) and aliphatics (AR9) was rapid from oil dispersed as small droplets into deep water, making those compounds more bioavailable to exposed pelagic organisms including microbes (see Appendix II, Annex C, evaluation of degradation rates), and degradation increased substantially as more SSDI was used. The small holes in the broken riser also facilitated the dispersion of oil into micro-droplets, and so degradation. Figure 4-2 as compared to Figure 4-4 shows substantial increases in degradation, especially after June 3 when the subsea dispersant was more effectively applied (Figure 2-9). Application of more dispersant subsea would have increased degradation further, as well as decreased the amount of floating and shoreline oil. Of course, the tradeoff of more hydrocarbon exposure to deep water biota would need to be considered, as compared to exposure of the more abundant water column biota and wildlife at and just below the water surface and in coastal waters.

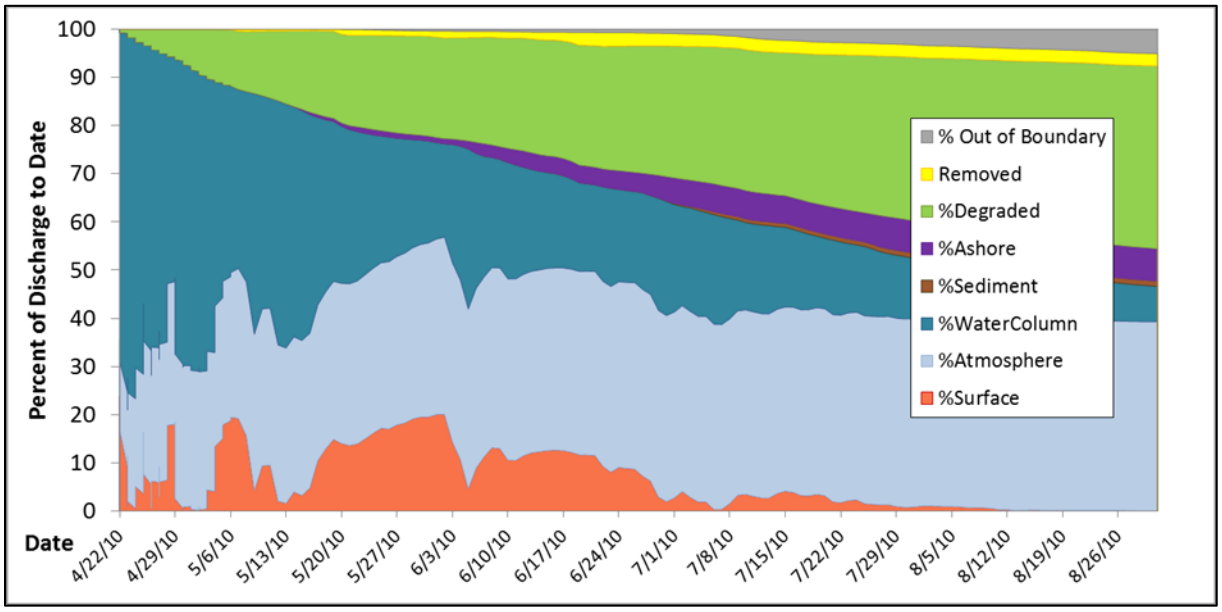

Figure 4-1. Modeled mass balance of oil over time, as percentages of oil released to date; base case simulation using HYCOM-FSU.

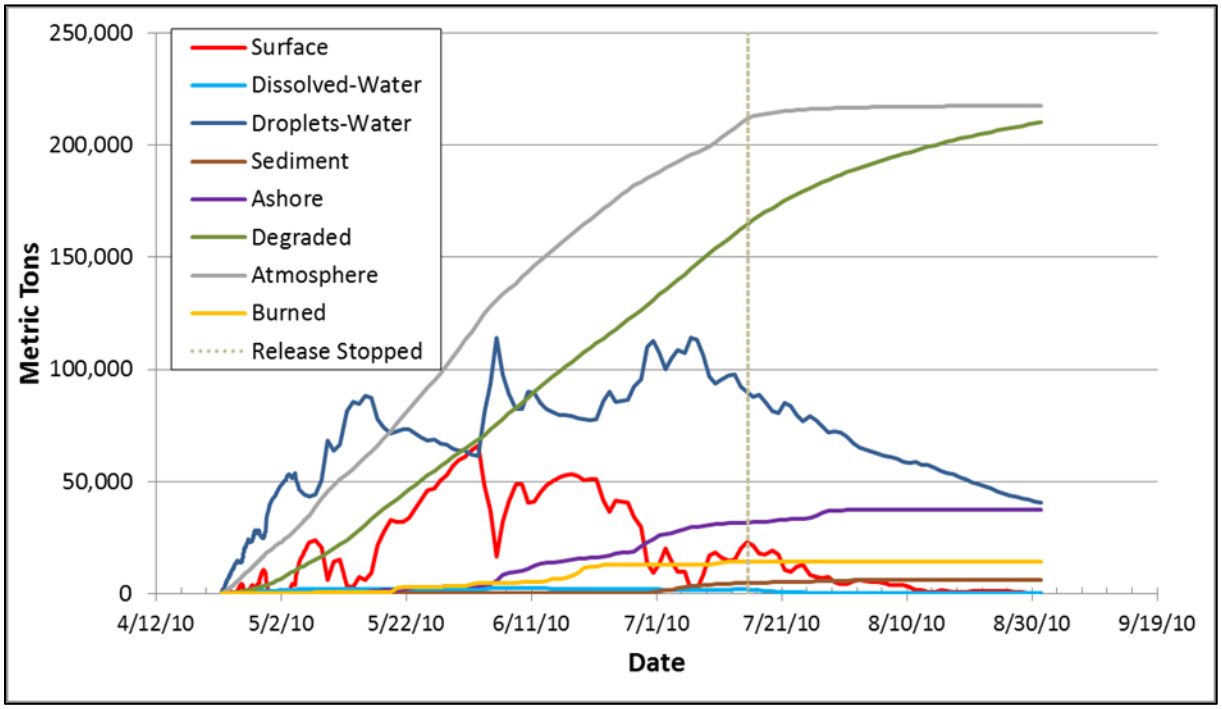

Figure 4-2. Modeled mass balance of oil over time, in metric tons; base case simulation using HYCOM- FSU.

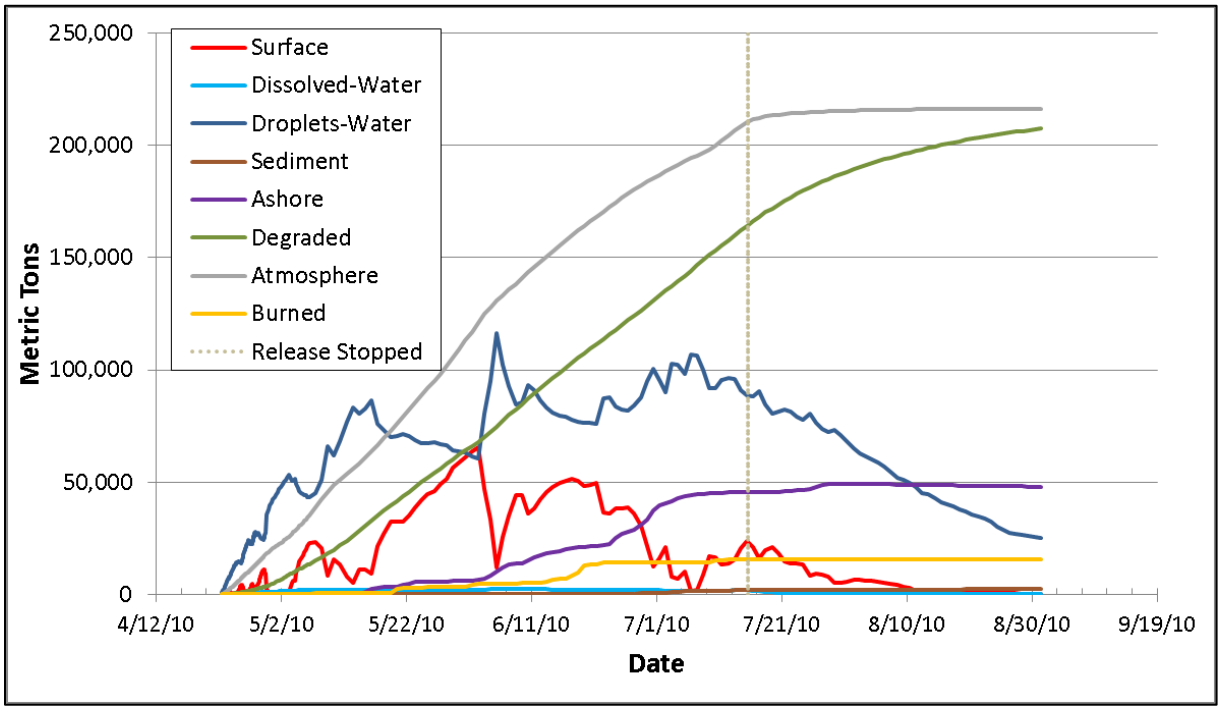

Figure 4-3. Modeled mass balance of oil over time, in metric tons; primary simulation using SABGOM.

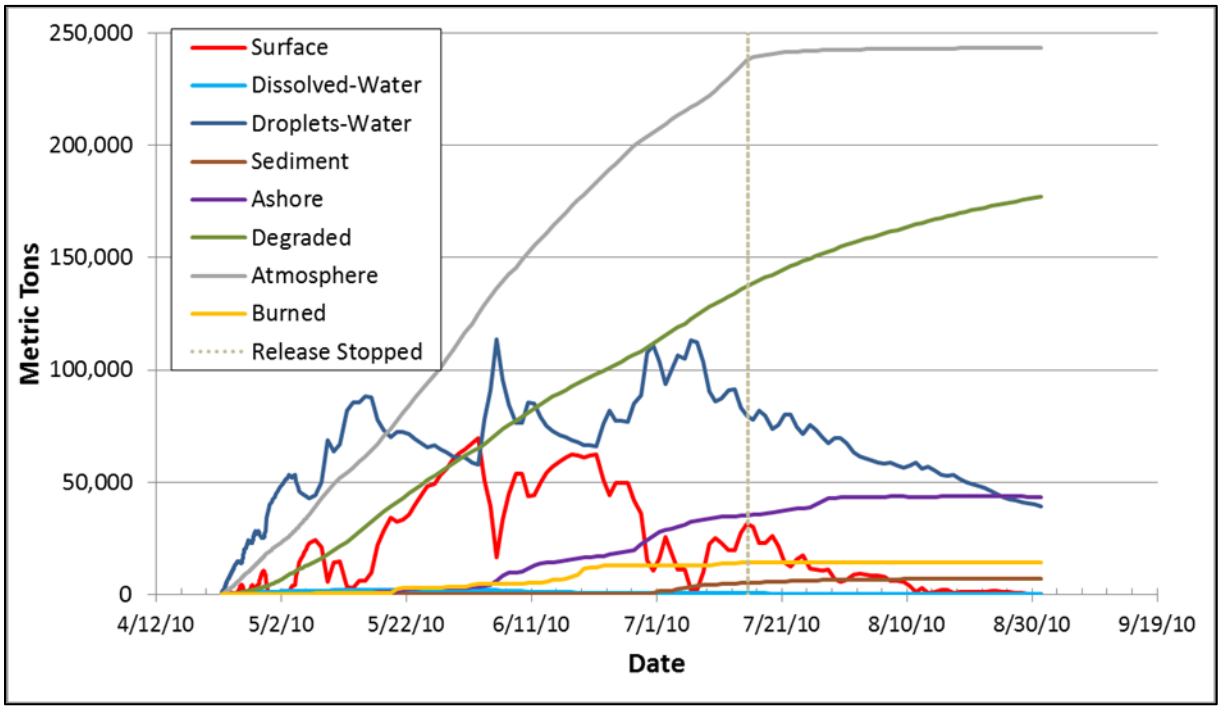

Figure 4-4. Modeled mass balance of oil over time, in metric tons; simulation using HYCOM-FSU but assuming no SSDI treatment.

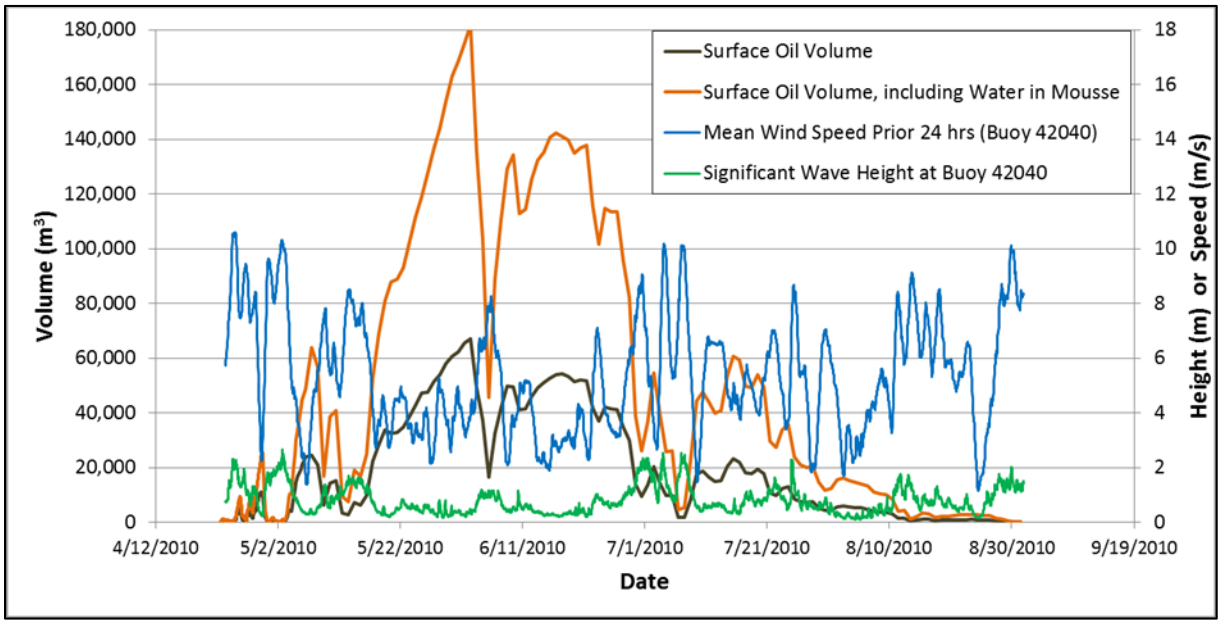

Figure 4-5. Modeled volume of surface oil over time, both including and not including the water volume in the mousse, compared to winds and waves–base case simulation using HYCOM-FSU.

The results for runs using alternative horizontal dispersion coefficients for surface floating oil (1-200 m^2/s) show very similar mass balances to those of Figures 4-1 and 4-2 (also see Table 4-2). Variation of the dispersion coefficients used for in-water spillets representing the subsurface oil does not affect the mass balance much (not shown).

Table 4-2 lists the mass balance on 31 August 2010, expressed as percent of the total oil released to the environment (modeled as 553,889 MT), for the model base case and five alternatives with varying currents and winds, plus the base case without inclusion of SSDI and with alternative assumptions regarding the effectiveness of the SSDI. All model runs listed include the best estimates of *in situ* burning and surface dispersant application, with the exception of the run with HYCOM-FSU, NARR, and Best SSDI but no surface dispersant included (the only change from the base case run).

In all simulations, there was little floating oil left by mid-August (Table 4-2). During the windy period of mid-August (Figure 4-5), the model indicates the remaining floating oil was for the most part dispersed as weathered oil and tar balls, with essentially all the volatiles and soluble-semi-solubles in the floating oil evaporated or degraded. When winds were calm, the model runs result in widely scattered weathered oil ("tarballs") floating or awash in the wave-mixed layer. Floating oil was "visible" in the remote sensing products offshore until the August 9 SAR observation (MacDonald et al 2015). Note that SAR and other remote sensing products would not identify areas of tarballs, only areas where fresher oil, mousse and sheens occur (see Garcia-Pineda et al. 2009, 2013a, b; Hu et al. 2009; Leifer et al. 2012; Svejkovsky et al. 2012, 2016; Marghany 2014; and MacDonald et al. 2015 for specifics). Overall, by the end of August 2010, the model estimates are that 68% of the remaining oil (5% of the spilled oil) was highly weathered ("tarballs"), containing <1% of the soluble and semi-soluble hydrocarbons (i.e., those with $\log(K_{ow})<6$) originally in the released oil, with 83% of the soluble and semi-soluble hydrocarbon mass being in the form of 3-ring PAHs.

The base case model indicates about 7% of the oil released to the environment came ashore, mostly at the end of June as the result of the strong southeasterly winds caused by Tropical Storm Alex (which also dispersed a substantial amount of the surfaced oil into the water column). Shoreline cleanup is not included in the simulation, nor are shoreline processes such as burial of oil in shoreline sediments which would slow weathering losses. Oil simply accumulated on the shoreline in the model simulations.

Table 4-2. Mass balance on 31 August 2010, as percent of the total oil released to the environment.

Model Run	Surface	Ashore	Burned	Atmos-phere	Sediment	Water Column	Degraded	Outside Grid
SABGOM, NARR, with Best SSDI	0.01	8.7	2.8	39	0.4	4.6	37	7.0
HYCOM-NRL, CFSR Reanalysis with Best SSDI	0.01	4.5	2.6	38	0.3	8.1	41	4.7
HYCOM-FSU, NARR, with Best SSDI	0.01	6.7	2.6	39	1.2	7.3	38	5.0
HYCOM-FSU, NARR, with Best SSDI; no surface dispersant	0.01	7.2	2.6	40	1.3	7.3	37	5.0
HYCOM-FSU, NARR, without SSDI	0.01	7.8	2.6	44	1.3	7.1	32	5.3
HYCOM-FSU, NARR, Low Effectiveness SSDI	0.0002	7.2	2.6	43	1.3	7.6	33	5.1
HYCOM-FSU, NARR, High Effectiveness SSDI	0.01	6.6	2.6	35	1.0	7.9	42	4.7
ADCPS, NARR, without SSDI	0.02	11	2.6	44	1.6	8.2	33	0.0
ADCPs, NARR, with Low Effectiveness SSDI	0.01	12	2.6	43	1.6	7.8	33	0.0
ADCPs, NARR, with Best SSDI	0.02	10	2.6	39	1.5	8.0	39	0.0
ADCPS, NARR, with High Effectiveness SSDI	0.01	11	2.9	35	1.3	7.7	43	0.0

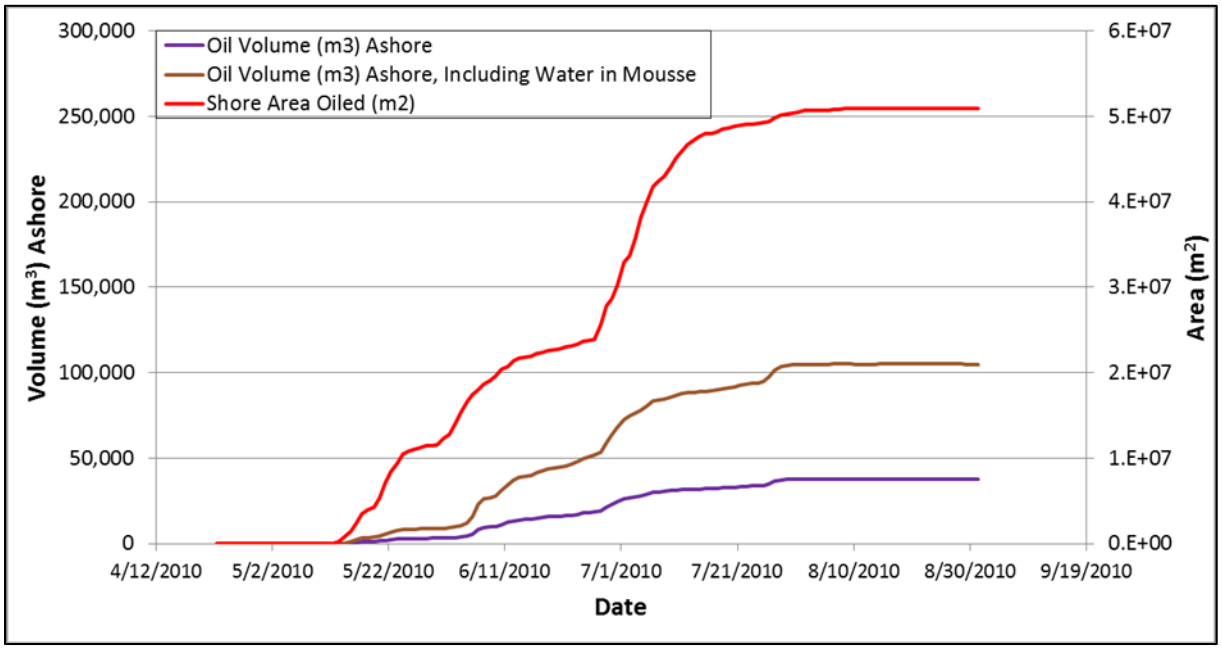

Figure 4-6. Volume of oil (not including water in mousse) and of mousse coming ashore, and area of shoreline habitat oiled, in the base case simulation.

Of the model inputs, the mass balance results are most sensitive to variation in the currents and associated winds. These inputs influence the trajectory path and the percentage of the oil going ashore, some of which evaporates and affects the fraction of mass in the atmosphere. The simulations using ADCP currents had considerably more oil come ashore than other simulations using hydrodynamic model currents, likely due to the lack of current data on the shelf and near shore such that along-shore current transport was missing from the ADCP-forced simulations. (Comparisons of shoreline oiling amongst model runs and with observations are discussed in Section 4.3 below.)

Some of the variation in the percentage in the water column compartment is due to variation in the amount exiting the model grid ("outside grid" in Table 4-2), where it was no longer tracked. The oil transported outside the model (habitat and bathymetry) grid was almost entirely in the water column. Most of the oil in the water column ultimately degraded, with a small fraction settling to the sediments. Thus, the percentage dispersed and ultimately degraded in the water column is the sum of water column, degraded, and outside the model grid from Table 4-2.

The simulation run with HYCOM-FSU currents and NARR winds, without SSDI (Figure 4-4), resulted in more floating oil exposure, more oil ashore, a higher percentage of oil volatilized, and a lower percentage of oil degraded than the same run including SSDI (with the best estimate of effectiveness, Figure 4-1, or with other assumptions regarding the SSDI

effectiveness, Table 4-2). The percentage of discharged oil dispersed by SSDI was 3% for the low effectiveness case, 21% for the high effectiveness case, and 12% for the base case with the best estimate of effectiveness. Application of dispersant at the water surface dispersed 3.6–3.7% of the discharged oil (all model runs using HYCOM-FSU currents and NARR winds). When surface dispersant application was not included in the base case simulation using HYCOM-FSU currents and NARR winds, about 2% more of the oil went ashore, evaporated, or settled to the sediments and about 1% less degraded by the end of August 2010. About half of the oil dispersed with surface dispersant later dispersed naturally.

In the base case model run including SSDI (as in most other model runs, Table 4-2), 2.6% (~14,000 MT) of the oil mass (~3.8 million gal) was removed by *in situ* burning. This estimate is about 1/3rd of the estimate made by Mabile and Allen (2010). In the model, sufficient oil thicker than the assumed minimum threshold was not available to meet the Mabile and Allen burn volume estimates on all burn dates. (Note that the details of the skimming that occurred to gather oil for burning are not available and were not simulated, which might account for some of the differences.) Mechanical removal was not simulated in these runs because accurate quantitative estimates of the amounts of oil removed by location and over time were not available. Lehr et al. (2010, OBC) estimated that about 2–5% of the oil was skimmed. However, the water content of the removed "oil" was not measured, such that Lehr et al. needed to make an assumption in order to make this estimate. As shown in Figure 4-7, the fraction burned of the floating oil was quite small, and mechanical removal was also a small fraction of the floating oil, such that it would have little influence on the mass balance if estimates were included.

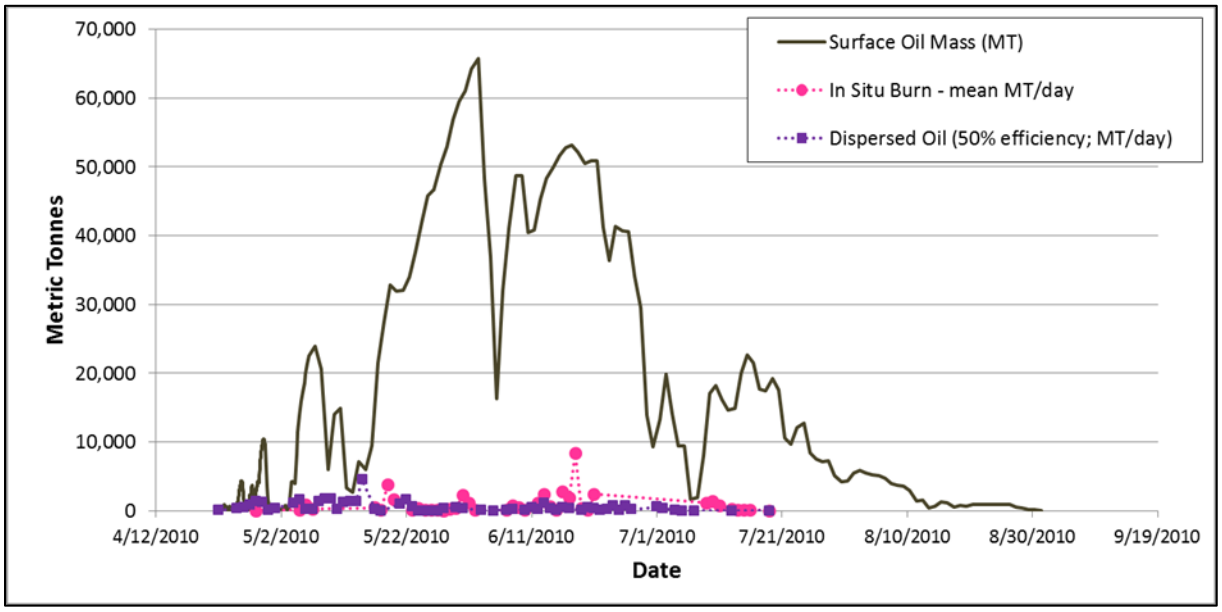

Figure 4-7. Estimated daily burn rate and amount of oil dispersed by aerial dispersant operations, as compared to the amount of floating oil on the water each day (base case model run).

Ryerson et al. (2011) used chemical analysis of hydrocarbon data to quantify the DWHOS hydrocarbon (gas and oil) flow rate and environmental distribution. They estimated that on June 10, 2010, the release rate of gas and oil was 10.1 million kg/day (76% of which by mass was oil), and of that after 2 days 10% surfaced and remained floating, 5% evaporated, 36% of the oil and gas remained in deep plumes, 27% was either flared or recovered, and the other 22% was not accounted for, with much of that likely degraded. The 10% of released hydrocarbons that was estimated floating would be 13% of the released oil. On June 10, the SIMAP model estimates (for the SSDI-included runs in Table 4-2) were that, of the oil released to that date, 9-11% of the oil was floating, 34-39% of the oil had evaporated, and 22-26% was degraded by that time. The Ryerson et al. (2011) estimates were characterized for the oil release 2 days prior and not cumulative for the spill to date. Thus, direct comparisons cannot be made. However, the floating oil estimates are in close agreement since a parcel of floating oil remained on the surface for just a few days before dispersing. The higher percent in the atmosphere and degraded in the SIMAP results are primarily due to the cumulative sum of those losses over the prior eight weeks of release.

Estimates were made by Lehr et al. (2010) in the Oil Budget Calculator (OBC) report of the amount of oil skimmed, burned, chemically dispersed, evaporated or dissolved, naturally dispersed, recovered from the well head, and other. The "other" category would include floating oil, oil that came ashore and oil in sediments. Lehr et al. (2010) discuss that much of the oil in the water column (dispersed or dissolved) would ultimately degrade. Table 4-3

provides a summary of the OBC results in terms of the amounts and percent of the total released to the environment, excluding the amount recovered at the wellhead. Estimates are provided by Lehr et al. (2010) for best, expected, and worse case assumptions. Best is defined as results that have the largest amounts of oil that are treated or removed and dispersed by the response activity (burned, skimmed, and chemically dispersed). The percentages in Table 4-3 were recalculated to exclude the amount of oil recovered at the source. The OBC mass balance estimates were recast in Table 4-4, assuming much of the "evaporated or dissolved" was evaporated, and combining the dispersed categories as contributing to water column.

The SIMAP model estimates for runs using HYCOM-FSU currents and NARR winds, including SSDI, in Table 4-2 are summarized as ranges in Table 4-5 using the OBC categories. Water column includes degradation and mass exiting the model boundary. The OBC estimates of amount evaporated are low compared to the range calculated by the SIMAP model, whereas the OBC estimates of amount on shorelines are high compared to the range calculated by the SIMAP model. As the volatiles made up 61% of the oil, it would be likely that more of the oil evaporated than the OBC estimates, leaving less in the "other" category, assumed to be on shore or in sediments. The water column estimates are in reasonable agreement.

Table 4-3. OBC estimates of the total volume and percent of total oil released to the environment for the best, expected, and worst-case assumptions from the view-point of the response.

Fate	Best	Expected	Worst
Naturally dispersed	16%	16%	14%
Chemically dispersed	35%	19%	12%
Evaporated or dissolved	24%	28%	30%
Burned	7%	6%	6%
Skimmed	5%	4%	2%
Other	13%	28%	36%
Total	100%	100%	100%

Table 4-4. OBC percentages recalculated to exclude the amount of oil recovered at the source and allocating water column and evaporated fractions.

Fate	Best	Expected	Worst
Evaporated	24%	28%	30%
Water column (dispersed or dissolved)	51%	35%	26%
Burned	7%	6%	6%
Skimmed	5%	4%	2%
Other (on shore and sediment)	13%	28%	36%

Table 4-5 Mass balance ranges for SIMAP model base case simulations, assuming low, best and high effectiveness for SSDI, combined into the categories described by the OBC.

Fate	Low	Best Estimate	High
Evaporated	43%	39%	35%
Water column (dispersed or degraded)	46%	50%	55%
Burned	2.6%	2.6%	2.6%
Skimmed (not simulated)	-	-	-
Other (on shore and sediment)	8.5%	7.9%	7.6%

Figure 4-8 compares the modeled (base case, HYCOM-FSU currents and NARR winds, with SSDI) amount of oil floating over time to estimates from interpretation of remote sensing data (described in Section 3.3.1). The comparison shows good agreement, indicating the oil droplet size distributions (based on the SSDI model) input to the SIMAP oil fate model and the oil fate model vertical transport and surface entrainment algorithms are producing reasonable results.

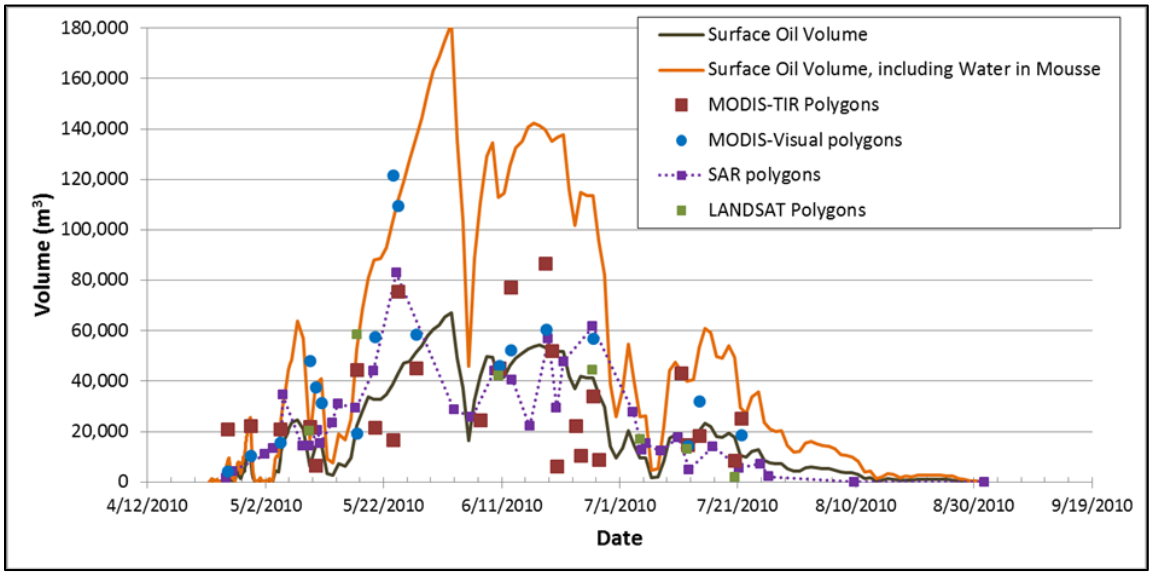

Figure 4-8. Estimates of oil mass floating based on remote sensing and the base case model predictions.

The estimates of oil thickness used for MVIS, MTIR, and Landsat TM are highly uncertain, being based on a representative thickness within broad thickness ranges (Table 3-2). The SAR-based thickness estimates developed by MacDonald et al. (2015) were more narrowly quantified and subjected to ground truthing based on field data, albeit they are estimates of average thickness for highly variable oil coverages. Thus, the volumes indicated by the sensors are approximate. Figure 4-9 shows the correlation of the model (base case) and

SAR-based floating oil volume estimates, comparing SAR-based estimates to the model predictions of both the oil alone and the volume of emulsified oil with water as mousse. Both are in generally good agreement overall. The model predictions of the oil alone are in most cases closer to the SAR-based estimates than the model-predicted mousse volume estimates. However, the thick oil category of SAR includes mousse and the MacDonald et al. (2015) estimate of 70 µm on average for thick oil is intended to reflect a mixture of mousse and fresh thick oil. Thus, one would expect the SAR-based estimates to fall between the oil-only and the mousse-volume model estimates (Figure 4-8).

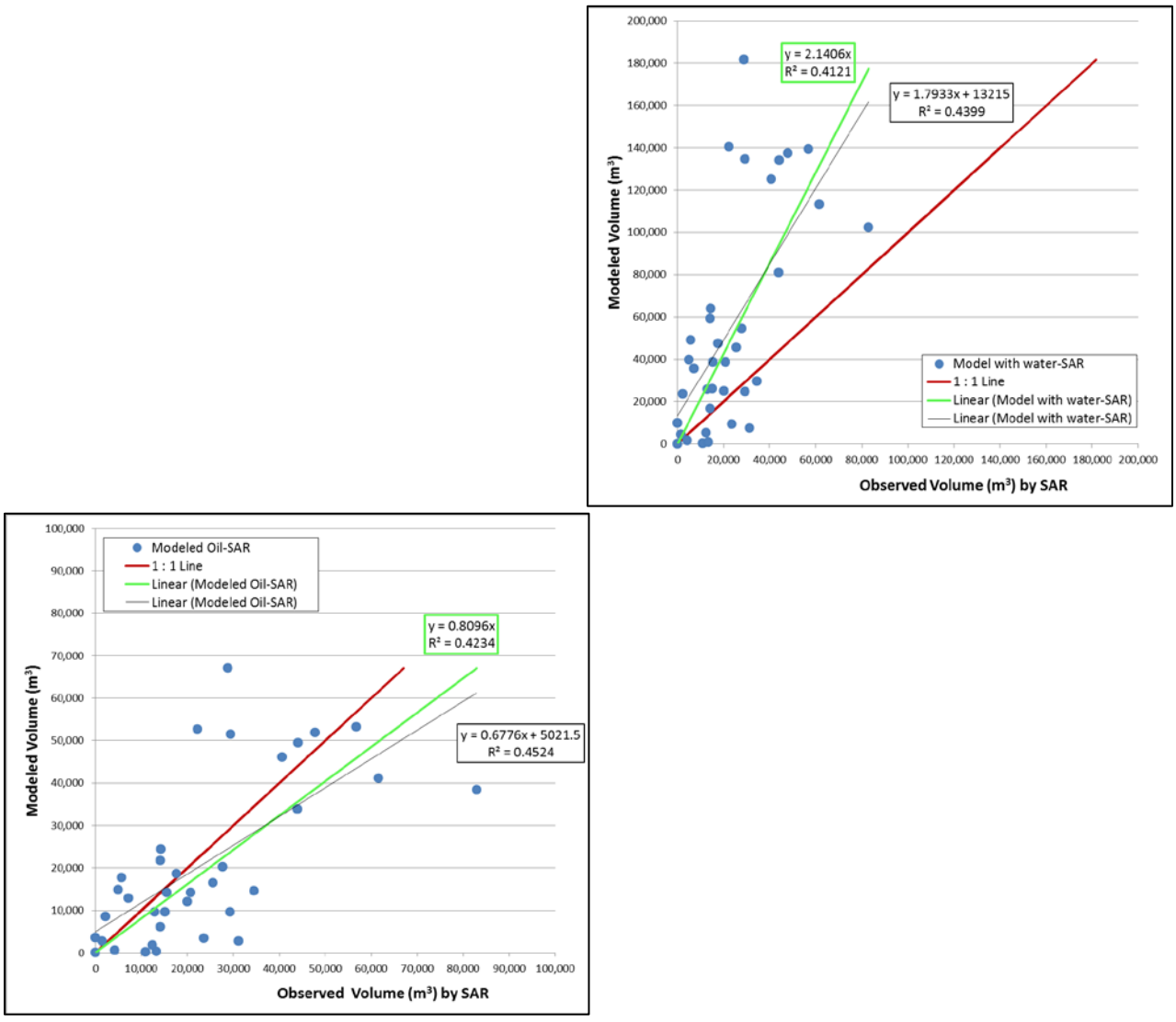

Figure 4-9 Correlation of the model (base case) predictions and SAR-based floating oil volume estimates.

(Oil-only, left panel; mousse volume, right panel.)

Figure 4-10 compares the model and SAR results to wave data recorded at an offshore buoy (42040) in the area of the floating oil. The modeled surface oil and mousse volumes, as well as the SAR estimates, increased in periods of calm and decreased when waves were higher during storm periods. This inverse relationship of SAR-based oil volume with wave height and winds was noted by MacDonald et al. (2015).

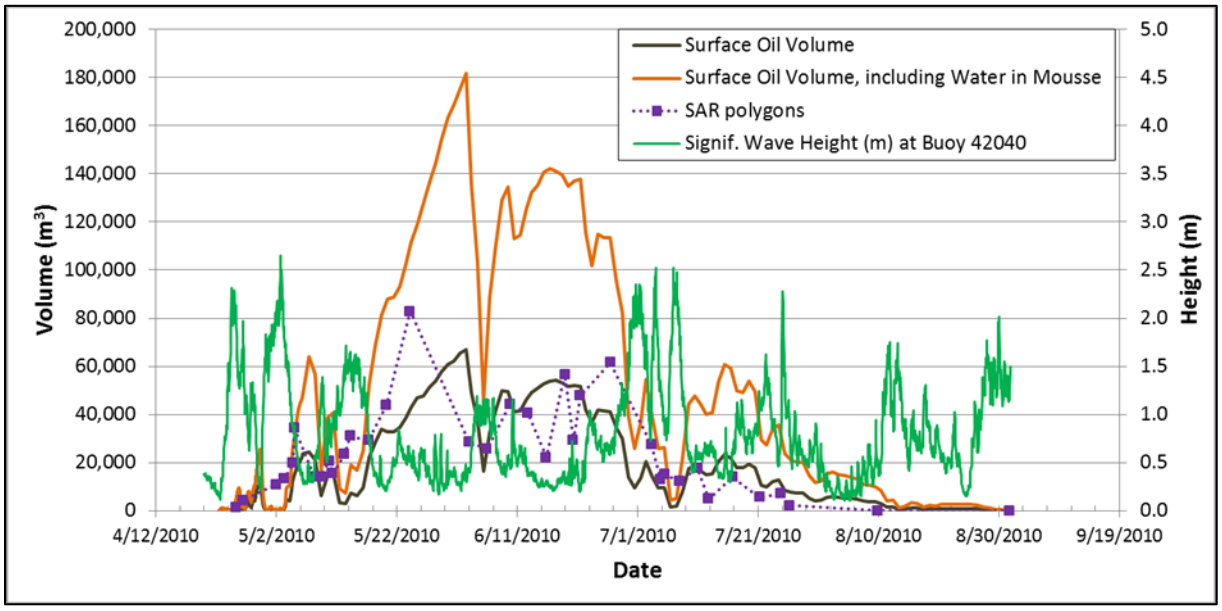

Figure 4-10. Model (base case) and SAR-based estimates of floating oil volume, with significant wave height recorded at buoy (42040).

4.2 Floating Oil

4.2.1 Remote Sensing Data Used for Model Comparisons

Derivations of the remote sensing data used for model comparisons are described in Section 3.3.1. Although remote sensing image acquisitions were focused on the DWHOS area during the emergency, not all images covered the entire extent of the surface oil, and satellite overpass periods were irregular. There were 34 SAR images where both TCNNA and OEDA analyses were performed (DWHOS Trustees 2016; ERMA 2016) and that were synoptic of the area of interest. Thus, these 34 SAR images were treated as statistical samples of the total surface oil, as were the 18 MVIS, 24 MTIR and 7 Landsat TM images analyzed by the DWHOS Trustees (2016; ERMA 2016) that were synoptic (or nearly so) of the area of floating oil (Table 4-6).

Graettinger et al. (2015) and MacDonald et al. (2015) aggregated the pixelated data as gridded data in a 5 x 5 km^2 geographic grid and developed statistical models to interpolate between observations in space and time. However, comparisons of the SIMAP model results to imagery results were made using the pixelated data based on the observational data, without use of the interpolations. These non-interpolated data were gridded in the same 5 km by 5 km grid used by the DWHOS Trustees (2016; Graettinger et al. 2015; ERMA 2016). The results are summarized in 34 SAR, 18 MVIS, 25 MTIR, and 7 Landsat TM maps, which are paired with gridded model results and presented in Annex C (attachments to Section C.3).

Table 4-6. Dates and times (local time, CDT) of 84 remote sensing products used for model comparisons.

Date/Time	Sensor	Date/Time	Sensor	Date/Time	Sensor	Date/Time	Sensor
4/25/10 6:50 AM	SAR_OEDA	5/11/10 1:55 PM	MVIS	6/10/10 11:17 AM	Landsat TM	7/3/10 6:56 AM	SAR_OEDA
4/25/10 1:55 PM	MTIR	5/13/10 6:51 AM	SAR_OEDA	6/10/10 2:05 PM	MTIR	7/4/10 11:18 AM	Landsat TM
4/25/10 1:55 PM	MVIS	5/14/10 6:51 AM	SAR_OEDA	6/10/10 2:05 PM	MVIS	7/4/10 6:47 PM	SAR_OEDA
4/26/10 10:58 AM	SAR_OEDA	5/17/10 6:45 AM	SAR_OEDA	6/12/10 1:50 PM	MVIS	7/5/10 10:58 AM	SAR_OEDA
4/29/10 11:55 AM	MTIR	5/17/10 11:18 AM	Landsat TM	6/12/10 1:55 PM	MTIR	7/7/10 10:44 PM	SAR_OEDA
4/29/10 1:30 PM	MVIS	5/17/10 11:40 AM	MTIR	6/12/10 6:56 PM	SAR_OEDA	7/10/10 10:49 PM	SAR_OEDA
5/1/10 10:51 PM	SAR_OEDA	5/17/10 11:40 AM	MVIS	6/15/10 6:41 PM	SAR_OEDA	7/11/10 11:04 AM	MTIR
5/3/10 6:53 AM	SAR_OEDA	5/20/10 6:56 AM	SAR_OEDA	6/18/10 11:40 AM	MTIR	7/12/10 11:17 AM	Landsat TM
5/4/10 1:45 PM	MVIS	5/20/10 1:45 PM	MTIR	6/18/10 1:50 PM	MVIS	7/12/10 2:05 PM	MTIR
5/4/10 1:50 PM	MTIR	5/20/10 1:45 PM	MVIS	6/18/10 10:41 PM	SAR_OEDA	7/12/10 2:05 PM	MVIS
5/4/10 6:57 PM	SAR_OEDA	5/23/10 1:55 PM	MVIS	6/19/10 2:00 PM	MTIR	7/12/10 6:53 PM	SAR_OEDA
5/4/10 10:57 PM	SAR_OEDA	5/23/10 2:20 PM	MTIR	6/20/10 6:52 AM	SAR_OEDA	7/14/10 1:55 PM	MTIR
5/8/10 6:59 AM	SAR_OEDA	5/24/10 11:45 AM	MTIR	6/20/10 11:30 AM	MTIR	7/14/10 1:55 PM	MVIS
5/9/10 10:50 AM	SAR_OEDA	5/24/10 11:45 AM	MVIS	6/21/10 11:13 AM	SAR_OEDA	7/16/10 6:45 PM	SAR_OEDA
5/9/10 11:17 AM	Landsat TM	5/24/10 6:57 PM	SAR_OEDA	6/23/10 1:35 PM	MTIR	7/20/10 11:18 AM	Landsat TM

Date/Time	Sensor	Date/Time	Sensor	Date/Time	Sensor	Date/Time	Sensor
5/9/10 2:05 PM	MTIR	5/27/10 1:55 PM	MTIR	6/24/10 11:05 AM	MTIR	7/20/10 11:40 AM	MTIR
5/9/10 2:05 PM	MVIS	5/27/10 1:55 PM	MVIS	6/26/10 11:17 AM	Landsat TM	7/21/10 6:55 AM	SAR_OEDA
5/10/10 11:35 AM	MTIR	6/2/10 10:44 PM	SAR_OEDA	6/26/10 11:25 AM	SAR_OEDA	7/21/10 2:00 PM	MTIR
5/10/10 11:35 AM	MVIS	6/5/10 10:49 PM	SAR_OEDA	6/26/10 2:05 PM	MTIR	7/21/10 2:00 PM	MVIS
5/10/10 6:53 PM	SAR_OEDA	6/7/10 12:00 PM	MTIR	6/26/10 2:05 PM	MVIS	7/24/10 7:05 PM	SAR_OEDA
5/11/10 7:03 AM	SAR_OEDA	6/9/10 6:50 PM	SAR_OEDA	6/27/10 11:03 AM	MTIR	7/26/10 6:56 AM	SAR_OEDA

4.2.2 Model Results

The fates model results of surface floating oil were compared to observed surface oil locations based on remote sensing information (Sections 3.3.1 and 4.2.1; Table 4-6) and other field data, as available. For the base case (using HYCOM-FSU currents and NARR winds), surface oil trajectory figures, showing snapshots of the modeled spillets' movements over time color-coded by time since release, show the oil pathway and indicate degree of weathering (Annex C, Figures C.1-1 to C.1-9). The modeled weathering of floating oil, as compared to field observations, is discussed in Section 4.2.7.

Surface oil distributions, as snapshots over time predicted by the model and based on remote sensing data, are shown in map figures comparing the two in Annex C, Section C.3 (see attachments, as listed in Table C-1). Figures C.2-1 to C.2-42 summarize the oiled footprints (north of 27°N) as cumulative days of oil presence on the water surface, maximum amount of oil, and mean amount of oil in each grid cell over the simulation.

Figure 4-11 summarizes the trajectory of the floating oil for the base case simulation using HYCOM-FSU currents and NARR winds, plotting number of days of oil presence using a 5 km by 3 km grid similar in resolution to the 5-km grid used by the DWHOS Trustees in summarizing the remote sensing data. Figure 4-12 maps the modeled maximum amount of oil in each grid cell at any time in the simulation (as g/m^2 averaged over the grid cell), which provides a summary of the pathways of the floating oil. Figure 4-13 maps the mean floating oil concentration (g/m^2) in each cell for the period when oil was observed by SAR, 24 April to 3 August 2010. Figure 4-11 may be compared to the SAR-based (Figure 3-1) and four sensor-based (Figure 3-3) summaries prepared by the DWHOS Trustees. Figure 4-13 may be compared with Figure 3-2 from MacDonald et al. (2015). Similar figures for other primary model simulations are in Annex C, Section C.2 (Figures C.2-1 to C.2-42), of this Volume II, and these may also be compared with Figures 3-1, 3-2 and 3-4.

The remote sensing data indicate the floating oil was primarily in a fairly circular area near and just north of the DWHOS wellhead. The simulations using HYCOM-FSU (Figures C.2-1 to C.2-3), HYCOM-NRL, Reanalysis (Figures C.2-4 to C.2-6), and IAS ROMS (Figures C.2-19 to C.2-21) show a similar pattern. The results of the simulations with other currents (Figures C.2-7 to C.2-18 in Annex C.2) show excursions too far northeast (SABGOM, NCOM Real-time), and too much dispersion in all directions (HYCOM-NRL, Real-time; NGOM). The three simulations using no currents and NAM, NARR or NOGAPS winds (Figures C.2-22 to C.2-30) are similar, and all three do not have enough transport of the floating oil to the east toward Florida or to the west towards western Louisiana and Texas. Otherwise, the no-current simulations result in realistic floating oil patterns centered just north of the wellhead. The simulation using ADCP currents and NARR winds generates results very

similar to no currents and NARR winds, because the ADCP currents are relatively weak in the offshore area and do not cover the shelf or nearshore (Figures C.2-31 to C.2-33). These results indicate the importance of the winds in transporting the floating oil, but that the currents used can change the patterns quite dramatically.

Figures C.2-34 to C.2-42 in Annex C.2, compared to Figures 4-11 to 4-13, show the effects of SSDI and the assumed relative effectiveness of the SSDI. Assuming no SSDI results in much more floating oil than the base case. Use of the low and high effectiveness assumptions for SSDI (see Section 2.8.3) results in more subtle but discernable changes in the amounts of thicker floating oil on the water.

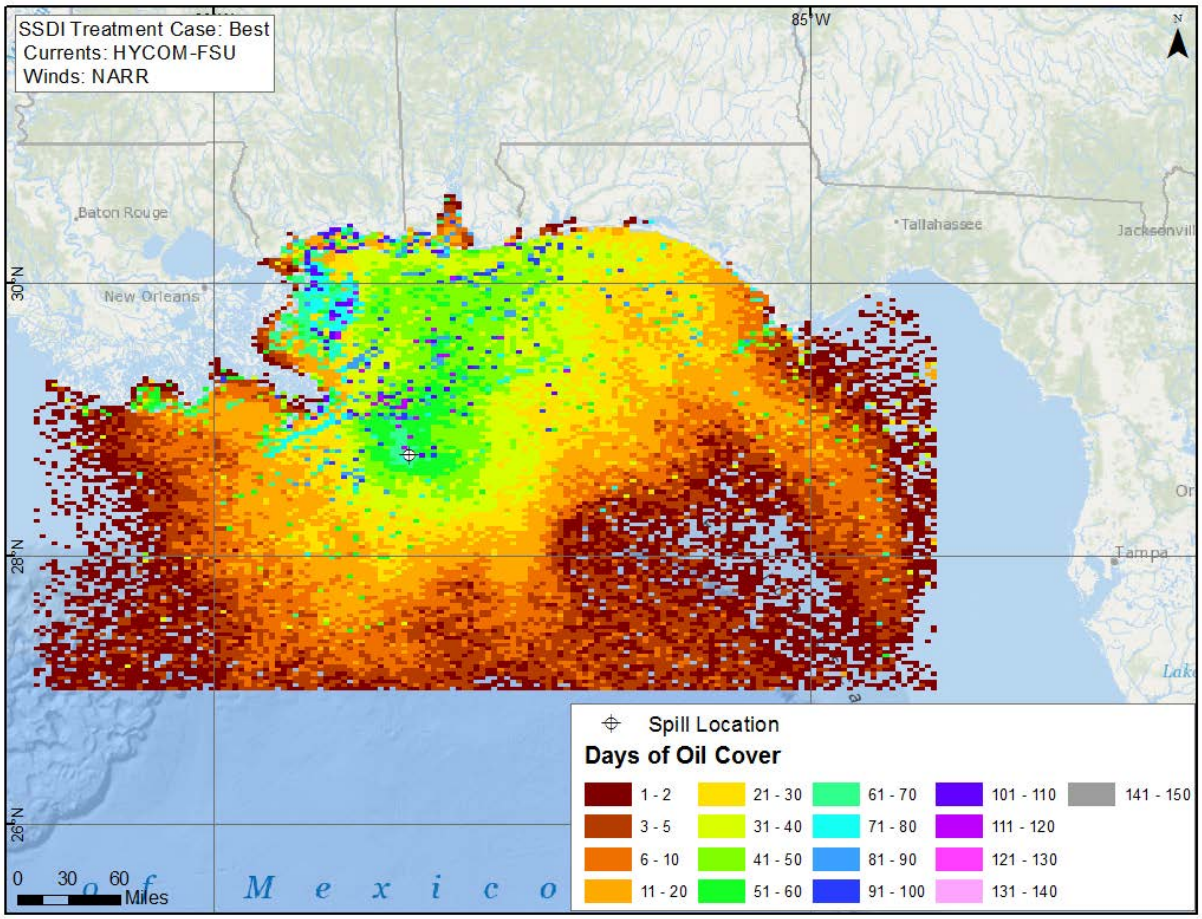

Figure 4-11. Cumulative days of oil presence on the water surface, based on the base case model simulation.

The modeled number of days of oil cover (Figure 4-11) is of the same range as the SAR-based estimates (Figure 3-1) around the wellhead and off the Louisiana delta. However, the duration of oil cover in the area near the coast of Mississippi and Alabama is higher in the

model than the SAR data indicate. Also, floating oil trapped near shore in the model remained longer than observed. Mechanical removal, on water or on shorelines, was not included in the simulations, and this could potentially account for the observed reduction in the nearshore floating oil.

The modeled time-averaged mean oil cover shown in Figure 4-13 is similar in pattern and of the same magnitudes as the estimates in Figure 3-2 based on SAR analysis. The units of volume per area (m^3/km^2) are equivalent to g/m^2, assuming the oil density is 1 g/cm^3.

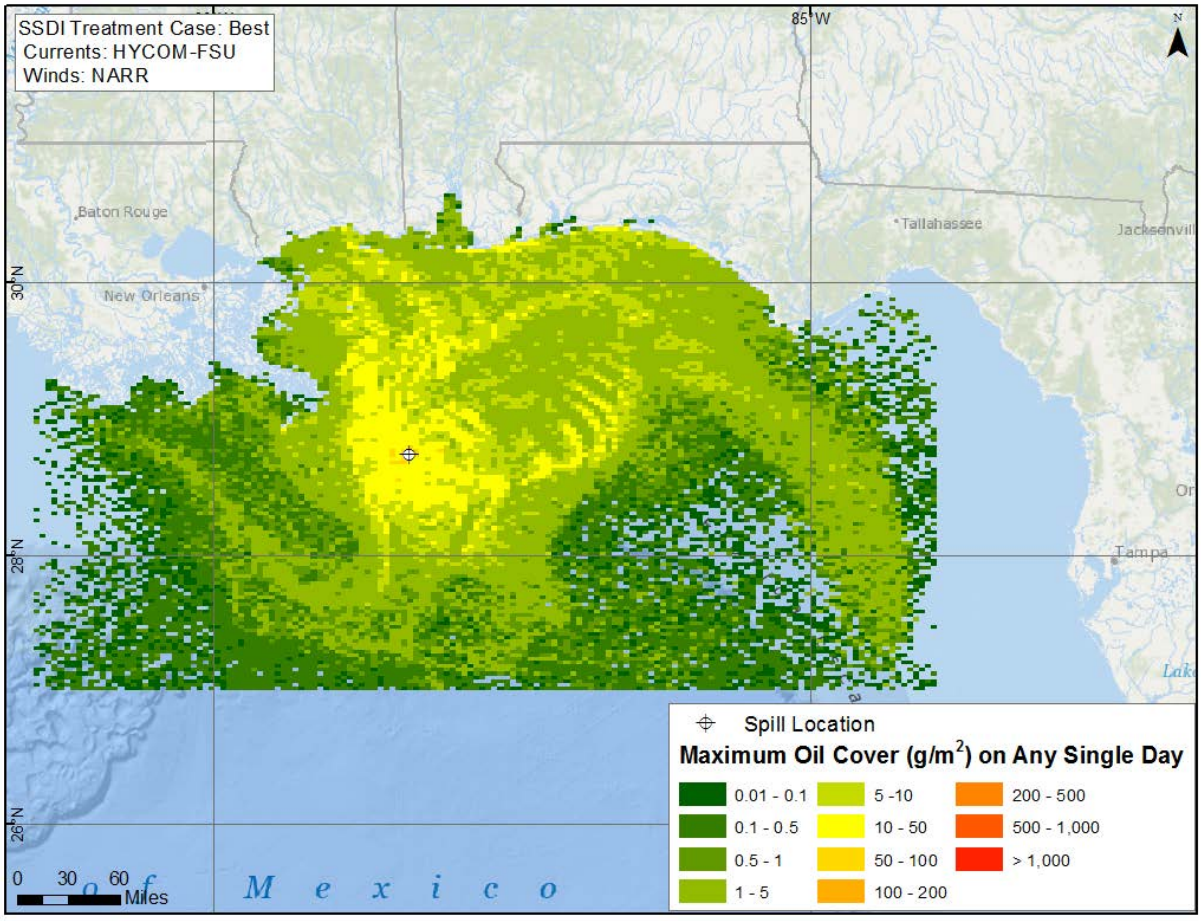

Figure 4-12. Modeled maximum amount of oil in each grid cell at any time in the simulation (as g/m^2 averaged over the grid cell), based on the base case model simulation.

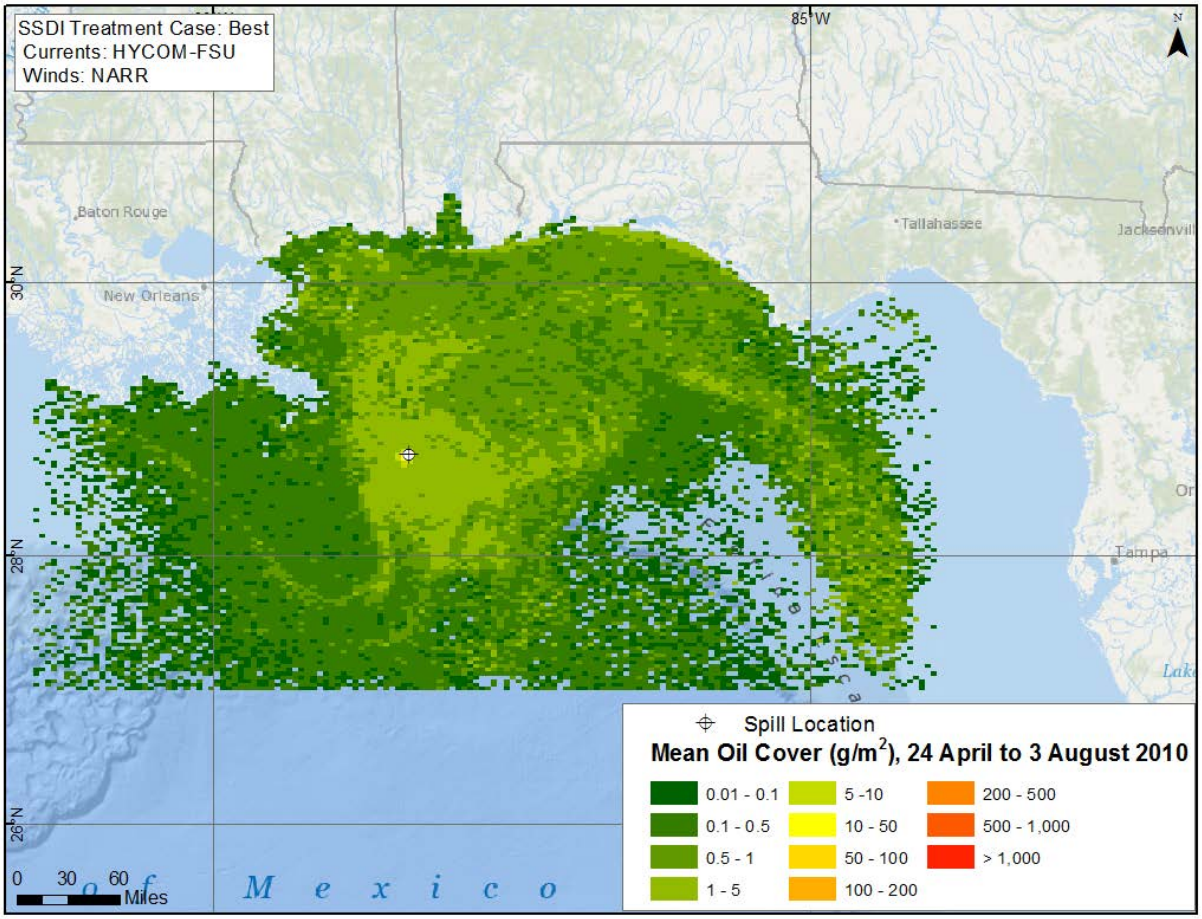

Figure 4-13. Time-averaged mean floating oil concentration (g/m2) in each cell for the period when oil was observed by SAR, 24 April to 3 August 2010, based on the base case model simulation.

Note that the gridded summaries of floating oil distributions, both for the model and for the remote sensing data, provided average amounts of oil mass over the cell area. They should not be interpreted as an actual oil thickness, as the oil is in reality patchy and of varying thicknesses within the cells. The remote sensing data are typically expressed as volumes per cell (e.g., Figure 3-2) for this reason. Furthermore, the total area of the cells where oil is present is larger than the actual oil coverage at any given time.

Annex C (attachments to Section C.3) contains comparisons of the modeled floating oil distributions with remote sensing products on dates and times when the remote sensing products were available. The SAR and MODIS coverages were typically synoptic views, or nearly so; however, the Landsat TM coverages were incomplete. This should be kept in mind when reviewing the results.

The comparisons of the primary model simulations to the remote sensing show generally good agreement, although there are displacements on some dates, and the degree of displacement varies with the primary forcing data, the winds and currents. Overall, the base case using HYCOM-FSU currents and NARR winds shows the best agreement with the remote sensing data. The simulation using HYCOM-NRL Reanalysis currents and CFSR winds is similar to that using the HYCOM-FSU currents and NARR winds. The IAS ROMS (hourly) simulation using NAM winds is an improvement over SABGOM (run with NARR winds), as SABGOM transports too much oil past Apalachicola and into the Big Bend area of Florida. IAS ROMS was derived from SABGOM, and includes data assimilation (see Section 2.2.3.2) of the ADCP data described in Section 2.2.3.1.

The model simulations using no currents replicate well the areas exposed to oil in the offshore and east of the bird's foot Delta area of Louisiana. However, the modeled transport of oil to the near-shore area west of the Bird's Foot appears to be less than indicated by the SAR remote sensing products. Sharma et al. (2010) noted that the winds from NDBC buoy 42040 showed periods of sustained winds in June and July that established strong westward coastal flows. These are observed in the surface drifter data they examined. Those near shore current features need to be replicated in current data in order to simulate that transport. Similarly, the trajectories without currents do not capture the eastward coastal movement of oil in late June indicated by the SAR data (see attachments to Annex C, Section C.3). However, the general patterns of the observed oil movements and majority of shoreline oiling are predicted in simulations using only the wind forcing and no current data, demonstrating the importance of the accuracy of the modeled winds used for simulations.

4.2.3 Methods for Comparison of Model to Observations

The modeled and observed oil distributions were gridded at each time a remote sensing map was available. The percentage of floating oil present in each grid cell was calculated as follows.

- The **relative area** of oil in each grid cell evaluates the distribution of oil cover, without the need to estimate oil thickness or volume from the satellite imagery:
    - Remote sensing data: The area of oil in the cell, calculated from the percentage of the cell covered by oil, was divided by the total area of oil in all cells estimated from the imagery.
    - Model: The area covered by spillets falling in the cell was divided by the total area of all floating spillets at that time step. (Area of each spillet, treated as a circle with a spillet-specific radius, was apportioned to multiple cells if they overlapped the cell edges. Overlaps of spillets within a cell were accounted for, i.e., the area in common that was covered was only counted once.)

- The **relative volume** of oil in each grid cell accounts for the relative distribution of thick versus thin oil:
    - Remote sensing data: The volume of oil in the cell, calculated from the area covered by each thickness category and the assigned mean thickness, was divided by the total volume of oil in all cells estimated from the imagery.
    - Model: The total mass in spillets falling in the cell was divided by the total mass of all floating spillets in all cells at that time step. The mass was not corrected for oil density to convert to volume. Thus, all spillets were assumed to be of equal density at a given time step.
- The **estimated volume of oil** in each grid cell was calculated as follows:
    - Remote sensing data: The volume of oil in the cell was calculated from the area of the cell covered by each thickness category and the assigned mean thickness.
    - Model: The total mass in spillets falling in the cell that time step. (Mass in each spillet was apportioned to multiple cells if they overlapped the cell edges.) The mass was not corrected for oil density to convert to volume. Thus, all spillets were assumed to be of equal density at a given time step.

Using the set of grids created from SIMAP output (modeled grids) and the remote sensing grids (observed grids), matching the closest date and time for each observation, the Root Mean Square Error (RMSE) was calculated for each date and time there was an observation available. The RMSE is a frequently-used measure of the differences between values predicted by a model and the values actually observed, and thus is a measure of accuracy. These individual differences are also called residuals, and the RMSE serves to aggregate them into a single measure of predictive power (Fitzpatrick 2009). For each pair of grids, the RMSE was calculated by summing the squares of the differences between modeled and the observed over all cells of the grid, where $\boldsymbol{n}$ = total number of cells in each grid:

$$\mathbf{RMSE} = \sqrt{\frac{\sum(\mathbf{observed} - \mathbf{modeled})^2}{\boldsymbol{n}}}$$

RMSE values were plotted for each date over time, and also summed for all dates, in order to judge relative fit comparing dates and/or among simulations, the minimum RMSE indicating the best fit. For example, Figures 4-14 and 4-15 show the RMSE calculated for relative area (fraction), relative volume (fraction) and oil volume (m^3), at the date and time

of each remote sensing observation for the base case model simulation. The RMSEs for relative area and relative volume are small fractions, <0.0025, indicating overall good agreement of the model and observations. The results show the best agreement in terms of relative area or volume distribution in early June, whereas the modeled estimated volume of oil was most similar to the remote-sensing based estimates in April-early May and in July. The results for other current-wind combinations showed similar temporal patterns. These results are discussed in more detail in the next section.

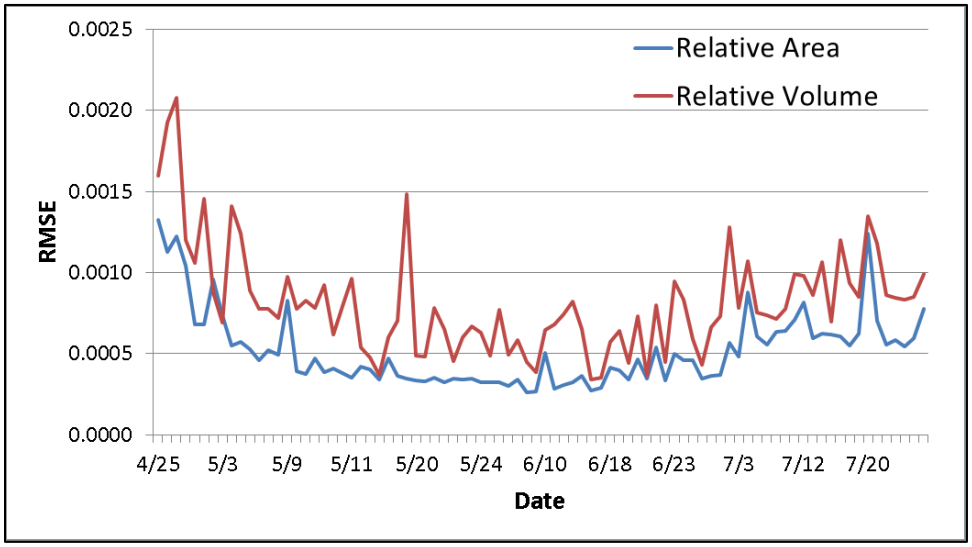

Figure 4-14. RMSE of relative area and relative volume (fractions) for the base case model simulation (using HYCOM-FSU) compared to remote sensing coverages.

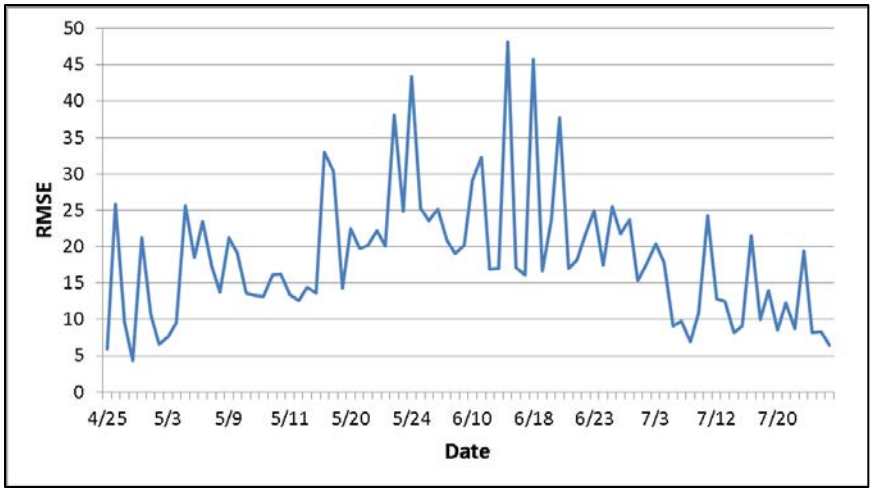

Figure 4-15. RMSE of oil volume (m^3) for the base case model simulation (using HYCOM-FSU) compared to remote sensing coverages.

4.2.4 Comparison to Oil Observations by Remote Sensing

Figure 4-14 shows that the (base case) modeled relative spatial coverage of oil was in less agreement with the remote sensing in April and July, and in better agreement during May and June. The relatively high RMSE values for spatial coverage in April were because the modeled distribution remained more localized around the wellhead than the remote sensing indicated. The relatively high RMSE value for relative volume on May 17 was for the MODIS visual image of that date, when the "Tiger Tail" feature (i.e., the extension to the southeast as oil sheen was drawn into a Loop Current ring) was seen in the imagery (Walker et al. 2011, Olascoaga and Haller 2012) but not indicated by the model (i.e., the hydrodynamic model did not locate the ring edge in the same location at that time).

In contrast, the volume RMSE (Figure 4-15) shows the better agreement in April and July and less agreement of the base case with the remote sensing in May and June. This is due to more predicted displacement (advection) of the thick oil in the model compared to the observed in May and June than in April or July, reflecting the currents and winds used to force the transport. These temporal trends were similar for other primary model simulations.

Table 4-7 lists, for all model runs, the mean RMSE over all dates of comparison, based on each of relative area, relative volume, and estimated volume of oil. Those runs used to evaluate sensitivity to the floating oil horizontal dispersion coefficient (varied in the range 5–200 m^2/s) are shaded in light grey at the top of the table. The mean RMSE decreased with increasing horizontal dispersion coefficient, indicating the largest rates tested resulted in the most agreement between the model and the remote sensing data. Runs listed as "Best (Hi)" under SSDI treatment were initialized with 800,000 spillets, while the rest of the runs were initialized with 100,000 spillets. Use of 800,000 spillets instead of 100,000 spillets slightly improved the model agreement with the observed, as the additional spillets filled in some of the areas where remote sensing data indicated oil was present.

Most of the variation in the mean RMSE was related to the currents and winds used for the simulation, as demonstrated by the results for the primary model runs, listed in unshaded rows in Table 4-7. The best agreement to the remote sensing data overall (minimum mean RMSE using all three metrics) was using HYCOM_FSU currents and NARR winds. IAS ROMS showed second best agreement to the remote sensing in terms of the relative spatial distribution of floating oil (second lowest set of mean RMSE values for relative area and relative volume). However, the HYCOM-NRL Reanalysis with CFSR winds showed the same degree of agreement with the remote-sensing data as the HYCOM_FSU/NARR simulation in terms of oil volume distribution (based on mean RMSE for volume, Table 4-7). As noted above, SABGOM moved much more oil northeast towards Florida in June than did other

hydrodynamics (see attachments to Annex C, Section C.3). The HYCOM-NRL real-time hydrodynamics transported more oil southeast towards southern Florida than was observed in the remote sensing. The tan rows at the bottom of the table show poorer agreement of the model with the floating oil distributions in remote sensing products when no currents and only winds are used, than for when any of the hydrodynamic models are used. The NAM winds, when used without currents, resulted in the best agreement between modeled and observed, while NOGAPS resulted in the lowest agreement (highest mean RMSE). Use of ADCP data for surface transport (extrapolated from below 40 m and from offshore stations where ADCPs recorded data) resulted in better agreement to the observational data than without currents, but there was no ADCP data on the shelf or nearshore, such that along-shore transport was not captured. Thus, the simulations using hydrodynamic modeled currents produced better agreement with the observed floating oil distributions than simulations using ADCP data for currents. However, as will be discussed in Section 4.4.1, modeled oil distributions below 40 m were in better agreement with observational data than simulations using any of the hydrodynamic models.

The movements of floating oil are the result of ocean currents, tidal currents (more important near shore), wind-forced currents and wave-induced transport. The hydrodynamic models do not resolve the Stokes Drift in the upper wave-mixed layer resulting from wave motions and Ekman flow induced by the wind. Simulations using the Youssef and Spaulding (1993, 1994) model (see Appendix II, Annex A, Section 2.1.3 for a description of the wind drift model) of these processes, as well as varying percentages-of-wind-speed drift rates and angles to the right of downwind, were examined to determine sensitivity and identify the inputs yielding the best agreement to the remote sensing data.

The results of the wind drift sensitivity analysis (not shown) were that the best fit was consistently that using the Youssef and Spaulding (1993, 1994) model algorithm, as opposed to using a constant wind drift percentage and angle for all dates, although the differences between the results were not large on most days. Of the tests varying an assumed constant percentage of wind speed and angle to the right of downwind, 3% and 0 angle showed the best agreement to the remote sensing data; hence the mean RMSE results for this set of runs is included in Table 4-7 (denoted as “3% wind speed”). Moreover, there was much more variation between runs with different currents and winds used for forcing than the differences due to variation in wind drift model or the horizontal dispersion coefficient (Table 4-7). Thus, variation of wind drift and horizontal dispersion coefficient assumptions was not examined further.

Table 4-7. RMSE (mean over all dates) comparing model to remote sensing data for floating oil distributions.

SSDI Treatment Case	Currents	Winds	Wind Drift Model	Floating Oil Horizontal Dispersion Coefficient (m^2/s)	RMSE: Relative Area	RMSE: Relative Volume	RMSE: Volume
Best	SABGOM	NARR	Modeled	5	0.00062	0.00102	23.0
Best	SABGOM	NARR	Modeled	10	0.00062	0.00101	22.5
Best	SABGOM	NARR	Modeled	50	0.00059	0.00094	20.4
Best	SABGOM	NARR	Modeled	100	0.00058	0.00090	19.3
Best	SABGOM	NARR	Modeled	200	0.00055	0.00085	18.5
Best	HYCOM-FSU	NARR	Modeled	5	0.00056	0.00091	19.8
Best	HYCOM-FSU	NARR	Modeled	10	0.00056	0.00089	19.4
Best	HYCOM-FSU	NARR	Modeled	50	0.00054	0.00084	18.0
Best [Base Case]	HYCOM-FSU	NARR	Modeled	100	0.00053	0.00082	17.3
Best	HYCOM-FSU	NARR	Modeled	200	0.00051	0.00080	16.8
Best (Hi)	HYCOM-FSU	NARR	Modeled	100	0.00052	0.00080	17.7
Best (Hi)	HYCOM-NRL, Real-time	NARR	Modeled	100	0.00058	0.00087	18.9
Best (Hi)	SABGOM	NARR	Modeled	100	0.00056	0.00087	19.7
Best (Hi)	NGOM-NOAA, Real-time	NARR	Modeled	100	0.00058	0.00087	18.2
High	HYCOM-FSU	NARR	Modeled	100	0.00052	0.00080	17.7
Low	HYCOM-FSU	NARR	Modeled	100	0.00054	0.00083	19.6
None	HYCOM-FSU	NARR	Modeled	100	0.00054	0.00084	20.2
Best [Base Case]	HYCOM-FSU	NARR	Modeled	100	0.00053	0.00082	17.3
Best	HYCOM-FSU	NARR	3% wind speed	100	0.00052	0.00082	19.0
Best	ADCP	NARR	Modeled	100	0.00068	0.00107	21.6
Best	SABGOM	NARR	3% wind speed	100	0.00056	0.00090	22.0
Best	SABGOM	NARR	Modeled	100	0.00057	0.00090	21.2

SSDI Treatment Case	Currents	Winds	Wind Drift Model	Floating Oil Horizontal Dispersion Coefficient (m^2/s)	RMSE: Relative Area	RMSE: Relative Volume	RMSE: Volume
Best	HYCOM-NRL, Reanalysis	CFSR	Modeled	100	0.00061	0.00100	17.3
Best	HYCOM-NRL, Real-time	NARR	3% wind speed	100	0.00059	0.00089	19.8
Best	HYCOM-NRL, Real-time	NARR	Modeled	100	0.00058	0.00088	19.4
Best	NCOM Real-Time	NARR	Modeled	100	0.00060	0.00090	21.3
Best	NGOM-NOAA, Real-time	NARR	3% wind speed	100	0.00058	0.00088	19.5
Best	NGOM-NOAA, Real-time	NARR	Modeled	100	0.00059	0.00088	19.1
Best	IAS ROMS-hourly	NAM	Modeled	100	0.00056	0.00087	19.7
Best	IAS ROMS-12 hourly	NAM	Modeled	100	0.00057	0.00090	20.3
Best	none	NAM	Modeled	100	0.00070	0.00104	22.9
Best	none	NARR	Modeled	100	0.00072	0.00109	25.3
Best	none	NAM	3% wind speed	100	0.00074	0.00109	25.2
Best	none	NARR	3% wind speed	100	0.00079	0.00118	27.4
Best	none	NOGAPS	3% wind speed	100	0.00080	0.00118	28.9
Best	none	NOGAPS	Modeled	100	0.00075	0.00112	25.5

The details of the comparisons may be seen in the paired figures of the model results and remote sensing data in Annex C (attachments to Section C.3). Perusal of the figures gives the viewer the sense that the modeled floating oil is in the general vicinity of the observed. As model simulations were free running, with no updates during the simulation to match observations, transport errors accumulated over the model runs. Given this approach and the fact that the simulations evaluating floating oil were run 131 days, the agreement between the model and the observed is quite good.

4.2.5 Areas Exposed to Floating Oil

It is important to recognize that the oil is not continuous in the 25 km^2 area of the remote sensing grid cells presented (Figures 3-1, 3-2, 3-4 and in attachments to Section C.3 of Annex C), but rather is patchy within them, and so the total area for the remote sensing in the grids is an over-estimate of the actual area oiled at a single instant in time. Resolution of individual pixels depended upon the satellite and collection mode, but was generally in the range of 25–1,000 m (625 m^2–1 km^2). The TCNNA processing of a SAR image yielded a set of pixels (typically ~100 x 100 m, 10,000 m^2) that were classified as oil-covered water (MacDonald et al. 2015). MODIS visual had a pixel resolution of 250 m or 500 m, depending on the spectral band. The MODIS sensors collect TIR data at a pixel resolution of 1,000 m (1 km^2). Landsat TM satellite data have a pixel resolution of about 30 m (900 m^2). Thus, the areas of oil coverage in the remote sensing products were at these resolutions if processed at the pixel level, or larger if gridded.

Combining all results using 25 km^2 grid cells from 24 April to 3 August 2010, MacDonald et al. (2015) estimated the aggregated floating oil and oil emulsion footprints extended over an area of 149,000 km^2, from offshore Louisiana west of the Mississippi River Delta and east northeast across the DWHOS site to the Florida Panhandle (Figure 3-2). The TCNNA composite in Figure 3-1 had a surface area of 112,115 km^2 (ERMA 2016). The daily footprint areas were much smaller than the cumulative area and were variable in size and location. The daily average footprint area was 11,200 km^2 (standard deviation (SD) 8,430; maximum 28,400 km^2) using 25 km^2 grid cells (MacDonald et al. 2015).

Similarly, the gridded model areas used to compare to the remote sensing products average the oil mass in the spillets over the grid cell, when in the model they are actually simulated as patches of oil in these spillets. Using grid cells of 15 km^2 area, the modeled daily estimates of floating oil exposure, averaged over the same date range, are presented in Table 4-8 (all runs use modeled wind drift and 100 m^2/s horizontal dispersion coefficient for floating oil). The results for the base case (HYCOM-FSU and NARR with Best SSDI) model run are compared to SAR and MVIS in Figure 4-16. The base case modeled areas exposed with an average of greater than 1.0 g/m^2 (mean 6,720 km^2; SD 4,960 km^2) are not significantly different from the remote sensing daily estimate (11,200 km^2; SD 8,430 km^2) for nominally >1 g/m^2, or from other simulations with various currents and winds used for forcing (Table 4-8). The case using HYCOM-FSU and NARR, without SSDI (Table 4-8), results in larger areas of exposure greater than 1 g/m^2, but *using gridding*, this difference is not significant. Note that for the best SSDI case, after mid-June, there was sufficient dispersant used in the SSDI to treat 30% of the release at a DOR near the target of 1:100. Thus, even with SSDI, 70% or more of the oil was estimated to be untreated (Spaulding et al. 2015, 2017) and rose the surface within hours.

For both model predictions and observed estimates based on remote sensing data, other areal estimates would result from different grid cell resolutions. The exposure areas would be larger with use of larger grid cells, and the average “thickness” would be lower.

Table 4-8. Average area (km^2) followed by standard deviation of sea surface exposed daily to floating oil from 24 April to 3 August 2010, calculated using 15 km^2 grid cells.

SSDI Treatment Case	Currents	Winds	Average Area with Threshold (0 g/m^2)	Average Area with Threshold (0.1 g/m^2)	Average Area with Threshold (1 g/m^2)	Average Area with Threshold (10 g/m^2)	Average Area with Threshold (100 g/m^2)
None	HYCOM-FSU	NARR	30,400 (15,300)	22,400 (12,400)	7,580 (5,180)	275 (289)	0.11 (1.3)
Low	HYCOM-FSU	NARR	32,500 (15,600)	23,700 (13,400)	7,480 (5,500)	242 (258)	0.07 (1.03)
High	HYCOM-FSU	NARR	32,100 (15,400)	25,300 (13,800)	7,020 (5,500)	139 (199)	0 (0)
Best [Base Case]	**HYCOM-FSU**	**NARR**	**32,700 (15,400)**	**23,700 (12,700)**	**6,720 (4,960)**	**196 (231)**	**0.036 (0.73)**
Best	ADCP	NARR	18,100 (9,080)	13,400 (6,820)	5,380 (3,280)	385 (411)	1.3 (5.1)
Best	SABGOM	NARR	29,200 (13,400)	19,800 (9,770)	5,730 (4,260)	239 (308)	0.41 (3.1)
Best	HYCOM-NRL, Re-analysis	CFSR	25,000 (14,900)	18,500 (12,000)	5,220 (4,870)	200 (328)	0.52 (4.1)
Best	HYCOM-NRL, Real-time	NARR	26,500 (10,800)	18,700 (8,210)	5,240 (3,450)	245 (233)	0 (0)
Best	NCOM Real-Time	NARR	34,100 (11,500)	14,400 (4,390)	4,010 (2,790)	327 (341)	0.036 (0.73)
Best	NGOM-NOAA, Real-time	NARR	22,600 (7,880)	15,180 (5,770)	4,490 (2,910)	312 (338)	0 (0)
Best	IAS ROMS-hourly	NAM	25,600 (8,900)	17,000 (6,500)	5,230 (3,540)	309 (305)	0.36 (2.4)
Mean and SD of the Means: Best (only)	Hydrody-namic Model Cases (only)	(as above)	28,000 (4,230)	18,200 (3,120)	5,230 (867)	261 (55)	0.20 (0.23)

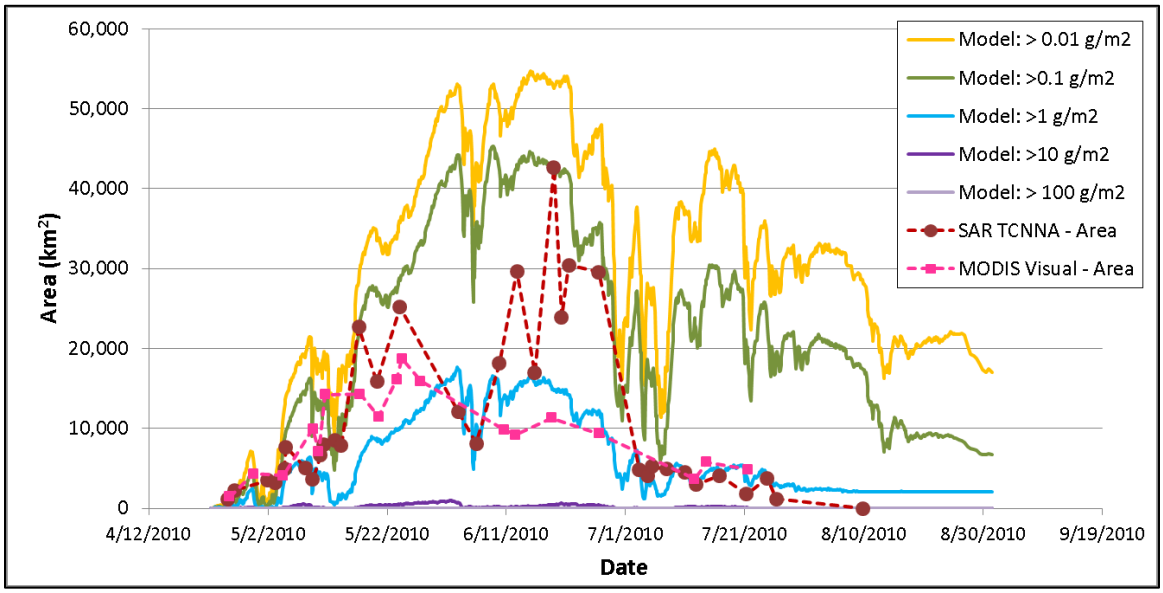

Figure 4-16. Surface area exposed, using 15 km^2 grid cells, for the base case model run compared to SAR and MVIS remote sensing product data.

To evaluate the surface area exposed at any single instant in time, one should consider the patchiness of the oil. In a gridded presentation, the average volume and area equivalent to a thickness of sheen is not actually continuous sheen, but patchy thicker oil and sheens with open water areas. Averaging over a cell area makes it appear that sheens are more continuous than they are in reality. This issue was recognized by MacDonald et al. (2015) and the DWHOS Trustees, and they processed the gridded data to record fractions of the cell covered by different thickness categories (Graettinger et al. 2015). However, this detail is difficult to present in simple maps, such as those in Figures 3-1, 3-2 and 3-4.

The sum of the area covered by spillets at a single time step provides the modeled area covered by oil at any instant in time (Figure 4-17). Summing the area swept between time steps (as the isosceles trapezoid defined by the circular spillet's radius at the prior time step, the radius at the present time step, and the distance moved), yields a metric quantifying exposure to floating oil (Table 4-9). The areas covered by oil spillets (i.e., oil patches, Figure 4-17) were an order of magnitude lower than those estimated from the gridding (Figure 4-16), i.e., patches average about 10% of the oil cover in a cell. The areas swept by oil are variable, depending on the currents and winds used. The mean swept area from 24 April to 3 August 2010 (101 days) was 1,960 km^2/day for the model base case. The swept area for the thick oil (>100 g/m^2) was significantly higher for the model run without SSDI, as compared to those run with SSDI (Table 4-9).

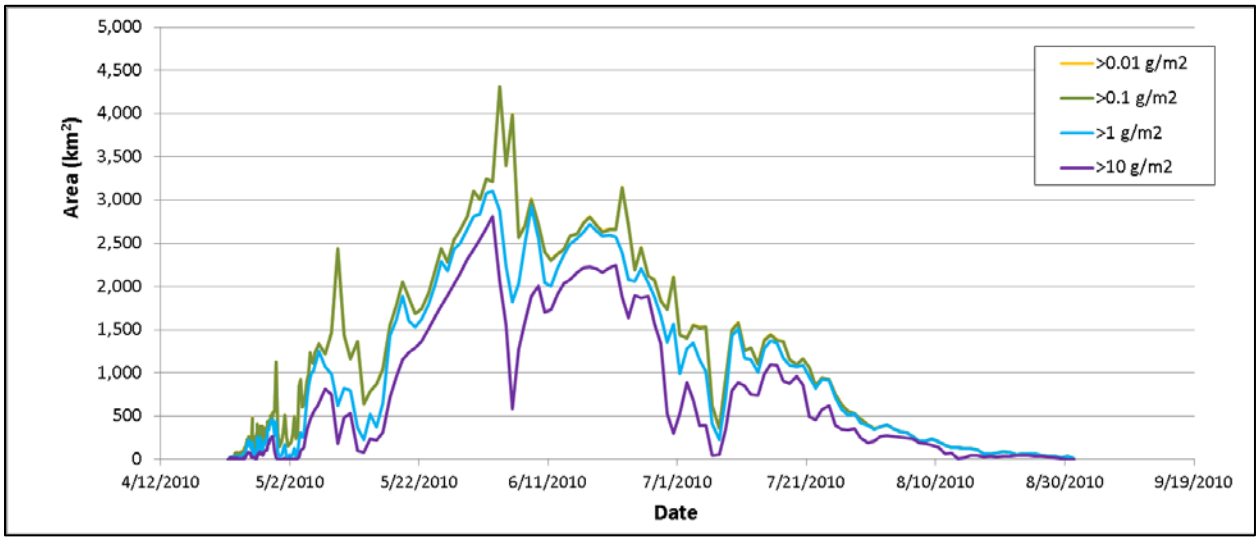

Figure 4-17. Area covered by spillets above specified thresholds at each time step for the base case model run.

Table 4-9. Sum of area swept (thousands of km^2-days) by floating oil based on areas and movements of modeled spillets, with no gridding used.

SSDI Treatment Case	Currents	Winds	Sum of Area Swept with Threshold (0 g/m^2)	Sum of Area Swept with Threshold (0.1 g/m^2)	Sum of Area Swept with Threshold (1 g/m^2)	Sum of Area Swept with Threshold (10 g/m^2)	Sum of Area Swept with Threshold (100 g/m^2)
None	HYCOM-FSU	NARR	206	206	203	165	17
Low	HYCOM-FSU	NARR	220	220	216	181	10
High	HYCOM-FSU	NARR	216	216	210	180	6
Best [Base Case]	HYCOM-FSU	NARR	198	197	194	161	12
Best	ADCP	NARR	158	158	154	120	9
Best	SABGOM	NARR	196	196	192	160	13
Best	HYCOM-NRL, Re-analysis	CFSR	202	202	198	162	10
Best	HYCOM-NRL, Real-time	NARR	193	193	189	178	14

SSDI Treatment Case	Currents	Winds	Sum of Area Swept with Threshold (0 g/m^2)	Sum of Area Swept with Threshold (0.1 g/m^2)	Sum of Area Swept with Threshold (1 g/m^2)	Sum of Area Swept with Threshold (10 g/m^2)	Sum of Area Swept with Threshold (100 g/m^2)
Best	NCOM Real-Time	NARR	166	166	161	153	11
Best	NGOM-NOAA, Real-time	NARR	239	238	234	219	14
Best	IAS ROMS-hourly	NAM	174	174	170	161	14
Mean and SD of the Means: Best (only)	Hydrody-namic Model Cases (only)	(as above)	195	195	191	171	13

As guidance for evaluating the model results based on the spillet areas, floating oil of 1 g/m^2 is about 1 μm thick (on average) and appears as sheen. Table 3-3 gives approximate thickness ranges for surface oil of varying appearance based on NOAA (2016) and the Bonn Agreement (2009); the scheme by NRC (1985) being similar. Crude oil >200 μm thick appears as black or blown oil. Once crude oils are emulsified as mousse, their color typically changes to orange or red, as was the case with the MC252 oil. Floating oil does not have these appearances indefinitely, however, as weathered oil would be in the form of scattered floating tar balls and tar mats where currents converge.

Note that in the model output displays and figures in Annex C (including the attachments), the floating oil mass is gridded and the mass is averaged over the 15 km^2 grid cell. The g/m^2 averages by grid cell should not be construed as an oil thickness with these appearances.

4.2.6 Floating Oil Weathering

Most of the oil surfaced within a 2-km radius of the wellhead in April, and within a 5-km radius in May–July. This is consistent with observations by Ryerson et al. (2012). Payne and Driskell (2015d) reported fresh oil surfacing between 1.5 and 4 km from the wellhead.

The age of the floating oil spillets, defined as hours since release at the trap height of the near-field plume, provides an indication of the degree of weathering the oil has undergone since release. Figures C.1-1 to C.1-9 in Annex C (Section C.1) show snapshots from the base

case simulation. In April 2010 (Figure C.1-1), most of the floating oil was relatively fresh (< a few days old), due to the rapid surfacing time of the large oil droplets released at that time and the two storms (see Figure 4-5) that entrained and dispersed oil into the water column. In May, June, and the first half of July, the freshest oil was offshore near the wellhead and trending toward the Louisiana delta (e.g., bird's foot); oil near the Mississippi, Alabama, and Florida coastlines was well weathered (over 7 days old, Figures C.1-2 to C.1-7). In late July and August, the oil remaining floating was highly weathered (Figures C.1-8 and C.1-9).

The average density and viscosity of the subsurface oil droplets in the model simulations increased over time as a higher percentage of the oil was lost to dissolution weathering (Figure 4-18). While the oil was being released, i.e., until July 15th, relatively fresh droplets rose from the release locations, weathering by dissolution of the more water-soluble components as they rose to the surface, where they mixed with well-weathered oil already on the water surface. The smooth lines after July 15th in Figure 4-18 show the weathering rate for micro-droplets remaining at depth and also re-entrained from floating oil at the surface. The peaks in oil viscosity and density in April and May are during times where high winds entrained more oil, reflecting the more weathered surface oil entering the water column. Figure 4-19 shows the modeled viscosity and density of floating oil, indicating rapid weathering and emulsification to form mousse when oil was on the water surface.

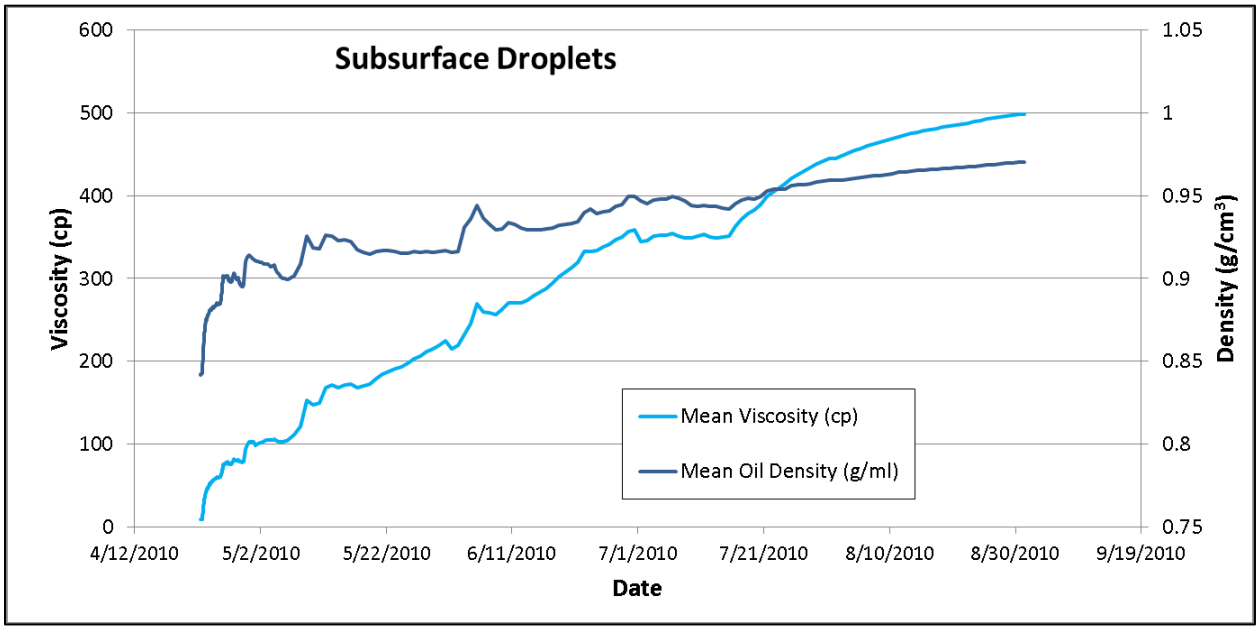

Figure 4-18. Mean viscosity and density of modeled subsurface oil droplets over time.

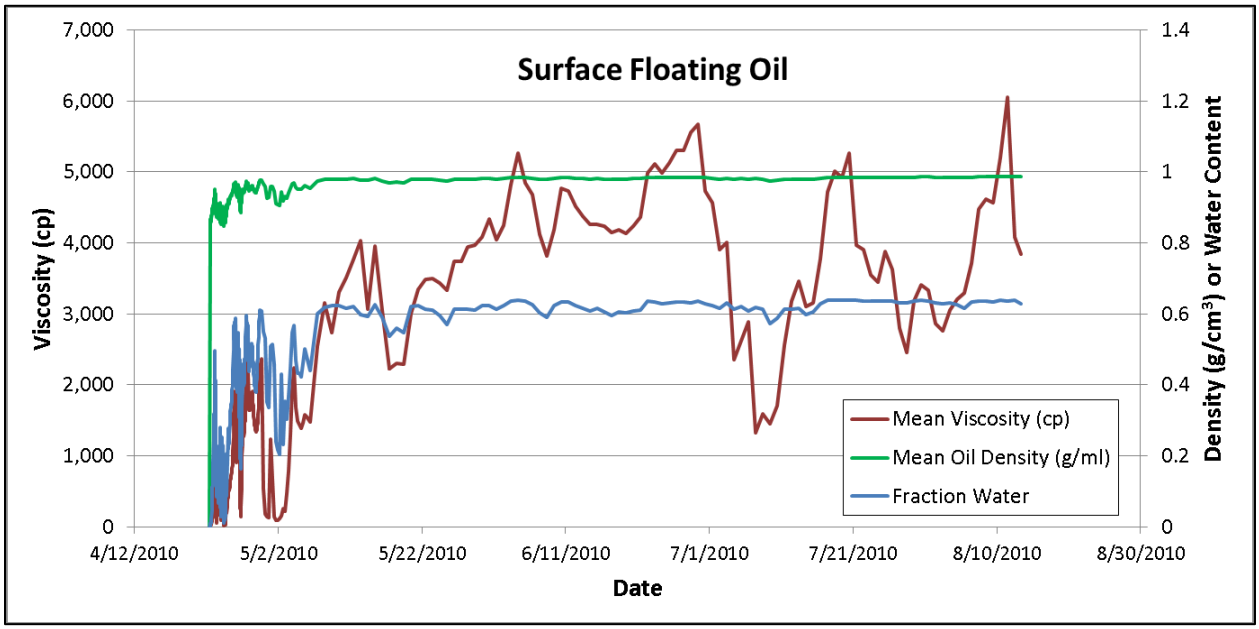

Figure 4-19. Mean viscosity, density, and fractional water content (reflecting emulsification) of modeled surface oil over time.

Figures 4-20 and 4-21 plot the composition of modeled surface oil over time. The soluble-semi-soluble and volatile-semi-volatile hydrocarbons are plotted in Figure 4-20. Table 2-3 lists the pseudo-component code definitions and compounds included; in short AR1 is BTEX, AR2-AR3 are substituted benzenes, AR4 is decalins, AR5-AR8 are the PAHs, and AR9 is comprised of soluble aliphatics. The aliphatic content plotted in Figure 4-21 is for insoluble and volatile-semi-volatile components, with the higher numbered pseudo-components (Table 2-4) having lower vapor pressures, so they remain longer in the oil as it weathers. The high degree of weathering in the model is in agreement with observations by Stout et al. (2016a) that floating oil samples had total PAH (TPAH) depletions averaging 69±23%, range 12 to 91%, caused by the combined effects of evaporation, dissolution, and photo-oxidation.

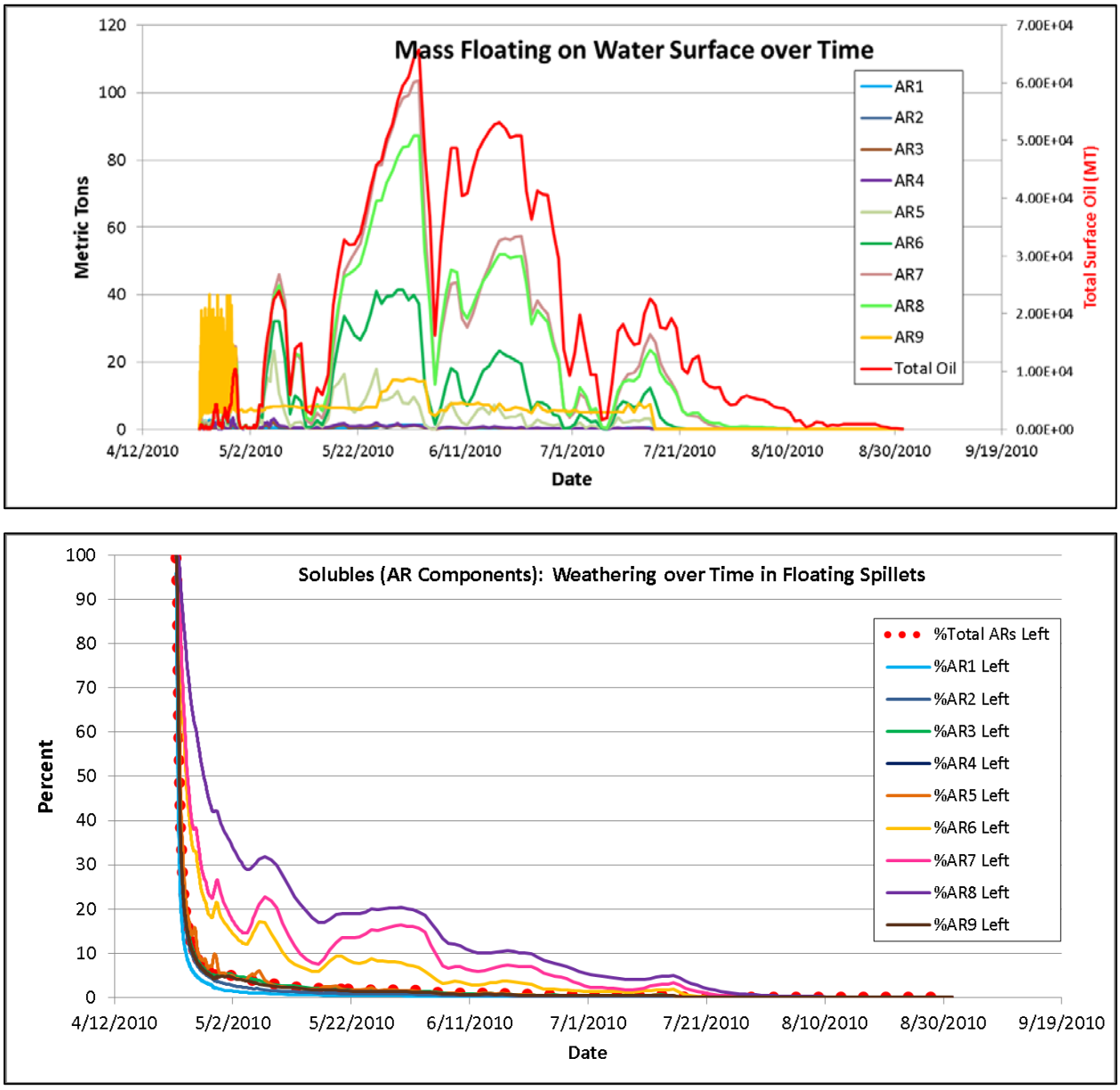

Figure 4-20. Composition of modeled surface oil over time.
Soluble hydrocarbons, as mass (upper panel) and percent of the component left (lower panel).

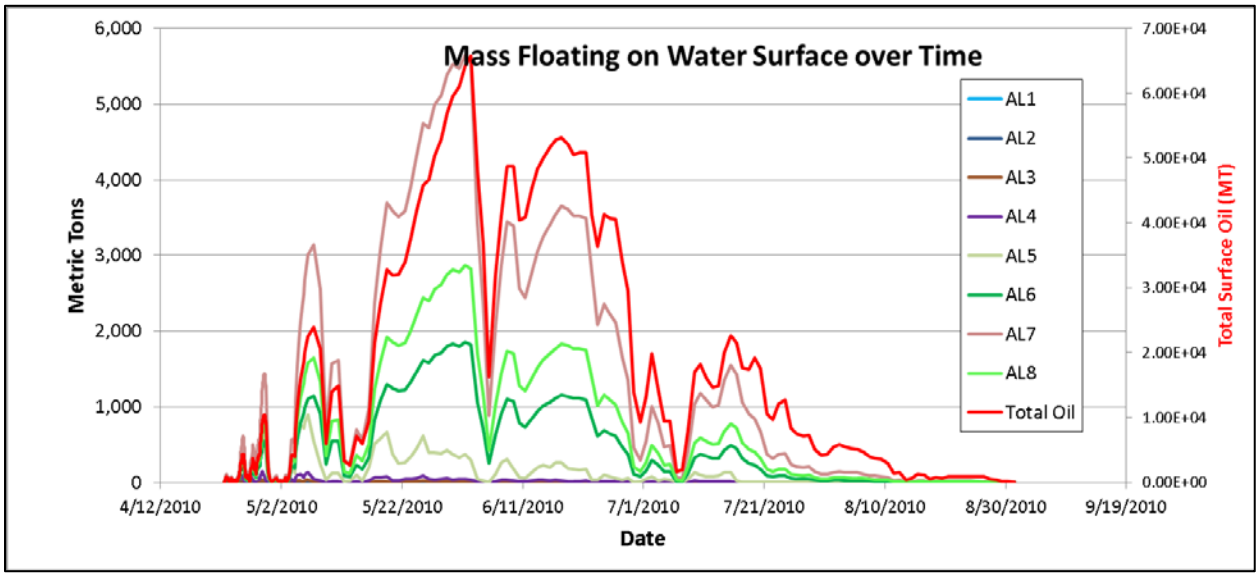

Figure 4-21. Composition of modeled surface oil over time; insoluble volatile hydrocarbons.

Figures 4-22 to 4-24 show maps indicating the typical weathering pattern of floating oil near the surfacing location around the wellhead and at further distances. The AR1 (BTEX), AR2 (C3-benzenes) and AR9 (soluble alkanes) components evaporated rapidly when oil surfaced, and so floating oil containing these components was only within a few to tens of kilometers from the wellhead and at the surfacing location, which depended on the current transport before surfacing (see example in Figure 4-22 for June 3, when oil surfaced in the HYCOM-FSU simulation out to ~30 km from the wellhead). The AR5-AR8 components (PAHs) remained in the floating oil for progressively longer, and so the model shows them to occur over a wider area than the AR1, AR2 and AR9 components (Figures 4-23 and 4-24).

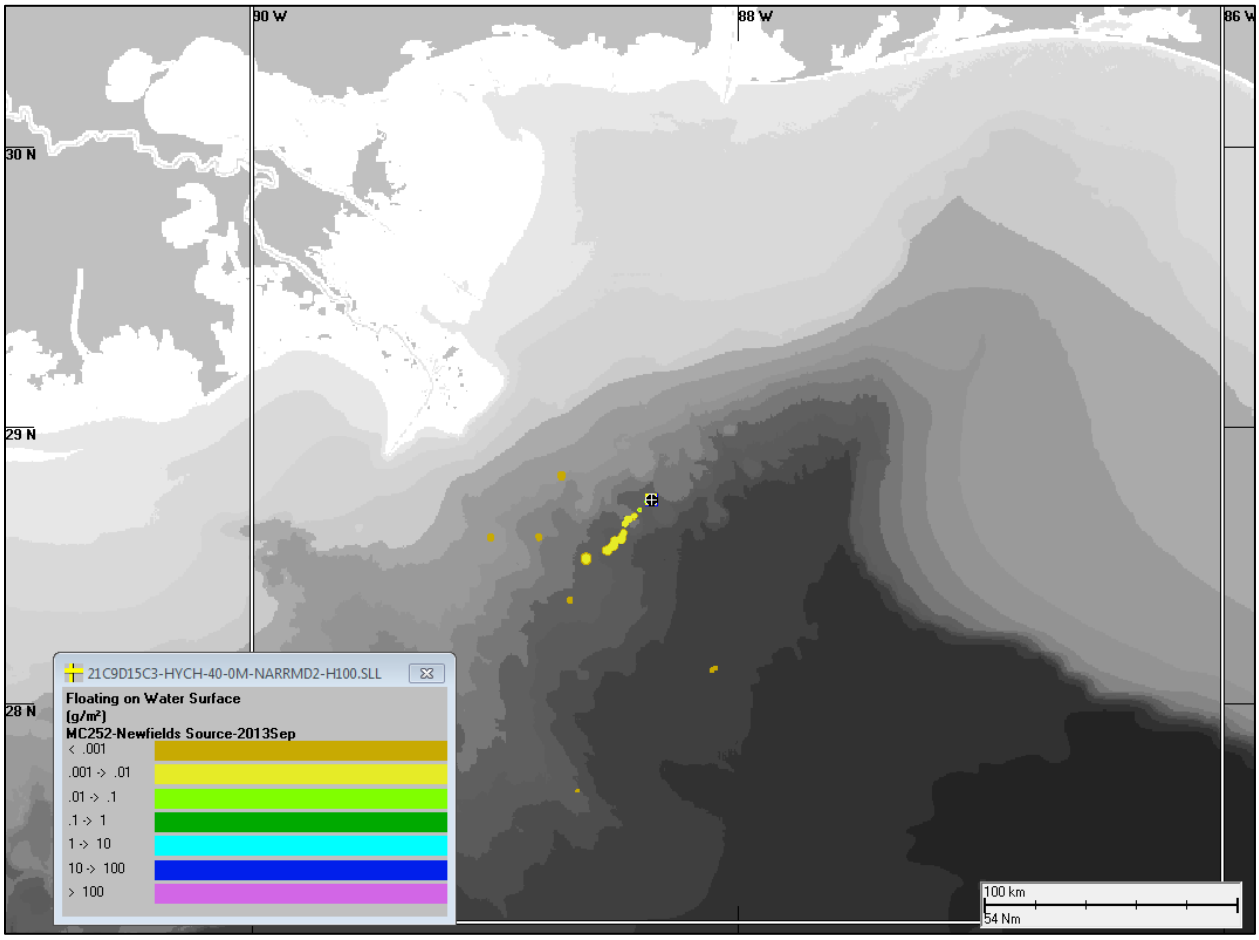

Figure 4-22. Modeled concentration of AR1 (BTEX) in floating oil (g/m^2) on the water surface on June 3 (base case simulation).

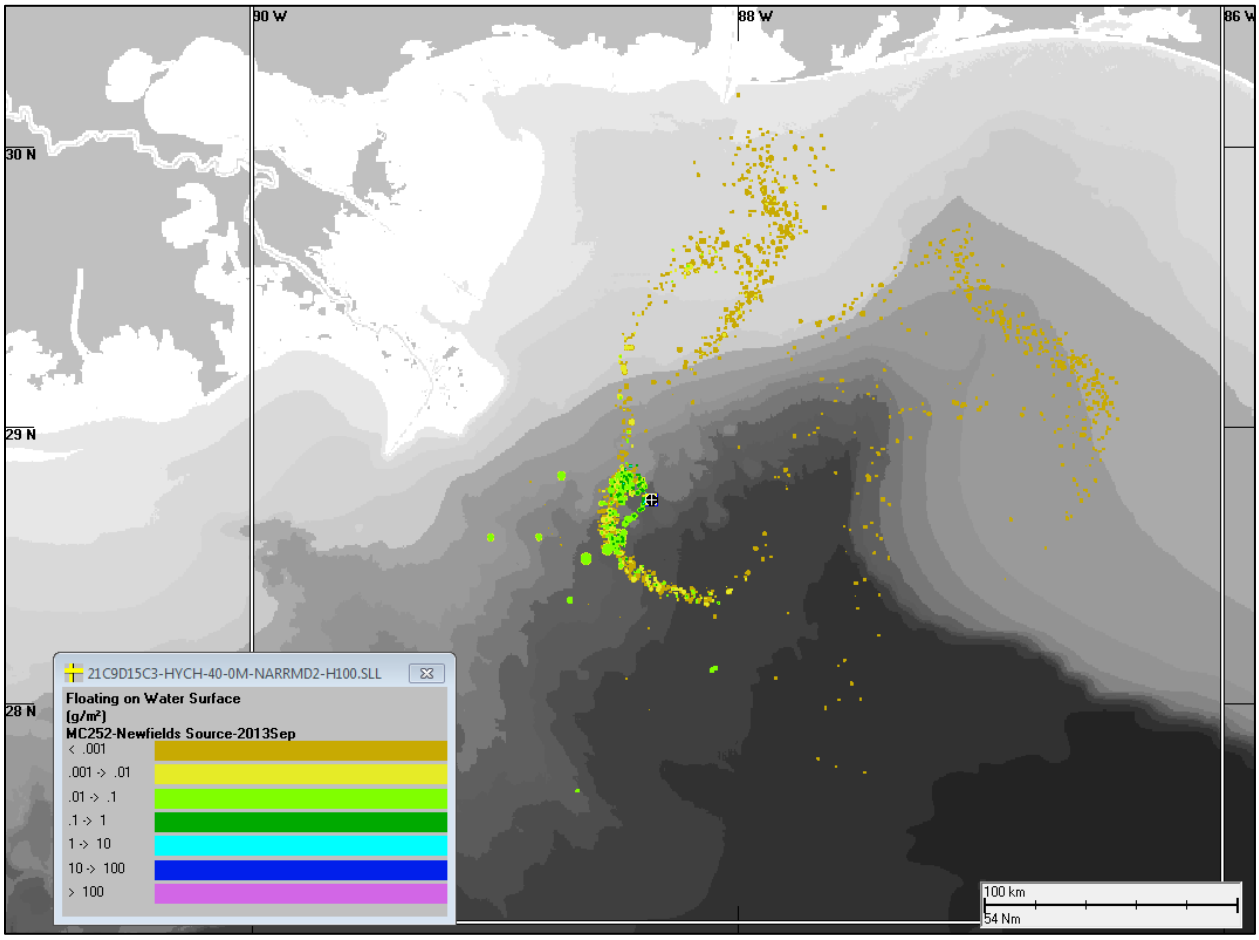

Figure 4-23. Modeled concentration of AR5 (C0–C2 naphthalenes) in floating oil (g/m^2) on the water surface on June 3 (base case simulation).

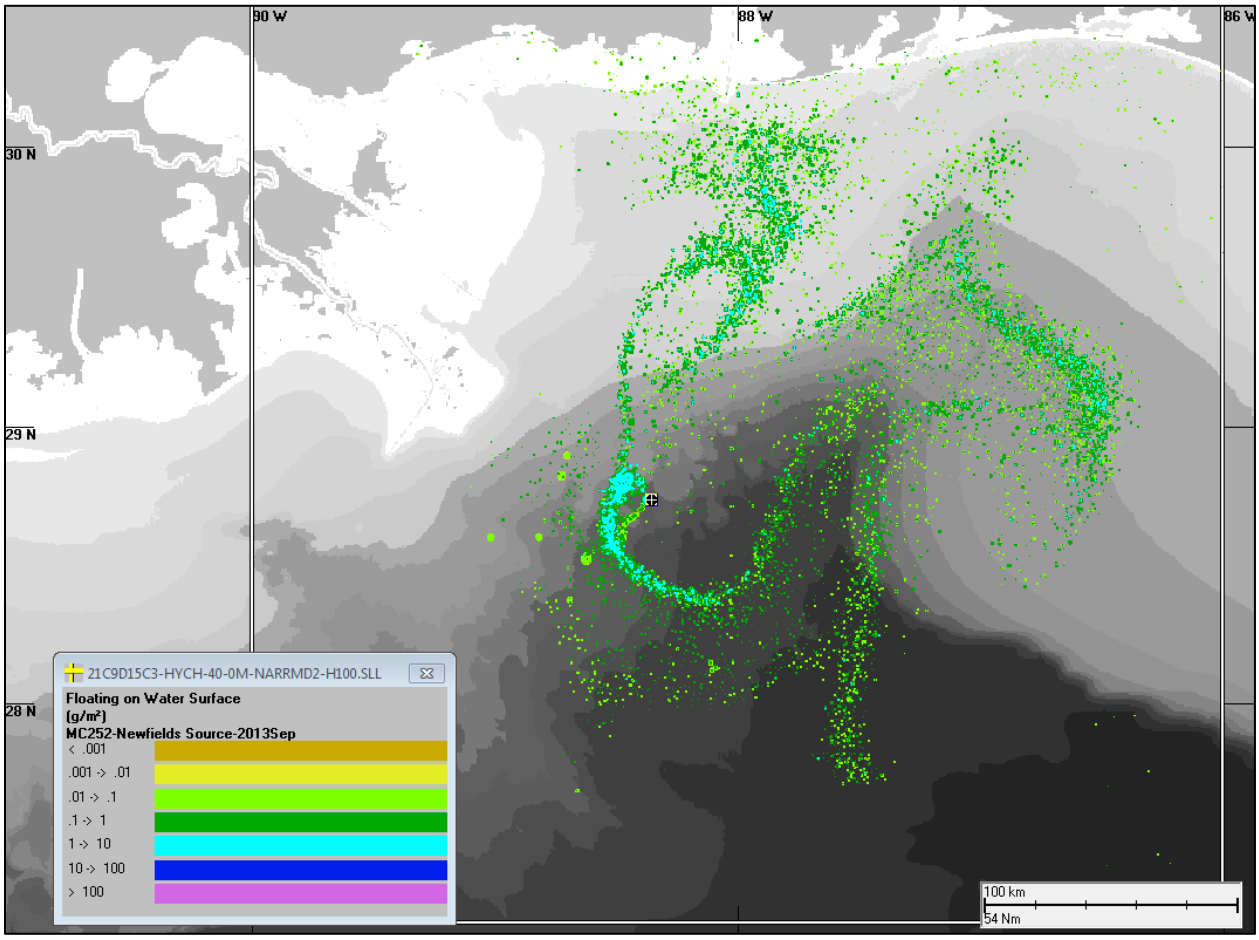

Figure 4-24. Modeled concentration of AR7 (Fluorenes & C0–C1 3-ring PAHs) in floating oil (g/m^2) on the water surface on June 3 (base case simulation).

The low content upon surfacing and rapid loss to evaporation of AR1, AR2 and AR9 components is consistent with the findings of Stout et al. (2016a) in their examination of 62 floating oil samples collected between April 22 and August 31 of 2010. Stout et al. (2016a) documented that floating oil samples collected less than 10 km from the wellhead exhibited a wide range of PAH depletions (12 to 91%, average 54 ± 20%), reflecting a mix of freshly surfaced and already weathered floating oil. The model predicted a range of degree of weathering in oil surrounding the wellhead because of mixing of highly weathered and fresher oil newly surfaced. Floating oil collected 10 to 75 km from the well exhibited 85 ± 14% depletion of PAH, on average, indicating that weathering of the floating oil quickly advanced as the oil moved away from the well (Stout et al. 2016a). The model predicted a high degree of weathering in floating oils greater than 10 km from the well.

4.3 Shoreline Oiling

4.3.1 Model Results: Cumulative Oil on Shorelines

Figures 4-25 to 4-27 show the amount of oil accumulated on shorelines for the base case simulation, as mass of total hydrocarbons per unit area (averaged in each habitat grid cell). No shoreline cleanup was simulated in the model. Thus, oil simply accumulates and remains on the shore. Figures D.1-1 to D.1-36 in Annex D map the amounts of oil accumulated on shorelines for the other primary simulations, showing the variability resulting from different current and wind inputs. The modeled shoreline oiling for the base case compares well with the observations (Figures 3-6 to 3-9), the model showing oiling from the Apalachicola Bay area of Florida to Terrebonne Bay area of Louisiana. Note that the model predicted oiling on shore inside Mobile Bay in areas where it was not observed. However, most of Mobile Bay's shoreline areas were not surveyed, so oiling of those areas is unknown.

Simulations using HYCOM-NRL Reanalysis currents with CFSR winds (Figures D.1-1 to D.1.3), HYCOM-NRL Real-time currents with NARR winds (Figures D.1-4 to D.1.6), and NCOM Real-Time with NARR winds (Figures D.1-10 to D.1.12), predict similar oiling patterns to the base case using HYCOM-FSU currents and NARR winds (Figures 4-25 to 4-27). SABGOM spreads oil to shorelines too far to the east (in the Big Bend of Florida) and into western Louisiana where no oiling was observed (Figures D.1-7 to D.1.9). NGOM currents with NARR winds and the IAS ROMS simulations carry too much oil to western Louisiana and Texas (Figures D.1-13 to D.1-21).

Simulations made with no currents, forced with winds only (Figures D.1-22 to D.1-27 in Annex D), and those forced with ADCP currents and NARR winds (Figures D.1-28 to D.1.30), do not bring as much oil ashore west of the bird's foot in Plaquemine's Parish (SCAT Division 1) and Lake Barre as was observed. Thus, coastal currents prevailing towards the west apparently transported the oil to the more western areas. Also, currents brought the oil east to Florida, as winds alone do not account for that shoreline oiling.

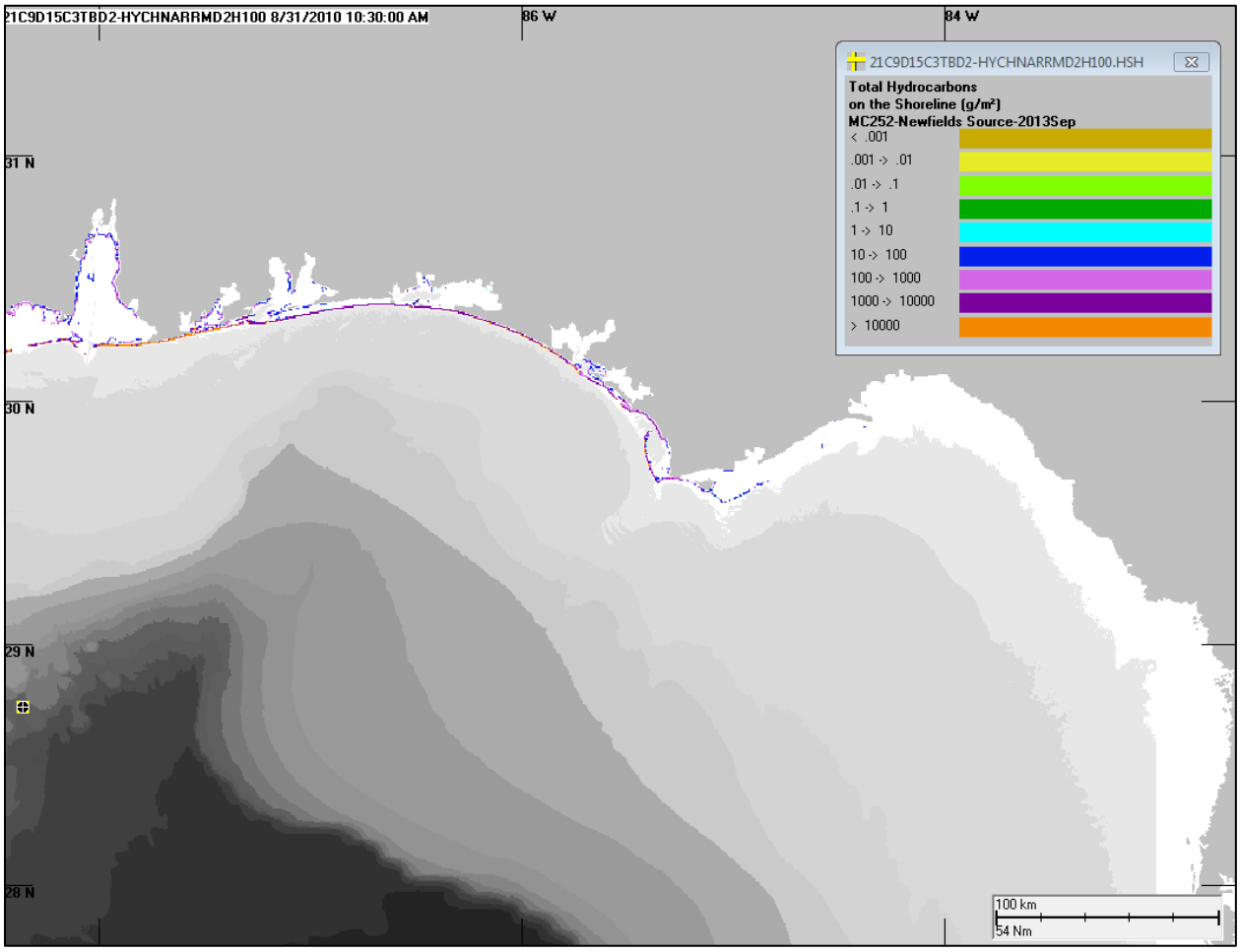

Figure 4-25. Amount of oil accumulated on shorelines for the base case simulation (east extent).

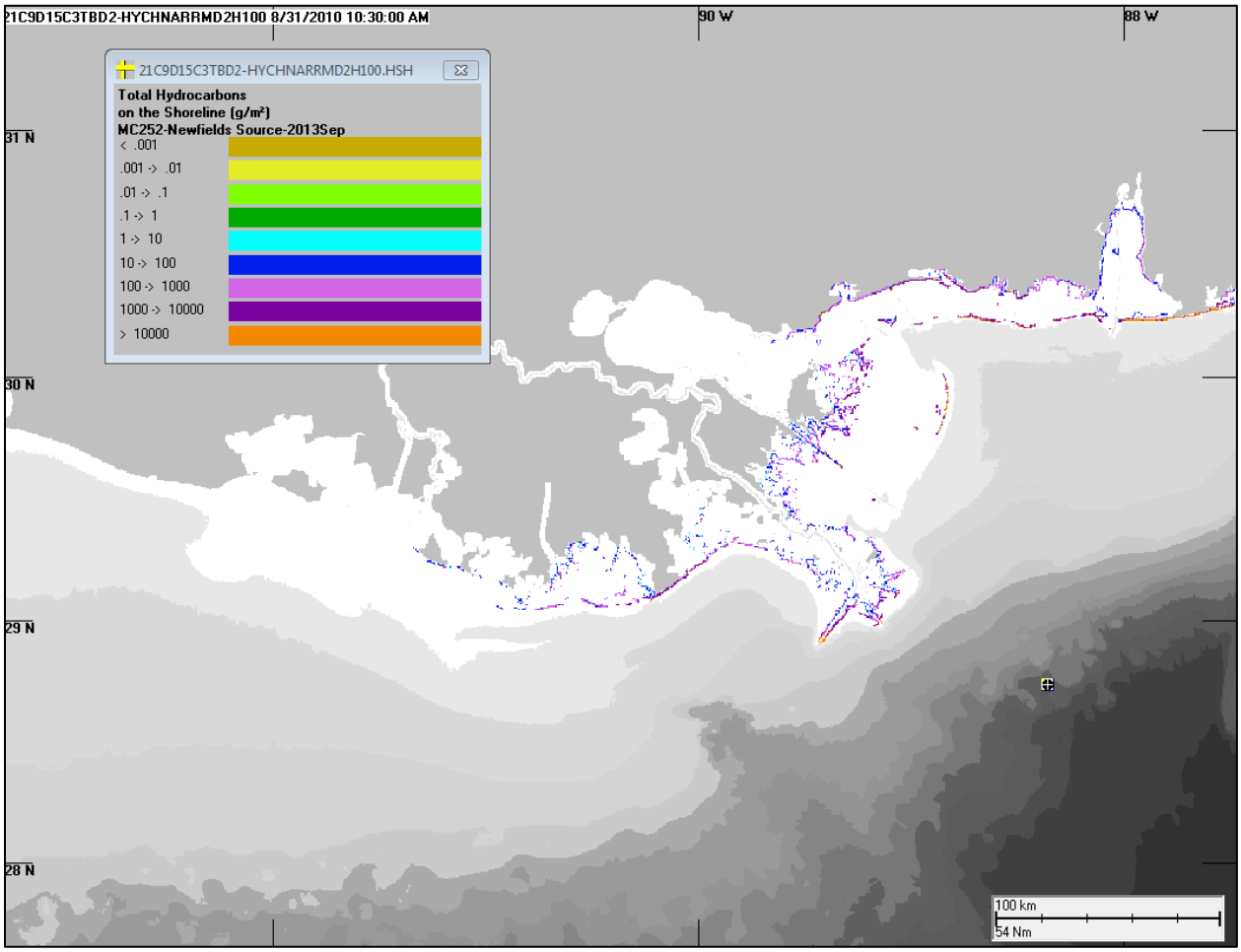

Figure 4-26. Amount of oil accumulated on shorelines for the base case simulation (central extent).

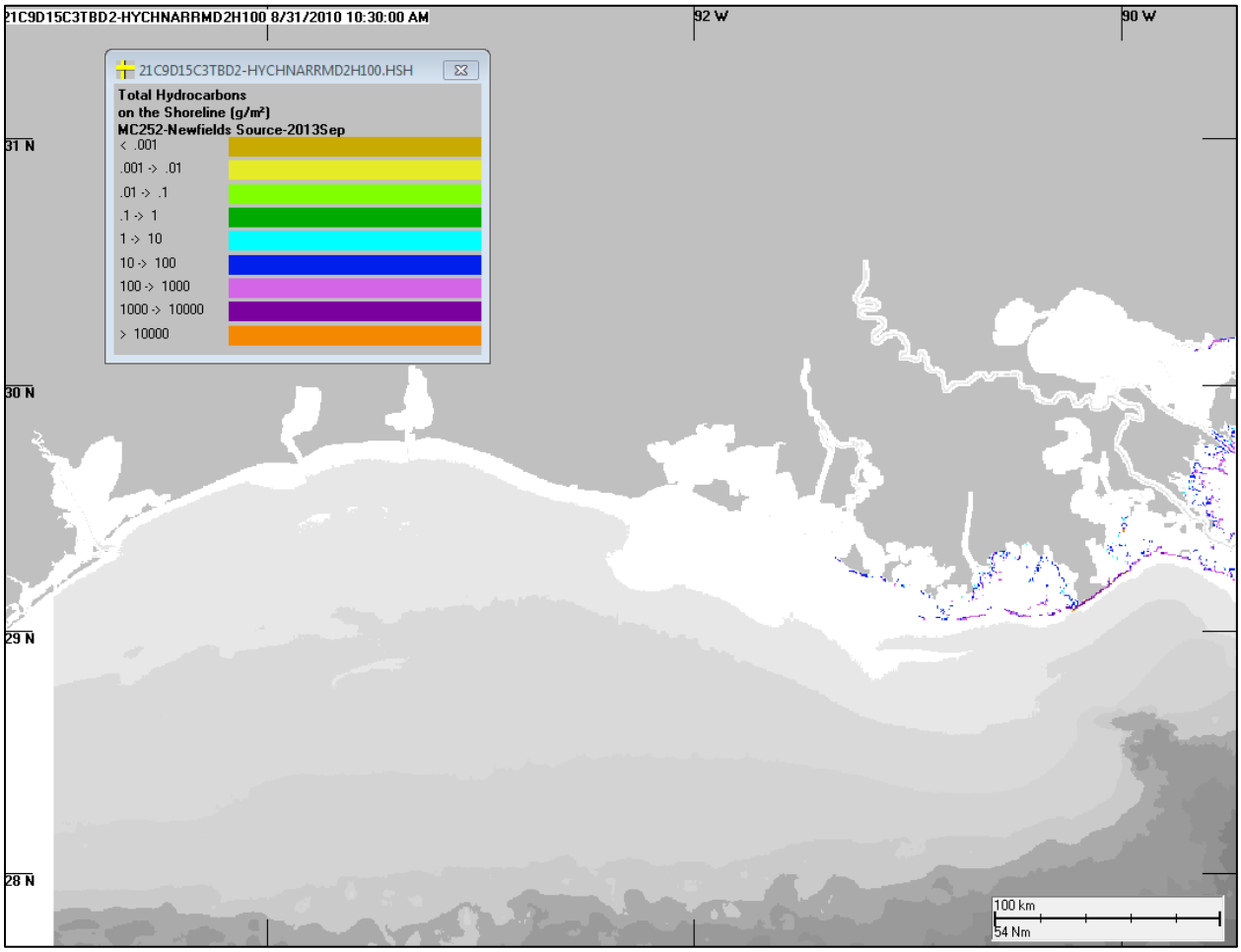

Figure 4-27. Amount of oil accumulated on shorelines for the base case simulation (west extent).

Shoreline oiling results are summarized in Table 4-10. For simulations run without currents, the length of shoreline oiled is smaller and focused on the area between the Bird's Foot and Alabama. The simulation using HYCOM-FSU currents and NARR winds, but assuming no SSDI was applied, oils the same length of shoreline as the SSDI case, but more heavily. This is evident when comparing Figures D.1-31 to D.1-33 in Annex D to Figures 4-25 to 4-27.

The estimated total length of shore oil estimated by the DWHOS Trustees (2016; Nixon et al. 2015) was 2,113 km. The categories of degree of oiling used by the Trustees cannot be translated to oil loading amounts (g/m^2). The total lengths of shoreline oiling predicted by the model using most of the hydrodynamic model currents (except NGOM) are 2,000–2,700 km oiled, with the base case predicting 2,568 km oiled. These results are in good agreement with the observations, considering some areas were not surveyed.

Table 4-10. Shoreline oiling results for primary model cases.

SSDI Treatment Case	Currents	Winds	Wind Drift Model	Length of Shore Oiled (km)	Mass of Oil Ashore (MT)
High	HYCOM-FSU	NARR	Modeled	2,504	60,741
Low	HYCOM-FSU	NARR	Modeled	2,458	70,679
None	HYCOM-FSU	NARR	Modeled	2,526	72,950
Best	HYCOM-FSU	NARR	Modeled	2,568	64,407
Best	HYCOM-NRL, Reanalysis	CFSR	Modeled	1,993	25,045
Best	HYCOM-NRL, Real-time	NARR	Modeled	2,698	58,164
Best	SABGOM	NARR	Modeled	2,658	91,677
Best	NCOM Real-Time	NARR	Modeled	2,385	85,485
Best	NGOM-NOAA, Real-time	NARR	Modeled	3,540	91,089
Best	IAS ROMS-hourly	NAM	Modeled	2,507	67,850
Best	IAS ROMS-12 hourly	NAM	Modeled	2,381	81,487
Best	none	NAM	Modeled	1,436	38,306
Best	none	NARR	Modeled	1,550	49,039
Best	none	NOGAPS	Modeled	1,013	33,483
Best	ADCPs	NARR	Modeled	1,857	56,189

4.3.2 Timing and Distribution of Oil on Shore

A binary discriminator test (Fitzpatrick 2009) was used to evaluate the timing of oil coming ashore in the model, as compared with observations made by the SCAT program. The presence or absence of oil according to SCAT observations and the model predictions was gridded using the 5 km by 5 km Albers grid (ERMA 2016) employed by the DWHOS Trustees (2016) in their evaluations of oil exposure after the DWHOS. A cell was considered to have oil presence if any shore segment within the cell was observed oiled by the SCAT teams.

SCAT observations of shoreline oiling were downloaded from ERMA in July of 2014 as shape files. The observational data were binned into 10-day intervals, from April 22 to September 30, 2010. In the analysis, only those SCAT segments where oil was observed to arrive before September 30 were considered as oiled. Segments checked during the 10-day interval, but where no oil was observed to arrive, were considered as “no oil”. Segments where oil was observed to arrive after September 30, but earlier observations showed it did not arrive there before September 30, were coded as “no oil”. Note that the shorelines

were not searched synoptically, and areas were not visited for days or weeks; thus, the time oil was first observed could have been a considerable time after the actual initial oiling. Also, note that the DWHOS Trustees (2016) used additional observations and SAR to identify where oil came ashore, to develop more comprehensive maps of the locations where oil came ashore during and after (including after September 30) the spill. The maps in Section 3.4 summarize the DWHOS Trustees' findings.

The results are shown in Figures D.2-1 to D.2-7 and D.3-1 to D.3-16 in Annex D. Note the maps color code where oil came ashore in the model but where the shoreline had not been surveyed ("no observed coverage, modeled oil"), as well as where both modeled and observed indicate oil ("match"), where both observed and the model indicate no oil ("no observed oil"), where there are false negatives (observed only), and where there are false positives (modeled only).

Figures D.2-1 to D.2-7 in Annex D show comparisons of the model to the observed, mapping the cumulative amount of oil on the shoreline over the period April 22 to September 30. The base case using HYCOM-FSU and NARR is summarized in Figure D.2-1 and other primary simulations are summarized in Figures D.2-2 to D.2-7.

As was evident in the maps of shore oiling (Figures 4-25 to 4-27 compared to Figures 3-6 to 3-9), the modeled shoreline oiling for the base case, compares well with the observations, the model showing oiling from the Apalachicola Bay area of Florida to Terrebonne Bay area of Louisiana. Note again that the model predicted oiling on shore inside Mobile Bay in areas where it was not observed; however, most of Mobile Bay's shoreline areas were not surveyed, so oiling of those areas is unknown. The patterns noted in Section 4.3.1 for the primary model simulations are more evident in Figures D.2.2 to D.2.7 of Annex D. Simulations using HYCOM-NRL Reanalysis currents with CFSR winds (Figure D.2-2), HYCOM-NRL Real-time currents with NARR winds (Figure D.2-3), and NCOM Real-Time with NARR winds (Figure D.2-5), predict similar oiling patterns to the base case using HYCOM-FSU currents and NARR winds (Figure D.2-1). NGOM (Figure D.2-6), SABGOM (Figure D.2-4) and IAS ROMS (Figure D.2-7) carry too much oil to western Louisiana and Texas, but otherwise show good agreement with the SCAT observations.

Figures D.3-1 to D.3-16 in Annex D map the results for the base case simulation for each of the 16 10-day intervals from April 22 to September 30. No oil came ashore in the first 10-day period, April 22–May 1, in either the model or SCAT observations. The oil's arrival to shore was in good agreement with the SCAT observations for most areas and observation periods. One exception is that the (base case) model did not bring as much oil ashore west of the Bird's Foot and Lake Barre during early to mid-June as was observed. Oil did come ashore in that simulation later in June and in July. The false negatives for the modeled oil

stranding in Louisiana in August and September may in part be due to delays before shorelines were first surveyed after oil arrived, given the remoteness of the shorelines.

4.4 Subsurface Hydrocarbon Concentrations

The following is a conceptual model of the deep plume and rising oil from the DWHOS blowout. The oil released from the trap height just above and near the wellhead rose through 1,140 to 1,320 m of water. Large oil droplets (greater than 1 mm in diameter) rose quickly—within a few hours to a day—to the ocean surface. Medium-sized oil droplets (between 100 μm and 1 mm in diameter) rose to the surface over the course of several days, during which time they were transported by currents away from the wellhead. High turbulence and the injection of dispersants at the source caused some of the oil to be dispersed as microscopic (<~100 μm) oil droplets at the trap height, which remained near the release depth. These micro-droplets and soluble hydrocarbons that rapidly dissolved from the droplets moved with the deep-sea currents, resulting in a deep-sea oil plume at about 1,100-1,300 m. Soluble hydrocarbons also dissolved from the rising oil droplets, and multiple "plumes" of hydrocarbons were sheared in various directions at higher depths of the water column. The oil droplets weathered during the rise as dissolution progressed, losing mass and bringing their density (Figure 4-18) much closer to that of the seawater than when the oil was fresh, which slowed their rise.

If there were no currents, the rising oil droplets would be in the shape of an inverted cone, with the vertex of the cone at the trap height and the widest radius just below the water surface. Rising oil droplets with the largest diameter would be in the center of the cone along the cone axis. Progressively smaller droplets would be found moving out from the axis, as the slower rise rates of smaller droplets increases their residence time in the water column, therefore increasing their dispersion. With no currents, concentrations of contaminants would be highest along the cone axis, decreasing toward the edges in a Gaussian shape that is typical of dispersion from a central source. Because the smaller oil droplets spread out considerably at the top of the cone, concentration profiles show much lower concentrations higher in the water column and farther from the axis of the inverted cone. With the addition of currents, however, this inverted cone would be bent and sheared at various depths.

Surface oil was transported rapidly away from the surfacing location by winds and currents, and at times circled back to over the surfacing oil droplets. When winds and waves were high, the floating oil was entrained back into the upper water column, most of it remaining in the upper mixed layer. The upper mixed layer in the area of the DWHOS in summer was about 40 m deep.

Thus, a cross section of the water column would show a cloud of micro-droplets and dissolved constituents at the depth of the trap height being transported with currents and dispersing in the deep water between 1,100 and 1,300 m. Above that were the droplets and dissolved hydrocarbon plumes advecting in various directions throughout the water column. The rising oil and dissolved hydrocarbons were more dispersed, i.e., in lower concentrations and patchier, as they moved up through the water column. In the upper 40-m mixed layer, re-entrained oil droplets and dissolved hydrocarbons were spread out, under floating oil, over many tens to hundreds of square kilometers.

In the following sections, model results of subsurface oil droplet and dissolved hydrocarbon distributions and concentrations are described. Model simulations were run separately above and below 40 m, so that higher numbers of model spillets and smaller concentrations grids could be used, maintaining high resolution for model results. Very little oil from above 40 m reached below that depth due to surface turbulence, and that which would do so would be so diluted as to be inconsequential. The model simulations above 40 m were initialized with outputs from the simulations initialized at the wellhead. The mass and weathering condition of all oil droplets passing through the 40-m model boundary was saved in output files, then used as input files for initializing the next simulation.

Section 4.4.1 describes the model results for simulations below 40 m. Section 4.4.2 describes the subsurface oil droplet and dissolved hydrocarbon distributions and concentrations above 40 m.

4.4.1 Model Results for Simulations below 40 Meters

4.4.1.1 Trajectories and Concentrations of Total Hydrocarbons

Concentrations of total hydrocarbons within oil droplets were highly variable in space and over time, as the currents shifted. The concentration at any point in space or time changed rapidly, as the water and oil moved during the continuing release. Therefore, it is difficult to portray the results in static figures. To portray the movement of the oil, the age of the spillets (time since each particle was released) was plotted. Snapshots of the trajectory, integrating spillets over the water column and color-coded by the age of spillets, are provided in the attachments to Annex E, Section 1, for three simulations: those using HYCOM-FSU (E.1.1), SABGOM (E.1.2) and ADCP (E.1.3) current data.

Figures showing the concentrations of total hydrocarbons in droplets are in the attachments to Annex E, Section E.2 for three simulations: those using HYCOM-FSU (E.2.1), SABGOM (E.2.2) and ADCP (E.2.3) current data. The figures depict top-down map views providing the vertical maximum dissolved hydrocarbon concentration in any 500 m x 500 m x 20 m cell within each of the indicated layers of the water column.

The simulations using currents depict the extent to which currents may transport and shear the rising oil. The conceptual model of a cone is instructive, but the shape of a cone was not depicted in the simulations (nor was it observed in the field data), as there was substantial horizontal displacement and spillets move in different directions. ADCP data in ~30-60 m vertical bins in the water column showed slow (<10 cm/s) currents in adjacent depths differing by as much as 120° in the May-June 2010 timeframe. Some of the described shear is evident in the figures (Annex E.1) that depict the age of the spillets as they move throughout the simulation.

The diameter of the hypothetical cone (which was more like the shape of a cylinder) of rising oil droplets was relatively small during April when subsea dispersants were not applied, the kink holes had not yet formed, and most droplets were > 1mm in diameter, rising to the surface within hours. The diameter of the cylinder (measured at the point where the vertical maximum total hydrocarbon concentrations were greater than 1 $\propto\gamma$/L, a conservatively low concentration) in the ADCP and HYCOM-FSU simulations was about 3 km on April 26 (smaller than the spill site symbol in the figures in the attachments to Annex E.2.1 and E.2.3). As such, the age-dated spillets below 800 m are mostly masked by the spill site symbol in the figures from April 22 through April 30, and they do not begin to appear until May 4, 2010. From May through mid-July, the area of rising oil was much larger and, in the ADCP and HYCOM-FSU simulations, was sheared in complex patterns as observed in the field-collected water-column data. In the SABGOM simulation, the currents were consistently strong towards the southwest, and the rising droplets streamed out to the southwest more than 100 km. After the discharge ended on July 15, the concentrations dispersed and components degraded. Total hydrocarbon concentrations were <10 $\propto\gamma$/L in most locations by the end of August.

Note that the total hydrocarbon concentrations in droplets that are predicted by the model are based on the total mass of the release (i.e., 553,889 MT), broken out by boiling point ranges (i.e., true boiling point [TBP] distillation cuts plus residual), much of which cannot be chemically measured in water samples. Thus, the modeled total hydrocarbon concentration is not directly comparable to a total petroleum hydrocarbon (TPH) measurement using, for example, gas chromatographic methods. For this reason, model-predicted concentrations of the measurable soluble and semi-soluble hydrocarbons, i.e., of the AR components, are compared to field sample measurements of those same chemical components. Note that because the aliphatic AL components are also defined by boiling point ranges, those components contain much more non-chromatographable mass than is measurable within the boiling ranges using GC/FID, GC/MS or other existing techniques to measure individual aliphatic hydrocarbons in the water.

4.4.1.2 Concentrations of Dissolved Hydrocarbons

Snapshots of the dissolved concentration distributions below 40 m produced by the base case simulation using HYCOM-FSU, the simulation using SABGOM, and the simulation using ADCPs are provided in the attachments to Annex E, Sections 3.1 (HYCOM), 3.2 (SABGOM) and 3.3 (ADCPs). The figures depict top-down map views providing the vertical maximum dissolved hydrocarbon concentration in any 500 m x 500 m x 20 m cell within each 200-m layer of the water column. Concentrations of total dissolved hydrocarbons include all 9 soluble and semi-soluble components (AR1 to AR9). Components AR5 to AR8 are the PAHs (the sum of which, TPAH, being termed TPAH50 by the DWHOS Trustees, 2016), AR1 is BTEX and AR9 includes the measurable soluble alkanes. The concentrations for each of these modeled chemical components are in Annex E.4. Only concentrations greater than 1 $\propto\gamma$/L (ppb) are plotted in the figures in the attachments for Annex E.2, E.3, and E.4.

In the simulations, dissolved concentrations move horizontally by current advection, as droplets rise out of the 1,100–1,300 m layer. Of the droplets, smaller droplets were transported farther from the wellhead before rising out of the layer. This makes the oil droplet (and resulting dissolved) concentrations highly patchy in 3-D space, and increasingly so moving up through the water column above the release point at the trap height. Successful sampling of such patches would be rare occurrences using a regularly-spaced sampling design. For this reason, NRDA sampling was focused on locations where fluorescence and dissolved oxygen sensors indicated the potential presence of in-water hydrocarbon concentrations (Payne and Driskell 2015d). This targeted sampling approach was used on NRDA *Jack Fitz* 1, 2, and 3 cruises of May and June 2010, but did not begin in earnest on the response vessels until late July and August of 2010 (Figure B.2-3 in Annex B).

Using the chemistry sample results (see Annex B), observations of particulate oil (Li et al. 2015, 2017a, and Payne and Driskell 2015d), and modeling analyses (Spaulding et al. 2015; summarized in Section 2.8.3.2), it was concluded that much of the oil was released in relatively large droplets, which rose rapidly to the surface near the wellhead. In April 2010, the oil was released primarily as >1 mm diameter droplets. Therefore, subsurface hydrocarbon concentrations below 1,100 m were only above 1 $\propto\gamma$/L within a radius of approximately 2 km of the wellhead. In May 2010, the progressively smaller oil droplet sizes released (see Section 2.8.3.2) resulted in increasing concentrations of oil in the deep-water plume. After May 2010, observed concentrations from field sampling extended further from the wellhead than previously, to a distance of at least 40 km on May 15 and 70 km on May 31 (see Annex B, Figures B.2.8 to B.2.11).

Transport to the southwest, particularly from July through the fall, was observed in fluorescence and dissolved oxygen indicators and chemistry samples collected in June

through September 2010 (Payne and Driskell, 2015a, and Annex B.1). Southwest transport was also observed in the deep plume of the model simulations at 1,000-1,400 m (see attachments to Annex E.3). Note that the concentration maps in the attachments to Annex E.3 only depict concentrations > 1 ∝γ/L.

In all three simulations, in the layer from 1,000–1,200 m, concentrations peaked at over 500 ∝γ/L near the release location and immediately downstream, but diluted rapidly such that concentrations over 100 ∝γ/L were transported in a narrow plume extending some distance from the release point. In the ADCP simulation, concentrations in the deep plume > 100 ∝γ/L total dissolved hydrocarbons remained within ~25 km of the release point, and those >10 ∝γ/L reached 30 -40 km from the wellhead (Annex E.3.3.2 attachments). In the HYCOM-FSU simulations, concentrations >100 ∝γ/L were transported to about 40 km from the wellhead on most dates and to about ~50 km on some days. Concentrations >10 ∝γ/L reached ~60 km from the wellhead on most dates and to about ~100 km in early July (Annex E.3.1.2). In the SABGOM simulations, concentrations >100 ∝γ/L were transported to ~60 km and to as much as 100 km from the wellhead. Concentrations >10 ∝γ/L reached ~110 km from the wellhead on many dates (Annex E.3.2.2 attachments). The SABGOM results reflect much higher current speeds than in the HYCOM-FSU simulation, and HYCOM-FSU currents at the depth of the deep plume were generally higher than the ADCP measurement data indicate.

At depths of >1,000 m, the majority of the field-measured concentrations greater than 10 µg/L were within approximately 30 km of the wellhead (Annex B, Figures B.2.8 to B.211, "Total Investigated" chemicals). Furthermore, at higher (shallower) depths in the water column but below 40 m, field-measured concentrations greater than 10 µg/L were within approximately 20 km of the wellhead. However, relatively few samples were taken between 40 m and 100 m at >25 km from the wellhead in April–July when the model depicts concentrations above 10 µg/L.

Thus, the simulation using ADCP current data produced concentrations in agreement with the distributions and concentrations measured in the field, whereas the simulations using the hydrodynamic models' currents (particularly for SABGOM) resulted in total dissolved hydrocarbon concentrations >10 ∝γ/L extending too far from the wellhead. While it is possible that the field sampling missed the narrow plumes indicated by the hydrodynamic model-forced simulations, that distribution is unlikely given the comparison of the current speeds predicted by the hydrodynamics models with measurement data showing the hydrodynamic models over-estimated current speeds.

Camilli et al. (2010) documented the plume at ~1,000- to 1,200-m depth during 23-27 June 2010. Elevated hydrocarbon concentrations identified with a mass spectrometer, combined

with the rosette profiling data, indicated a continuous, plume as much as 200 m thick and in certain areas more than 2 km wide, moving with a southwestern trend for a distance of more than 35 km from its source. At approximately 27 km from the source, petroleum hydrocarbon values rapidly diminished. The HYCOM-FSU and SABGOM-forced simulations both show narrow plumes about 2 km wide, but they stretch well past 27 km without diminishing in concentration. The highest concentrations in the ADCP-forced model simulation are in a narrow plume on the order of 2 km wide, which diminishes in concentrations rapidly at just over 20 km from the source.

The concentrations of individual modeled chemical components are depicted in the figures in the attachments for Annex E.4. Results for AR1 (BTEX), AR5 (C0-C2 naphthalenes), AR7 (fluorenes & C0-C1 3-ring PAHs) and AR9 (soluble alkanes) are mapped over time. The soluble and semi-soluble hydrocarbon concentrations were in low concentrations in a narrow cylinder rising toward the surface in April, when the release was mostly of large droplets (Spaulding et al. 2015; Section 2.8.3.2). During May when the kink holes appeared and subsea dispersant began to be applied, the dissolved-phase concentrations were much higher and over a wider area (from a bird's-eye view). The higher concentrations continued in June when more effective subsea dispersant applications were used (Spaulding et al. 2015). The highest dissolved concentrations were of BTEX and soluble alkanes, whereas most of the 3-ring PAHs were still in the particulate phase.

During May, concentrations of BTEX (AR1) produced by the base case simulation show two vertical maxima at the two depths of release: the deeper (~1,300 m) from the kink holes in the riser and the shallower ~1,200 m from the end of the broken riser. BTEX dissolution rates were obviously rapid based on the relatively high concentrations at depth close to the source predicted by the model, in agreement with published accounts of field observations, such as those by Reddy et al. (2011), and the NRDA chemistry data (Annex B, Figures B.2.8 to B.2.11). Outside of the 2-km circle around the release location (where field samples could not be taken because of safety constraints), the maximum BTEX concentrations in the plume below 1,000 m were predicted by the model to be 25-100 $\propto\gamma$/L (Annex E.4.1), in agreement with observations by Reddy et al. (2012) during June 19–28, 2010, which had a plume layer concentration as high as 78 μg/L. This is also consistent with the NRDA cruise data (Horn et al. 2015a, b), in which, the pre-cut (i.e., prior to June 3) plume layer median BTEX concentration value was 92 μg/L (range 4.5–228 μg/L) and the post-cut plume layer median value 60 μg/L (range 4.9–176 μg/L).

After the riser was cut June 3, new oil was released at about 1,200m. However, some concentrations persisted at ~1,200–1,300 m because the oil released in that depth range in May was in very small droplets that had very slow rise rates. The small droplets (<100 μm) remained in the deep plume layer of ~1,100–1,300 m.

In the model results, the maximum dissolved PAH concentrations in the deep plume layer (at ~1,100–1,200 m) are generally 80–140 ∝γ/L from May to July. Higher in the water column (shallower), concentrations are much lower than these maxima. Between 600 m and 800 m, modeled concentrations of PAHs >1 µg/L were patchy and diffuse. Between 600 m and 40 m, modeled concentrations of PAHs were <1 µg/L because of cumulative current shearing and other dispersion processes diluting the small oil droplets and dissolved components below and in that depth zone. Large droplets containing PAHs passed through the 600 m to 40 m layer in just a few hours, such that their residence time in the layer was short, and little PAH dissolution occurred during their transit.

Careful consideration should be used when comparing the model results to measurements from samples. Samples were not collected at the maxima directly at or above the release points at the trap height, and therefore much lower concentrations would be anticipated further from the release site. The highest PAH concentrations below 40 m (up to ~5 ∝γ/L) were consistently measured in water samples taken at depths between approximately 1,000–1,300 m, but elevated PAHs were also measured at shallower depths in lower concentrations (Annex B, Figures B.2.8 to B.211; "PAH50" in these figures corresponds to TPAH). Further comparisons to observations are made in the paragraphs below.

The highest measurements of total investigated (i.e., measured) hydrocarbons (including BTEX, other MAHs, PAHs, and soluble alkanes) in the deep plume were >100-700 µg/L, and concentrations up to ~80 µg/L were measured at other depths between 200–1,000 m. Fluorescence peaks and dissolved oxygen sags in the depth zone where the highest BTEX and PAH concentrations were measured, were observed between 1,000–1,300 m (compare figures in Annex E.4 with Figures B.2.8 to B.211 in Annex B). The model-simulated concentrations (Annex E.4) depict similar distributions and concentrations.

The modeled concentrations of BTEX remaining in the oil droplets above 1,100 m were very low throughout the simulations. Comparisons between the BTEX content of the oil droplets and the dissolved concentrations indicate that the BTEX was rapidly dissolved below 1,100 m in the deep plume. Dissolution continued at shallower depths as oil droplets rose through the water column. As may be seen in the figures in the attachments to Annex E.4.4, semi-soluble components (i.e., C2-benzenes, C3-benzenes, naphthalenes, low molecular weight alkanes, isoalkanes, cycloalkanes) partially dissolved while the oil droplets were at depths below 1,100 m. In the simulations, the sparingly soluble 3-ring PAHs were primarily in the droplet phase. With the exception of a few scattered patches, dissolved concentrations of components AR6, AR7 and AR8 (PAHs) were only >1 µg/L below 800 m. These partitioning patterns are generally consistent with the weathering models and analyses of chemistry samples, where dissolved and particulate fractions were measured (Payne and Driskell 2015a, b, c)

4.4.1.3 Comparison of the Modeled Concentrations to Field Measurements

The modeled concentrations of oil components were compared to measurement data reported in the literature, as available, and from chemistry samples collected for the NRDA chemistry program (described in Horn et al. 2015a and Payne and Driskell 2015a, b, c). Comparisons to literature reports are discussed in Section 5. Results of comparisons of the model results to the NRDA chemistry data are presented in this section and discussed further in Section 5.

The modeled concentrations of each of the pseudo-components were compared to measurement data (summed by component) from chemistry samples collected for the NRDA chemistry program (see Horn et al. 2015a for a description of the sample data sets and QA/QC procedures, as well as Horn et al. 2015b for presentation of the chemical measurement results). Due to the differences between the modeled and actual field conditions and the patchiness of observed chemistry, there is the potential for displacement between modeled and observed concentrations in both space and time. Therefore, a direct overlay of the detectable chemistry measurements on the model would be insufficient for evaluating if the concentrations produced by the model are reasonable. To account for this displacement, results within a spatial and temporal window, containing a population of chemistry samples, are plotted as cumulative and non-cumulative frequency distributions. The chemistry samples and modeled results were ordered by concentration so that the distributions may be compared. Such cumulative density functions have been suggested and found useful for evaluating model performance in other contexts (Fitzpatrick 2009).

Most of the chemistry samples were analyzed as whole water samples, which includes both the in-droplet and dissolved concentrations. The chemistry sampling was targeted at fluorescence peaks and dissolved oxygen sags, which indicated the presence of oil and preferentially targeted regions with above-background concentrations (Payne and Driskell 2015d). If a randomized sampling plan were used both horizontally and vertically, then many more samples would likely be present with non-detectable hydrocarbons. Therefore, only the modeled concentrations with hydrocarbon concentrations greater than zero were compared to the chemistry results.

The comparisons were made for five vertical intervals within a 25 km by 25 km box centered on the wellhead. Table 4-11 summarizes the three-time domains (based on the response-ordered Observable Chemistry Regimes [OCRs], described in Section 3.1.2) considered for the statistical analysis. Each of the OCR1, OCR2 and OCR3 time intervals had sufficient samples (>5 samples in each depth interval and the domain considered) for meaningful comparisons. The single latitude-longitude domain and depth intervals used are:

- Longitude: 88.628° to 88.130° W
- Latitude: 28.51° to 28.96° N
- Depth range: 40-1,400 m (divided into 5 depth intervals: 40-200 m, 200-500 m, 500-800 m, 800-1,100 m, 1,100-1,400 m)

Table 4-11. Time domains considered for the comparison of modeled to observed component concentrations.

Time Period	Date Range		Description
	Starting Date	Ending Date	
OCR1	4/22/2010	5/26/2010	Before Top Kill
OCR2	5/26/2010	6/6/2010	Top Kill, Riser-cutting, and Initial Top Hat operations
OCR3	6/6/2010	7/15/2010	Post-cut and Collection until Discharge Stopped

Figures in the attachments to Annex F graphically depict the comparisons of modeled to observed chemistry values. A single figure is provided within this section of the report as an example (Figure 4-28). The depth range listed in the figure legend specifies the investigated region as a layer of the ocean. Only chemistry samples and SIMAP prediction data within this depth interval and the geographic bounds are presented for the specified time period.

Histograms are used to compare the frequency distribution of the modeled concentrations within each grid cell to the frequency distribution of the measured samples. This is presented in a cumulative percentile format (left panel) and in a histogram of percentages in each concentration bin, as indicated on the x-axis of the upper-right panel (Figure 4-28). The maximum modeled chemistry concentration is listed along the right vertical axis of the left panel figure. Selected percentiles (representative values between 50-100%) of modeled concentration are plotted as horizontal lines (minty green). For example, if the observed chemistry data, plotted as points in the left panel, are above the frequency distribution for the SIMAP model, it indicates that the observed chemistry values as a whole are higher than the modeled values.

In the top right panel of Figure 4-28, a histogram of binned chemistry concentrations ($\propto\gamma$/L) for observed samples (blue) and gridded model results (green) are plotted as the percentage of the total number of samples and grid cells. Results have been binned into concentration ranges. The first bar on the left represents all concentrations between 0.1 and 0.5 $\propto\gamma$/L. Note the range increases non-linearly to the right and that the sum of all percentages may not add up to 100%. A large number of observed samples and modeled grid cells may fall below 0.1 µg/L and are not presented here. In this example, the model

results (green) are higher than the observed chemistry (blue) in the concentration interval 0.1 to 0.5 $\propto\gamma$/L, indicating that there are more model results in this concentration bin than there are observed chemistry sample results. For the 0.5-1.0 $\propto\gamma$/L bin, the model results match the observed chemistry, i.e., about 7.5% of samples and 7.5% of modeled values are in the concentration bin 0.5-1.0 $\propto\gamma$/L.

The two spatial maps in Figure 4-28 depict the 95th percentile (left) and maximum (right) modeled concentrations in the vertical direction (over the specified depth range) for each of the horizontal grid cells (500 m x 500 m) of the 25 km by 25 km box centered on the wellhead, evaluated over the specified time interval (OCR). Overlaid on the model predictions are dots representing the concentrations of measured chemistry samples. Open symbols depict chemical concentrations that were greater than zero, but below the analytical method detection limit (MDL). In other words, open symbols represent the qualitative presence of analytes that make up the component grouping, as the concentration was not high enough to report a quantified value. The modeled concentration in each horizontal grid cell considers all of the 20 m vertical layers over each time step in the OCR. Each grid cell (in 3D), at each time step, is considered an individual sample for the model at the location in the map. Note that the variation in the magnitudes (concentrations) and spatial distribution of the chemistry sample measurements is typically much higher than that shown by the model results in the maps, because all samples are plotted whereas only the maximum (or 95th percentile) over time is presented for the model result in each grid cell. Thus, good agreement of the model and measurements is indicated when the sample results are the same or lower in concentration than the modeled maximum or 95th percentile. However, in the probability distributions (left and upper right panels), where model-predicted concentrations for all grid cells and time steps in the overall depth range and time interval of the OCR are treated as the set of predictions, the variance of the modeled results is completely characterized.

In the example in Figure 4-28, from the left panel, 18% of the model predictions for the AR5 PAH group (C0-C2 naphthalenes; where TPAH includes AR5- AR8) in the depth interval 800-1,100 m and time interval May 26-Jun 6 are <10^{-3} $\propto\gamma$/L, whereas approximately 7% of chemistry sample measurements in the same domain are below that concentration. About 6% (left panel) of both the model predictions and the sample measurements exceed 1 $\propto\gamma$/L, with the distribution shown in the upper right panel. The 40% of chemistry samples and the 47% of modeled values with concentrations >0.1 $\propto\gamma$/L are plotted in the upper right panel histogram. The maps show peak concentrations of the same magnitude and that the modeled location of the plume is partially offset to the north of the contaminated area indicated by the samples.

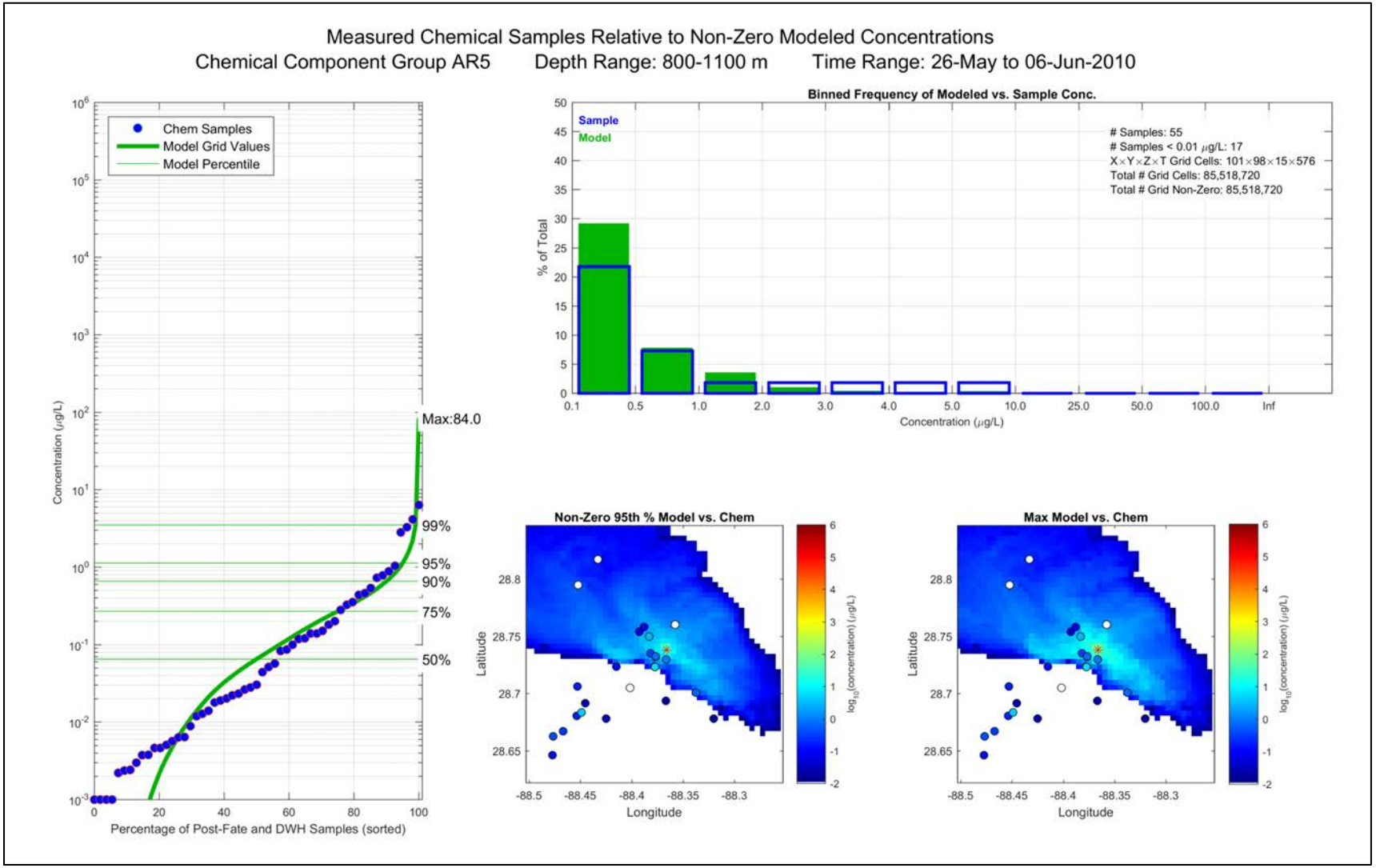

Figure 4-28. Comparison of modeled AR5 (C0-C2 naphthalenes) concentrations for the ADCP simulation to those measured in chemistry samples.

Figures in Annex F depict comparisons of results to data for April–July 2010 (OCR1 through OCR3), for the simulations using HYCOM-FSU (Annex F.1), SABGOM (Annex F.2) and the ADCP currents (Annex F.3). It is clear from these figures that statistical analyses of the comparisons would be complex and dependent on the resolution of the model concentration grid cells; they are not attempted herein.

In general, the modeled concentrations of the various pseudo-components were of the same order of magnitude as the measured concentrations. In order to be meaningful, comparisons need to be made on a component basis, as the components have different properties and behaviors (e.g., dissolution rates) that would cause their concentration distributions to vary. In many instances, the frequency distributions between the modeled concentrations and the measured samples compared well. However, in some cases the model overestimated concentrations observed in the samples, whereas in others it underestimated the concentrations. Overall, the differences between observed and modeled concentrations were not large and there was no obvious bias.

The frequency distributions of concentrations between the three modeled simulations with the different currents were similar for these analyses close to (within the 25 km x 25 km box surrounding) the wellhead. The currents moved the oil and dissolved concentrations along different pathways, but the frequency distributions of the concentrations in the evaluated domain were not greatly affected by the specifics of the transport. This was not the case further from the wellhead, as discussed above. However, on close inspection of the figures in the attachments to Annex F, it is evident that the SABGOM simulation resulted in higher concentrations than indicated by the samples or in the HYCOM-FSU and ADCP simulations. The SABGOM plume (e.g., 800–1,100 m and 1,100–1,400 m depth intervals, attachments F.2.1 and F.2.2 to Annex F) was narrower than the samples indicated occurred, and SABGOM consistently moved the plume southwestward even when ADCPs (and HYCOM) indicated the currents were moving oil in other directions. The model simulations using ADCPs and HYCOM-FSU predicted very similar concentrations. The spatial distributions of the high concentrations in the ADCP simulation were more closely aligned with the deep plume as indicated by the concentrations in the samples than the spatial distributions of the high concentrations in the HYCOM-FSU simulation (attachments F.1.1, F.1.2, F.3.1 and F.3.2 to Annex F).

The frequency distributions of the modeled and measured concentrations were more similar for PAH components than for some of the other components. Additionally, the modeled and measured concentrations compared more favorably in the deep plume (800–1,100 m and 1,100–1,400 m depth intervals) than higher in the water column. There also

were far fewer chemistry samples available from depths of 40 m to 800 m, and those samples were typically taken on a vertical cast that was targeting sampling of the deep plume contamination. That sampling strategy would miss sampling rising oil, and components dissolving from them, above the deep plume that was displaced by currents, particularly when those shallower "plumes" were relatively narrow moving through a vast ocean (features evident in the model results, see figures in the attachments to Annex E, comparing depth zones for the same model simulation). There were many more chemistry measurements below MDL in samples taken between 40 and 800 m than there were in deeper water. Thus, comparisons of modeled peak concentrations to samples in the lower layers where sampling targeted fluorescence peaks and dissolved oxygen sags are much more meaningful than those in upper layers where sampling was infrequent, not targeted at peaks, and partially biased.

The maximum BTEX (AR1) concentrations predicted by the model were generally ~25–100 $\propto\gamma$/L, with the exception of the core of the deep plume within 800–1,000 m where concentrations were up to ~300 $\propto\gamma$/L. AR2 and AR3 concentrations showed similar distributions to those for AR1. Hazen et al. (2010) measured volatile hydrocarbon concentrations in 17 deep-water samples from 10 locations May 25–June 2. They detected a deep-sea oil plume from 1,099 m–1,219 m at distances up to 10 km from the wellhead, with a mean of 139 µg/L volatile aromatic hydrocarbon concentration.

Components AR5 and AR6 include the C0-C4 naphthalenes and C0-C4 benzothiophenes (i.e., the semi-soluble PAHs), whereas AR7 and AR8 (the 3-ring PAHs) are slightly soluble. The measured and modeled concentrations include dissolved and, in the deep plume, particulate PAHs in micro-droplets. The highest concentrations of modeled and observed AR5 in the deep plume were in the range ~50–100 $\propto\gamma$/L. The highest concentrations of modeled and observed for each of AR6 and AR7 in the deep plume were in the range ~20–50 $\propto\gamma$/L, whereas for AR8, highest concentrations were ~15–30 $\propto\gamma$/L. As addition corroboration, GC/MS analyses of water samples collected by Diercks et al. (2010) at depths at which fluorescence and beam attenuation showed anomalies confirmed the presence of PAHs at concentrations up to 189 µg/L in discrete depth layers between 1,000 and 1,400 m southwest of the wellhead site and extending at least as far as 13 km.

Components AR7 and AR8 include the 3-ring PAHs. The comparisons at 1,100–1,400 m show a similar pattern as the naphthalenes (AR5 and AR6), whereas for the 800–1,000 m depth range the model and observed frequency distributions of concentrations overlay well. For all chemical components, the closest results to the observed are in this depth range.

For the AR9 component, below 800 m the maximum modeled concentrations compare favorably with the observations. The highest concentrations of modeled and observed AR9 in the deep plume were in the range ~1,000–3,000 ∝γ/L (1–3 mg/L). However, the comparisons of frequency distributions of AR9 concentrations are somewhat variable. In some time windows the model and observed are very similar, whereas in others the model tends to over-predict the volume where high concentrations were observed (assuming the samples are representative). The model may have overestimated the volume with these higher concentrations (perhaps due to underestimation of biodegradation rates for compounds included in AR9) or the samples may not have been taken in areas where high concentrations occurred. The latter was the case for within 1 km of the wellhead and likely for sampling between 40 m and 800 m. In addition, the measured percentage of the compounds included in AR9 was often well below 100% of the chemicals examined, which biases the chemistry results low as compared to the model results that include 100% of the chemicals listed as measured in at least a few samples. With the gaps in sampling and incomplete chemistry analyses, it is not possible to definitively determine which of these explanations are true. The AR9 component contributes the most to the total soluble and semi-soluble hydrocarbon concentrations, so the comparisons of modeled to observed are similar for total soluble and semi-soluble hydrocarbon concentrations as well.

There was a statistically significant (α= 0.01) decrease in both the sample concentrations and the percent detectable results in samples taken in and just above the deep plume (800–1,100 m) after the June 3 riser cut and Top Hat #4 placement when oil recovery from depth began and the volume of oil released to the environment decreased substantially (Figure 2-7). A decrease after June 6 (i.e., in OCR3) is evident in the model results and the compared chemistry samples.

Uncertainties in these comparisons may result from the modeled transport or rate processes, field measurements of hydrocarbon chemistry (e.g., the GC/MS only reported the target analytes amenable to analytical methods that can be measured, see details in Payne and Driskell 2015b), or the input data used for modeling (e.g., currents, droplet size distribution of dispersant-treated and untreated oil released at depth, microbial degradation rates). In addition, the large gaps between sampling locations in both space and time contributed a considerable amount of uncertainty, which precludes any interpolation of the sample concentrations in this dynamic environment. Furthermore, the sampling efforts to depict hydrocarbon distributions within the water column may be complicated by the unavoidable heterogeneity in the water column and sampling artifacts (e.g., shipboard sample contamination or inclusion of surface oil from passing an open Niskin bottle through a slick when attempting to collect a water sample at depth, etc.). For these reasons, sampling gaps in space and time can make conclusive interpretation of field

observations quite difficult when attempting to assess the contaminant conditions on a larger scale. Furthermore, there is no evidence of either the presence or absence of oil in regions that were not sampled.

4.4.1.3 Mass Balance in Deep Water

By 30 September 2010, 15% of the released oil remained in waters below 40 m in the model simulation, primarily as biodegradation products and microbial biomass deriving from dissolved components and hydrocarbons from dispersed micro-droplets. This falls within the estimated range of 4–31% of the released oil that was sequestered in the deep-sea based on field data analysis by Valentine et al. (2014). Daling et al. (2014) estimated dissolution loss into the water during the ascent from 1,500 m water depth to the surface was ~15% of the oil with the oil composed of: saturates < C7 (10 weight % of the stabilized source oil), BTEX (3 weight % of the source oil), and C-3-Benzenes (1.5 weight % of the source oil). The 15% estimate accounts for all the water-soluble hydrocarbons in the released oil, so the implicit assumption made by Daling et al. was that dissolution of the soluble hydrocarbons was complete for all droplet sizes before the oil surfaced. Additionally, Daling et al. (2014) estimated about 18% of the total PAH's (PAHs representing 1.1 weight % of the total oil), corresponding to about 0.2 weight % of the source oil, was dissolved in the water before the oil surfaced. Based on analysis of freshly-surfaced oil sampled in June 2010, Stout et al. (2016a) estimated that 20–25 weight % of the oil was lost to dissolution before the (larger droplets of) oil reached the surface.

In the SIMAP model results, 36% of the degraded mass below 40 m derived from dissolved soluble (AR1, AR2, AR3, AR5, and AR9) and semi-soluble (AR4, AR6, AR7, and AR8, i.e., PAHs) hydrocarbons. On average over the entire spill, ~5% of the total oil hydrocarbons released into the environment dissolved before oil droplets reached 40 m on the way to the water surface. Since 18% of the released oil was soluble and semi-soluble hydrocarbons, the remaining 72% of the soluble and semi-soluble hydrocarbons rose through 40 m to the surface water, and either dissolved in the upper 40 m or volatilized. All soluble and semi-soluble hydrocarbons in droplets remaining below 40 m dissolved and eventually biodegraded in the model simulation, whereas soluble components did not completely dissolve from the large droplets that rose to the surface in a few hours. One would expect this to be the case, as surfaced fresh oil did contain measurable BTEX and soluble alkanes (Stout 2015c, Stout et al., 2016), which volatilized rapidly. Ryerson et al. (2012) measured these volatiles in the atmosphere above the rising oil and fresh oil slicks.

Ryerson et al. (2012) estimated that, on June 10, 19–20% of the total oil hydrocarbon mass released to the environment was trapped in the deep plume, 8–9% was in the surface slicks, and 17.4–18.4% was evaporated. This left ~54% unaccounted for in their analysis. The missing fraction of oil would presumably be biodegraded, suspended in the water

column other than in the intrusion layer deep plume, and/or sunken to the seabed (see Annex B, Section 2.1.1 for further detail). The Ryerson et al. (2012) mass balance analysis has a number of sources of uncertainty, including that it depends on: (1) an estimate of the total integrated dissolved oxygen anomaly by Kessler et al. (2011) and (2) Hazen et al.'s (2010) estimated ratios of alkanes to toluene in the plume phase versus in the leaking fluid phase (assumed to reflect the ratio of droplet to dissolved phase hydrocarbons–on the premise of the co-location of the dissolved versus droplet phases). To the extent that droplets rose out of the deep plume preferentially leaving dissolved-phased hydrocarbons at depth (a process known to have occurred), the Ryerson et al. (2012) estimate of 19–20% being in the deep plume is an overestimate. The SIMAP model estimates for June 10 (Figure 4-1) are that about 24% was in the water column (at all depths, with 15% below 40 m), 23% had degraded (at all depths, with 9% below 40 m), 11% was on the water surface, 38% was in the atmosphere and 3% had gone ashore. As 61% of the fresh MC252 oil was volatile, at least 62% (38%/0.61) of the oil released to date surfaced by June 10, leaving less than 38% in deep water.

4.4.2 Model Results for Simulations above 40 meters

4.4.2.1 Model-predicted Concentrations

The model-predicted concentrations in the upper 40 m are presented in Annex E.5. Only results from the simulation using HYCOM-FSU currents and NARR winds are presented. Though the locations of the oil and dissolved components vary with the different currents and winds used, all simulations resulted in similar characteristic patterns and patchiness in the distributions. The concentration in the upper 40 m of the water column show distributions indicated by the trajectories of floating oil in Annex C.1.

Annex E.5.1 shows the modeled total hydrocarbon concentrations in oil droplets, most of which are entrained by waves from surface oil. Annex E.5.2 shows the modeled total dissolved hydrocarbon concentrations, including all 9 soluble and semi-soluble components (AR1 to AR9). These concentrations are almost entirely of PAHs, as concentrations of AR1, AR2, AR3 and AR9 components are largely lost to dissolution as the oil rose to the surface and they are depleted immediately after oil surfaces by evaporation. Thus, only TPAH is presented. For both total and dissolved hydrocarbons, only concentrations greater than 1 $\propto\gamma$/L (ppb) are plotted in the figures.

The figures are snapshots each 4 days of the simulation, depicting top-down map views of the vertical maximum dissolved hydrocarbon concentration in the upper 40-m mixed layer of the water column. The grid cells are 500 m x 500 m x 5 m deep, and the vertical maximum is for the highest 5-m interval, typically that just under the surface. Concentrations are generally fairly uniform with depth in the upper mixed layer.

Modeled total hydrocarbon concentrations in oil droplets were primarily <100 ∝γ/L and under fresh oil in the range 100–1,000 ∝γ/L. The modeled dissolved PAHs concentrations were very patchy in distribution and ephemeral. Most of the concentrations were <25 ∝γ/L, with some concentrations under fresh oil in the range 25–100 ∝γ/L, occasionally between 100 and 200 ∝γ/L in small volumes (i.e., in a few 500 m x 500 m cells).

4.4.2.2 Comparison of the Modeled Concentrations to Field Measurements

A similar approach to that used for concentrations below 40 m was used to evaluate the modeled concentrations of PAHs in the upper 40 m as compared to samples. Because the sampling in the upper 40 m was not synoptic or representative of the entire modeled domain, the comparison was performed using NRDA samples collected within the 25 km by 25 km box centered on the wellhead between April 22 and July 15 of 2010. In the domain of interest, there were 196, 19 and 32 samples with PAH measurements made and quality checked in the upper 10 m, 10–20 m and 20–40 m, respectively. To ensure a sufficiently large enough number of samples for a frequency distribution, samples collected in the upper 10 m and (all) model results in the 625 km^2 x 10 m box around the wellhead were compared. Table 4-12 and Figure 4-29 show the frequency distribution of the 196 NRDA samples with PAH measurements collected within the domain and period of interest. Twelve bins of logarithmically increasing concentration ranges were used. The twelve bins used in Figures 4-29 and 4-30 are defined in Table 4-12.

The DWHOS Trustees (2016; Travers et al. 2015 a, b) identified 338 PAH-measurements from the NRDA quality checked data set, as well as other data sets obtained from the literature and BP's public database, which were of samples taken in the upper 20 m in areas of surface oil. These data were used to characterize exposure of plankton to PAHs in the upper 20 m of the water column. Figure 4-30 shows the frequency distribution of the 283 detectable PAH-measurements in the sample set, which was downloaded from ERMA (2016) in September 2106. The concentration frequencies are similar to the 196 NRDA samples in the 625 km^2 x 10 m box around the wellhead. The area around the wellhead was exposed to floating oil throughout the period of interest (April 22 and July 15 of 2010).

Note that for both sets of samples, there is a lower frequency of PAH concentrations <0.1 ∝γ/L than for concentrations in the range 0.1–10 ∝γ/L. This suggests a bias in the sample chemistry results, potentially due to sampling under and near oil and to some analytes being below the detection limit. The DWHOS Trustees (2016; Travers et al. 2015 a, b), of course, purposely biased the sample set to be associated with floating oil.

The samples are of whole water, so would include dissolved PAHs and micro-droplets that did not surface from the sample during handling. Thus, comparisons of the modeled

concentrations to these samples were made considering PAHs in the particulate phase (i.e., in dispersed droplets) and the dissolved phase.

Table 4-12. Frequency distribution of PAH concentrations in field samples from the 10-m surface layer of a 625 km^2 box centered on the wellhead.

Range	Concentration (µg/L)		Fraction of Samples in Each Concentration Bin				
Bin Range #	Minimum	Maximum	AR5	AR6	AR7	AR8	TPAH
0	0	0.001	0.026	0.092	0.051	0.117	0.005
1	0.001	0.005	0.036	0.020	0.036	0.051	0.010
2	0.005	0.01	0.056	0.061	0.046	0.046	0.026
3	0.01	0.05	0.163	0.179	0.173	0.138	0.117
4	0.05	0.1	0.082	0.112	0.056	0.112	0.061
5	0.1	0.5	0.255	0.362	0.245	0.357	0.184
6	0.5	1	0.117	0.107	0.184	0.071	0.107
7	1	5	0.240	0.061	0.204	0.102	0.367
8	5	10	0.020	0.000	0.000	0.000	0.087
9	10	50	0.000	0.005	0.005	0.005	0.031
10	50	100	0.005	0.000	0.000	0.000	0.000
11	100	500	0.000	0.000	0.000	0.000	0.005
12	500	>1000	0.000	0.000	0.000	0.000	0.000
Total>0.001	0.001	>1000	0.974	0.908	0.949	0.883	0.995
Total >= 0	0	>1000	1.000	1.000	1.000	1.000	1.000

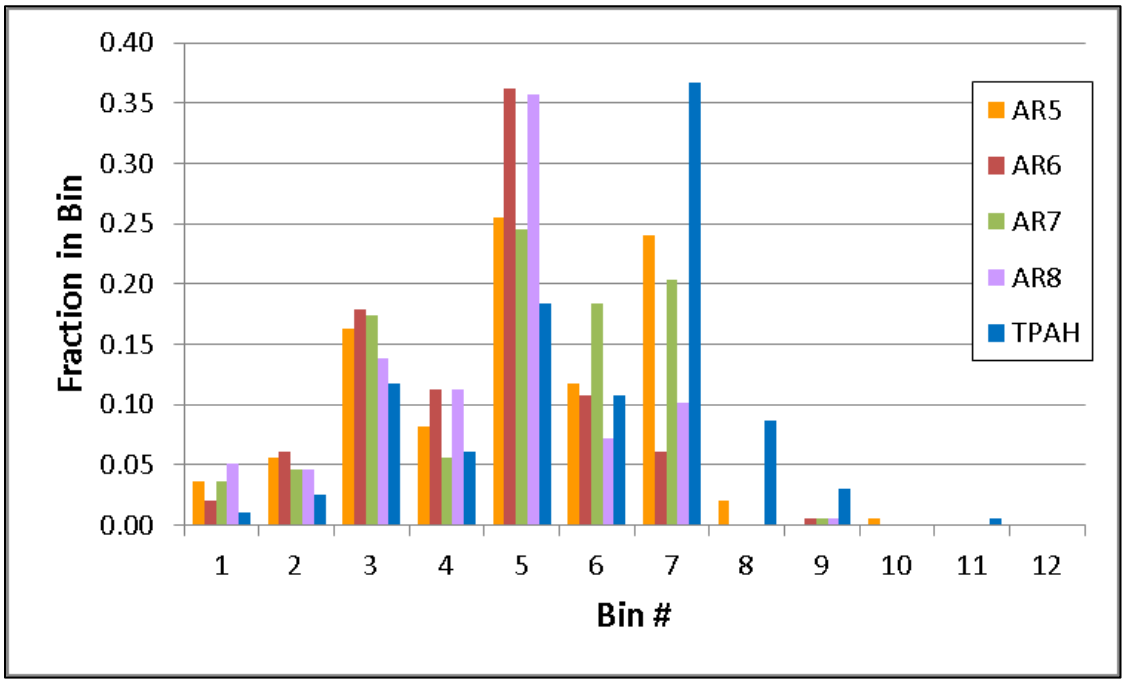

Figure 4-29. Frequency distribution of detectable PAH concentrations >0.001 ∝γ/L in field samples from the 10-m surface layer of a 625 km^2 box centered on the wellhead.

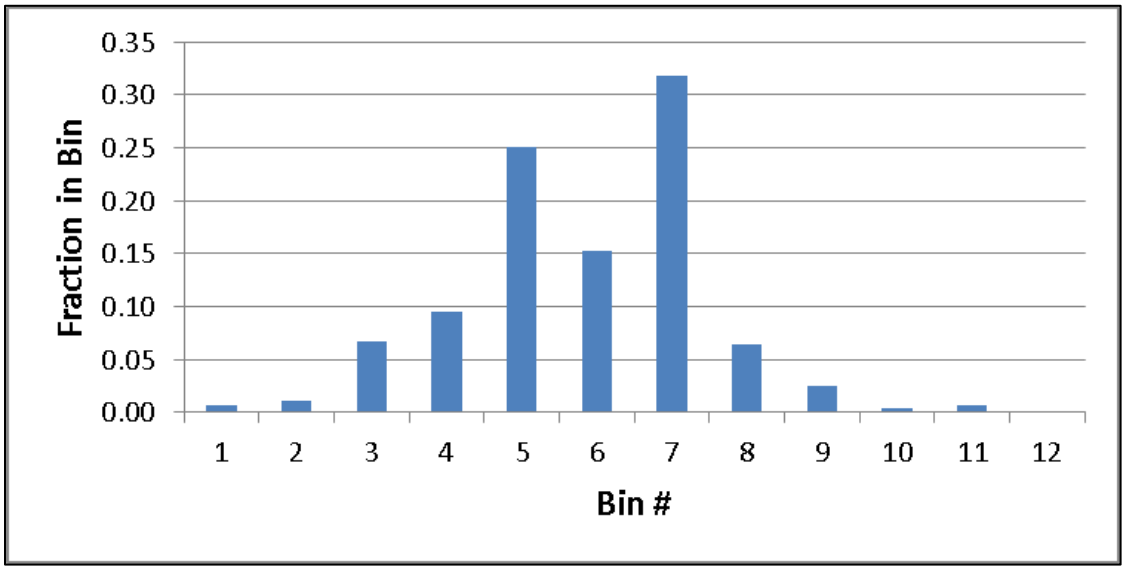

Figure 4-30. Frequency distribution of detectable PAH concentrations >0.001 ∝γ/L in the sample set identified by Travers et al. (2015a) taken in areas of surface oil.

The modeled concentrations of PAHs in both the dissolved phase and in droplets were calculated to determine their contribution to the total concentrations and to compare to the observations. For this calculation, PAH mass was assumed evenly distributed over the volume of water occupied by the Lagrangian Element (LE) representing the cloud of droplets or the dissolved mass. The LE volume was approximated by a cylinder, circular in the horizontal dimension. The radius of the LE volume at a given time step was estimated as the dispersive distance, D_h, defined as 2 standard deviations of a Gaussian-shaped spread of mass, which increases over time since release (or dissolving), t_a, at a rate scaled by the horizontal dispersion coefficient, D_{xy}:

$$D_h = \sqrt{2\, D_{xy}\, t_a}$$

The vertical spread (height of the cylinder, h_z) is calculated similarly using the vertical dispersion coefficient, D_z.

$$h_z = \sqrt{2\, D_z\, t_a}$$

Modeled concentrations of PAHs in the volume of water within the box (6.25 x 10^9 m^3) were calculated for each of 4,800 half-hour time steps over 100 days of simulation. The volume of water in the box occupied by LEs of a given concentration range (i.e., for each bin in Table 4-12) were summed over all time steps of the 100 days, and divided by the total volume of the box times 4,800 "sampling" times (i.e., by 3.0 x 10^{13} m^3). This yielded an average (over the time of the simulation) fraction of the volume of the box where total PAH

concentration fell within the concentration bin. For the purposes of this calculation, if the fraction of the box volume was less than 1.0, it was assumed that the LEs were not overlapping. If the fraction exceeded 1.0, the LE volumes were overlapping, and the entire box was assumed contaminated to that bin level over the 100 days of simulation.

For the simulation with HYCOM-FSU and NARR winds, the entire water volume of the 625 km^2 x 10 m box, on average, was affected by dispersed droplets, and 71% of the water volume had TPAH concentrations in droplets > 0.1 $\propto\gamma$/L. Figures 4-31 and 4-32 show the frequency distributions of particulate phase and the dissolved phase concentrations, with the particulate phase clearly dominating, in the box (note the difference in the concentration scales in the figures). Just 1.5% of the box volume had dissolved PAH concentrations >0.001 $\propto\gamma$/L, with 1.4% being > 0.1 $\propto\gamma$/L. Figure 4-33 shows the frequency distribution of the total of dissolved and particulate phase PAH concentrations in the box volume (indistinguishable from Figure 4-31). The shape of the frequency distribution of model results is what one would expect as concentrations dilute and degrade over time.

Figure 4-33 may be compared with the chemistry sample frequency distribution in the box shown in Figure 4-29. However, the clear bias in the chemistry sample results compromises the comparisons below 0.1 $\propto\gamma$/L. Above this concentration threshold, the modeled fraction of water contaminated to the binned concentration levels is similar to the fraction of measurements falling within those bins. The model predicts that about 71% of the water samples would have concentrations >0.1 $\propto\gamma$/L, whereas 78% of the NRDA samples and 82% of the 338 samples used by the DWHOS Trustees (2016) exceeded this threshold.

Figures 4-34 to 4-37 show the frequency distributions in the box volume of the total of dissolved and particulate phase concentrations for AR5, AR6, AR7 and AR8, respectively, for the simulation with HYCOM-FSU and NARR winds. The dissolved phase concentrations for the AR5, AR6, AR7 and AR8 components were > 0.001 $\propto\gamma$/L in 1.4–1.5% of the 625 km^2 x 10 m box (i.e., in 9 x 10^7 m^3), on average. The particulate concentrations > 0.1 $\propto\gamma$/L occurred in 11% (AR5), 41% (AR6), 41% (AR7), and 52% (AR8) of the box, on average. Thus, the particulate PAHs made up the majority of the concentrations. Based on the simulation using HYCOM-FSU and NARR winds, the volume in which TPAH concentrations exceed 0.1 $\propto\gamma$/L averaged 4.4 x 10^9 m^3.

For the simulation with SABGOM and NARR winds, dispersed droplets only occupied 0.0004% of the 625 km^2 x 10 m box around the wellhead (i.e., in 1.3 x 10^8 m^3) on average. Dissolved phase PAH concentrations > 0.001 $\propto\gamma$/L occupied 3.8% of the box. The very low droplet concentrations were due to the strong SABGOM currents at depth that advected the released oil toward the southwest out of the wellhead area (and 625 km^2 box) very quickly.

This resulted in surface oil stretched to the southwest, as well (see SABGOM figures in Annex C.2 and C.3). The concentrations in the box are mostly 10–50 ∝γ/L because dispersion by the SABGOM current field is very low. The SABGOM results do not appear to be as realistic as the HYCOM-FSU results.

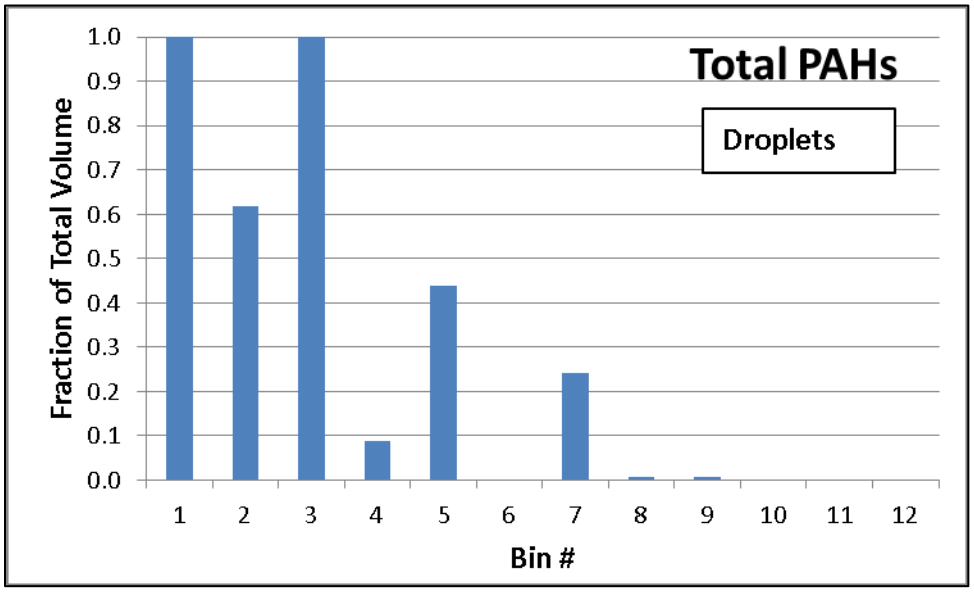

Figure 4-31. Frequency distribution of modeled PAH concentrations >0.001 ∝γ/L in the particulate phase in the 10-m surface layer of a 625 km^2 box centered on the wellhead–HYCOM-FSU simulation.

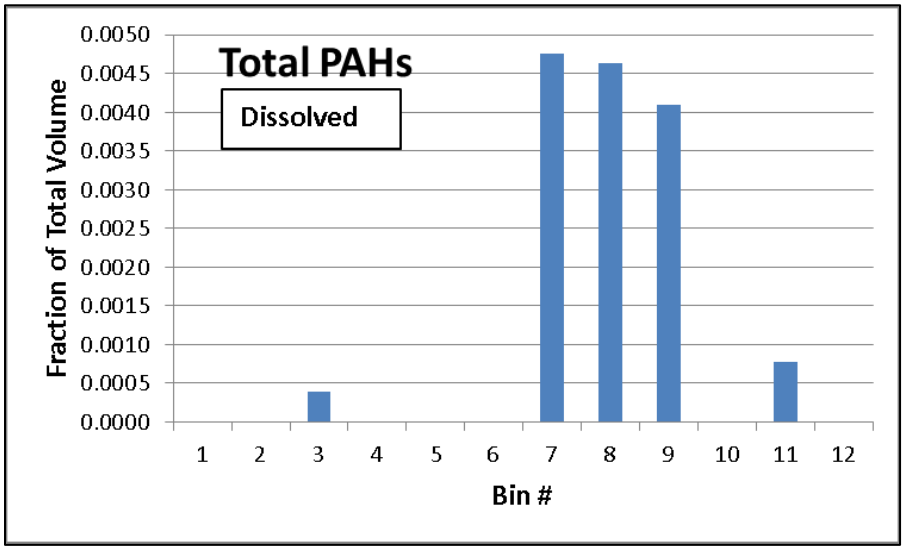

Figure 4-32. Frequency distribution of modeled PAH concentrations >0.001 ∝γ/L in the dissolved phase in the 10-m surface layer of a 625 km^2 box centered on the wellhead.

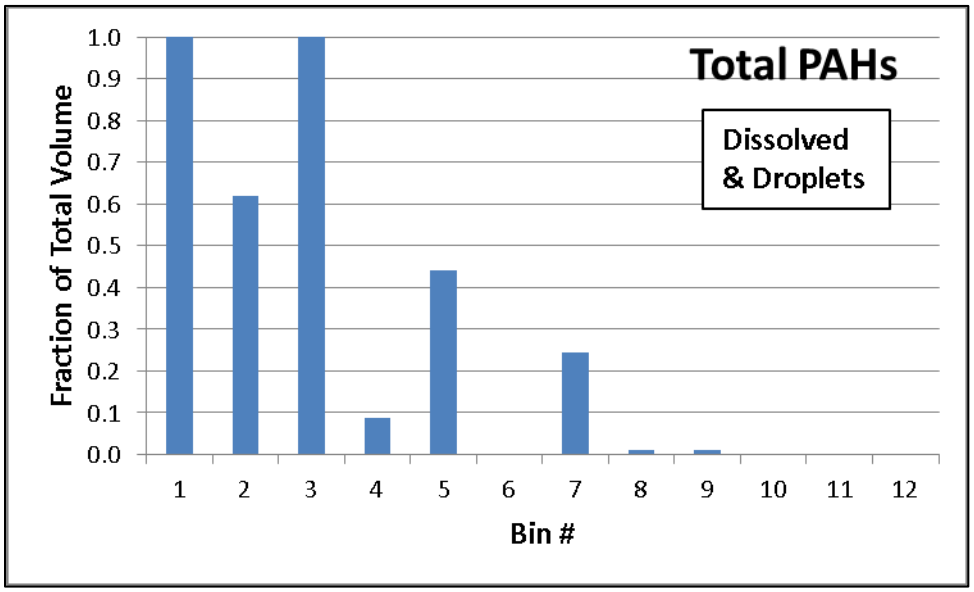

Figure 4-33. Frequency distribution of modeled PAH concentrations >0.001 ∝γ/L in both the dissolved and particulate phases in the 10-m surface layer of a 625 km^2 box centered on the wellhead.

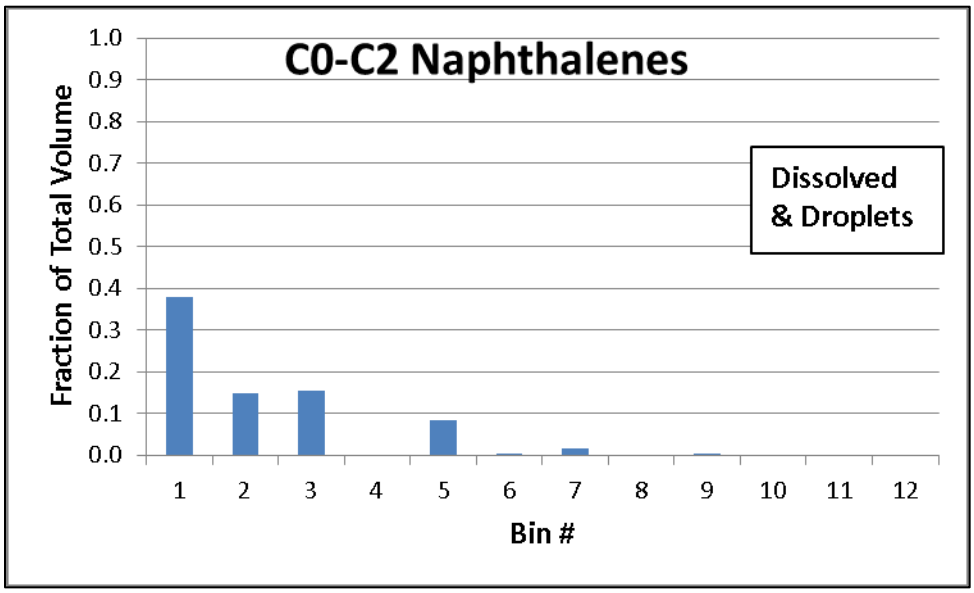

Figure 4-34. Frequency distribution of modeled AR5 concentrations >0.001 ∝γ/L in both the dissolved and particulate phases in the 10-m surface layer of a 625 km^2 box centered on the wellhead.

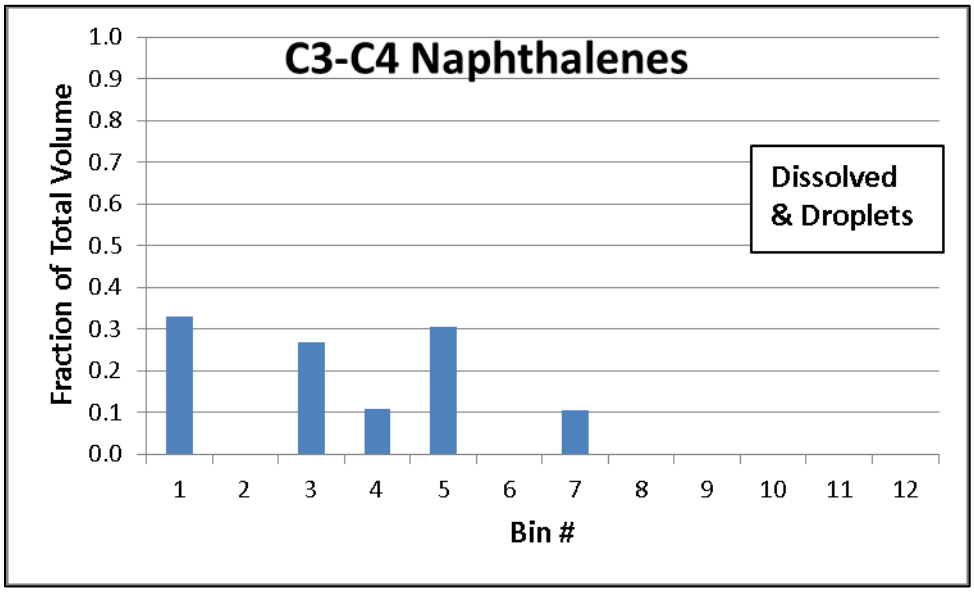

Figure 4-35. Frequency distribution of modeled AR6 concentrations >0.001 ∝γ/L in both the dissolved and particulate phases in the 10-m surface layer of a 625 km² box centered on the wellhead.

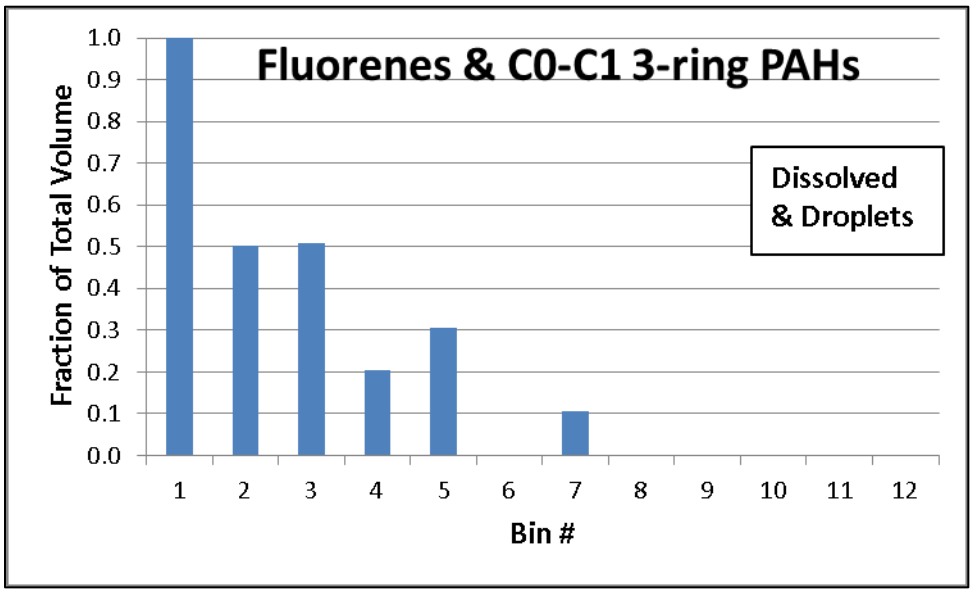

Figure 4-36. Frequency distribution of modeled AR7 concentrations >0.001 ∝γ/L in both the dissolved and particulate phases in the 10-m surface layer of a 625 km² box centered on the wellhead.

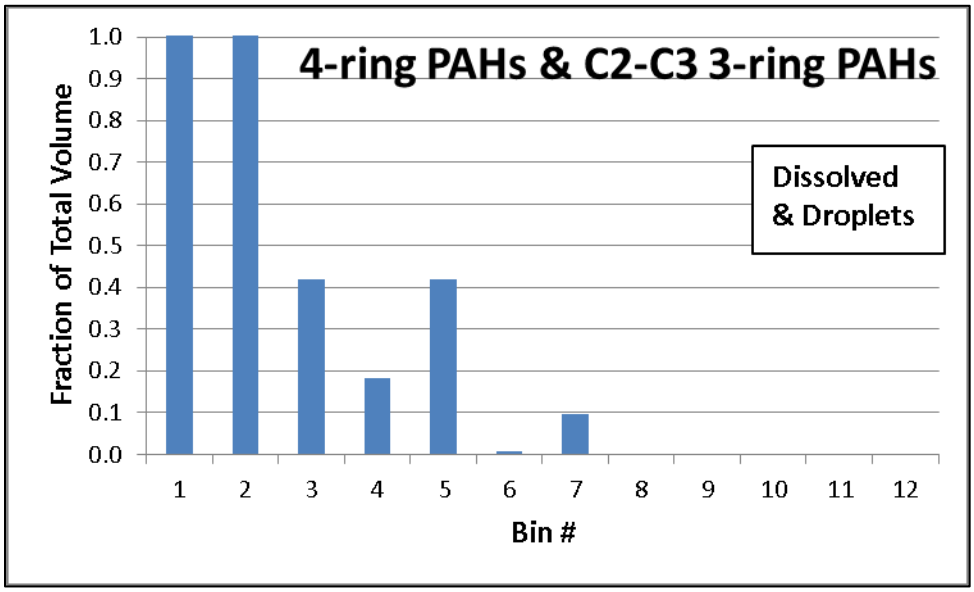

Figure 4-37. Frequency distribution of modeled AR8 concentrations >0.001 ∝γ/L in both the dissolved and particulate phases in the 10-m surface layer of a 625 km² box centered on the wellhead.

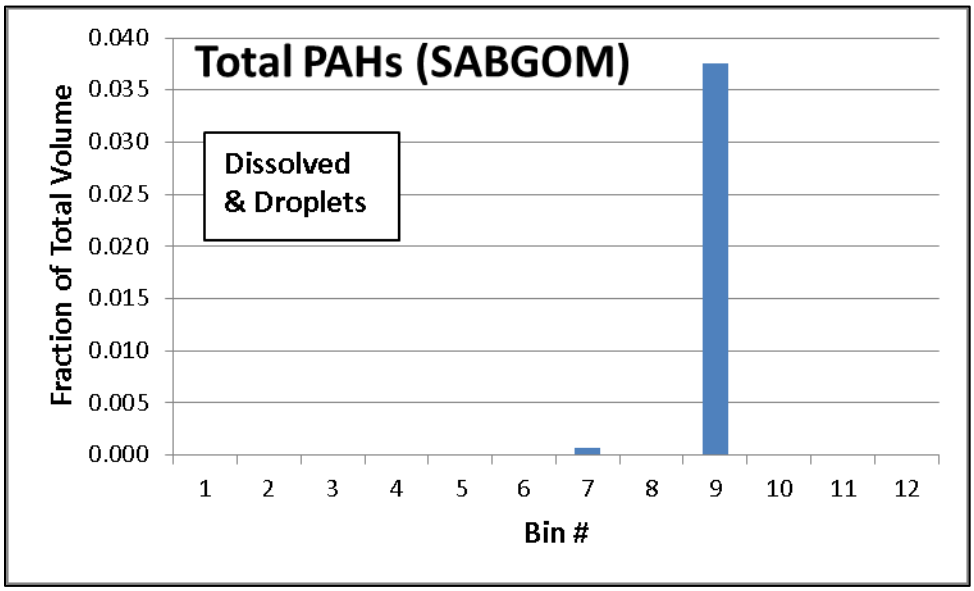

Figure 4-38. Frequency distribution of modeled PAH concentrations >0.001 ∝γ/L in the particulate phase (in water containing dispersed droplets) in the 10-m surface layer of a 625 km² box centered on the wellhead.

4.5 Sedimented Oil

The model estimated the mass of oil hydrocarbons settling to subtidal sediments, which was about 1% of the released oil. Stout et al. (2015) estimated ~7% of the released oil settled near the wellhead by 2011 with most settling before late August 2010. Some of that settled oil would be accounted for by the junk shots and oil associated with drilling muds (Stout and Payne 2017), a flux not included in the modeling. The SIMAP model simulation ended September 30, 2010. Estimates of organic SPM concentrations needed to model oil flux in marine snow were unavailable prior to September 30, 2010; therefore organic-born oil flux is not included in the modeling.

The deposition of total hydrocarbons to the sediments, as predicted by the model simulations, is mapped for four simulations in Figures 4-39 (HYCOM-FSU), 4-40 (SABGOM), 4-41 (IAS ROMS), and 4-42 (ADCPs). The map in the upper panel depicts settling from depths of 200-800m; the lower panel shows settling from depths >800m. The sedimentation patterns for the simulations using HYCOM-FSU and the ADCPs are very similar, indicating the net transport by the HYCOM-FSU model at depth is reasonable. The sedimentation pattern for the simulation using SABGOM is highly stretched to the SW and NE, aligned with and indicating strong current transport. The simulation using IAS ROMS is similar, but less extreme. IAS ROMS was derived from SABGOM and it assimilated ADCP data, which apparently reduced the flow somewhat towards the southwest. This highly-stretched pattern was not seen in the sediment chemistry results (Valentine et al. 2014; Stout 2015d; Stout et al. 2015, 2016b; Stout and Payne 2016a).

MC252 oil from the spill was identified on the sediments in the offshore area surrounding and down-stream of the well site, primarily within the basin area around the well, but also extending somewhat southwest and northeast (Joye et al. 2011; Montagna et al. 2013; Valentine et al. 2014; Stout 2015d). Thus, the sedimentation pattern in the HYCOM-FSU and ADCP simulations appear to be more comparable to the observations than the IAS ROMS or SABGOM simulations.

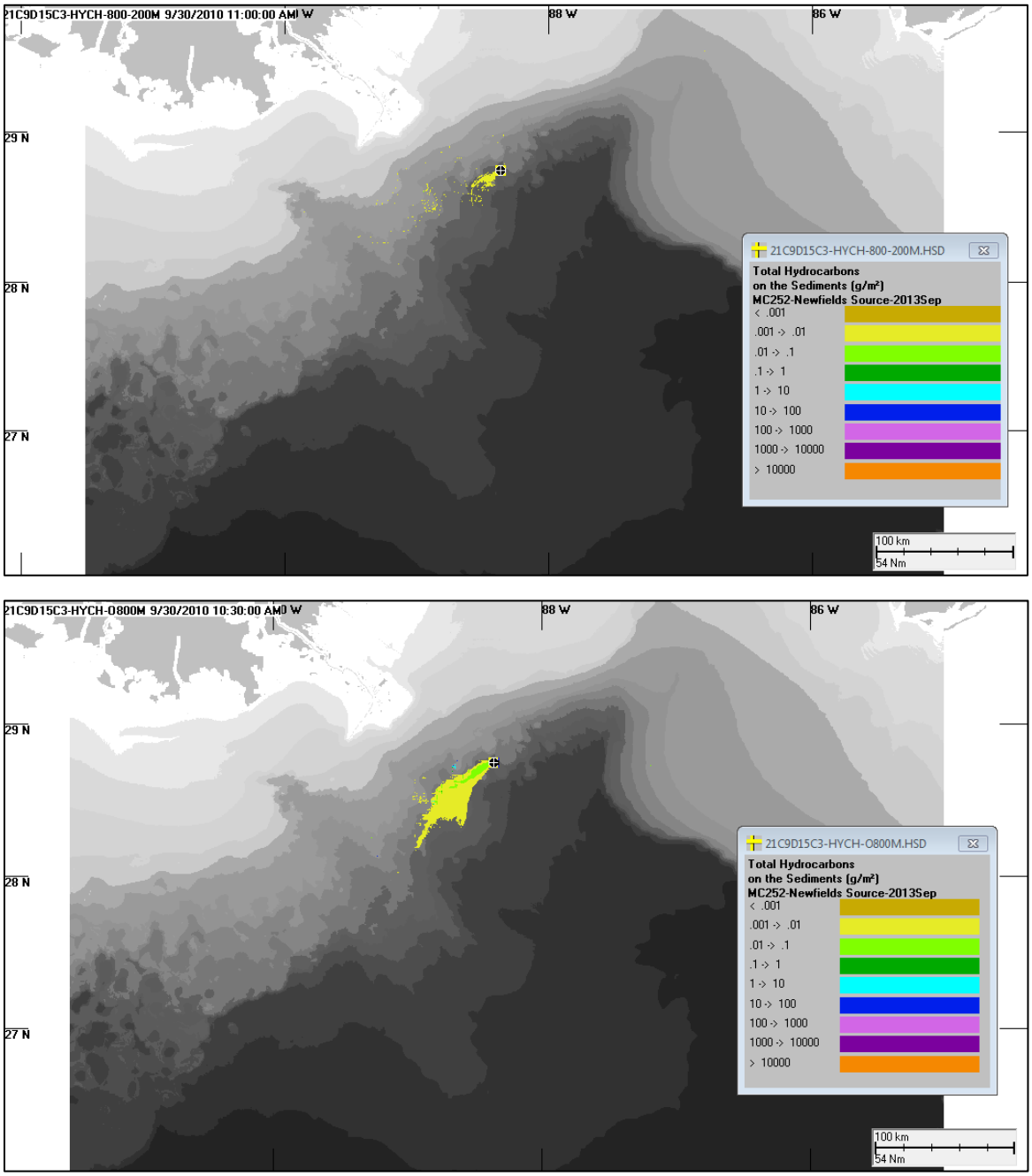

Figure 4-39. Modeled mass distribution of total hydrocarbons settled to the sediments by September 30, 2010.
Upper panel depicts settling from depths of 200-800m; the lower panel shows settling from depths >800m.

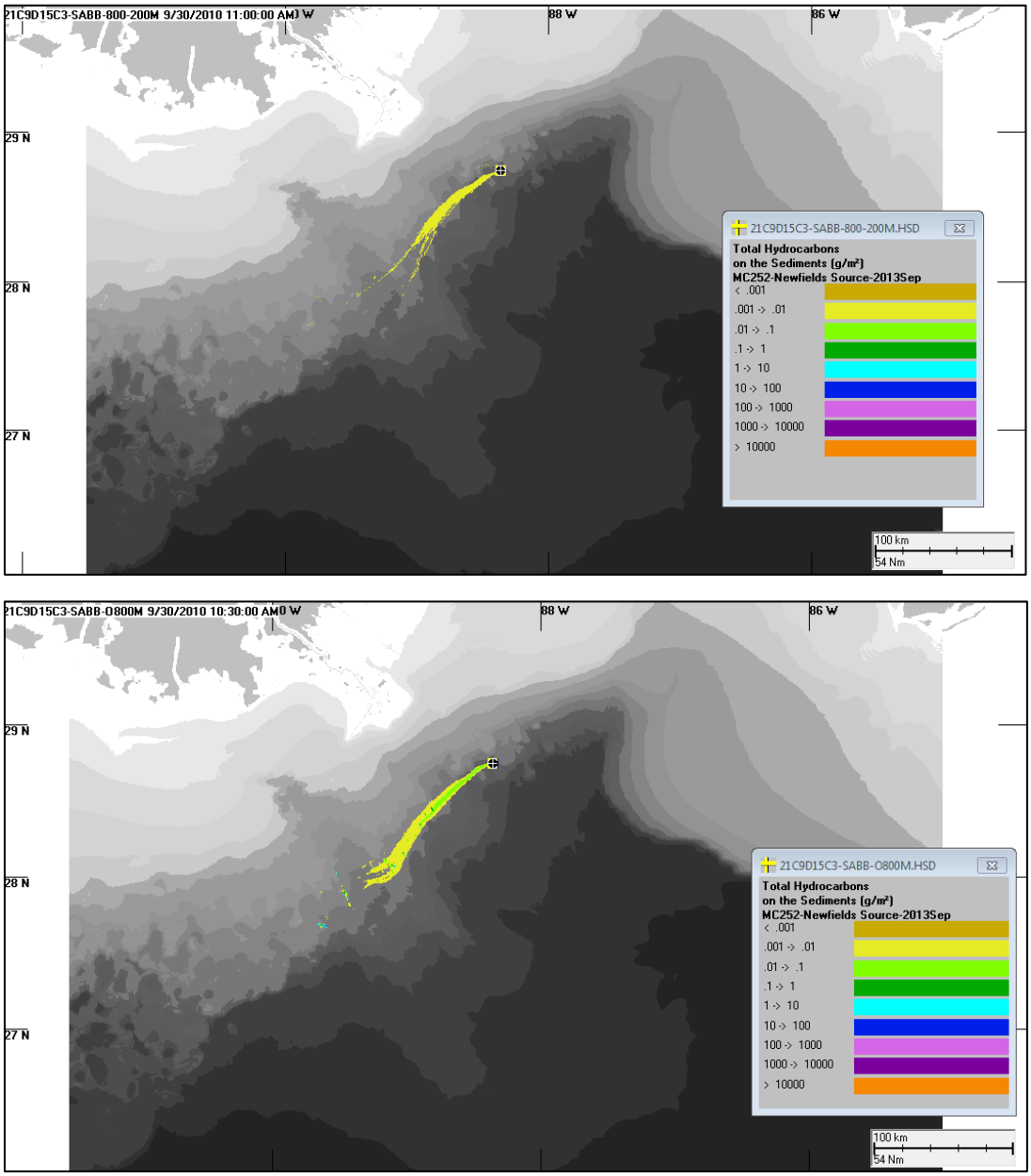

Figure 4-40. Modeled mass distribution of total hydrocarbons settled to the sediments by September 30, 2010.
Upper panel depicts settling from depths of 200-800m; the lower panel shows settling from depths >800m.

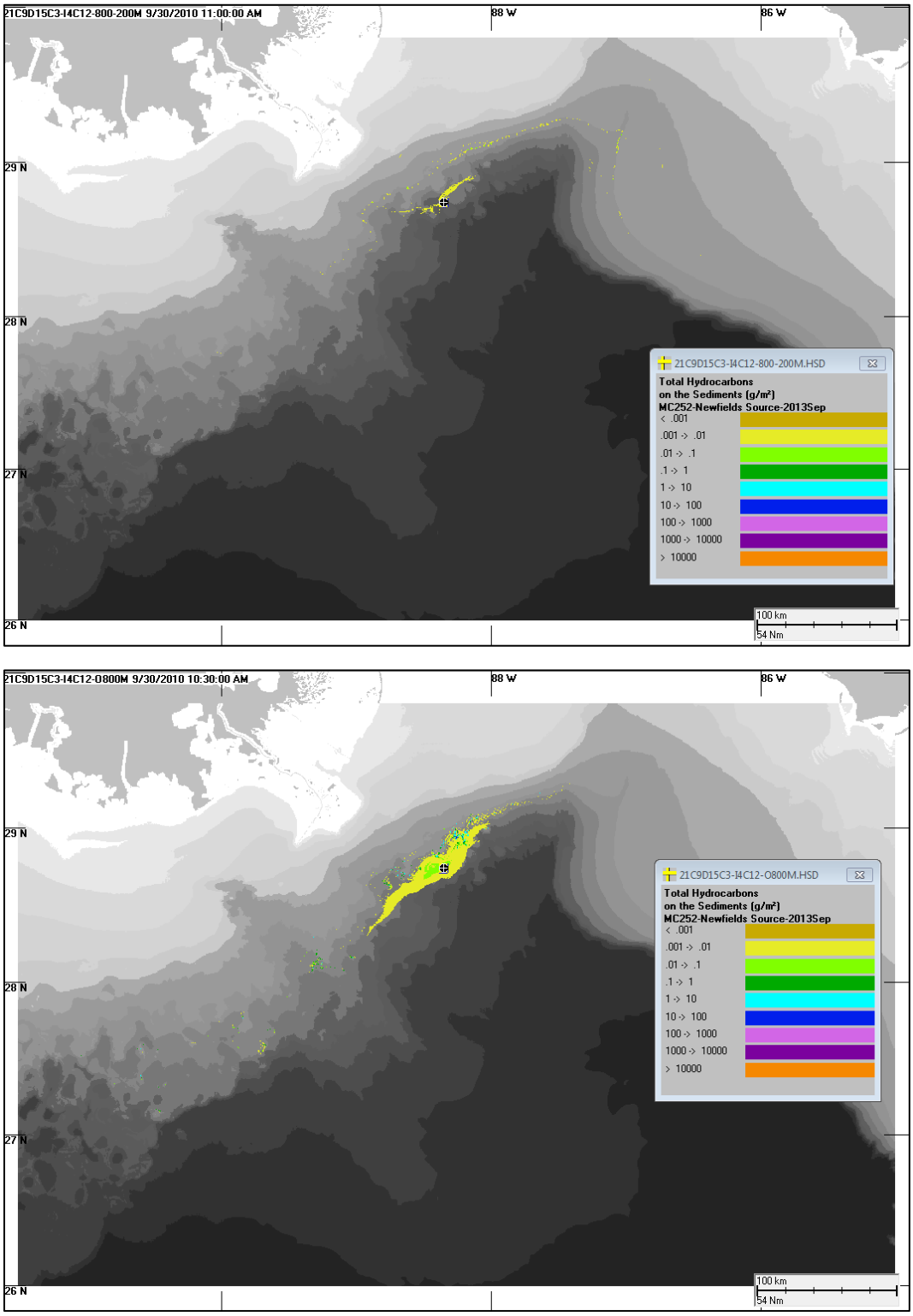

Figure 4-41. Modeled mass distribution of total hydrocarbons settled to the sediments by September 30, 2010.

Upper panel depicts settling from depths of 200–800m; the lower panel shows settling from depths >800m.

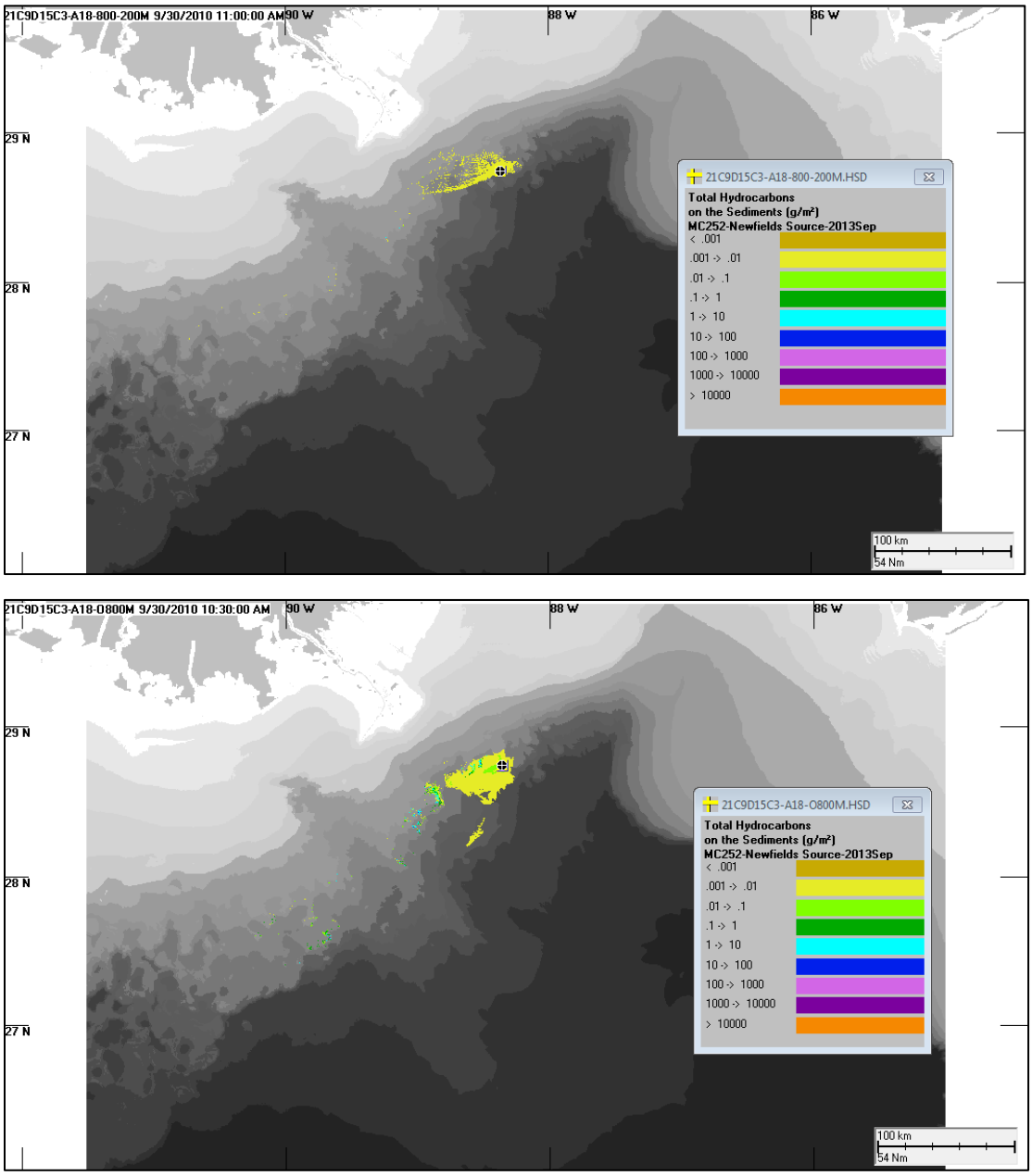

Figure 4-42. Modeled mass distribution of total hydrocarbons settled to the sediments by September 30, 2010.
Upper panel depicts settling from depths of 200–800m; the lower panel shows settling from depths >800m.

5. Summary and Conclusions

A modeling analysis of the transport and fate of the DWHOS was undertaken, using the SIMAP oil fate model to evaluate the distribution and mass of oil in the water column, on the water surface, on shorelines, and in the sediments through time. Pipe-discharge, blowout and droplet size models (Spaulding et al. 2015; 2017; Li et al. 2017a) were used to provide needed initial release conditions (i.e., oil mass and droplet sizes released at depth from the blowout) to the SIMAP oil fate model calculations. In the model, the oil is treated as being comprised of 9 soluble (and volatile, including 8 aromatic and 1 aliphatic) pseudo-components and 9 insoluble (8 volatile and one non-volatile residual oil) saturated pseudo-components, described in Section 3.1. Processes simulated in the physical fates model include oil droplet and surface oil transport and dispersion, oil surfacing, surface oil spreading, evaporation of volatiles from surface oil to the atmosphere, stranding of oil on shorelines, emulsification of oil, entrainment of oil as droplets into the water column, re-surfacing of oil, dissolution of soluble components into the water column, volatilization from the water column to the atmosphere, partitioning of oil between water and sediment, sedimentation of oil droplets, and degradation. Output of the fate model includes the location and dimensions of floating oil, mass and concentrations of hydrocarbon constituents in water, and fluxes of hydrocarbons to air and sediment over time. Concentrations of particulate (oil droplet) and dissolved hydrocarbon concentrations are saved to files for later viewing and evaluations.

5.1 Model Inputs

The oil fate model requires geographic information, environmental conditions, oil properties and degradation rates, winds and currents as inputs. Geographic information and environmental conditions were readily mapped from government data sources (Section 2.1, 2.2, 2.5). Physical-chemical properties and degradation rates are described in Appendix II, and specifics for DWHOS are described in Section 2.3 of Volume II. Winds and waves were available from wind and wave models, as well as other wind products and measurement data. Wind data were available for six stations in the area affected by the spill. Current data were available for the offshore continental slope area of the northern GOM from ADCPs that were moored or attached to offshore platforms. The ADCP and other field current data sets did not adequately characterize shelf or near shore waters, nor did they characterize parts of the GOM outside of areas of measurement data. Thus, existing meteorological and hydrodynamic models were evaluated and used in the modeling of transport in surface waters, as well as deep waters near the wellhead where there was coverage with ADCP measurement data.

Specifics for the spill scenario included release rate and duration, response activities, and the initial conditions provided by the blowout model. Government estimates of the release volume to the environment and volumes burned or dispersed (Lehr et al. 2010) were used as model input assumptions. The amount of oil released to the environment was assumed to be ~559 thousand metric tons (4.26 million bbl).

The analysis by Spaulding et al. (2015, 2017) provided the initial release conditions (i.e., oil mass and droplet sizes released at the trap height) that were used as input to the SIMAP oil fate model calculations. The blowout modeling analysis estimated the nearfield plume was trapped between ~1,150 and 1,350 m. The droplet size distributions of the release were estimated daily, based on the sizes of the holes in the broken riser pipe where oil and gas were released, environmental conditions, and amount and method of dispersant application each day.

5.2 Observational Data Related to the DWHOS

5.2.1 Subsurface Oil

During the DWHOS blowout release, a considerable amount of oil was dispersed as oil droplets into the water column. The smaller droplets remained in the water column for an extended period due to their slow rise velocities, while larger droplets rose to the surface on the time scale of hours. The data reviewed in this report support the conceptual model that large droplets rose quickly in the immediate vicinity of the leaking wellhead, intermediate-sized droplets were transported further afield in the mid water column as they were subject to dissolution weathering and continued to rise through the water column, and a number of small droplets remained suspended in the deep water column intrusion layer (deep plume), where they weathered by dissolution processes, were colonized by microbes and degraded, and in some cases combined with SPM to eventually settle to the sea floor as marine snow. Observational data were compiled and reviewed for use in validation the model results.

Changes in the chemical composition of the MC252 oil at depth also support the preceding description of the transport of dissolved compounds, dispersed oil, and larger droplets. Most water-soluble compounds such as benzene, alkylated mono-aromatics, and soluble C5-C10 alkanes were enriched in the deep plume. Compounds with lower water solubility were present both in the deep water and in the upper water column as mixtures of dissolved and particulate oil droplets.

Considerable spatial heterogeneity was evident in the observed distribution of hydrocarbons at various depths. These resulted from variations in the oil release rate and subsea dispersant applications over time (changing droplet size distributions of the oil over time), slow (< 5–20 cm/s) but spatially- and temporally-varying currents throughout the

water-column, as well as dissolution, dispersion, and degradation of hydrocarbon constituents, and irregularly positioned sampling stations and different sampled depths. The multiple "plumes" that were observed moving in various directions presumably originated at different times, and indicated that complex and meandering current patterns were present in the area before sampling.

Maximum hydrocarbon and dispersant concentrations were observed in samples taken at the surface (<20 m) and at depths between roughly 1,000 and 1,400 m deep (Payne and Driskel 2015a; Horn et al. 2015b). The highest observed values were near the wellhead, and the concentrations typically decreased as distance from the wellhead increased. While some surface observations of hydrocarbons exceeded method detection limits beyond 150 km from the wellhead, the majority of concentrations greater than 1–10 µg/L were within approximately 50 km of the wellhead. The highest concentrations at depth were of the BTEX group (i.e., benzene, toluene, ethylbenzene and xylene) and soluble alkanes. Elevated dispersant concentrations were also identified between 1,000–1,300 m.

5.2.2 Surface Floating Oil

Remote sensing data (satellite imagery) data were used to: (1) indicate where oil surfaced which is useful for evaluating the model's predictions of the net transport of oil droplets to the surface (i.e., rise rates of various droplet sizes and subsurface movements), (2) evaluate the transport and spatial distribution of surface oil, and (3) estimate the amount of oil floating for comparison to the model's mass balance predictions that are functions of weathering and entrainment processes. For comparisons with model results, floating oil distributions from 84 dates and times were used, these being times where the image was judged sufficiently synoptic of the area of the floating oil and where volume estimates could be derived for comparison with model results.

Chemical analyses of samples of surface floating oil showed that the oil was considerably weathered (i.e., most of the more soluble components had dissolved from the oil and some microbial degradation had occurred) before it reached the water surface. The oil also emulsified to form a water-in-oil emulsion after weathering at the surface.

5.2.3 Shoreline Oiling

Approximately 2,100 km of beaches and coastal wetlands were exposed to MC252 oil in 2010 (DWHOS Trustees 2016; Nixon et al. 2015). DWHOS Trustees (2016) mapped maximum observed oiling on shoreline (beaches and wetlands), which was categorized as not surveyed, no oil seen, or with various degrees of oiling. With respect to the timing of when oil came ashore, available data consist of maps of where oil was first observed on various shoreline segments and assessments by the SCAT program during Response. However, the shorelines were not searched synoptically, and areas were not visited for

days or weeks; thus, the time oil was first observed could have been a considerable time after the actual initial oiling. These data sets were used for model comparisons.

5.2.4 Sediment Oil

MC252 oil from the spill was identified on the sediments in the offshore area surrounding and down-stream of the well site. Stout (2015d) and Stout et al. (2015, 2016b) estimated the extent of Macondo oil from the DWHOS in benthic sediments as about 6.9–7.7% of the released oil mass.

5.3 Model Results and Validation

5.3.1 Subsurface Oil

In the model simulations, the highest total hydrocarbon concentrations were near the wellhead (as was observed in field chemistry samples), decreasing with distance from the spill site as oil droplets rose to the surface, diluted and degraded. Smaller droplets were transported farther from the wellhead by currents before rising to the surface. Complex patterns arose as rising droplets were transported and sheared by the variable currents at different depths. This made the oil droplet (and resulting dissolved) concentrations highly patchy in 3-D space and time.

In April 2010, the oil was released in relatively large droplets, which rapidly rose to the surface. Because of the transient nature of large droplets, subsurface hydrocarbon concentrations below 40 m were only above 1 $\propto\gamma$/L within a few km of the wellhead. Between May and July 2010, progressively smaller droplet sizes, produced by flow through small holes in the riser at the kink and due to subsea dispersant applications, increased hydrocarbon concentrations in waters below 40 m. Based on field sample observations, elevated concentrations extended further from the wellhead to at least 70 km from the well during June and July 2010.

The modeled concentrations of BTEX remaining in the oil droplets were very low throughout the simulations. Comparison of the BTEX content between the oil droplets and dissolved concentrations in the water column indicates that the BTEX was mostly in the dissolved phase at all depths of the water column and in highest concentrations below 1,100 m in the deep plume. BTEX dissolved quickly in the deep plume and at shallower depths as the oil droplets rose through the water column. The semi-soluble components (i.e., C2-benzenes, C3-benzenes, naphthalenes, low molecular weight alkanes, isoalkanes, and cycloalkanes) had partially dissolved while the oil droplets were at depths below 1,100 m, but there was additional dissolution as droplets continued to rise to shallower depths. The sparingly soluble 3-ring PAHs were primarily in the droplet phase in the simulations. Dissolved concentrations of PAH components were for the most part below 1 µg/L between 800 m and 40 m. These partitioning patterns are consistent with the weathering

models and analyses of chemistry samples, where dissolved and particulate fractions were measured (Payne and Driskell 2015a, b, c).

The highest hydrocarbon concentrations below 40 m were consistently measured in water samples taken at a depth of approximately 1,000-1,300 m. Elevated concentrations at depth were observed in each of the investigated chemical groups ranging from BTEX through PAHs to the soluble alkanes. When considered together, the total soluble compounds, total investigated compounds, and PAH groups all had highest observed concentrations between 1,000–1,300 m. Elevated concentrations were also measured at shallower depths, however they had lower concentrations than those found between 1,000–1,300 m. The highest measurements of total investigated compounds in the deep plume were >100–700 µg/L, with concentrations up to ~80 µg/L between 200–1,000 m. When considered individually, soluble alkanes typically had the highest concentrations between 1,000–1,300 m with values of >100–400 µg/L, while BTEX were typically >100–200 µg/L, and PAHs were typically <120 µg/L. Peaks in fluorescence data and sags in dissolved oxygen data were observed between 1,000–1,300 m in the same depth zone where the highest BTEX and PAH concentrations were measured. The model-simulated hydrocarbons have similar distributions and concentrations.

The modeled concentrations of each of the oil components were compared to measurement data from chemistry samples collected for the NRDA chemistry program. Due to the differences between the modeled and actual field conditions and the patchiness of observed chemistry, there is the potential for displacement between modeled and observed concentrations in both space and time. Therefore, a direct overlay of the detectable chemistry measurements on the model would be insufficient for evaluating if the concentrations predicted by the model were realistic. To account for likely displacement, results are plotted as frequency distributions within a spatial and time window, containing a population of chemistry samples. The chemistry samples and modeled results were ordered by concentration so that the distributions could be compared.

Comparisons of model and observational chemistry were made for five vertical intervals within a 25 km by 25 km box centered on the wellhead. As components have different properties and dissolution rates, their concentration distributions varied. Therefore, to be meaningful, comparisons needed to be made on a component-by-component basis.

The modeled concentrations of the various components were generally of the same order of magnitude as the measured concentrations. In many instances, the frequency distributions of the modeled concentrations compared well to the frequency distribution of the measured samples, particularly in the deep-plume regions of 1,200–1,400 m and 1,000–1,200m. Agreements between observed and modeled concentrations in shallower

waters were more variable. In some cases, the model overestimated concentrations, whereas in others it underestimated the concentrations described by the samples. There were far fewer chemistry samples available from depths of 40 m to 800 m than in deeper waters, and those samples were typically taken on a vertical cast that was targeting sampling the deep plume contamination. That sampling strategy would miss sampling rising oil, and components dissolving from them, above the deep plume that was displaced by currents, particularly when those shallower "plumes" were relatively narrow moving through a vast ocean. However, overall, the differences between observed and modeled concentrations were not large and there was no obvious bias. The frequency distributions of the modeled and measured concentrations were more similar for PAH components than for some of the other components. Additionally, the frequency distributions of the concentrations produced by the model simulations using different currents, within the 25 km by 25 km box centered on the wellhead, were similar. Further from the wellhead, spatial distributions of concentrations above 0.1 $\propto\gamma$/L were more variable with the current dataset used.

Overall, the results and sensitivity analyses show that the most important input contributing to uncertainty is the current dataset used. Results from each of the hydrodynamic datasets were quite different from each other and from the available measurement data from the ADCPs.

5.3.2 Mass Balance

The modeled amount of floating oil over time is in good agreement with estimates from interpretation of remote sensing data, and the predicted water column concentrations of hydrocarbon components are in good agreement with sample measurements, indicating the model algorithms and inputs are producing reasonable results. Among the most influential of these are oil droplet size distributions input to the SIMAP oil fate model, the oil weathering process algorithms and their input assumptions, and the algorithm modeling natural and dispersant-mediated surface oil entrainment (Li et al. 2017b).

Table 5-1 summarizes the mass balance on August 30, 2010, predicted by the SIMAP model simulations using HYCOM-FSU currents and NARR winds, assuming low, best and high effectiveness for SSDI. Results assuming the SSDI was not effective are listed for comparison. These estimates are consistent with mass balance estimates by Ryerson et al. (2011) and OBC estimates by Lehr et al. (2010) of the amount dispersed and degraded in the water column (26–51%). The OBC estimates of amount evaporated are low compared to the range calculated by the SIMAP model, whereas the OBC estimates of the amount on shorelines are high compared to the range calculated by the model. As the volatiles made up 61% of the oil, it would be likely that more of the oil evaporated than the OBC estimates

(which were 24–30%), leaving less in the "other" category, assumed in the OBC to be on shore or in sediments.

The model simulations did not include consideration of the large amount of drilling muds, sediment and other materials (e.g., "junk") discharged with the oil during the several Top Kill attempts made to stop the flow from the broken riser (primarily between May 26 and June 1). Those materials would have bound with some of the oil and carried it to the sediments. Based on field sampling, Stout et al. (2015) estimated ~7% of the released oil settled near the wellhead. Thus, accounting for this additional oil settlement would reduce the model estimates of oil remaining in the water column (ultimately degrading) by about 6%.

Table 5-1 Mass balance on August 30, 2010, for SIMAP model base case simulations, assuming no, low, best, and high effectiveness for SSDI.

Fate	None	Low	Best Estimate	High
Evaporated	44%	43%	39%	35%
Water column (dispersed or degraded)	44%	46%	50%	55%
Burned	2.6%	2.6%	2.6%	2.6%
Skimmed (not simulated)	–	–	–	–
Shoreline	7.8%	7.2%	6.7%	6.6%
Sediment	1.3%	1.3%	1.2%	1.0%

Table 5-2 presents a modified mass balance that accounts for the oil settled with drilling muds and sediment ejected from the well during failed Top Kill operations, as well as additional mechanical removal (by oil skimming) not included in the modeling. Lehr et al. (2010 OBC) estimated that 2–5% (4% being the best estimate) of the oil was removed mechanically (skimmed), assuming 20% of the fluids skimmed were oil. This removal would have reduced the floating oil, which ultimately was dispersed in the model naturally or by surface dispersant application, and the oil ultimately coming ashore. For the purposes of estimating a comprehensive mass balance table (Table 5-2) based on the model estimates and the missing Top Kill and skimming influences, the amount skimmed was assumed to be 4% of the discharge, amounting to a 2% reduction in the water column and a 2% reduction of oil ultimately reaching the shoreline (assuming much of the skimming prevented oil from coming ashore). The actual distribution of skimming effort is unknown. Table 5-2 represents the best estimate of the fate of the DWHOS discharge, accounting for the uncertainty in the initial droplet size distribution resulting from SSDI. Uncertainties due to currents and winds used and other inputs are quantified by the data in Table 4-2.

Table 5-2 Best estimate of mass balance on August 30, 2010, accounting for oil sedimentation and skimming, assuming low, best, and high effectiveness for SSDI.

Fate	None	Low	Best Estimate	High
Evaporated	44%	43%	39%	35%
Water column (dispersed or degraded)	44%	46%	50%	55%
Burned	2.6%	2.6%	2.6%	2.6%
Skimmed (not simulated)	–	–	–	–
Shoreline	7.8%	7.2%	6.7%	6.6%
Sediment	1.3%	1.3%	1.2%	1.0%

5.3.3 Surface Floating Oil

The remote sensing data indicate the floating oil was primarily in a near-circular area near and just north of the DWHOS wellhead. The simulations using HYCOM-FSU, HYCOM-NRL Reanalysis and IAS ROMS show a similar pattern. The results of the simulations with other currents show excursions, too far northeast (SABGOM, NCOM Real-time), and too much dispersion in all directions (HYCOM-NRL, Real-time; NGOM). The three simulations using no currents and NAM, NARR or NOGAPS winds are similar, and none of the three have enough transport of the floating oil to the east toward Florida or to the west towards western Louisiana and Texas. Otherwise, the no-current simulations result in realistic floating oil patterns centered just north of the wellhead. These results indicate the importance of the winds in transporting the floating oil, but that the currents used can change the patterns quite dramatically.

Using gridding with a cell size of 25 km^2, MacDonald et al. (2015) estimated the footprint of aggregated floating oil and oil emulsions, where oil coverage exceeded about 1 g/m^2 at some time during the spill and extended over an area of 149,000 km^2. They estimated the daily average footprint area was 11,200 km^2 (SD = 8,430 km^2). The model estimate (using the base case) of the daily average surface area affected by floating oil >1.0 g/m^2, using gridding of similar resolution, was 6,720 km^2 (SD = 4,960 km^2), not significantly different from the remote sensing daily estimate.

To evaluate the surface area exposed at any single instant in time, one should consider the patchiness of the oil. In a gridded presentation, the average volume and area equivalent to a thickness of sheen is not actually continuous sheen, but patchy thicker oil and sheens with open water areas. Averaging over a cell area makes it appear that sheens are more continuous than they are. The sum of the area covered by spillets at a single time step provides the modeled area covered by oil at any instant in time. The areas covered by oil spillets (i.e., oil patches) were an order of magnitude lower than those estimated from the

gridding. The mean swept area from 24 April to 3 August 2010 (101 days) was 1,960 km^2/day for the model base case.

5.3.4 Shoreline Oiling

The modeled shoreline oiling for the base case (2,000–2,700 km oiled) compares well with the observations (~2,100 km oiled), with the model showing oiling from the Apalachicola Bay area of Florida to the Terrebonne Bay area of Louisiana. The model predicted oiling on shore inside Mobile Bay in areas where it was not observed. However, most of Mobile Bay's shoreline areas were not surveyed, so oiling of those areas is unknown. Simulations using HYCOM-NRL Reanalysis currents with CFSR winds, HYCOM-NRL Real-time currents with NARR winds, and NCOM Real-Time with NARR winds, predict similar shoreline oiling patterns to the base case using HYCOM-FSU currents and NARR winds. SABGOM spreads oil to shorelines too far to the east (in the Big Bend of Florida) and into western Louisiana where no oiling was observed. NGOM currents with NARR winds and the IAS ROMS simulations carry too much oil to western Louisiana and Texas.

5.3.5 Sediment Oil

The model estimated the mass of oil hydrocarbons settling to subtidal sediments, which was about 1% of the released oil. Stout et al. (2015, 2016a) estimated ~7% of the released oil settled near the wellhead by 2011 with most settling before late August 2010. Most of that settled oil would be accounted for by oil associated with settled drilling muds discharged following the Top Kill attempts (Stout and Payne 2017), a flux not included in the modeling. The SIMAP model simulation ended on September 30, 2010. Estimates of organic SPM concentrations needed to model oil flux in marine snow were unavailable prior to September 30, 2010; therefore, organic-born oil flux is not included in the modeling.

5.3.6 Uncertainty and Research Needs

Evaluation of the sensitivity of the model results to the environmental, geographical and physical-chemical input data showed that the greatest variability and uncertainty was due to the current dataset used for transport calculations in the oil spill model. The available hydrodynamic models varied considerably in their predictions of current patterns. Below 40 m, in the offshore area affected by the rising oil, none of the hydrodynamic models aligned well with the ADCP current measurements with respect to specific speeds and directions, although HYCOM-FSU performed the best of the hydrodynamic models in terms of overall transport around the DWHOS subsurface plume. Below 40 m, the best agreement of the oil spill model results with observational data was obtained using the ADCP data as current input. However, for surface waters above 40 m, the measurement data from ADCPs (and other measurements, such as drifters) were insufficient to characterize the currents over the entire domain of oil exposure. The best agreement to observational data (i.e.,

floating and shoreline oil distributions) was obtained using the HYCOM-FSU modeled data as current input, with the HYCOM-NRL Reanalysis model providing very similar results. Considering both below and above 40 m, HYCOM-FSU provided the most accurate inputs for transport of the oil.

Winds accounted for most of the transport of the floating oil. Uncertainties due to the wind data used were examined by running simulations with winds from each of the meteorological models alone, without currents. These simulations predicted surface and shoreline oiling distributions similar to the results including HYCOM-FSU currents with the NARR winds, absent the along-shore transport to the west past the Bird's Foot and to the east to the Florida coast. Winds also affect all the surface weathering processes. Hence wind data were the most influential of all model inputs. Variation among the wind data sets, which were derived from complex meteorological models, was much less than for the currents. All the wind models examined provided realistic model simulations of the event, as measured by comparisons to floating oil observations based on remote sensing.

The modeled mass balance of oil over time (i.e., the percent of total mass spilled to date that was on the water surface, in the water column, on shorelines, in the sediment, in the atmosphere, and degraded) was relatively insensitive to the floating oil dispersion coefficient, wind drift transport assumptions, and current data used (to the degree that amount transported ashore was unaffected). However, there was a bit more variation in mass balance depending on the potential range of assumptions for SSDI (Table 5-1 and 5-2), which reflects differences in droplet size distributions and therefore surfacing and weathering rates of the oil.

Locations of surface oil and water column contamination (i.e., the trajectories) varied spatially with the various current data sets used. However, exposure metrics such as concentrations in the water and areas exposed to floating oil above concentration thresholds varied much less with the current data used. The contamination was displaced by the differing transport, while weathering processes and dilution were similar, as evidenced by comparing results using ADCPs and HYCOM-FSU, as well as other simulations with various currents that transported oil to different places but resulted in similar floating oil exposure.

Thus, the mass balance and degree of exposure to surface oil and water column concentrations predicted by the model are quantitatively realistic and reliable for evaluating short-term (2010) exposure and effects on biological and socioeconomic resources. The modeled exposure estimates (e.g., areas swept by floating oil and volume of water affected above concentrations of concern) are not highly sensitive to the uncertainties of the currents used (among the current data sets providing realistic results

compared to the observations), as well as many of the other inputs tested. While the sensitivity analysis presented here is not exhaustive, it covers the inputs causing most of the uncertainties in model results.

The modeling reported here was predictive, and not calibrated or adjusted to fit observational data as the simulation proceeded. This approach was used so that the model could be validated, justifying its use for predictive simulations as part of the risk assessment. An alternative approach to modeling this (or any) spill would be to use data assimilation techniques for the transport, i.e., to adjust the locations of the floating oil to positions where oil was observed by remote sensing. For hind casts of a real event, this could be performed as the model runs, or the model could be reinitialized and restarted from observed locations. That approach was in fact tried, and the trajectory followed the oil observations, while the mass balance was not materially altered. During response to a spill, trajectory modeling is used to forecast where oil will go, to inform response activities. For that purpose, updating the model with observational information is the most appropriate approach.

This modeling study demonstrates the state-of-the-art for oil trajectory and fate modeling. The results and analyses shed light on areas where research is needed and on important data collections that should be made during a spill. Some of these are highlighted below.

While the accuracy of hydrodynamic models (particularly HYCOM) is quite good for surface waters, below 40 m the models did not perform well. The models routinely assimilate (calibrate to) data indicating surface conditions (e.g., sea surface height, temperature, and salinity) but typically do not assimilate ADCP or other subsurface data. For the DWHOS, the IAS ROMS modelers used the ADCP data measured during and after the spill, but the ROMS model predicted much faster current speeds at depth and so the assimilation was not successful in substantially improving the accuracy of the ROMS results. The ADCP data were not assimilated by the HYCOM model simulations. However, potentially such data assimilation would improve subsurface current predictions.

There was sufficient ADCP data available to use for the oil spill modeling below 40 m, but that current data needed to be interpolated both horizontally and vertically for it to be used. However, the interpolation did not conserve mass and momentum in the manner of a hydrodynamic model. Thus, the small-scale details of the subsurface transport remain uncertain for this spill.

In future spills, it would be preferable to have a field of ADCPs deployed in the area of interest, measuring currents at all depths. Hydrodynamic models could assimilate this data along with the surface measurements routinely used, and thus provide better hydrodynamic simulations to input to oil spill modeling. Unmanned autonomous vehicles

could also be useful in collecting needed physical data, as well as in profiling the distribution of oil using sensors such as fluorometers that employ appropriate wavelengths to detect hydrocarbons.

Another important uncertainty in the modeling was in the quantification of the flux of oil to the sediments. While there is sufficient information to identify the processes that occur, and that microbial exudates stimulated by the oil play an important role in binding and potentially transporting oil to the sediments, quantitative data useful for modeling this pathway are lacking. There would need to be an algorithm quantifying the production of the exudates by microbes in response to presence of oil, the binding rate of the oil as a function of oil and exudate concentrations, and the rate at which those oil-SPM agglomerates would settle. The measurement data needs to be under conditions similar to the offshore open ocean area of the DWHOS in order to be useful for quantifying the rates for that or similar spills.

Improvements in data collections to support modeling, over and above those performed during the DWHOS event, include the following:

- To include mechanical removal in the modeling, tabulate daily amounts of oily liquids skimmed, as well as measure the water content in the skimmed liquids.
- To better document the oil droplet sizes released from the deep plume, perform sampling closer to the release. During the DWHOS safety concerns precluded sampling closer than 2 km from the wellhead, but unmanned vehicles could be directed to perform such sampling.
- Perform water sampling, for chemically characterizing both particulate (droplet) and dissolved oil components, near the sea surface under surface floating oil that is also sampled and physically and chemically characterized, specifically documenting these co-located samples. This would allow better verification of surface entrainment and dissolution processes with field data.
- Perform similar water sampling near the sea surface in areas where surface floating oil was dispersed by chemical dispersant *within minutes* of the dispersant application, so as to capture the dispersant effects on entrainment and dissolution. Because of safety concerns, this may necessitate use of remotely-operated unmanned vehicles.
- Quantify physical-chemical changes and degradation rates of floating oil, including measurement of degradation products, so that floating oil behavior (e.g., bulk properties and emulsification) may be better modeled as the oil weathers.
- To quantify sedimentation of oil-SPM aggregates, deploy sediment traps and take water samples at multiple depths in areas with heavy surface oil and high subsurface oil concentrations, measuring mass accumulation rates and

concentrations (respectively) of a full suite of hydrocarbons, as well as dissolved and particulate organic carbon and mineral matter.

- Spill contingency planning needs to consider the vessels and equipment needed to perform these and the actual types of sampling that occurred for the DWHOS, as vessels and equipment were limiting factors in sampling the DWHOS.

Though these suggestions for monitoring future spills are not comprehensive, they point out some of the areas where more information could improve the accuracy of oil trajectory and fate modeling. That said, the model system as it stands is robust and has been verified with the best-studied deep-water oil and gas blowout to date, world-wide.

6. References

Adams EE, Socolofsky SA, Boufadel M. 2013. Comment on Evolution of the Macondo well blowout: simulating the effects of the circulation and synthetic dispersants on the subsea oil transport. Environ. Sci. Tech. 47(20): 11905–11905.

Aman ZM, Paris CB. 2013. Response to Comment on Evolution of the Macondo well blowout: simulating the effects of the circulation and synthetic dispersants on the subsea oil transport. Environ. Sci. Tech. 47(20): 11906–11907.

Aman ZM, Paris CB, May EF, Johns ML, Lindo-Atichati D. 2015. High-pressure visual experimental studies of oil-in-water dispersion droplet size. Chem. Eng. Sci. 127(0):392–400.

Antonov JI, Seidov D, Boyer TP, Locarnini RA, Mishonov AV et al. 2010. World ocean atlas 2009, volume 2: salinity. Sydney. Levitus (ed.). NOAA Atlas NESDIS 69. Washington (DC): U.S. Government Printing Office. 184 pp.

American Petroleum Institute (API), National Oceanic and Atmospheric Administration (NOAA), U.S. Coast Guard (USCG), U.S. Environmental Protection Agency (USEPA). 2001. Characteristics of response strategies: a guide for spill response planning in marine environments. Washington (DC): Joint Publication of API, NOAA, USCG, and USEPA. 80p.

ASCE Task Committee on Modeling Oil Spills. 1996. State-of-the-art review of modeling transport and fate of oil spills, Water Resources Engineering Division. ASCE, J. Hydraul. Eng. 122(11): 594–609.

ASTM International. 2006. Standard guide for visually estimating oil spill thickness on water. In ASTM Committee F20 on Hazardous Substances and Oil Spill Response, edited, p. 4, ASTM Int'l, West Conshohocken, PA.

Belore RC, Trudel BK, Morrison J. 2011. Weathering, emulsification, and chemical dispersibility of Mississippi Canyon 252 crude oil: Field and Laboratory studies. International Oil Spill Conference Proceedings, March 2011. Vol 2011(1):247.

Bonn Agreement. 2009. Bonn agreement aerial operations handbook, 2009. London, UK. Available: http://www.bonnagreement.org/site/assets/files/1081/ba-aoh revision 2 April 2012-1.pdf, Accessed 4 June 2015.

Boyer T, Levitus S, Garcia H, Locarnini RA, Stephens C et al. 2005. Objective analyses of annual, seasonal, and monthly temperature and salinity for the world ocean on a 0.25 degree grid. Int. J. Clim., 25, 931–945.

Boyer TP, Antonov JI, Baranova OK, Garcia HE, Johnson DR et al. 2009: World Ocean Database 2009. S. Levitus, Ed., NOAA Atlas NESDIS 66. Washington (DC): U.S. Government Printing Office. 216 p.

Brandvik PJ, Johansen Ø, Leirvik F, Farooq U, Daling PS. 2013. Droplet breakup in subsurface oil releases–Part 1: Experimental study of droplet breakup and effectiveness of dispersant injection. Marine Poll Bull (73): 319–326.

Boehm PD, Murray KJ, Brown JS, Royer L. 2012. Distribution and fate of PAH and chemical dispersants in the water column following the Deepwater Horizon Oil Spill. In: Presentation at the 243rd American Chemical Society National Meeting, San Diego, CA. March 26–29, 2012.

Brown JS, Beckmann D, Bruce L, Cook L, Mudge S. 2011. PAH depletion ratios document the rapid weathering and attenuation of PAHs in Oil Samples Collected after the Deepwater Horizon. In International Oil Spill Conference Proceedings (IOSC) 2011(1), Abs336. American Petroleum Institute.

Bryden HL. 1973. New polynomials for thermal expansion, adiabatic temperature gradient, and potential temperature of sea water. Deep-Sea Research 20: 401–408.

Camilli R, Reddy CM, Yoerger DR, Van Mooy BAS, Jakuba MV et al. 2010. Tracking hydrocarbon plume transport and biodegradation at Deepwater Horizon. Science 330:201–204.

Chassignet EP, Hurlburt HE, Metzger EJ, Smedstad OM, Cummings JA et al. 2009. US GODAE: Global ocean prediction with the HYbrid Coordinate Ocean Model (HYCOM). Oceanography 22(2):64–75, http://dx.doi.org/10.5670/oceanog.2009.39.

Chassignet EP, Srinivasan A. 2015. Data assimilative hindcast for the Gulf of Mexico. US Dept. of the Interior, Bureau of Ocean Energy Management, OCS Study BOEM 2015-035, 2015, 40 pp.

Chao Y, Li Z, Farrara JD, McWilliams JC, Bellingham J, Capet X et al. 2009. Development, implementation and evaluation of a data-assimilative ocean forecasting system off the central California coast. Deep-Sea Res. II 56, 100–126, doi: 10.1016/j.dsr2.2008.08.011.

Chao Y, He R, Farrara J, Zhang C. 2014. ROMS hydrodynamic modeling. Report to NOAA OR&R NRDA program, June 5, 2014, 64p.

Chan G, Chow A, Adams EE. 2014. Effects of droplet size on intrusion of subsurface oil spills. Environ Fluid Mech. 15: 959–973. http://dx.doi.org/10.1007/s10652-014-9389-5.

Csanady GT. 1973. Turbulent diffusion in the environment. Dordrecht (Holland): D. Reidel Publishing Company,

Cummings JA, Smedstad OM. 2013. Variational data assimilation for the global ocean. In: Data Assimilation for Atmospheric, Oceanic and Hydrologic Applications Vol II, Chapter 13: 303–343.

Cummings JA. 2005. Operational multivariate ocean data assimilation. Q J R Meteorol Soc , Part C, 131(613): 3583–3604.

Daling PS, Leirvik F, Almås IK, Brandvik PJ, Hansen BH et al. 2014. Surface weathering and dispersibility of MC252 crude oil. Marine Poll Bull 87(1-2): 300–310.

Davis CS, Loomis NC. 2014. Deepwater Horizon Oil Spill (DWHOS) Water Column Technical Working Group Image Data Processing Plan: Holocam, Description of data processing methods used to determine oil droplet size distributions from *in situ* holographic imaging during June 2010 on cruise *M/V Jack Fitz* 3. Loomis (NC): Davis CS, Woods Hole Oceanographic Institution. 15 pages + Appendix.

Deepwater Horizon Natural Resource Damage Assessment Trustee Council (DWH Trustees). 2016. The *Deepwater Horizon* Oil Spill final programmatic damage assessment and restoration plan and final programmatic environmental impact statement. National Oceanic and Atmospheric Administration, Office of Response and Restoration. (accessed February 2016). Available at: http://www.gulfspillrestoration.noaa.gov/restoration-planning/gulf-plan/.

Diercks AR, Highsmith RC, Asper VL, Joung D, Zhou Z. 2010. Characterization of subsurface polycyclic aromatic hydrocarbons at the *Deepwater Horizon* site. Geophysical Research Letters 37, L20602:1–6.

D'Sa EJ, Ko DS. 2008. Short-term influences on suspended particulate matter distribution in the northern Gulf of Mexico: satellite and model observations. Sensors 8: 4249–4261.

D'Sa EJ, Miller RL, McKee BA. 2007. Suspended particulate matter dynamics in coastal waters from ocean color: application to the northern Gulf of Mexico. Geophysical Research Letters 34: 6.

Dubinsky EA, Conrad ME, Chakraborty R, Bill M, Borglin SE et al. 2013. Succession of hydrocarbon-degrading bacteria in the aftermath of the *Deepwater Horizon* Oil Spill in the Gulf of Mexico. Environ. Sci. Tech. 47(19): 10860–10867.

ERMA. 2016. The ERMA® Deepwater Gulf Response Web Application. (accessed 20 March 2016). Available at: https://gomex.erma.noaa.gov/erma.html#/x=-88.40092&y=30.46988&z=7&layers=16+16056+16402.

Faksness LG, Altin D, Nordtug T, Daling PS, Hansen BH. 2015. Chemical comparison and acute toxicity of water accommodated fraction (WAF) of source and field collected Macondo oils from the *Deepwater Horizon* spill. Marine Poll Bull. 91(1): 222–229.

FNMOC. 2013. The Fleet Numerical Meteorology and Oceanography Center (FNMOC). Data for 2010 were downloaded and then converted into NetCDF format. (accessed 15 September 2013). Available at: http://www.usno.navy.mil/FNMOC

Fitzpatrick JJ. 2009. Assessing skill of estuarine and coastal eutrophication models for water quality managers. J. Mar. Syst. 76: 195–211.

Forth H, Morris J, Lay C, Lipton J, Mitchelmore C. 2015a. Characterization of oil and water accommodated fractions used to conduct aquatic toxicity testing in support of the *Deepwater Horizon* Natural Resource Damage Assessment. DWH NRDA Toxicity Technical Working Group Report. Prepared for National Oceanic and Atmospheric Administration by Abt Associates, Boulder, CO. August.

Forth HP, Morris JM, Cacela D. 2015b. Explanation of analytes included in the total polycyclic aromatic hydrocarbon sums used by the *Deepwater Horizon* Natural Resource Damage Assessment Toxicity Group. DWH NRDA Toxicity Technical Working Group Report. Prepared for National Oceanic and Atmospheric Administration by Abt Associates, Boulder, CO. August.

French D, Reed M, Jayko K, Feng S, Rines H et al. 1996. The CERCLA type A natural resource damage assessment model for coastal and marine environments (NRDAM/CME), Technical Documentation, Vol. I–V. Final Report. Washington (DC): USDOI. April 1996. Report No.: PB96-501788. Contract No.: Available from: NTIS, Springfield, VA 22161.

French DP, Rines H. 1997. Validation and use of spill impact modeling for impact assessment. In: Proceedings, 1997 International Oil Spill Conference, Washington. (DC): American Petroleum Institute. Publication No. 4651. p. 829–834.

French DP, Rines H, Masciangioli P. 1997. Validation of an orimulsion spill fates model using observations from field test spills. In: Proceedings of 20th Arctic and Marine Oil Spill Program (AMOP) Technical Seminar, 10–12 June 1997. Emergencies Science Division, Environment Canada; Ottawa, ON, Canada. p. 933–961

French McCay DP. 2002. Development and application of an oil toxicity and exposure model, OilToxEx. Environl Toxicol and Chem. 21(10): 2080–2094.

French McCay DP. 2003. Development and application of damage assessment modeling: example assessment for the North Cape Oil Spill. Marine Poll. Bull. 47 (9-12): 341–359.

French McCay DP. 2004. Oil spill impact modeling: development and validation. Environ Toxicol and Chem. 23 (10): 2441–2456.

French McCay DP. 2009. State-of-the-art and research needs for oil spill impact assessment modeling. In: Proceedings of the 32nd AMOP technical seminar, 9–11 June 2009. Emergencies Science Division, Environment Canada; Ottawa, ON, Canada. p. 601–653.

French McCay DP, Rowe JJ. 2004. Evaluation of bird impacts in historical oil spill cases using the SIMAP oil spill model. In: Proceedings of the 27th Arctic and Marine Oil Spill Program (AMOP) Technical Seminar, Emergencies Science Division, Environment Canada, Ottawa, ON, Canada, pp. 421–452.

French McCay D, Whittier N, Sankaranarayanan S, Jennings J, Etkin DS. 2004. Estimation of potential impacts and natural resource damages of oil. J. Hazard. Mater. 107(1-2): 11–25.

French-McCay DP, Rowe JJ, Whittier N, Sankaranarayanan S, Etkin DS et al. 2005a. Evaluation of the consequences of various response options using modeling of fate, effects and NRDA costs of oil spills into Washington waters. In: Proceedings, International Oil Spill Conference, May 2005, Paper 395, American Petroleum Institute, Washington, DC.

French-McCay DP, Whittier N, Dalton D, Rowe JJ, Sankaranarayanan S. 2005b. Modeling fates and impacts of hypothetical oil spills in Delaware, Florida, Texas, California, and Alaska waters, varying response options including use of dispersants. In: Proceedings, International Oil Spill Conference, May 2005, Paper 399, American Petroleum Institute, Washington, DC.

French-McCay DP, Mueller C, Jayko K, Longval B, Schroeder M et al. 2007. Evaluation of field-collected data measuring fluorescein dye movements and dispersion for dispersed oil transport modeling. In: Proceedings of the 30th Arctic and Marine Oil Spill Program (AMOP) Technical Seminar, Emergencies Science Division, Environment Canada, Ottawa, ON, Canada, pp.713–754.

French McCay DP, Jayko K, Li Z, Horn M, Kim Y et al. 2015. Technical reports for *Deepwater Horizon* water column injury assessment–WC_TR14: Modeling oil fate and exposure concentrations in the deepwater plume and cone of rising oil resulting from the *Deepwater Horizon* Oil Spill. DWH NRDA Water Column Technical Working Group Report. September 29, 2015. Administrative Record no. DWH-AR0285776.pdf [https://www.doi.gov/deepwaterhorizon/adminrecord].

French McCay DP, Li Z, Horn M, Crowley D, Spaulding M et al. 2016. Modeling oil fate and subsurface exposure concentrations from the *Deepwater Horizon* Oil Spill. In:

Proceedings of the 39th AMOP Technical Seminar on Environmental Contamination and Response, Environment Canada. 39, 2016, 115–150.

Garcia HE, Locarnini RA, Boyer TP, Antonov JI, Baranova OK. 2010a. World ocean atlas 2009, volume 3: dissolved oxygen, apparent oxygen utilization, and oxygen saturation. Sydney Levitus (ed.). NOAA Atlas NESDIS 70. Washington (DC): U.S. Government Printing Office. 344 p.

Garcia HE, Locarnini RA, Boyer TP, Antonov JI, Zweng MM. 2010b. World ocean atlas 2009, volume 4: nutrients (phosphate, nitrate, silicate). S. Levitus, Ed. NOAA Atlas NESDIS 71, Washington (DC): U.S. Government Printing Office. 398 pp.

Garcia-Pineda O, Zimmer B, Howard M, Pichel W, Li X et al. 2009. Using SAR images to delineate ocean oil slicks with a texture classifying neural network algorithm (TCNNA). Canadian Journal of Remote Sensing 35(5), 411–421.

Garcia-Pineda O, MacDonald I, Hu C, Svejkovsky J, Hess M et al. 2013a. Detection of floating oil anomalies from the *Deepwater Horizon* oil spill with synthetic aperture radar. Oceanography 26(2):124–137.

Garcia-Pineda O, MacDonald IR, Li X, Jackson CR, Pichel WG. 2013b. Oil spill mapping and measurement in the Gulf of Mexico with Textural Classifier Neural Network Algorithm (TCNNA). IEEE Journal of Selected Topics in Applied Earth Observations and Remote Sensing 6(6): 2517–2525.

Graettinger G, Holmes J, Garcia-Pineda O, Hess M, Hu C et al. 2015. Integrating data from multiple satellite sensors to estimate daily oiling in the Northern Gulf of Mexico during the *Deepwater Horizon* Oil Spill. DWH Natural Resource Exposure NRDA Technical Working Group Report, FE_TR.31, NOAA, August 31, 2015, 46p. [DWH-AR0062925].

Grennan M, Zamorski S, Decker L, Horn M, Kim Y. 2015. Technical reports for eepwater Horizon water column injury assessment–FE_TR.39: Volume II. Water Column CTD and Sensor Data from the *Deepwater Horizon* Oil Spill. South Kingstown (RI): RPS ASA. DWH-AR0293108.pdf. (accessed 1 September 2015). Available at: https://www.doi.gov/deepwaterhorizon/adminrecord.

Hazen TC, Dubinsky EA, Desantis TZ, Andersen GL, Piceno YM et al. 2010. Deep-sea oil plume enriches indigenous oil-degrading bacteria. Science 330:204–208.

Horn M, Grennan M, Decker L, Zamorski S, French McCay D et al. 2015a. Technical reports for *Deepwater Horizon* water column injury assessment –Volume I. Water Column Chemistry Data from the *Deepwater Horizon* Blowout. RPS ASA, South Kingstown, RI, USA, August 2015. DWH-AR0023907.pdf (main), DWH-AR0290546.pdf (Appendix A), DWH-AR0290744.pdf (Appendix B), DWH-AR0291867.pdf (Appendix C), DWH-

AR0292430.pdf (Appendix D), DWH-AR0292881.pdf (Appendix E), [https://www.doi.gov/deepwaterhorizon/adminrecord]

Horn M, French McCay D, Payne J, Driskell W, Li Z et al. 2015b. Technical reports for *Deepwater Horizon* water column injury assessment –Volume III. Water Column Chemical and Physical Data from the Deep Water Horizon Blowout. RPS ASA, South Kingstown, RI, USA, August 2015. DWH-AR0024617.pdf (main), (Appendix A is missing), DWH-AR0024364.pdf (Appendix B), DWH-AR0024462.pdf (Appendix C), DWH-AR0023990.pdf (Appendix D) [https://www.doi.gov/deepwaterhorizon/adminrecord]

Hu C, Li X, Pichel WG, Muller-Karger FE. 2009. Detection of natural oil slicks in the NW Gulf of Mexico using MODIS imagery. Geophysical Research Letters 36. doi:10.1029/2008gl036119.

Hyun KH, He R. 2010. Coastal upwelling in the South Atlantic Bight: A revisit of the 2003 cold event using long term observations and model hindcast solutions. J. Mar. Syst. 83(1–2):1–13.

JAG. 2010. Joint Analysis Group (JAG) Review of R/V Brooks McCall data to examine subsurface oil. (accessed 10 September 2010). Available at: http://www.ncddc.noaa.gov/activities/healthy-oceans/jag/reports.

Jernelov A, Linden O. 1981. Ixtoc I: A case study of the world's largest oil spill. Ambio 10(6):299–306.

Joye S, MacDonald IR, Leifer I, Asper V. 2011. Magnitude and oxidation potential of hydrocarbon gases released from the BP oil well blowout. Nature Geoscience, Letters, published online 13 February 2011.

Kessler JD, Valentine DL, Redmond MC, Du M et al. 2011. A persistent oxygen anomaly reveals the fate of spilled methane in the deep Gulf of Mexico. Science 331:312–315.

Kujawinski EB, Kido Soule MC, Valentine DL, Boysen AK, Longnecker K et al. 2011. Fate of dispersants associated with the *Deepwater Horizon* Oil Spill. Environ. Sci. Technol. 45(4): 1298–1306.

Lehr B, Bristol S, Possolo A. 2010. *Deepwater Horizon* oil budget calculator: A report to the national incident command. (Oil Budget Calculator, OBC) The Federal Interagency Solutions Group, Oil Budget Calculator Science and Engineering Team. (accessed 1 April 2012). Available at: http://www.restorethegulf.gov/sites/default/files/documents/pdf/OilBudgetCalc_Full_HQ-Print_111110.pdf

Leifer I, Lehr WJ, Simecek-Beatty D, Bradley E, Clark R et al. 2012. State of the art satellite and airborne marine oil spill remote sensing: Application to the BP *Deepwater Horizon* oil spill. Remote Sens Environ. 124: 185–209. Available at: doi: http://dx.doi.org/10.1016/j.rse.2012.03.024.

Li Z, et al. 2008a. A three-dimensional variational data assimilation scheme for the Regional Ocean Modeling System: Implementation and basic experiments. J. Geophys. Res.C: Oceans 113(5).

Li Z, et al. 2008b. A three-dimensional variational data assimilation scheme for the regional ocean modeling system. J. Atmos. Oceanic Tech. 25(11): 2074–2090.

Li Z, Bird A, Payne JR, Vinhateiro N, Kim Y et al. 2015. Technical reports for *Deepwater Horizon* water column injury assessment–Volume IV. Oil Particle Data from the *Deepwater Horizon* Oil Spill. South Kingstown (RI): RPS ASA. DWH-AR0024715.pdf Available at: https://www.doi.gov/deepwaterhorizon/adminrecord.

Li Z, Spaulding M, French McCay D, Crowley D, Payne JR. 2017a. Development of a unified oil droplet size distribution model with application to surface breaking waves and subsea blowout releases considering dispersant effects. Marine Poll Bull 114 (1): 247–257.

Li Z, Spaulding M, French McCay D. 2017b. An algorithm for modeling entrainment and naturally and chemically dispersed oil droplet size distribution under surface breaking wave conditions. Marine Poll Bull. available online. pii: S0025-326X(17)30268-0. doi: 10.1016/j.marpolbul.2017.03.048.

Lindo-Atichati D, Paris CB, Le Hénaff M, Schedler M, Valladares Juárez AG et al. 2014. Simulating the effects of droplet size, high-pressure biodegradation, and variable flow rate on the subsea evolution of deep plumes from the Macondo blowout. Deep-Sea Res. II (0).

Locarnini RA, Mishonov AV, Antonov JI, Boyer TP, Garcia HE et al. 2010. World ocean atlas 2009, volume 1: temperature. S. Levitus (ed.). NOAA Atlas NESDIS 68. Washington (DC): U.S. Government Printing Office. 184 pp.

Mabile N, Allen A. 2010. Controlled burns after action report, Burns on May 28th–August 3, 2010, Controlled Burn Group, Report prepared by Nere' Mabile & Al Allen, August 8, 2010, 28p. (accessed 10 September 2012). Available at: http://gomex.erma.noaa.gov/erma.html#/x=88.34691&y=29.41717&z=7&layers=2301.

MacDonald IR, Garcia-Pineda O, Beet A, Daneshgar Asl S, Feng L et al. 2015. Natural and unnatural oil slicks in the Gulf of Mexico. J. Geophys. Res.Oceans 120 (8):364–368. doi:10.1002/2015JC011062.

Mackay D, Shiu WY, Ma KC. 1992. Illustrated handbook of physical-chemical properties and environmental fate for organic chemicals, Vol. I–IV. Chelsea [MI]: Lewis Publishers, Inc. 120 p.

Mackay D, Shiu WY, Ma KC, Lee SC. 2006a. Handbook of Physical-Chemical Properties and Environmental Fate for Organic Chemicals. Vol. I, Introduction and Hydrocarbons. Baton Rouge (FL): CRC Press, Taylor & Francis Group. 4216p.

Mackay D, Shiu WY, Ma KC, Lee SC. 2006b. Handbook of physical-chemical properties and environmental fate for organic chemicals. Vol. IV, Nitrogen and Sulfur Containing Compounds and Pesticides. Baton Rouge (FL): CRC Press, Taylor & Francis Group.

Marghany M. 2014. Utilization of a genetic algorithm for the automatic detection of oil spill from RADARSAT-2 SAR satellite data, Marine Poll Bull. 89(1–2): 20–29. doi: http://dx.doi.org/10.1016/j.marpolbul.2014.10.041.

McKenna AM, Nelson RK, Reddy CM, Savory JJ, Kaiser NK et al. 2013. Expansion of the analytical window for oil spill characterization by Ultrahigh Resolution Mass Spectrometry: beyond gas chromatography. Environ. Sci. Tech. 47 (13): 7530–7539.

McNutt M, Camilli R, Guthrie G et al. 2011. Assessment of flow rate estimates for the *Deepwater Horizon* / Macondo Well Oil Spill. Flow Rate Technical Group report to the National Incident Command, Interagency Solutions Group, March 10, 2011.

Michel J, Owens EH, Zengel S, Graham A, Nixon Z et al. 2013. Extent and degree of shoreline oiling: *Deepwater Horizon* oil spill, Gulf of Mexico, USA. PLoS ONE, 8(6), e65087, doi:10.1371/journal.pone.0065087.

Montagna PA, Baguley JG, Cooksey C, Hartwell I, Hyde LJ, et al. 2013. Deep-sea benthic footprint of the *Deepwater Horizon* blowout. PLoS ONE 8(8): e70540. doi: 10.1371/journal.pone.0070540

Mulcahy R. 2010. Water column injury ephemeral data collection: ADCP monitoring pPlan (M/V Bunny Bordelon) (May 26, 2010). Originated as a Requirement by D. French McCay, Y. Kim, and Laurie Sullivan, 2010. *Deepwater Horizon* NRDA > Administrative Record > Pre-assessment -- Water Column: http://www.doi.gov/deepwaterhorizon/adminrecord/Pre-assessment-Water-Column.cfm

National Oceanic and Atmospheric Administration (NOAA). 2010. Characteristics of response strategies: a guide for spill response planning in marine environments. U.S. Department of Commerce, U.S. Coast Guard, U.S. Environmental Protection Agency, American Petroleum Institute. 75p.

National Oceanic and Atmospheric Administration (NOAA). 2016. Open water oil identification job aid for aerial observation. U.S. Department of Commerce, Office of Response and Restoration [http://response.restoration.noaa.gov/oil-and-chemical-spills/oil-spills/resources/open-water-oil-identification-job-aid.html]

National Research Council (NRC). 1985. Oil in the sea: inputs, fates and effects. National Academy Press, Washington, D.C. 601p.

NCEI. 2013. Climate Forecast System. (accessed 3 October 2013). Available at: https://www.ncdc.noaa.gov/data-access/model-data/model-datasets/climate-forecast-system-version2-cfsv2.

NDBC. 2011. National Data Buoy Center. ADCP data. (accessed March 2011). Available at: http://www.ndbc.noaa.gov/

NDBC. 2013. National Data Buoy Center. Meteorological data. (accessed 2013). Available at: http://www.ndbc.noaa.gov/.

Nixon Z, Zengel SA, Michel J. (2015). Categorization of shoreline oiling from the *Deepwater Horizon* Oil Spill. (NS_TR.31). DWH Shoreline NRDA Technical Working Group Report.

North EW, Adams EE, Schlag Z, Sherwood CR, He R et al. 2011. Simulating oil droplet dispersal from the *Deepwater Horizon* Spill with a Lagrangian approach. Monitoring and Modeling the *Deepwater Horizon* Oil Spill: A Record-Breaking Enterprise. American Geophysical Union, pp. 217–226.

North EW, Adams EE, Thessen A, Schlag Z, He R et al. 2015. The influence of droplet size and biodegradation on the transport of subsurface oil droplets during the *Deepwater Horizon* spill: a model sensitivity study. Environmental Research Letters 10(2): 024016.

Okubo A, Ozmidov RV. 1970. Empirical dependence of the coefficient of horizontal turbulent diffusion in the ocean on the scale of the phenomenon in question. Atmospheric and Ocean Physics 6(5): 534–536.

Okubo A. 1971. Oceanic diffusion diagrams. Deep-Sea Research 8: 789–802.

Olascoaga M, Haller G. 2012. Forecasting sudden changes in environmental pollution patterns. In: Proceedings of the National Academy of Sciences 109 (13): 2738–2743.

Paris CB, Hénaff ML, Aman ZM, Subramaniam A, Helgers J et al. 2012. Evolution of the Macondo well blowout: simulating the effects of the circulation and synthetic dispersants on the subsea oil transport. Environ. Sci. Technol. 46(24): 13293–13302.

Passow U. 2014. Formation of rapidly-sinking, oil-associated marine snow. Deep-Sea Res. II. (0).

Passow U, Ziervogel K, Asper V, Diercks A. 2012. Marine snow formation in the aftermath of the *Deepwater Horizon* oil spill in the Gulf of Mexico. Environmental Research Letters 7.

Patton JS, Rigler MW, Boehm PD, Fiest DL. 1981. Ixtoc 1 oil spill: flaking of surface mousse in the Gulf of Mexico. Nature 290(5803): 235–238.

Payne JR, Kirstein BE, McNabb Jr GD, Lambach JL, Redding R et al. 1984. Multivariate analysis of petroleum weathering in the marine environment–sub Arctic. Environmental Assessment of the Alaskan Continental Shelf, OCEAP, Final Report of Principal Investigators, Vol. 21 and 22, Feb. 1984, 690p.

Payne JR, Kirstein BE, Clayton Jr JR, Clary C, Redding R et al. 1987. Integration of suspended particulate matter and oil transportation study. Final Report. Minerals Management Service, Environmental Studies Branch, Anchorage, AK. Contract No. 14-12-0001-30146. 216 p.

Payne JR, Terrill E, Carter M, Otero M, Middleton W et al. 2007. Evaluation of field-collected drifter and subsurface fluorescein dye concentration data and comparisons to high frequency radar surface current mapping data for dispersed oil transport modeling. In: Proceedings of the Thirtieth Arctic and Marine Oil Spill Program (AMOP) Technical Seminar, Emergencies Science Division, Environment Canada, Ottawa, ON.

Payne JR, Driskell WB. 2015a. 2010 DWH offshore water column samples—forensic assessments and oil exposures. PECI Technical Report to the Trustees in support of the pDARP.

Payne JR, Driskell WB. 2015b. Forensic fingerprinting methods and classification of DWH offshore water samples. PECI Technical Report to the Trustees in support of the pDARP.

Payne JR, Driskell WB. 2015c. Dispersant effects on waterborne oil profiles and behavior. PECI Technical Report to the Trustees in support of the pDARP.

Payne JR, Driskell WB. 2015d. Offshore adaptive sampling strategies. PECI Technical Report to the Trustees in support of the pDARP.

Reddy CM, Arey JS, Seewald JS, Sylva SP, Lemkau KL et al. 2011. Composition and fate of gas and oil released to the water column during the *Deepwater Horizon* oil spill. In: Proceedings of National Academy of Sciences PNAS early edition: 1–6. (accessed August 2011). Available at: www.pnas.org/cgi/doi/10.1073/pnas.1101242108.

Reddy CM, Arey JS, Seewald JS, Sylva SP, Lemkau KL et al. 2012. Composition and fate of gas and oil released to the water column during the *Deepwater Horizon* oil spill. In: Proceedings of National Academy of Sciences 109(5): 20229–20234.

Ryerson TB, Aikin KC, Angevine WM, Atlas EL, Blake DR et al. 2011. Atmospheric emissions from the Deepwater Horizon spill constrain air-water partitioning, hydrocarbon fate, and leak rate. Geophys. Res. Lett. 38(7): L07803.

Ryerson TB, Camilli R, Kessler JD, Kujawinski EB, Reddy CM et al. 2012. Chemical data quantify *Deepwater Horizon* hydrocarbon flow rate and environmental distribution. In: Proceedings of the National Academy of Sciences 109(50): 20246–20253.

Saha S, et al. 2010. NCEP Climate Forecast System Reanalysis (CFSR) 6-hourly products, January 1979 to December 2010. Research Data Archive at the National Center for Atmospheric Research (NCAR), Computational and Information Systems Laboratory. (accessed March 2011). Available at: https://doi.org/10.5065/D69K487J.

Salisbury JE, Campbell JW, Linder E, Meeker LD, Muller-Karger FE et al.. 2004. On the seasonal correlation of surface particle fields with wind stress and Mississippi discharge in the northern Gulf of Mexico. Deep-Sea Research II 51: 1187–1203.

Schmitz Jr WJ, Biggs DC, Lugo-Fernandez A, Oey LY, Sturges W. 2005. A Synopsis of the circulation in the Gulf of Mexico and on its continental margins. In W. Sturges and A. Lugo-Fernandez, Circulation in the Gulf of Mexico: Observations and Models (pp. 11–29). Washington, D.C., United States: American Geophysical Union.

Sharma N, Brickley P, Owen G, Coholan P. 2010. Use of air-deployed drogued drifting buoys for oil spill tracking. In OCEANS 2010, 1–9, 2010. (accessed October 2011). Available at: http://ieeexplore.ieee.org/xpls/abs_all.jsp?arnumber=5663921.

Socolofsky SA, Jirka GH. 2005. Environmental fluid mechanics. Part I: mass transfer and diffusion. Engineering–Lectures. Publisher: Texas A&M University 2005, 184 p.

Socolofsky SA, Adams EE, Sherwood CR. 2011. Formation dynamics of subsurface hydrocarbon intrusions following the *Deepwater Horizon* blowout. Geophysical Research Letters 38(9): L09602.

Socolofsky SA, Adams EE, Boufadel MC, Aman ZM, Johansen Ø et al. 2015. Intercomparison of oil spill prediction models for accidental blowout scenarios with and without subsea chemical dispersant injection. Marine Poll Bull 96(1–2): 110–126. (accessed April 2016). Available at : doi:http://dx.doi.org/10.1016/j.marpolbul.2015.05.039.

Spaulding MS, Mendelsohn D, Crowley D, Li Z, Bird A. 2015. Draft technical reports for *Deepwater Horizon* water column injury assessment: WC_TR.13: Application of OILMAP DEEP to the *Deepwater Horizon* Blowout. RPS ASA, 55 Village Square Drive, South Kingstown, RI 02879. Administrative Record no. DWH-AR0285366.pdf . (accessed March 2016). Available at: https://www.doi.gov/deepwaterhorizon/adminrecord.

Spaulding M, Li Z, Mendelsohn D, Crowley D, French-McCay D et al. 2017. Application of an integrated blowout model system, OILMAP DEEP, to the *Deepwater Horizon* (DWH) Spill. Marine Poll Bull. (accessed October 2017). Available at pii: S0025-326X(17)30350-8. doi: 10.1016/j.marpolbul.2017.04.043.

Spier C, Stringfellow WT, Hazen TC, Conrad M. 2013. Distribution of hydrocarbons released during the 2010 MC252 oil spill in deep offshore waters. Environ. Pollut. 173(0): 224–230.

Stout SA. 2015a. Physical and chemical properties of the fresh MC252 Macondo-1 well crude oil. NewFields Technical Report to the Trustees in support of the pDARP.

Stout SA. 2015b. Bulk chemical and physical properties of fresh and weathered Macondo crude oil. NewFields Technical Report to the Trustees in support of the pDARP.

Stout SA. 2015c. Range in composition and weathering among floating Macondo oils during the *Deepwater Horizon* oil spill. NewFields Technical Report to the Trustees in support of the pDARP.

Stout SA. 2015d. Chemical evidence for the presence and distribution of Macondo oil in deep-sea sediments following the *Deepwater Horizon* oil spill. Newfields Technical Report to the Trustees in support of the pDARP

Stout S, Rouhani S, Liu B, Oehrig J. 2015. Spatial Extent ("Footprint") and volume of Macondo oil found on the deep-sea floor following the *Deepwater Horizon* Oil Spill. Newfields Technical Report to the Trustees in support of the pDARP.

Stout SA, Payne JR, Emsbo-Mattingly SD, Baker G. 2016a. Weathering of field-collected floating and stranded Macondo oils during and shortly after the *Deepwater Horizon* oil spill. Marine Poll Bull. 105(1):7–22. (accessed January 2017). Available at: http://dx.doi.org/10.1016/j.marpolbul.2016.02.044.

Stout SA, Payne JR. 2016a. Macondo oil in deep-sea sediments: Part 1–sub-sea weathering of oil deposited on the seafloor. Marine Poll Bull. 111, 365–380. (accessed April 2017). Available at: http://dx.doi.org/10.1016/j.marpolbul.2016.07.041.

Stout SA, Payne JR, Ricker RW, Baker G, Lewis C. 2016b. Macondo oil in deep-sea sediments: Part 2–Distribution and distinction from background and natural oil seeps. Marine Poll Bull. 111, 381–401. (accessed September 2017). Available at: http://dx.doi.org/10.1016/j.marpolbul.2016.07.041.

Stout SA, Payne JR. 2016b. Chemical composition of floating and sunken in-situ burn residues from the *Deepwater Horizon* oil spill. Marine Poll Bull 108, 186–202. (accessed September 2017). Available at: http://dx.doi.org/10.1016/j.marpolbul.2016.04.031

Stout SA, Payne JR. 2017. Footprint, weathering, and persistence of synthetic-base drilling mud olefins in deep-sea sediments following the *Deepwater Horizon* disaster. Marine Poll Bull 118(1-2): 328–340.

Svejkovsky J, Lehr W, Muskat J, Graettinger G, Mullin J. 2012. Operational utilization of aerial multispectral remote sensing during oil spill response: lessons learned during the *Deepwater Horizon* (MC-252) spill. Photogramm Eng Remote Sensing 78(10): 1089–1102.

Svejkovsky J, Hess M, Muskat J, Nedwed TJ, McCall J, Garcia O. 2016. Characterization of surface oil thickness distribution patterns observed during the *Deepwater Horizon* (MC-252) oil spill with aerial and satellite remote sensing. Marine Poll Bull.110(1): 162–176.

Travers C, Forth H, Rissing M, Cacela D. 2015a. Polycyclic aromatic hydrocarbon concentrations in the upper water column during the *Deepwater Horizon* Oil Spill. DWH NRDA Water Column Technical Working Group Report. Prepared for National Oceanic and Atmospheric Administration by Abt Associates, Boulder, CO. August 2015.

Travers C, Wobus C, Morris. 2015b. Mortality estimates of invertebrates and early life stage fish and other injury metrics in the upper mixed layer of the water column during the *Deepwater Horizon* Oil Spill. DWH NRDA Water Column Technical Working Group Report. Prepared for National Oceanic and Atmospheric Administration by Abt Associates, Boulder, CO. August 2015.

USDC. 2015. The US District Court for Eastern District of Louisiana, Case 2:10-md-02179-CJB-SS Document 14021 Filed 01/15/15, Findings of fact and conclusions of law phase two trial. pp 1–44. (accessed February 2016). Available at: http://www2.epa.gov/sites/production/files/2015-01/documents/phase2ruling.pdf

Valentine DLK, JD, Redmond MC, Mendes SD, Heintz MB et al. 2010. Propane respiration jump-starts microbial response to a deep oil spill. Science 330: 208–211.

Valentine DL, Fisher GB, Bagby SC, Nelson RK, Reddy CM et al. 2014. Fallout plume of submerged oil from *Deepwater Horizon*. PNAS vol. 111, No. 45, pp. 15906–15911, (accessed October 2017). Available at: doi: 10.1073/pnas.1414873111.

Walker N, Pilley C, D'Sa E, Leben R, Coholan P et al. 2011. Impacts of loop current frontal cyclonic eddies and wind forcing on the 2010 Gulf of Mexico oil spill. Geophysical Monograph Series 195: 103–116.

Xue Z, He R, Fennel K, Wei C, Lorentz S et al. 2013. Modeling ocean circulation and biogeochemical variability in the Gulf of Mexico. Biogeosciences 10(11): 7219–7234.

Youssef M. 1993. The behavior of the near ocean surface under the combined action of waves and currents in shallow water, (PhD Dissertation) Department of Ocean Engineering, University of Rhode Island, Narragansett, RI, 212 p.

Youssef M, Spaulding ML. 1993. Drift current under the action of wind waves. In: Proceedings of the 16th Arctic and Marine Oil Spill Program Technical Seminar, Calgary, Alberta, Canada, pp. 587–615.

Youssef M, Spaulding ML. 1994. Drift current under the combined action of wind and waves in shallow water. In: Proceedings of the Seventeenth Arctic and Marine Oilspill Program (AMOP) Technical Seminar, Environment Canada, Ottawa, ON, Canada, pp. 767–784.

Ziervogel K, Mckay L, Rhodes B, Osburn CL, Dickson-Brown J et al. 2012. Microbial activities and dissolved organic matter dynamics in oil-contaminated surface seawater from the *Deepwater Horizon* Oil Spill site. PLoS ONE 7(4): e34816.

Ziervogel K, Arnosti C. 2014. Enhanced protein and carbohydrate hydrolyses in plume-associated deepwaters initially sampled during the early stages of the *Deepwater Horizon* oil spill. In: Deep Sea Research Part II: Topical Studies in Oceanography. Amsterdam (Netherlands): Elsevier. (accessed 2 December 2016). Available at: DOI: 10.1016/j.dsr2.2013.09.003

Annex A: SIMAP Model Inputs for *Deepwater Horizon* Oil Spill Simulations: Environmental Data and Response Activities

A.1. Water Temperature and Salinity

A.1.1 Data Source and Grid Resolution

Data were obtained from the National Oceanographic Data Center (NODC) Ocean Climate Laboratory's, World Ocean Atlas, Monthly Climatology data set for the Gulf of Mexico. Objectively-analyzed mean data in the monthly 1/4° gridded data set of the NODC database (NODC 2015). Data were reformatted into a text file format suitable for input to SIMAP. The extents of the grids are: 99.000°W to 81.000°W; 21.000°N to 31.000°N.

Processing of the data was performed, as follows:

- Many grid cells within this extent did not have any data. It was required that all cells that cover any water at all need a temperature and salinity value. Therefore, all cells that touched any water within the model input habitat grid had the values extrapolated. Other cells with no data that did not have any data and were either outside of the habitat grid extent or were completely over land were excluded from the output file.

  Extrapolation Method: A total of 102 cells needed values extrapolated. For each of these cells, a mapping was defined to a nearby cell from which to use the data.
  - The nearby cell to use was determined by selecting the closest reasonable cell with data values. Typically, this was the nearest cell directly to the south. In some cases, the nearest cell was a diagonal. And in other cases (i.e. around the Bird's Foot), the nearest cell was the one to the east. In some cases, the nearest cell with data was actually several cells away.
- Because all vertical layers of each of the cells needed a value, and in some locations the atlas data did not reach the bathymetry, the value from the deepest depth where data were available was used for all depths below it. (SIMAP will not use data below the depth present in the depth grid.)

A.1.2 Temperature

Figure A.1.1 shows the resolution of the 1–4° grid, and the locations of three grid cells for which average vertical temperature profiles are shown in Figure A.1.2.

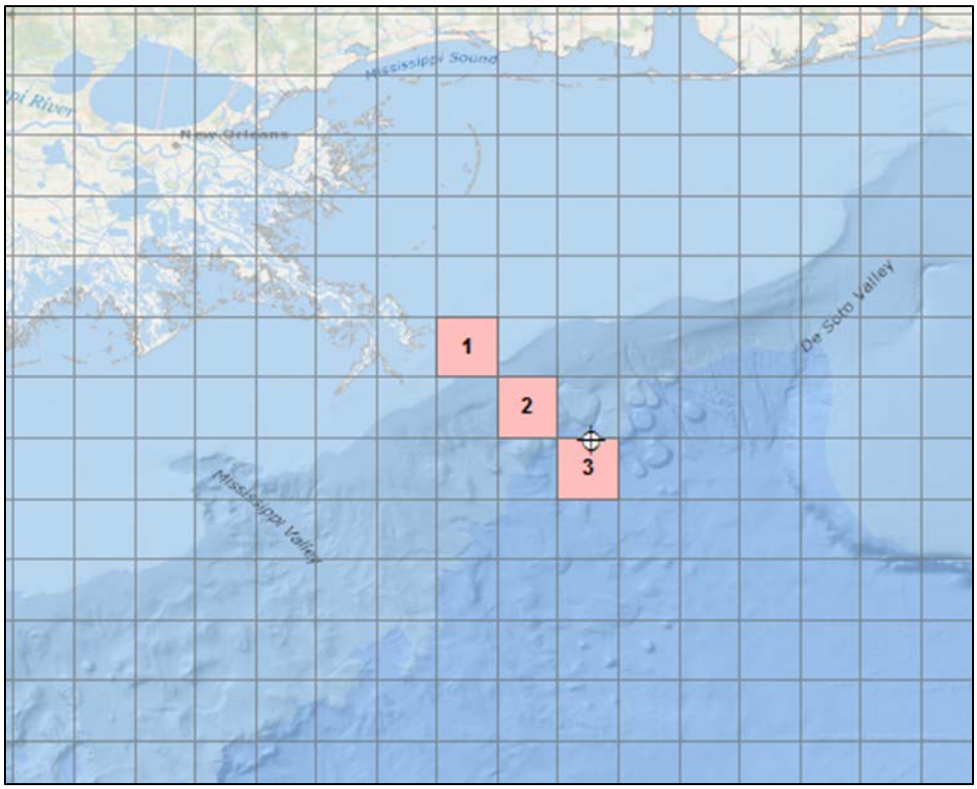

Figure A.1.1 Resolution of the 1/4° grid, and the locations of three grid cells for which vertical temperature profiles are shown in Figure A.2.2.

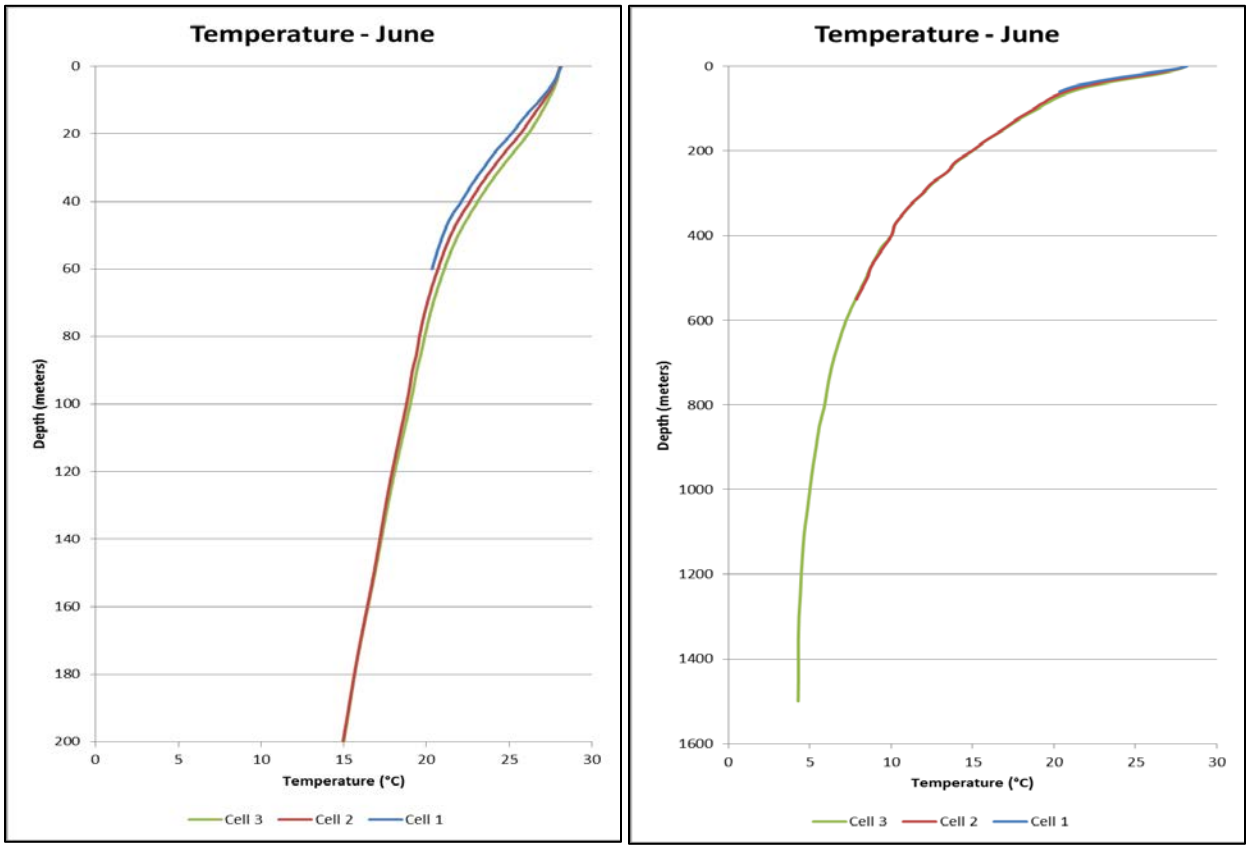

Figure A.1.2 Average vertical temperature profiles for June for cells shown in Figure A.1.1.

Figures A.1.3 to A.1.8 show the ¼° surface water temperature data included in the SIMAP input file, obtained from the NODC World Ocean Atlas 2013. WOA13 temperature values were extrapolated to shore.

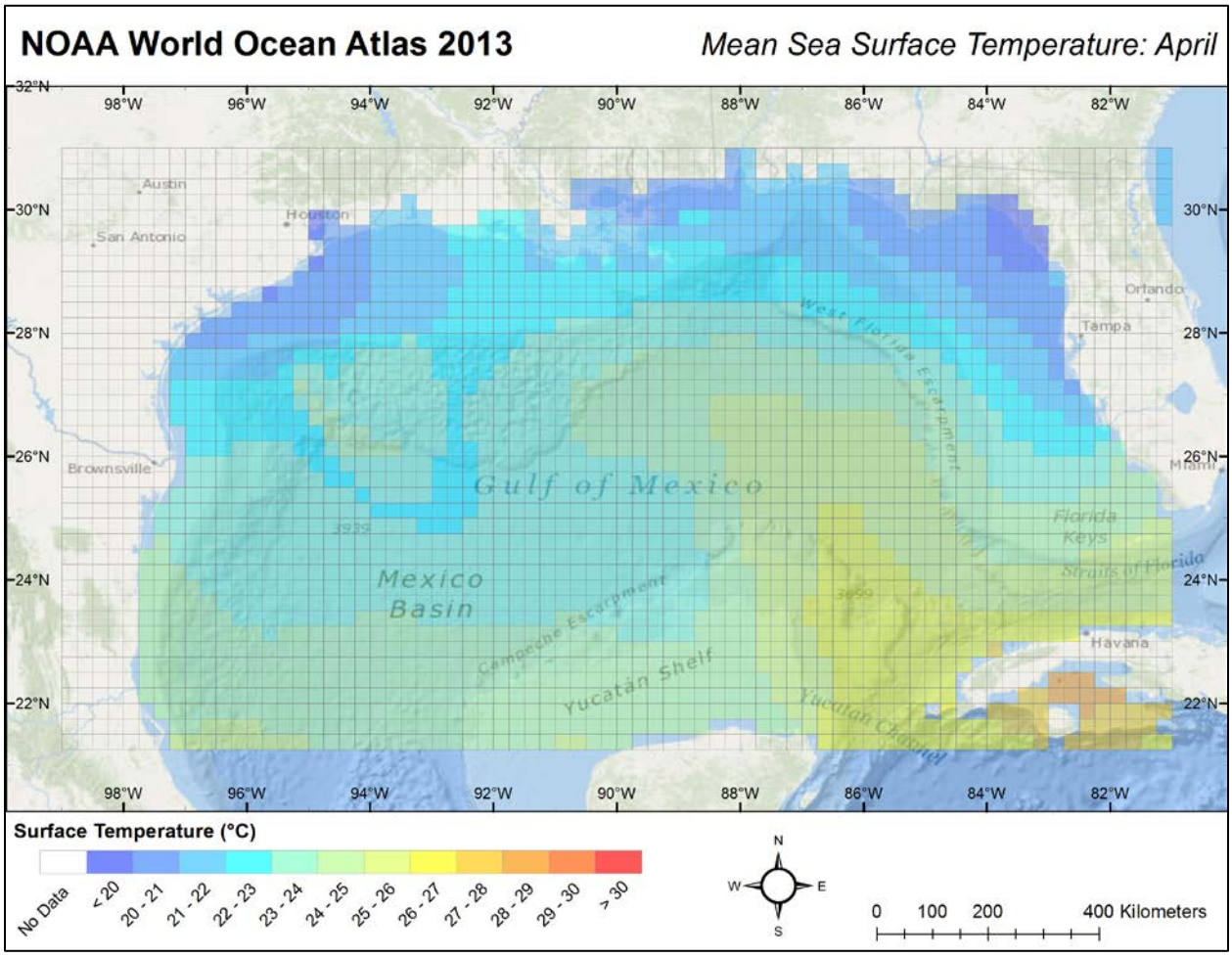

Figure A.1.3 Climatic mean surface water temperature data for April.

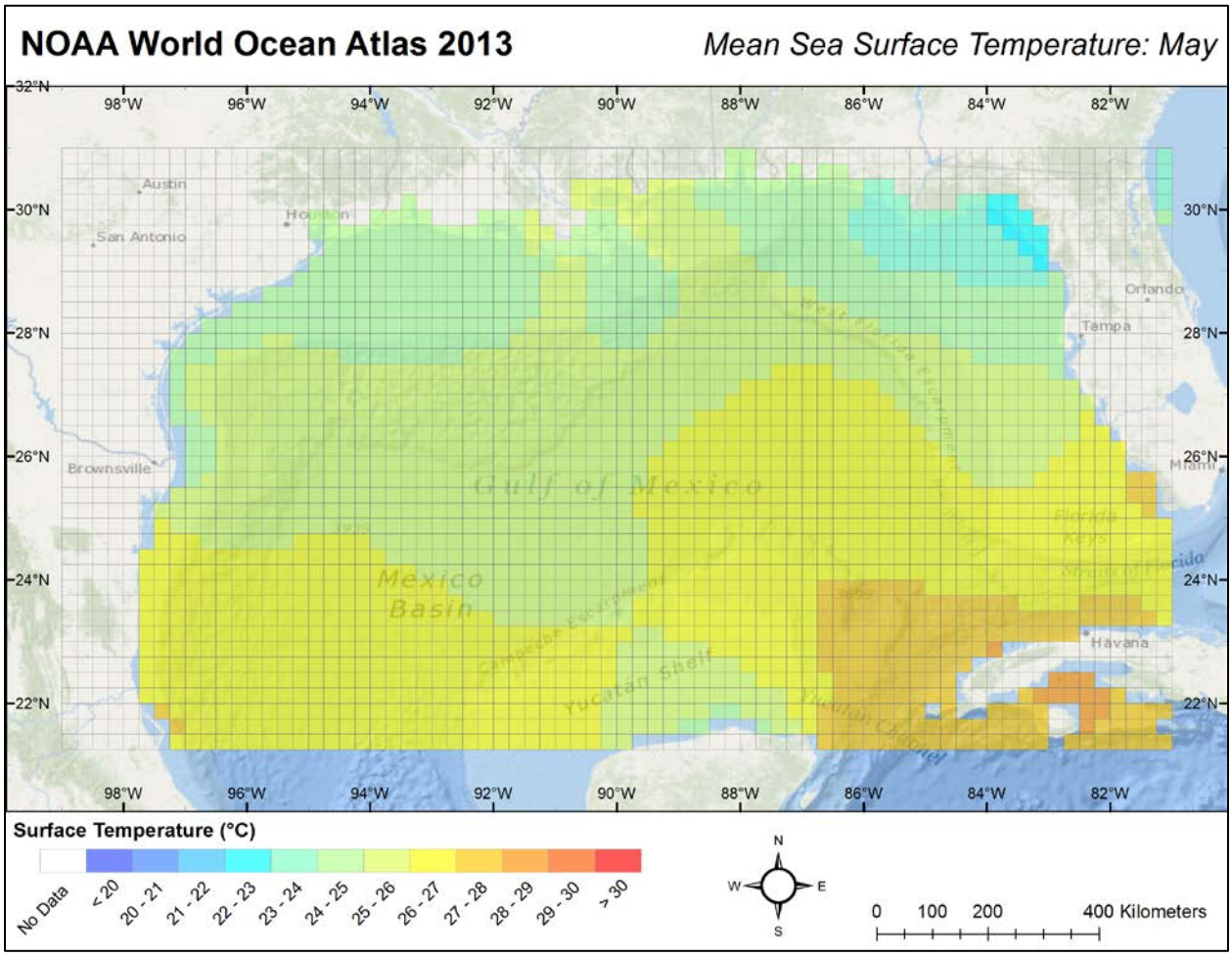

Figure A.1.4 Climatic mean surface water temperature data for May.

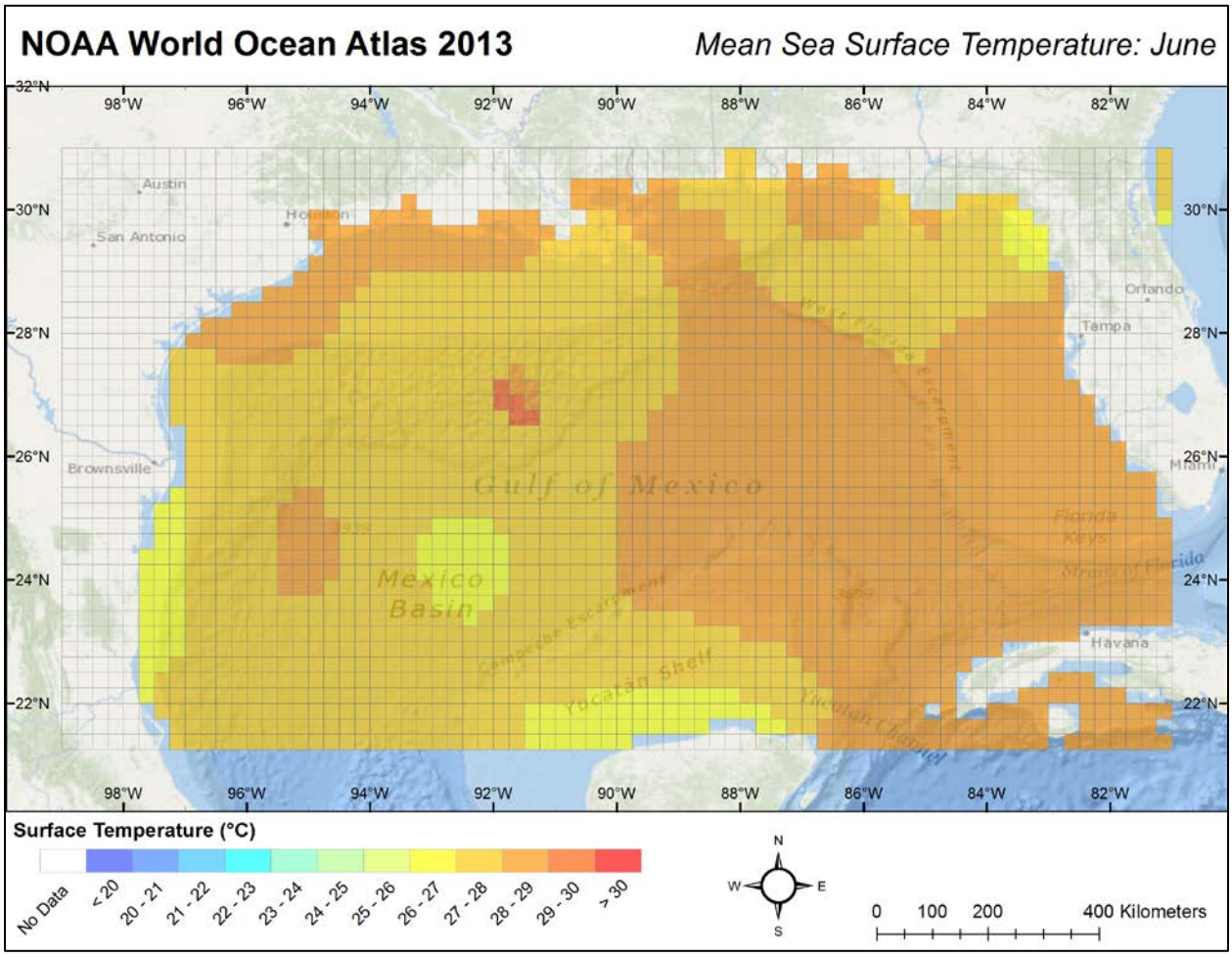

Figure A.1.5 Climatic mean surface water temperature data for June.

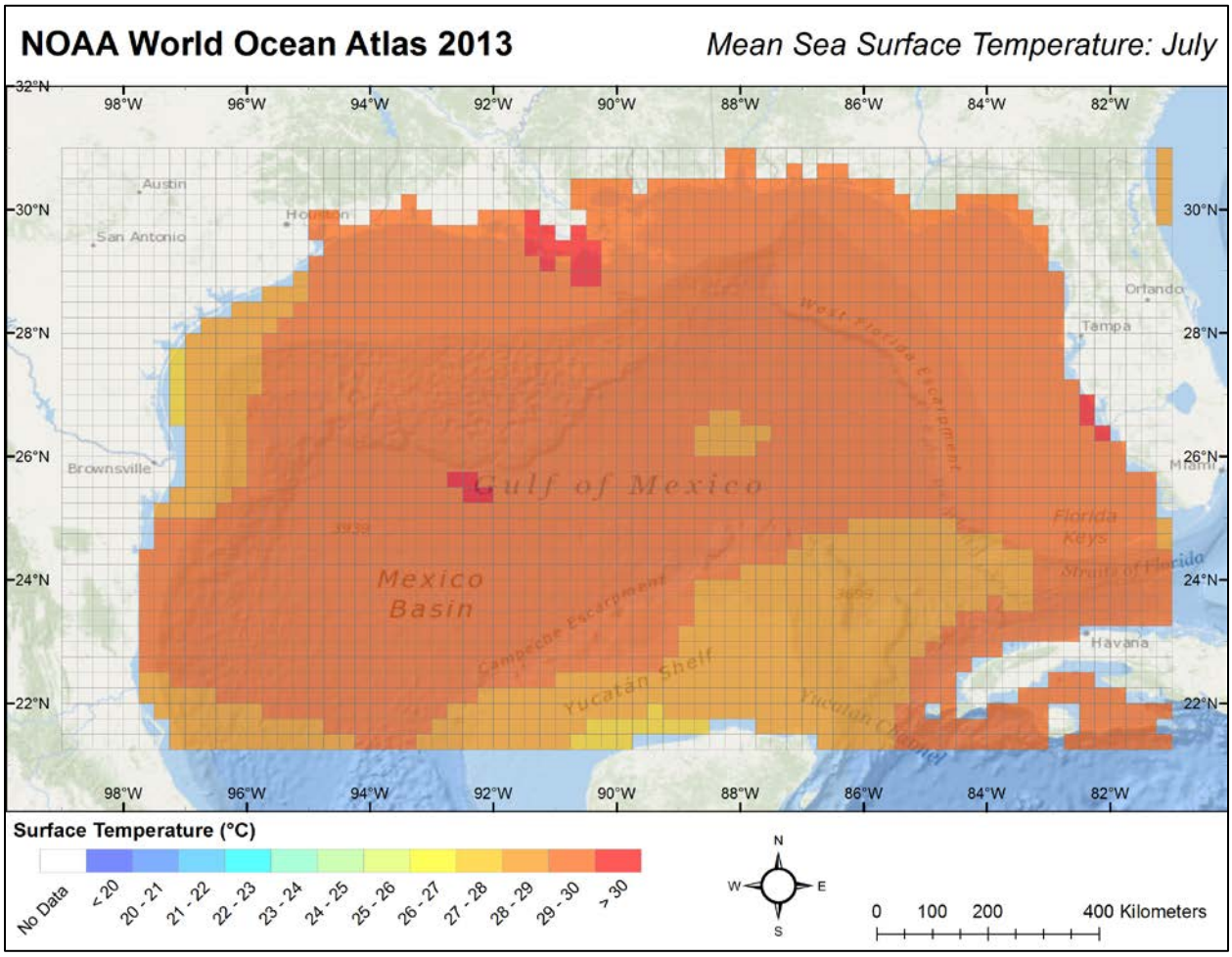

Figure A.1.6 Climatic mean surface water temperature data for July.

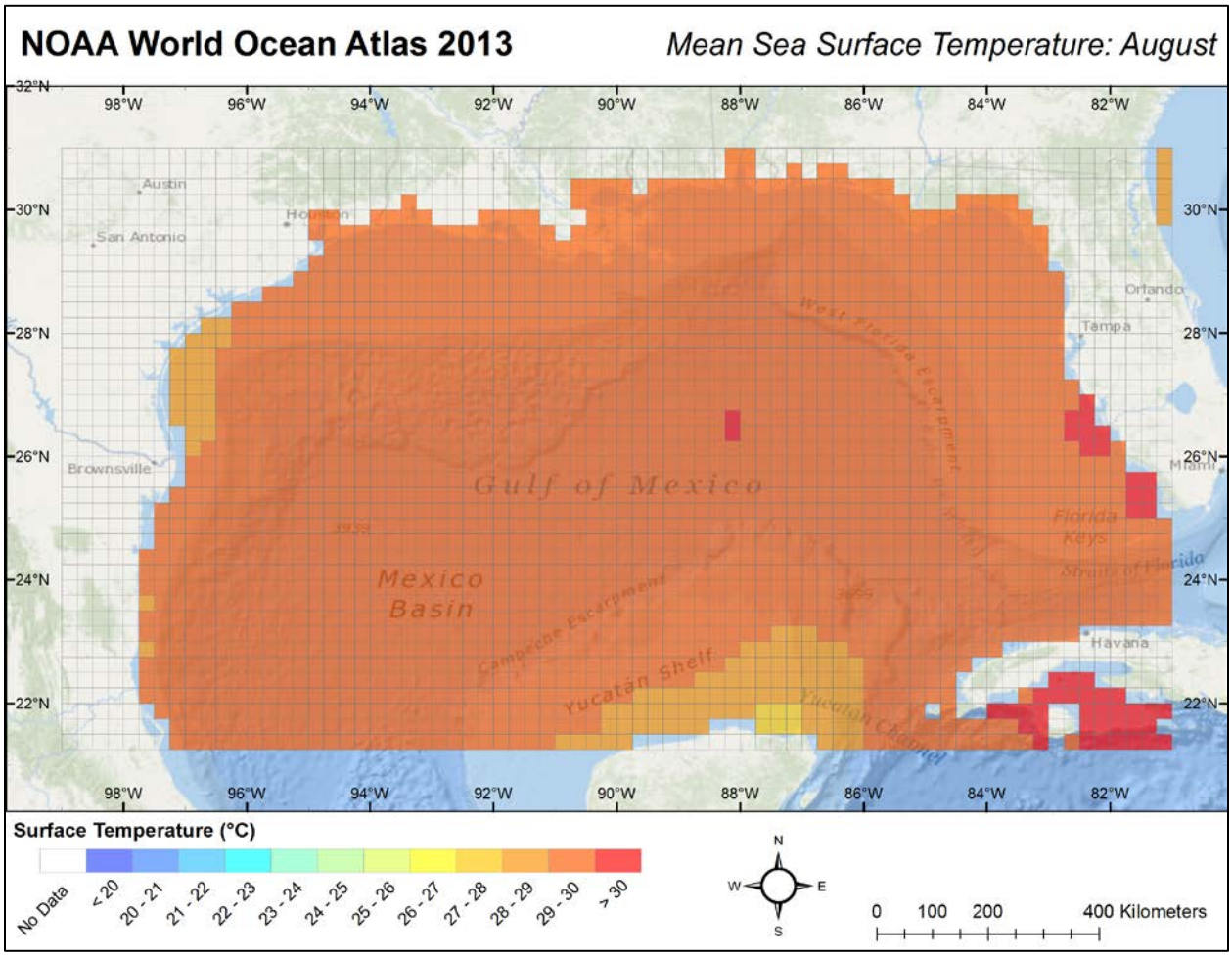

Figure A.1.7 Climatic mean surface water temperature data for August.

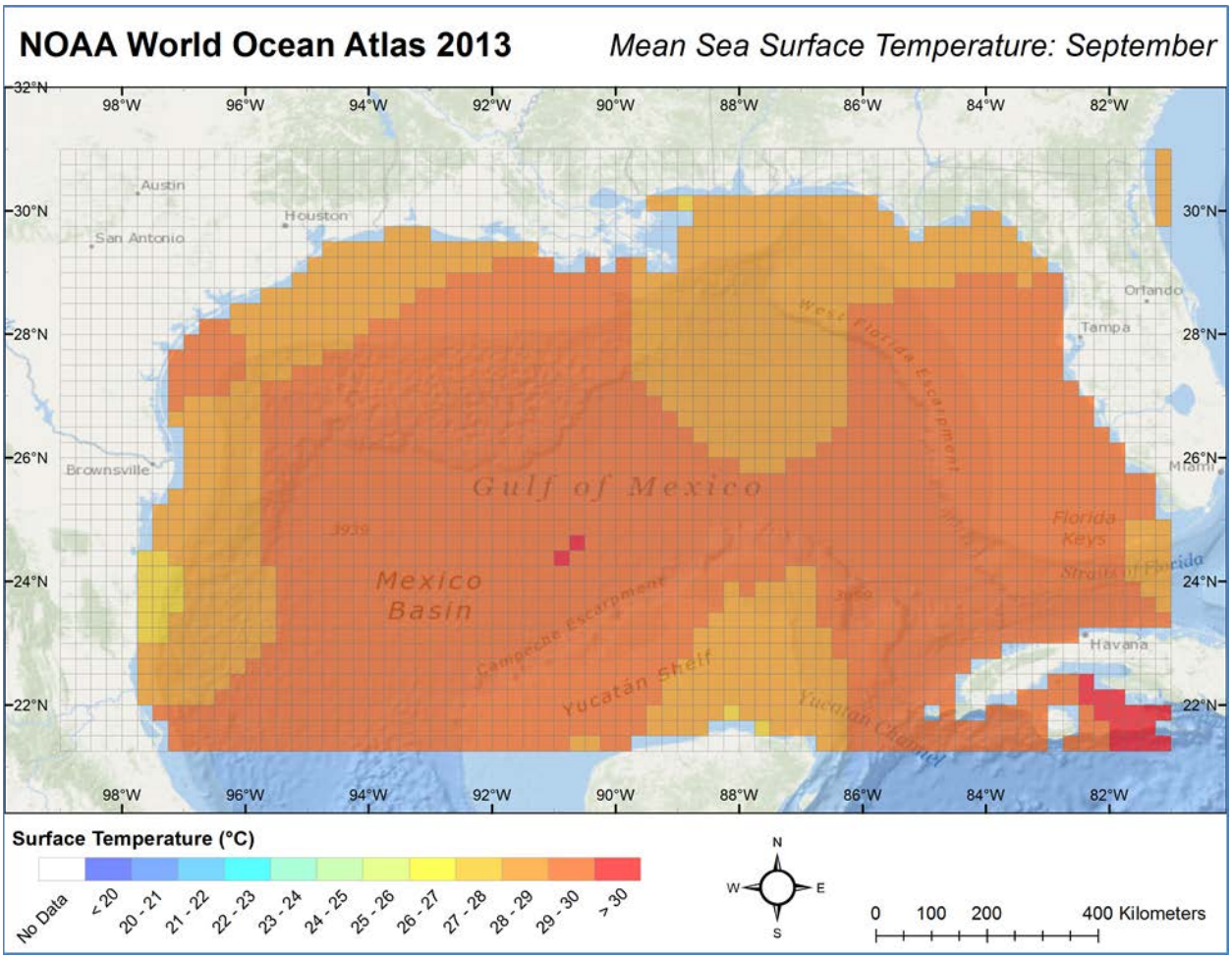

Figure A.1.8 Climatic mean surface water temperature data for September.

A.1.3 Salinity

Figure A.1.9 shows average vertical salinity profiles for grid cells shown in Figure A.2.2. The strong salinity gradient in the upper 20 m is typical of Mississippi plume-influenced waters near the Louisiana delta (e.g., bird's foot).

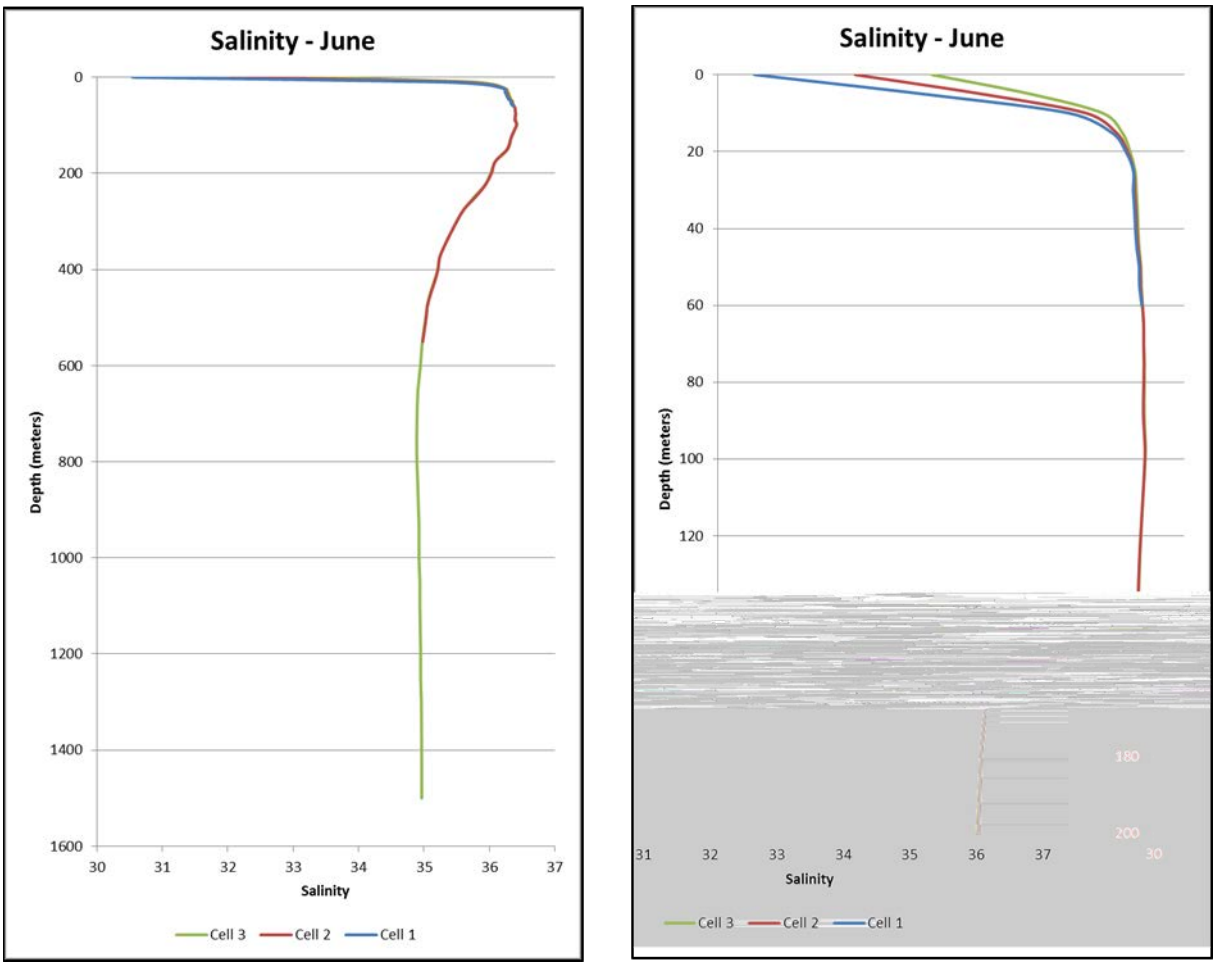

Figure A.1.9 Average vertical salinity profiles in June for cells shown in Figure A.2.1.

Figures A.1.10 to A.1.15 show the ¼-degree surface salinity data in the SIMAP input file, obtained from the World Ocean Atlas 2013. The WOA13 temperature values were extrapolated to shore. The influence of river discharges is seen near the Texas and Louisiana coastlines.

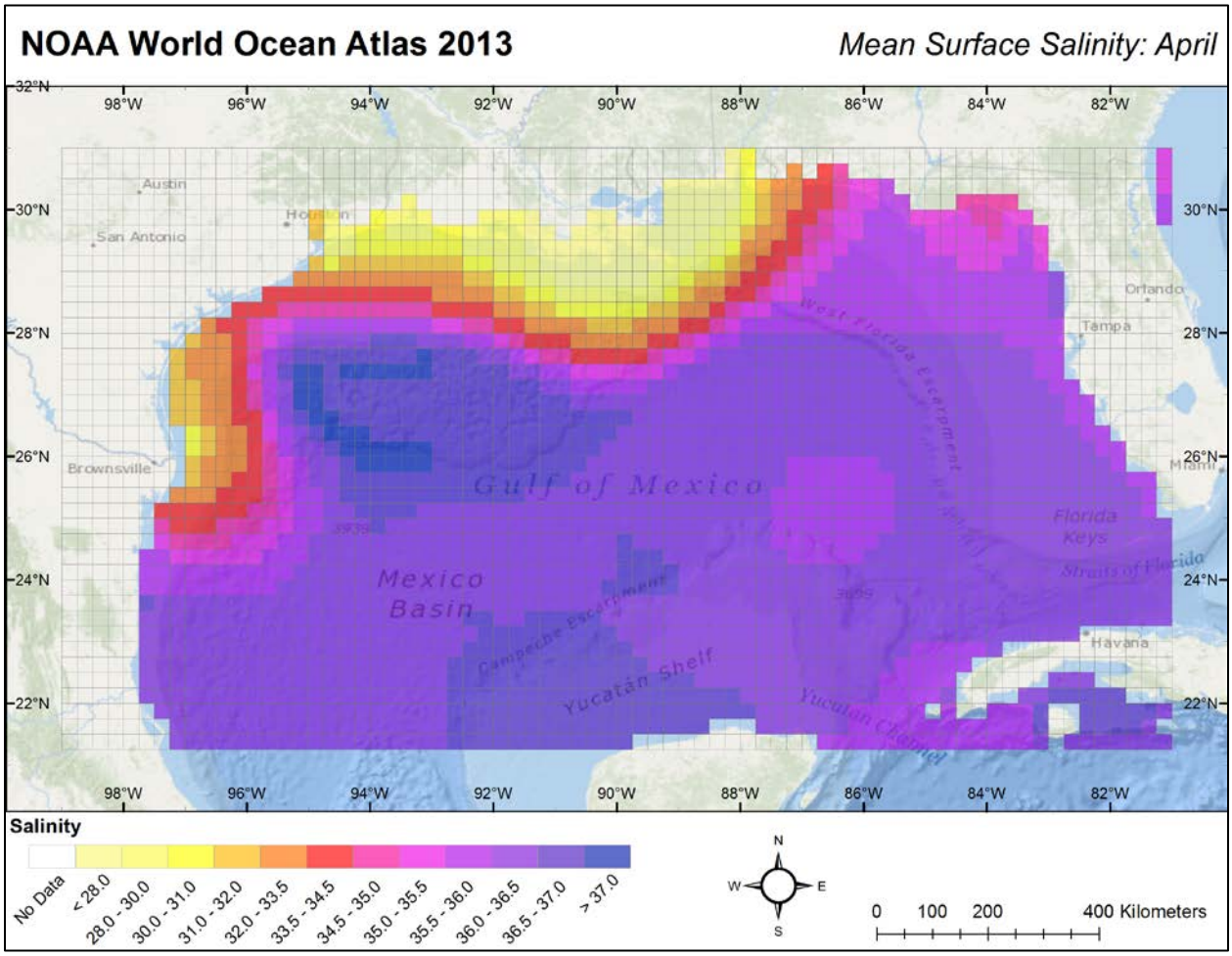

Figure A.1.10 Climatic mean surface salinity data for April.

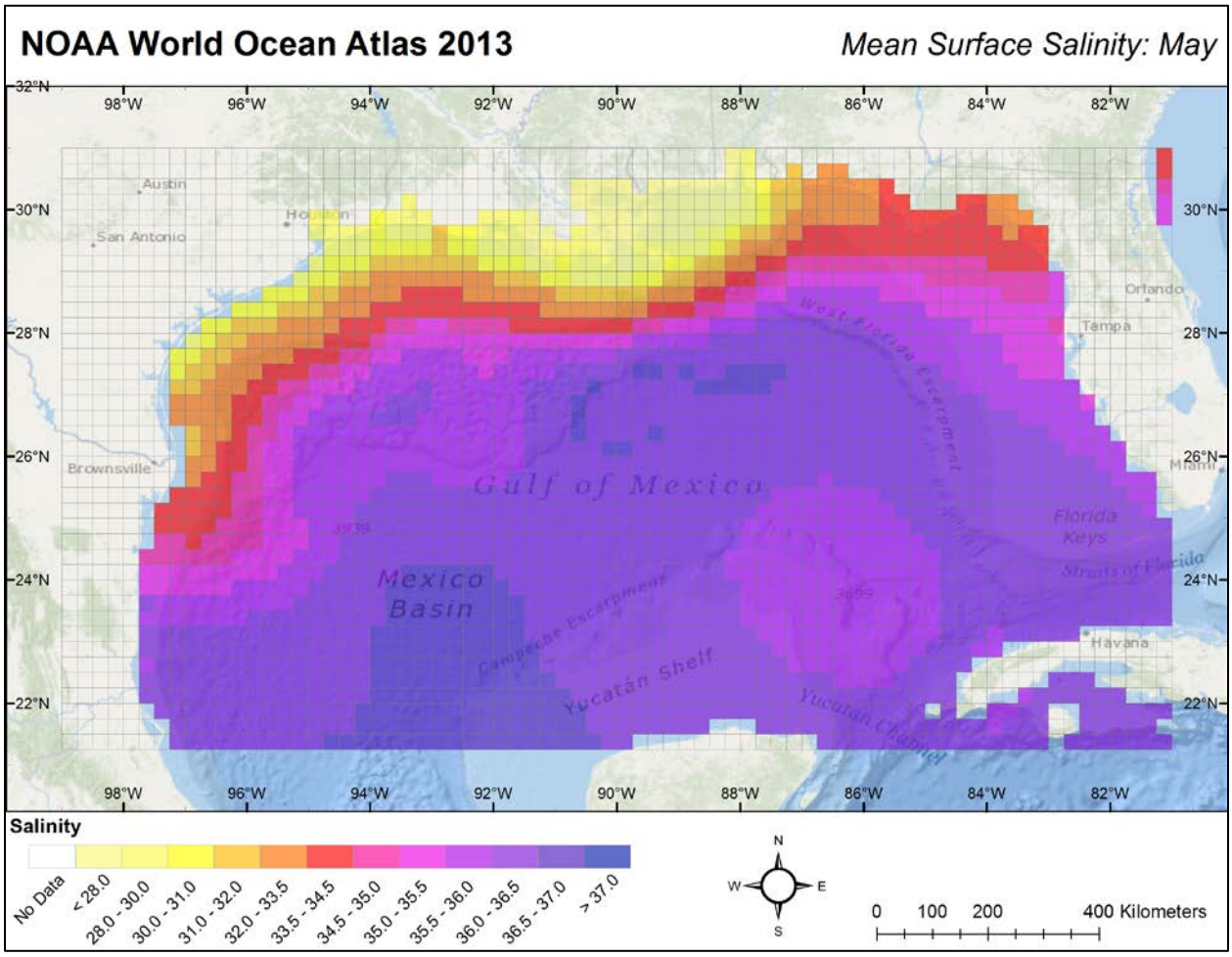

Figure A.1.11 Climatic mean surface salinity data for May.

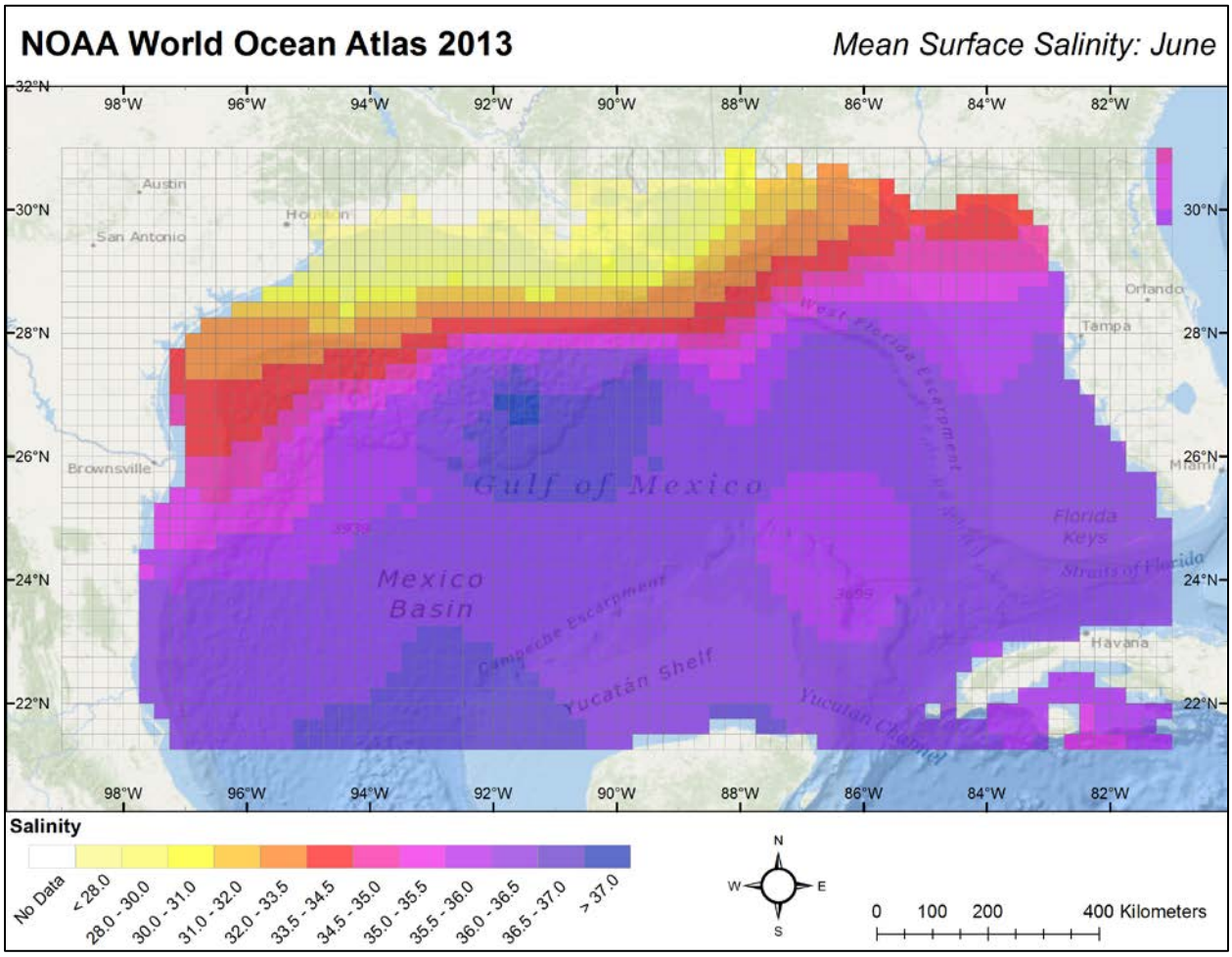

Figure A.1.12 Climatic mean surface salinity data for June.

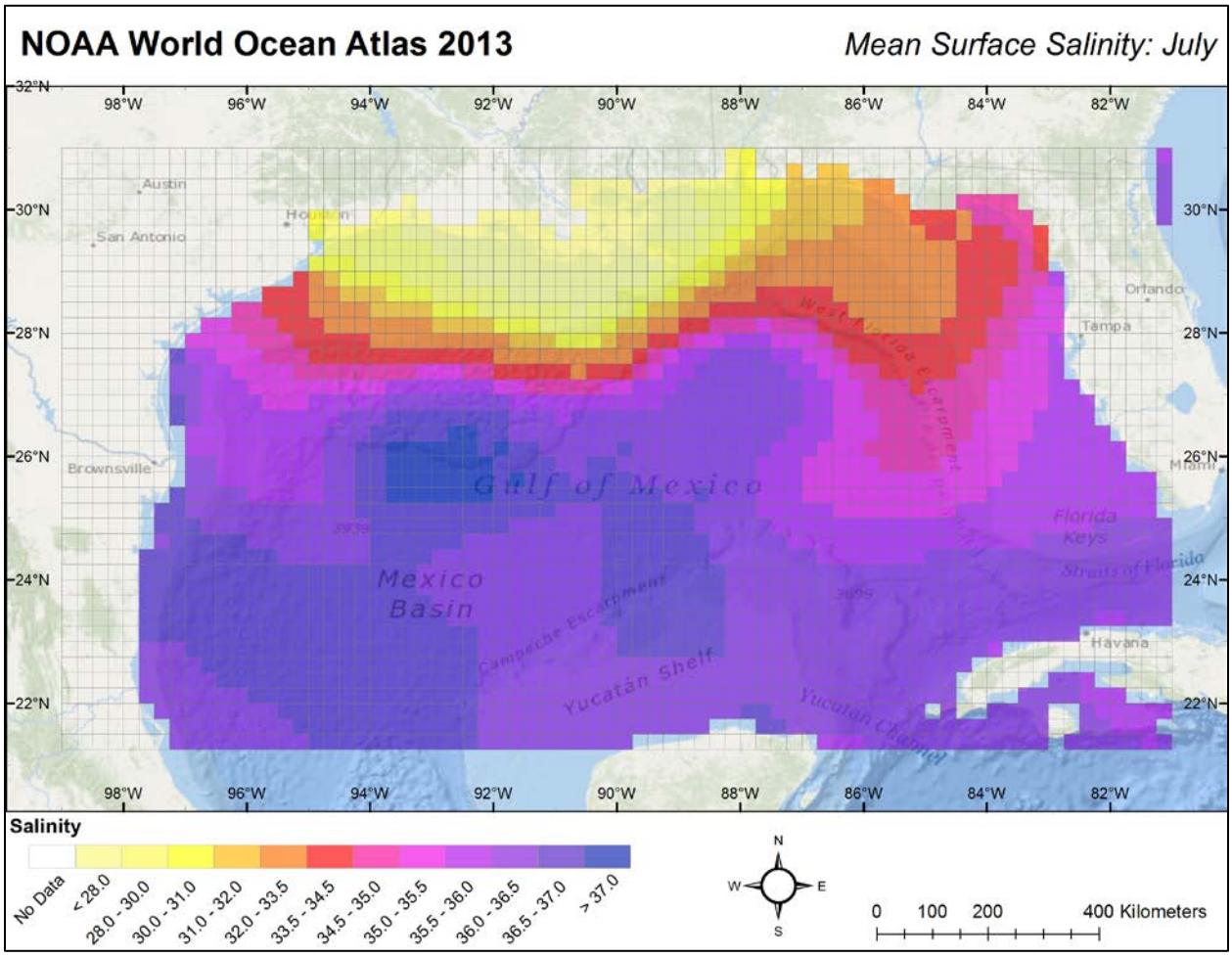

Figure A.1.13 Climatic mean surface salinity data for July.

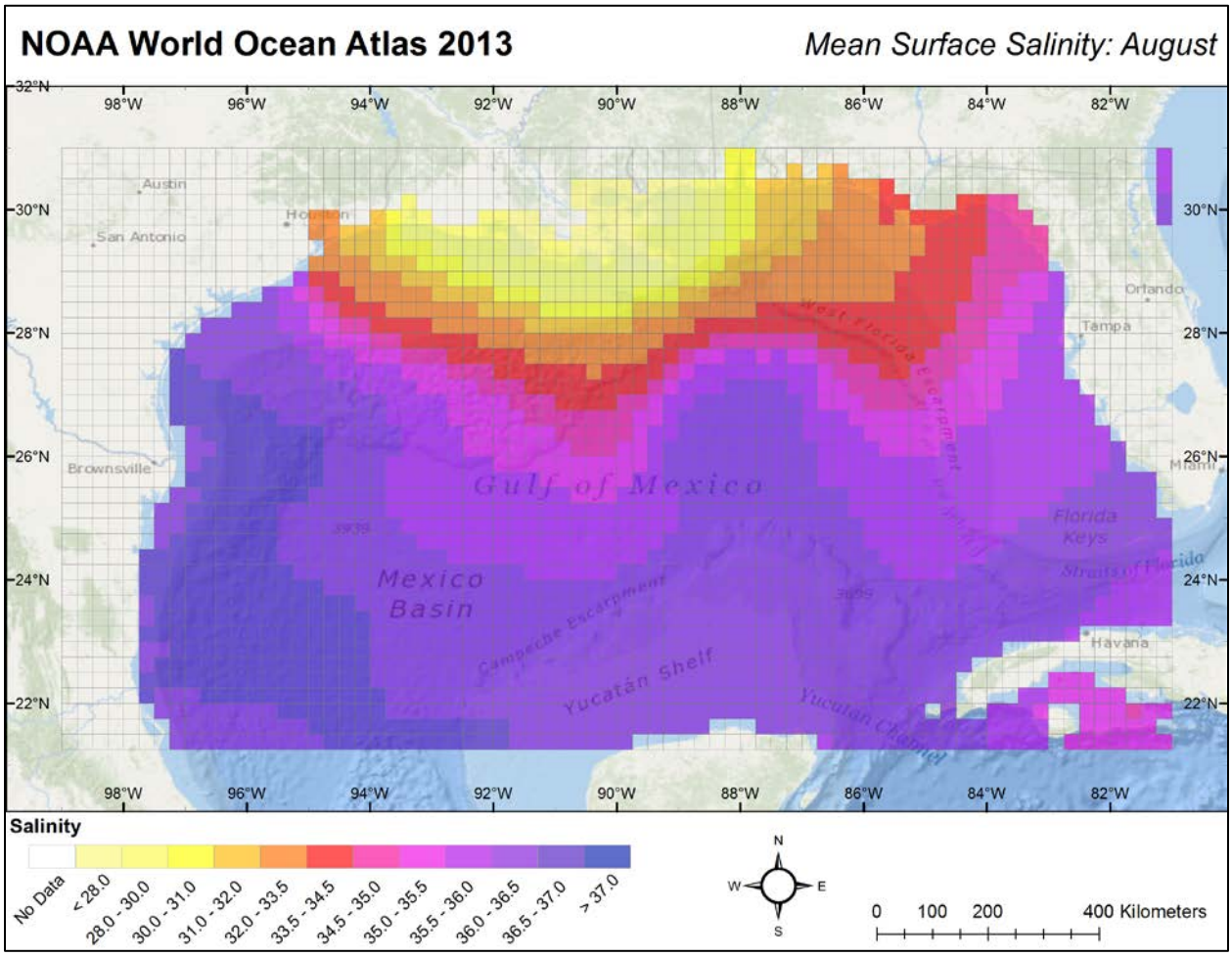

Figure A.1.14 Climatic mean surface salinity data for August.

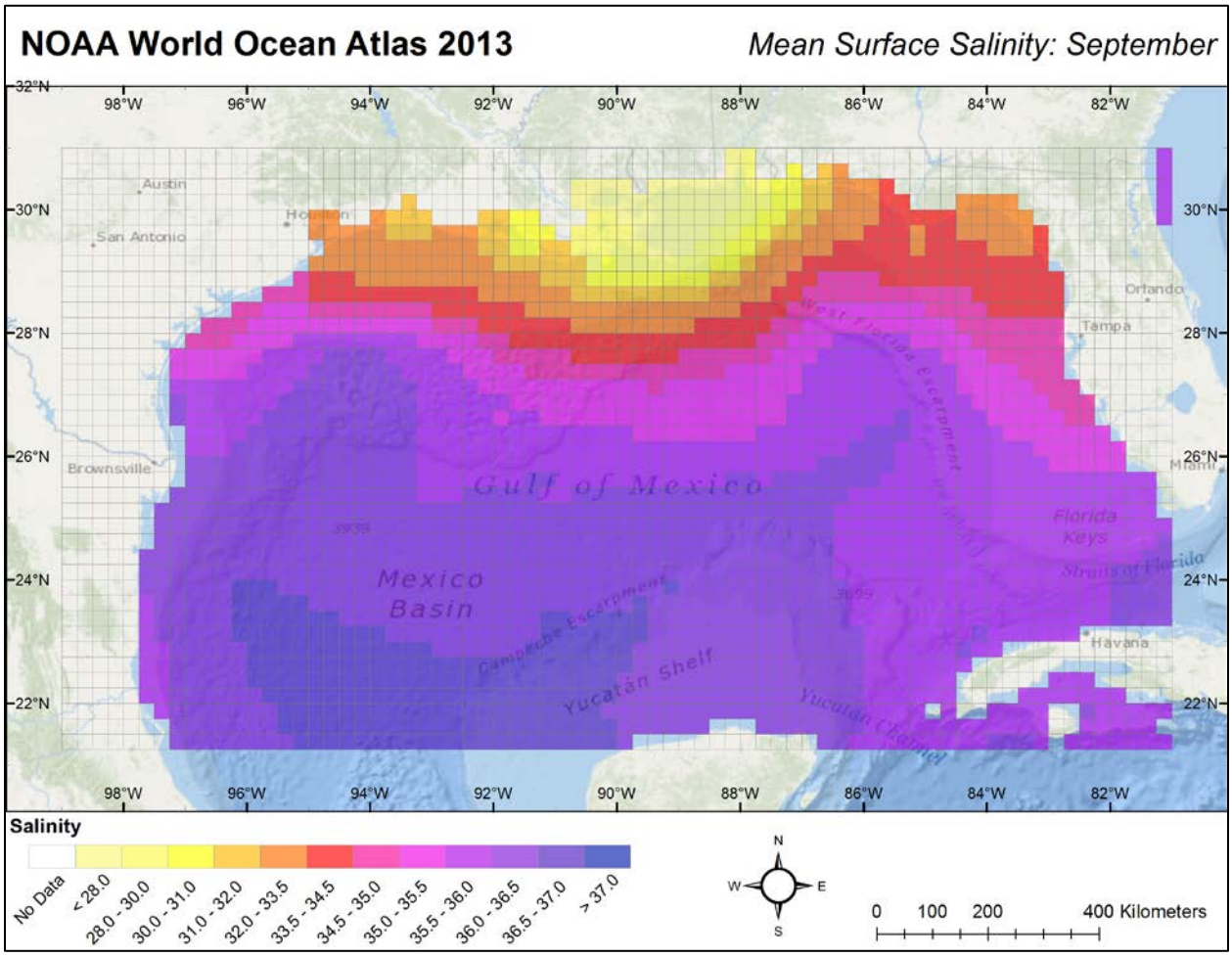

Figure A.1.15 Climatic mean surface salinity data for September.

A.1.4 Water Density

Figure A.1.16 shows a composite of all water density (as sigma-t) profiles based on CTD (conductivity, temperature and depth) data that were reviewed and validated in the Quality Assurance/Quality Control (QA/QC) DWHOS NRDA program.

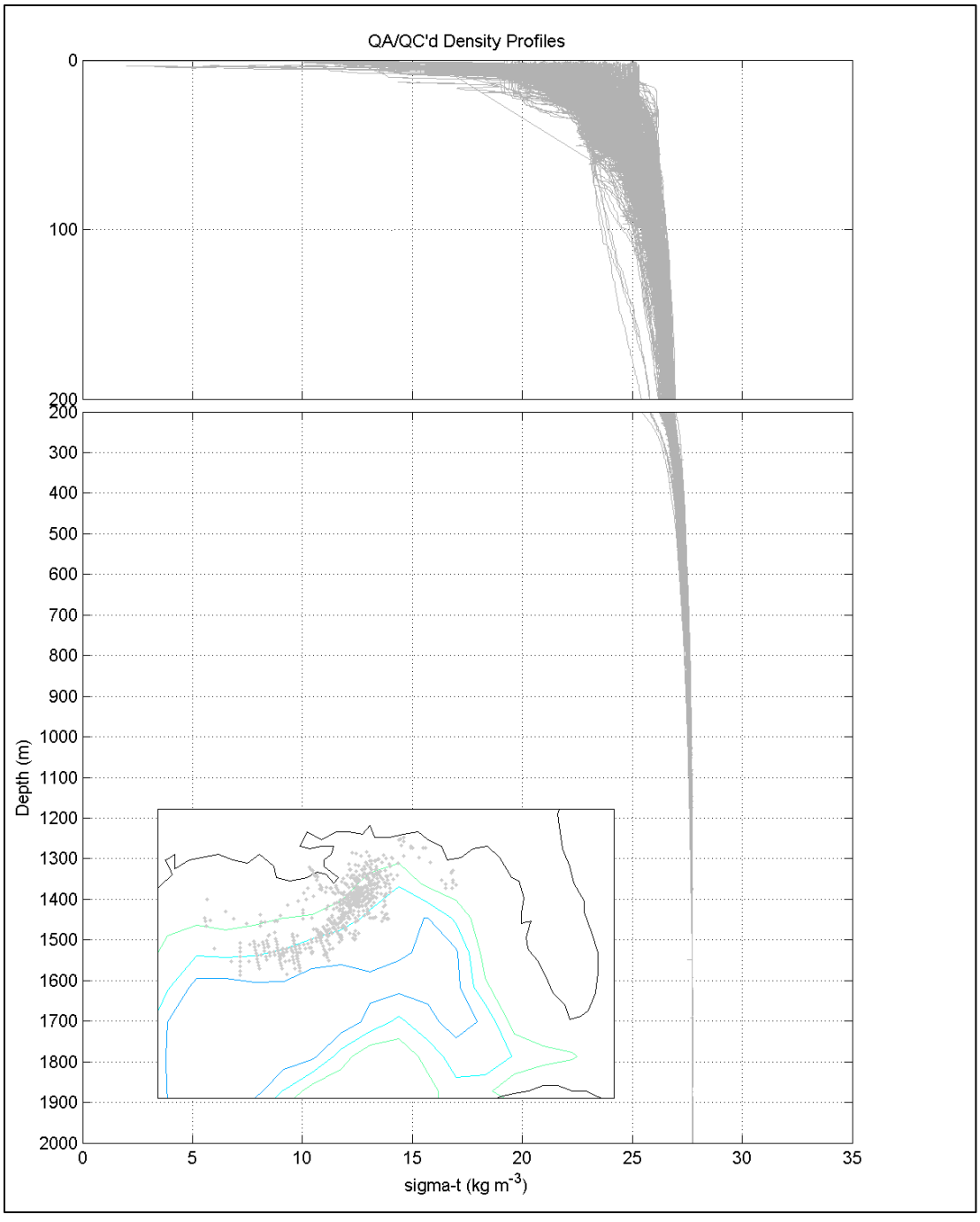

Figure A.1.16 Water density (as sigma-t) profiles based on conductivity, temperature and depth (CTD).

A.2. Response Activities

This section describes how response operation data for in situ burning and aerial dispersant applications were collected and developed into inputs for modeling oil fate. Section 4.7 of the main report describes the algorithms, as well as environmental and oil property constraints assumed for the modeling.

A.2.1 In-Situ Burning

Data collected on in-situ burning collected during the DWHOS response were obtained from the ERMA web site (ERMA 2014). The values from the final burn report (Mabile and Allen 2010) for 411 burns were used for the calculations of burning inputs for the model. Appendix D in Mabile and Allen (2010) contains the burns table. The entire table from 4/28/2010 to 7/19/2010 was imported into MS Excel™ (Table A.2.1). Burn times (CDT) were available for all but the burns on May 19. For that date, the typical burning period for days in May was assumed.

Table A.2.1 In situ burn volumes from Mabile and Allen (2010).

Burn No.	Date	Approximate Burn Volume Minimum (bbl)	Approximate Burn Volume Maximum (bbl)	Burn Start (CDT)	Burn End (CDT)	Burn Duration (hr:min)
1	4/28/2010	77	108	16:40	17:08	0:28
2	5/5/2010	512	716	11:38	12:20	0:42
3	5/5/2010	10	13	14:45	14:53	0:08
4	5/5/2010	1	2	15:11	15:16	0:05
5	5/5/2010	147	364	19:00	19:34	0:34
6	5/6/2010	1,760	3,285	10:43	12:51	2:08
7	5/6/2010	1,031	1,925	13:43	14:58	1:15
8	5/6/2010	1,723	2,413	14:10	15:44	1:34
9	5/6/2010	41	131	18:11	19:00	0:49
10	5/7/2010	371	519	8:52	9:50	0:58
11	5/7/2010	25	35	13:18	13:28	0:10
12	5/7/2010	113	158	15:05	15:40	0:35
13	5/7/2010	170	237	15:09	15:55	0:46
14	5/7/2010	1	2	16:55	17:02	0:07
15	5/7/2010	994	1,392	18:44	19:50	1:06
16	5/17/2010	1,851	2,591	11:30	12:56	1:26
17	5/17/2010	166	232	11:58	12:20	0:22
18	5/17/2010	136	190	13:15	14:32	1:17
19	5/17/2010	0	0	14:09	14:28	0:19
20	5/17/2010	0	0	15:45	16:00	0:15
21	5/17/2010	297	416	17:01	17:10	0:09
22	5/17/2010	210	293	17:51	18:43	0:52
23	5/18/2010	235	329	9:53	10:33	0:40

Burn No.	Date	Approximate Burn Volume Minimum (bbl)	Approximate Burn Volume Maximum (bbl)	Burn Start (CDT)	Burn End (CDT)	Burn Duration (hr:min)
24	5/18/2010	368	515	10:54	12:07	1:13
25	5/18/2010	51	72	17:04	17:41	0:37
26	5/18/2010	0	0	17:54	18:24	0:30
27	5/19/2010	303	425	11:30	14:00	N/A
28	5/19/2010	11,700	16,380	12:30	15:00	N/A
29	5/19/2010	3,800	5,319	13:30	16:00	N/A
30	5/19/2010	769	1,076	14:30	17:00	N/A
31	5/19/2010	1,423	1,992	15:30	18:00	N/A
32	5/19/2010	4,809	6,733	16:30	19:00	N/A
33	5/20/2010	2,940	4,116	11:41	13:33	1:52
34	5/20/2010	678	950	12:56	14:02	1:06
35	5/20/2010	864	1,210	14:45	15:51	1:06
36	5/20/2010	0	0	16:25	17:43	1:18
37	5/20/2010	4,783	6,696	16:43	17:01	0:18
38	5/20/2010	1	2	17:50	18:09	0:19
39	5/20/2010	179	251	18:33	18:55	0:22
40	5/23/2010	160	224	13:05	13:42	0:37
41	5/23/2010	293	410	15:27	15:45	0:18
42	5/23/2010	34	84	16:23	16:50	0:27
43	5/23/2010	139	195	16:57	17:30	0:33
44	5/23/2010	125	176	18:04	19:09	1:05
45	5/23/2010	10	14	18:24	18:38	0:14
46	5/23/2010	2	3	19:10	19:20	0:10
47	5/23/2010	8	11	19:30	19:48	0:18
48	5/24/2010	172	240	8:24	8:55	0:31
49	5/24/2010	75	105	9:35	9:58	0:23
50	5/24/2010	382	534	9:49	11:27	1:38
51	5/24/2010	179	250	10:14	11:25	1:11
52	5/24/2010	280	392	11:14	12:03	0:49
53	5/24/2010	76	106	12:17	13:23	1:06
54	5/24/2010	7	10	12:38	13:43	1:05
55	5/24/2010	458	641	12:58	15:04	2:06
56	5/24/2010	132	185	14:47	15:17	0:30
57	5/24/2010	40	56	15:30	16:10	0:40
58	5/24/2010	19	26	15:51	16:35	0:44
59	5/24/2010	0	0	16:24	16:35	0:11
60	5/24/2010	77	108	17:35	18:00	0:25
61	5/24/2010	153	214	18:45	19:29	0:44
62	5/25/2010	49	68	13:08	13:51	0:43
63	5/25/2010	73	103	14:34	15:11	0:37
64	5/25/2010	0	0	15:30	15:51	0:21
65	5/25/2010	0	0	16:06	16:14	0:08
66	5/25/2010	180	253	16:25	17:25	1:00
67	5/25/2010	0	0	17:22	17:31	0:09
68	5/26/2010	20	28	12:15	12:46	0:31

Burn No.	Date	Approximate Burn Volume Minimum (bbl)	Approximate Burn Volume Maximum (bbl)	Burn Start (CDT)	Burn End (CDT)	Burn Duration (hr:min)
69	5/26/2010	117	163	13:30	14:14	0:44
70	5/26/2010	0	0	16:33	17:25	0:52
71	5/26/2010	75	105	17:50	18:06	0:16
72	5/26/2010	24	33	18:36	18:56	0:20
73	5/26/2010	14	20	19:17	19:25	0:08
74	5/26/2010	114	160	19:40	20:00	0:20
75	5/27/2010	57	80	10:42	11:11	0:29
76	5/27/2010	55	77	13:15	13:33	0:18
77	5/27/2010	217	304	13:20	14:25	1:05
78	5/27/2010	177	248	14:34	15:40	1:06
79	5/27/2010	11	15	14:46	15:07	0:21
80	5/27/2010	10	14	15:17	15:40	0:23
81	5/27/2010	3	4	15:38	16:18	0:40
82	5/27/2010	10	13	16:07	16:28	0:21
83	5/27/2010	27	38	16:33	17:00	0:27
84	5/27/2010	0	0	17:01	17:24	0:23
85	5/27/2010	11	16	17:42	18:04	0:22
86	5/27/2010	16	23	18:53	19:16	0:23
87	5/27/2010	0	0	18:56	19:35	0:39
88	5/28/2010	0	0	13:17	13:35	0:18
89	5/29/2010	0	0	10:51	11:37	0:46
90	5/29/2010	1	1	11:30	11:57	0:27
91	5/29/2010	81	113	11:59	12:16	0:17
92	5/29/2010	284	397	13:40	15:22	1:42
93	5/29/2010	0	0	16:35	16:52	0:17
94	5/29/2010	560	703	15:53	16:10	0:17
95	5/29/2010	95	133	16:24	16:44	0:20
96	5/30/2010	93	130	13:08	13:25	0:17
97	5/30/2010	68	95	14:16	15:18	1:02
98	5/30/2010	95	133	15:43	16:04	0:21
99	5/30/2010	257	360	15:48	16:39	0:51
100	5/30/2010	32	44	16:05	16:45	0:40
101	5/30/2010	207	290	17:30	18:03	0:33
102	5/30/2010	95	133	17:29	18:25	0:56
103	5/30/2010	116	162	18:03	18:38	0:35
104	5/30/2010	325	455	19:09	19:40	0:31
105	5/31/2010	186	261	8:09	9:27	1:18
106	5/31/2010	720	1,008	8:17	10:55	2:38
107	5/31/2010	0	0	8:29	8:56	0:27
108	5/31/2010	59	83	10:15	10:44	0:29
109	5/31/2010	187	262	10:47	12:00	1:13
110	5/31/2010	501	702	11:10	12:10	1:00
111	5/31/2010	9	12	13:03	13:33	0:30
112	5/31/2010	73	102	13:31	14:01	0:30
113	5/31/2010	97	136	14:00	14:18	0:18

Burn No.	Date	Approximate Burn Volume Minimum (bbl)	Approximate Burn Volume Maximum (bbl)	Burn Start (CDT)	Burn End (CDT)	Burn Duration (hr:min)
114	5/31/2010	424	594	14:04	14:59	0:55
115	5/31/2010	513	719	14:39	16:19	1:40
116	5/31/2010	144	202	14:43	15:06	0:23
117	5/31/2010	8,512	11,916	15:40	19:32	3:52
118	5/31/2010	101	142	16:44	17:01	0:17
119	5/31/2010	750	1050	17:15	17:50	0:35
120	5/31/2010	254	356	18:17	19:54	1:37
121	5/31/2010	1,248	1,748	18:30	19:36	1:06
122	6/1/2010	3,849	5,389	10:45	12:08	1:23
123	6/1/2010	138	193	12:21	13:17	0:56
124	6/1/2010	2,451	3,431	13:45	15:15	1:30
125	6/1/2010	132	185	14:17	15:08	0:51
126	6/2/2010	571	800	11:55	12:05	0:10
127	6/7/2010	231	323	13:38	14:11	0:33
128	6/7/2010	66	92	13:47	15:03	1:16
129	6/7/2010	18	26	15:08	15:42	0:34
130	6/7/2010	157	220	16:22	17:22	1:00
131	6/7/2010	36	51	17:21	18:05	0:44
132	6/7/2010	61	85	17:55	18:30	0:35
133	6/7/2010	180	252	18:50	19:06	0:16
134	6/8/2010	45	63	10:36	11:06	0:30
135	6/8/2010	109	153	10:44	11:26	0:42
136	6/8/2010	65	92	11:26	12:15	0:49
137	6/8/2010	127	178	12:34	13:24	0:50
138	6/8/2010	3	4	12:34	12:49	0:15
139	6/8/2010	1,621	2,270	12:46	19:25	6:39
140	6/8/2010	367	513	13:00	15:48	2:48
141	6/8/2010	469	656	13:11	14:40	1:29
142	6/8/2010	322	451	13:26	17:28	4:02
143	6/8/2010	70	98	15:02	15:37	0:35
144	6/8/2010	604	846	15:25	16:15	0:50
145	6/8/2010	503	704	15:48	16:28	0:40
146	6/8/2010	90	126	17:05	18:03	0:58
147	6/8/2010	65	91	17:14	17:59	0:45
148	6/8/2010	84	118	17:28	18:05	0:37
149	6/9/2010	75	106	9:57	10:19	0:22
150	6/9/2010	1,156	1,618	10:14	12:22	2:08
151	6/9/2010	119	167	12:37	14:06	1:29
152	6/9/2010	123	173	12:46	13:15	0:29
153	6/9/2010	29	41	13:02	13:41	0:39
154	6/9/2010	60	85	13:27	13:56	0:29
155	6/9/2010	266	372	13:31	13:37	0:06
156	6/9/2010	52	73	14:00	14:47	0:47
157	6/9/2010	99	139	14:09	15:07	0:58
158	6/9/2010	116	162	14:16	14:43	0:27

Burn No.	Date	Approximate Burn Volume Minimum (bbl)	Approximate Burn Volume Maximum (bbl)	Burn Start (CDT)	Burn End (CDT)	Burn Duration (hr:min)
159	6/9/2010	343	480	14:40	16:34	1:54
160	6/9/2010	103	144	15:11	15:49	0:38
161	6/9/2010	64	89	15:25	15:45	0:20
162	6/9/2010	106	148	16:32	17:04	0:32
163	6/9/2010	68	95	17:00	18:10	1:10
164	6/9/2010	66	93	17:18	17:49	0:31
165	6/9/2010	93	131	17:41	18:26	0:45
166	6/10/2010	300	400	15:45	16:04	0:19
167	6/12/2010	2	3	10:22	10:32	0:10
168	6/12/2010	6	8	10:35	10:50	0:15
169	6/12/2010	218	305	11:32	13:22	1:50
170	6/12/2010	32	45	12:38	13:09	0:31
171	6/12/2010	909	1,272	13:20	14:38	1:18
172	6/12/2010	255	357	13:46	14:30	0:44
173	6/12/2010	14	20	14:00	14:16	0:16
174	6/12/2010	19	27	14:48	15:19	0:31
175	6/12/2010	33	46	15:00	15:31	0:31
176	6/12/2010	4,597	6,436	17:03	20:15	3:12
177	6/12/2010	85	120	17:28	17:52	0:24
178	6/12/2010	19	26	17:46	18:40	0:54
179	6/12/2010	31	44	18:08	18:16	0:08
180	6/12/2010	55	77	17:46	18:40	0:54
181	6/12/2010	5	7	18:03	18:16	0:13
182	6/13/2010	4,774	6,683	9:05	20:26	11:21
183	6/13/2010	15	21	9:35	9:49	0:14
184	6/13/2010	888	1,244	10:08	12:46	2:38
185	6/13/2010	2,283	3,196	10:14	17:34	7:20
186	6/13/2010	4,692	6,568	11:00	17:15	6:15
187	6/13/2010	171	240	11:35	12:06	0:31
188	6/13/2010	26	36	11:42	12:08	0:26
189	6/13/2010	64	89	13:45	14:29	0:44
190	6/13/2010	360	504	14:41	16:28	1:47
191	6/13/2010	35	49	14:15	15:11	0:56
192	6/13/2010	120	168	15:27	16:22	0:55
193	6/13/2010	342	479	16:41	20:15	3:34
194	6/13/2010	32	45	17:07	17:31	0:24
195	6/13/2010	21	30	18:25	18:41	0:16
196	6/14/2010	88	123	10:35	11:36	1:01
197	6/14/2010	61	86	10:38	12:14	1:36
198	6/14/2010	20	27	11:23	12:06	0:43
199	6/14/2010	73	102	11:24	12:06	0:42
200	6/14/2010	11	16	12:06	12:27	0:21
201	6/14/2010	264	370	12:09	13:30	1:21
202	6/14/2010	92	129	12:29	12:56	0:27
203	6/14/2010	106	148	12:51	15:27	2:36

Burn No.	Date	Approximate Burn Volume Minimum (bbl)	Approximate Burn Volume Maximum (bbl)	Burn Start (CDT)	Burn End (CDT)	Burn Duration (hr:min)
204	6/14/2010	1,133	1,586	13:14	14:18	1:04
205	6/14/2010	20	29	14:19	14:50	0:31
206	6/14/2010	19	27	15:39	15:58	0:19
207	6/14/2010	3	5	15:41	16:15	0:34
208	6/14/2010	186	261	16:02	16:50	0:48
209	6/14/2010	1	1	17:05	17:20	0:15
210	6/14/2010	1,041	1,457	17:05	19:15	2:10
211	6/14/2010	387	542	17:31	20:18	2:47
212	6/14/2010	54	75	18:06	18:22	0:16
213	6/14/2010	20	27	18:13	18:32	0:19
214	6/15/2010	344	482	9:05	12:08	3:03
215	6/15/2010	111	156	13:43	14:53	1:10
216	6/15/2010	169	236	14:03	15:56	1:53
217	6/15/2010	43	60	14:11	14:30	0:19
218	6/15/2010	8	11	15:04	15:56	0:52
219	6/15/2010	143	200	15:31	16:50	1:19
220	6/15/2010	1	1	16:19	16:39	0:20
221	6/15/2010	12	17	16:24	17:13	0:49
222	6/15/2010	1	2	16:43	17:09	0:26
223	6/15/2010	14	19	17:22	17:38	0:16
224	6/16/2010	5,956	8,339	9:19	21:07	11:48
225	6/16/2010	5	7	10:17	10:34	0:17
226	6/16/2010	214	299	11:00	11:31	0:31
227	6/16/2010	705	986	11:57	15:54	3:57
228	6/16/2010	2,508	3,512	12:13	15:53	3:40
229	6/16/2010	1,014	1,420	13:09	23:29	10:20
230	6/16/2010	81	113	13:17	14:02	0:45
231	6/16/2010	292	409	13:33	17:52	4:19
232	6/16/2010	5,968	8,355	15:00	23:30	8:30
233	6/16/2010	33	46	17:29	17:48	0:19
234	6/17/2010	2,237	3,132	11:30	18:24	6:54
235	6/17/2010	1,251	1,751	13:28	15:52	2:24
236	6/17/2010	7,492	10,488	16:43	21:12	4:29
237	6/17/2010	59	83	16:46	17:06	0:20
238	6/17/2010	44	62	18:02	18:24	0:22
239	6/18/2010	121	170	8:47	9:34	0:47
240	6/18/2010	69	96	9:40	10:12	0:32
241	6/18/2010	147	205	10:44	11:17	0:33
242	6/18/2010	148	207	12:59	13:57	0:58
243	6/18/2010	420	588	13:14	14:16	1:02
244	6/18/2010	49	69	13:24	13:44	0:20
245	6/18/2010	820	1,148	13:30	14:20	0:50
246	6/18/2010	4,333	6,066	15:07	20:43	5:36
247	6/18/2010	255	357	15:07	16:32	1:25
248	6/18/2010	842	1,178	15:11	16:52	1:41

Burn No.	Date	Approximate Burn Volume Minimum (bbl)	Approximate Burn Volume Maximum (bbl)	Burn Start (CDT)	Burn End (CDT)	Burn Duration (hr:min)
249	6/18/2010	16,097	22,536	15:18	18:01	2:43
250	6/18/2010	21,932	30,705	15:30	18:00	2:30
251	6/18/2010	127	178	16:56	17:27	0:31
252	6/18/2010	1,705	2,388	17:05	18:23	1:18
253	6/18/2010	2,133	2,986	18:03	21:37	3:34
254	6/18/2010	422	591	18:13	18:54	0:41
255	6/19/2010	360	504	13:30	14:02	0:32
256	6/19/2010	83	116	13:42	14:08	0:26
257	6/19/2010	1,226	1,716	15:10	16:57	1:47
258	6/19/2010	39	55	15:30	15:54	0:24
259	6/19/2010	36	50	15:32	15:38	0:06
260	6/19/2010	204	286	16:57	17:25	0:28
261	6/20/2010	37	52	11:51	12:10	0:19
262	6/20/2010	198	278	13:02	13:44	0:42
263	6/20/2010	24	33	13:42	13:50	0:08
264	6/20/2010	75	105	14:25	14:40	0:15
265	6/20/2010	18	25	15:11	15:20	0:09
266	6/20/2010	74	104	15:26	15:57	0:31
267	6/20/2010	85	120	16:31	16:45	0:14
268	6/21/2010	2,975	4,165	7:52	12:52	5:00
269	6/21/2010	1,350	1,889	7:59	12:37	4:38
270	6/21/2010	1,139	1,595	8:03	9:17	1:14
271	6/21/2010	1,550	2,170	9:02	12:35	3:33
272	6/21/2010	1,237	1,731	9:50	14:31	4:41
273	6/21/2010	473	662	10:05	11:05	1:00
274	6/21/2010	1,141	1,597	10:17	11:54	1:37
275	6/21/2010	468	655	11:58	12:45	0:47
276	6/21/2010	292	409	13:04	13:50	0:46
277	6/21/2010	160	224	13:30	14:16	0:46
278	6/21/2010	51	71	13:33	13:44	0:11
279	6/21/2010	54	76	13:40	14:39	0:59
280	6/21/2010	0	0	14:25	14:35	0:10
281	6/21/2010	41	57	14:07	14:33	0:26
282	6/21/2010	395	553	14:48	15:07	0:19
283	6/21/2010	774	1,083	15:07	16:27	1:20
284	6/21/2010	13	18	15:30	15:44	0:14
285	6/21/2010	744	1,041	15:36	16:36	1:00
286	6/21/2010	625	876	15:47	16:16	0:29
287	6/21/2010	638	893	16:36	19:06	2:30
288	6/21/2010	78	110	16:59	18:04	1:05
289	7/8/2010	0	0			
290	7/9/2010	346	484	10:20	12:12	1:52
291	7/9/2010	2,067	2,894	11:16	12:30	1:14
292	7/9/2010	361	506	12:04	13:31	1:27
293	7/9/2010	413	579	13:34	14:33	0:59

Burn No.	Date	Approximate Burn Volume Minimum (bbl)	Approximate Burn Volume Maximum (bbl)	Burn Start (CDT)	Burn End (CDT)	Burn Duration (hr:min)
294	7/9/2010	357	500	14:24	15:20	0:56
295	7/9/2010	157	220	14:31	15:13	0:42
296	7/9/2010	58	81	14:44	15:10	0:26
297	7/9/2010	294	411	15:34	16:20	0:46
298	7/9/2010	25	34	16:01	16:12	0:11
299	7/9/2010	928	1,299	16:55	17:55	1:00
300	7/9/2010	277	387	16:58	17:09	0:11
301	7/9/2010	25	36	17:53	18:29	0:36
302	7/9/2010	422	591	17:52	18:20	0:28
303	7/9/2010	50	71	18:03	18:47	0:44
304	7/9/2010	1,150	1,611	18:34	19:25	0:51
305	7/10/2010	140	197	8:26	9:00	0:34
306	7/10/2010	3,794	5,312	8:30	10:21	1:51
307	7/10/2010	4	6	9:05	10:15	1:10
308	7/10/2010	940	1,316	9:12	10:22	1:10
309	7/10/2010	311	436	9:56	11:49	1:53
310	7/10/2010	61	86	10:31	11:04	0:33
311	7/10/2010	2,646	3,705	11:39	14:52	3:13
312	7/10/2010	176	246	12:08	12:27	0:19
313	7/10/2010	76	106	12:48	13:02	0:14
314	7/10/2010	59	83	13:14	13:25	0:11
315	7/11/2010	46	65	9:05	10:22	1:17
316	7/11/2010	578	810	10:29	11:34	1:05
317	7/11/2010	61	85	10:50	10:54	0:04
318	7/11/2010	72	101	10:30	11:03	0:33
319	7/11/2010	660	924	11:28	12:38	1:10
320	7/11/2010	0	0	12:06	12:11	0:05
321	7/11/2010	1,136	1,590	12:26	13:36	1:10
322	7/11/2010	550	771	12:31	13:27	0:56
323	7/11/2010	50	70	13:02	13:16	0:14
324	7/11/2010	66	92	13:57	14:17	0:20
325	7/11/2010	81	114	13:49	14:41	0:52
326	7/11/2010	772	1,081	14:15	14:18	0:03
327	7/11/2010	50	70	14:36	15:25	0:49
328	7/11/2010	242	339	16:15	17:00	0:45
329	7/11/2010	72	100	16:32	16:51	0:19
330	7/13/2010	47	65	11:47	11:57	0:10
331	7/13/2010	45	64	12:16	13:09	0:53
332	7/13/2010	43	60	12:23	12:37	0:14
333	7/13/2010	2	2	12:34	12:40	0:06
334	7/13/2010	20	27	12:47	13:01	0:14
335	7/13/2010	3	4	13:08	13:13	0:05
336	7/13/2010	0	0	13:08	13:15	0:07
337	7/13/2010	20	28	13:20	13:36	0:16
338	7/13/2010	0	0	13:20	13:37	0:17

Burn No.	Date	Approximate Burn Volume Minimum (bbl)	Approximate Burn Volume Maximum (bbl)	Burn Start (CDT)	Burn End (CDT)	Burn Duration (hr:min)
339	7/13/2010	32	44	13:28	13:55	0:27
340	7/13/2010	160	224	13:50	14:05	0:15
341	7/13/2010	66	92	14:54	15:17	0:23
342	7/13/2010	2	3	14:16	14:40	0:24
343	7/13/2010	1	1	15:16	15:29	0:13
344	7/13/2010	0	0	15:59	16:07	0:08
345	7/13/2010	75	105	16:21	16:53	0:32
346	7/13/2010	27	38	16:31	17:17	0:46
347	7/13/2010	67	93	16:33	16:56	0:23
348	7/13/2010	105	147	16:50	17:22	0:32
349	7/13/2010	18	25	17:17	17:29	0:12
350	7/13/2010	0	0	18:19	18:46	0:27
351	7/13/2010	435	609	18:28	19:00	0:32
352	7/14/2010	2	3	9:30	9:45	0:15
353	7/14/2010	54	75	10:20	10:40	0:20
354	7/14/2010	14	20	11:04	11:11	0:07
355	7/14/2010	81	114	10:21	11:03	0:42
356	7/14/2010	89	124	13:16	14:07	0:51
357	7/14/2010	0	0	12:30	12:58	0:28
358	7/14/2010	7	10	13:46	14:05	0:19
359	7/14/2010	0	0	13:40	13:58	0:18
360	7/14/2010	43	60	14:24	14:52	0:28
361	7/14/2010	22	31	14:45	15:00	0:15
362	7/14/2010	103	144	14:55	15:13	0:18
363	7/14/2010	16	23	14:45	14:58	0:13
364	7/14/2010	12	17	14:29	14:39	0:10
365	7/14/2010	0	0	15:45	16:16	0:31
366	7/14/2010	20	28	17:07	17:34	0:27
367	7/14/2010	10	14	17:50	18:05	0:15
368	7/14/2010	48	67	18:00	18:18	0:18
369	7/14/2010	56	79	18:05	18:32	0:27
370	7/14/2010	42	59	19:12	19:50	0:38
371	7/14/2010	0	0	19:31	19:44	0:13
372	7/14/2010	10	13	19:31	19:46	0:15
373	7/14/2010	74	103	18:45	19:17	0:32
374	7/14/2010	18	25	19:24	19:38	0:14
375	7/14/2010	50	69	19:47	20:34	0:47
376	7/14/2010	77	107	19:58	20:10	0:12
377	7/14/2010	55	78	20:43	21:12	0:29
378	7/15/2010	19	26	13:25	13:50	0:25
379	7/15/2010	41	57	14:29	15:18	0:49
380	7/15/2010	0	0	15:07	15:25	0:18
381	7/15/2010	0	0	16:05	16:09	0:04
382	7/15/2010	27	37	16:45	17:26	0:41
383	7/15/2010	8	11	17:03	17:15	0:12

Burn No.	Date	Approximate Burn Volume Minimum (bbl)	Approximate Burn Volume Maximum (bbl)	Burn Start (CDT)	Burn End (CDT)	Burn Duration (hr:min)
384	7/15/2010	0	0	18:40	18:51	0:11
385	7/15/2010	37	52	19:23	20:03	0:40
386	7/15/2010	79	110	19:25	20:00	0:35
387	7/15/2010	83	117	19:39	20:42	1:03
388	7/15/2010	0	0	17:30	18:15	0:45
389	7/15/2010	0	0	16:14	16:18	0:04
390	7/16/2010	7	10	9:30	9:43	0:13
391	7/16/2010	473	662	9:12	10:15	1:03
392	7/16/2010	56	79	10:43	11:15	0:32
393	7/16/2010	32	44	10:44	11:05	0:21
394	7/16/2010	21	30	12:51	13:21	0:30
395	7/16/2010	11	16	13:51	14:00	0:09
396	7/16/2010	0	0	13:07	13:14	0:07
397	7/16/2010	11	15	14:00	14:12	0:12
398	7/16/2010	1	1	14:07	14:27	0:20
399	7/16/2010	16	23	14:33	14:50	0:17
400	7/16/2010	63	89	14:06	14:46	0:40
401	7/16/2010	0	0	14:50	15:05	0:15
402	7/16/2010	0	0	14:37	14:47	0:10
403	7/16/2010	82	115	14:37	15:10	0:33
404	7/16/2010	55	78	15:44	15:55	0:11
405	7/16/2010	0	0	15:54	17:10	1:16
406	7/16/2010	13	18	16:02	16:12	0:10
407	7/16/2010	8	12	17:10	17:23	0:13
408	7/16/2010	50	70	17:36	17:53	0:17
409	7/17/2010	0	0	16:00	16:25	0:25
410	7/19/2010	106	148	11:09	11:43	0:34
411	7/19/2010	0	0	14:15	14:28	0:13
	Total	219,986	309,457			

Individual burn volumes had been estimated by Mabile and Allen (2010) as a range (minimum to maximum) of oil burned in barrels (bbl). Cumulative daily burn volumes were calculated by summing the individual burns each day. The average burn volume was calculated using the mean of the minimum and maximum daily volume. The model input was the daily average volume burned, simulated to occur between the start of the first burn of the day and the end of the last burn of the day.

The SIMAP model input file uses metric tons (MT) of oil burned for the units, so the data was converted to MT. The daily values were converted assuming an oil density of 0.97 MT/m^3, which was the density of the surface oil sample "Slick A" measured by Stout (2015). Slick A was weathered oil but collected in an area near the wellhead where burning operations were performed.

Daily value in MT = (Daily value in bbl) * (0.158987 m^3/bbl) * (0.97 MT/m^3)

SIMAP defines the start and stop time of a burning response operation as the number of hours from the scenario start time (i.e., 10:30 am CDT on April 22, 2010). The range of times listed in Table A.2.1 was used to calculate the start and stop time of burning operations on each day. The daily volume burned was divided by the hours of burning operations that day to obtain a burn rate in MT/hr.

Mabile and Allen (2010) mapped the burn locations, as shown in Figure A.2.1, which was taken from that report. The burning information on ERMA included the BP_Provided_burns.shp file that defined the area of in situ burns as being within the longitude-latitude box in Table A.2.2. The rounded values (degrees) defined an area where surface oil was removed from the model, during the time window of the day's burning and up to the amount of oil floating at the time in the model, to simulate burning.

Table A.2.2. The longitude-latitude bounding box used to model in situ burning.

		Shape File (degrees)	Rounded Values Input to Model (degrees)
Longitude	minimum	-88.755	-89.0
Longitude	maximum	-88.182393	-88.0
Latitude	minimum	28.0453335	28.0
Latitude	maximum	28.9506334	29.0

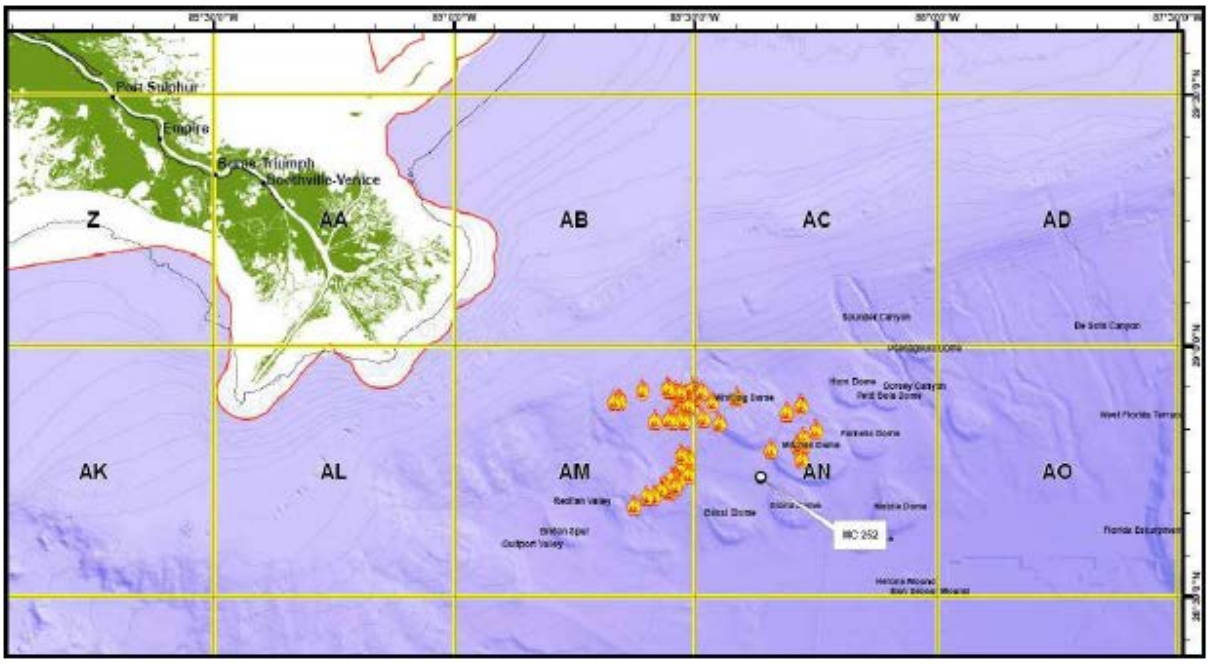

Appendix B – Burn Locations

Figure A.2.1 Locations of in-situ burns in 2010
Source: Mabile and Allen 2000

A.2.2 Aerial Dispersants

Aerial dispersant daily application data were obtained from the Environmental Response Management Application (ERMA 2013). The daily dispersant applications tracks were downloaded from ERMA in shapefile format and merged into a single shapefile. The file was converted from polyline tracks into polygon tracks using a buffer around each track so dispersant could be applied to an area of water surface. If multiple tracks existed for a single day they were merged together creating an area that encompassed all tracks with a single value for dispersant volume application equal to the sum of the individual track volumes for that day (Table A.2.3). The *.dbf file associated with the created shapefiles contained the date and dispersant amount applied (gallons). The *.dbf file containing the dispersant application data from 4/22/2010–7/19/2010 was opened in Excel to add the information required to input to SIMAP.

Table A.2.3. Daily surface dispersant application volumes.

Day	Date	Dispersant Amount Applied (gal)
Day 1	4/22/2010	1,800
Day 2	4/25/2010	11,604
Day 3	4/26/2010	14,486
Day 4	4/26/2010	27,078
Day 5	4/28/2010	42,143
Day 6	4/29/2010	41,098
Day 7	4/30/2010	4,900
Day 8	5/1/2010	11,653
Day 9	5/4/2010	34,273
Day 10	5/5/2010	49,645
Day 11	5/6/2010	28,770
Day 12	5/7/2010	7,270
Day 13	5/8/2010	41,690
Day 14	5/9/2010	55,932
Day 15	5/10/2010	56,220
Day 16	5/11/2010	7,940
Day 17	5/12/2010	39,710
Day 18	5/13/2010	41,620
Day 19	5/14/2010	44,031
Day 20	5/15/2010	14,208
Day 21	5/17/2010	6,591
Day 22	5/18/2010	209
Day 23	5/21/2010	28,892
Day 24	5/22/2010	50,246
Day 25	5/23/2010	18,104
Day 26	5/24/2010	638
Day 27	5/25/2010	200
Day 28	5/26/2010	229
Day 29	5/27/2010	200
Day 30	5/28/2010	10,259
Day 31	5/30/2010	15,131
Day 32	5/31/2010	11,676
Day 33	6/3/2010	1,900
Day 34	6/4/2010	125
Day 35	6/7/2010	3,998
Day 36	6/8/2010	5,505
Day 37	6/10/2010	4,506
Day 38	6/11/2010	14,305
Day 39	6/12/2010	6,996
Day 40	6/13/2010	35,212
Day 41	6/14/2010	10,706
Day 42	6/15/2010	2,608
Day 43	6/16/2010	13,380
Day 44	6/17/2010	12,123
Day 45	6/19/2010	2,604
Day 46	6/20/2010	15,403

Day	Date	Dispersant Amount Applied (gal)
Day 47	6/21/2010	10,355
Day 48	6/22/2010	2,008
Day 49	6/23/2010	5,099
Day 50	6/24/2010	21,088
Day 51	6/25/2010	4,633
Day 52	6/26/2010	23,022
Day 53	6/27/2010	6,623
Day 54	7/1/2010	17,852
Day 55	7/2/2010	12,737
Day 56	7/4/2010	3,000
Day 57	7/5/2010	803
Day 58	7/13/2010	999
Day 59	7/19/2010	200

The Dispersant Amount Applied (gal) was converted to Dispersant Amount Applied (bbl) using the following formula:

Dispersant Amount Applied (bbl) = Dispersant Amount Applied (gal) / 42

The SIMAP model uses metric tons (MT) as the units for dispersant application so the data was converted to MT assuming an oil density of 0.86 MT/m^3, which is the density for relatively fresh MC252 oil (the target of dispersant operations):

Dispersant Amount Applied (MT) =

Dispersant Amount Applied (BBLS) * (0.158987 m^3/bbl) * (0.86 MT/m^3)

To calculate the amount of oil dispersed from the dispersant amount applied, the following formula was used:

Amount of oil dispersed = DOR * (Dispersant Volume) * (Fraction of Oil Treated)

Where DOR is the dispersant-to-oil ratio (volume of oil treated per dispersant volume). The following formulas were used to create three versions of the DOR (based on assumptions in Lehr et al. 2010):

- 100% treated assuming target DOR of 20: DOR=20,
- 50% treated assuming target DOR of 20: DOR=10, and
- 25% treated assuming target DOR of 20: DOR=5.

The input to the model includes the start time and end time of a daily dispersant application (as the number of hours from the scenario start time of 4/22/2010 10:30 CDT). For each daily dispersant application, the start time was set to 7:30 and was carried out for 12 hours. This default time frame was chosen due to a lack of information on specific

dispersant application times. Each daily volume in MT was then divided by the 12 hours of dispersant application to give MT per hour.

The daily shapefile that was created with the day's polygon dispersant tracks was used to define the area where surface dispersant applications were modeled. The model dispersed oil into the water column (see Annex A of Appendix II in Volume II for the entrainment algorithm used for this process) during the daily time window for operations, if sufficient floating oil was present (see Section 2.7.2 of Appendix V). Figure A.2.2 shows the locations of the daily dispersant operations simulated.

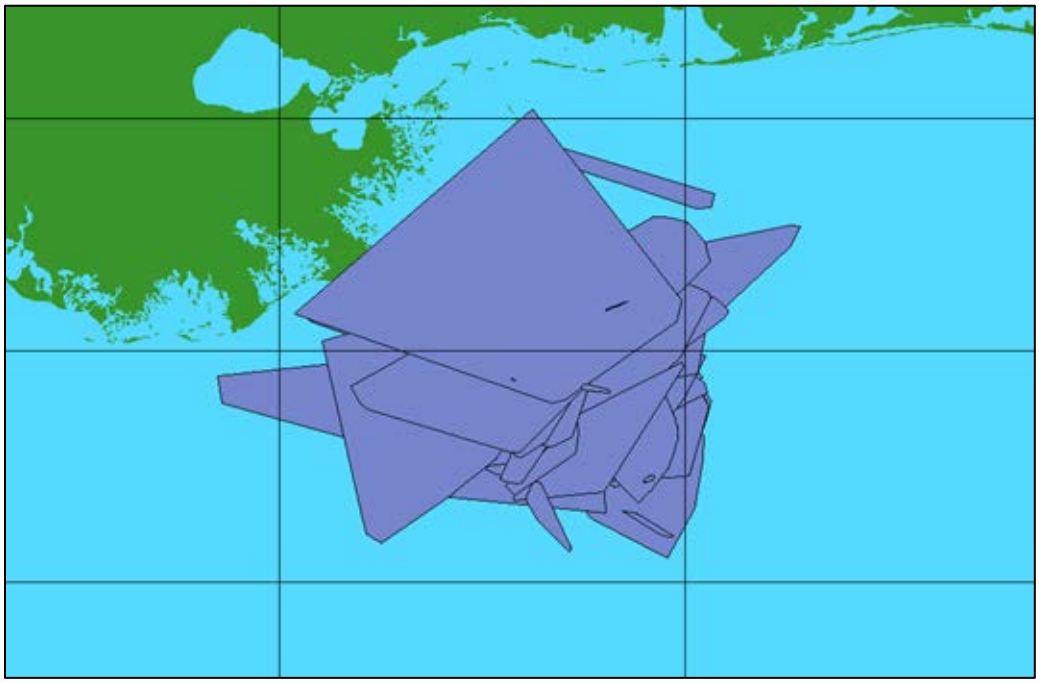

Figure A.2.2 Locations of the daily dispersant operations simulated in the model.

A.3. References

ERMA. 2013. Environmental Response Management Application. Aerial dispersant data; [data downloaded from: *Deepwater Horizon* MC 252 Incident/Response Operations/Dispersant Operations/Aerial Dispersant Applications]. (accessed 17 December 2013). Available at: https://www.erma.noaa.gov/dwh/erma.html

ERMA. 2014. Environmental Response Management Application. In-situ burning data; [data downloaded 28 January 2014 from: *Deepwater Horizon* MC 252 Incident/Response Operations/Burn; Locations/Cumulative *In Situ* Burns (BP Provided)]. (accessed 28 January 2014). Available at: https://www.erma.noaa.gov/dwh/erma.html.

Lehr B, Bristol S, Possolo A. (Oil Budget Calculator, OBC) 2010. *Deepwater Horizon* oil budget calculator: A report to the national incident command. The Federal Interagency Solutions Group, Oil Budget Calculator Science and Engineering Team. (Accessed on April 1, 2012). Available at: http://www.restorethegulf.gov/sites/default/files/documents/pdf/OilBudgetCalc_Full_HQ-Print_111110.pdf

Mabile N, Allen A. 2010. Controlled burns after action report, burns on May 28th–August 3, 2010, controlled burn group. Report prepared by Nere' Mabile & Al Allen, August 8, 2010, 28p. (accessed March 2011). Available at: http://gomex.erma.noaa.gov/erma.html#/x=88.34691&y=29.41717&z=7&layers=2301

NODC. 2015. World ocean atlas 2013, Version 2. (accessed 19 January 2015 in CSV format). Available at: https://www.nodc.noaa.gov/OC5/woa13/

Stout SA. 2015. Range in composition and weathering among floating Macondo oils during the *Deepwater Horizon* oil spill. NewFields Technical Report to the Trustees in support of the pDARP.

Annex B: Chemistry and Sensor-Based Observation Data

B.1. Observational Data

B.1.1 CTD and Sensor Data for Water Column Properties and Fluorescence

Conductivity-Temperature-Depth (CTD) data were collected on nearly every cruise conducted in response to the DWHOS to gain insight into the water column properties of the GOM, specifically focusing on the area around the release site. CTD and sensor (including fluorescence, dissolved oxygen, and transmissometer) data are summarized in the technical report by Grennan et al. (2015).

Figure B.1-1 shows vertical temperature profiles as measured by cruises in 2010 and from climatology. The temperature data is presented in grey scale, with the more common profiles appearing darker than the less common; the yearly climatology data envelope is presented as red lines. Temperature data are shown with mean climatological data +/- 3 standard deviations. Typical temperatures in the upper mixed layer were 20–31°C, in the thermocline below the mixed layer 7–20°C, and in deep water (>800 m) 4–7°C. Figure B.1-2 shows water density (as sigma theta) profiles for the Brooks McCall cruise data. The data is presented in grey scale, with the more common profiles appearing darker than the less common. Additional description of the data is in Grennan et al. (2015).

There were consistently observed fluorescence anomalies, as relative high values or "peaks", at depths between approximately 1,000–1,300 m. Figures B.1-3 to B.1-6 summarize the observed fluorescence anomalies. In Figure B.1-3, the blue line is an actual fluorescence profile with a significant increase in signal at depth. The green line is a separate fluorescence profile, representing a normal response at depth, in the absence of a fluorescence anomaly. The grey lines include all the 2010 fluorometer measurements for each specific sensor, emphasizing observed fluorescence anomalies between roughly 1,000–1,300 m. WET Labs ECO-CDOM measurements (left panel) are presented alongside Chelsea AquaTracka (AT) data (right). Regime 1 indicates the typical baseline condition and Regime 2 includes distinct fluorescence peaks at depth. Note that the calibrated units of the AquaTracka are different from that of the Colored Dissolved Organic Matter (CDOM) fluorometer. While the magnitude of the signal is lower than the CDOM in the sample designated by the blue line, the AquaTracka is more sensitive.

In Figures B.1-4 to B.1-6, the CDOM anomaly is plotted on a log-10 scale, due to the large range in reported values. Maximum anomalies occurred between roughly 1,100–1,200 m. The highest values were observed near the wellhead; the anomalies decreased as distance from the wellhead increased. Note that most samples collected between April 20 and July 15, 2010 were within 20 km of the wellhead. More distant sampling in the far-field occurred after July 15, 2010 (Figure B.1-6). Anomalies of high fluorescence values at depths

of 1,000–1,300 m were typically associated with elevated hydrocarbon concentrations in the water column, when water samples were collected concurrently with fluorescence measurements. These fluorescence peaks were observed mainly to the southwest of the wellhead and frequently out to approximately 150 km, with Payne and Driskell (2015a) reporting a small dissolved oxygen (DO) sag and fluorescence anomaly at the deep-plume depth to the southwest all the way out to 412 km. Although maximum fluorescence peaks were identified within a narrow range at depth, significantly elevated fluorescence values were noted throughout large portions of profiles. Peak fluorescence values at depth typically tapered to lower values in shallower waters. It was very common to observe significantly elevated fluorescence values up to 600 m and occasionally shallower.

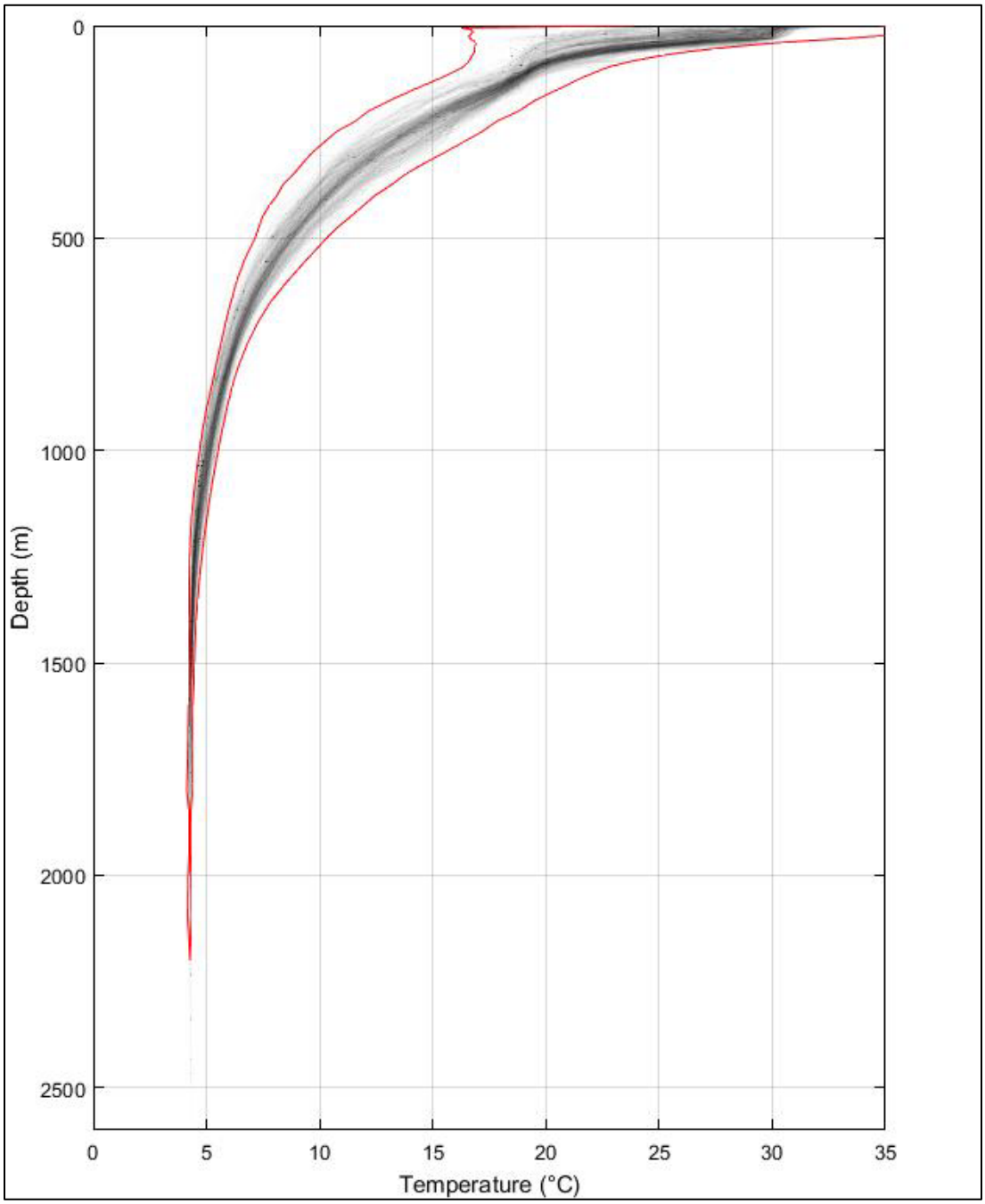

Figure B.1-1. Temperature data from cruises and climatology.

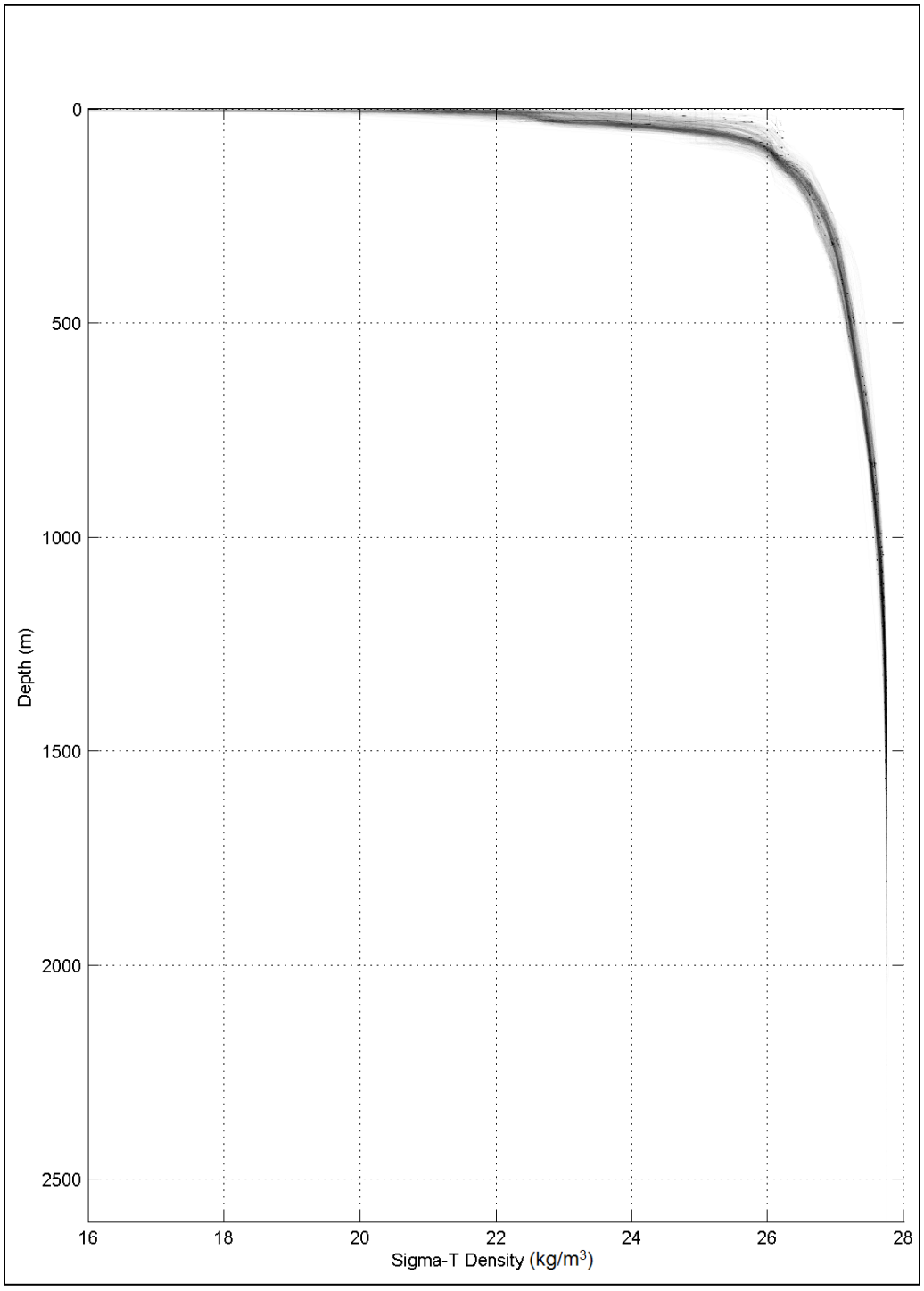

Figure B.1-2. Density profiles measured by cruises in 2010.

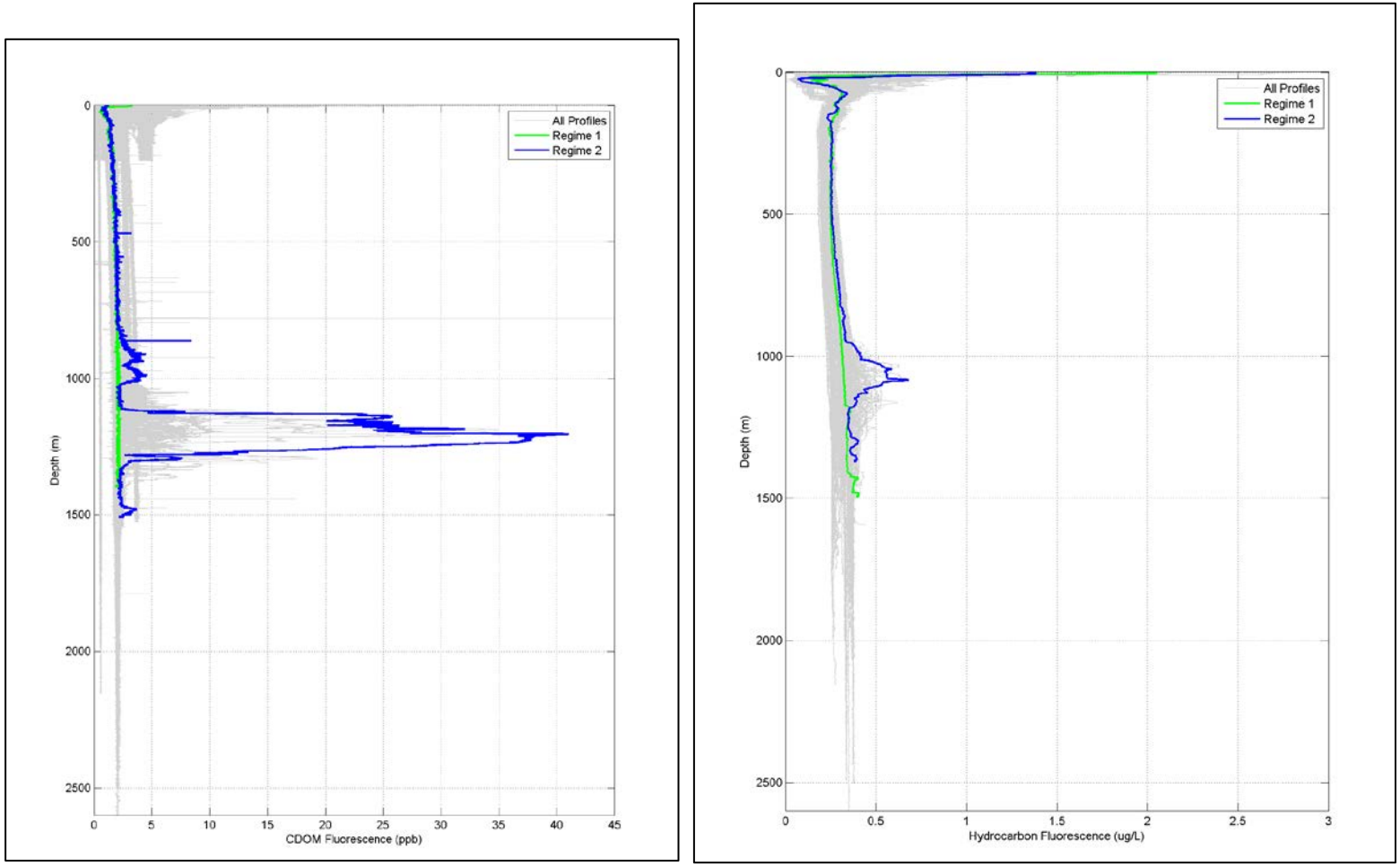

Figure B.1-3. Fluorometer data collected around the DWHOS site with two representative profiles highlighted in each.

(Blue and green lines.)

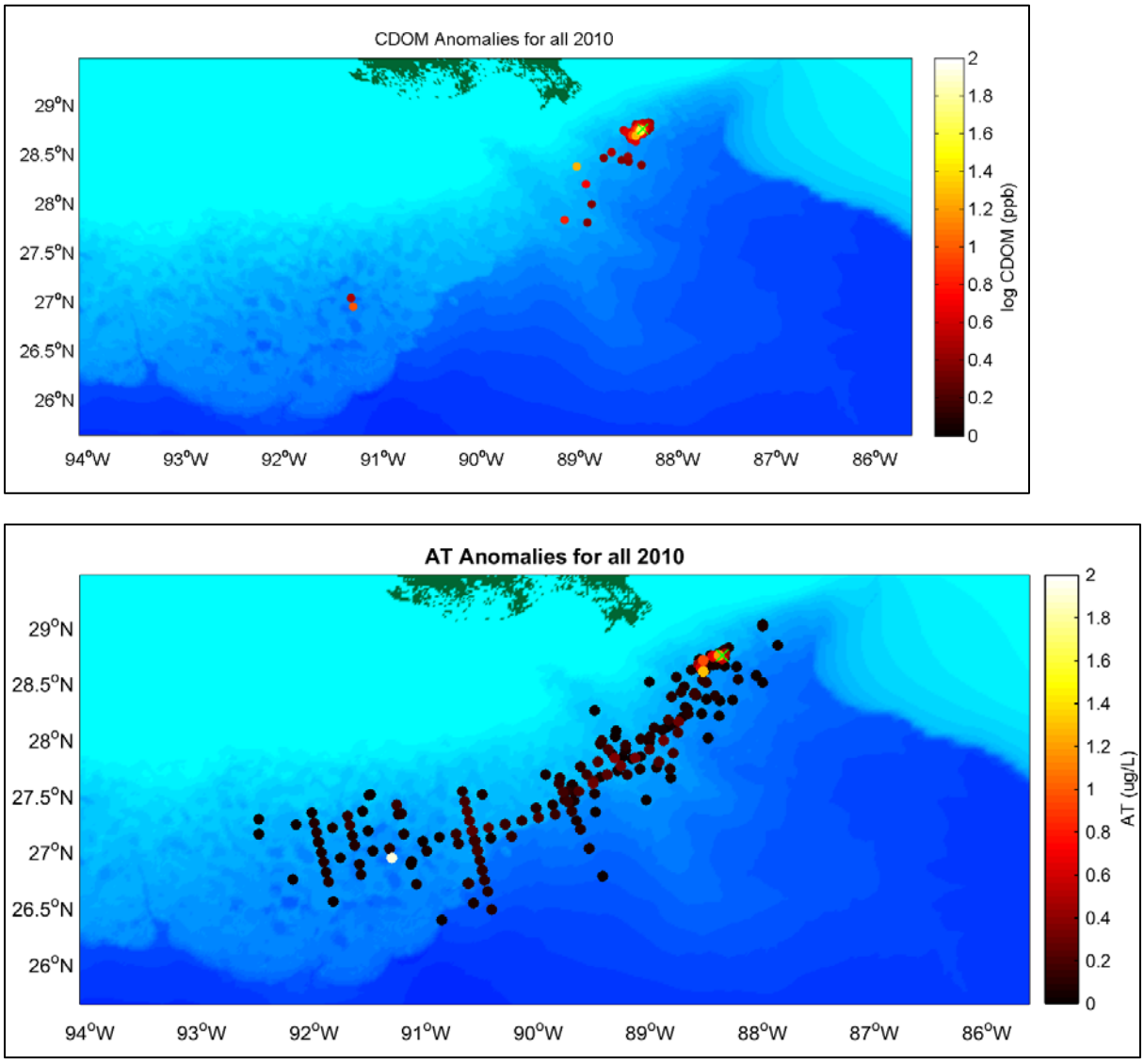

Figure B.1-4. The maximum CDOM (top) and AT (bottom) anomalies for each cast are displayed as single points in a map view.

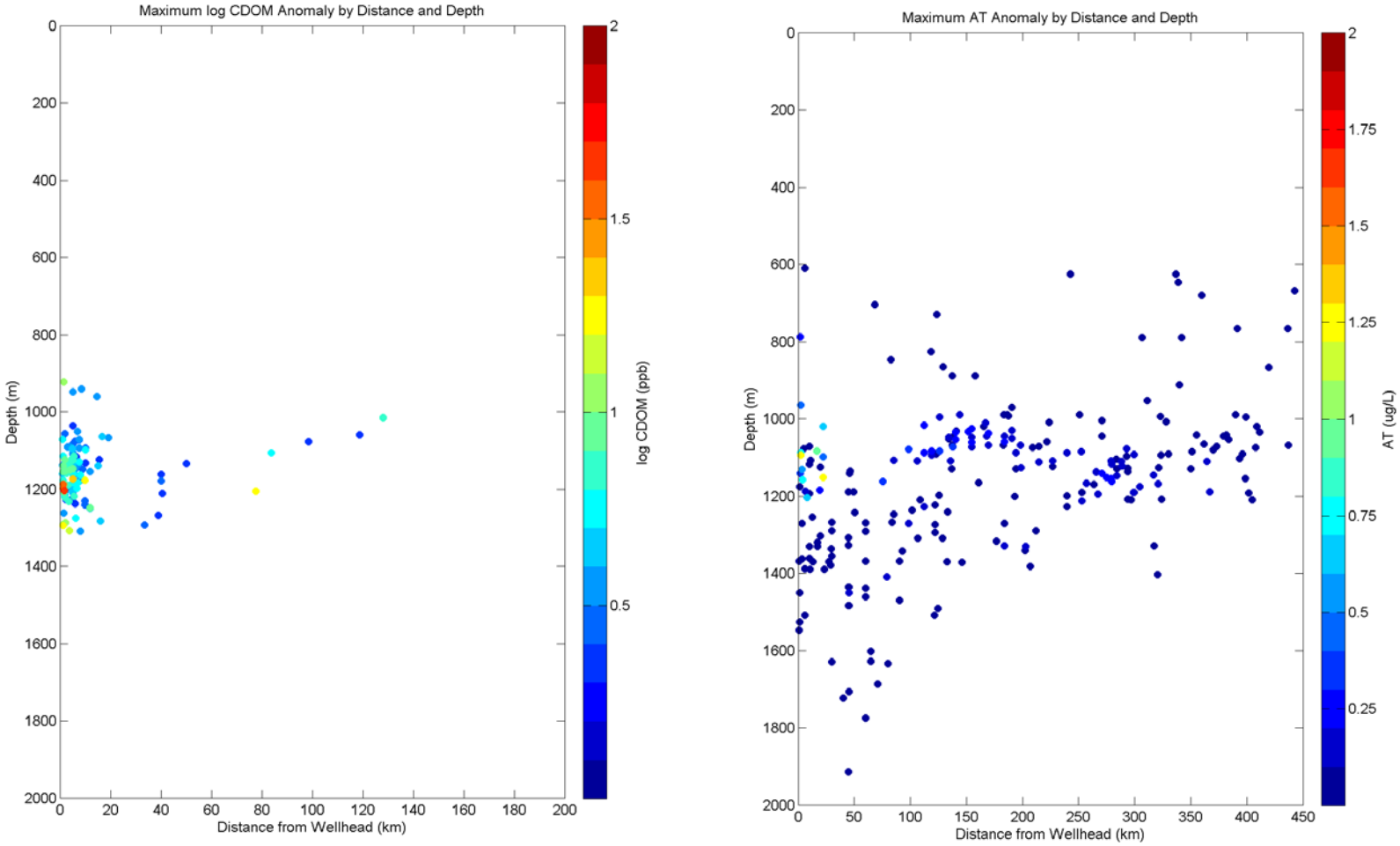

Figure B.1-5. The maximum CDOM anomalies (left) and AT anomalies (right) for each cast are displayed as single points in a depth profile view.

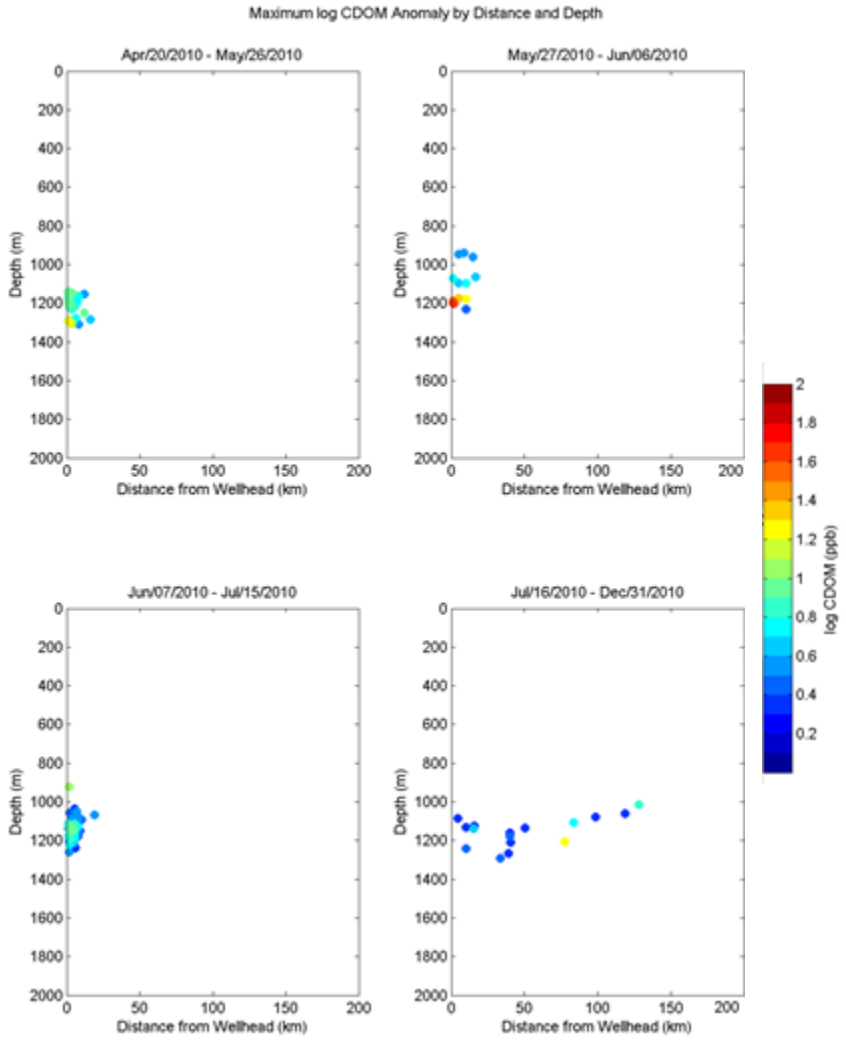

Figure B.1-6. Maximum CDOM Anomaly as a profile, broken out by date range.
Log (CDOM Anomaly) (ppb) and depth (m) are displayed over the distance to the wellhead (km).

There were consistent anomalous dissolved oxygen "sags" (i.e., relatively low values of dissolved oxygen in vertical profiles when compared to baseline profiles) at depths between approximately 700–1,300 m. Figures B.1-7 and B.1-8 summarize the dissolved oxygen anomalies. In Figure B.1-7, the maximum dissolved oxygen anomaly (ml/L) for each station is displayed on the map over the investigated depth range of 600–2,000 m. In Figure B.1-8, dissolved oxygen anomalies (ml/L) and corresponding depths (m) are displayed with distances to the wellhead (km). The maximum anomalies occurred between ~1,100 and 1,200 m deep. These anomalies first increased up to approximately 50–100 km from the wellhead and then decreased as distance from the wellhead increased to approximately 350 km. Anomalies calculated greater than one standard deviation below the profile-specific-baseline were identified out to greater than 500 km from the wellhead. As distance from the wellhead increased, dissolved oxygen anomalies increased and then decreased. As sags decreased in magnitude, they frequently became slightly broader, covering larger depth ranges. These observations are indicative of microbial degradation (i.e., hydrocarbon consumption) at depth followed by mixing with surrounding waters.

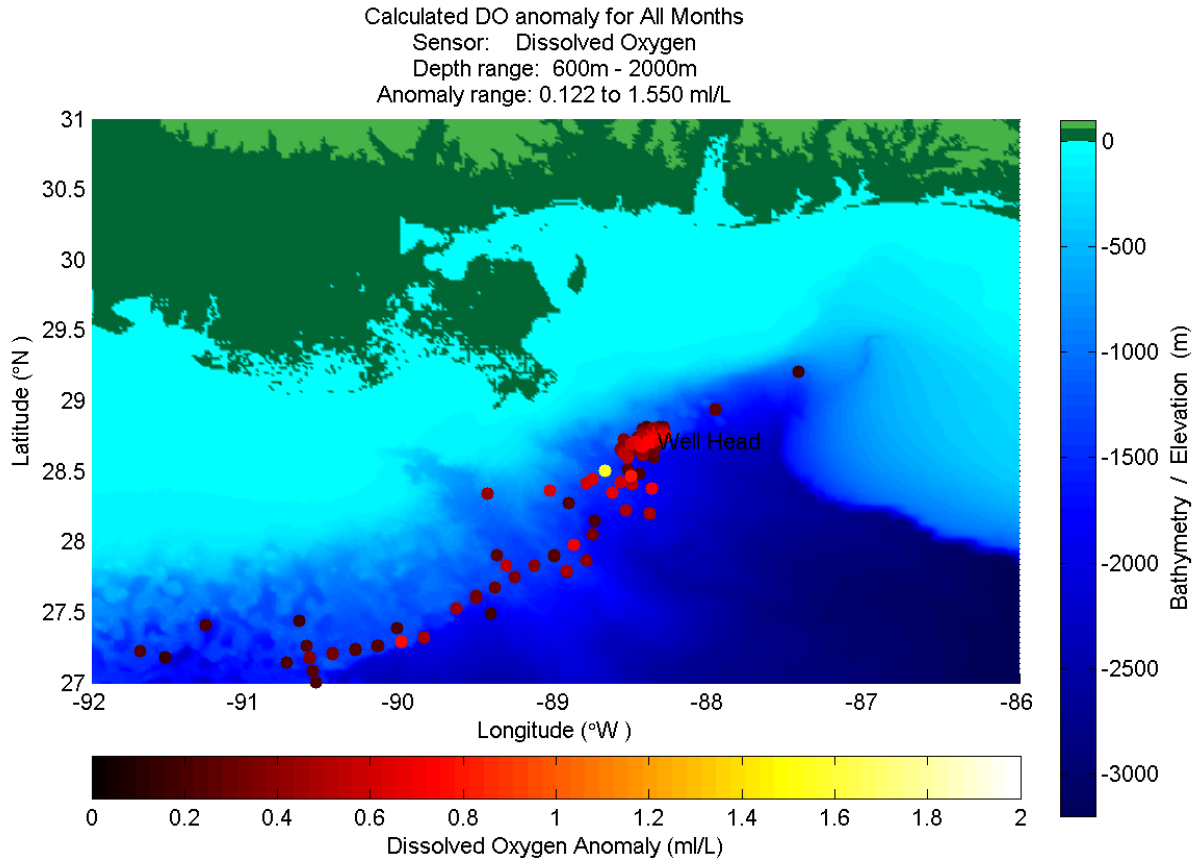

Figure B.1-7. Maximum dissolved oxygen anomaly (ml/L) from individual casts around the wellhead as a map view.

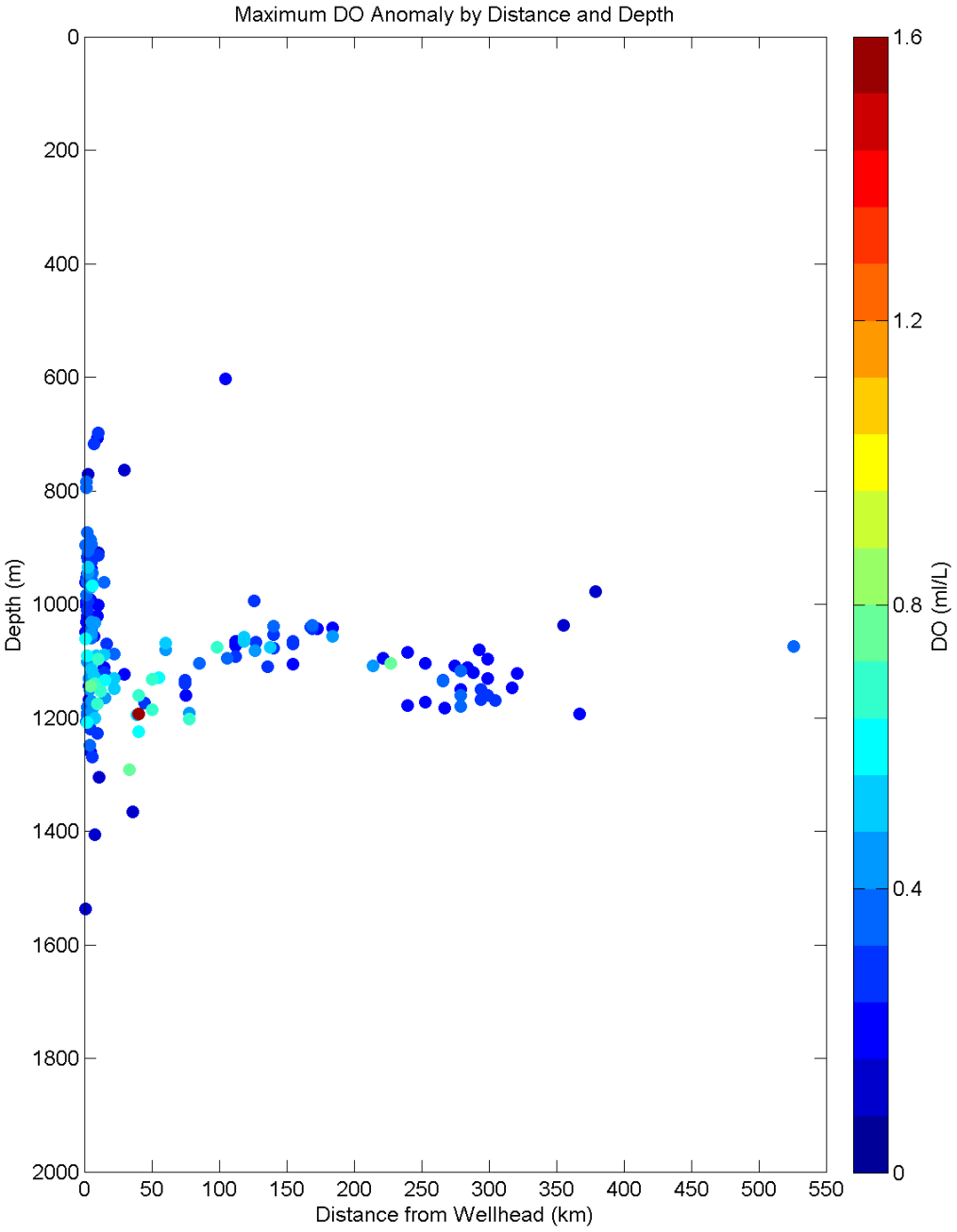

Figure B.1-8. Maximum dissolved oxygen anomaly from each individual cast as a profile view.

B.2. Chemistry Data

B.2.1 Chemistry Data Reported in the Literature

Chemistry data published in the peer-reviewed literature include oil hydrocarbons and chemical dispersant constituents that have been measured in samples collected from the subsurface intrusion plume, other depths in the water column, and from samples collected from the surface.

B.2.1.1 Hydrocarbon Chemistry

B.2.1.1.1 Source Oil Hydrocarbon Chemistry

Reddy et al. (2012) collected discrete source oil and gas release samples directly above the Macondo well on June 21, 2010 and analyzed oil and gas components in these samples. Analysis of selected compounds in Macondo well samples indicated that the released liquid from the wellhead included total C1–C5 compounds at a concentration of 0.24 g/g, of which methane was 0.15 g/g. All the other 140 hydrocarbon compounds measured totaled 0.24 g/g. Thus, together, characterized (i.e., where concentrations were measured) oil and gas compounds only accounted for 0.48 g/g or slightly less than half of the total mass of released fluid. This is consistent with analyses reported by Stout (2015a).

B.2.1.1.2 Hydrocarbon Chemistry in the Water Column

Oil-related hydrocarbon compounds were detected in the water column in the area surrounding the wellhead, especially in the intrusion-layer deep plume below 1,000 m. Observations in published literature include: May 9 –16, 2010, PAHs were detected up to 13km southwest of the wellhead by Diercks et al. (2010); May 25–June 2, 2010, BTEX and other volatiles were found in the DWHOS hydrocarbon plume, also supported by CDOM (Hazen et al., 2010); June 11–21, 2010, C_1–C_4 hydrocarbon gases were detected at depths of 800–1,200 m (Valentine et al. 2010, 2012); June 19–28, 2010, vertical rosette profiling including grab samples and *in situ* mass spectrometry measurements revealed elevated hydrocarbons between 1,100–1,200 m and lower concentrations of hydrocarbons between 50–500 m (Camilli et al. 2010).

Diercks et al. (2010) reported observations of concentrations of PAHs in subsurface waters near the DHW oil spill site. Profiles of *in situ* CDOM fluorescence and beam attenuation "indicating the presence of light-scattering dispersed oil droplets" during May 9–16, 2010 had distinct peaks at depths greater than 1,000 m. The highest intensities were close to the wellhead and the intensities decreased with increasing distance from the wellhead. Their GC and MS analyses of water samples collected at depths at which fluorescence and beam attenuation showed anomalies confirmed the presence of PAHs at concentrations up to 189 µg/L in discrete depth layers between 1,000 and 1,400 m southwest of the wellhead site

and extending at least as far as 13 km. Diercks et al. (2010) noted that the PAHs in the deep plume were enriched in naphthalenes, as compared to surface samples where 3-ring PAHs were relatively enriched, a pattern consistent with water partitioning of more water soluble PAH compounds during transport to the surface.

Hazen et al. (2010) collected and analyzed 17 deep-water samples from 10 locations during May 25–June 2. They detected a deep-sea oil plume from 1,099 m–1,219 m at distances up to 10 km from the wellhead. In their samples, extractable hydrocarbons (e.g., n-C18) ranged from non-detectable in non-plume samples to 9.21 µg/L in the plume and volatile aromatic hydrocarbon concentrations were significantly higher in the plume (mean 139 µg/L) than in the non-plume samples.

Camilli et al. (2010) performed a subsurface sampling effort during June 19–28, 2010 using *in situ* mass spectrometry and a rosette sampler, including three Sentry surveys conducted during June 23–27 at depths exceeding 1,000 m. Based on mass spectra and aromatic fluorometer data, the strongest hydrocarbon readings were encountered at ~1,100-m depth, west-southwest of the well site, and a weaker signal was detected northeast of the well site. The first long-range Sentry survey, conducted as an east-northeast radial projection from the well at three separate depth intervals (1,000, 1,150, and 1,300 m), did not encounter petroleum hydrocarbons significantly above background levels. Their mass spectrometric and fluorescence data taken ~ 4 km southwest of the leak source "confirmed a large plume at ~1,000- to 1,200-m depth, as well as a more diffuse plume existing between 50- and 500-m depth" (Camilli et al. 2010). Hydrocarbon mixture changes in composition between the deep plume and the near surface suggested (low molecular weight) aromatic hydrocarbons in greater abundance at depth. Elevated hydrocarbon concentrations identified with the mass spectrometer on Sentry dives 2 and 3, combined with the rosette profiling data, indicate a continuous, plume as high as 200 m and in certain areas more than 2 km wide, moving with a southwestern trend for a distance of more than 35 km from its source. Approximately 27 km from the source, petroleum hydrocarbon values rapidly diminished at this 1,120-m survey depth. Sentry executed track lines at differing depths until it identified a hydrocarbon maximum at 1,160 m. Sentry's Doppler Velocimetry recorded a southwest trending current at 1,100m depth, averaging 7.8 cm/s and at 247° from true north. The plume's horizontal stability and limited cross-sectional area increase as a function of distance from the well site suggest Lagrangian transport. The plume track is coincident with the water current direction at this depth, indicative of topographically-controlled transport (German et al. 1998) along an iso-depth contour line at the continental slope. Sentry's methane m/z signal at 35km from the source was only 53% less than that at 5.8km, suggesting that plume extended considerably beyond 35km survey bound. GC analysis on mono-aromatic hydrocarbons confirmed the presence of

BTEX (50 μg/L) within the plume at 16 km downrange from the wellhead, suggesting a mechanism for direct hydrocarbon transfer to the deep plume. However, DO anomaly estimates from the plume layer (±2μM or 0.8μM O_2/d) were significantly lower than reported by Du and Kessler (2012).

Reddy et al. (2012) collected discrete water samples within a southwest trending hydrocarbon-enriched plume (that defined by Camilli et al. 2010) at a depth of 1,100 m in June 19–28, 2010. The most abundant compounds larger than C5 were BTEX, which had a plume layer concentration as high as 78 μg/L. This is consistent with the NRDA cruise data (Horn et al. 2015a,b), in which, the pre-cut (i.e., before June 3) plume layer median BTEX concentration value was 92 μg/L (range 4.5–228 μg/L) and the post-cut plume layer median value 60 μg/L (range 4.9–176 μg/L). To quantify the relative abundance of compounds in the intrusion layer in comparison to the source release, Reddy et al. (2012) defined a benzene-normalized fractionation index (Fi) for a given compound (c_i) as,

$$F_{i,benzene} = \frac{\left(\frac{c_i}{c_{benzene}}\right)_{plume}}{\left(\frac{c_i}{c_{benzene}}\right)_{source\ liquid}} \quad (1)$$

An F_i value of unity indicates the compound completely channeled into the deep-water plume to the same extent as benzene, whereas an F_i value of zero indicates the compound was completely retained in ascending oil (particles) and likely reached the sea surface (or alternatively may have sunk to the seafloor bound to particulates). Benzene was nearly absent at depths less than 1,000 m in the water column (Camilli et al. 2010) and very little reached the sea surface (Ryerson et al. 2011), suggesting that benzene was predominantly retained in the deep water (intrusion layer) plume. F_i values for BTEX were benzene (1.00), toluene (0.505), o-xylene (0.378), ethylbenzene (0.369), and p/m-xylene (0.359). The compound mass fractions (M_i) of BTEX in source oil (μg/g) were benzene (2,300), toluene (6,540), o-xylene (1,880), ethylbenzene (950), and p/m-xylene (5,100). These values result in combined BTEX benzene-normalized fraction index as $\sum(Fi*Mi)/\sum Mi$ = 50.65%.

Comparison of wellhead liquid and plume water sample chemistry by Reddy et al. (2012) showed that the plume was preferentially enriched with water-soluble components, indicating that dissolution played a major role in the formation of the horizontal intrusion layer plume. There was only 1 out of 20 sampling locations (with unique x, y, and z-coordinates) where benzene was found with the co-presence of n-alkanes. Uniquely, their 1,201-m depth sample at 2.3 km SW of the wellhead contained significant levels of n-alkanes and other sparingly soluble compounds but was depleted in water-soluble compounds such as BTEX, suggesting that this sample might have been an “aged” rather than a “fresh” sample. Reddy et al. (2012) asserted that their results demonstrate that most of the C1–C3 hydrocarbons and a significant fraction of water-soluble aromatic compounds

were retained in the deep-water column, whereas relatively insoluble petroleum components were predominantly transported to the sea surface or deposited on the seafloor.

Ryerson et al. (2012) used airborne and subsurface chemical measurements from May–June 2010 to quantify initial hydrocarbon compositions and fate and transport processes. Note that all the oil and gas phase compounds from methane to n-C42 (as opposed to oil hydrocarbons ≥ C5) were included in their hydrocarbon mass balance analysis. About 25% of the leaking oil and gas mixture by mass was soluble, this would mainly be the gas fraction (assuming a mass ratio of [(gas+oil)/oil] = 1.31, the gas fraction is estimated as 0.31/[1.31] = ~23.7%) plus BTEX compounds (1.92%/[1.31] = 1.47%; Ryerson et al., 2012). This is based on a mass ratio of [(gas + oil)/oil] = 1.31 ± 0.08 measured at 1 atmosphere and 15.6 °C from the Woods Hole Oceanographic Institution (WHOI) sample of leaking fluid (Reddy et al 2011).

Among different environmental compartments, the evaporated mass was estimated by Ryerson et al. (2012) based on shipboard or aircraft measurements of atmospheric volatiles. As the bulk of gas phase compounds were dissolved, the evaporated fraction was mainly attributable to the volatile oil fraction. The oil slick mass at the surface was estimated by: Initial surface slick = [initial buoyant plume mass flux]–[dissolved mass flux + evaporated mass flux]. In this estimation, the initial buoyant plume mass flux was the *Slope* of Fig. S4 in Ryerson et al. (2012), estimated as follows: compound-specific atmospheric flux (kg/d) = *Slope* * compound-specific leaking fluid mass fraction (g/g), therefore the *Slope* has units of (kg leaking fluid/day). The evaporated mass flux was estimated as described above. Any compounds that are more soluble than 2-methylheptane were assumed to partition either in the intrusion layer plume as a dissolved fraction or in the atmosphere as an evaporated fraction, but not trapped in oil (including droplets and surface slick); so for these compounds, [dissolved] = 1–[evaporated], and a sum of dissolved (∑dissolved) provides an estimate of the fraction of compounds dissolved in plume water.

Deep sea plume intrusion layer mass was estimated by Ryerson et al. (2012) based on: (1) measurements of the compound mass fraction in leaking fluids (g/g_{total}), (2) compounds above n-C6 assumed completely insoluble, methane and ethane completely soluble, and estimated partial solubility for others, and (3) total environmental release based on total integrated DO anomaly as reported by Kessler et al. (2011), scaled up with oxidation stoichiometry of hydrocarbons, and summing all characterized compound mass fractions among the total mass. In their estimation, 14.415% (=0.15*0.9610) of the total insoluble hydrocarbon mass released from the wellhead (including those that were recovered) was trapped in the deep plume, where 0.15 = [($C_{10\text{-}32}$ n-alkane/Toluene in plume)/($C_{10\text{-}32}$ n-

alkane/Toluene in source)] was based on the samples reported in Hazen et al. (2010) for $C_{10\text{-}32}$ n-alkane vs toluene data, with a range from 0.05 to 0.25. The value 0.9610 is the fraction of toluene dissolved in seawater samples from the deep sea.

The mass balance analysis of *oil* released on June 10, 2010 was estimated by Ryerson et al. (2012) as: Total release = 1.007×10^7 kg/d /1.31 = 7.687×10^6 kg/d (59×10^3 bbl/d); Recovered oil = 2.1×10^6 kg/d (16×10^3 bbl/d); Total environmental release = 7.687×10^6 kg/d - 2.1×10^6 kg/d = 5.587×10^6 kg/d (43×10^3 bbl/d); Oil in the deep plume = 1.09×10^6 kg/d (which is, 1.09/5.587 = 19.5% *(1±0.3)); Oil evaporated = 0.46×10^6 kg/d (which is, 0.46/5.587 = 8.23% *(1±0.5)); and oil in surface slick = 1.0×10^6 kg/d (which is, 1.0/5.587 = 17.9% *(1±0.5)).

The Ryerson et al. (2012) mass balance analysis has a number of sources of errors and uncertainties, including: (1) the Kessler et al. (2011) estimated total DO Anomaly = 3.0 ~3.9 $\times 10^{10}$ mole O_2, and (2) the Hazen et al. (2010) ratio of alkanes to toluene in the plume phase versus the ratio of alkanes to toluene in the leaking fluid phase of 0.05 ~ 0.25, being a surrogate of the droplet to dissolved phase hydrocarbons–on the premise of the co-location of the dissolved versus droplet phases. Note that in the above analysis the tracked mass fraction would be equal to [19.5%*(1±0.3) + 8.23%*(1±0.5) + 17.9%*(1±0.5)] = 54.4% ± 18.9% of the release. In other words, nearly half of the oil mass (45.6%) was not accounted for in the analysis. The missing fraction of oil would presumably be biodegraded, suspended in the water column other than in the intrusion layer deep plume, and/or sunken to the seabed.

As an extension of Hazen et al.'s (2010) plume layer hydrocarbon data analysis, Spier et al. (2013) compiled hydrocarbon data from NOAA and BP datasets and conducted analyses to compare monitoring data with model prediction results. The NRDA data were collected during May 9–June 28, from 16 missions, and included over 150 chemical compounds ranging from C5–C40 hydrocarbons; the BP data were from Ocean Veritas cruises 1–3 (May 27–June 10) and Brooks McCall cruises 1–8 (May 9–June 10). After compiling and editing, 138,257 individual results remained, coming from 1,967 samples, each collected at a unique location, depth, and date.

Spier et al. (2013) investigated the spatial distribution of hydrocarbons using the following three zoning strategies: (1) Two separate regions broadly defined within a 45 km radius of the well head, i.e., Region 1, the rising cone and a 250 m deep subsurface plume layer centered at 1,175 m, which were predicted to contain the majority of the subsurface hydrocarbon mass, and Region 2 all other areas within a 45 km radius of the blowout; (2) Eight directions from the wellhead, namely N, NE, E, SE, S, SW, W, and NW; and (3) Layered vertical depth intervals, including every 100m, plus 50m and 25m binning in the top 100m.

Comparison of hydrocarbons in the two broad regions indicated that Region 1 did have the highest concentrations of hydrocarbons, and Region 2 also contained substantial proportions of hydrocarbons. Vertically, contour analysis indicated the presence of hydrocarbon plumes with mid-depths of 25, 265, 865, and 1,175 m. After Top Hat #4 became operational (i.e., post-cut on June 3), both the sample concentration and the percentage of detectable results decreased for the 865 and 1,175 m plumes.

The percentage of detectable measurements in each of Spier et al.'s (2013) identified plumes varied by direction from the wellhead, summarized as follows: (A) 0.5–50 m plume-carried in all directions from the blowout, probably due to influence from surface currents and wind; (B) 240–290 m plume had the highest concentrations and the highest frequency of detectable results primarily southeast and secondarily northwest; (C) 850–880 m plume had the highest sample concentration and the highest frequency of detectable results primarily to the northwest, but was lacking data in the southeast and northeast directions; and (D) 1050–1300 m plume-consistently had the highest concentration and the highest frequency of detectable results southwest and secondarily to the west of the blowout.

Spier et al. (2013) also noted that chemical composition changed with respect to depth (Figure B.2-1). Most water soluble compounds such as benzene, alkylated mono-aromatics, and C5–C8 alkanes were enriched in the deep plume. Less water soluble compounds were present both in the deep water plumes and in the upper water column; C13–C22 PAHs and C9–C22 alkanes were found in both 1,175-m and 865-m plumes as well as even deeper water and near the surface; C23–C40 alkanes were found in 1,175 m and 265 m, near the surface and also in lower concentrations in the 865-m plume.

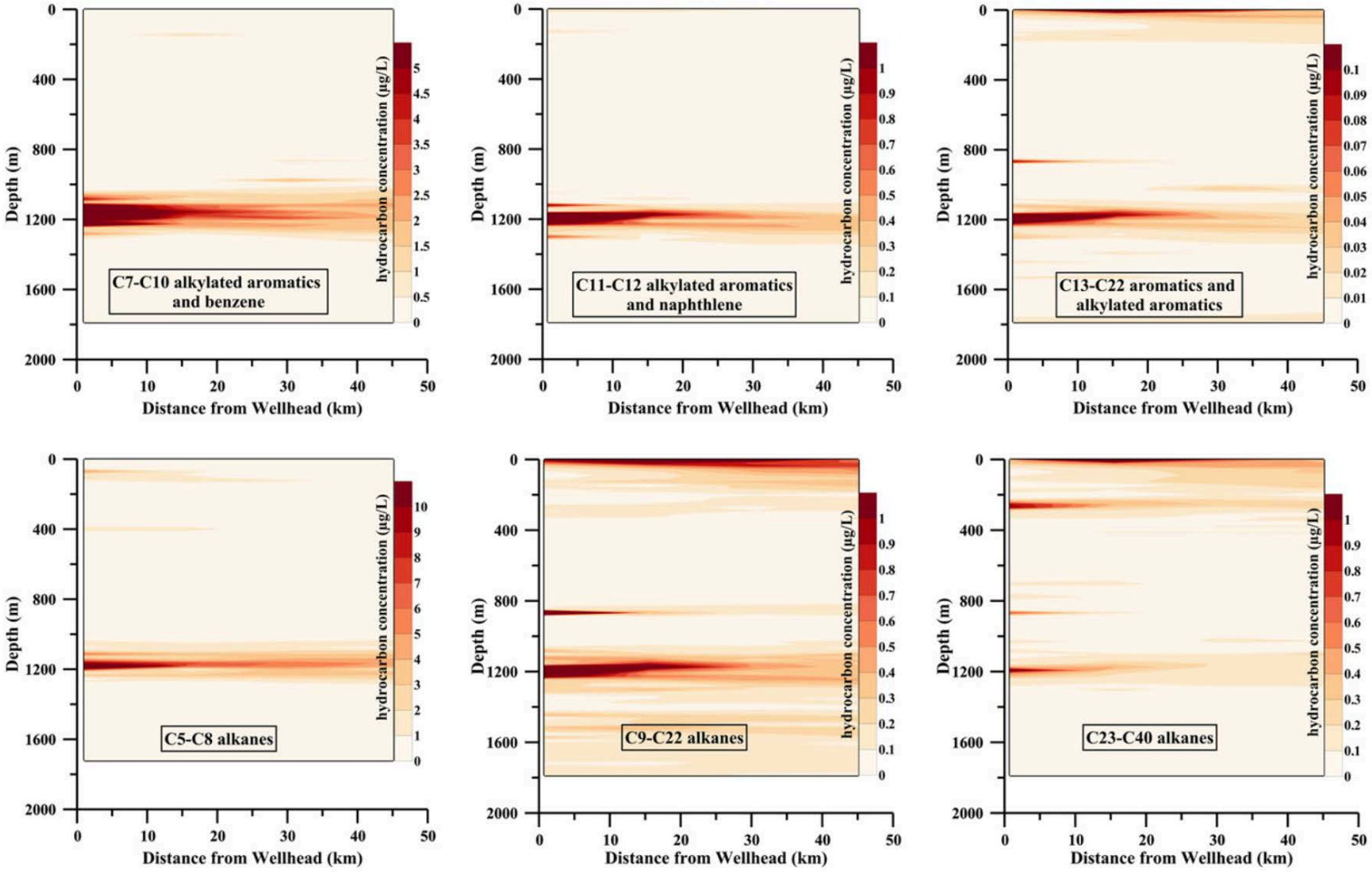

Figure B.2-1: Different hydrocarbon group concentrations in the water column, as summarized by Spier et al. (2013).

There was a statistically significant (α= 0.01) decrease in both the sample concentrations and the percent detectable results for the 865-m and 1,175-m plumes in the samples taken after the June 3 riser cut and Top Hat #4 placement. Before June 4th, the overall average sample hydrocarbon concentration was 46.1µg/L, and 17.5% of results were detectable. After Top Hat #4 began collecting oil the overall average sample hydrocarbon concentration was reduced to 5.5µg/L on average, and 10.1% of results were above detection limits. Overall, there was a significant increase in frequency of detects and sample concentration with higher dispersant application rates, specifically associated with less water soluble compounds including di-and polycyclic aromatics and alkylated aromatics and alkanes >C8.

From June 11–21, 2010, Valentine et al. (2010) investigated dissolved hydrocarbon gases at depth using chemical and isotopic surveys and on-site biodegradation studies. In the vicinity of the leaking well, propane, ethane, and methane were most abundant at depths greater than 799 m and formed plume structures with dissolved concentrations as high as 8 µM, 16 µM, and 180 µM for the three gases, respectively. Gases were orders of magnitude less concentrated at shallower depths. They also observed deep (>799 m) hydrocarbon plumes at 29 of the 31 stations (Figure 3A in Valentine et al., 2010) where methane measurements were made. In addition to the persistent plume at 1,000- to 1,200-m depth located to the southwest of the spill site, consistent with other reports (Camilli et al. 2010; Hazen et al. 2010), they also identified separate plumes at similar depths to the north and to the east, as well as a distinctive shallower plume at 800-to 1,000-m depth located to the east, suggesting multiple plumes in opposing directions presumably originated at different times, and indicating complex current patterns in the area before sampling.

Propane and ethane were identified by Valentine et al. (2010) as the primary drivers of microbial respiration, accounting for up to 70% of the observed oxygen depletion in “fresh” plumes. Regression of the observed oxygen anomaly data against the propane anomaly data indicated that 58% of the oxygen anomaly can be linked to propane, 70% of the oxygen anomaly can be linked to respiration of ethane and propane together in the fresh plume, and the remaining oxygen anomaly presumably derives from other HCs such as butane. Assuming that the subsurface plume contained 100% released gases and 23.6% of released oil that had been dispersed as fine droplets at the subsurface release point, Valentine et al. (2010) calculated that gases released from the DWHOS leak exerted a Biological Oxygen Demand (BOD) in the deep plume of up to 8.3×10^{11}g O_2 for methane, 1.3×10^{11}g O_2 for ethane, 1.0×10^{11} g O_2 for propane, and 4.4×10^{11} g O_2 for oil respiration. The sum of these values, $\sim 15 \times 10^{11}$ g of O_2, provides an estimate of the maximum integrated deep-water O_2 anomaly expected from this event, with ~15% of the oxygen loss occurring

in fresh plumes from respiration of propane and ethane, and ~two-thirds of the ultimate microbial productivity in deep plumes arising from metabolism of natural gases.

The Joint Analysis Group (JAG) Report (JAG, 2010), prepared during the spill, estimated that TPH (Total Petroleum Hydrocarbon, water-insoluble heavy saturate fraction) from GC-MS ranged between <1–1,000 ppb, with concentrations in the subsea plume (900–1,300 m) at a maximum of 485 ppb at 1.2 km from the wellhead and detectable levels extending >10 km from the source. In the plume, total volatile organic analysis (tVOA; water-soluble fraction) concentrations were higher than speciated Total Petroleum Hydrocarbon (sTPH), with a maximum of 2,112 ppb.

Boehm et al. (2012) reported highest concentration of total PAH (TPAH) in field chemistry samples as10–100 ppb; TPAH levels greater than 10 ppb were largely observed during the release and then close to the wellhead. Diercks et al. (2010) observed concentrations of TPAH of 189 ppb at 1,320 m depth and 29 ppb at 1,160 m near the wellhead site during the release. Spier et al. (2013) reported that in 422 samples from the rising cone of oil droplets and deep-water plume, the average concentration of measured hydrocarbons was 68.3 µg/L, and more than 28% of these samples contained ≥10 µg/L benzene. In 420 samples of the plume observed at 1,050–1,300 m depth, the average concentration was 65.8 µg/L.

B.2.1.2 Dispersant Chemistry in Subsurface Waters

Kujawinski et al. (2011) collected water samples throughout the water column on three research cruises in the GOM in May (27–30), June (1, 11–21), and September 2010. A total of 25 dispersant-constituent dioctyl sodium sulfosuccinate (DOSS) samples taken in May–June during the spill and 21 samples taken in September after the spill indicated that DOSS was found at elevated levels between depths of 1,000–1,200 m. Kujawinski et al. (2011) concluded that DOSS was sequestered in deep water hydrocarbon plumes at 1,000–1,200 m water depth and did not intermingle with surface dispersant applications. Kujawinski et al.'s (2011) DOSS measurements are consistent with the presence of chemically-dispersed small (<100 µm) droplets in the deep plume.

B.2.1.2.1 NRDA Water Sample Chemistry Data

During the DWHOS blowout and resulting spill, a variety of environmental data were collected aboard numerous ships. Discrete surface and water column samples were collected, sub-sampled, and analyzed from various vessels using NRDA protocols. While similar sampling protocols were followed, each vessel had slightly different objectives and sampling equipment. Alongside collected chemical and forensic data, concurrent and continuous measurements of dissolved oxygen and UV fluorescence were recorded.

In total, sampling on 165 cruises was conducted in support of either Response, academic or the NRDA effort. A complete summary of the 48 cruises where NRDA sampling was conducted in 2010 is presented in Figure B.2-2. Important events and tropical storms have been included for reference. The data included in this report are from samples collected in 2010, upon which physical measurements were collected concurrently with chemical samples, and where Quality Assured data were available at the time this data set was prepared (December 2014). Chemistry sampling locations throughout the GOM totaled 2,440 stations and nearly 14,000 discrete sampling locations (latitude, longitude, depth).

Based on the analysis of the water column chemical and physical data, as well as the consideration of major events during response, four distinct periods of time are identifiable during the spill period in 2010. These are described as separate Observable Chemistry Regimes (OCR):

a. OCR 1: pre-top-kill (Apr-20 to May-26)
b. OCR 2: top-kill, riser-cutting, and initial top-hat (May-26 to June-6)
c. OCR 3: post-cut and collection (June-6 to July-15)
d. OCR 4: post-cap (after July-15)

In April and May, oil was released from the broken riser (at 1,509 m deep) and from holes that developed at the kink in the riser pipe (at 1,503 m deep). Several times during May 26–28, the spill responders attempted to fill the riser pipe with heavy drilling mud and bridging material, but the procedures did not stop the release, and the well forced the mud and "junk" out of the riser. Relatively high hydrocarbon concentrations were observed during this period. During June 1–3, while the riser pipe was being cut, oil flowed freely from the riser, and this is evident in the data as elevated hydrocarbon concentrations compared to periods prior to and after this event. In OCR 3, oil was released from the blowout preventer (BOP) at a depth of 1,506 m from the opening of the Top Hat oil recovery installation or the gap between the Top Hat and the BOP. During OCR 4, after the release was stopped on July 15, in-water hydrocarbon concentrations decreased with increasing time and space.

Sampling of the active release of oil and gas during the three phases (OCR 1–3) was focused around the wellhead (<20 km); more extensive and broad-scale sampling into the far-field (focused to the south and southwest) did not commence until after the well shut-in was completed (OCR 4). Figures B.2-3–B.2-7 show the distribution of sampling overall and by OCR period.

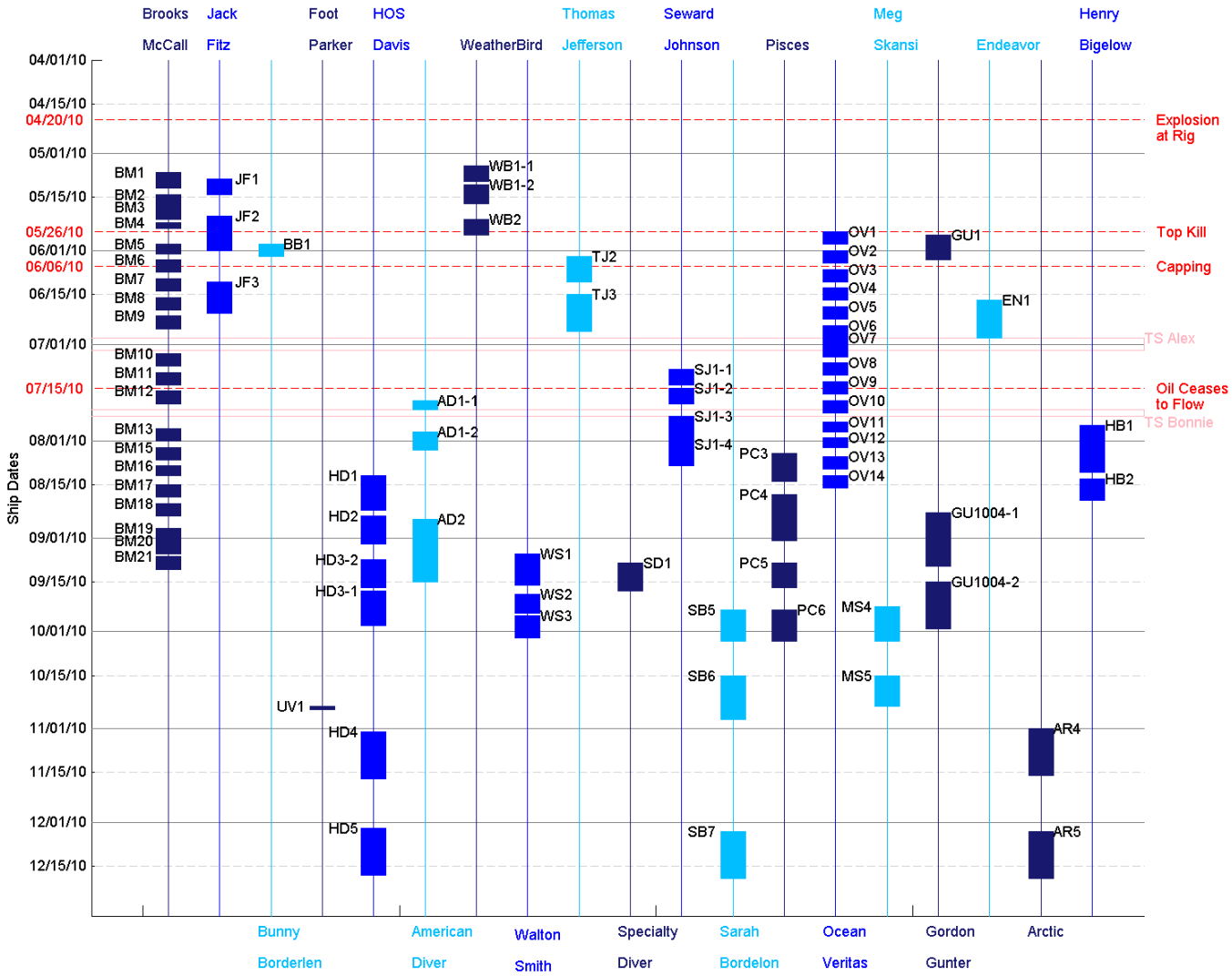

Figure B.2-2. List of 2010 cruises and associated dates where chemistry samples were collected.

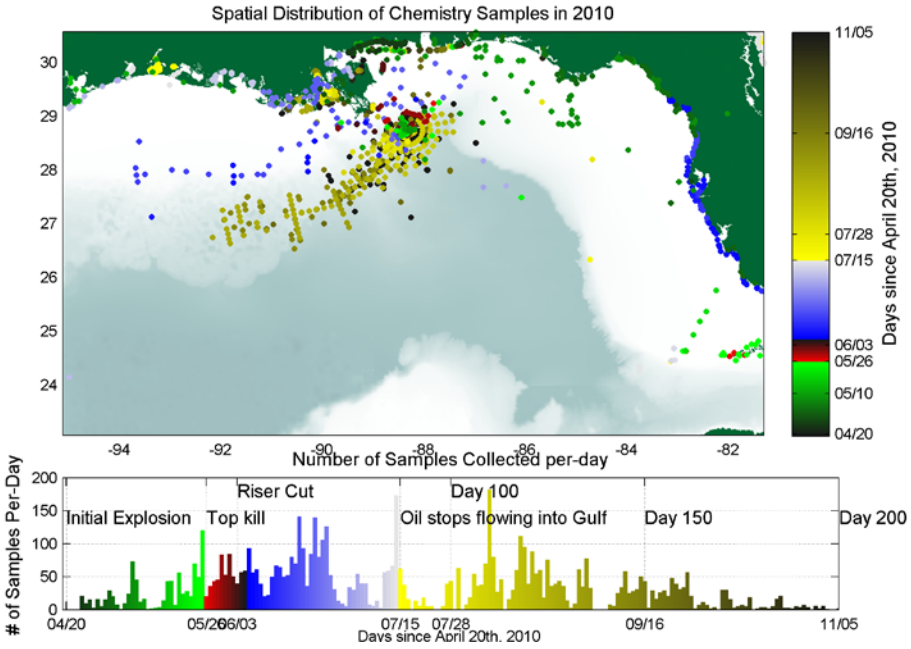

Figure B.2-3. Chemistry sampling location points in the GOM. Shaded colors represent date of collection, the four observed chemistry regimes are broken out by color.

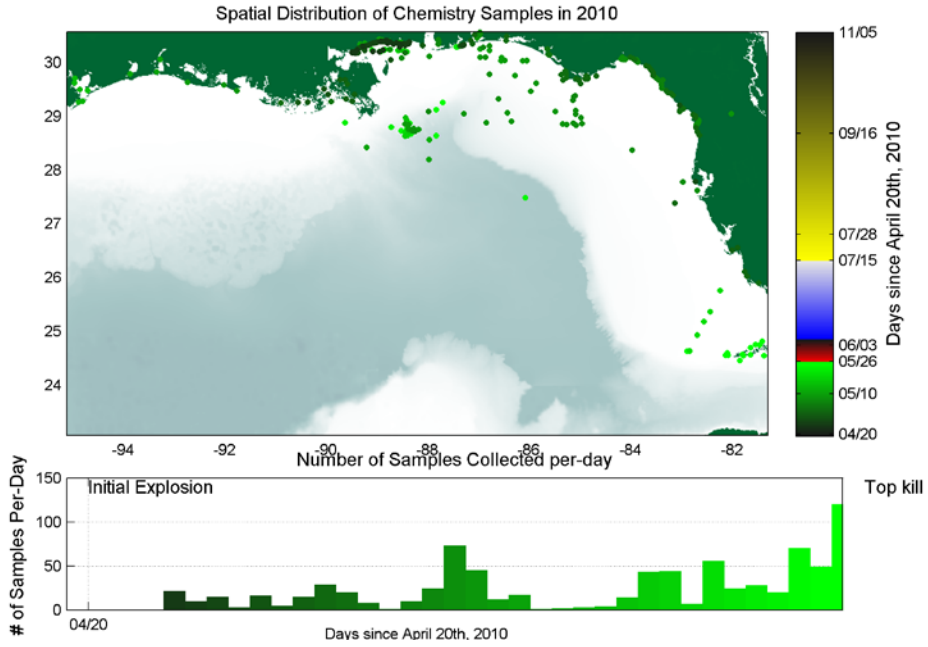

Figure B.2-4. Locations of chemistry sampling between April 20 and May 26, 2010. This period encompassed the initial explosion and pre-top-kill phase.

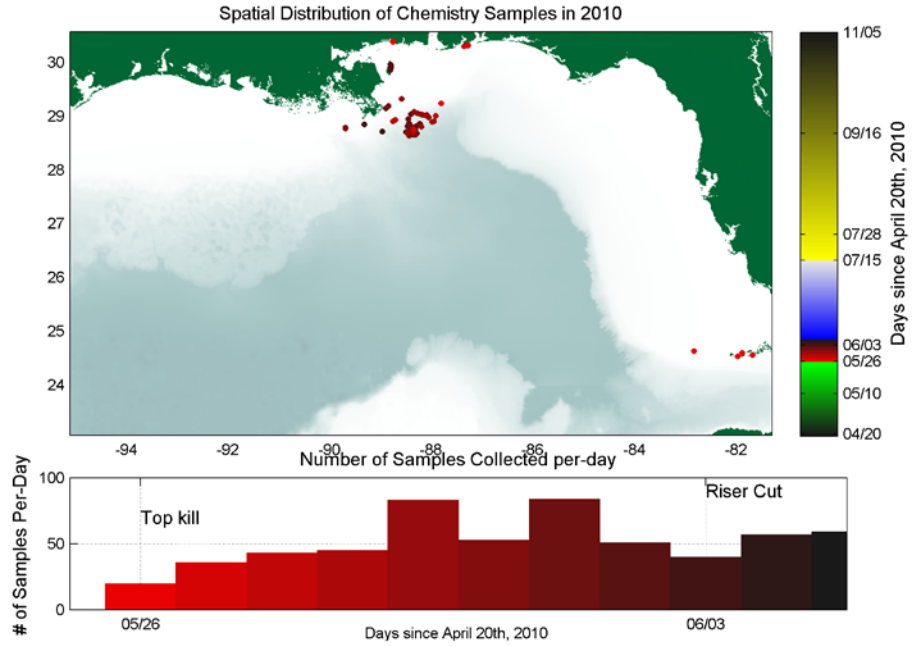

Figure B.2-5. Locations of chemistry sampling between May 26 and June 6, 2010. This period encompassed the top-kill, riser-cutting, and initial top-hat phase.

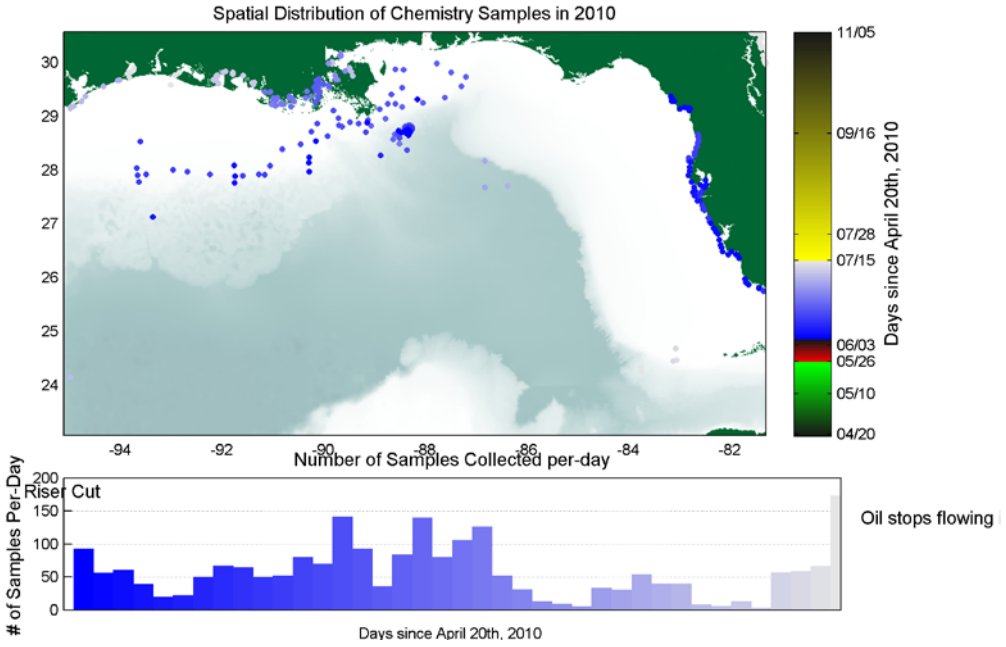

Figure B.2-6. Locations of chemistry sampling between June 6 and July 15, 2010. This period encompassed the post-cut and collection phase.

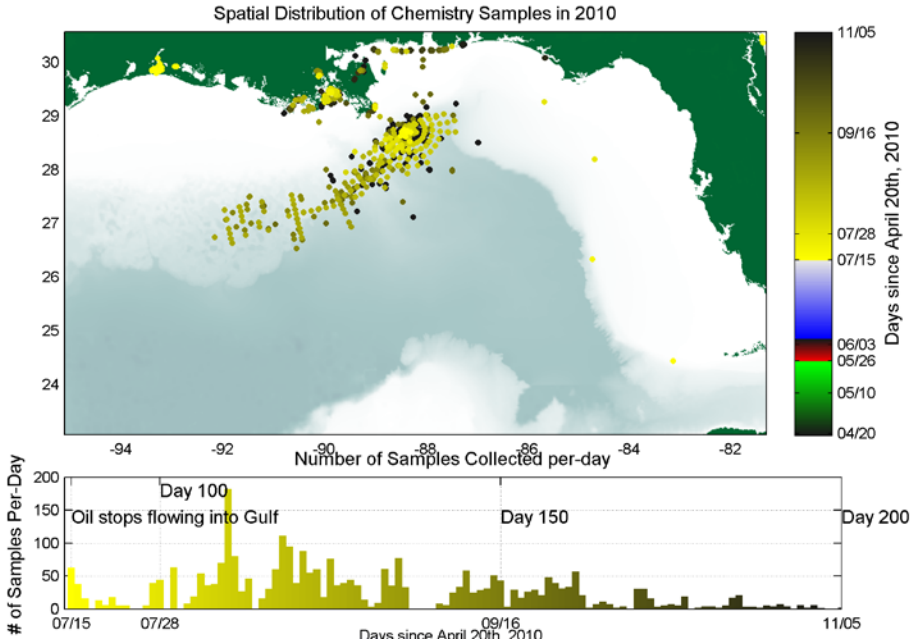

Figure B.2-7. Locations of chemistry sampling between July 15 and November 5, 2010. This period encompassed the post-cap and successful shut-in phase.

Thus, discrete sampling was not continuous, nor was it evenly distributed throughout the GOM. The spatial and temporal pattern of chemical sampling aliases data and does not lend itself to appropriately determining the distribution of hydrocarbons. The large gaps between samples in space and time likely introduce some bias in the results in such a dynamic environment. Without sampling specific locations, it is not possible to determine whether hydrocarbons were present or absent. As an example, limited spatial sampling during June–July 2010 may inappropriately lead one to conclude that there were no hydrocarbons present greater than ~50 km from the well head. However, it is likely that there were hydrocarbons at depth and that they were merely not sampled.

Although sampling was not comprehensive in space and time, several patterns in the data may be discerned. In-water concentrations remained elevated during the blowout and the released hydrocarbons began to dissipate just after the well was contained and eventually capped.

Summaries of the concentration data are in Figures B.2-8 to B.2-11. Note that all points represent significant hydrocarbon and dispersant concentrations, above the method detection limit for each investigated compound. The maximum hydrocarbon and dispersant concentrations occurred at the surface (<40 m) and at depths between ~1,100

and 1,200 m deep (Figure B.2-8 and Figure B.2-10). Though surface observations of hydrocarbons exceeded method detection limits at some locations beyond 150 km from the wellhead (Figure B.2-8), the majority of concentrations greater than 1–10 µg/L were within approximately 50 km of the wellhead (Figure B.2-10). The highest concentrations at depth were in the BTEX group and soluble alkanes (Figure B.2-8). Elevated dispersant concentrations were identified between 1,000-1,300 m near the wellhead and between 1,100–1,200m to out beyond 150 km.

There were relatively high hydrocarbon and dispersant concentrations at depths between approximately 1,000-1,300 m. The highest observed values were near the wellhead, and the concentrations decreased as distance from the wellhead increased. In late summer and fall 2010, hydrocarbons were consistently present southwest of the wellhead, where the sampling effort was highest. Forensically-identified MC252 oil was commonly observed radially within roughly 50 km of the wellhead (Figures B.2-8 and B.2-10).

Elevated concentrations in excess of the method detection limits were identified throughout the water column to beyond 150 km (Figure B.2-9). Sampling in the depth range between 100–1,000 m was much more sporadic than for 1,000–1,300m. The highest concentrations at depths of 100–1,000m were for the BTEX group and soluble alkanes (Figure B.2-11). The spatial extent in these intermediate waters is slightly more proximal to the wellhead, with highest concentrations observed typically within 25 km of the wellhead.

A detailed summary of the chemical analysis and data may be found in Horn et al. (2015a). A detailed summary of forensic findings may be found in Payne and Driskell (2015a,b,c) who, after examining 5,332 offshore water samples, identified MC252 oil in subsurface water samples as particulate-phase hydrocarbons up to 155 km from the wellhead, and as dissolved-phase as far as 267 km from the wellhead. Furthermore, based solely on dispersant indicators, fluorescence, and DO features, the presence of the deep plume was detected 412 km from the wellhead. Payne and Driskell (2015c) also documented that dispersant indicators, measured for the first time in field-collected, particulate-phase oil samples at depth, document the utility of dispersant injections at the wellhead. In addition, they found that dispersant application at depth also resulted in significantly enhanced dissolution of lower-and intermediate-molecular weight PAH contributing to enhanced bioavailability to both benthic and pelagic organisms. Chemistry and sensor data are compared and synthesized in the combined chemical and physical report by Horn et al. (2015b).

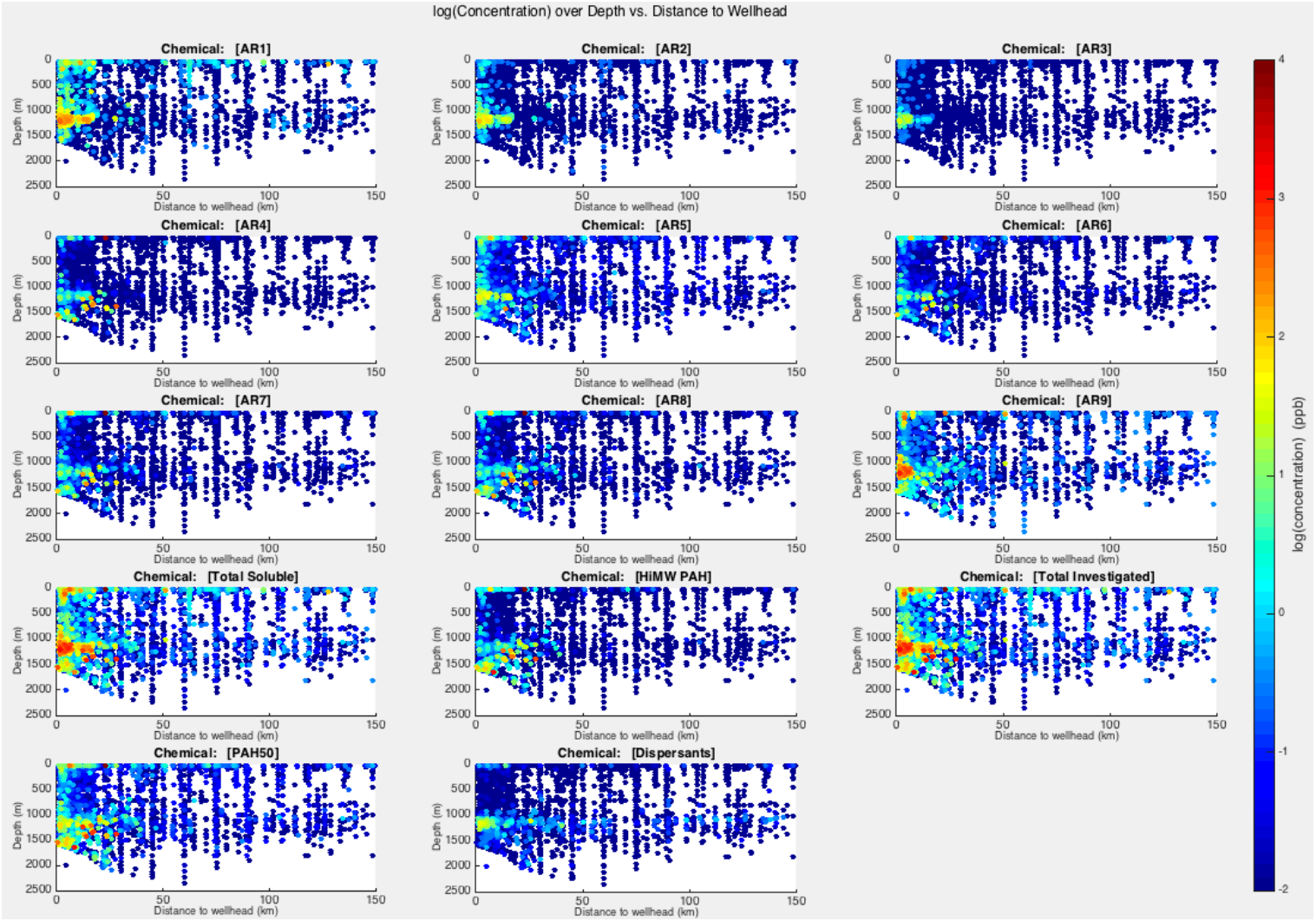

Figure B.2-8. Observed chemical concentrations (µg/L, or ppb) by grouping on a log-10 scale (color) through the full water column as a function of distance from the wellhead. (0-2,500m vertical axis; 0-150km horizontal axis)

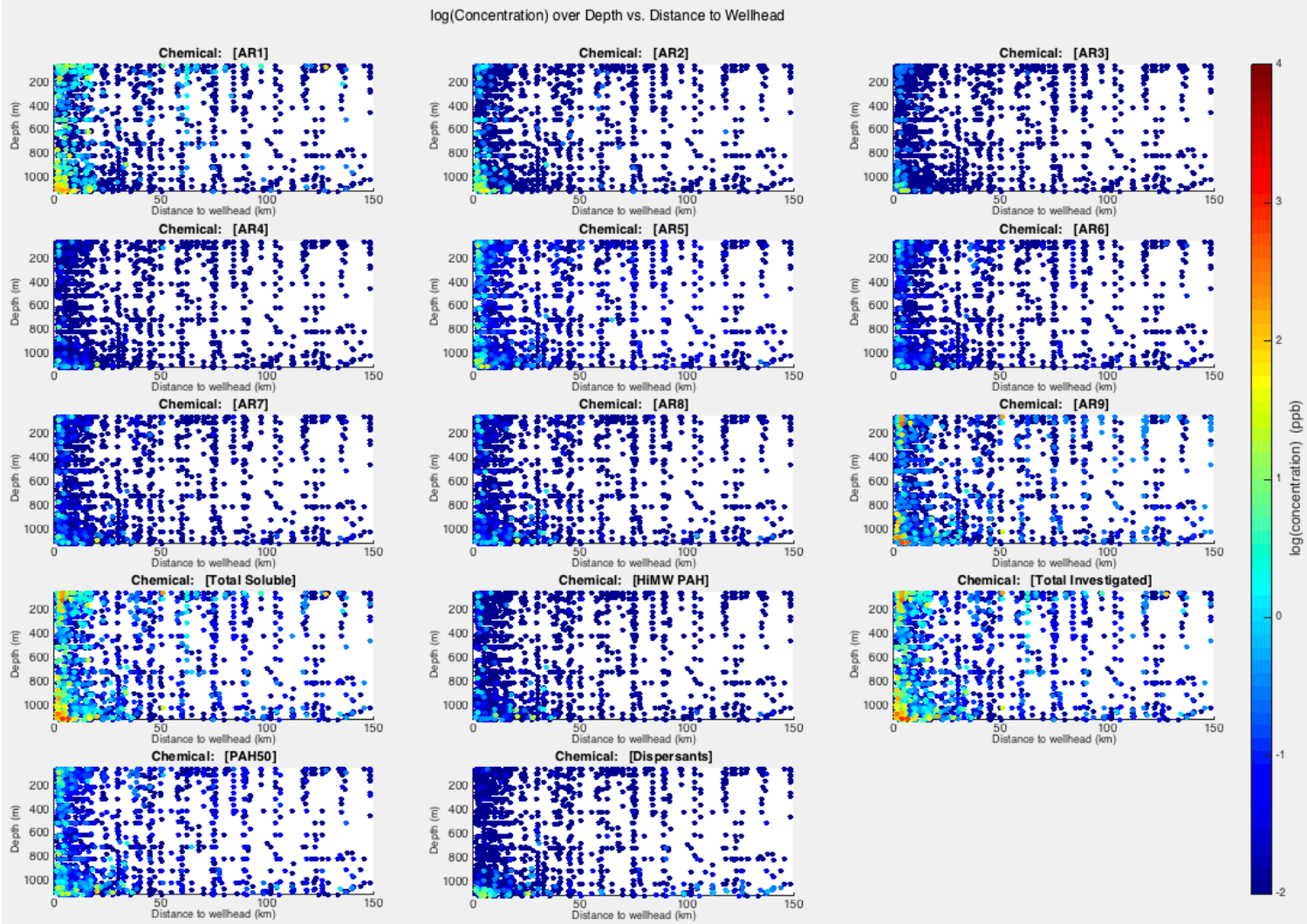

Figure B.2-9. Observed chemical concentrations (µg/L, or ppb) by grouping on a log-10 scale (color) through the water column as a function of distance from the wellhead. (40-1,100m vertical axis; 0-150km horizontal axis)

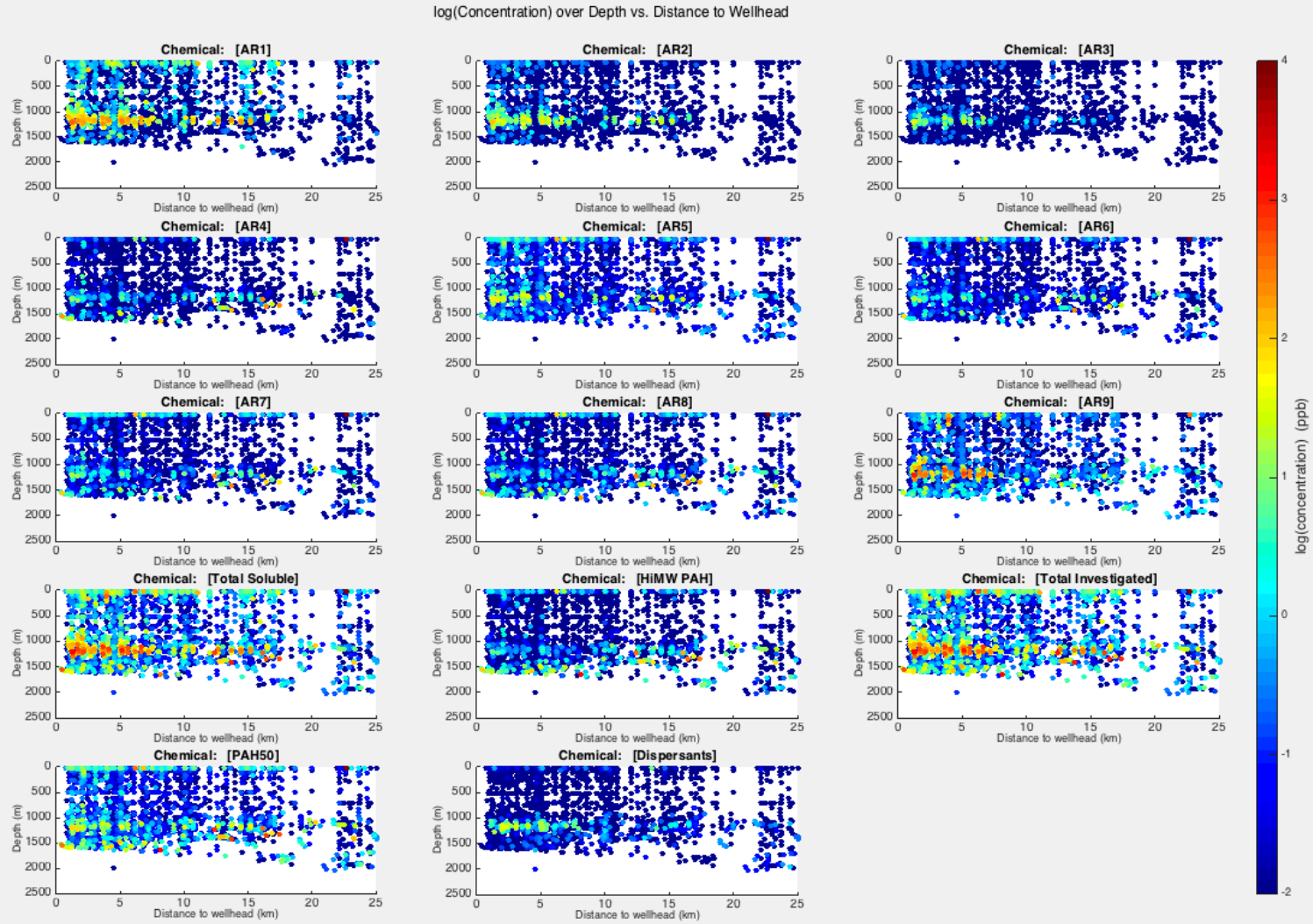

Figure B.2-10. Observed chemical concentrations (µg/L, or ppb) by grouping on a log-10 scale (color) through the full water column as a function of distance from the wellhead.
0-2,500m vertical axis; 0-25km horizontal axis

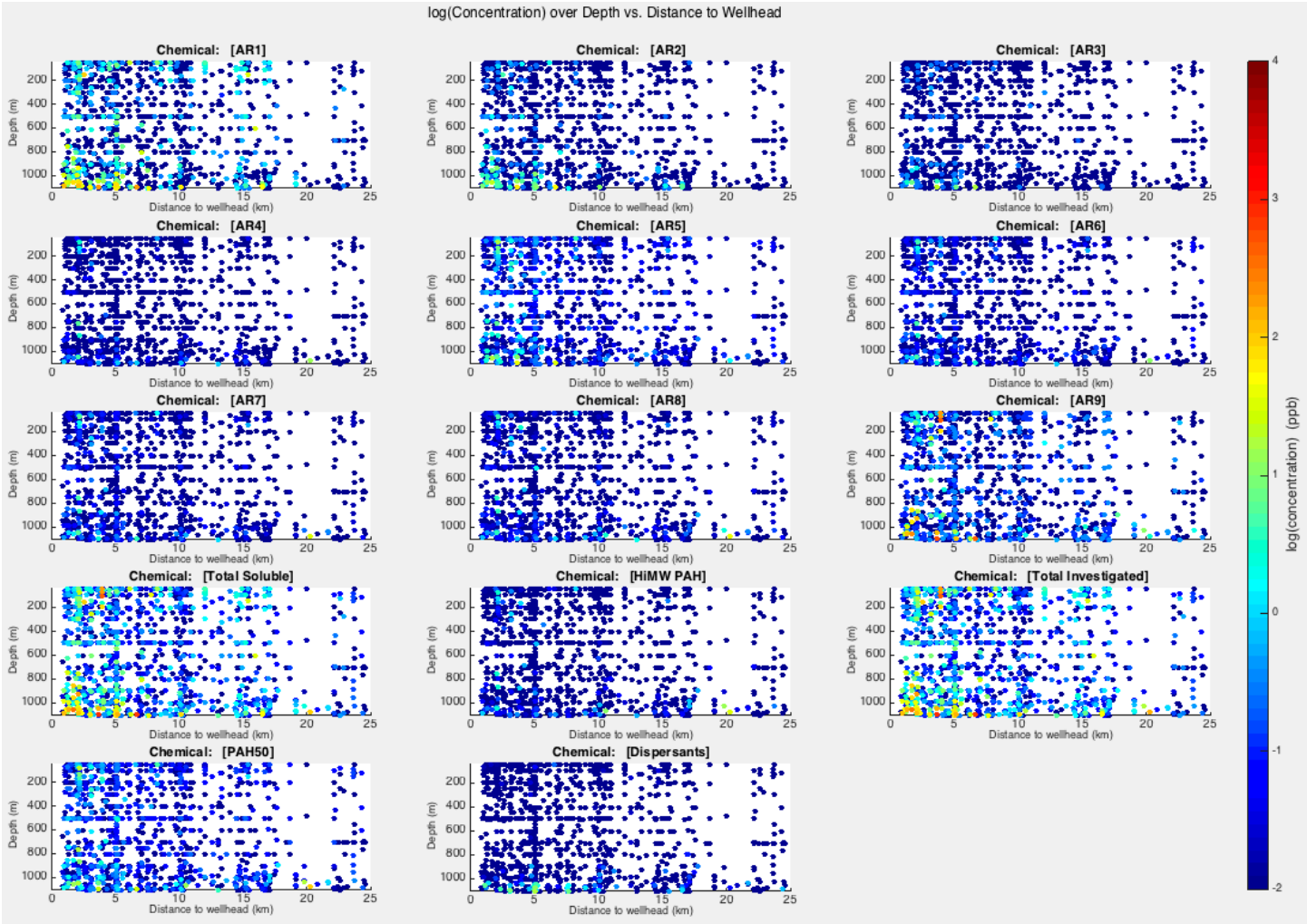

Figure B.2-11. Observed chemical concentrations (µg/L, or ppb) by grouping on a log-10 scale (color) through the water column as a function of distance from the wellhead.
40-1,100m vertical axis; 0-25km horizontal axis

B.3. Particle Data

A variety of field sampling programs have collected particle size information in the water column in the areas surrounding the DWHOS (Li et al. 2015, 2017). The particle measurements included: (1) ROV video and camera analysis of suspended particles in the water column and sessile droplets in contact with a roughly 4 cm x 4 cm oil quantitation grid attached to the ceiling of the ROV video and camera housing on M/V *Jack Fitz* 2 (JF2) during May 22–31, 2010, (2) Holographic camera analysis of suspended particles in the water column that was performed on M/V *Jack Fitz* 3 (JF3) during June 14–20, 2010, (3) Laser In-Situ Scattering and Transmissometry (LISST)-100X analysis of oil droplets or suspended particulate material (SPM) in the near-field shallow depths (within 300 m from the surface) on M/V *JF2 and JF3*, and (4) LISST-100X analysis of small particle concentrations (SPC) in the water column that was conducted on R/V *Brooks McCall* during May–August 2010 with discrete samples retrieved from the water column and at the surface.

The *JF*2 ROV dive data clearly showed particulates, including oil droplets, in the water column based on the recorded images and videos. These data indicated that: (1) higher concentrations of oil droplets occurred at certain depths in the water column, and (2) large oil droplets (>1 mm) tended to be more prevalent in the upper water column.

The Holocam analysis (of 30–1000+ μm particles) showed the presence of round particles throughout the water column, which had count (number) median diameters around 45–50 μm. For Dives 5 & 6, increased number of category 1 (round object) and category 2 (possible oil) particles were measured both in the deep subsurface (i.e., 1,100–1,500 m) and the surface mixed layer, whereas the oil droplets were rare in the 250–850 m depth range (Davis and Loomis, 2014).

All *in situ* deployments of LISST-100X (2.5–500 μm detection limit) indicated presence of suspended particles throughout the water column, with relatively higher integrated particle concentrations at the surface and near the maximum deployment depth (~250 m). The particle size distributions have peaks (i.e., mode) between 300 and 400 μm.

The spill response vessel's LISST-100X analyses on the R/V *Brooks McCall* indicated that higher small particle concentrations (i.e., diameter ≤ 70 μm) were observed in the surface waters and the plume layer, in the close vicinity of the leaking wellhead.

The data reviewed herein generally support the hypothesis that large droplets ascend quickly surrounding the immediate vicinity of the leaking wellhead, while a considerable number of smaller droplets remain suspended in the water column.

B.3.1 Field Data

B.3.1.1 JF2 Cruise ROV Video and Camera Imagery Data on Marked Grid

Three cruises aboard the M/V *Jack Fitz* were conducted as part of the DWHOS NRDA program. The *Jack Fitz* 2 (May 22–31, 2010) and *Jack Fitz* 3 cruises (June 14–20, 2010) employed an ROV with a video camera to observe oil in the water column along with deploying sampling gear and collecting temperature, salinity, dissolved oxygen, fluorescence, and other sensor data (Payne and Driskell, 2015d; Li et al. 2015). The *Jack Fitz* 2 cruise deployed 17 casts and dives with the ROV; the majority of the ROV video recorded on this cruise was in color, at a resolution of 720x480. *Jack Fitz* 3 deployed nine dives, again with the majority of the ROV video recorded in color at a resolution of 720x480. (However, the majority of the *Jack Fitz* 3 video contained a video water mark which obstructed the underlying video and persisted for the duration of the recorded video. This water mark is a visibly black artifact present in more than one location on the video.)

The ROV video data starting with JF2 Dive#6 on May 24, 2010 were fitted with a roughly 4 cm x 4 cm red-taped marked grid including a metal ruler with centimeter (cm) and millimeter (mm) lineation on one side as a reference scale. The oil quantitation grid (Marked Grid) was taped to the underside of the ROV housing, above and behind the camera, and during the dives the ROV was positioned to pan the camera to view the grid. The reference grid and scale next to the grid allow for visual estimations of droplet sizes in the water column, and those droplets that have collided with the grid. The grid-referenced oil droplets were identified either from the presence of visibly brown particulates in the water column, or from the sessile drops in contact (collided) with the surface of the grid. The advantage of the video over static imagery is the capability of tracking the movement of the droplets. For these droplets to be visible in this video footage, the droplet size must be greater than around 500 μm (see Li et al. 2015).

In JF2 ROV Dives 1 to 5, brown particulates indicative of oil were observed in the water column. In Dives 6–17, which were equipped with the Marked Grid, oil droplets were also observed in the water column and examined in more detail. Larger droplets ($d \geq 1$mm) were found present close to the surface and smaller droplets ($d < 1$mm) were present throughout the majority of the water column at different frequencies. Certain dives (particularly Dives 8, 10, 15 and 16) contained clear boundaries between low and high droplet densities.

JF2 Dive #8 (on May 27, 2010) was located at about 3 km northwest of the wellhead, and it had surveyed depths ranging from the surface to the seafloor (1,419 m). Two elevated peaks in numbers of droplets were observed: the first one was between the depths of 802 to 1,006 m, and the second was identified between depths from 1,168 to 1,390 m. However,

brown particulates were visible throughout the water column in addition to within these two distinct peak depth intervals.

Dive #10 (on May 28, 2010) was located at approximately 4 km northwest of the wellhead and had a maximum depth of 1,444 m. A number of large droplets (diameter ≥ 1mm) were observed at depths less than 261 m, and the oil droplet number density increased between 305 and 382 m, followed by a visibly decreased yet still visible number of droplets in the water column at deeper depths, extending to the maximum depth of the dive. Figures B.3-1 and E.3-2 illustrate the captured video and camera imagery data of the dive at different depths of the water column.

Figure B.3-1: A cloud of oil droplets captured by the ROV camera of JF2 Dive#10 from about 3 m below the surface.

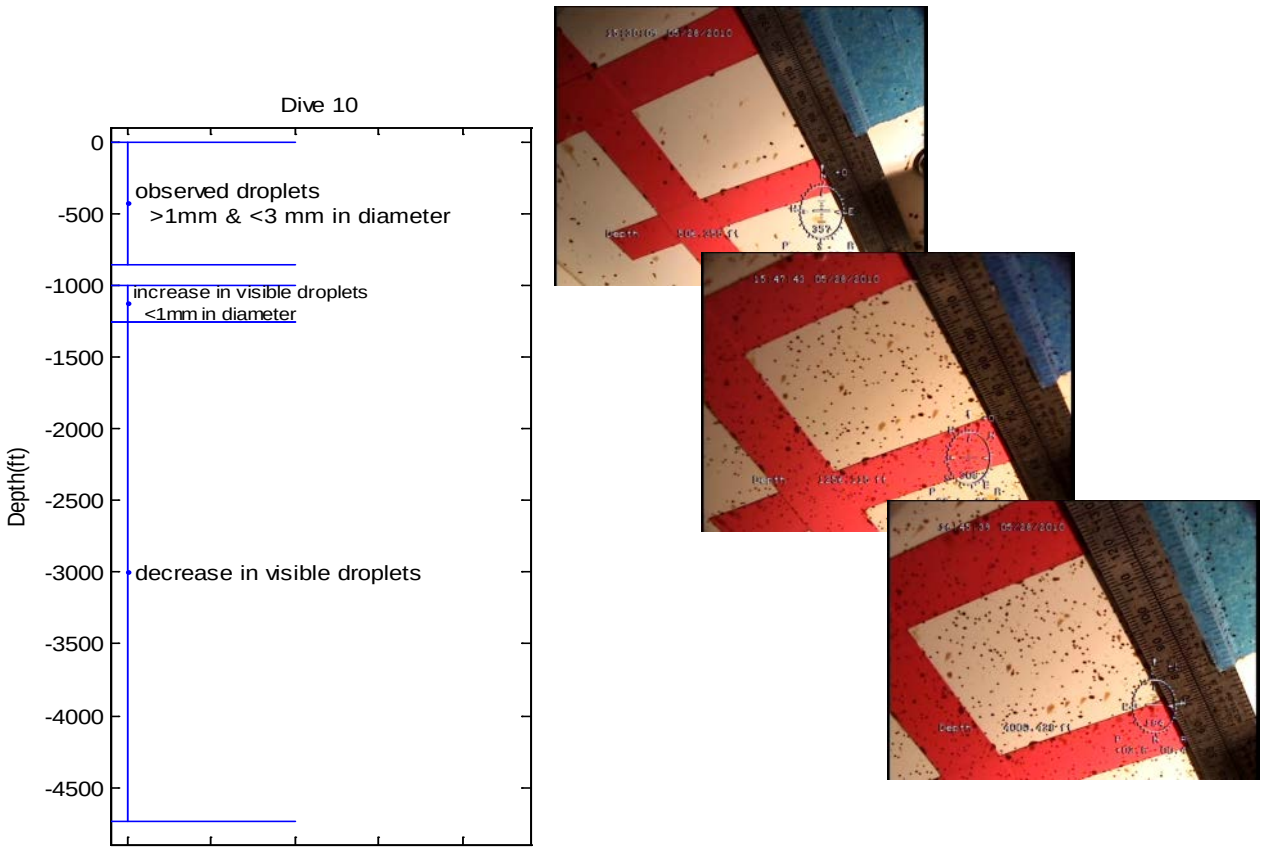

Figure B.3-2: Dive # 10 ROV video imagery data depth range (left, in feet) and representative images showing the oil droplets collided onto the roughly 4 cm x 4 cm red-tapped Marked Grid (right).

Dives #15 and 16 (on May 30, 2010) were located approximately 2 km southwest of the wellhead, with the maximum depth 1,601m for #15 and 1,212m for #16. There was very little surface oil at that location (Payne and Driskell, 2015d) and only small amounts of droplets were observed on the grid at depths less than 1,038.2 m during Dive 15, and at depths less than 990 m for Dive 16. For Dive #15, the greatest number of droplets was observed in the deep plume and on the Marked Grid in depths from 1,038 to 1,219 m, with a large number of small droplets still readily visible in the water column until the maximum depth. For Dive#16, as the ROV descended past the depth of 990m, the amount of droplets that were visible in the water column from the forward-facing camera visually increased, as were the number of droplets seen on the Marked Grid. At the maximum depth of the dive, however, the number of droplets appeared reduced. These dives clearly showed the decoupling of the deep plume from the surface manifestation of the released MC252 oil.

B.3.1.2 JF3 Holographic Camera Imagery Data

As part of the overall NOAA NRDA sampling program, a unique set of data on size distributions of oil droplets was collected and processed by Davis and Loomis (2014). On the M/V *Jack Fitz* 3 from June 14–20, 2010, an *in situ* digital holographic camera (Holocam) collected data from nine dives, at distances of 1–10 km from the wellhead. Among these nine dives, two were shallow dives that collected data within the upper 300 m, two dives were to 1,100 m, and the other five went deeper than 1,400 m.

During the dives, the Holocam was mounted on the front of an ROV and the unit was programmed to take an image at a set time interval over the entire dive. Objects were detected, and the roundness of each detected object was used as a constraint for particle detection. Classifier truth rates (i.e., identification of particles as oil) depended on droplet size, with droplets smaller than 30 μm having too few pixels for accurate human identification and droplets larger than 150 μm much less abundant in the imaged volume. Detailed description of the data processing is presented in Davis and Loomis (2014).

The Holocam analysis showed that droplets (i.e., particulates defined by their roundness with a minimum diameter of 30 μm, a subset of those plotted here) were found throughout the water column with count (by number) median diameters from all the dives between 44.5–52 μm. The number-based particle size distributions at each depth generally followed lognormal number size distributions. The depth at which the peak numbers of particles were measured varied for different stations. For most dives, increased numbers of particles were measured at both the subsurface plume layer (below 1,000 m) and in the surface mixed layer.

B.3.1.2.1 LISST-100X SPM Data

The LISST-100X instrument, manufactured by Sequoia Scientific Inc., uses the technique of laser diffraction to obtain size distributions of particulate material in the water column. Processed results from the LISST instrument provide a volume concentration (μL/L) of particles in each of 32 size classes. The size classes are log-spaced over the range 2.5–500 μm (for Type-C instrument).

As part of the DWHOS NRDA program, a LISST-100X was deployed *in situ* on the *Jack Fitz* 2 and 3 cruises during May and June 2010. The instrument was attached to a descending ROV to a depth between 250 and 300 m while recording and/or transmitting nearly continuous measurements. In general, SPM concentrations were large and variable in the upper 30–40 m of the water column, likely due to the increased productivity and active turbulence from winds in the surface mixed layer as compared to deeper water. Below the mixed layer, SPM concentrations dropped to 50–100 ppm, then gradually increased up to the depth

limits of the instrument (200–300 m). At each individual sampling depth of the LISST data, there is a noticeable increase in SPM concentrations in the 300–400 μm range. In other words, the mode of particle size distribution is approximately between 300 and 400 μm. It was not possible to identify oil droplets within these observations of SPM.

B.3.1.2.2 LISST-100X SPC Data

The R/V *Brooks McCall* (and its alternative R/V *Ocean Veritas*) was dispatched at the request of BP and US Environment Protection Agency (EPA) to meet the US EPA Directive to monitor subsurface dispersant use (EPA 2010). The period of data analyzed in this report extends from May 8 to August 24, 2010. The monitoring program (including *Brooks McCall* and *Ocean Veritas*) collected a total of 3,197 water samples from 404 stations at depths down to 2,000 m (NCEI 2013).

The measured small particle concentrations (SPC, i.e., d ≤ 70 μm) were plotted as a function of sampling depth below the sea surface, sampling distance from the wellhead, and the sampling date. All samples with high SPC (≥ 2.4 μl/L) were found at the surface, where the maximum was 14.2 μl/L. In comparison, the maximum SPC observed at the subsurface was 2.4 μl/L. All samples with SPC > 4.0 μl/L were within 15 km of the wellhead.

Results are included in the JAG report (JAG, 2010) regarding the "Review of R/V *Brooks McCall* Data to Examine Subsurface Oil". The plots illustrate the vertical profiles of fluorescence and oxygen measurements from CTD casts at stations with LISST-100X and laboratory analytical data from Niskin bottle samples. The JAG report concluded that: "Taken as a whole, fluorometry, TPH, and VOA measurements indicate that the anomaly observed near the wellhead is consistent with oil associated with the spill site, this signal decreases with distance from the source, and it decreases towards the southwest beyond 10 km within the area sampled. …The water sample analysis for dispersed oil particles in the range of 2.5–60 μm using the LISST shows a correspondence with peaks in the in-situ fluorescence. See in particular stations B45-46, and B48-50."

B.3.2 Summary of the Field Observation Particle Data

Li et al. (2015) compiled four sets of data that were collected during the DWHOS time period: ROV video and camera imagery, the ROV holographic camera, the LISST-100X SPM data, and the LISST-100X SPC data. The discrete sampling methods for the LISST-100X analysis of SPC were not suitable for quantifying the entire droplet size distribution using a device meant for *in situ* deployment. Specifically, when discrete aliquots were pulled from GoFlo or Niskin bottles and examined with a bench-top LISST on the vessel, the samples placed in the cuvettes were fraught with degassing bubbles and rapidly rising oil droplets confounding the analysis. That is one reason why *in situ* LISST measurements were used on the *Jack Fitz* cruises. However, this approach was depth limited (to the upper 250–300 m of the water column) because of instrumental constraints.

All *Jack Fitz* 2 ROV video data show particulates identifiable as oil in the water column. Several *Jack Fitz* 2 dives show that higher concentrations of oil droplets are present in certain depth ranges in the water column. The dive profiles also indicate large droplets (>1 mm) are more prevalent in the upper part of the water column.

Digital Holocam data were obtained by Davis and Loomis (2014) as part of the deployment of ROV in the water column during the *Jack Fitz* 3 NRDA monitoring program. The digital holographic camera data were collected in real time and *in situ* from nine different dives, including seven deep dives reaching depths of more than 1,000 m. The final results are reported as the number of round particles in the water column per size interval at each of the different depth intervals. These data clearly demonstrate the presence of round particles throughout the water column, and indicate some depths have higher numbers of particles than other depths.

In summary, during the DWHOS blowout release, a considerable amount of oil may have been dispersed as oil droplets into the water column. Some of these smaller droplets may have remained in the water column for an extended period because of their slow rise-times, while other larger droplets would have risen to the surface. The data reviewed generally support the contention that large droplets rose quickly surrounding the immediate vicinity of the leaking wellhead, intermediate-sized droplets extended further afield in the mid water column as they continued to rise, and a considerable number of small droplets remained suspended in the water column.

B.4. References

Belore RC, Trudel BK, Morrison J. 2011. Weathering, emulsification, and chemical dispersibility of Mississippi Canyon 252 crude oil: Field and Laboratory studies. International Oil Spill Conference Proceedings, March 2011. Vol 2011(1):247.

Boehm PD, Murray KJ, Brown JS, Royer L. 2012. Distribution and fate of PAH and chemical dispersants in the water column following the *Deepwater Horizon* Oil Spill. In: proceedings of Presentation at the 243rd American Chemical Society National Meeting, San Diego, CA. March 26–29, 2012.

Brown JS, Beckmann D, Bruce L, Cook L, Mudge S. 2011. PAH depletion ratios document the rapid weathering and attenuation of PAHs in oil samples collected after the *Deepwater Horizon*. In: International Oil Spill Conference Proceedings (IOSC), vol. 2011, no. 1, Abs336. American Petroleum Institute.

Camilli R, Reddy CM, Yoerger DR, Van Mooy BAS, Jakuba MV et al. 2010. Tracking hydrocarbon plume transport and biodegradation at *Deepwater Horizon*. Science 330:201–204.

Daling PS, Leirvik F, Almås IK, Brandvik PJ, Hansen BH et al. 2014. Surface weathering and dispersibility of MC252 crude oil. Marine Poll Bull. 87(1-2):300–310.

Davis CS, Loomis NC. 2014. *Deepwater Horizon* Oil Spill (DWHOS) water column technical working group image data processing plan: Holocam, description of data processing methods used to determine oil droplet size distributions from *in situ* holographic imaging during June 2010 on cruise *M/V Jack Fitz* 3. Cabell S. Davis, Woods Hole Oceanographic Institution; Nick Loomis, MIT/WHOI Joint Program in Oceanography. 15 pages + Appendix.

Diercks AR, Highsmith RC, Asper VL, Joung D, Zhou Z et al.2010. Characterization of subsurface polycyclic aromatic hydrocarbons at the *Deepwater Horizon* site. Geophys. Res. Lett. 37: L20602:1–6.

Du M, Kessler JD. 2012. Assessment of the spatial and temporal variability of bulk hydrocarbon respiration following the *Deepwater Horizon* Oil Spill. Environ. Sci. Tech. 46(19):10499–10507.

Dubinsky EA, Conrad ME, Chakraborty R, Bill M, Borglin SE et al. 2013. Succession of hydrocarbon-degrading bacteria in the aftermath of the *Deepwater Horizon* Oil Spill in the Gulf of Mexico. Environ. Sci. Tech. 47(19):10860–10867.

EPA. 2010. Dispersant monitoring and assessment directive for subsurface dispersant application. US Environmental Protection Agency Archive Document, 10 May 2010. https://archive.epa.gov/bpspill/web/html/

Grennan M, Zamorski S, Decker L, Horn M, Kim Y. 2015. Technical reports for *Deepwater Horizon* Water column injury assessment–FE_TR.39: Volume II. Water Column CTD and Sensor Data from the *Deepwater Horizon* Oil Spill. RPS ASA, South Kingstown, RI, USA, August 2015.

Hazen TC, Dubinsky EA, Desantis TZ, Andersen GL, Piceno YM et al. 2010. Deep-sea oil plume enriches indigenous oil-degrading bacteria. Science 330:204–208.

Horn M, Grennan M, Decker L, Zamorski S, French McCay D et al. 2015a. Technical reports for *Deepwater Horizon* Water column injury assessment–FE_TR.38: Volume I. Water Column Chemistry Data from the *Deepwater Horizon* Blowout. RPS ASA, South Kingstown, RI, USA, August 2015.

Horn M, French McCay D, Payne J, Driskell W, Li Z et al. 2015b. Technical reports for *Deepwater Horizon* water column injury assessment–FE_TR.40: Volume III. Water Column Chemical and Physical Data from the *Deepwater Horizon* Blowout. RPS ASA, South Kingstown, RI, USA, August 2015.

JAG. 2010. Joint Analysis Group (JAG) Review of R/V Brooks McCall data to examine subsurface oil. (accessed 10 September 2010). Available at: http://www.ncddc.noaa.gov/activities/healthy-oceans/jag/reports.

Kessler JD, Valentine DL, Redmond MC, Du M, Chan EW et al. 2011. A persistent oxygen anomaly reveals the fate of spilled methane in the deep Gulf of Mexico. Science 331:312–315.

Kujawinski EB, Kido Soule MC, Valentine DL, Boysen AK, Longnecker K et al. 2011. Fate of dispersants associated with the *Deepwater Horizon* Oil Spill. Environ. Sci. Tech. 45(4):1298–1306.

Li Z, Bird A, Payne JR, Vinhateiro N, Kim Y et al. 2015. Technical reports for *Deepwater Horizon* water column injury assessment–Volume IV. Oil Particle Data from the *Deepwater Horizon* Oil Spill. South Kingstown (RI): RPS ASA. DWH-AR0024715.pdf Available at: https://www.doi.gov/deepwaterhorizon/adminrecord.

Li Z, Spaulding M, French McCay D, Crowley D, Payne JR. 2017a. Development of a unified oil droplet size distribution model with application to surface breaking waves and subsea blowout releases considering dispersant effects. Marine Poll Bull 114 (1): 247–257.

NCEI. 2013. National Centers for Environmental Information. Ship Data: *Deepwater Horizon* Support. (accessed September 2013). Available at: http://www.nodc.noaa.gov/General/DeepwaterHorizon/ships.html.

Payne JR, Driskell WB. 2015a. 2010 DWH offshore water column samples—Forensic assessments and oil exposures. PECI Technical Report to the Trustees in support of the PDARP.

Payne JR, Driskell WB. 2015b. Forensic fingerprinting methods and classification of DWH offshore water samples. PECI Technical Report to the Trustees in support of the PDARP.

Payne JR, Driskell WB. 2015c. Dispersant effects on waterborne oil profiles and behavior. PECI Technical Report to the Trustees in support of the PDARP.

Payne JR, Driskell WB. 2015d. Offshore adaptive sampling strategies. PECI Technical Report to the Trustees in support of the PDARP.

Reddy CM, Arey JS, Seewald JS, Sylva SP, Lemkau KL et al. 2012. Composition and fate of gas and oil released to the water column during the *Deepwater Horizon* oil spill. In: Proceedings of National Academy of Sciences 109(5):20229–20234.

Ryerson TB, Aikin KC, Angevine WM, Atlas EL, Blake DR et al. 2011. Atmospheric emissions from the *Deepwater Horizon* spill constrain air-water partitioning, hydrocarbon fate, and leak rate. Geophys. Res. Lett. 38(7): L07803.

Ryerson TB, Camilli R, Kessler JD, Kujawinski EB, Reddy CM et al. 2012. Chemical data quantify *Deepwater Horizon* hydrocarbon flow rate and environmental distribution. In: Proceedings of the National Academy of Sciences 109(50):20246–20253.

Spier C, Stringfellow WT, Hazen TC, Conrad M. 2013. Distribution of hydrocarbons released during the 2010 MC252 oil spill in deep offshore waters. Environ. Pollut. 173:224–230.

Stout SA. 2015a. Physical and chemical properties of the fresh MC252 Macondo-1 well crude oil. NewFields Technical Report to the Trustees in support of the pDARP.

Stout SA. 2015b. Bulk chemical and physical properties of fresh and weathered Macondo crude oil. NewFields Technical Report to the Trustees in support of the pDARP.

Stout SA. 2015c. Range in composition and weathering among floating Macondo oils during the *Deepwater Horizon* oil spill. NewFields Technical Report to the Trustees in support of the pDARP.

Valentine DL, Kessler JD, Redmond MC, Mendes SD, Heintz MB et al. 2010. Propane respiration jump-starts microbial response to a deep oil spill. Science 330:208–211.

Valentine DL, Mezic I, Macesic S, Crnjaric-Zic N, Ivic S et al. 2012. Dynamic autoinoculation and the microbial ecology of a deep water hydrocarbon irruption. In: Proceedings of the National Academy of Sciences of the United States of America 109(50):20286–20291.

Annex C: *Deepwater Horizon* Oil Spill Model Results and Comparison to Observation: Floating Oil

C.1. Age of Floating Oil

The "age" of the floating oil spillets, defined as hours since release at the trap height of the near-field plume, provides an indication of the degree of weathering the oil has undergone since release. Figures C.1-1 to C.1-16 show snapshots from the base case simulation using HYCOM-FSU currents and NARR winds. See Section 4.2.7 of Volume II for discussion.

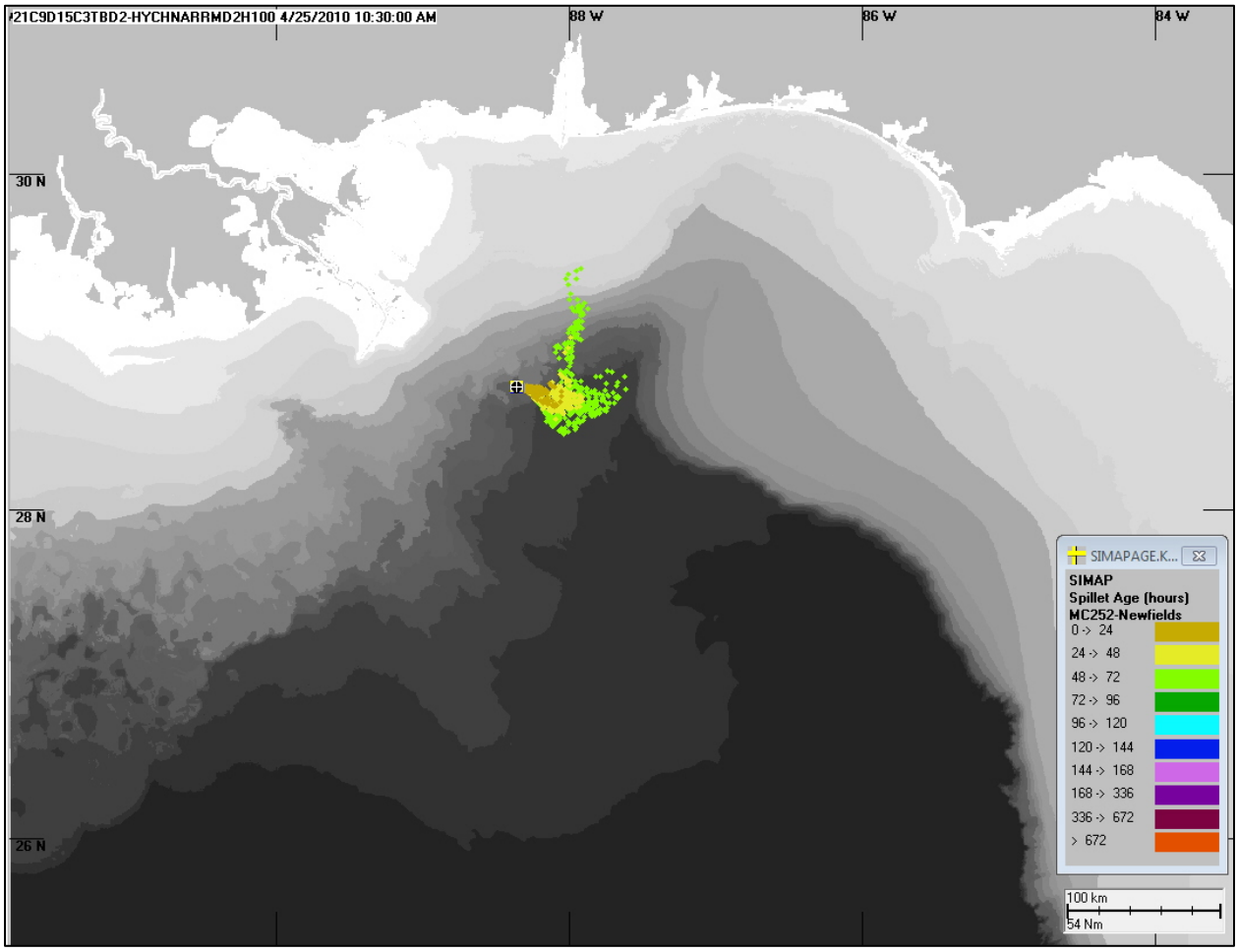

Figure C.1-1. Locations and age (hours since release) of floating oil spillets on April 25 (10:30 CDT).

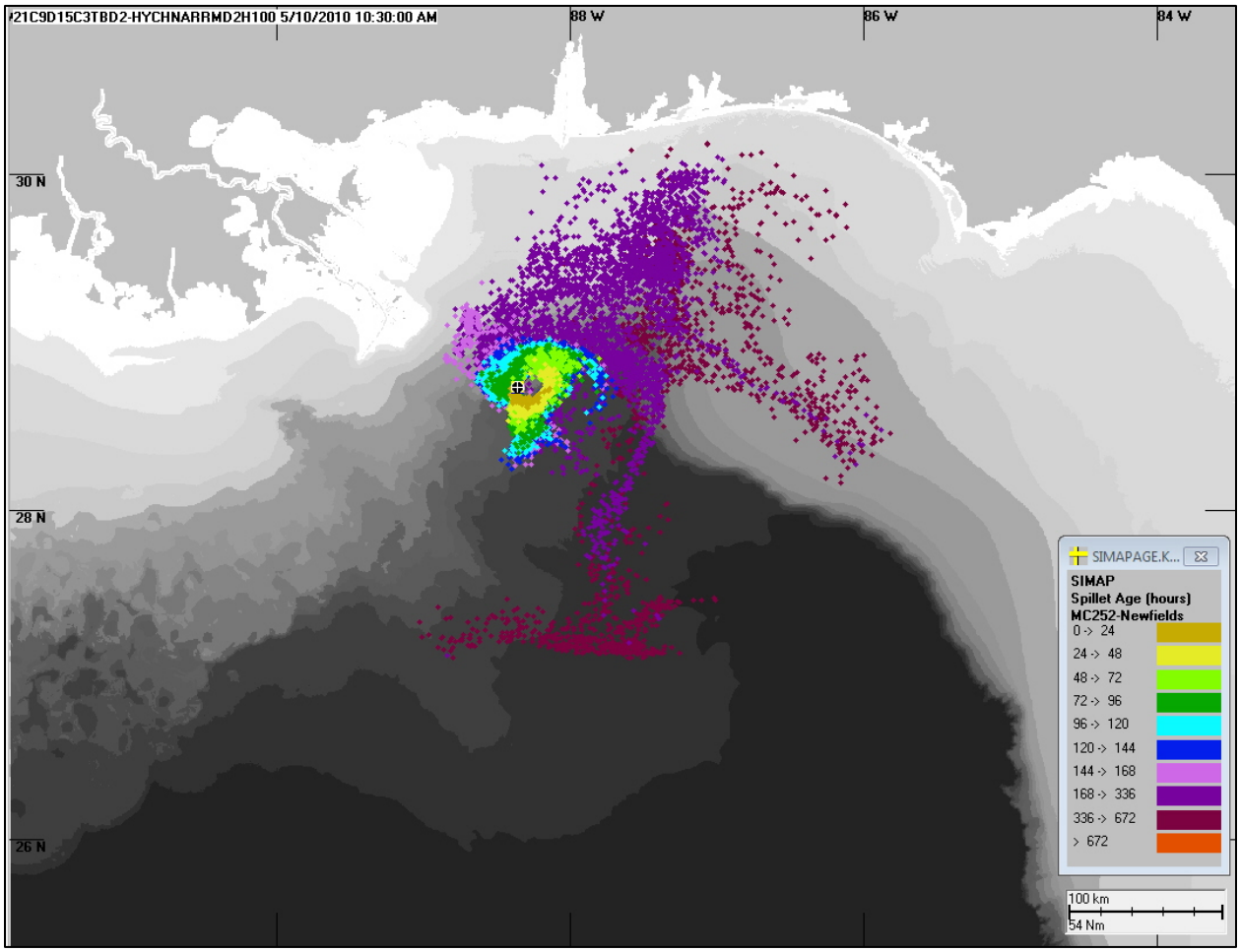

Figure C.1-2. Locations and age (hours since release) of floating oil spillets on May 10 (10:30 CDT).

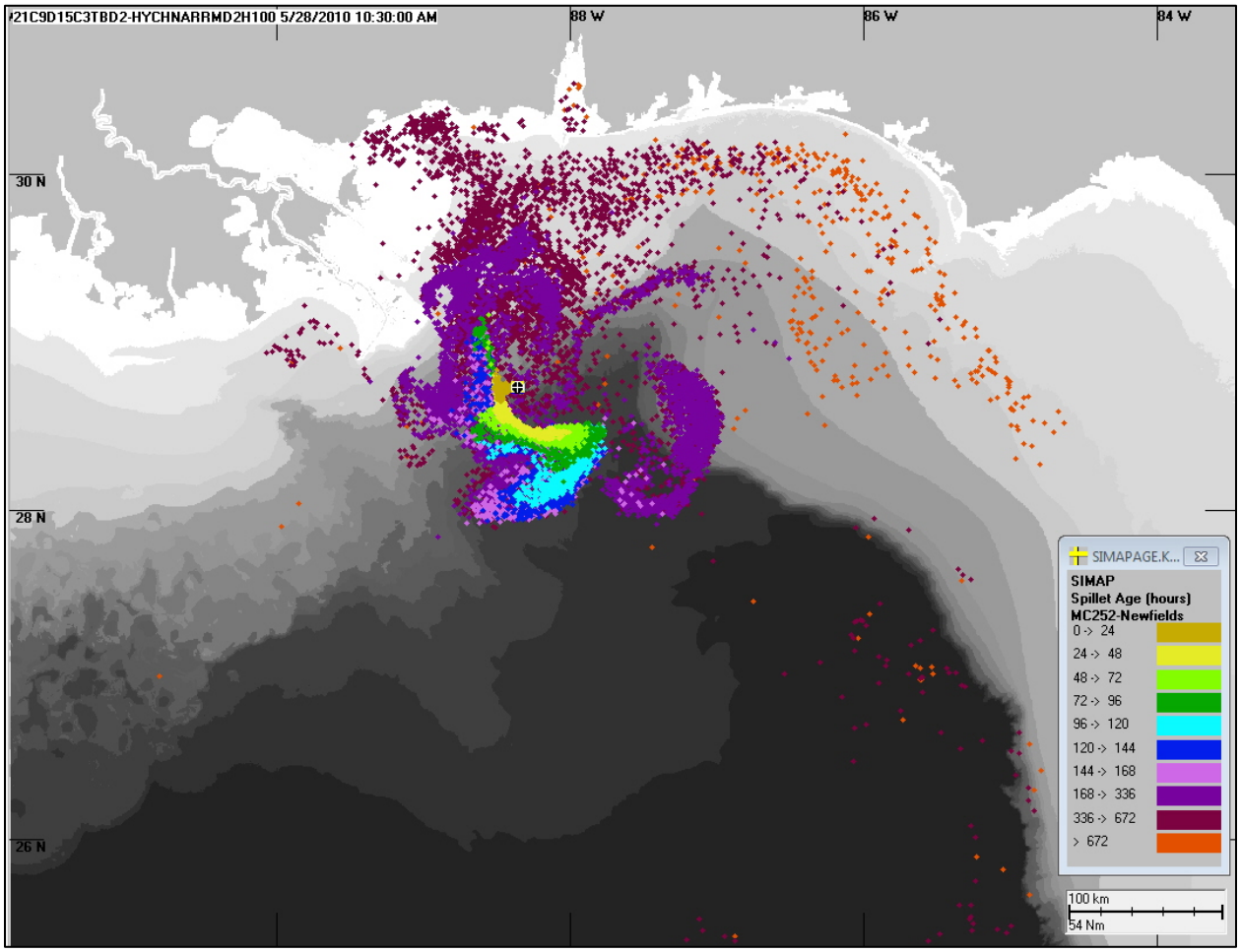

Figure C.1-3. Locations and age (hours since release) of floating oil spillets on May 28 (10:30 CDT).

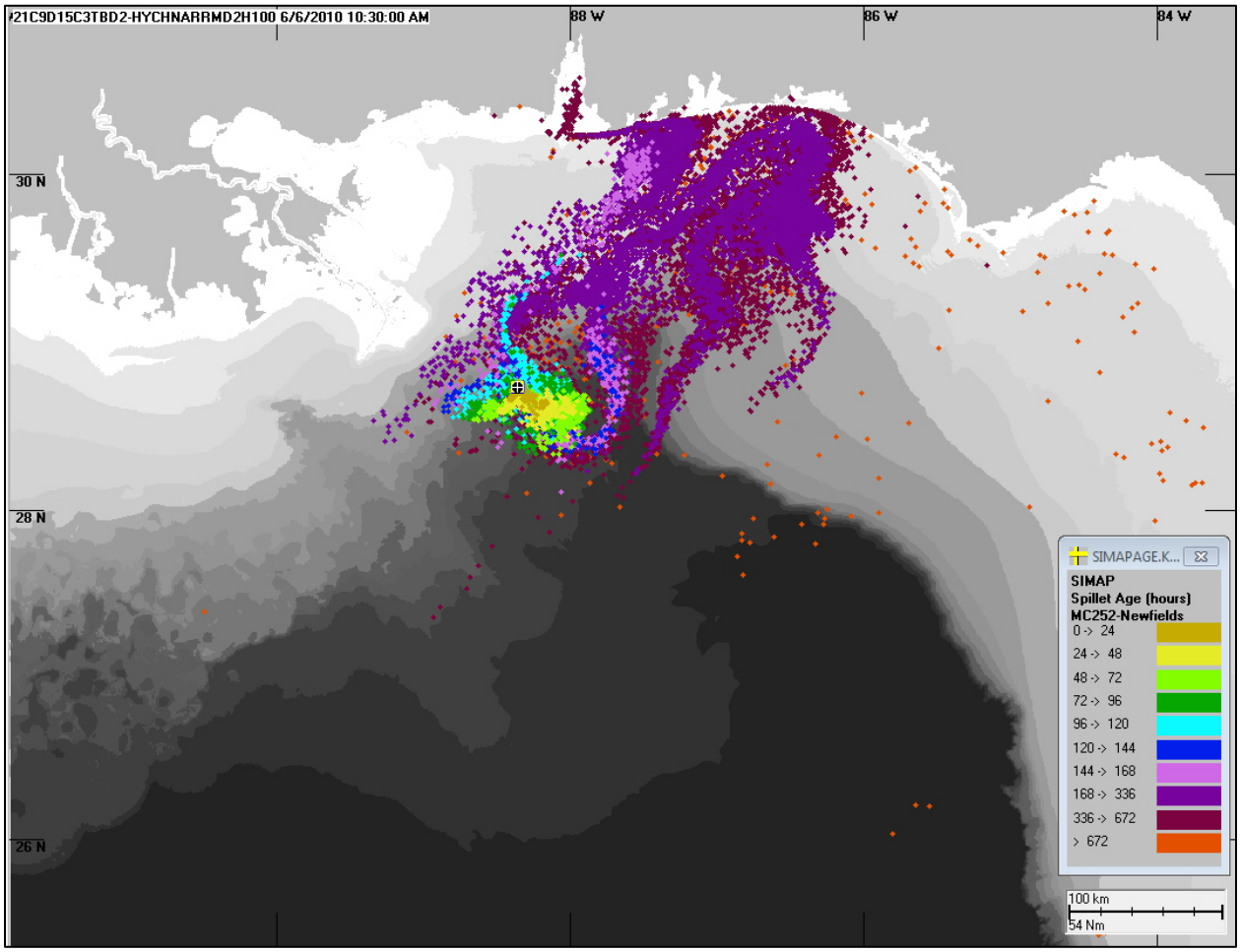

Figure C.1-4. Locations and age (hours since release) of floating oil spillets on June 6 (10:30 CDT).

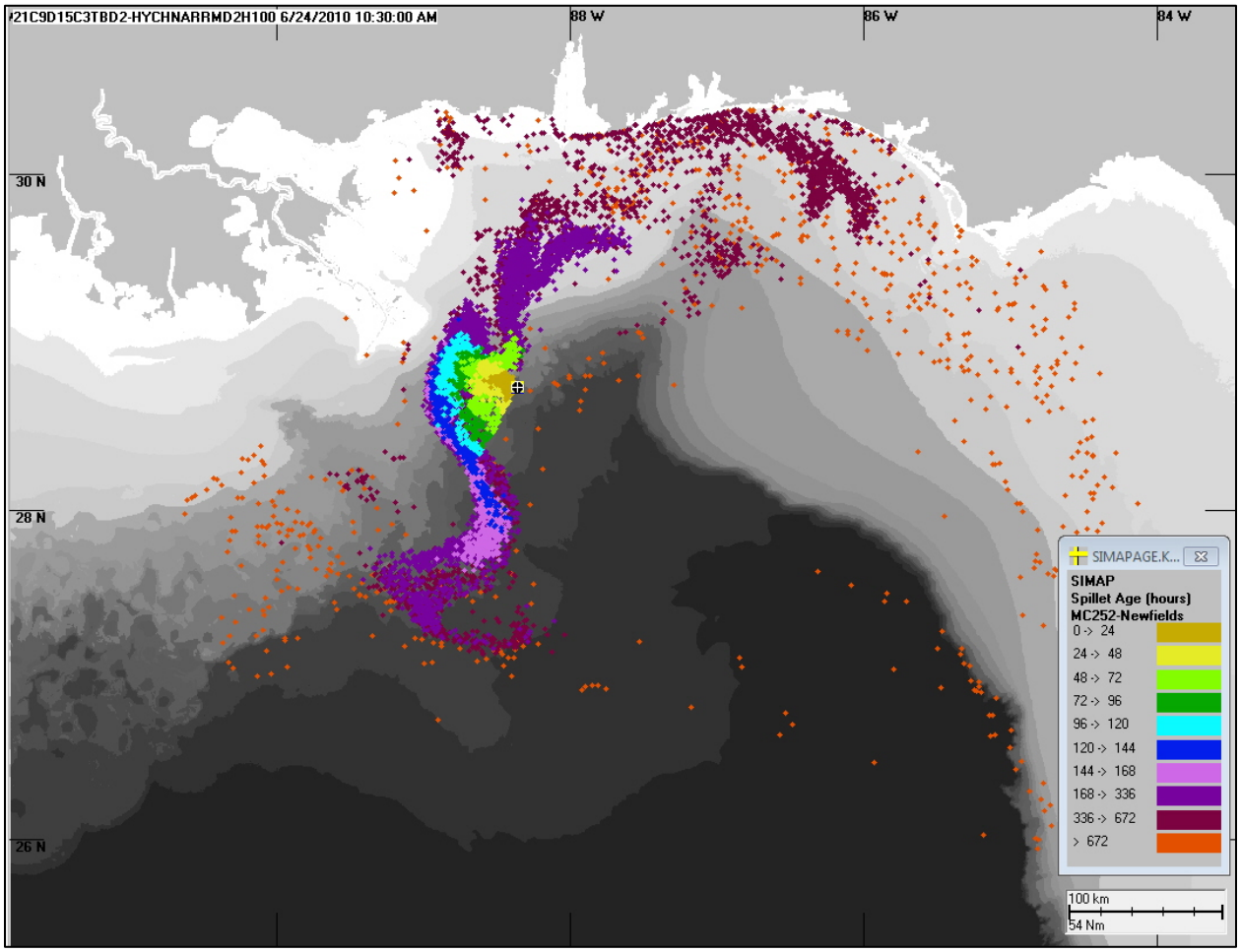

Figure C.1-5. Locations and age (hours since release) of floating oil spillets on June 24 (10:30 CDT).

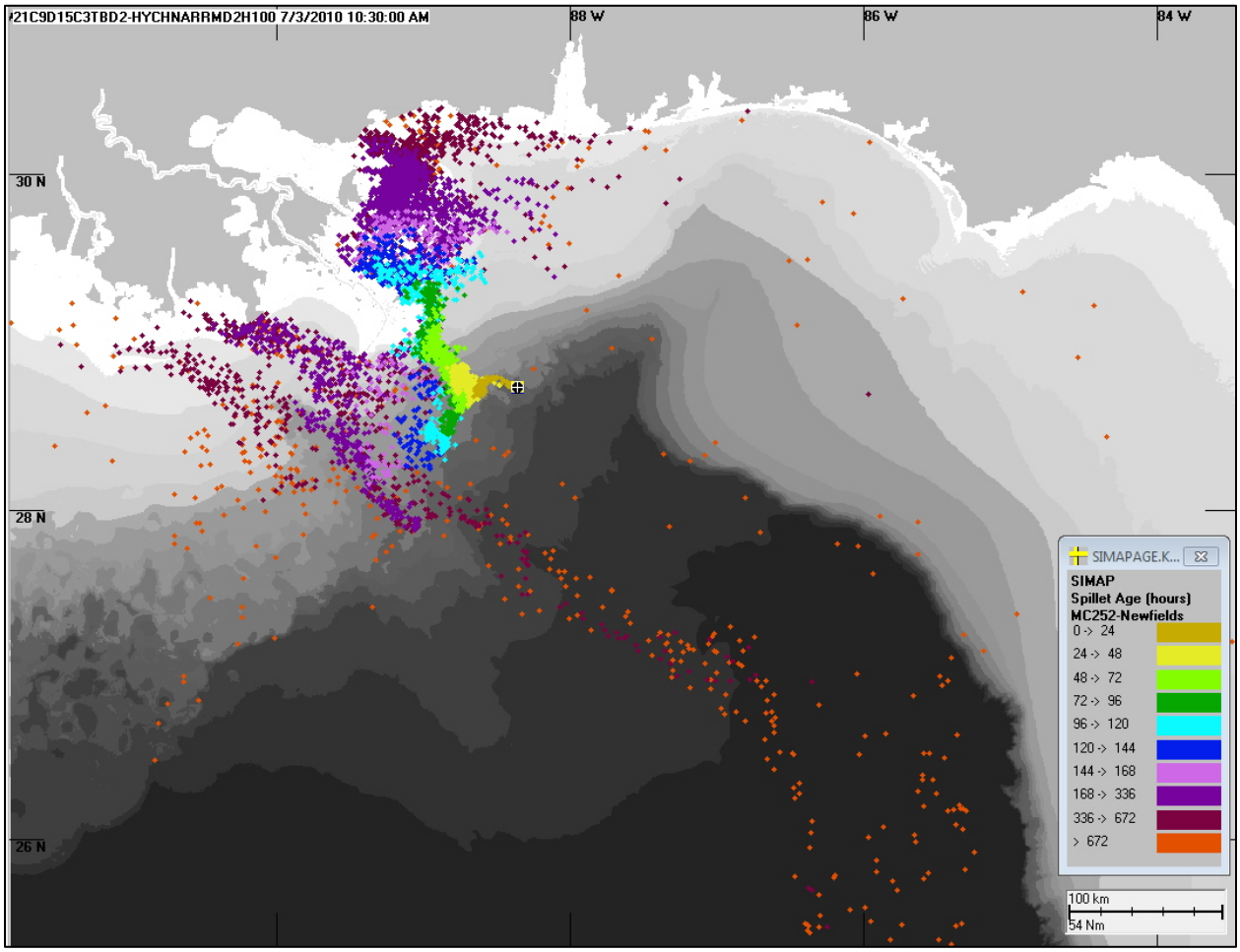

Figure C.1-6. Locations and age (hours since release) of floating oil spillets on July 3 (10:30 CDT).

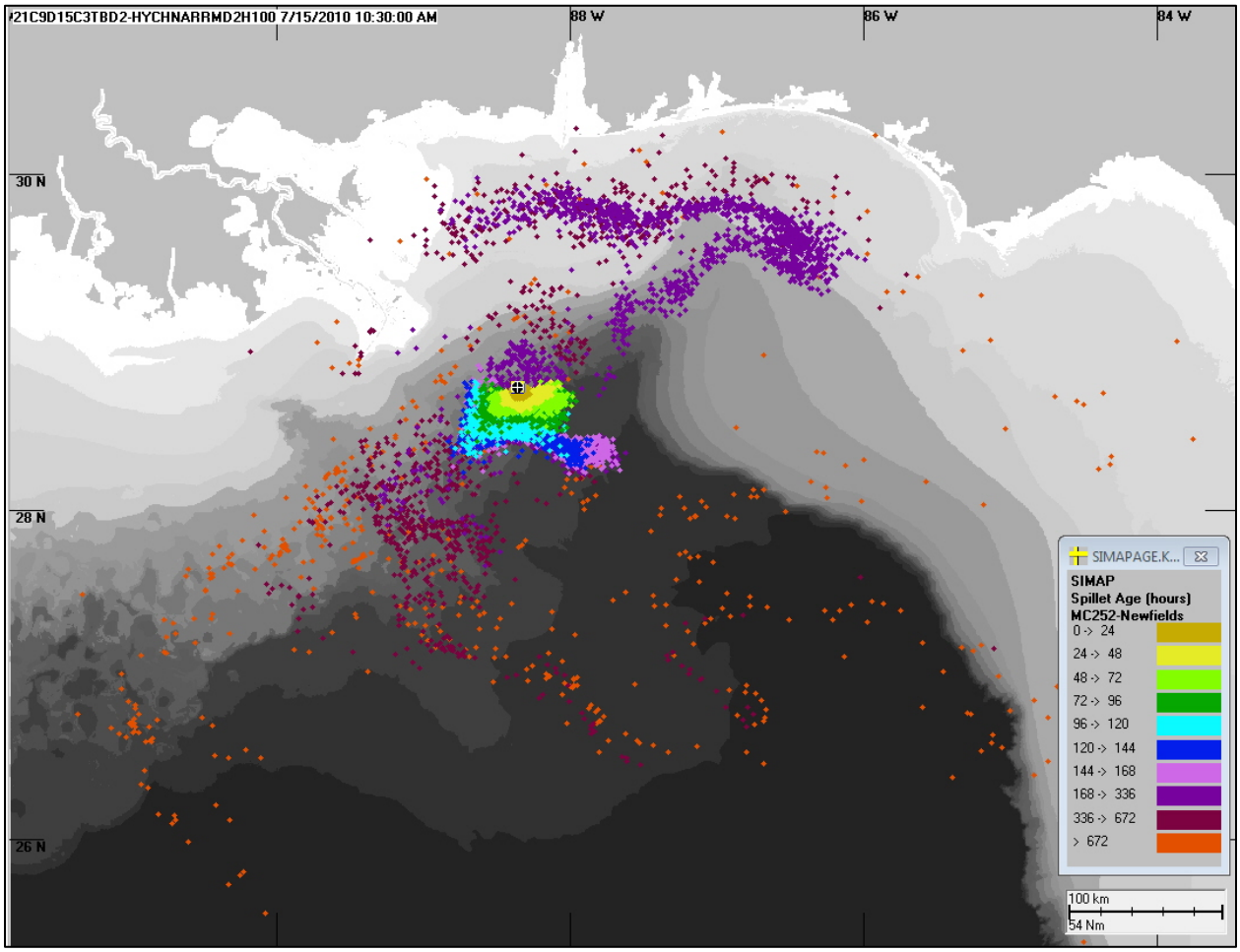

Figure C.1-7. Locations and age (hours since release) of floating oil spillets on July 15 (10:30 CDT).

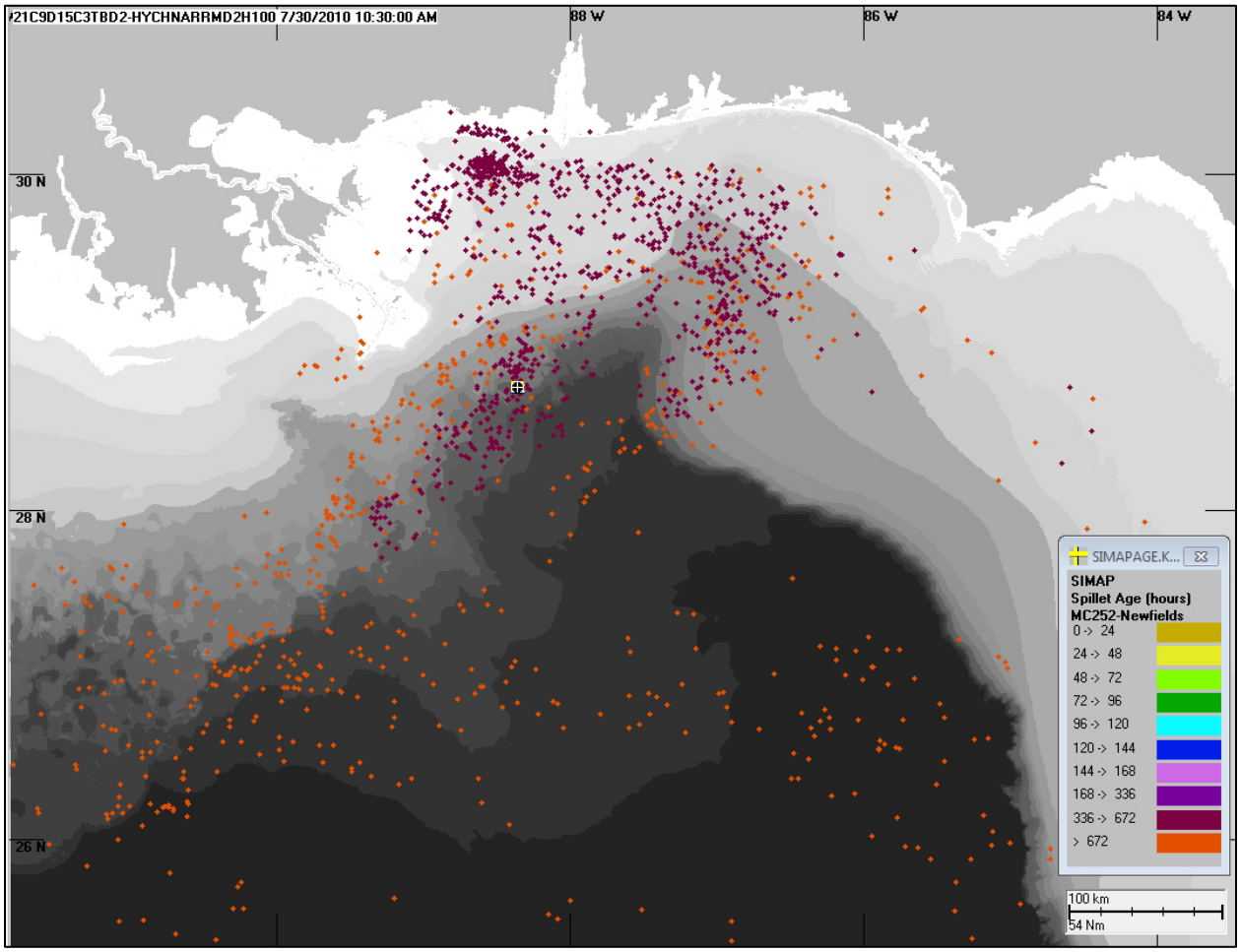

Figure C.1-8. Locations and age (hours since release) of floating oil spillets on July 30 (10:30 CDT).

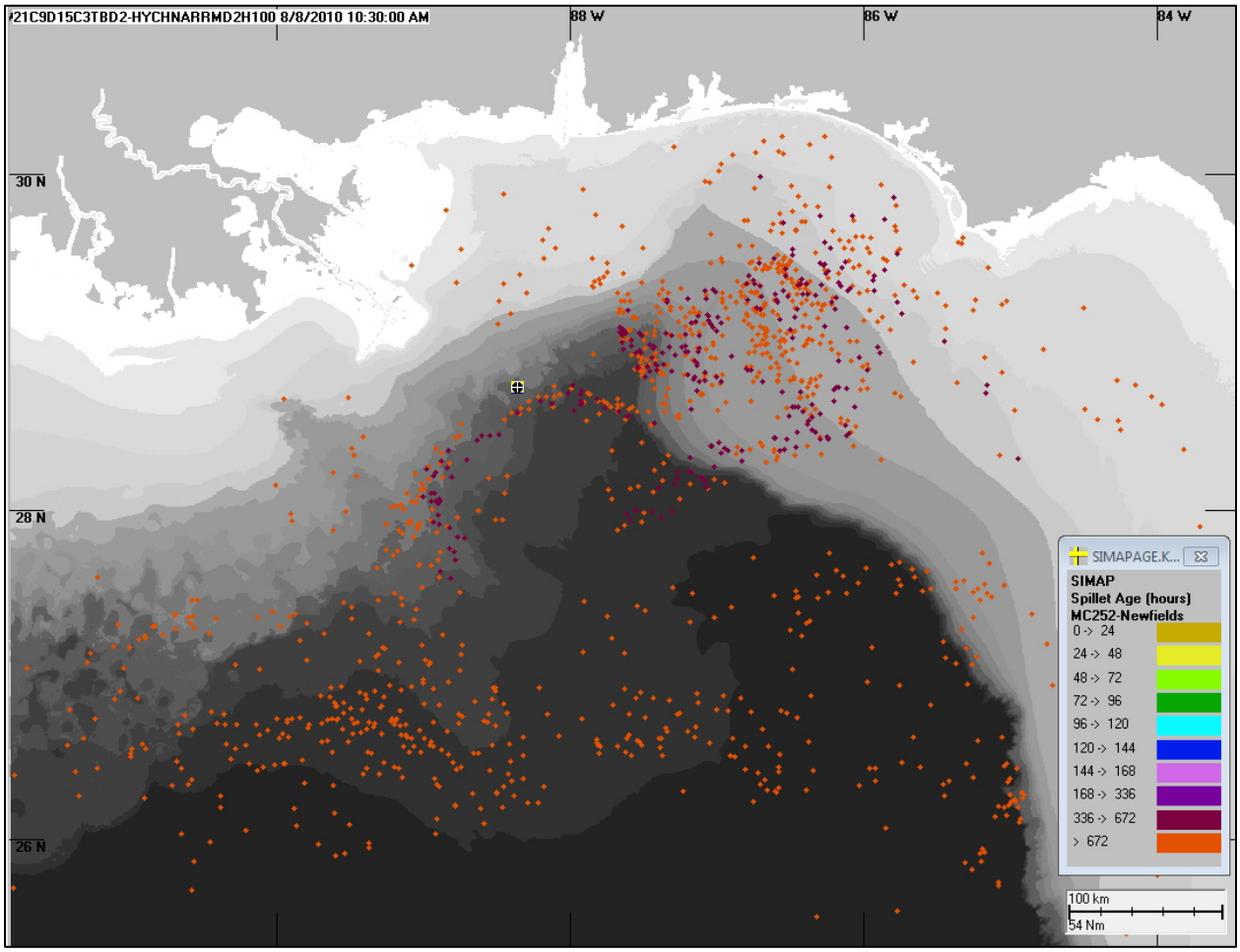

Figure C.1-9. Locations and age (hours since release) of floating oil spillets on August 8 (10:30 CDT).

C.2. Cumulative Exposure for Modeled Floating Oil Distributions

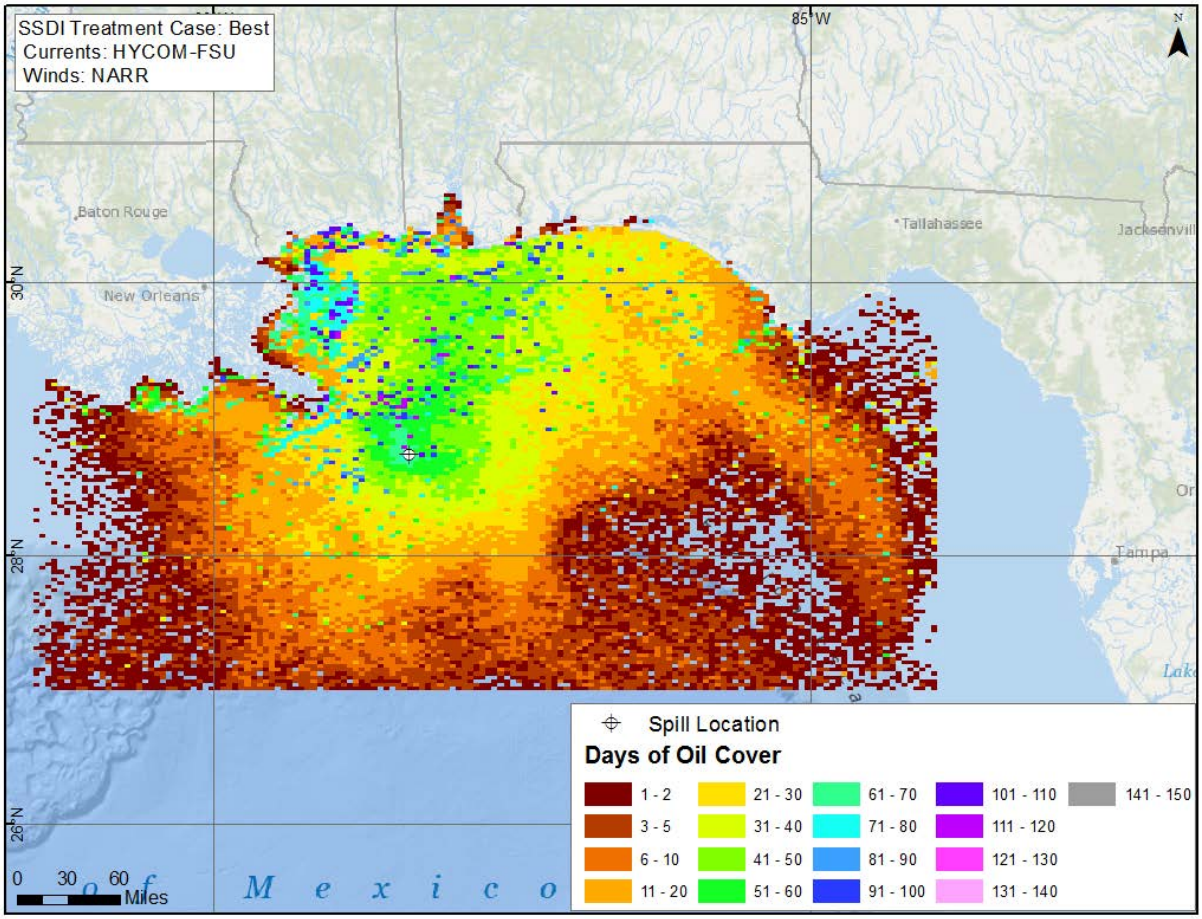

Figure C.2-1. Cumulative days of oil presence on the water surface, based on the base case model simulation.
Model simulation used SSDI, HYCOM-FSU currents and NARR winds.

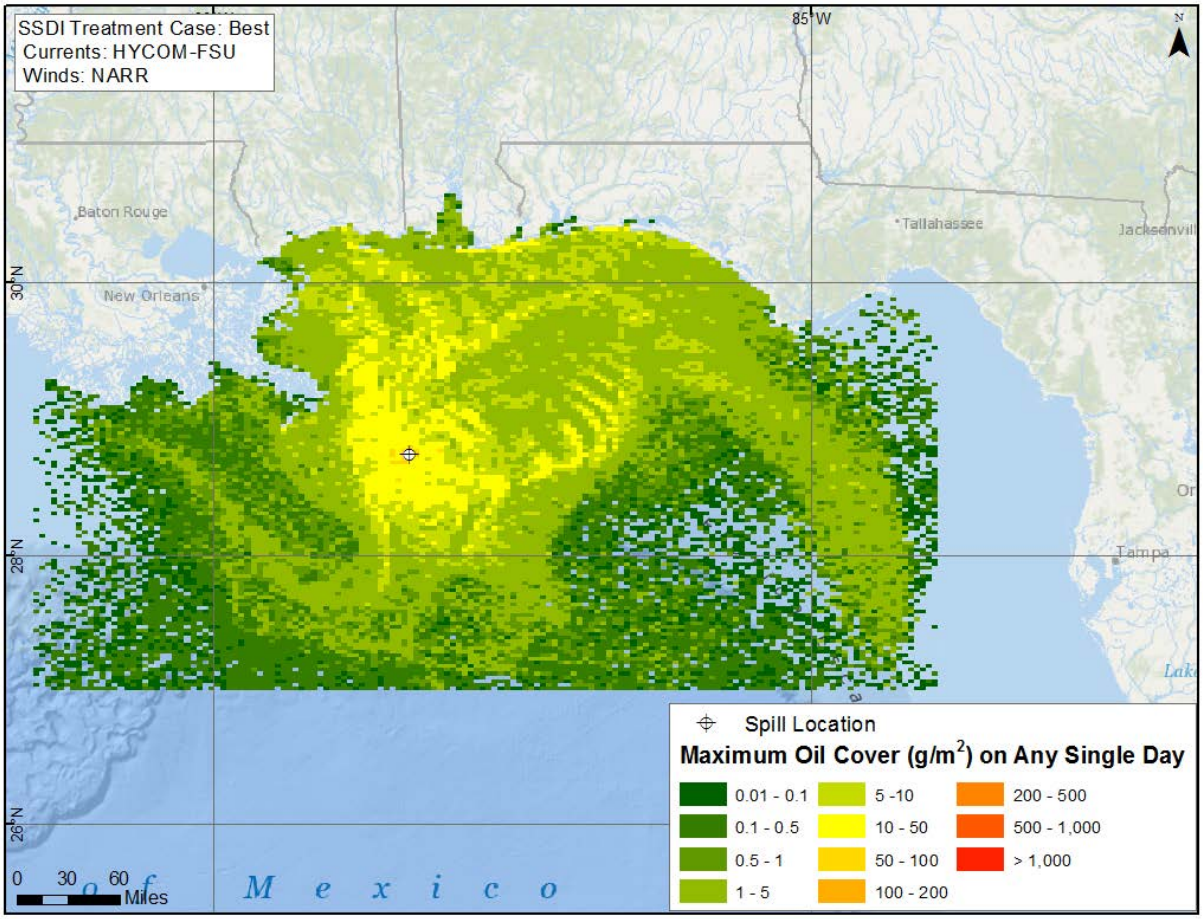

Figure C.2-2. Modeled maximum amount of oil in each grid cell at any time in the simulation based on the base case model run.
Gridded values are g/m^2 averaged over the cell. Model used SSDI, HYCOM-FSU currents and NARR winds.

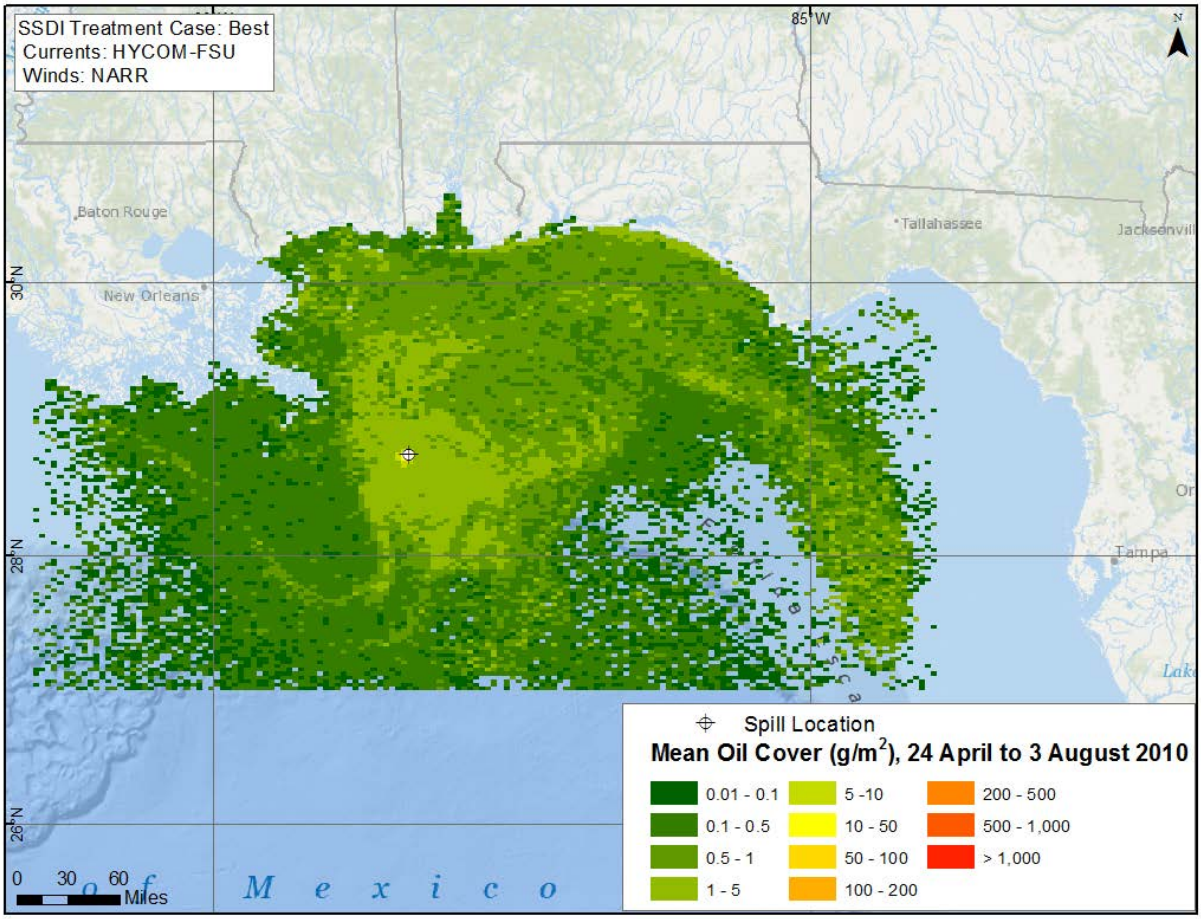

Figure C.2-3. Mean floating oil concentration (g/m^2) in each cell for the period when oil was observed by SAR, 24 April to 3 August 2010.
Base case model simulation with SSDI, HYCOM-FSU currents and NARR winds**.**

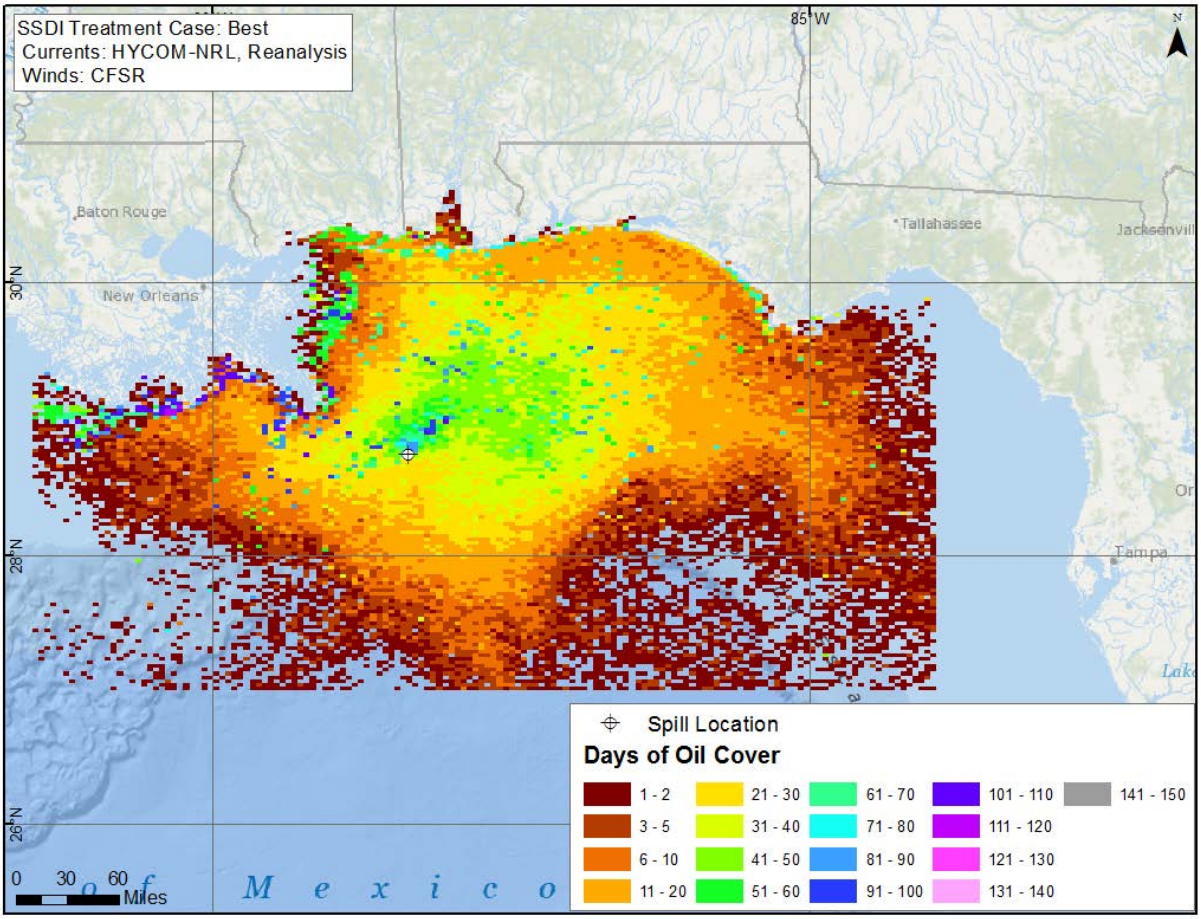

Figure C.2-4. Cumulative days of oil presence on the water surface.
Base model simulation with SSDI, HYCOM-NRL Reanalysis currents and CFSR winds.

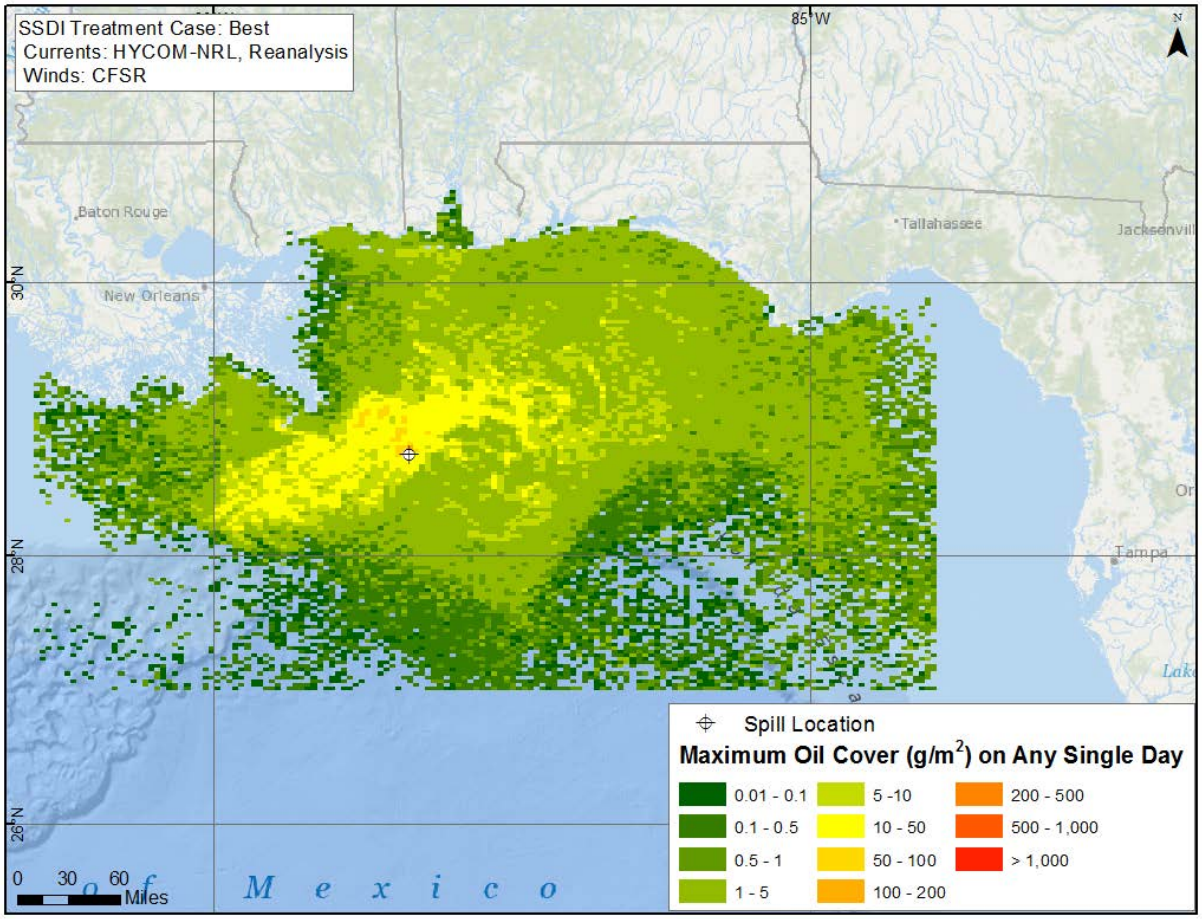

Figure C.2-5. Modeled maximum amount of oil in each grid cell at any time in the simulation. Grid values are g/m^2 averaged over the grid cell. Based on the model simulation with SSDI and using HYCOM-NRL, Reanalysis currents and CFSR winds.

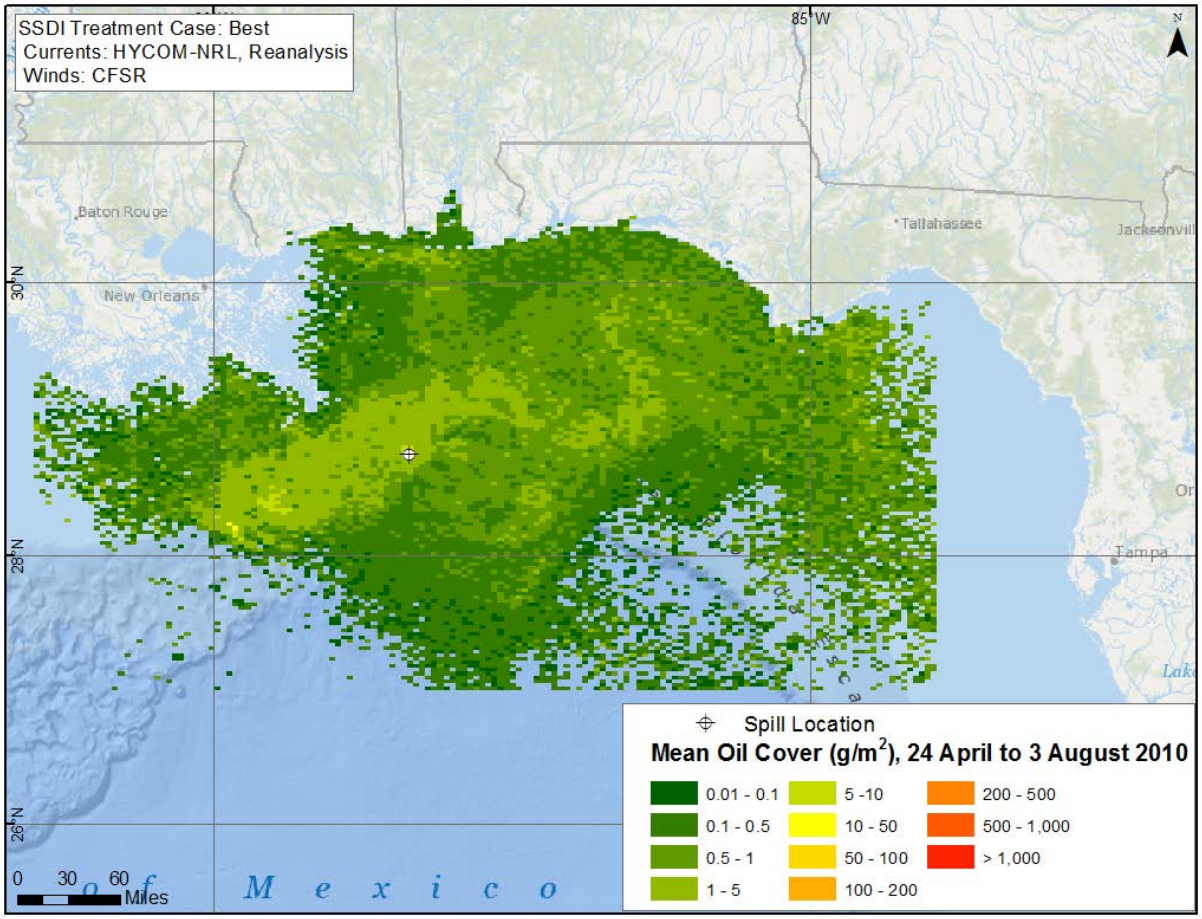

Figure C.2-6. Mean floating oil concentration (g/m^2) in each cell for the period when oil was observed by SAR, 24 April to 3 August 2010.
Based on the model simulation with SSDI and using HYCOM-NRL, Reanalysis currents and CFSR winds.

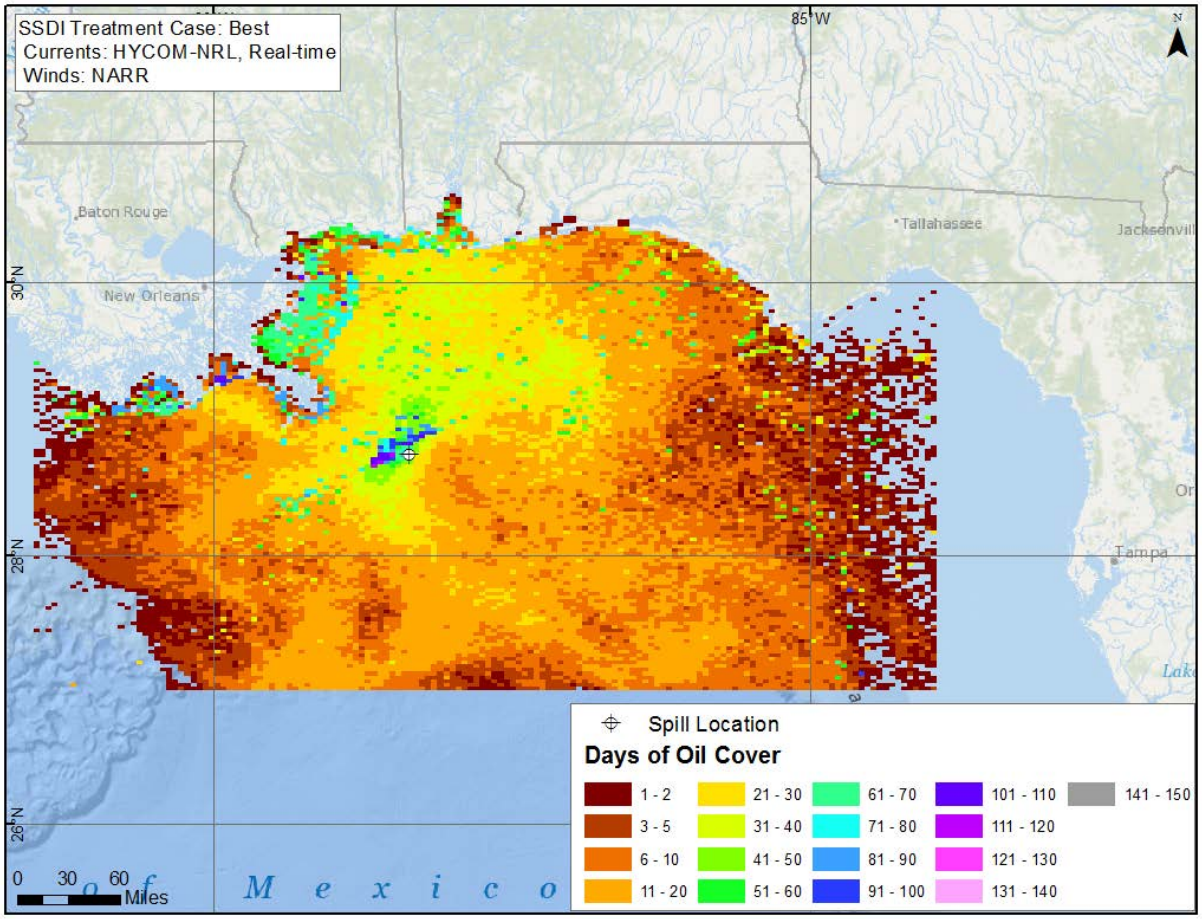

Figure C.2-7. Cumulative days of oil presence on the water surface.
Based on the model simulation with SSDI and using HYCOM-NRL, Real-time currents and NARR winds.

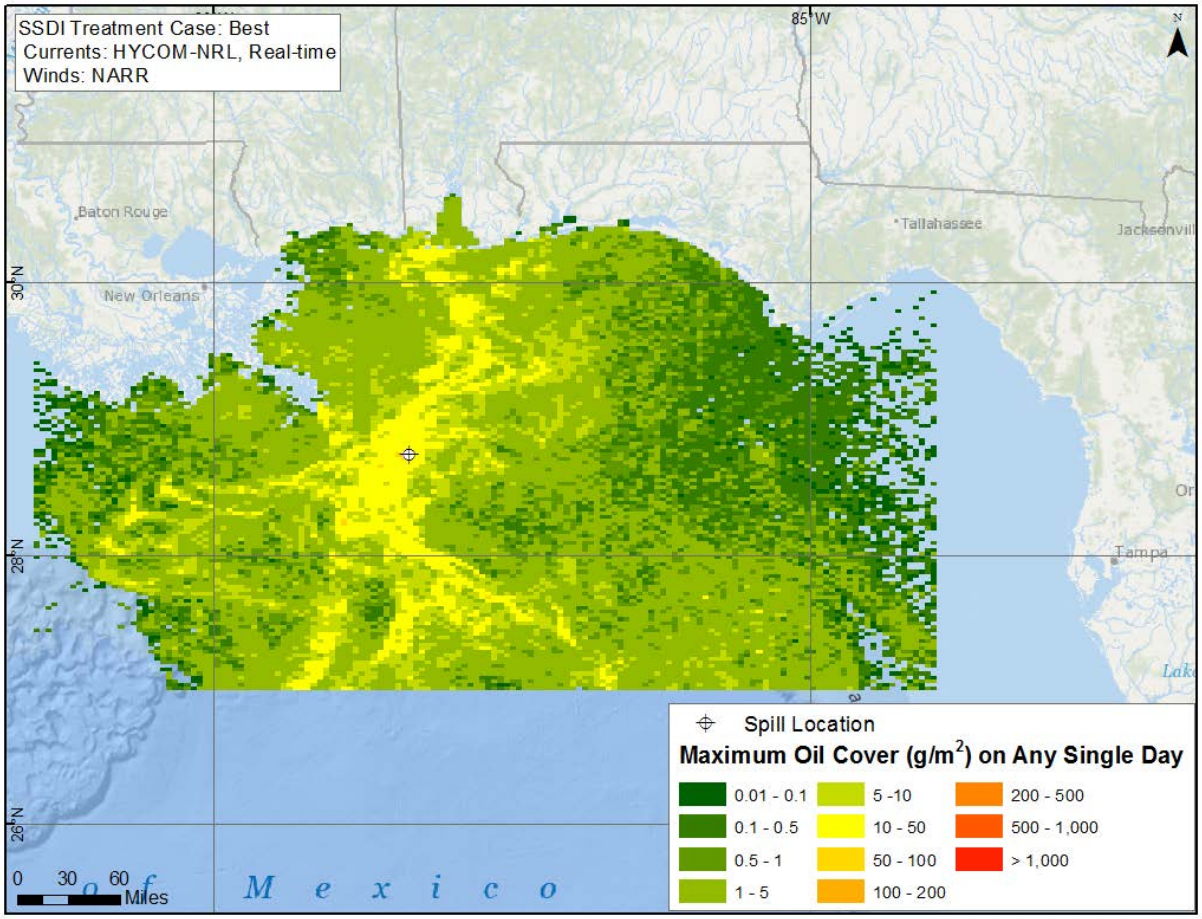

Figure C.2-8. Modeled maximum amount of oil in each grid cell at any time in the simulation. Grid values are g/m^2 averaged over the grid cell. Based on the model simulation with SSDI and using HYCOM-NRL, Real-time currents and NARR winds.

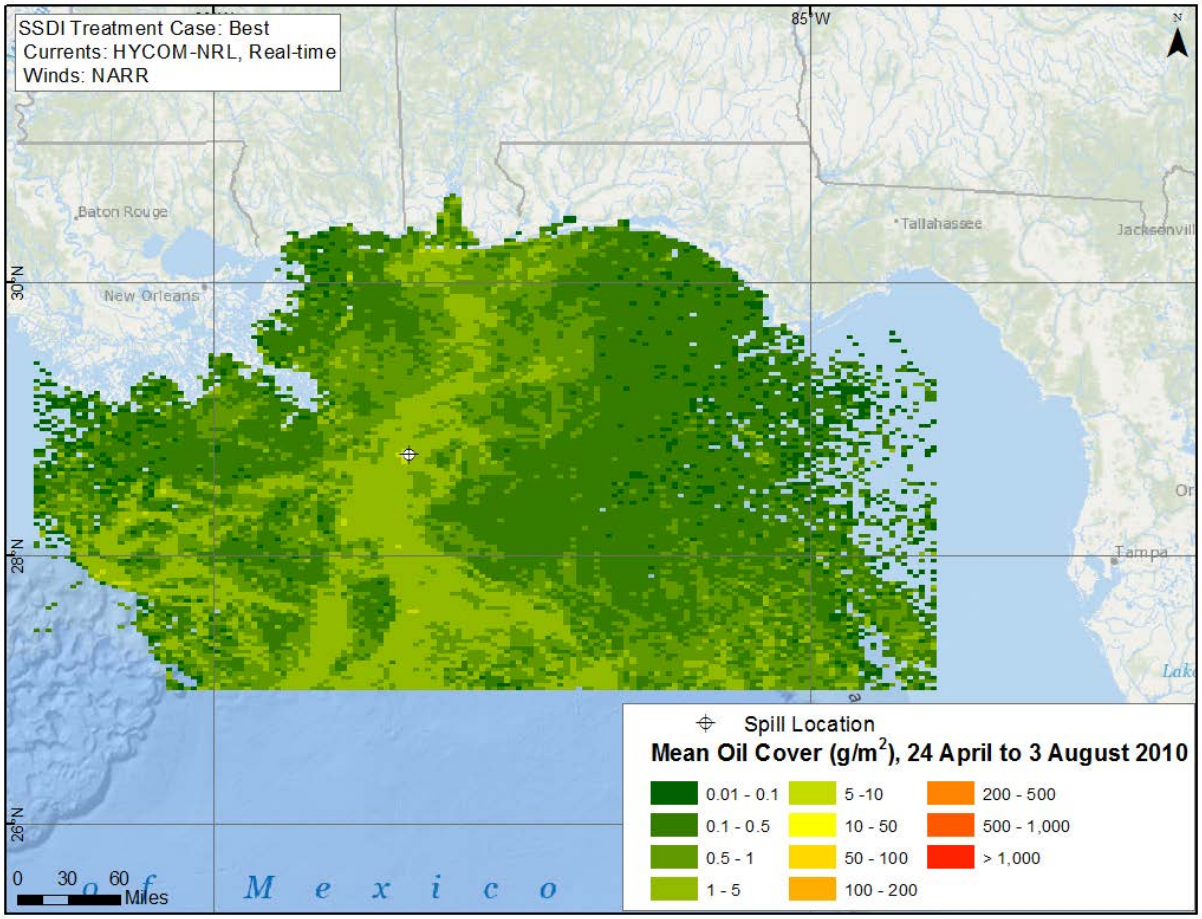

Figure C.2-9. Mean floating oil concentration (g/m^2) in each cell for the period when oil was observed by SAR, 24 April to 3 August 2010.
Based on the model simulation with SSDI and using HYCOM-NRL, Real-time currents and NARR winds.

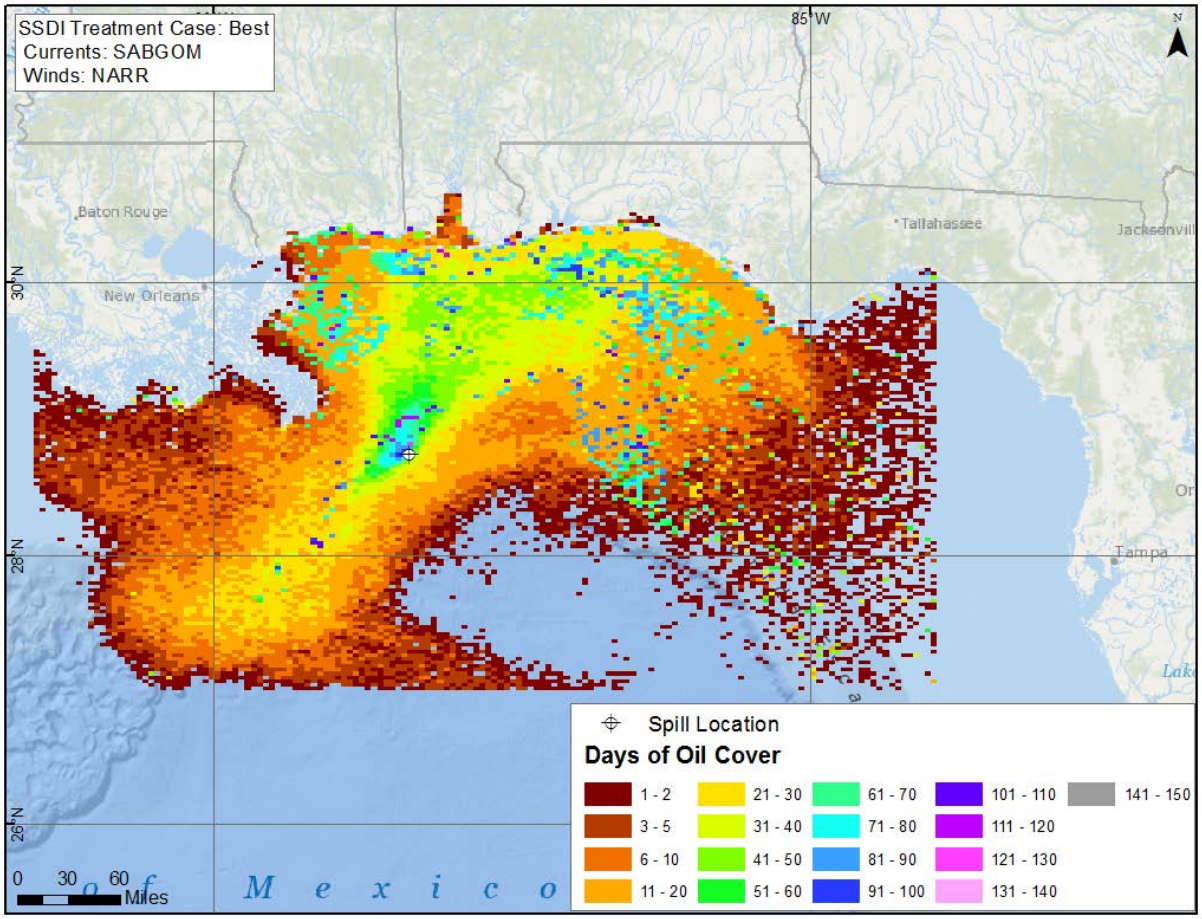

Figure C.2-10. Cumulative days of oil presence on the water surface.
Based on the model simulation with SSDI and using SABGOM currents and NARR winds.

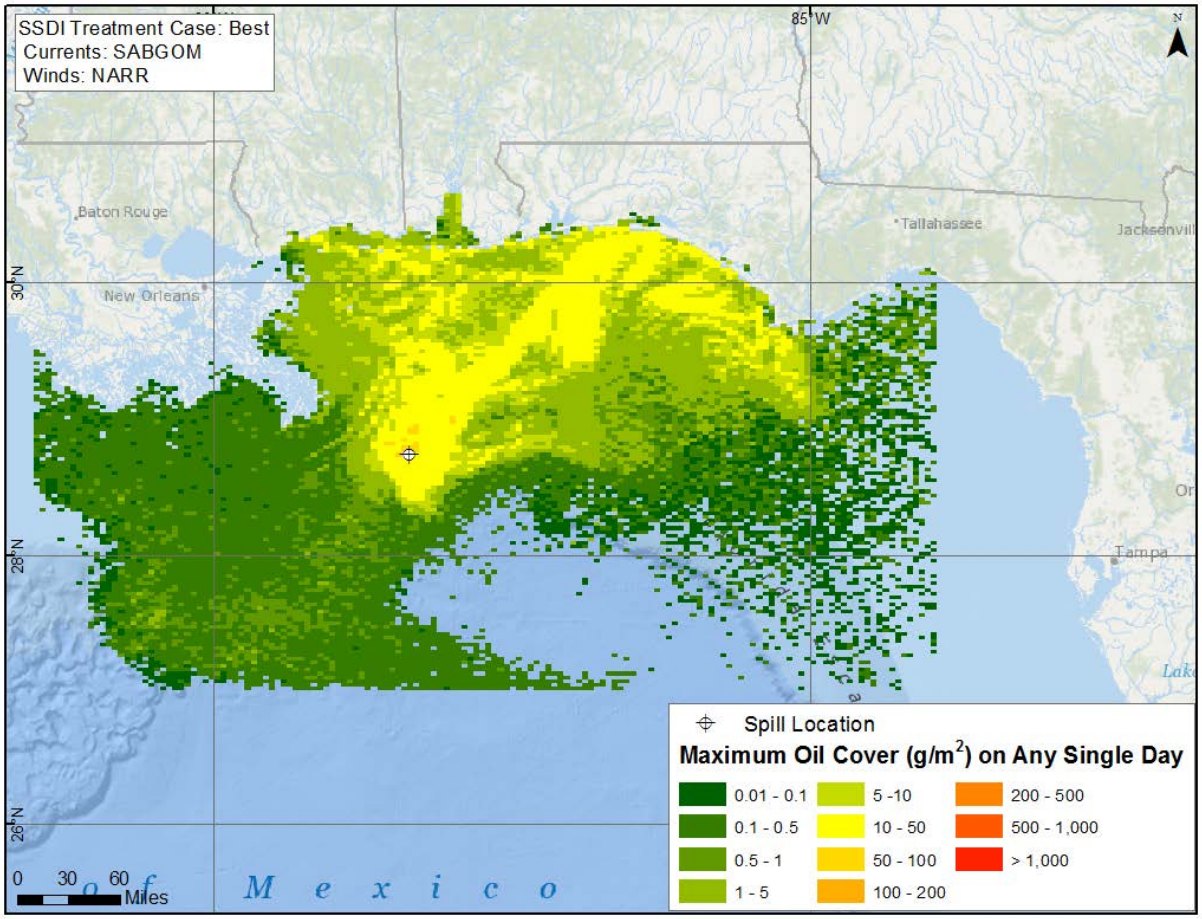

Figure C.2-11. Modeled maximum amount of oil in each grid cell at any time in the simulation. Grid values are g/m^2 averaged over the grid cell. Based on the model simulation with SSDI and using SABGOM currents and NARR winds.

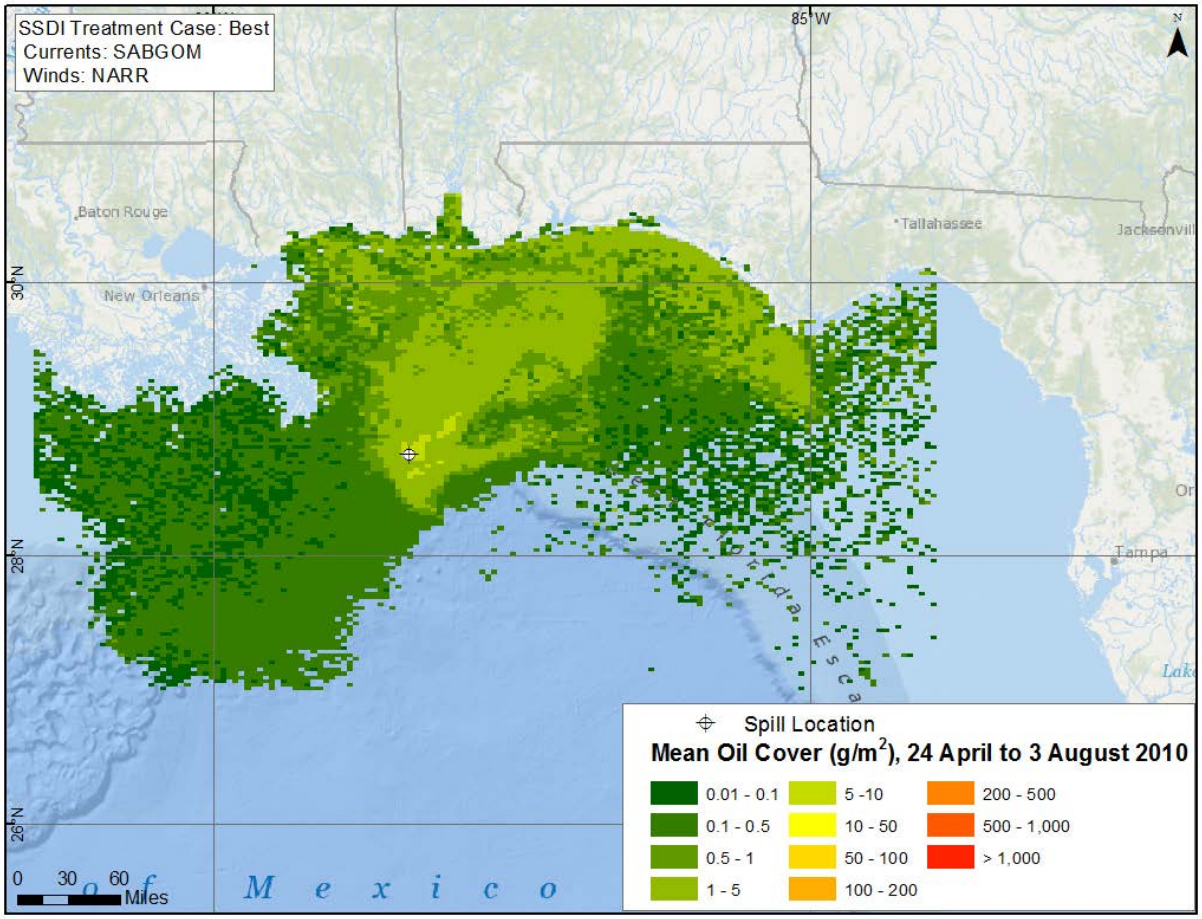

Figure C.2-12. Mean floating oil concentration (g/m^2) in each cell for the period when oil was observed by SAR, 24 April to 3 August 2010.
Based on the model simulation with SSDI and using SABGOM currents and NARR winds.

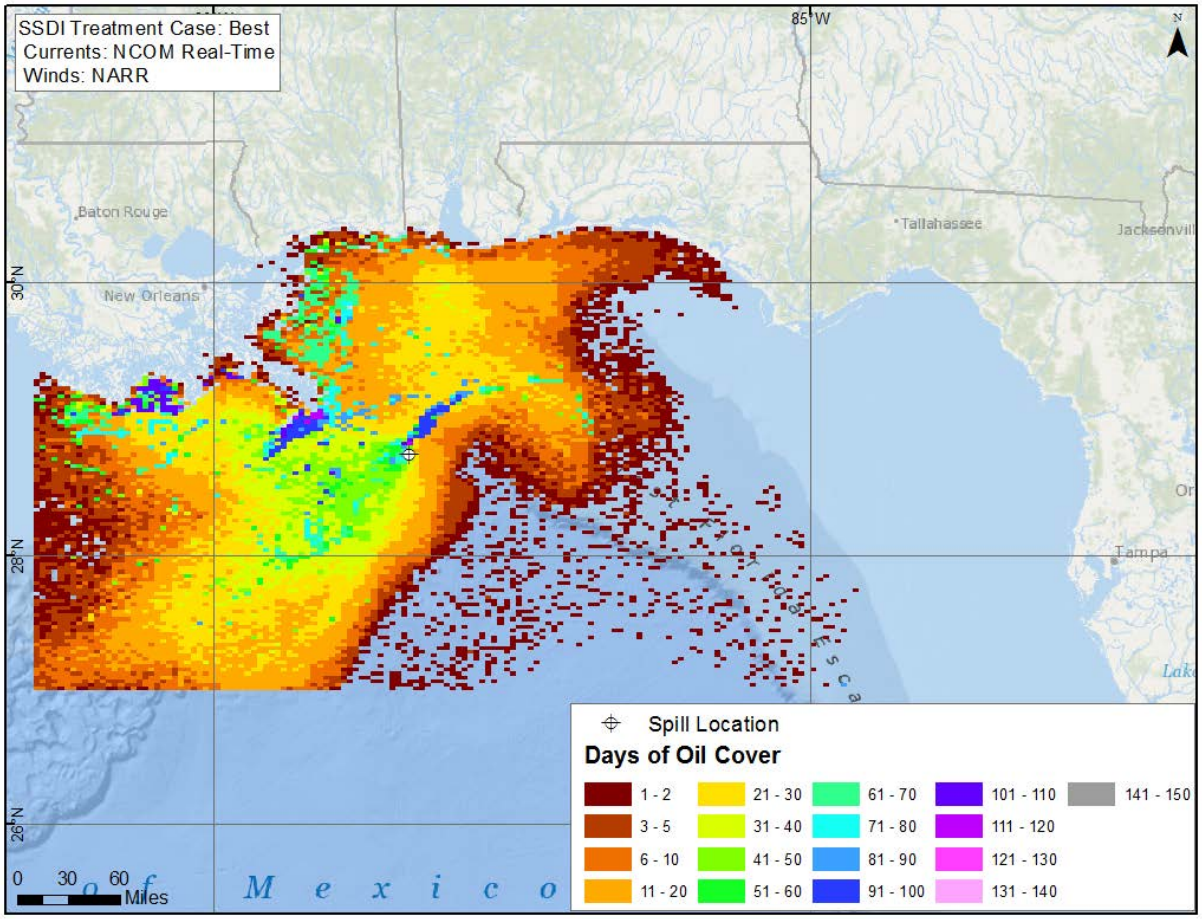

Figure C.2-13. Cumulative days of oil presence on the water surface.
Based on the model simulation with SSDI and using NCOM Real-time currents and NARR winds.

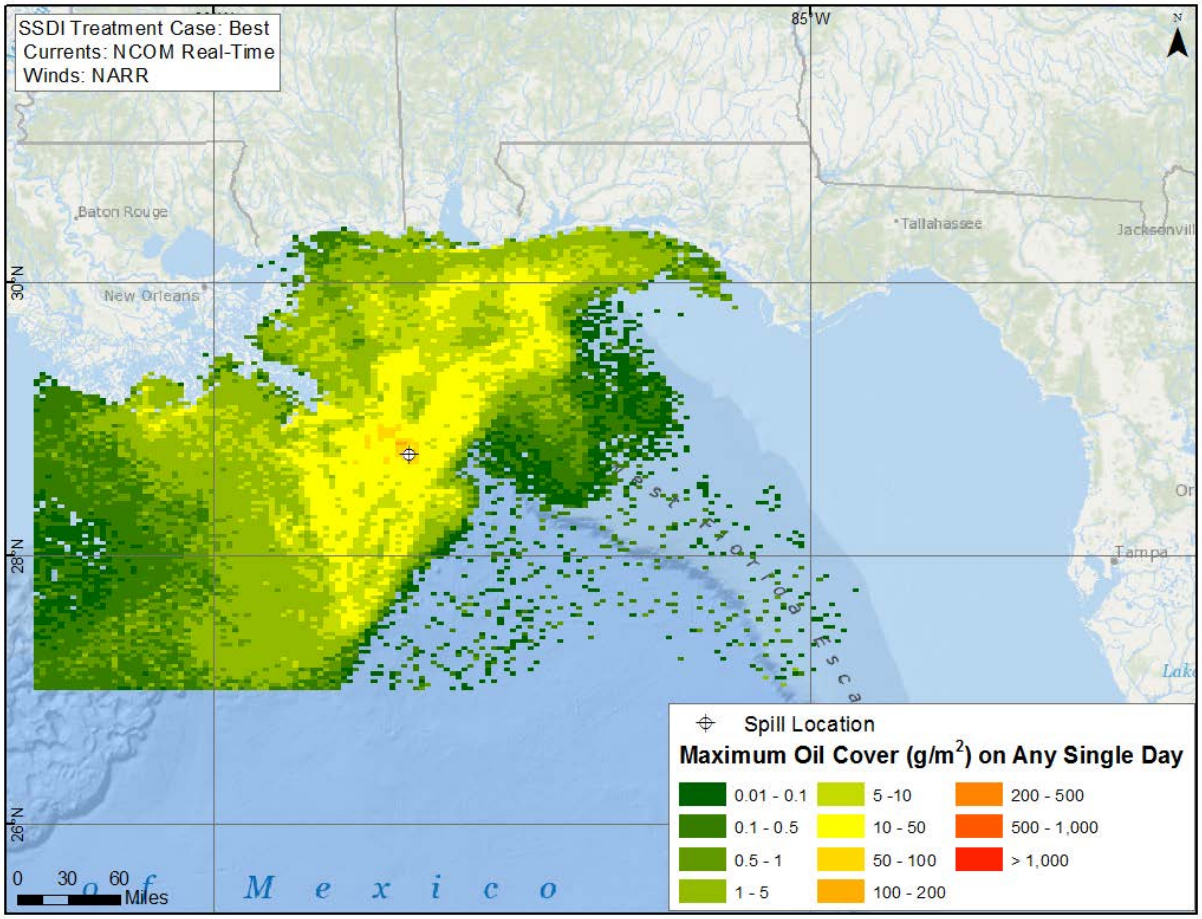

Figure C.2-14. Modeled maximum amount of oil in each grid cell at any time in the simulation. Grid values are g/m^2 averaged over the grid cell. Based on the model simulation with SSDI and using NCOM Real-time currents and NARR winds.

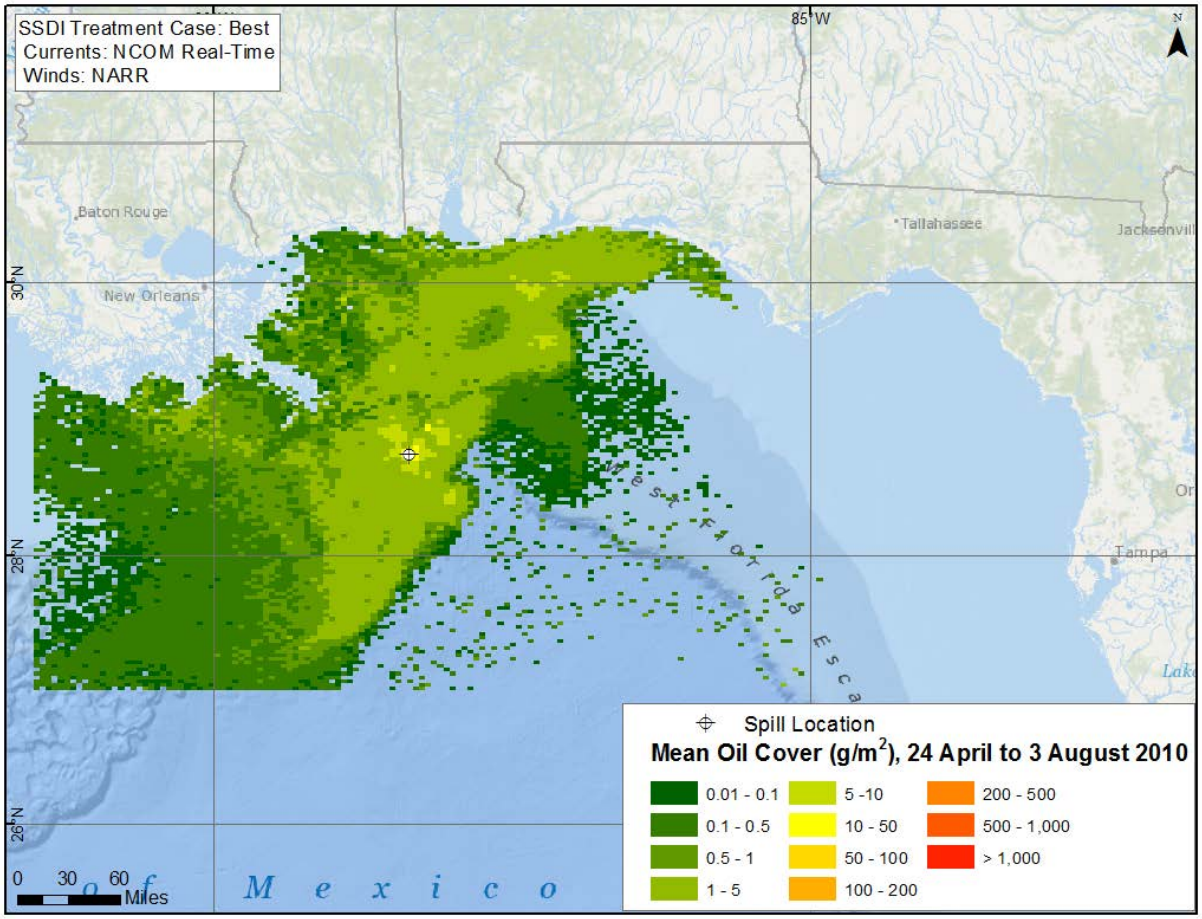

Figure C.2-15. Mean floating oil concentration (g/m^2) in each cell for the period when oil was observed by SAR, 24 April to 3 August 2010.
Based on the model simulation with SSDI and using NCOM Real-time currents and NARR winds.

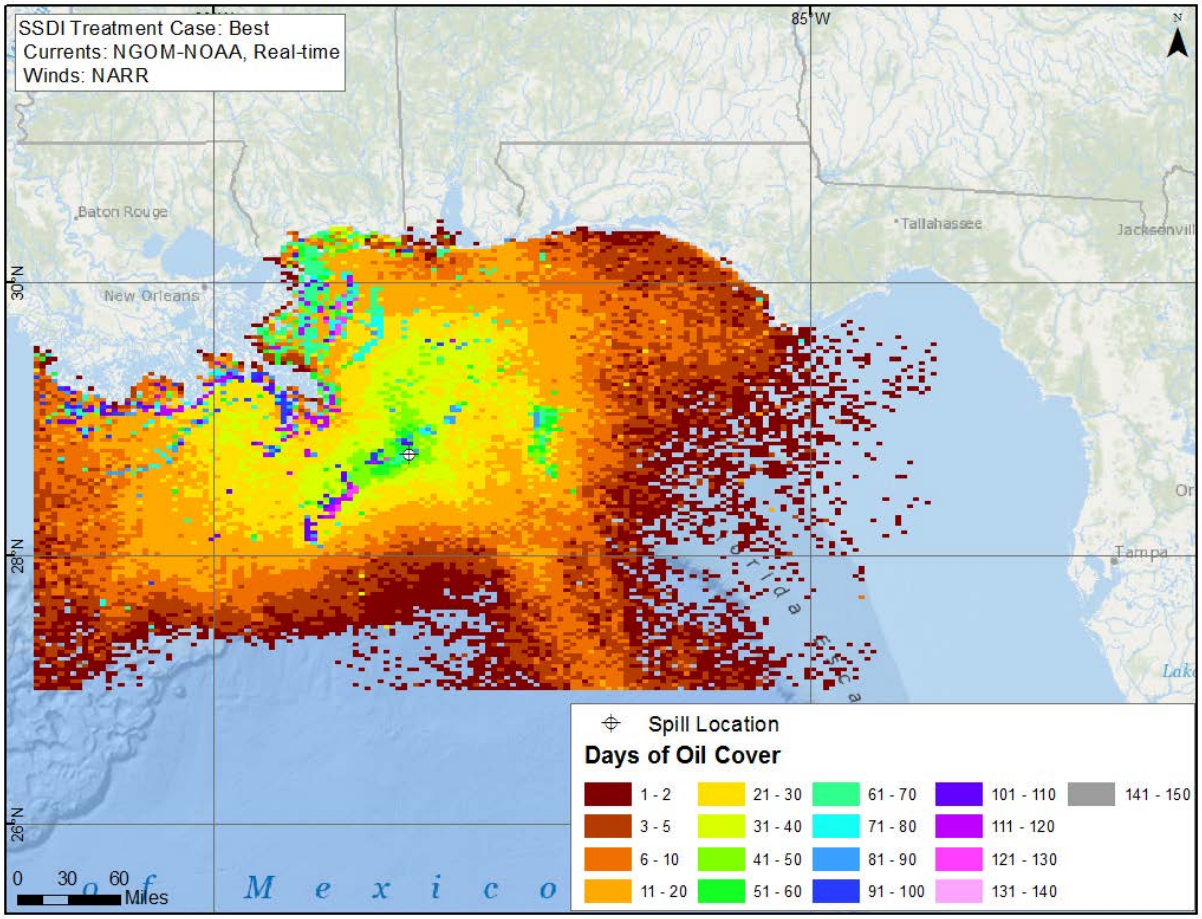

Figure C.2-16. Cumulative days of oil presence on the water surface.
Based on the model simulation with SSDI and using NGOM currents and NARR winds.

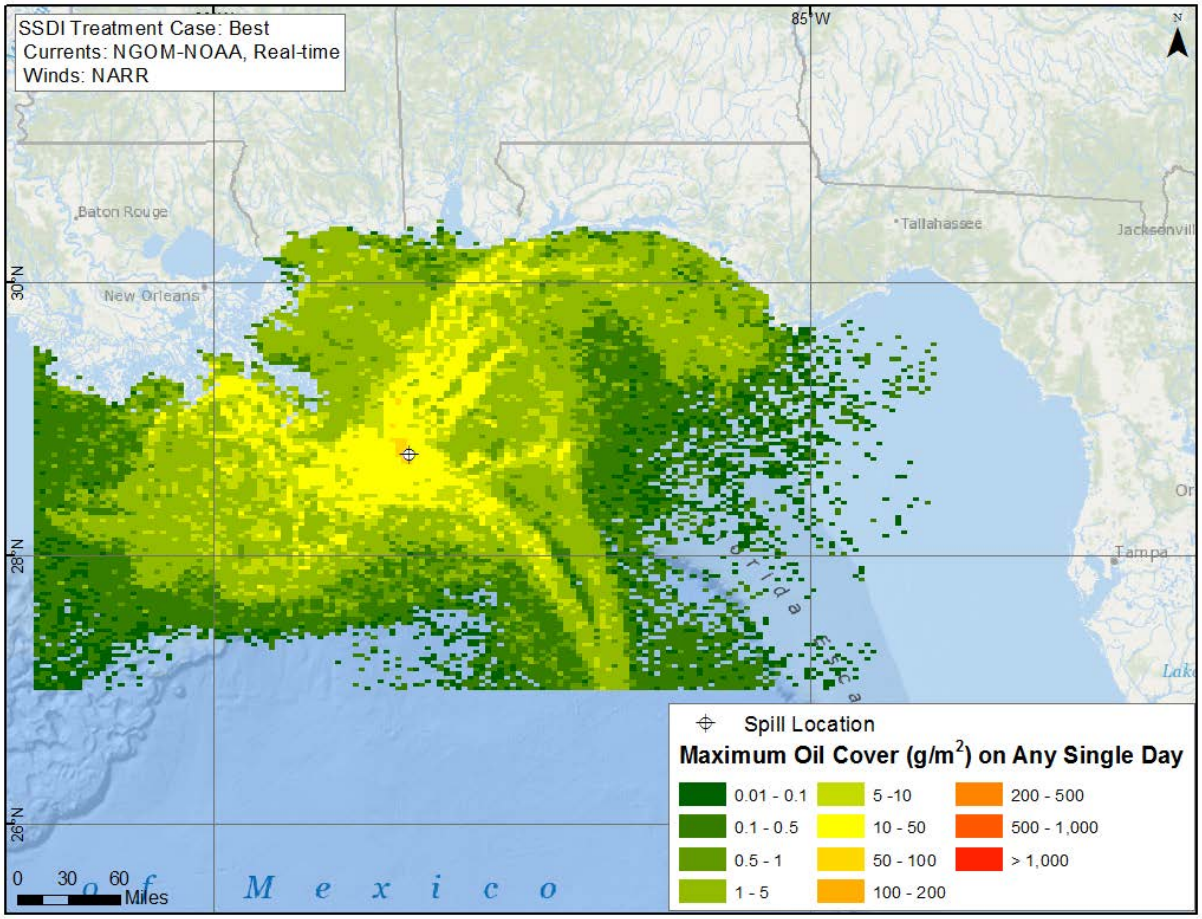

Figure C.2-17. Modeled maximum amount of oil in each grid cell at any time in the simulation. Grid values are g/m^2 averaged over the grid cell.
Based on the model simulation with SSDI and using NGOM currents and NARR winds.

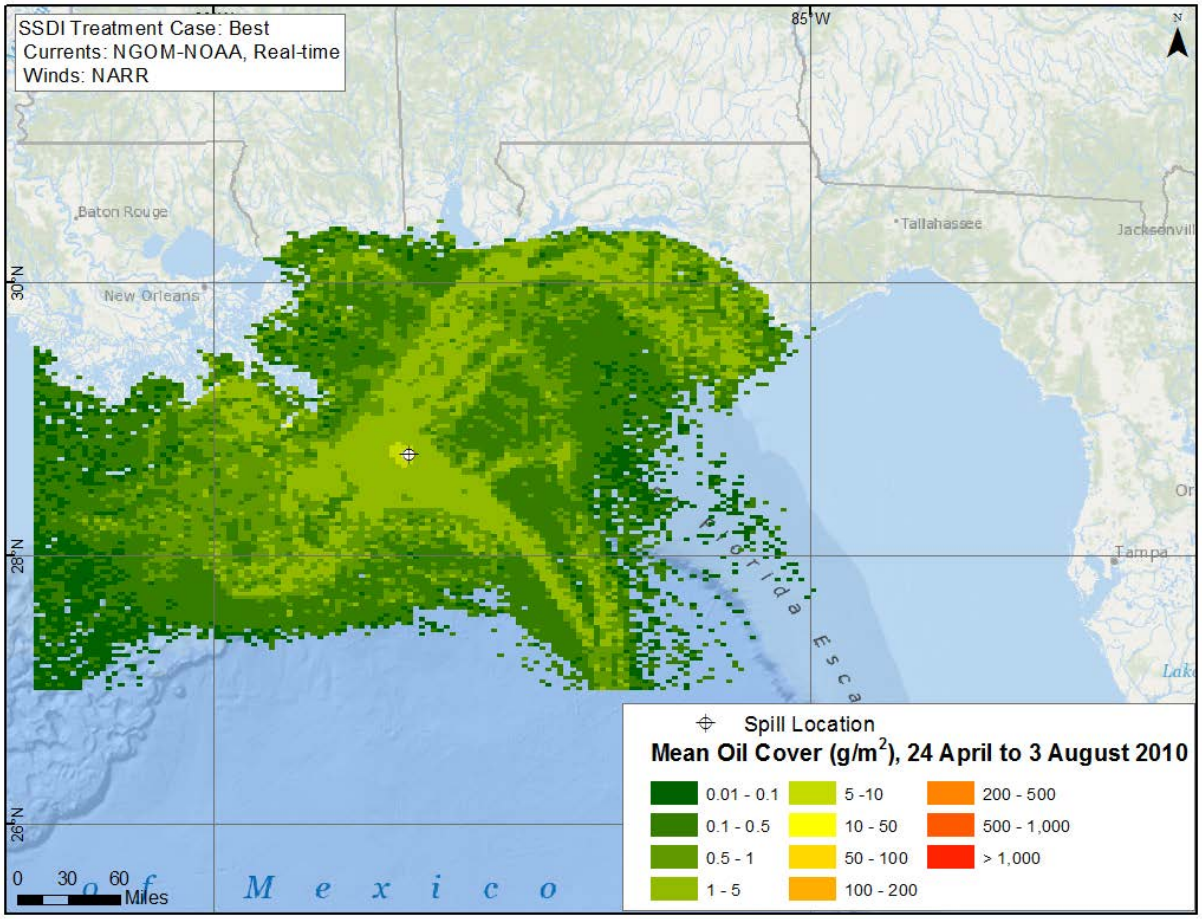

Figure C.2-18. Mean floating oil concentration (g/m^2) in each cell for the period when oil was observed by SAR, 24 April to 3 August 2010.
Based on the model simulation with SSDI and using NGOM currents and NARR winds.

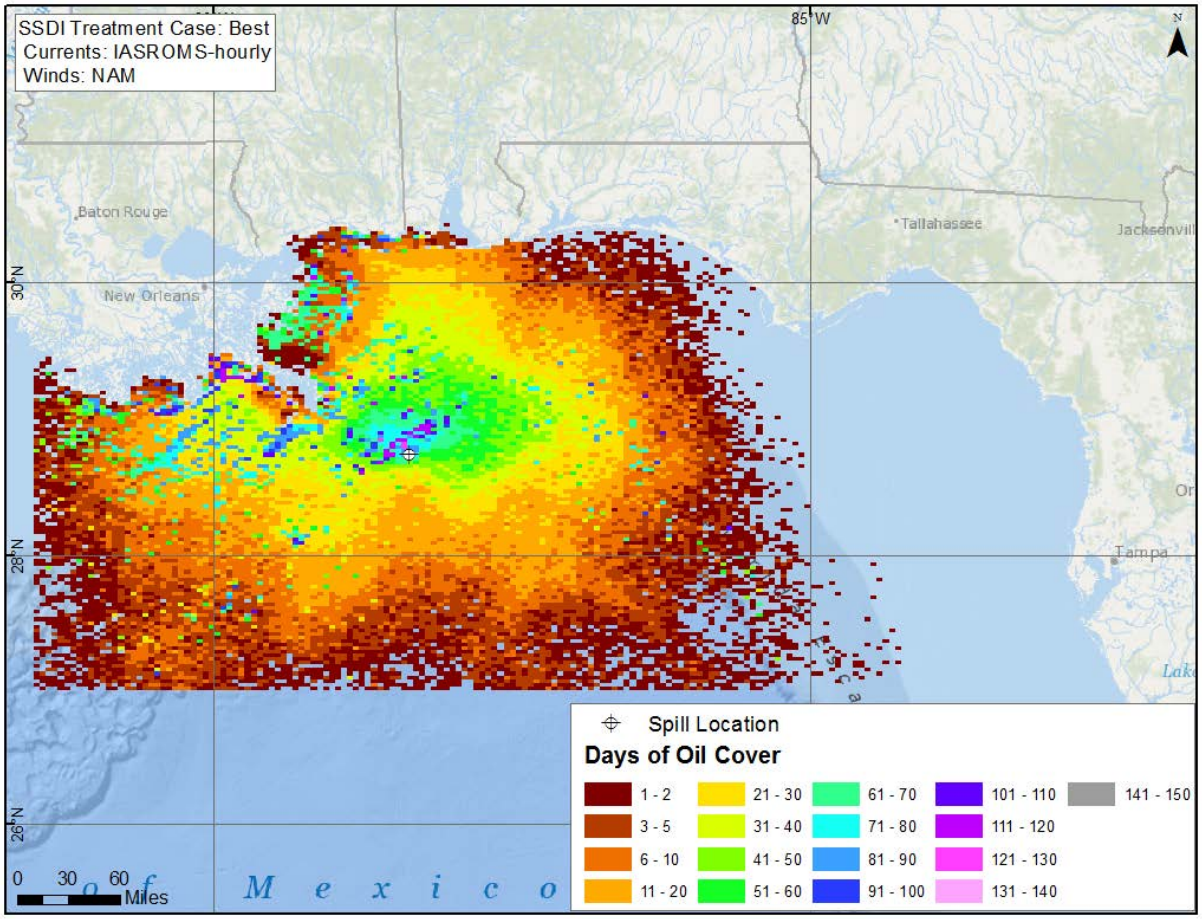

Figure C.2-19. Cumulative days of oil presence on the water surface.
Based on the model simulation with SSDI and using IAS ROMS-hourly currents and NARR winds.

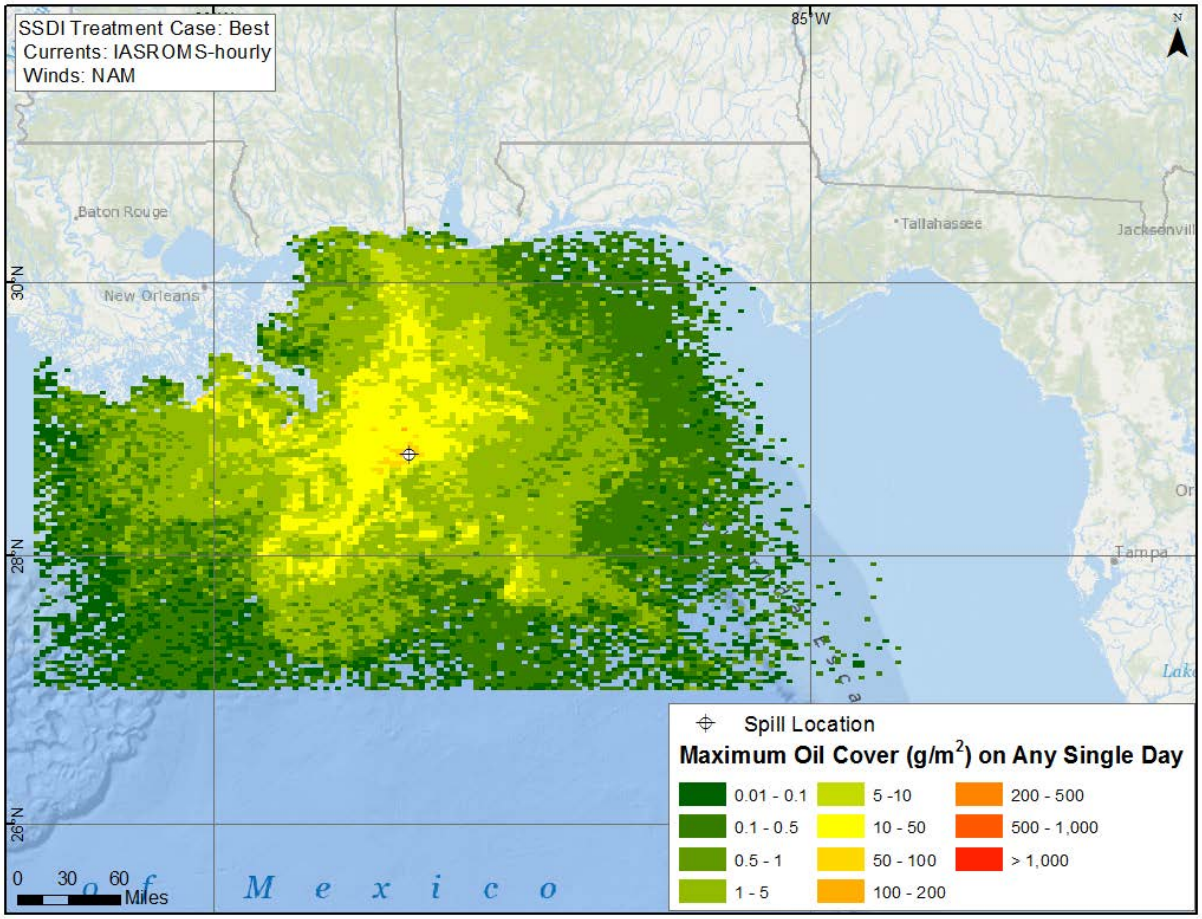

Figure C.2-20. Modeled maximum amount of oil in each grid cell at any time in the simulation. Grid values are g/m^2 averaged over the grid cell. Based on the model simulation with SSDI and using IAS ROMS-hourly currents and NARR winds.

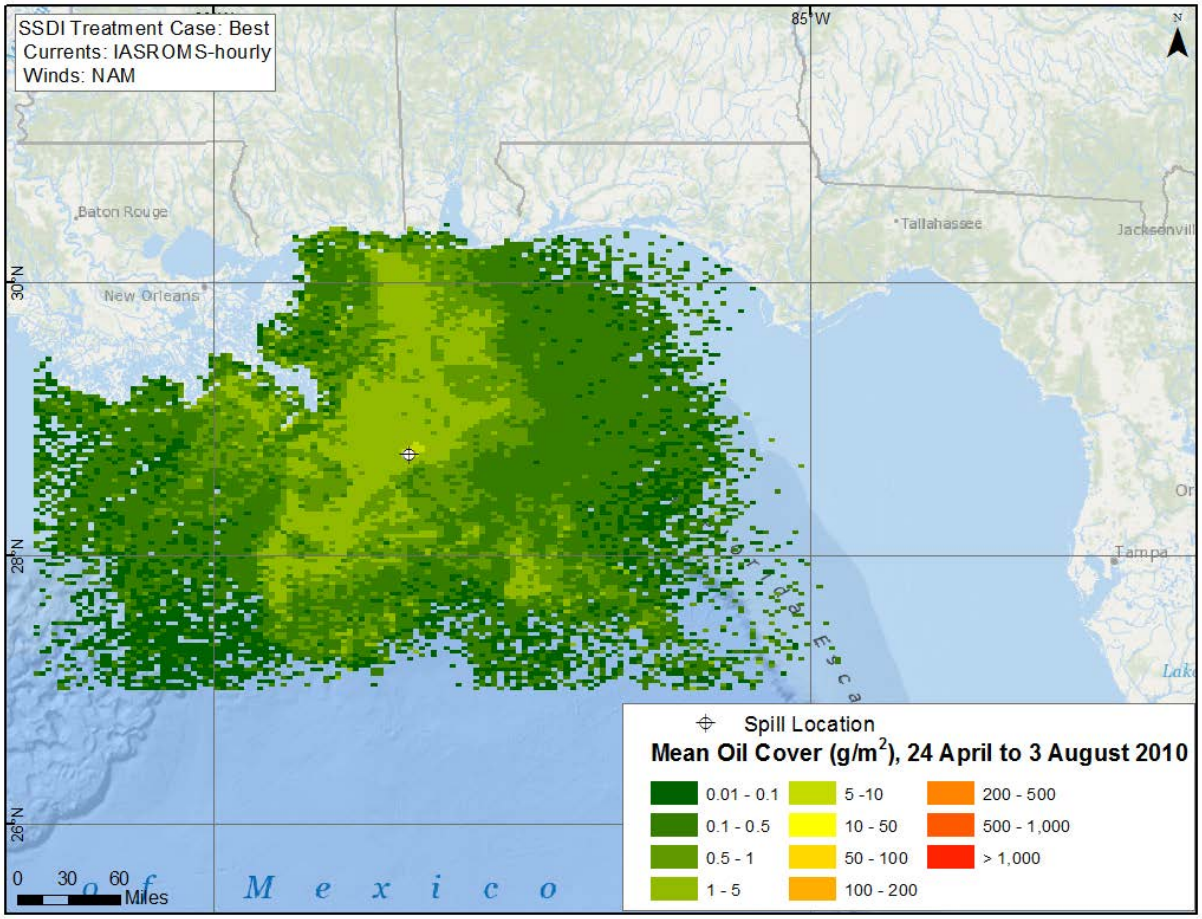

Figure C.2-21. Mean floating oil concentration (g/m^2) in each cell for the period when oil was observed by SAR, 24 April to 3 August 2010.
Based on the model simulation with SSDI and using IAS ROMS-hourly currents and NARR winds.

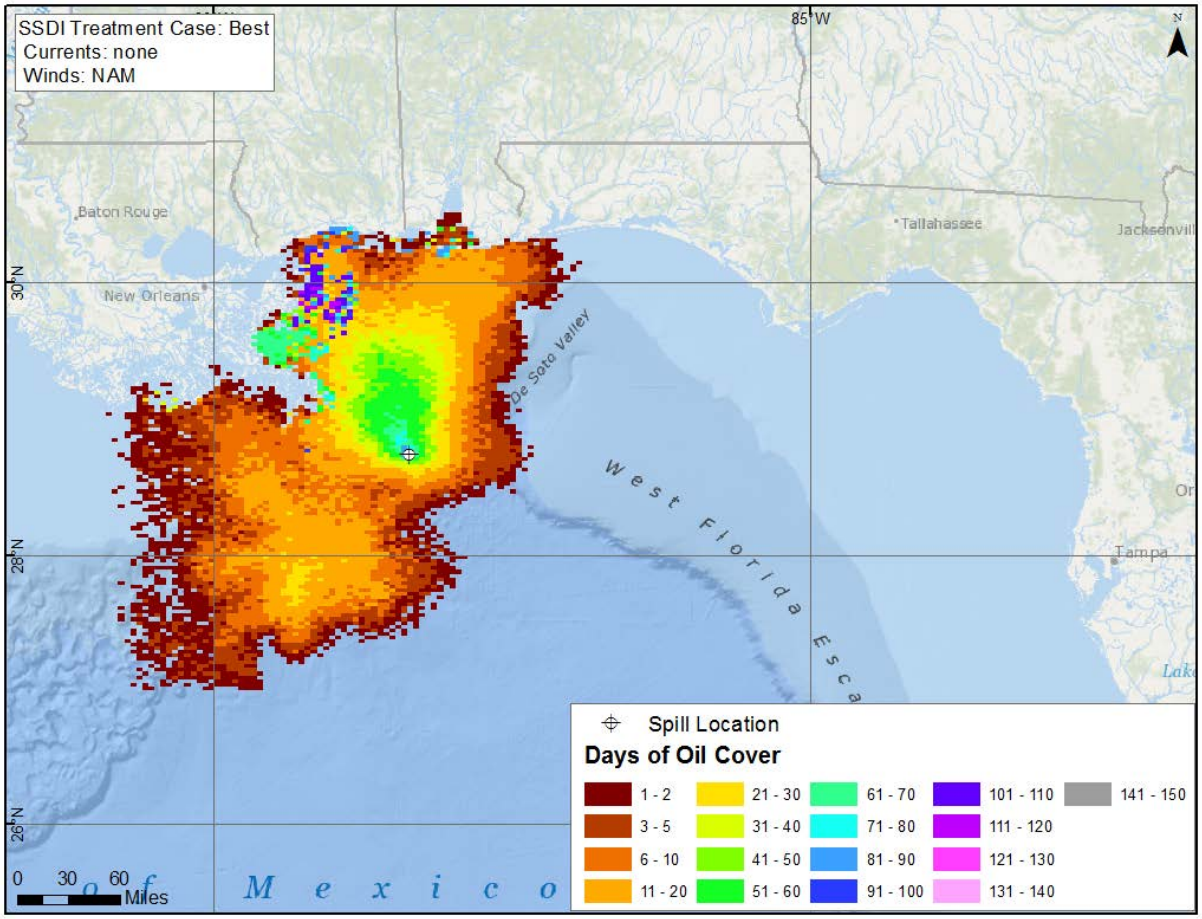

Figure C.2-22. Cumulative days of oil presence on the water surface.
Based on the model simulation with SSDI and using no currents and NAM winds.

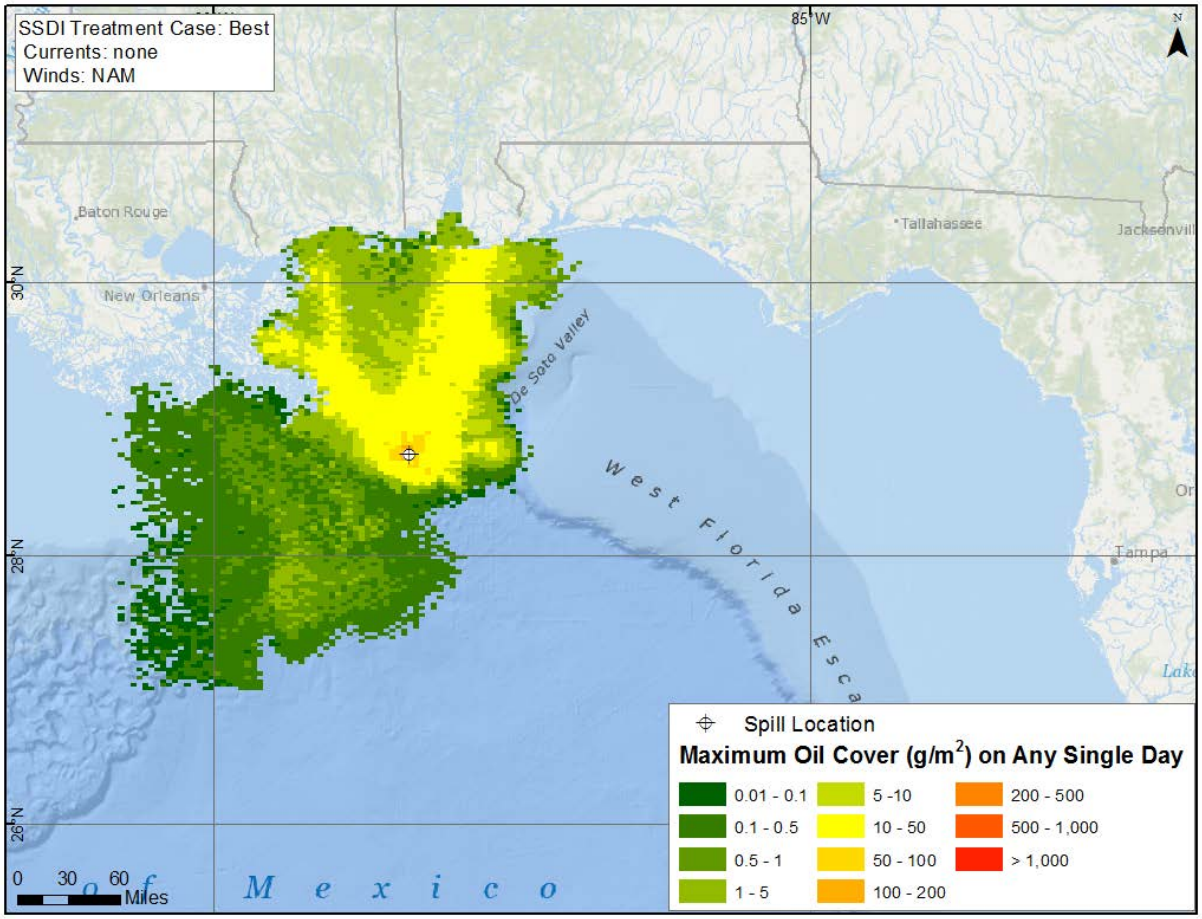

Figure C.2-23. Modeled maximum amount of oil in each grid cell at any time in the simulation. Grid values are g/m^2 averaged over the grid cell. Based on the model simulation with SSDI and using no currents and NAM winds.

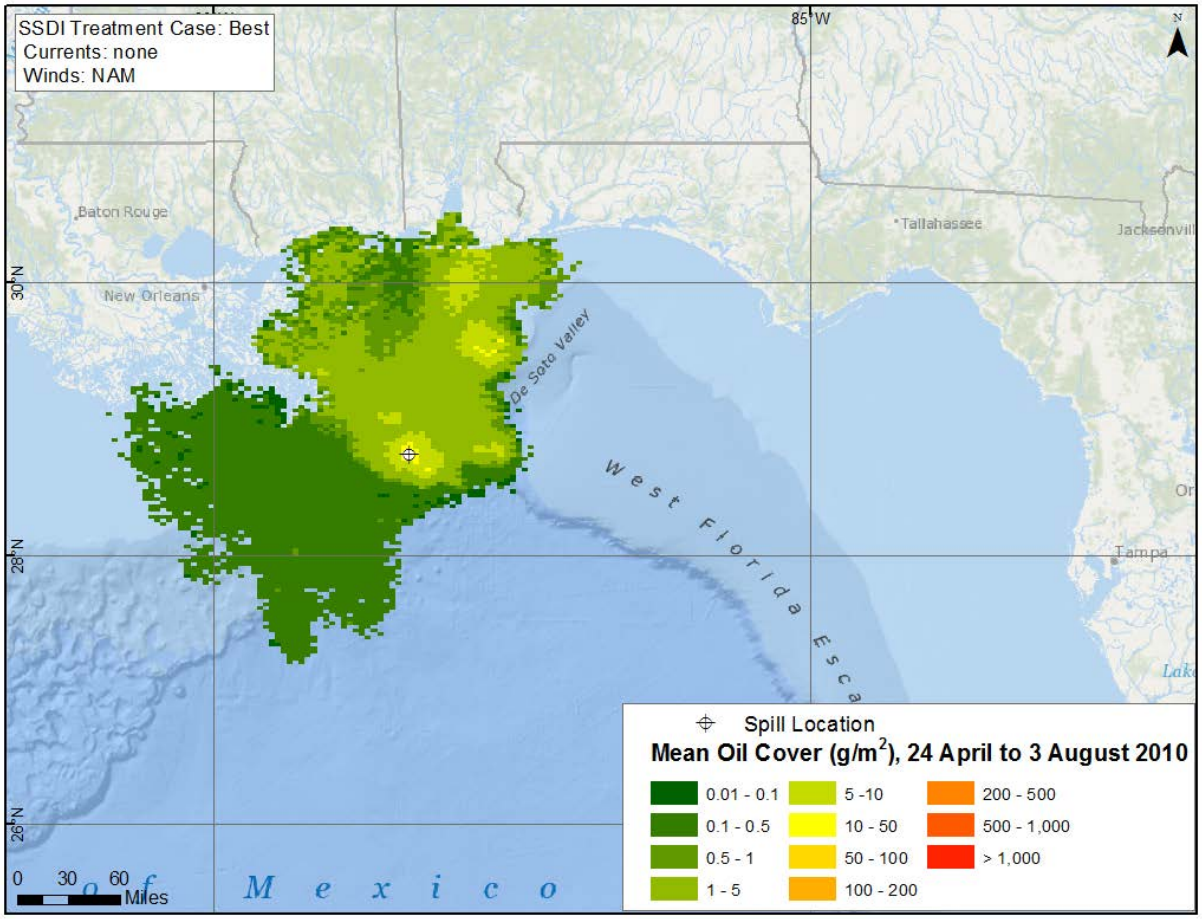

Figure C.2-24. Mean floating oil concentration (g/m^2) in each cell for the period when oil was observed by SAR, 24 April to 3 August 2010.
Based on the model simulation with SSDI and using no currents and NAM winds.

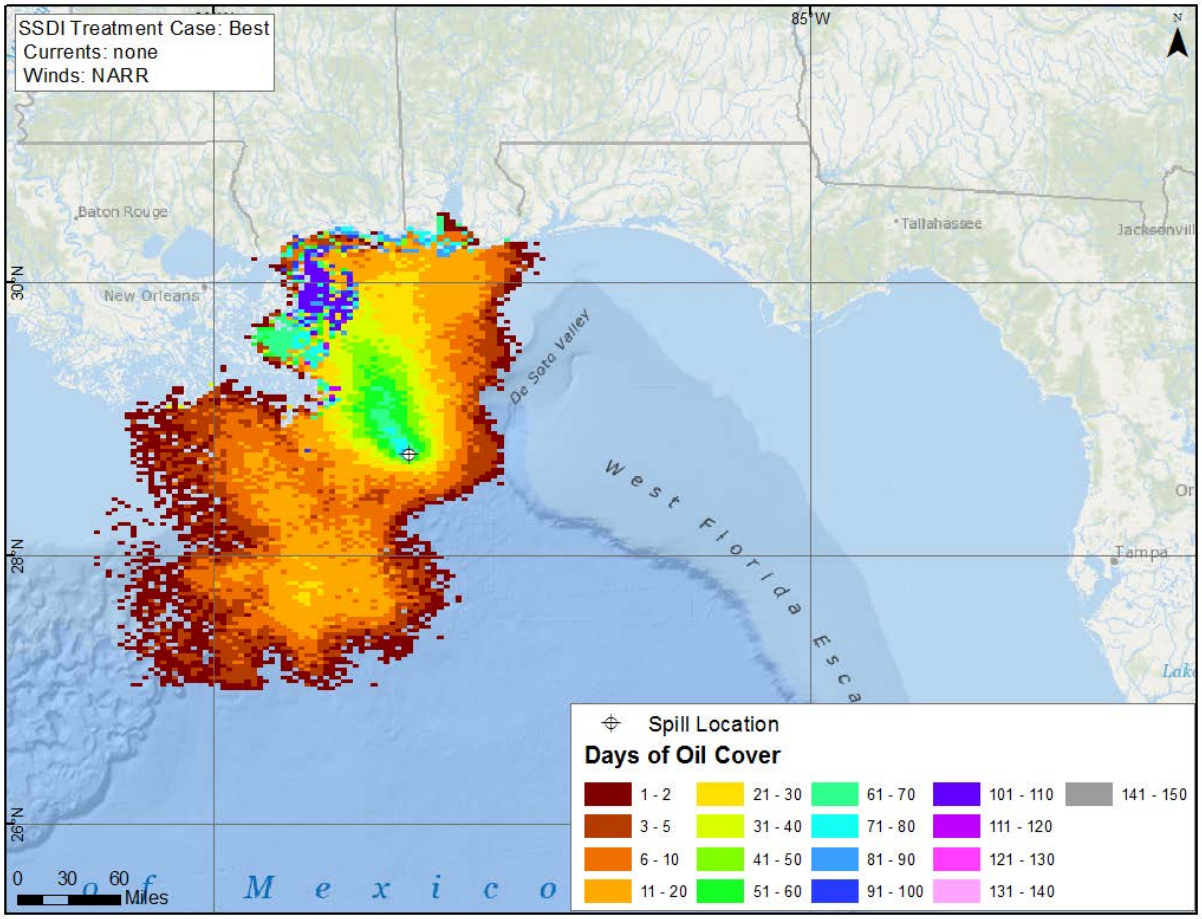

Figure C.2-25. Cumulative days of oil presence on the water surface.
Based on the model simulation with SSDI and using no currents and NARR winds.

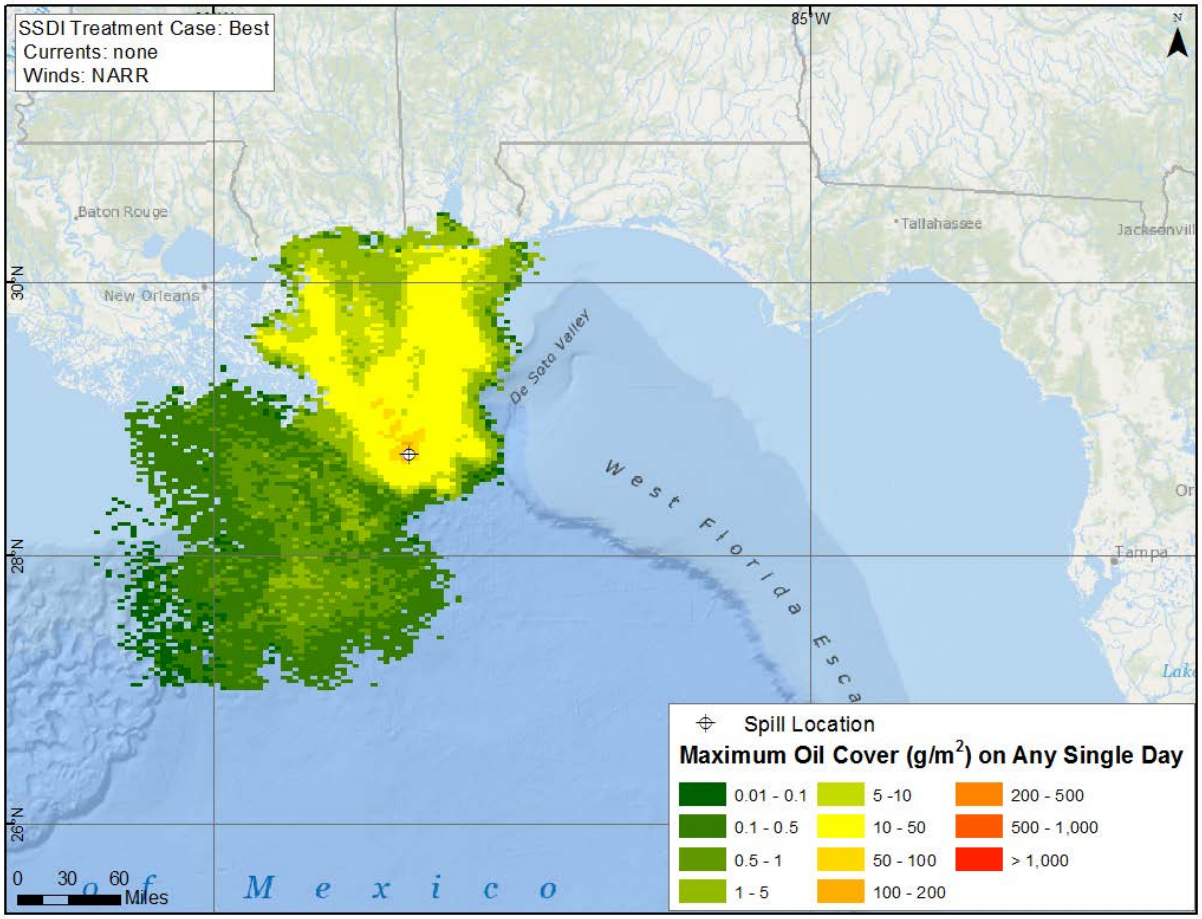

Figure C.2-26. Modeled maximum amount of oil in each grid cell at any time in the simulation. Grid values are g/m^2 averaged over the grid cell. Based on the model simulation with SSDI and using no currents and NARR winds.

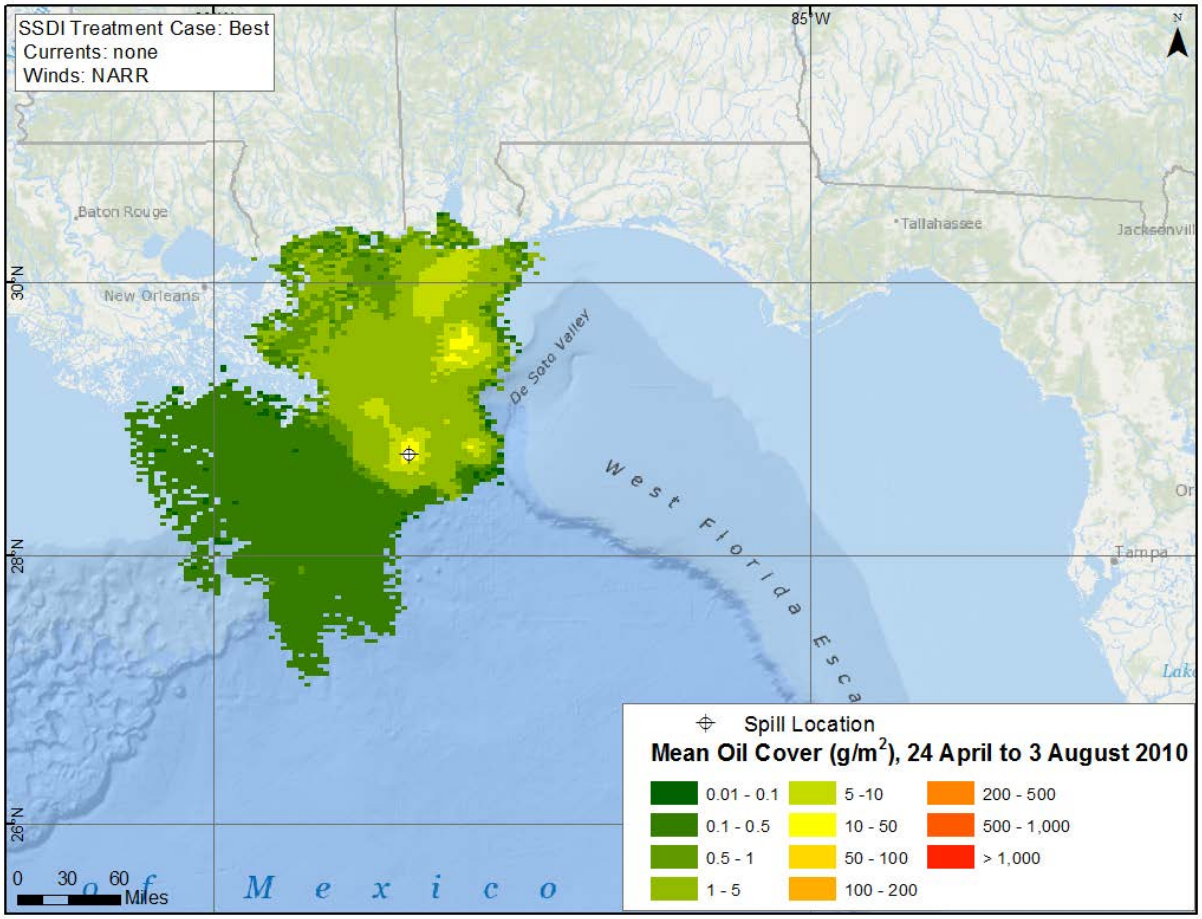

Figure C.2-27. Mean floating oil concentration (g/m^2) in each cell for the period when oil was observed by SAR, 24 April to 3 August 2010.
Based on the model simulation with SSDI and using no currents and NARR winds.

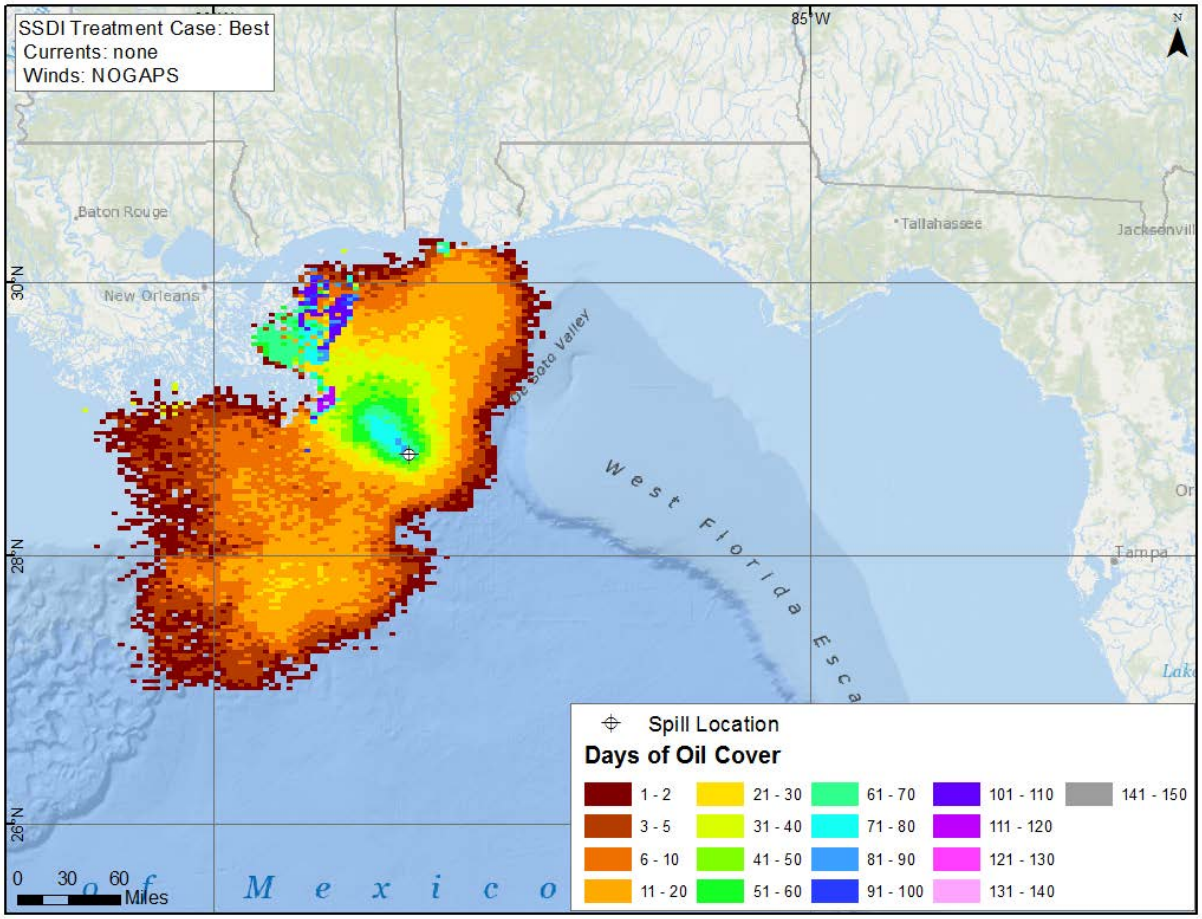

Figure C.2-28. Cumulative days of oil presence on the water surface.
Based on the model simulation with SSDI and using no currents and NOGAPS winds.

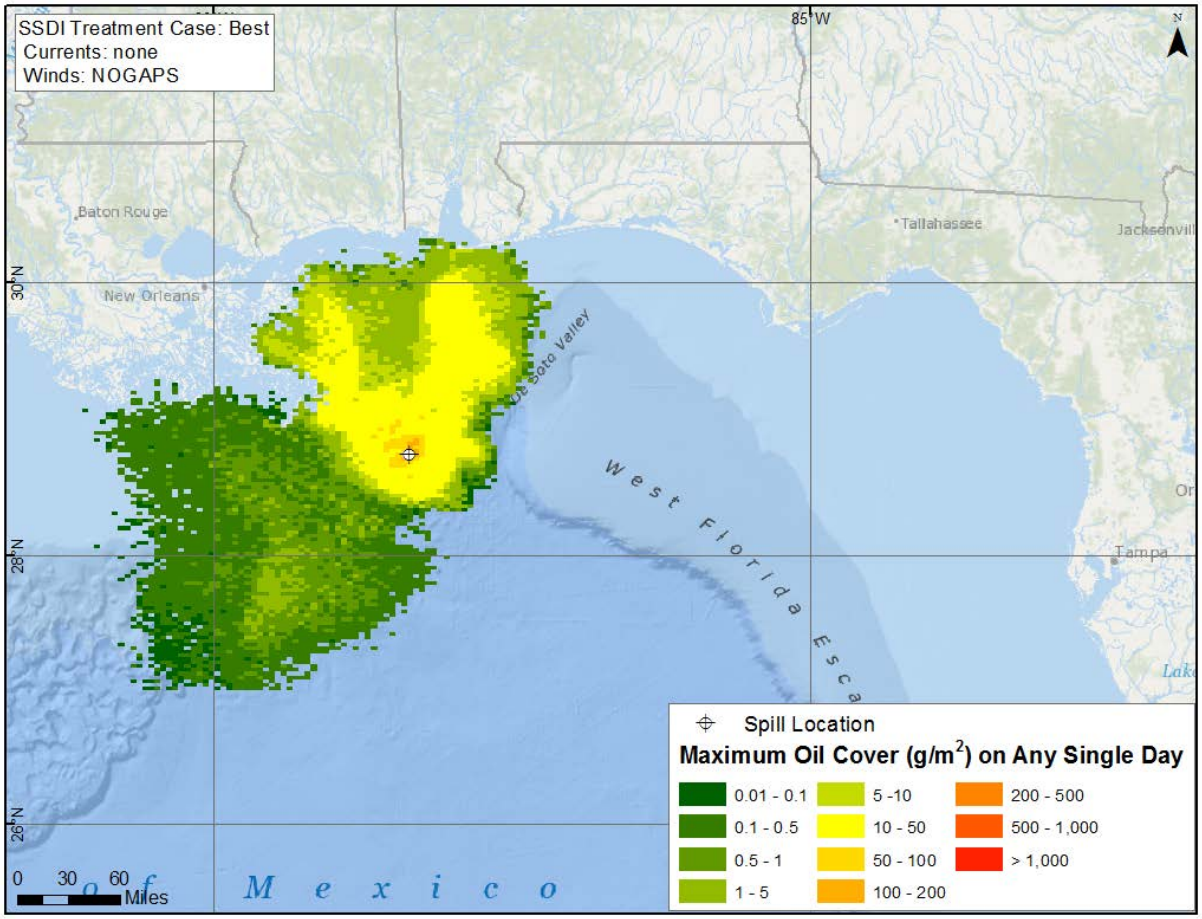

Figure C.2-29. Modeled maximum amount of oil in each grid cell at any time in the simulation. Grid values are g/m^2 averaged over the grid cell. Based on the model simulation with SSDI and using no currents and NOGAPS winds.

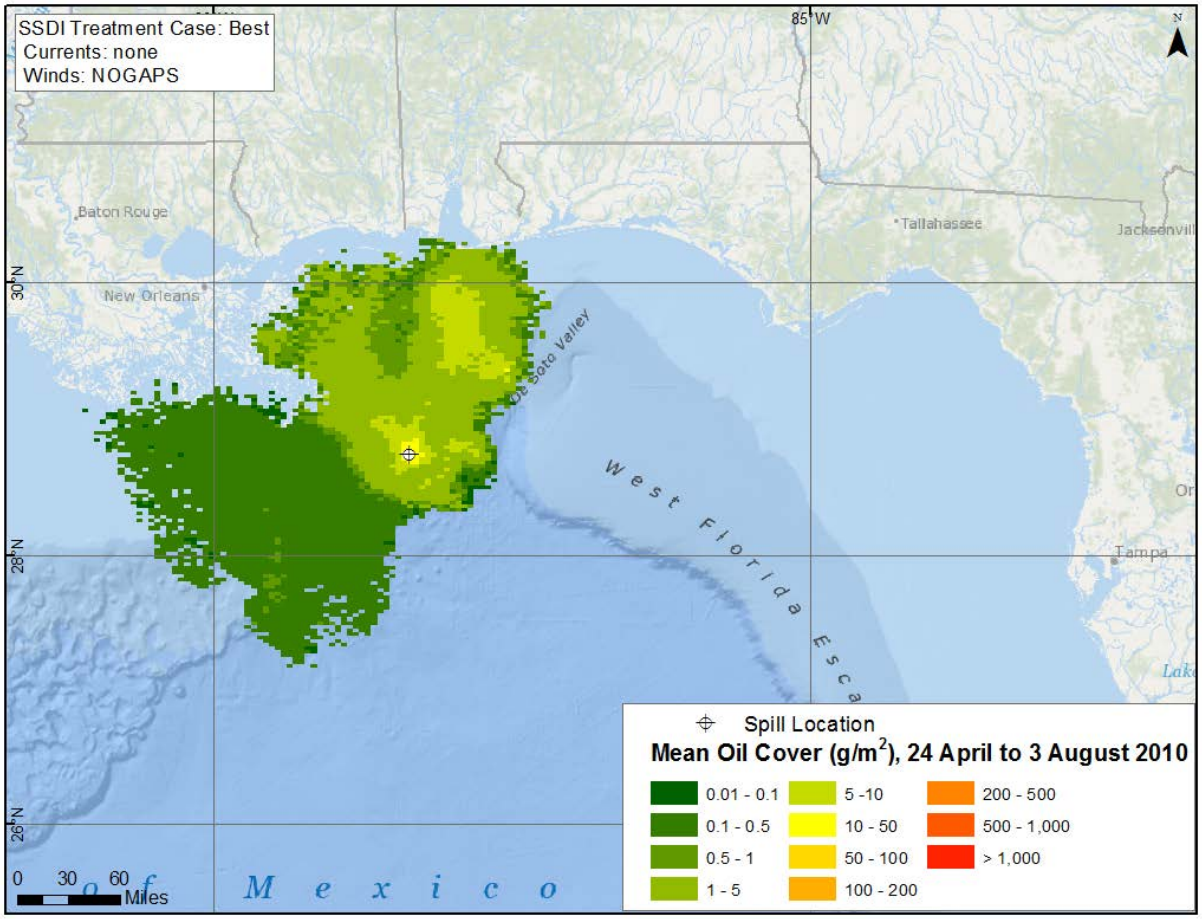

Figure C.2-30. Mean floating oil concentration (g/m^2) in each cell for the period when oil was observed by SAR, 24 April to 3 August 2010.
Based on the model simulation with SSDI and using no currents and NOGAPS winds.

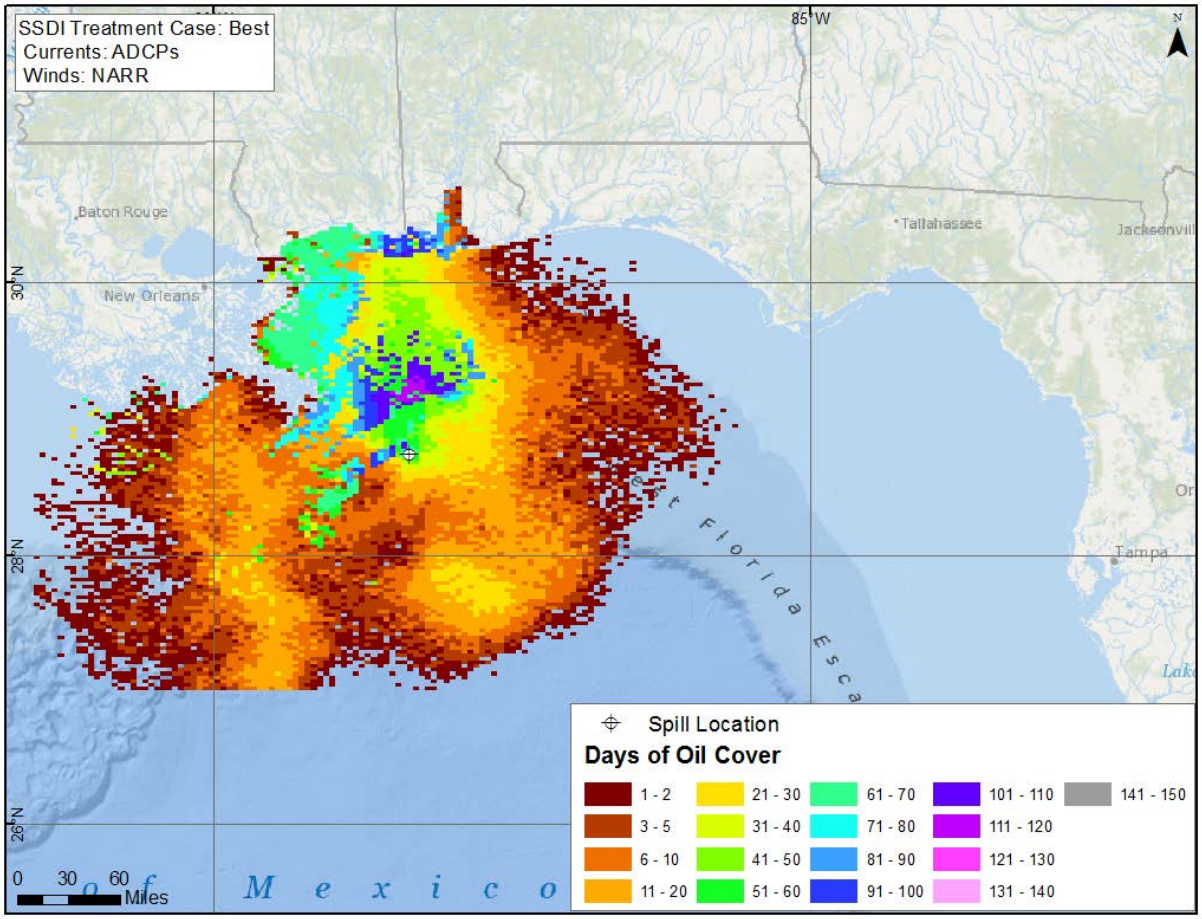

Figure C.2-31. Cumulative days of oil presence on the water surface.
Based on the model simulation with SSDI and using ADCP currents and NARR winds.

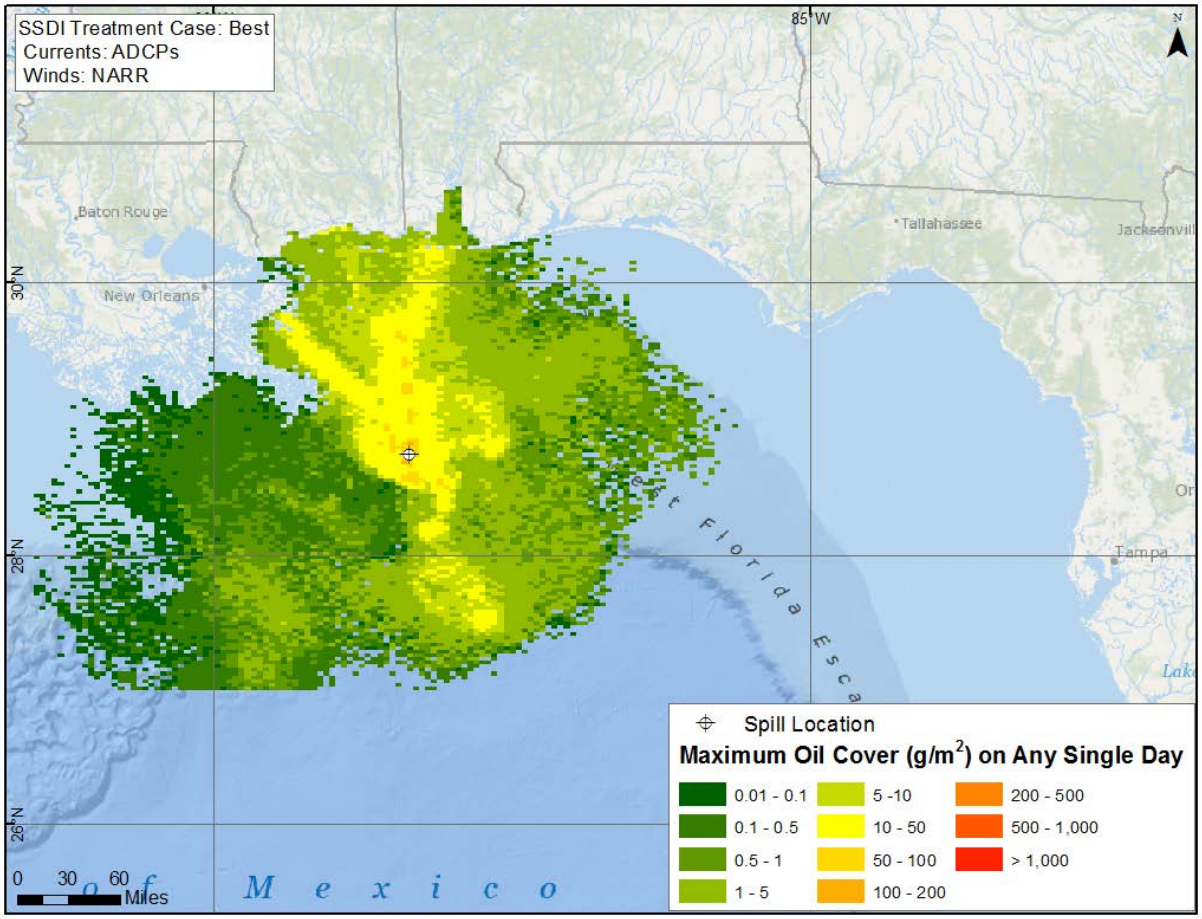

Figure C.2-32. Modeled maximum amount of oil in each grid cell at any time in the simulation. Grid values are g/m^2 averaged over the grid cell. Based on the model simulation with SSDI and using ADCP currents and NARR winds.

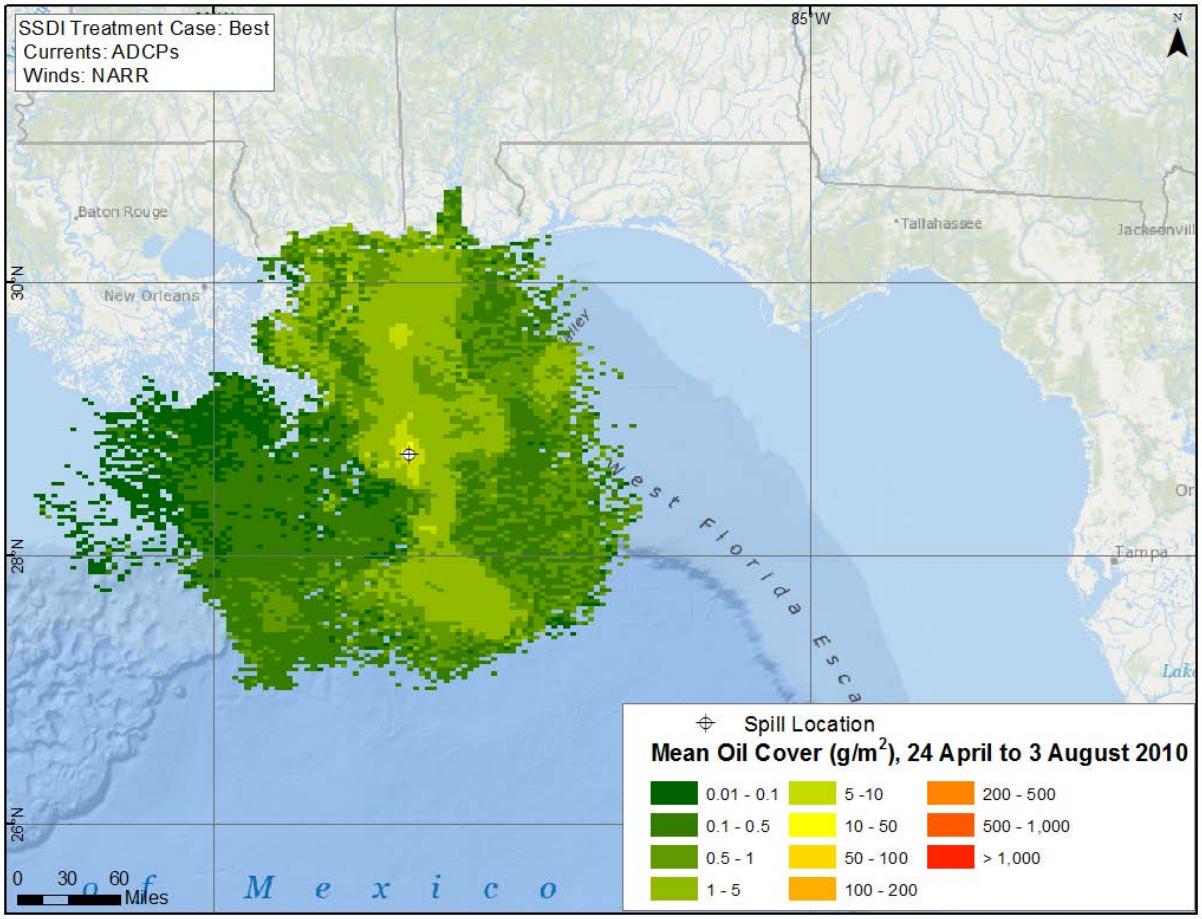

Figure C.2-33. Mean floating oil concentration (g/m^2) in each cell for the period when oil was observed by SAR, 24 April to 3 August 2010.
Based on the model simulation with SSDI and using ADCP currents and NARR winds.

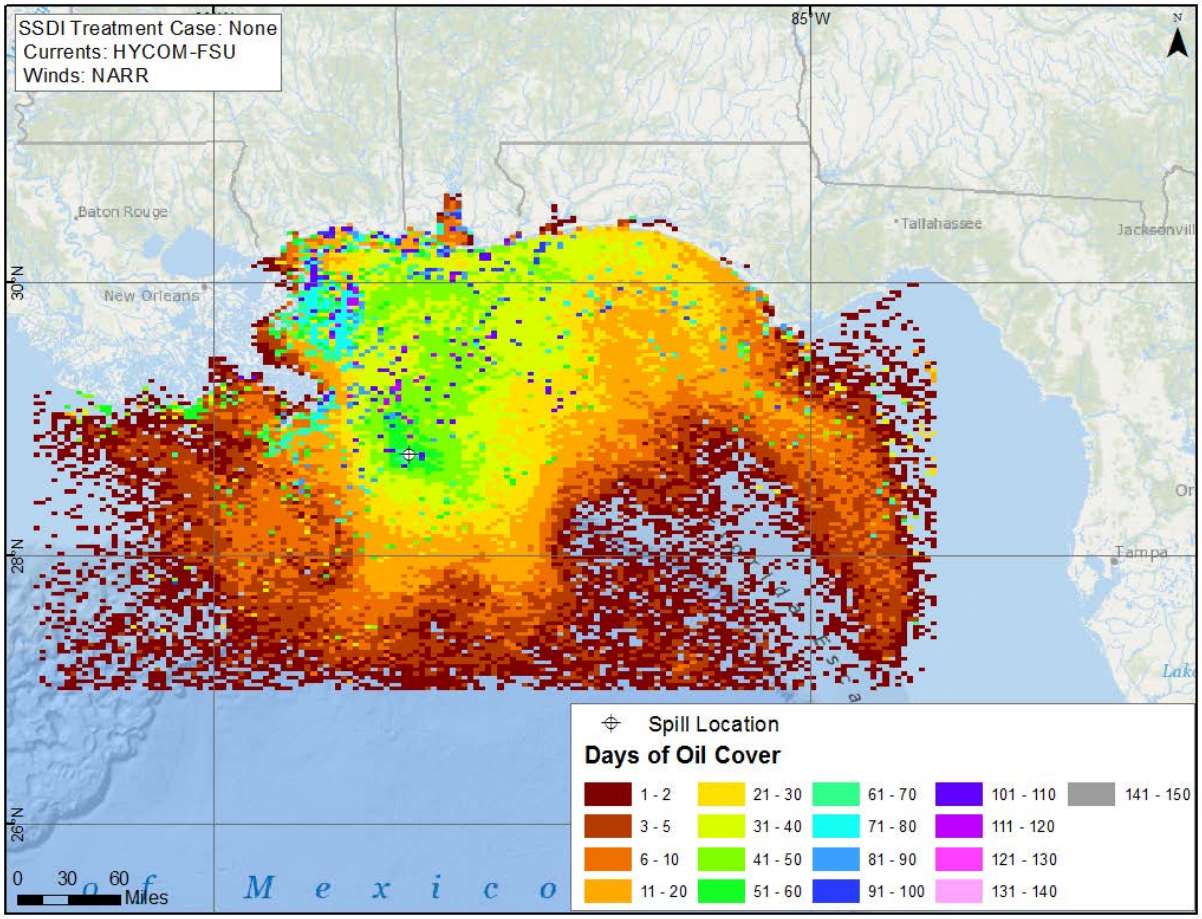

Figure C.2-34. Cumulative days of oil presence on the water surface.
Based on the simulation without SSDI and using HYCOM-FSU currents and NARR winds.

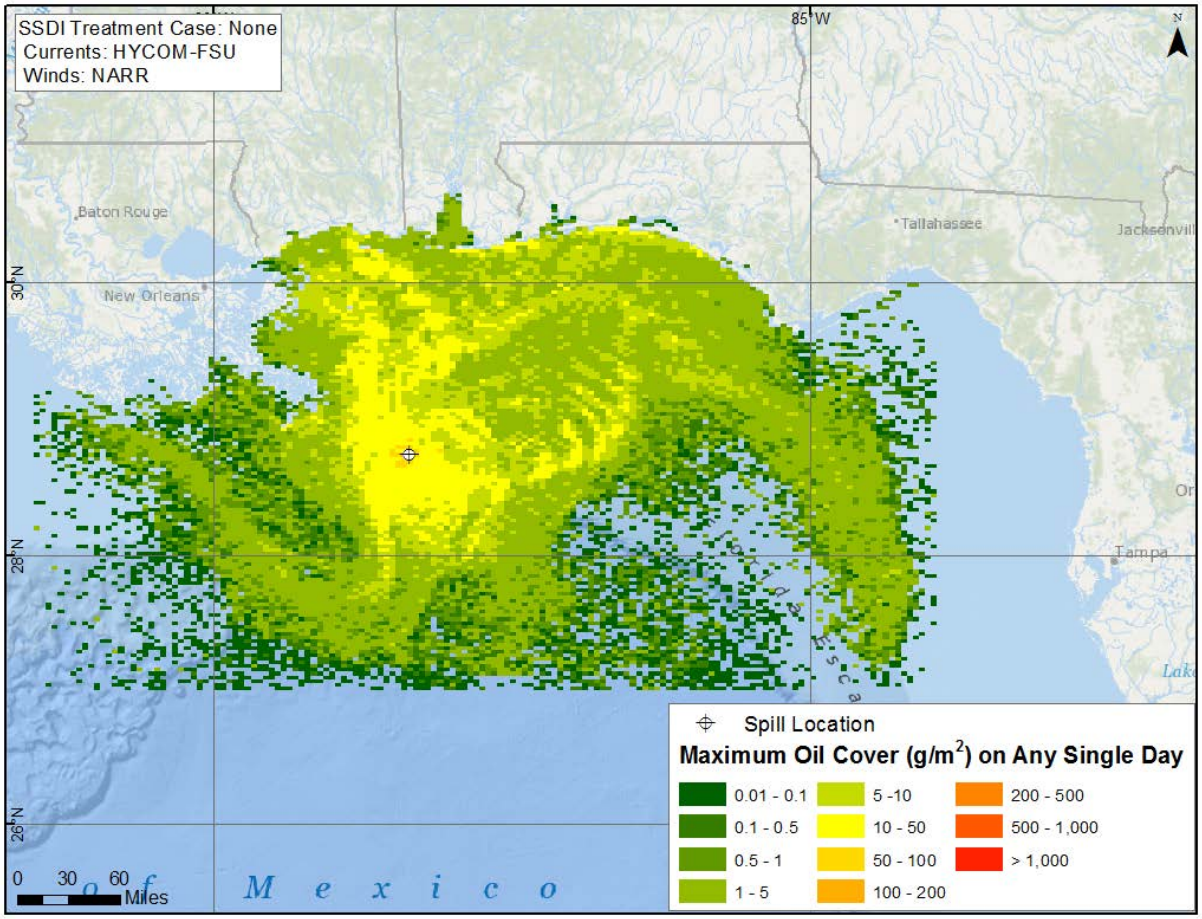

Figure C.2-35. Modeled maximum amount of oil in each grid cell at any time in the simulation. Grid values are g/m2 averaged over the grid cell. Based on the simulation without SSDI and using HYCOM-FSU currents and NARR winds.

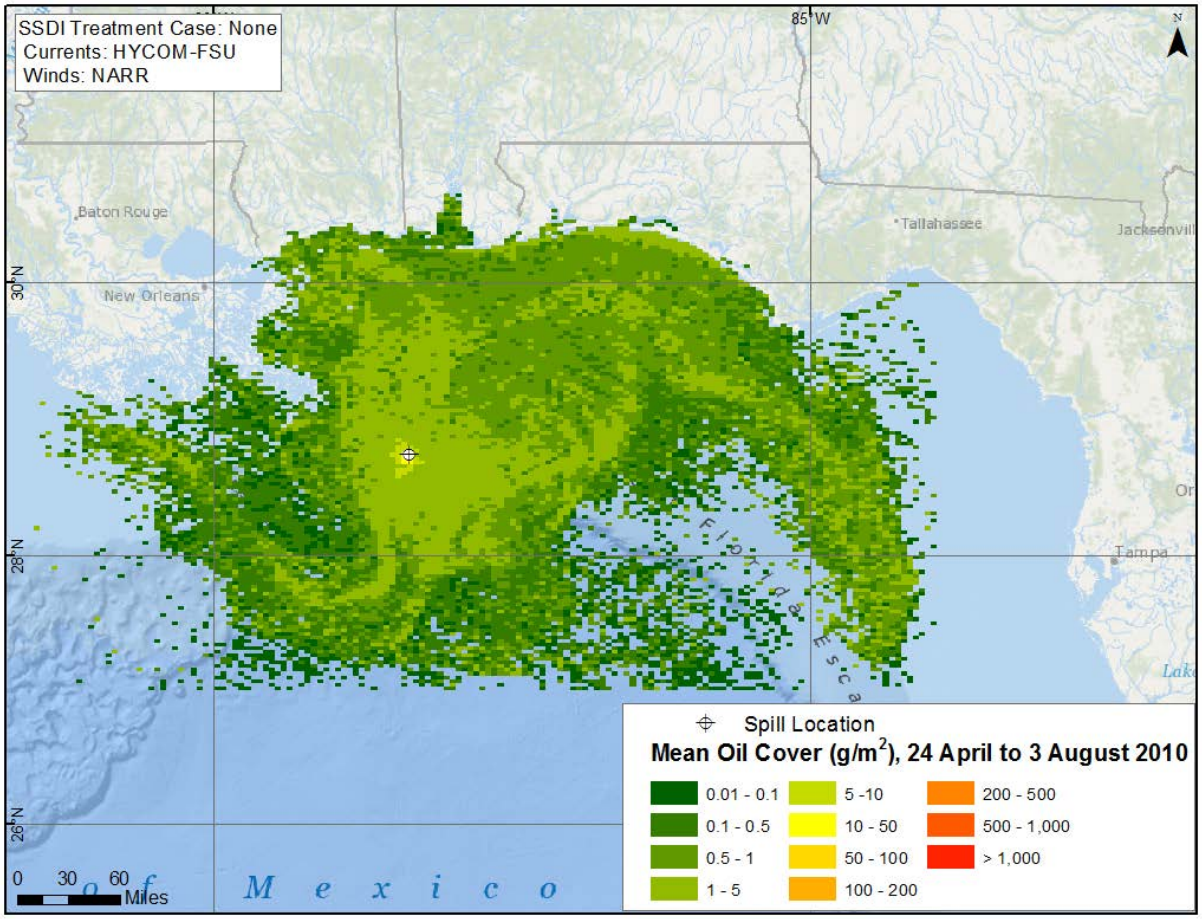

Figure C.2-36. Mean floating oil concentration (g/m^2) in each cell for the period when oil was observed by SAR, 24 April to 3 August 2010.
Based on the simulation without SSDI and using HYCOM-FSU currents and NARR winds.

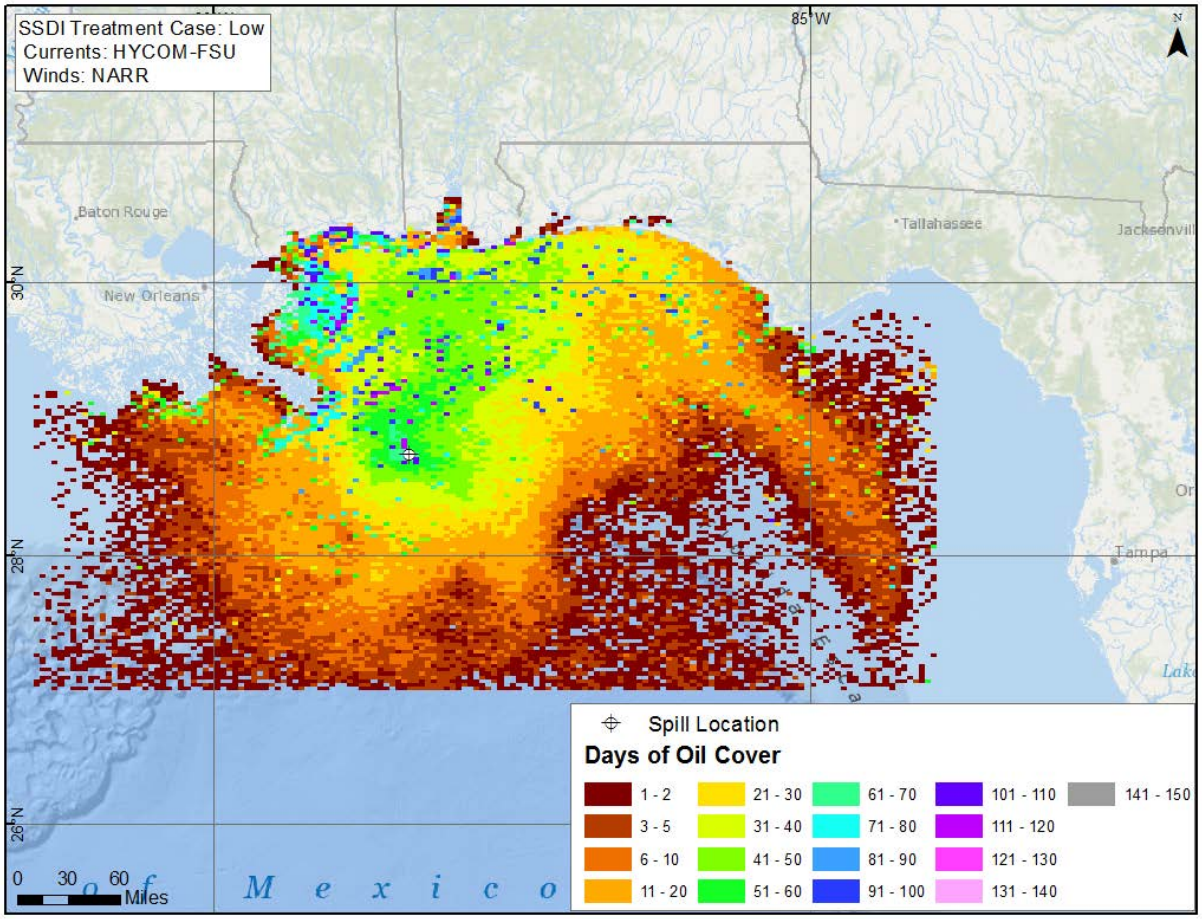

Figure C.2-37. Cumulative days of oil presence on the water surface.
Based on the simulation with low effectiveness SSDI and using HYCOM-FSU currents and NARR winds.

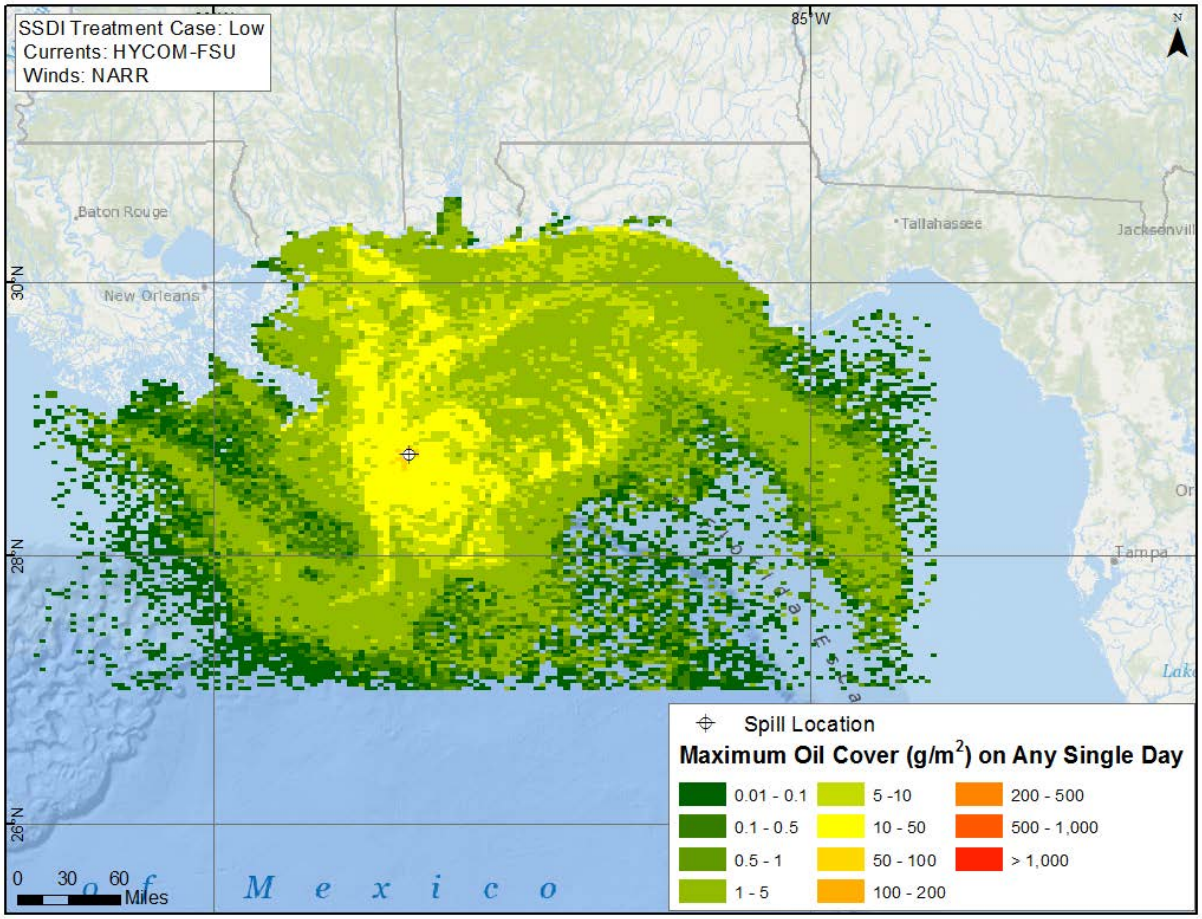

Figure C.2-38. Modeled maximum amount of oil in each grid cell at any time in the simulation. Grid values are g/m^2 averaged over the grid cell. Based on the simulation with low effectiveness SSDI and using HYCOM-FSU currents and NARR winds.

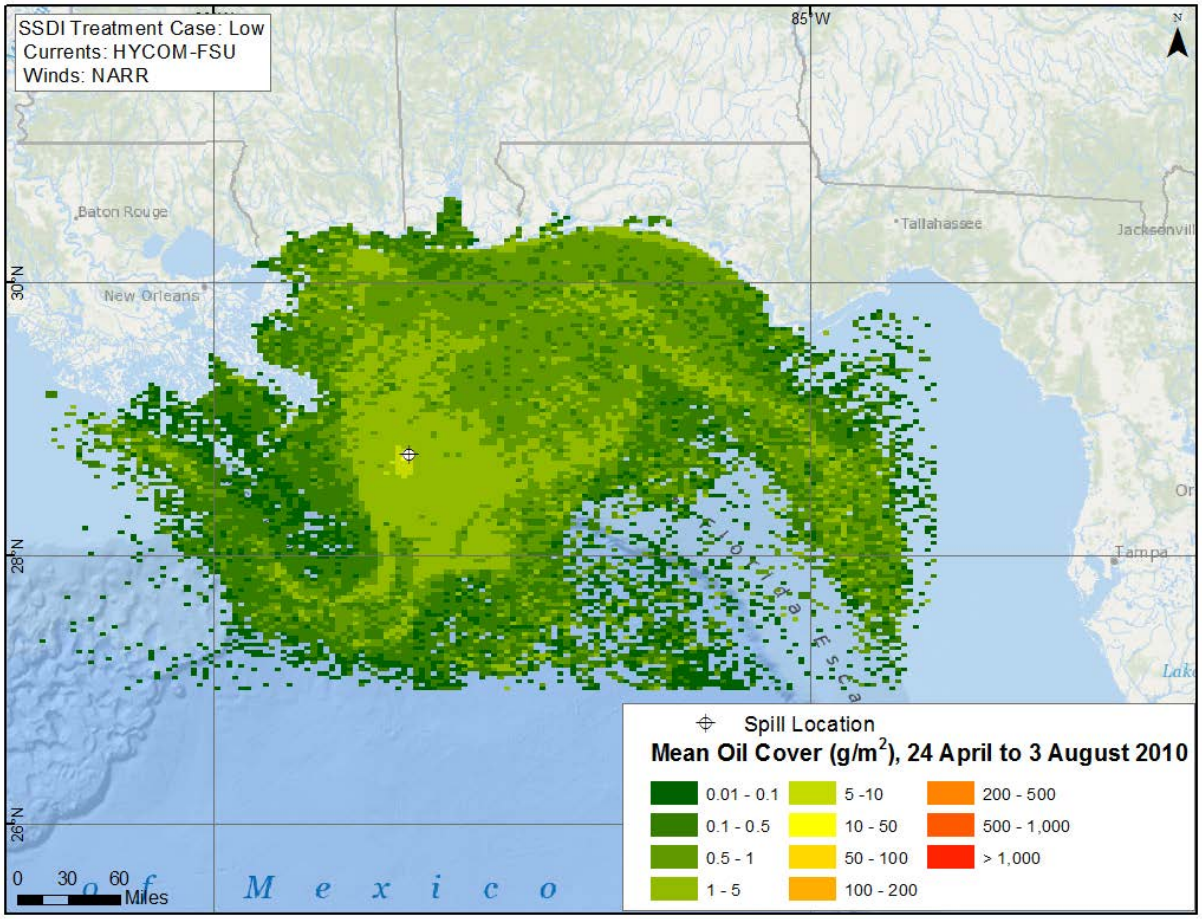

Figure C.2-39. Mean floating oil concentration (g/m^2) in each cell for the period when oil was observed by SAR, 24 April to 3 August 2010.
Based on the simulation with low effectiveness SSDI and using HYCOM-FSU currents and NARR winds.

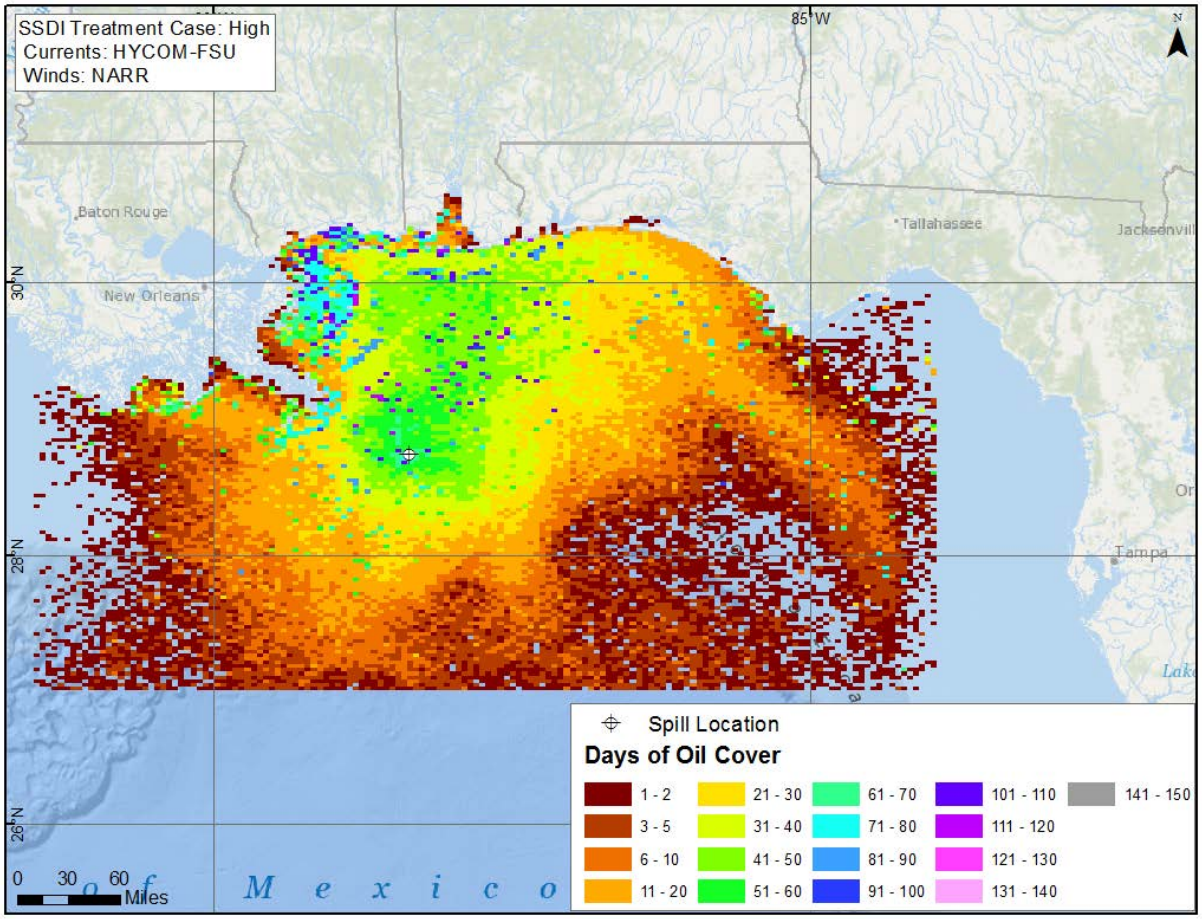

Figure C.2-40. Cumulative days of oil presence on the water surface.
Based on the simulation with high effectiveness SSDI and using HYCOM-FSU currents and NARR winds.

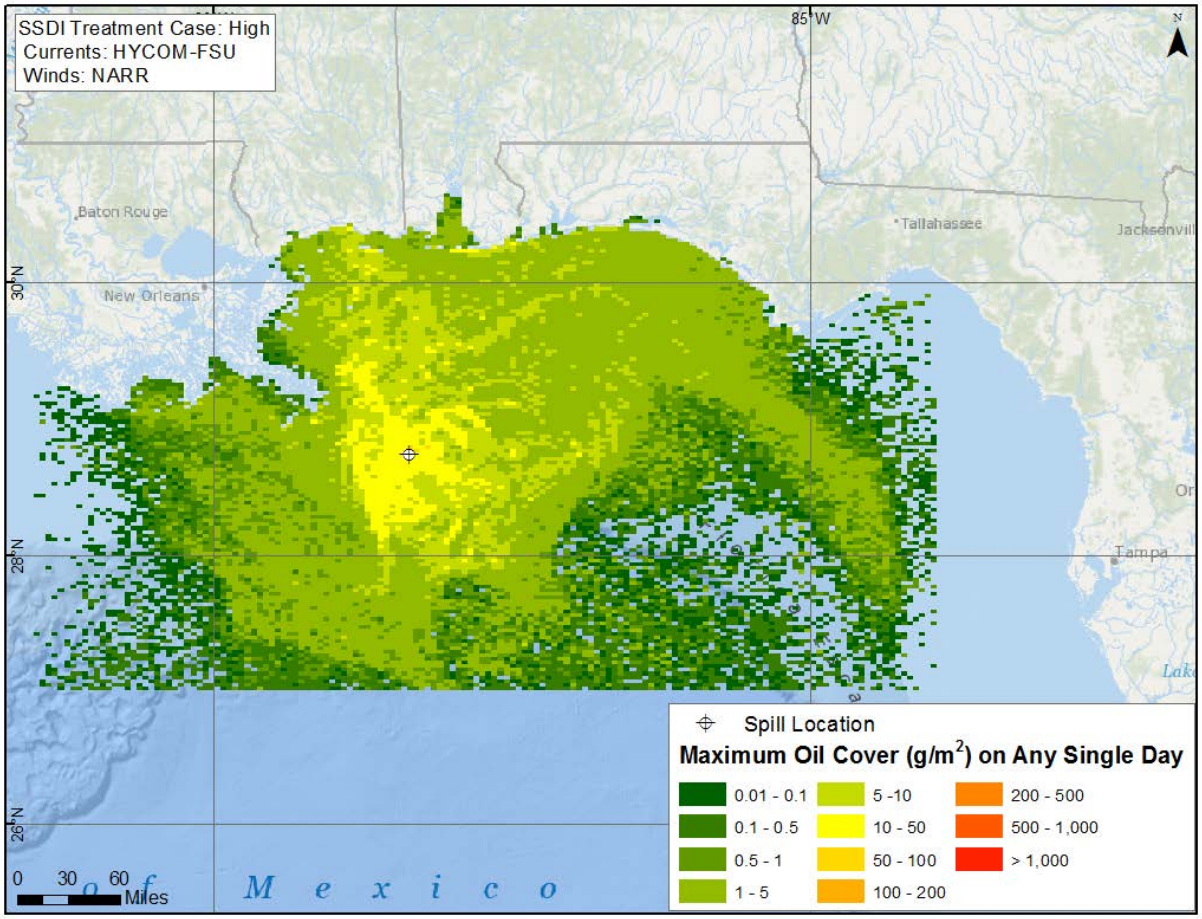

Figure C.2-41. Modeled maximum amount of oil in each grid cell at any time in the simulation. Grid values are g/m^2 averaged over the grid cell. Based on the simulation with high effectiveness SSDI and using HYCOM-FSU currents and NARR winds.

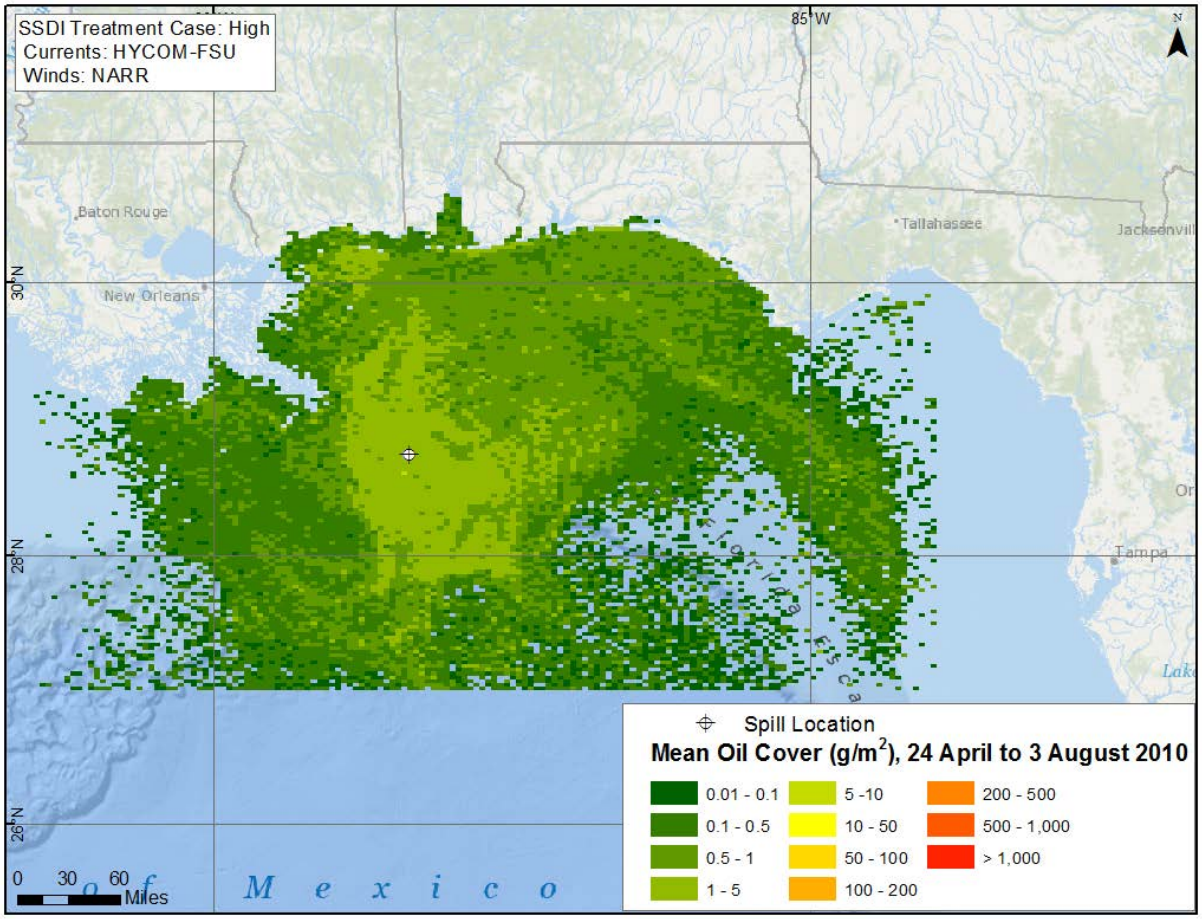

Figure C.2-42. Mean floating oil concentration (g/m^2) in each cell for the period when oil was observed by SAR, 24 April to 3 August 2010.
Based on the simulation with high effectiveness SSDI and using HYCOM-FSU currents and NARR winds.

C.3. Comparisons of Modeled Floating Oil Distributions to Remote Sensing Data

Figures were prepared comparing model results of floating oil distributions on 84 dates and times where remote sensing data were available and the image was judged sufficiently synoptic of the area of the floating oil. These included 34 SAR OEDA,18 MODIS-visual, 25 MODIS-TIR and 7 LANDSAT TM images analyzed by the DWHOS Trustees (2016; ERMA 2016) (Table 4-6 of Volume II). Paired figures showing modeled and remote sensing analyses of floating oil distributions, both gridded in the same 25 km^2 cell-size grid, are presented in the attachments to this Annex. Table C-1 describes these attachments. For all these model runs, the best-estimate SSDI was assumed, the floating oil horizontal diffusion coefficient was assumed 100 m^2/s, and the modeled wind drift was used.

Table C-1. List of attachments with paired figures showing modeled and remote sensing analyses of floating oil distributions on 84 dates and times.

Annex C.3 Attachment	Currents	Winds
Annex C.3.1 Floating oil-HYCOM-FSU and NARR	HYCOM-FSU	NARR
Annex C.3.2 Floating oil-HYCOM-NRL Reanalysis and CFSR	HYCOM-NRL, Reanalysis	CFSR
Annex C.3.3 Floating oil-HYCOM-NRL Real Time and NARR	HYCOM-NRL, Real-time	NARR
Annex C.3.4 Floating oil-SABGOM and NAM	SABGOM	NAM
Annex C.3.5 Floating oil-NCOM and NARR	NCOM Real-Time	NARR
Annex C.3.6 Floating oil-NGOM and NARR	NGOM-NOAA, Real-time	NARR
Annex C.3.7 Floating oil-IAS ROMS and NAM	IAS ROMS-hourly	NAM
Annex C.3.8 Floating oil-No Currents and NAM	None	NAM
Annex C.3.9 Floating oil-No Currents and NARR	None	NARR
Annex C.3.10 Floating oil-No Currents and NOGAPS	None	NOGAPS
Annex C.3.11 Floating oil-ADCPs and NARR	ADCPs	NARR

Annex D: *Deepwater Horizon* Oil Spill Model Results and Comparison to Observations: Shoreline Oil

D.1. Model Predictions of Shoreline Oiling

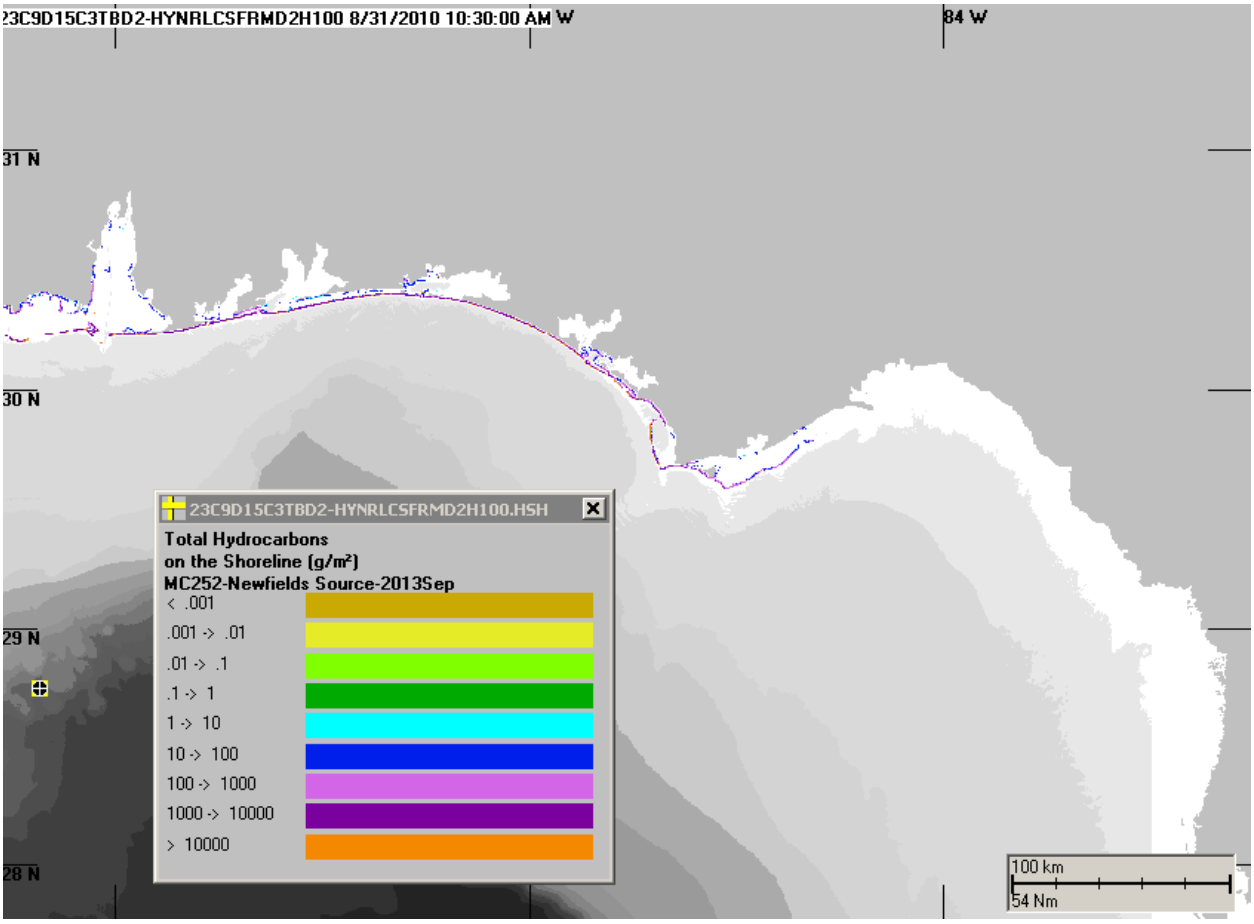

Figure D.1-1 Amount of oil accumulated on shorelines for the simulation using HYCOM-NRL Reanalysis currents and CFSR winds (east extent).

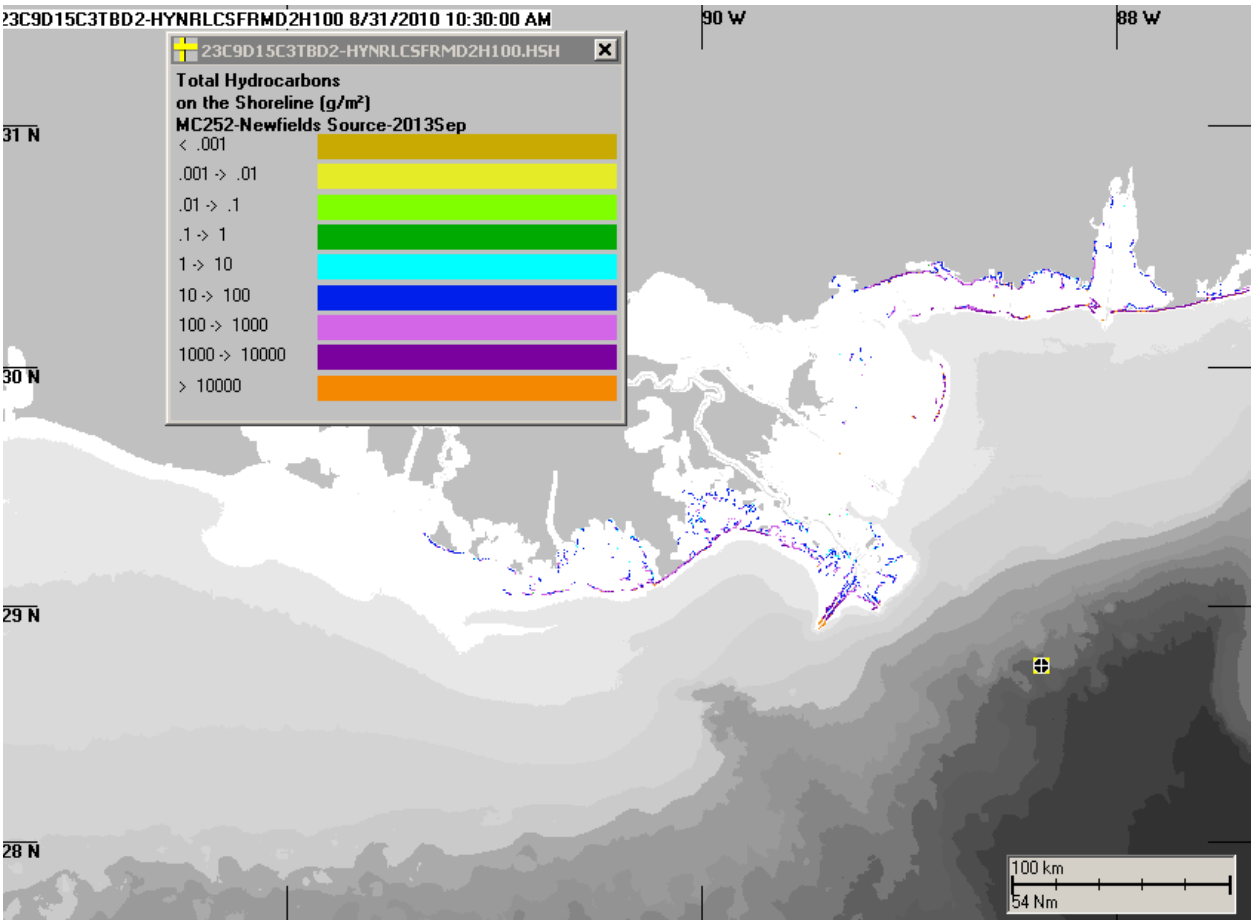

Figure D.1-2 Amount of oil accumulated on shorelines for the simulation using HYCOM-NRL Reanalysis currents and CFSR winds (central).

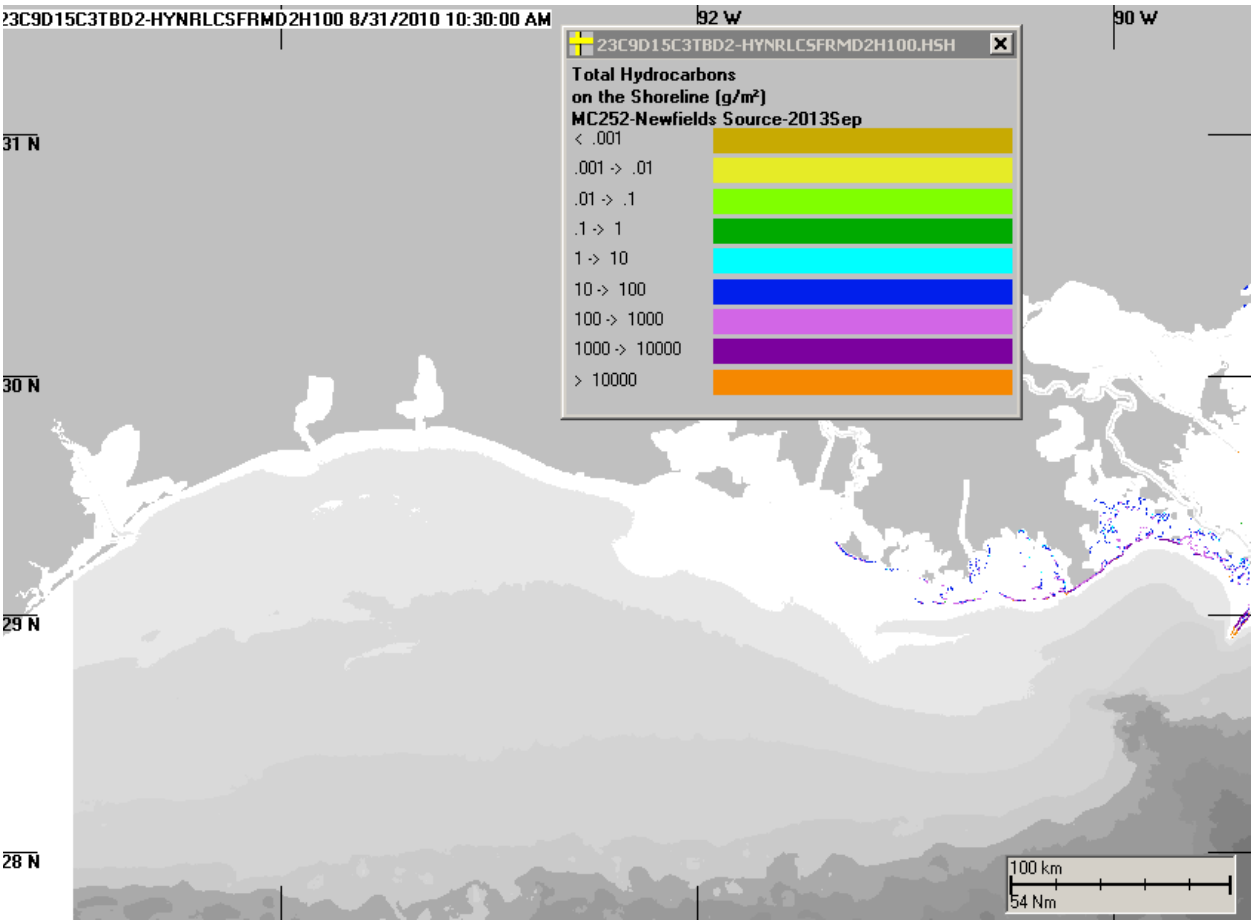

Figure D.1-3 Amount of oil accumulated on shorelines for the simulation using HYCOM-NRL Reanalysis currents and CFSR winds (west extent).

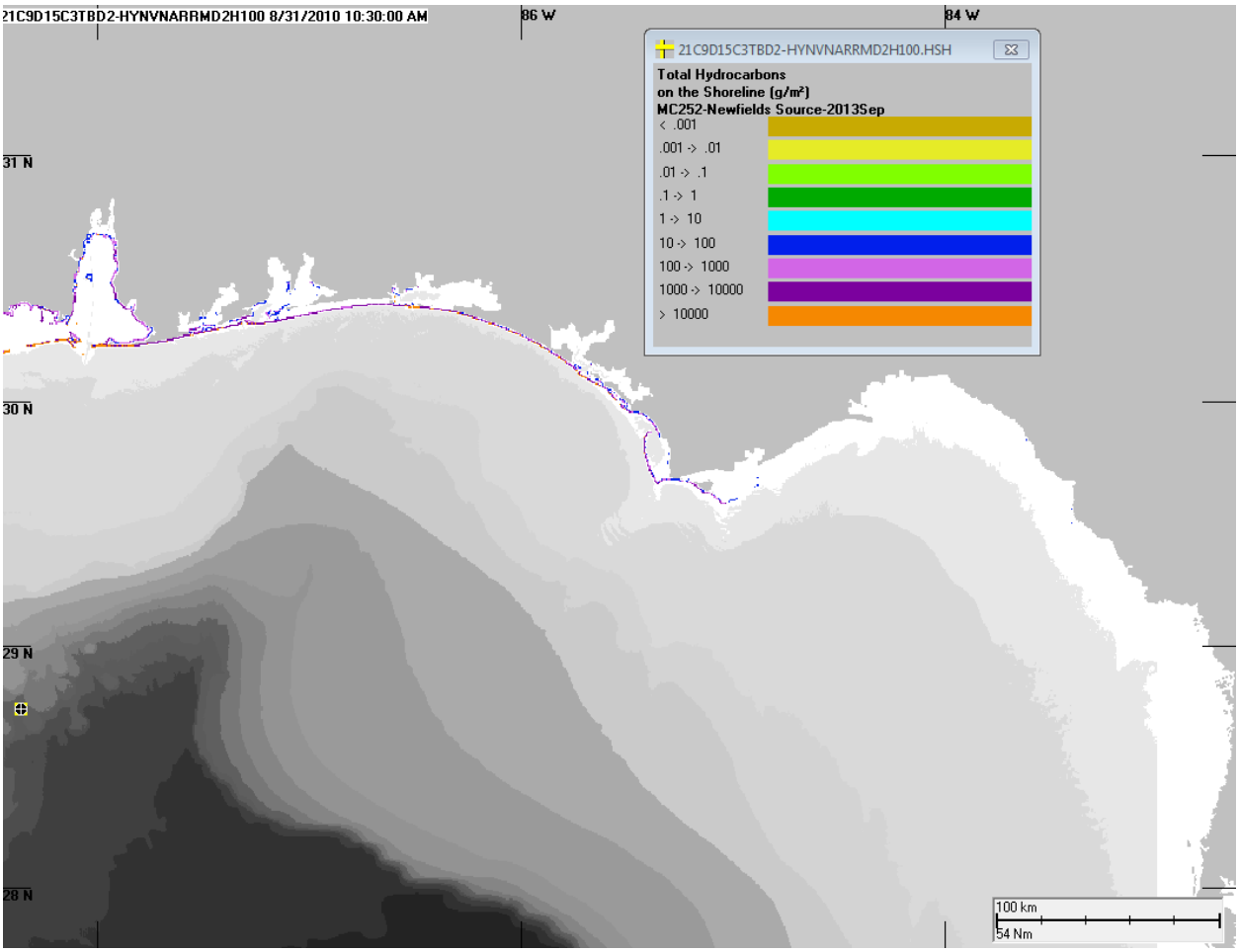

Figure D.1-4 Amount of oil accumulated on shorelines for the simulation using HYCOM-NRL Real-time currents and NARR winds (east extent).

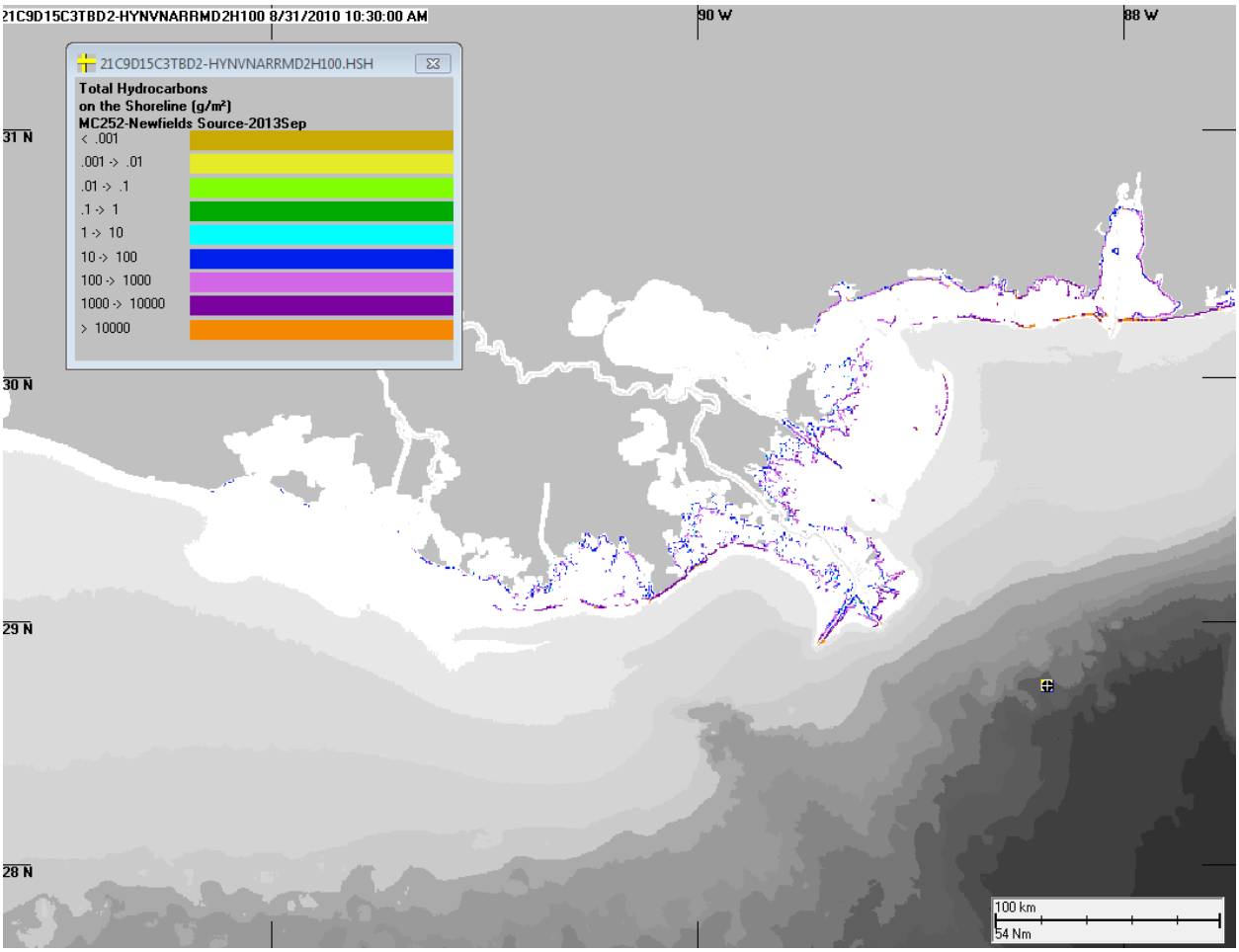

Figure D.1-5 Amount of oil accumulated on shorelines for the simulation using HYCOM-NRL Real-time currents and NARR winds (central).

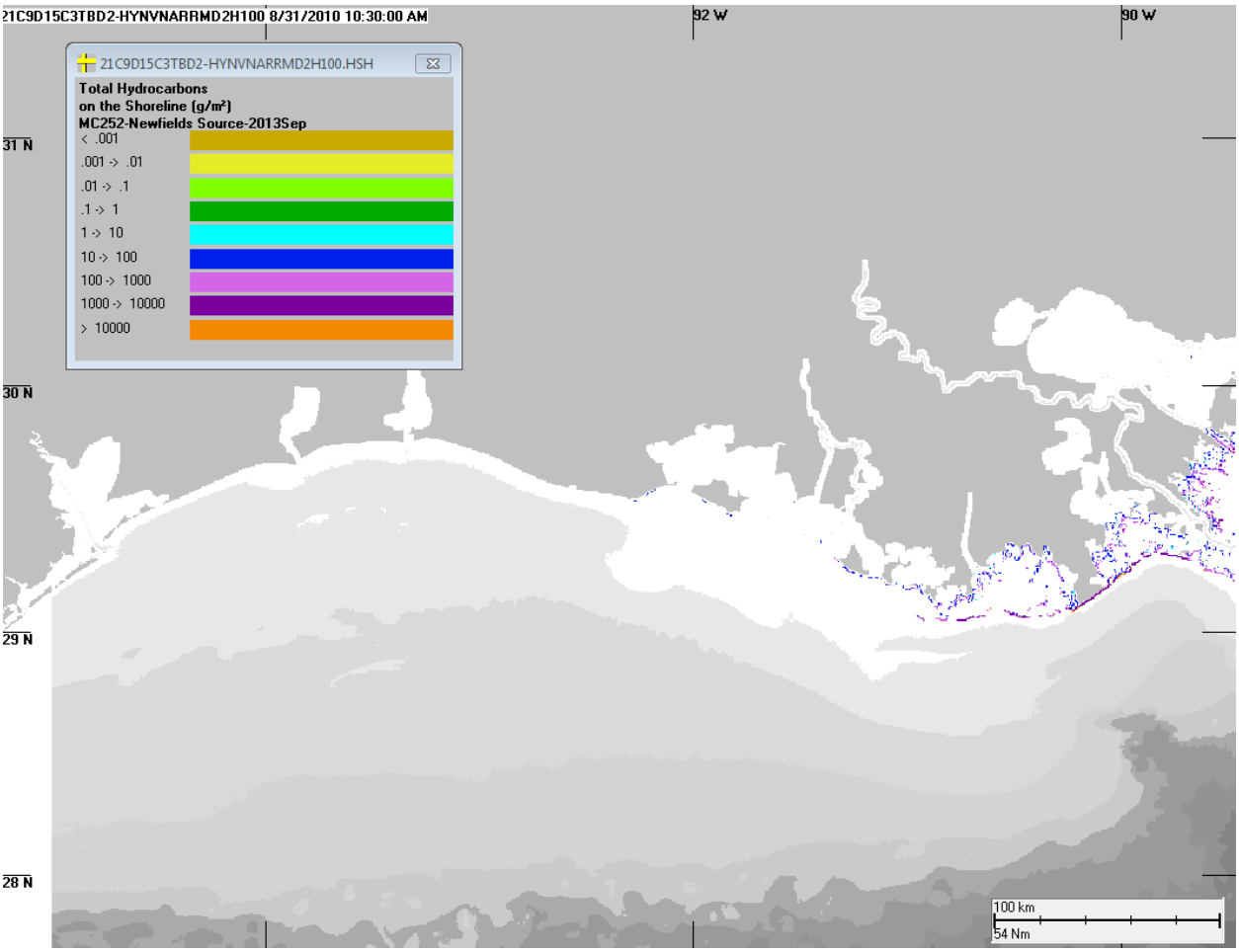

Figure D.1-6 Amount of oil accumulated on shorelines for the simulation using HYCOM-NRL Real-time currents and NARR winds (west extent).

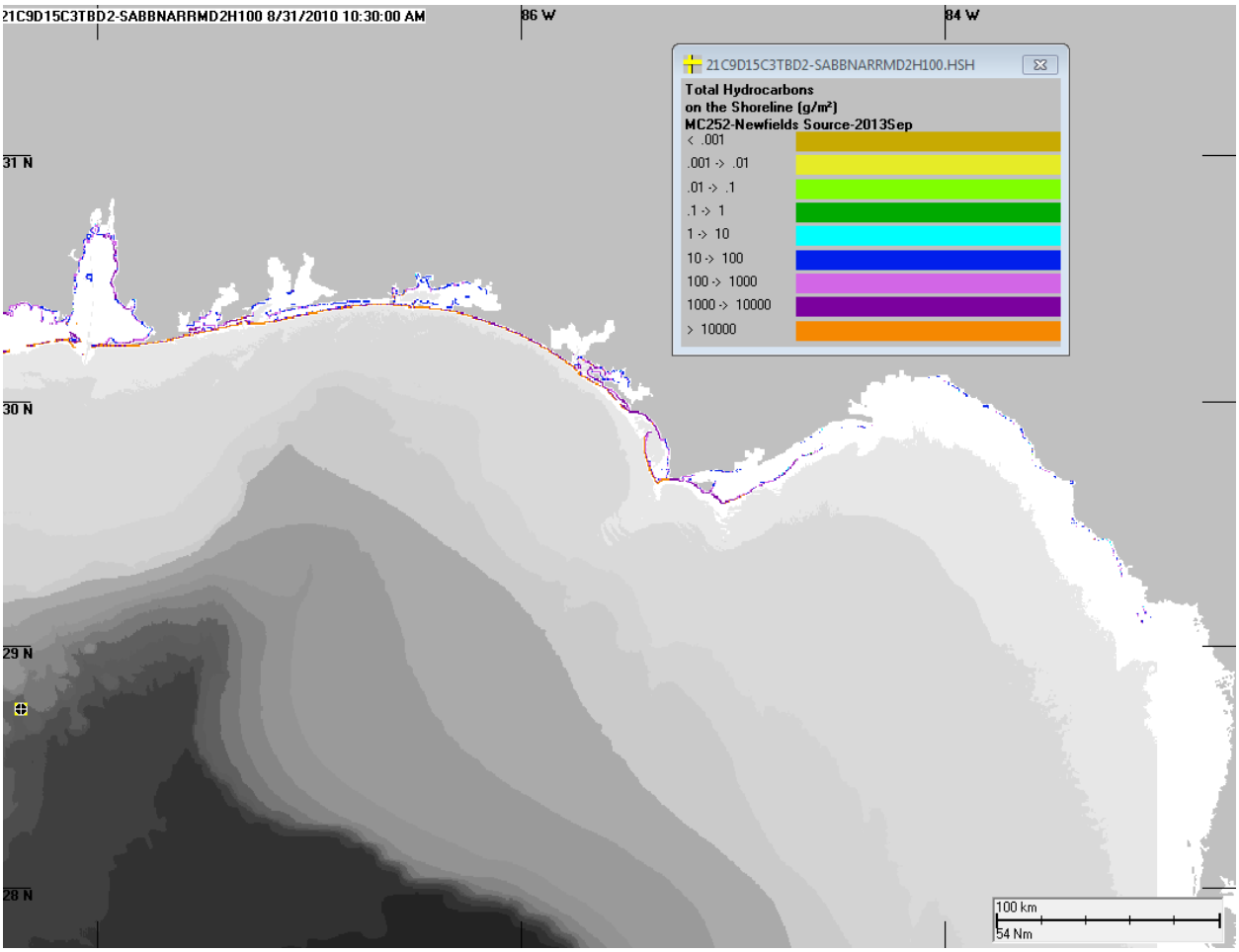

Figure D.1-7 Amount of oil accumulated on shorelines for the simulation using SABGOM currents and NARR winds (east extent).

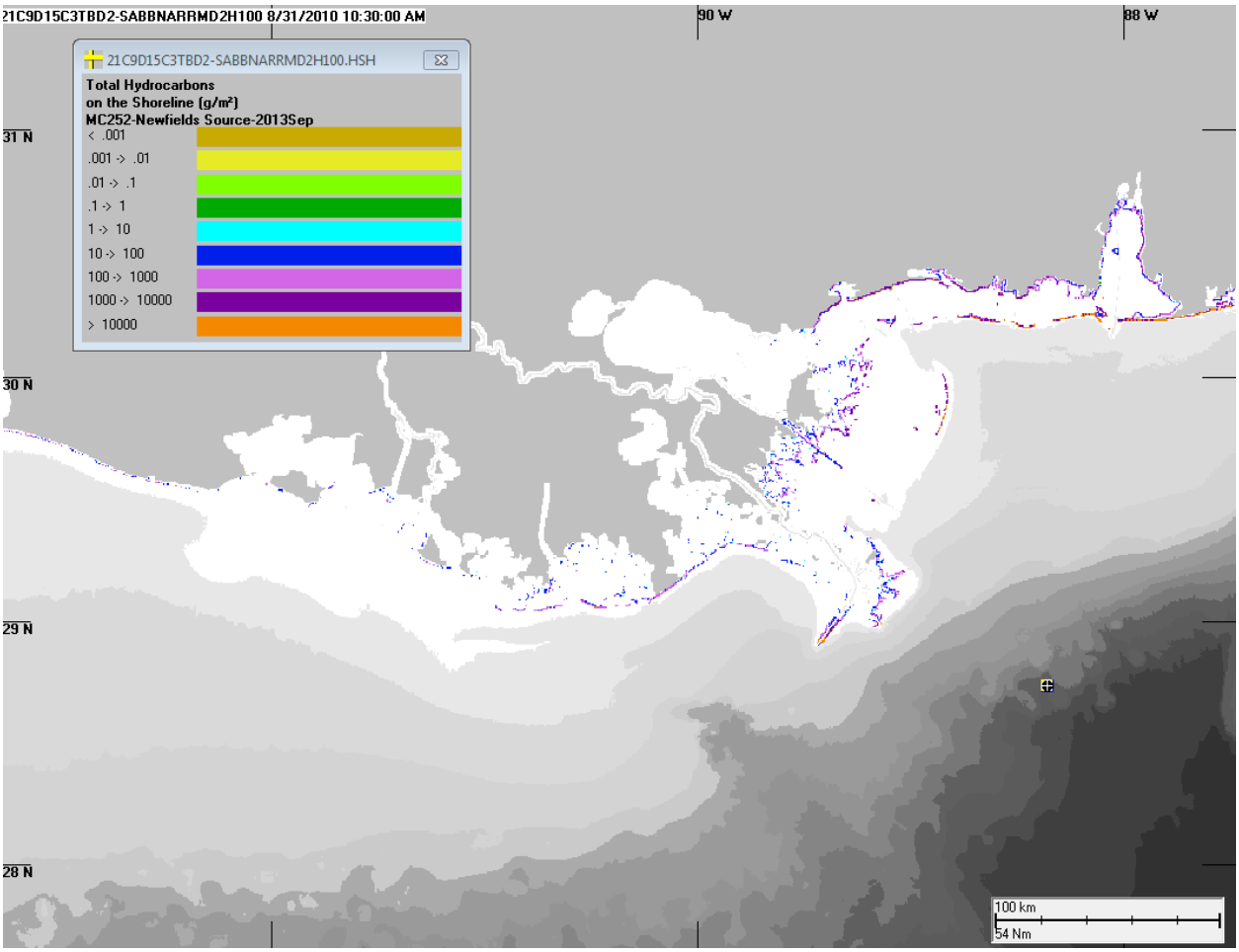

Figure D.1-8 Amount of oil accumulated on shorelines for the simulation using SABGOM currents and NARR winds (central).

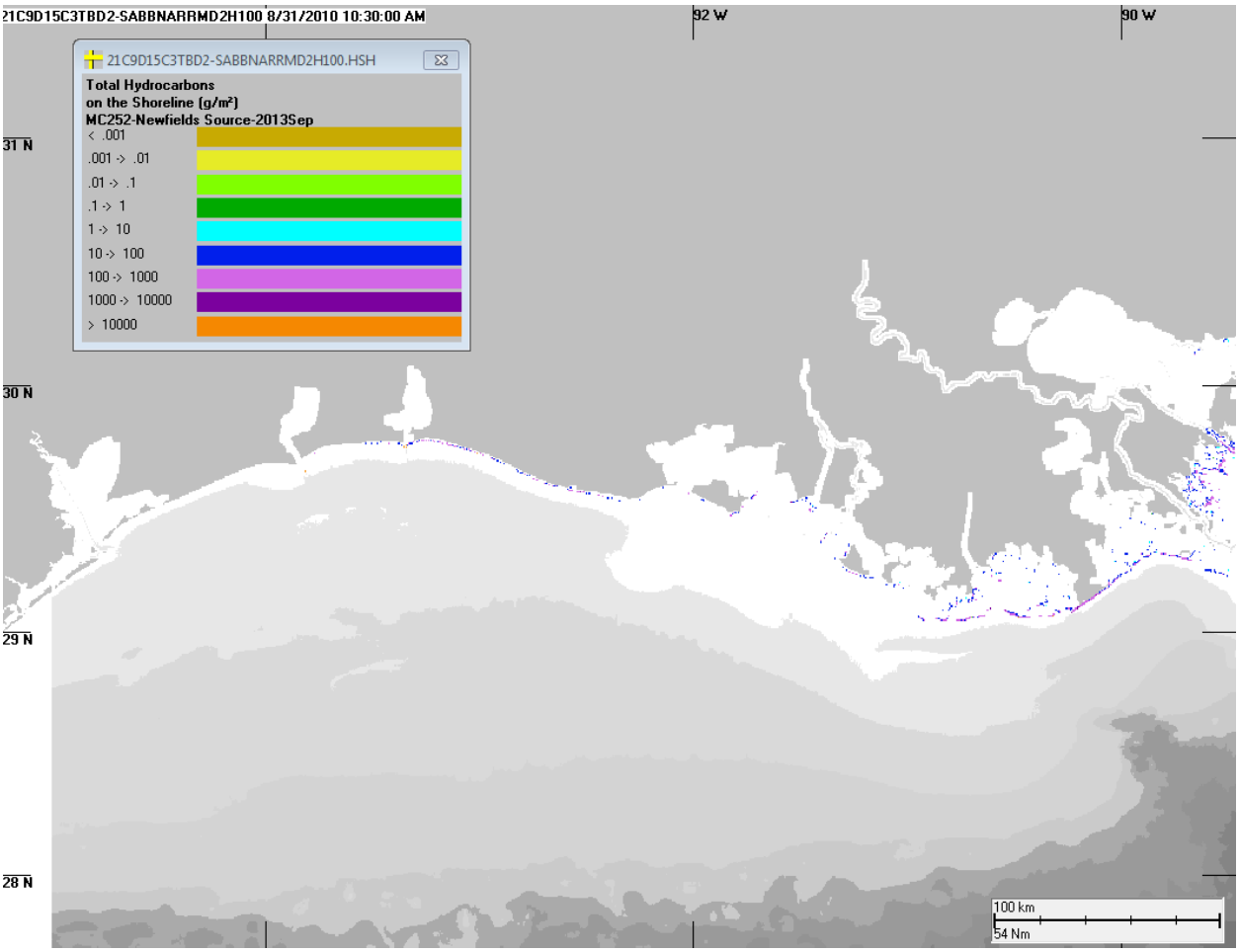

Figure D.1-9 Amount of oil accumulated on shorelines for the simulation using SABGOM currents and NARR winds (west extent).

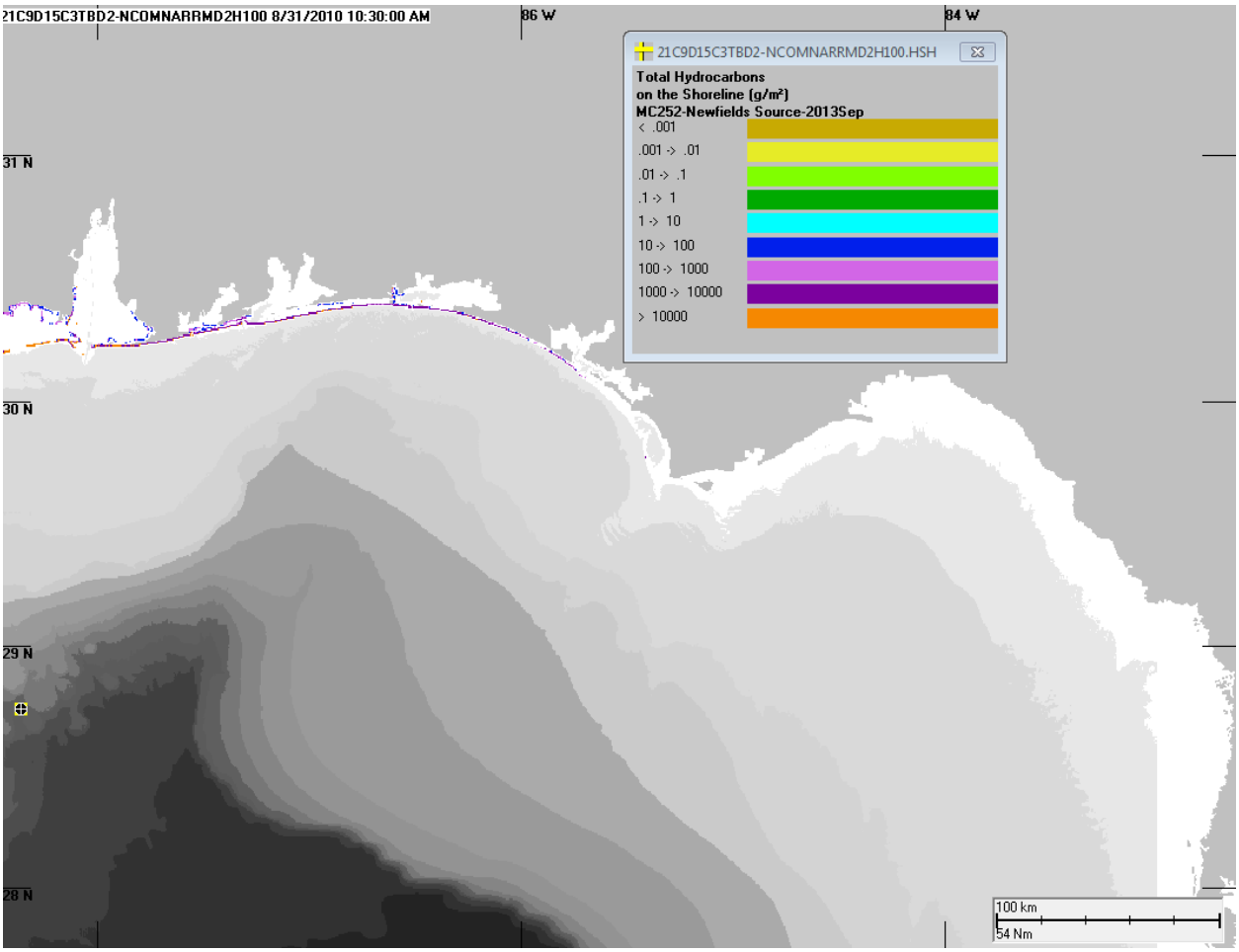

Figure D.1-10 Amount of oil accumulated on shorelines for the simulation using NCOM Real-Time currents and NARR winds (east extent).

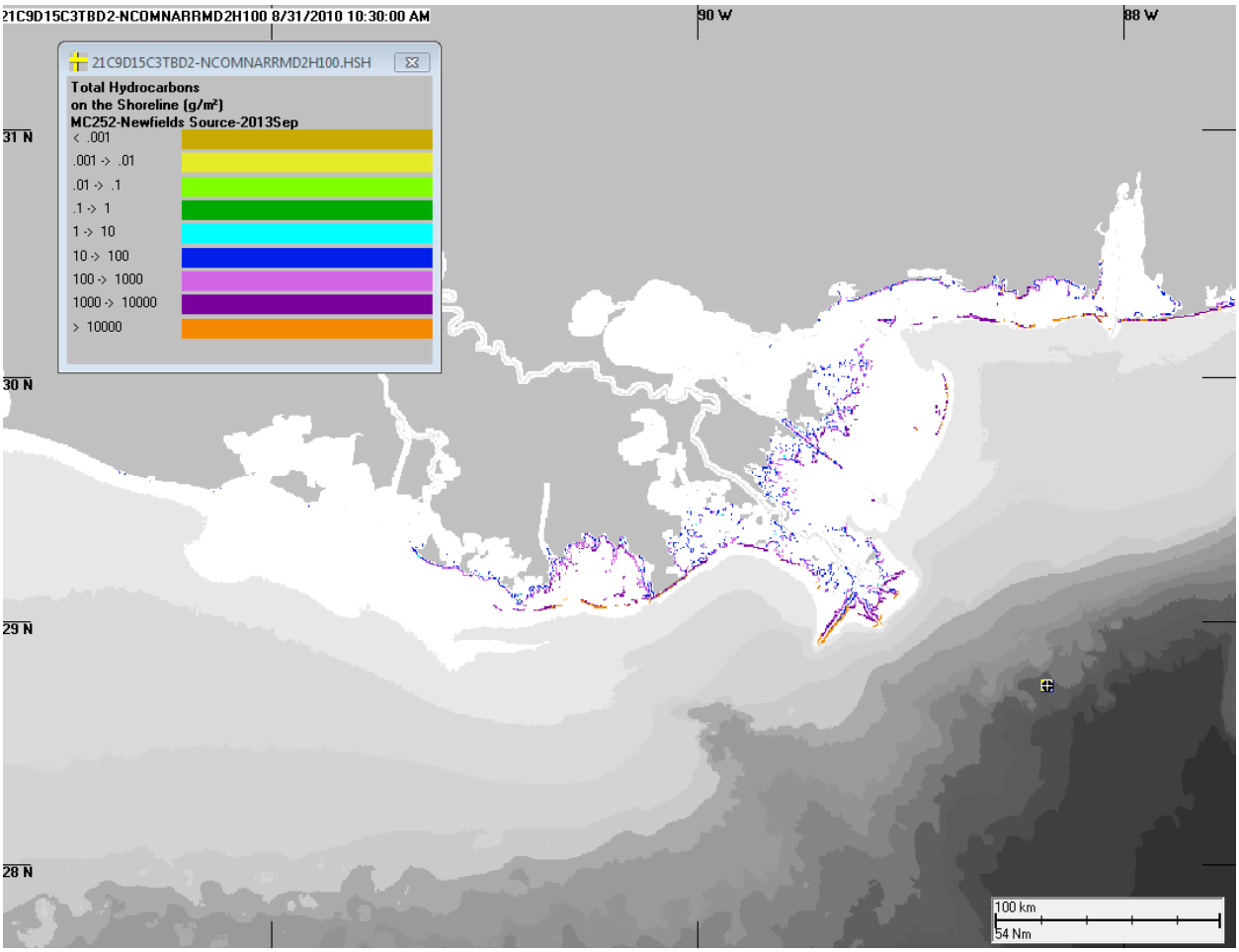

Figure D.1-11 Amount of oil accumulated on shorelines for the simulation using NCOM Real-Time currents and NARR winds (central).

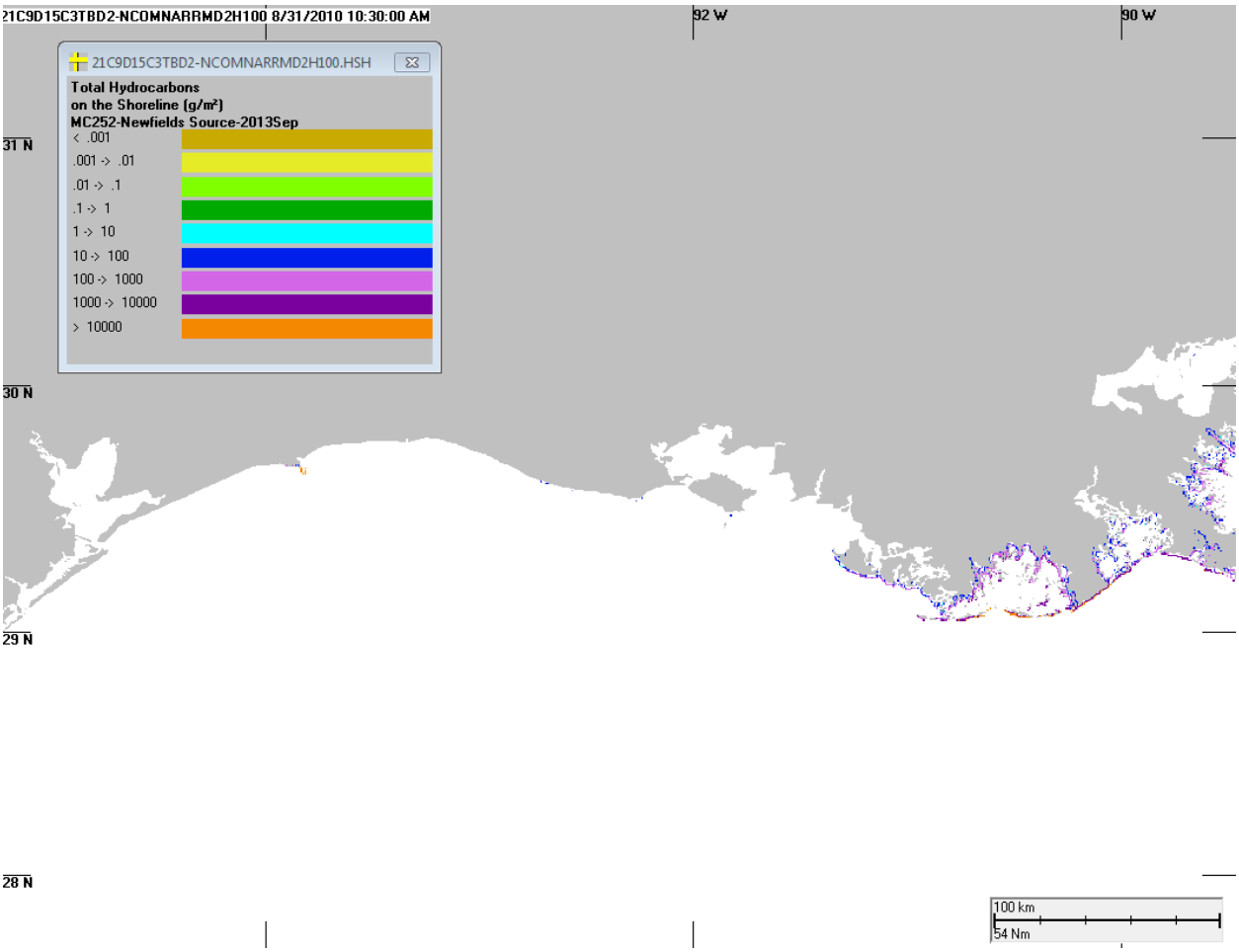

Figure D.1-12 Amount of oil accumulated on shorelines for the simulation using NCOM Real-Time currents and NARR winds (west extent).

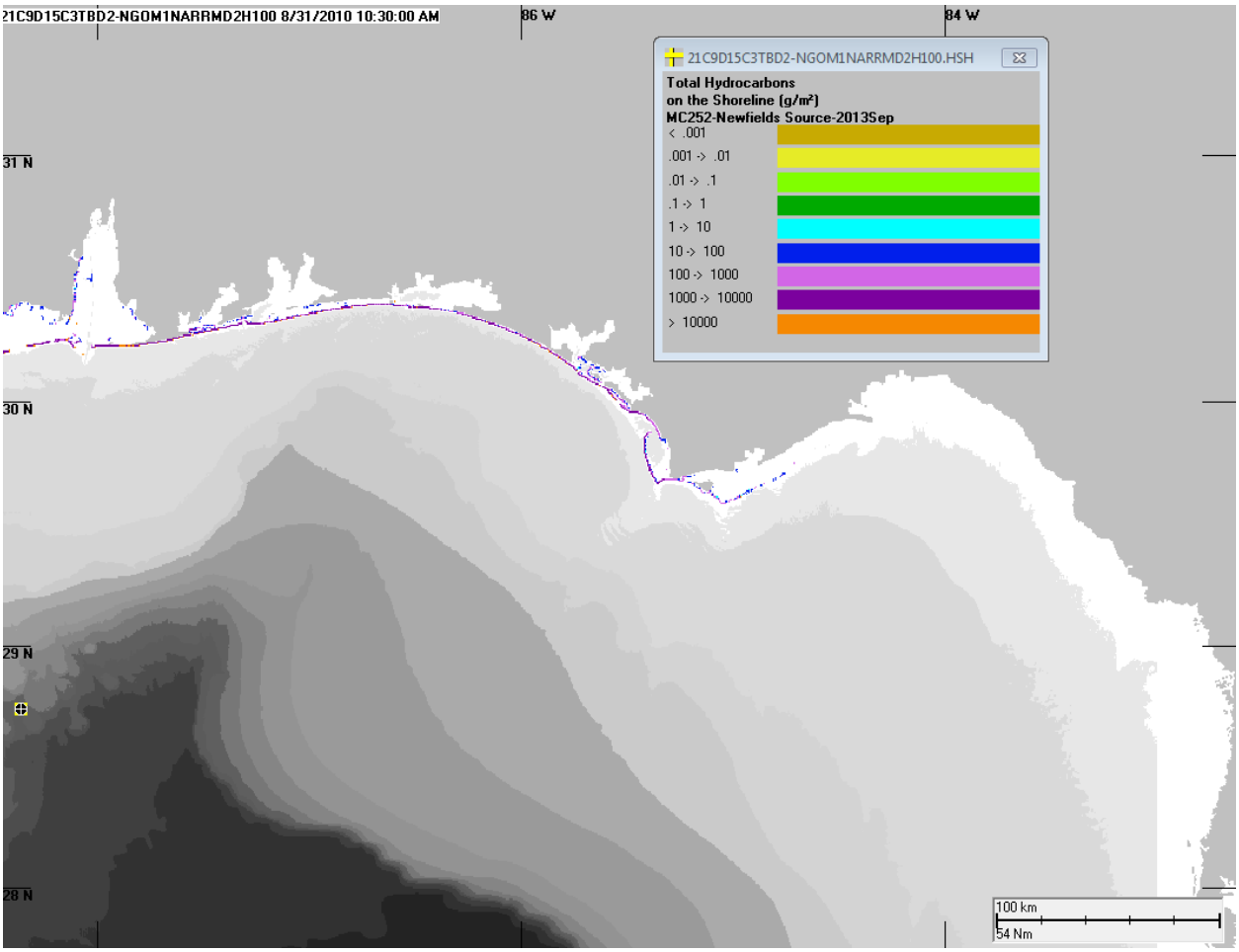

Figure D.1-13 Amount of oil accumulated on shorelines for the simulation using NGOM currents and NARR winds (east extent).

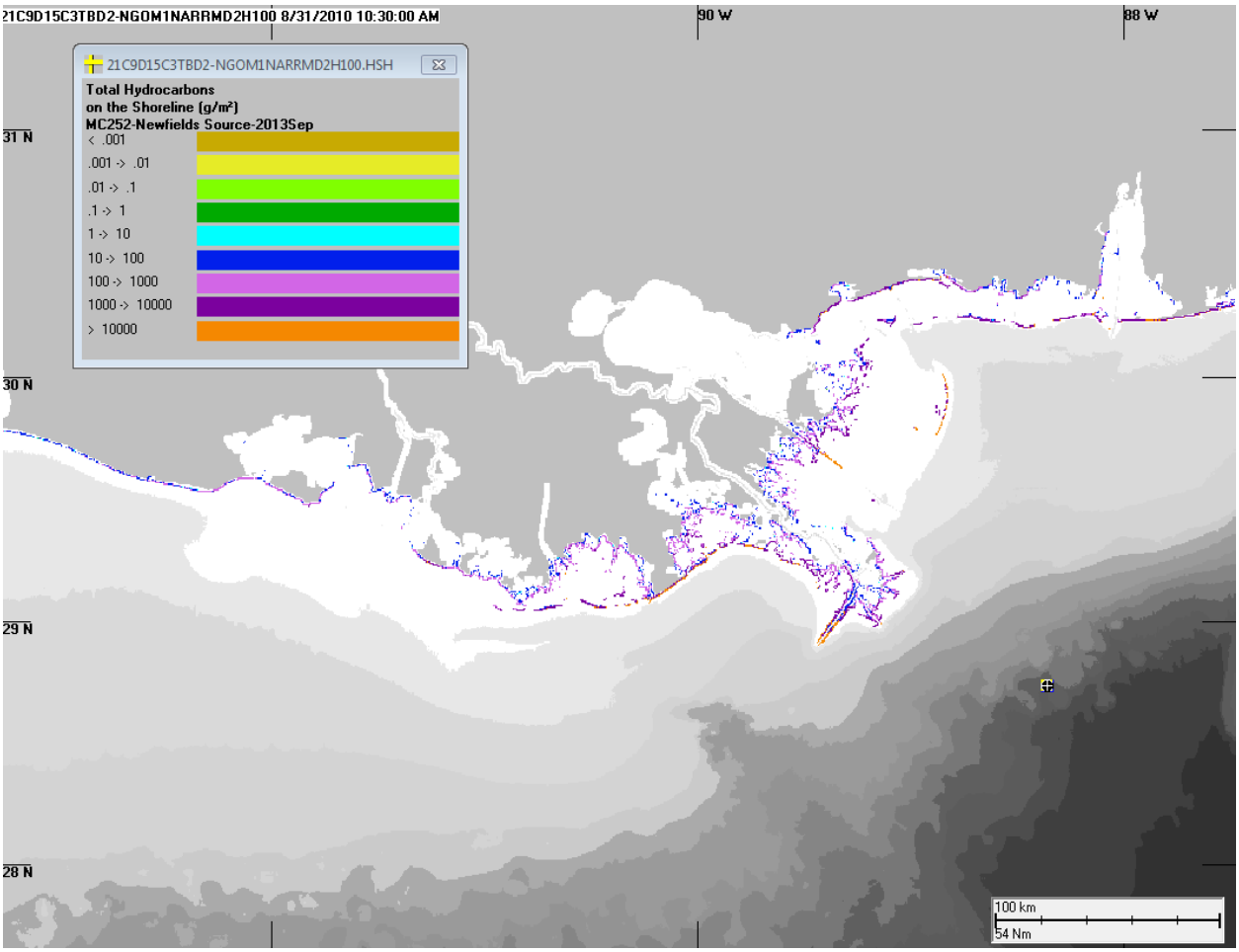

Figure D.1-14 Amount of oil accumulated on shorelines for the simulation using NGOM currents and NARR winds (central).

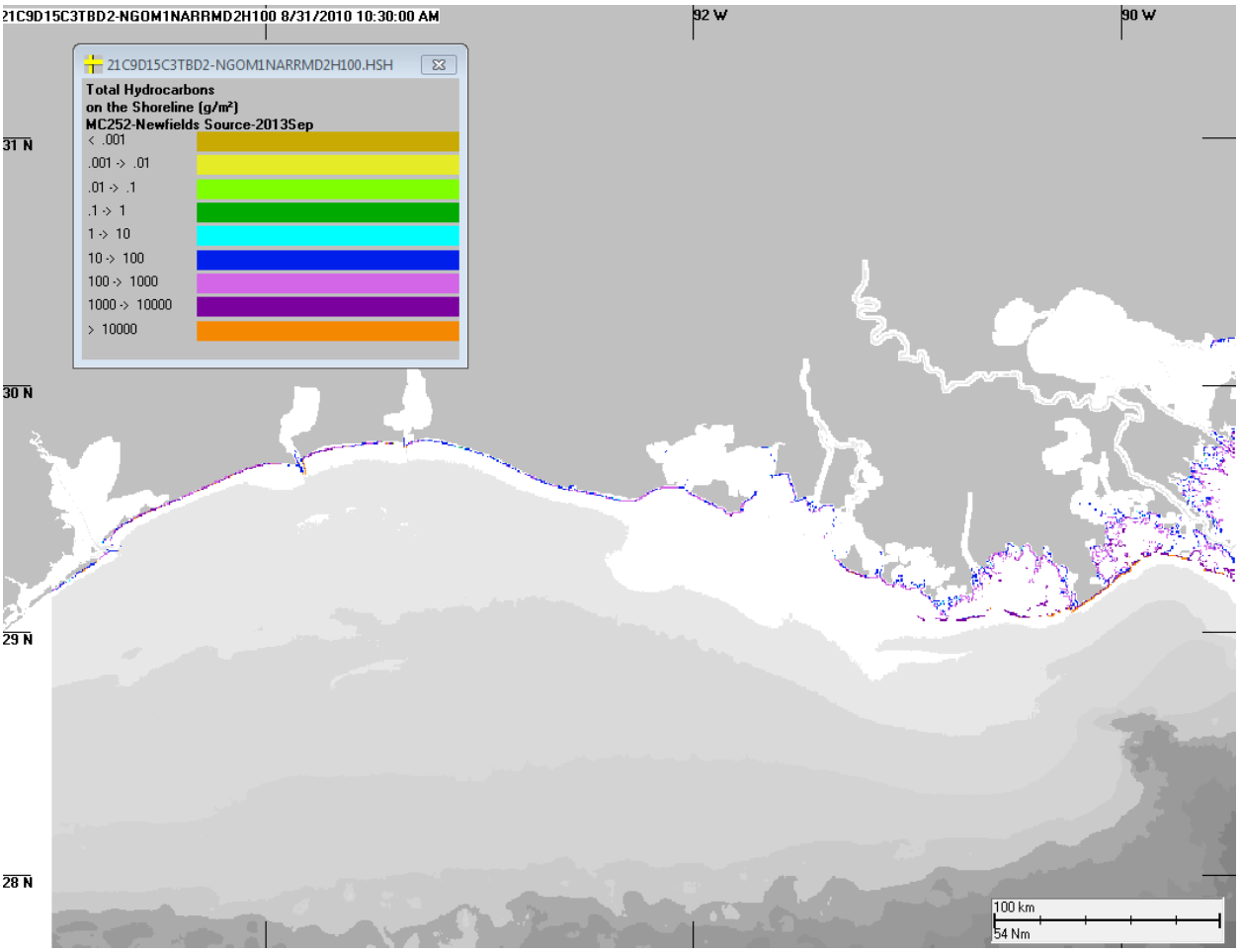

Figure D.1-15 Amount of oil accumulated on shorelines for the simulation using NGOM currents and NARR winds (west extent).

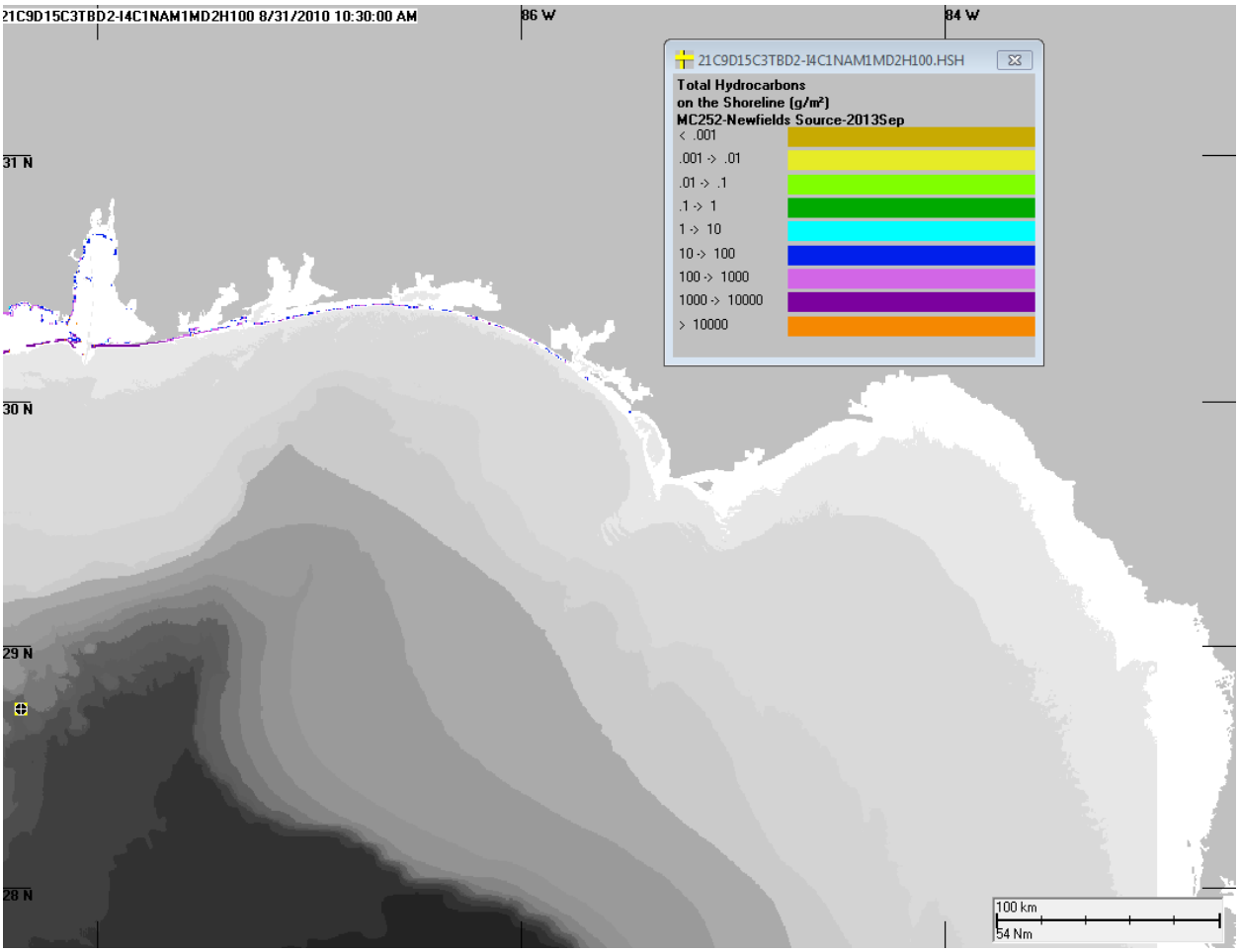

Figure D.1-16 Amount of oil accumulated on shorelines for the simulation using IASROMS-hourly currents and NAM winds (east extent).

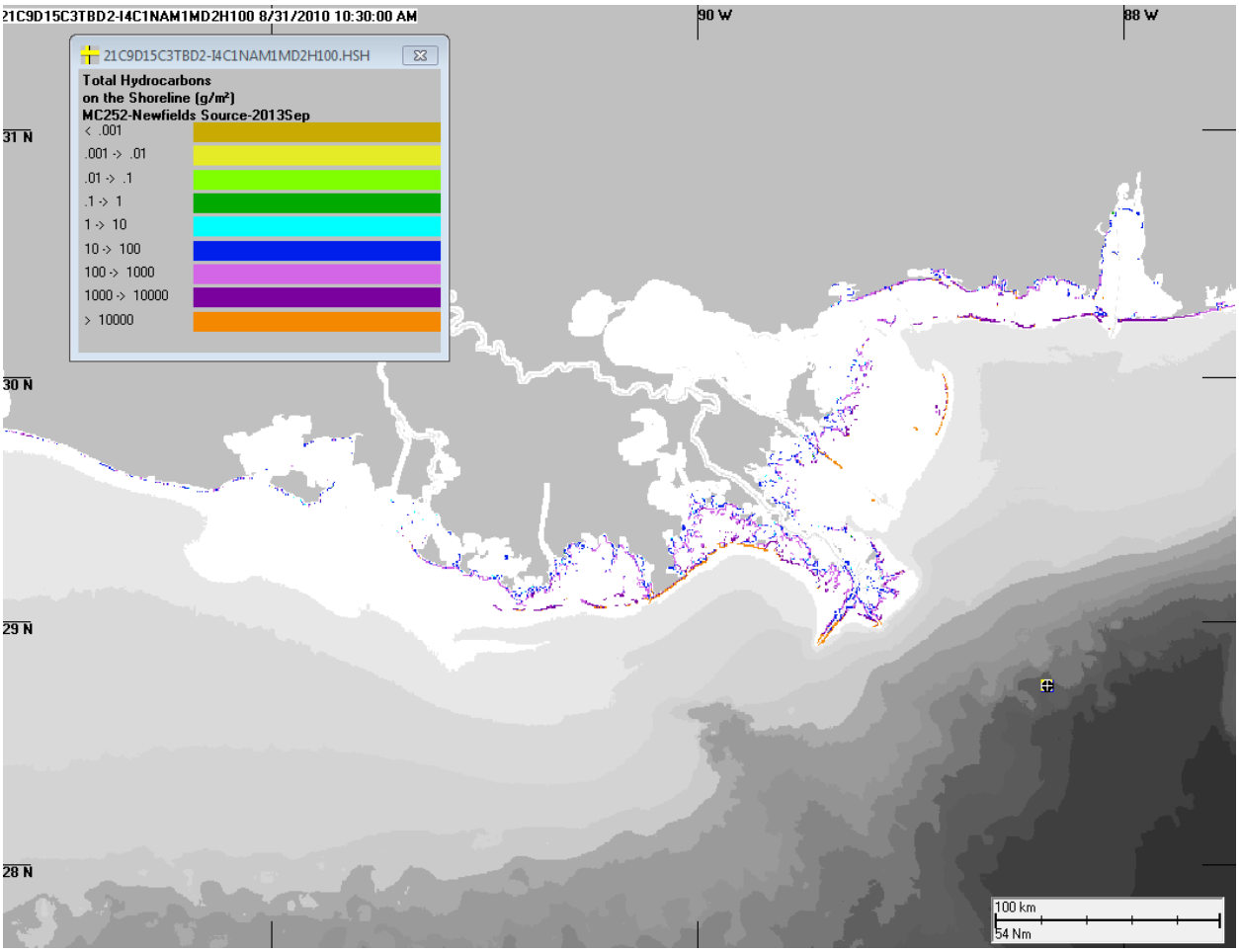

Figure D.1-17 Amount of oil accumulated on shorelines for the simulation using IASROMS-hourly currents and NAM winds (central).

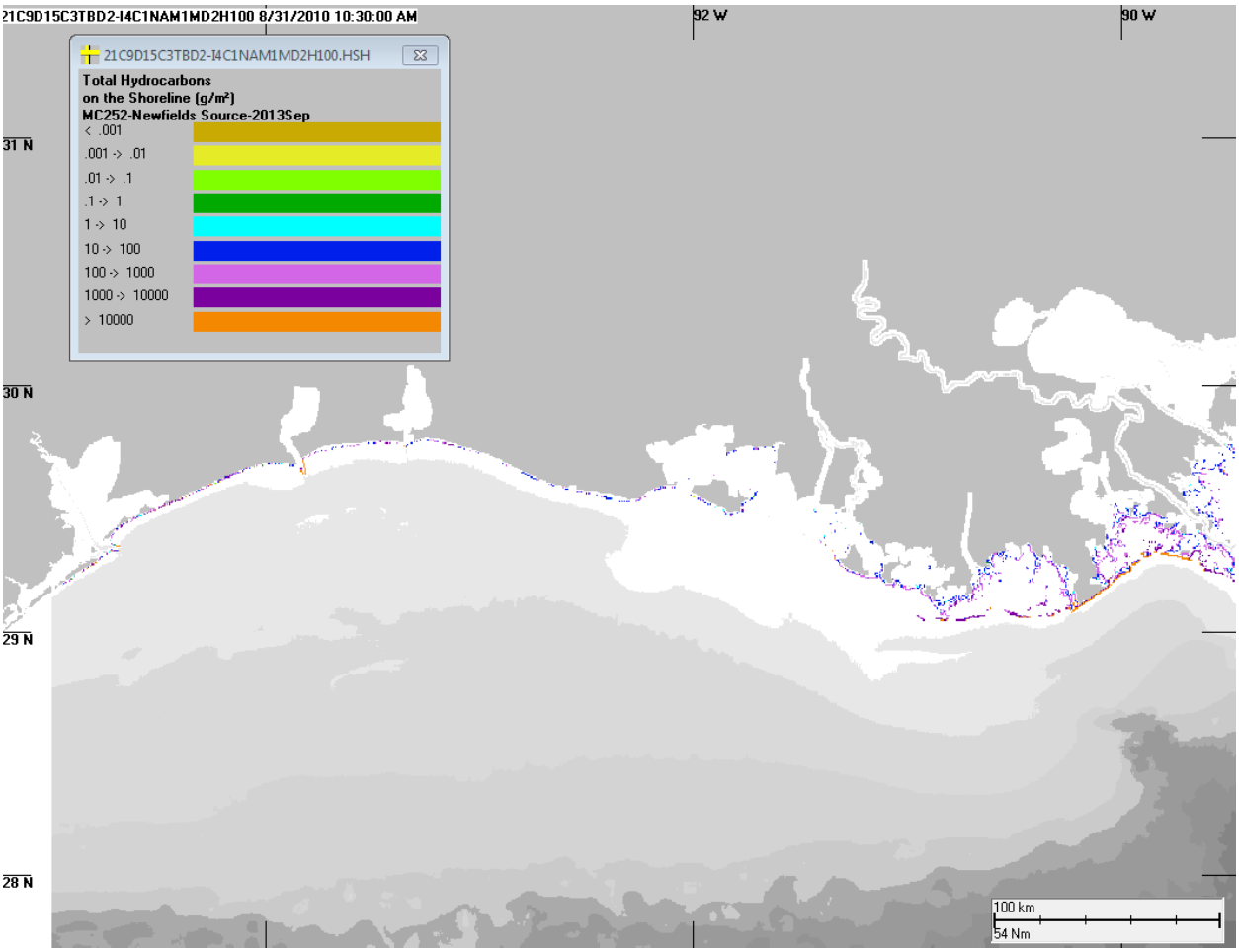

Figure D.1-18 Amount of oil accumulated on shorelines for the simulation using IASROMS-hourly currents and NAM winds (west extent).

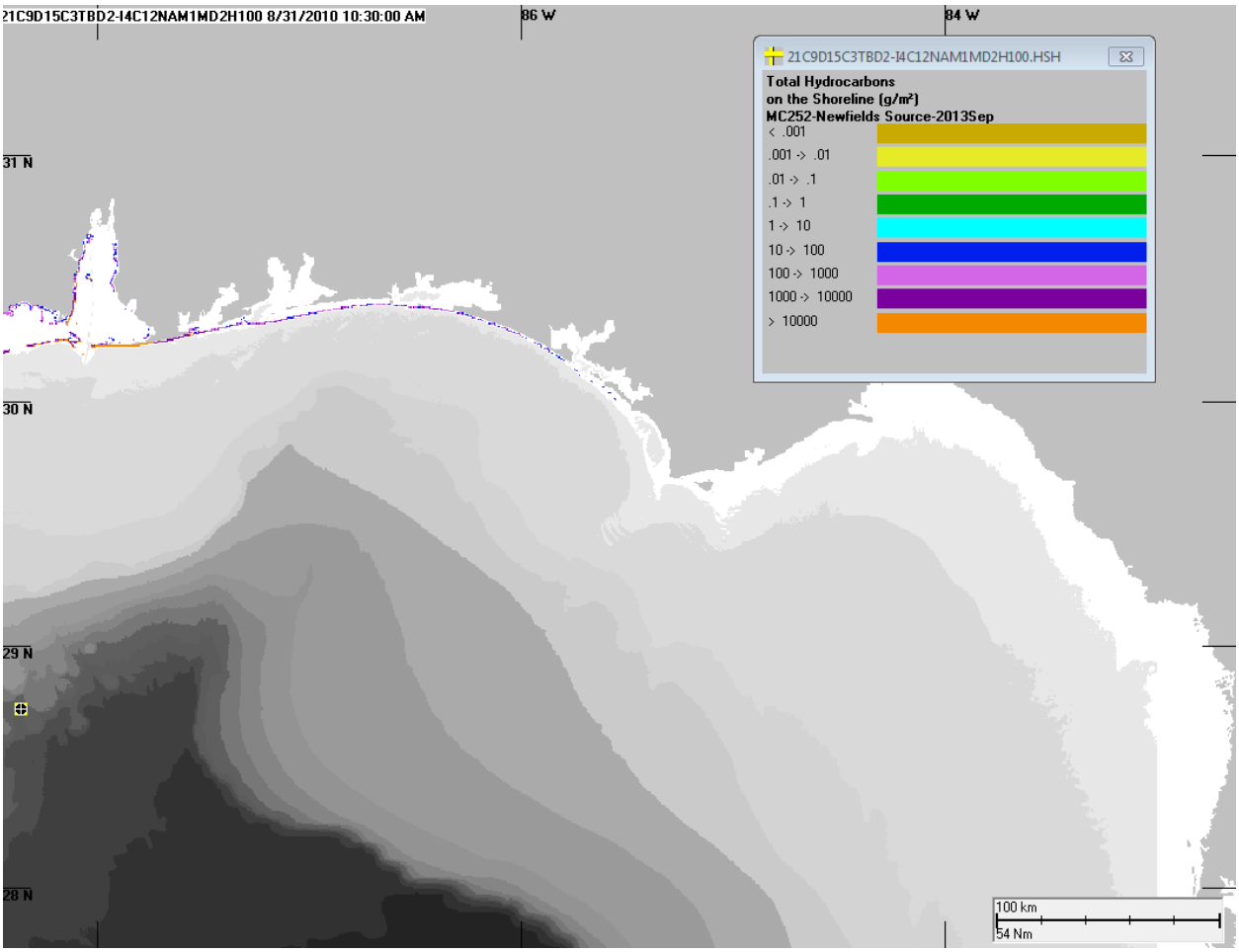

Figure D.1-19 Amount of oil accumulated on shorelines for the simulation using IASROMS-12 hourly currents and NAM winds (east extent).

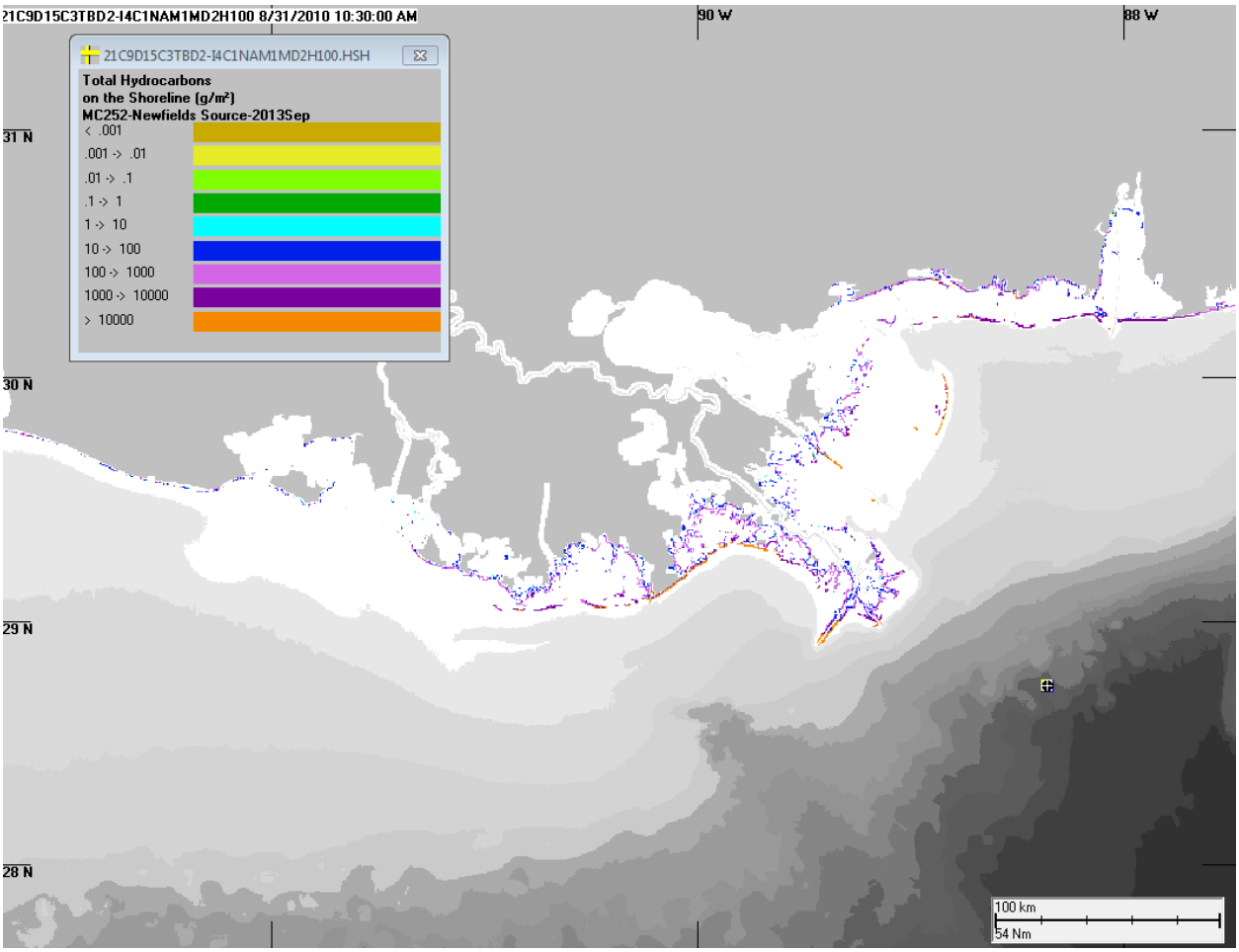

Figure D.1-20 Amount of oil accumulated on shorelines for the simulation using IASROMS-12 hourly currents and NAM winds (central).

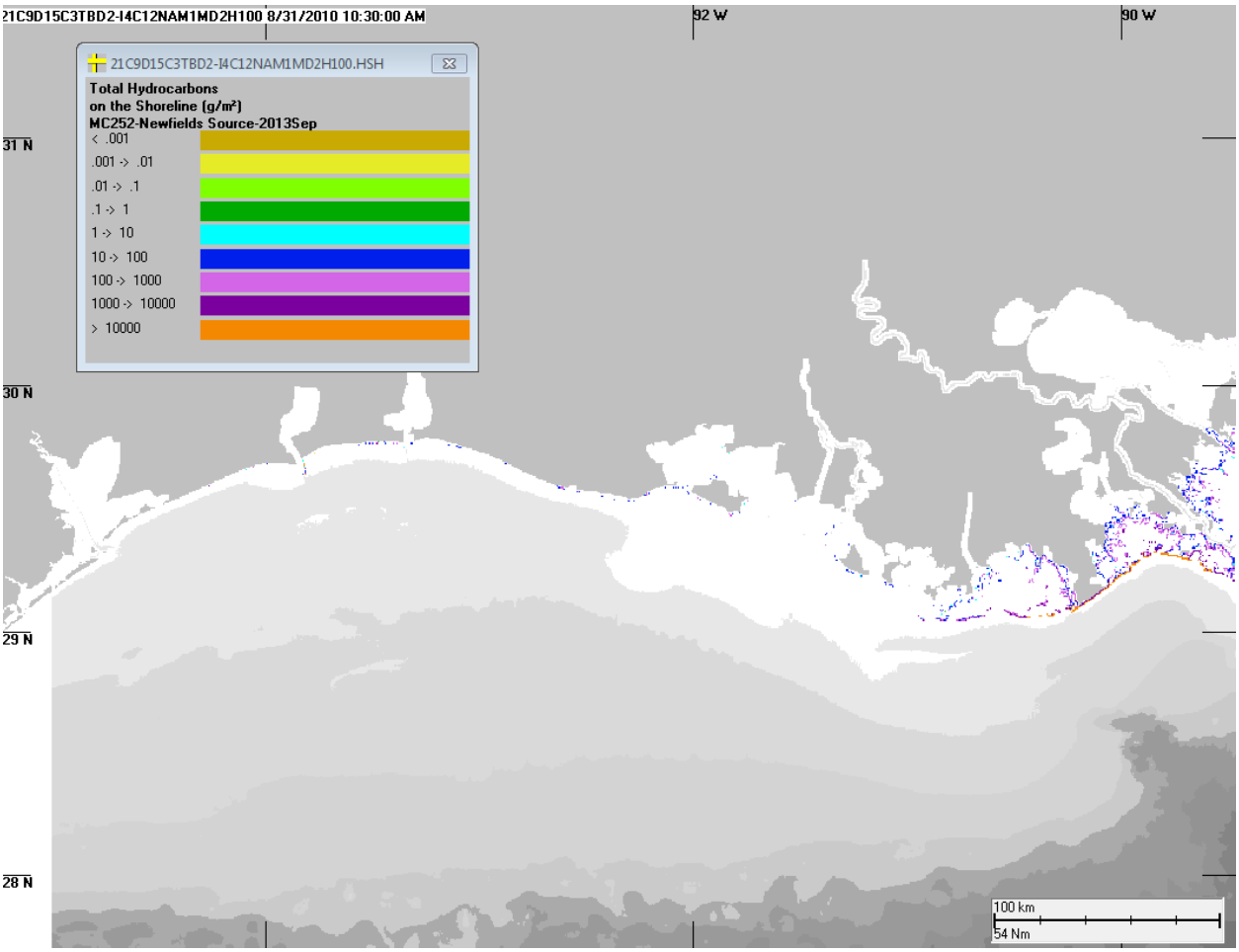

Figure D.1-21 Amount of oil accumulated on shorelines for the simulation using IASROMS-12 hourly currents and NAM winds (west extent).

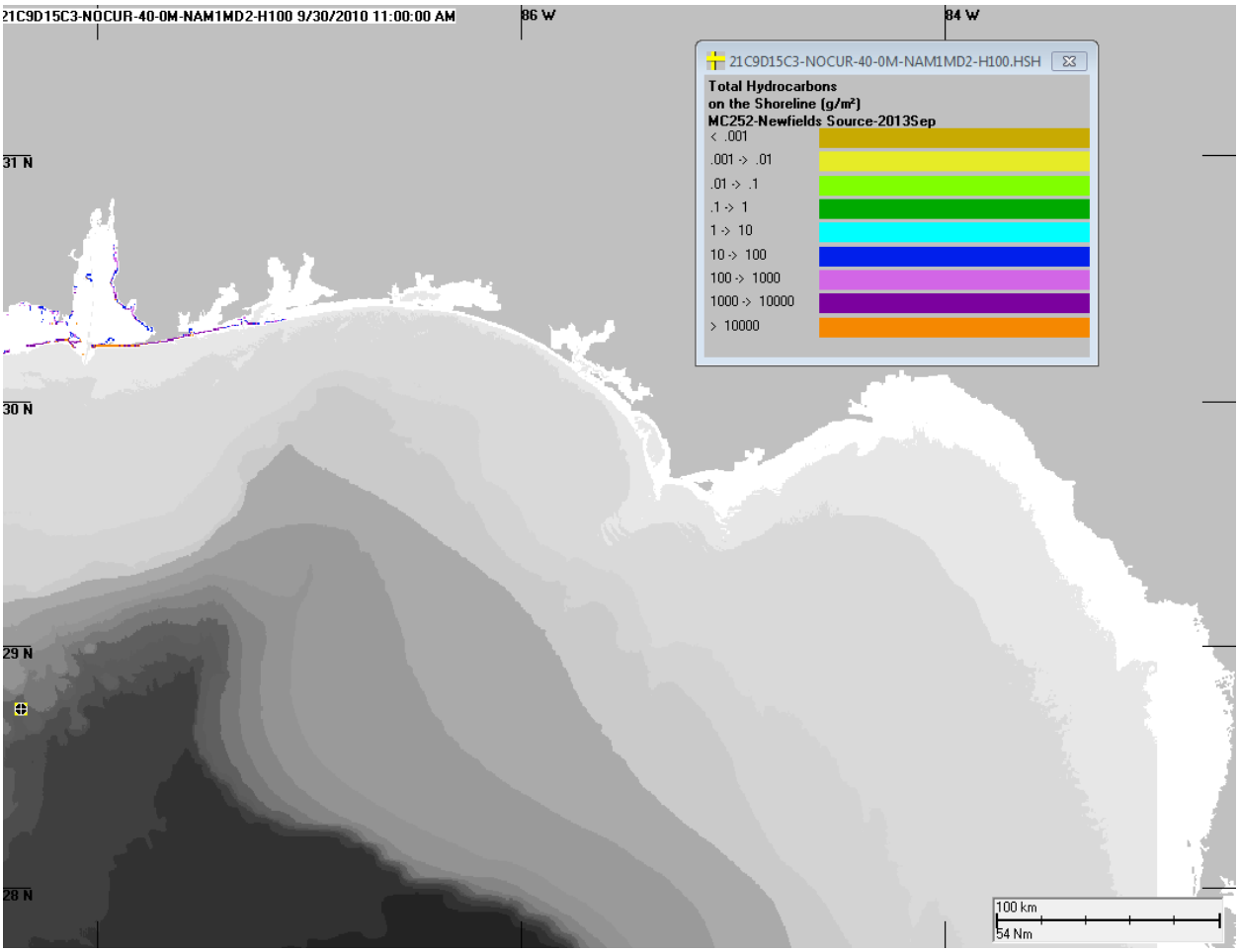

Figure D.1-22 Amount of oil accumulated on shorelines for the simulation using no currents and NAM winds (east extent).

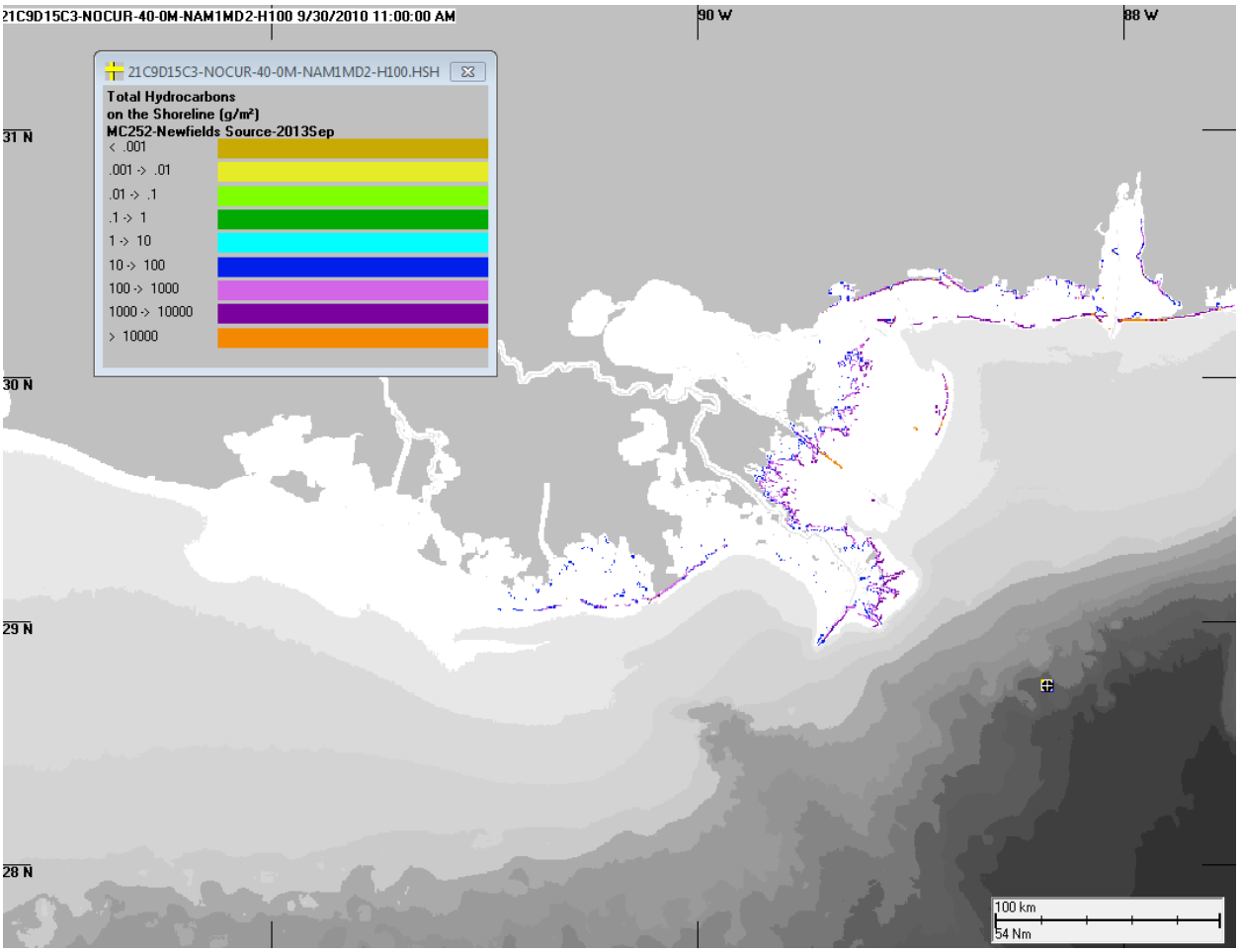

Figure D.1-23 Amount of oil accumulated on shorelines for the simulation using no currents and NAM winds (central).

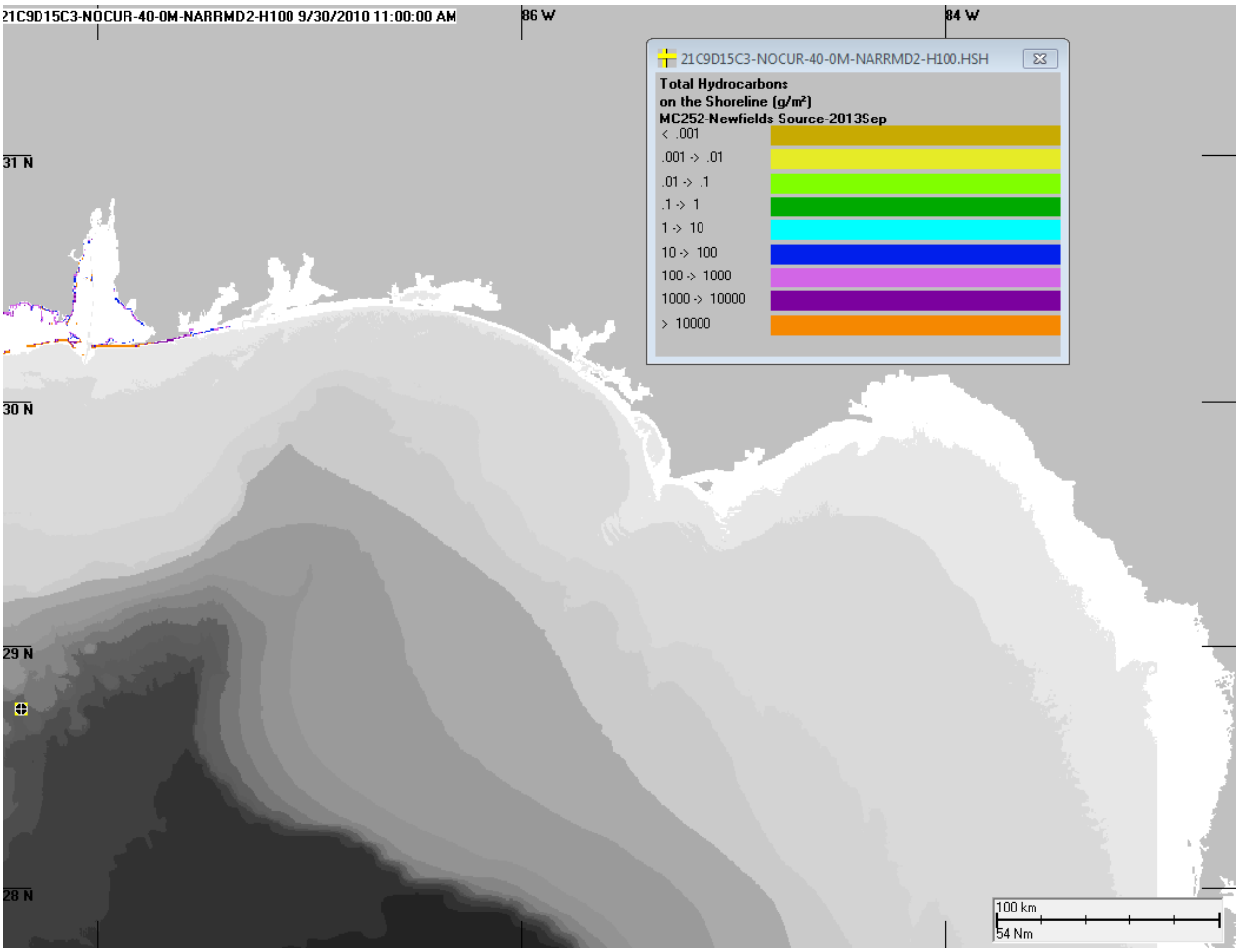

Figure D.1-24 Amount of oil accumulated on shorelines for the simulation using no currents and NARR winds (east extent).

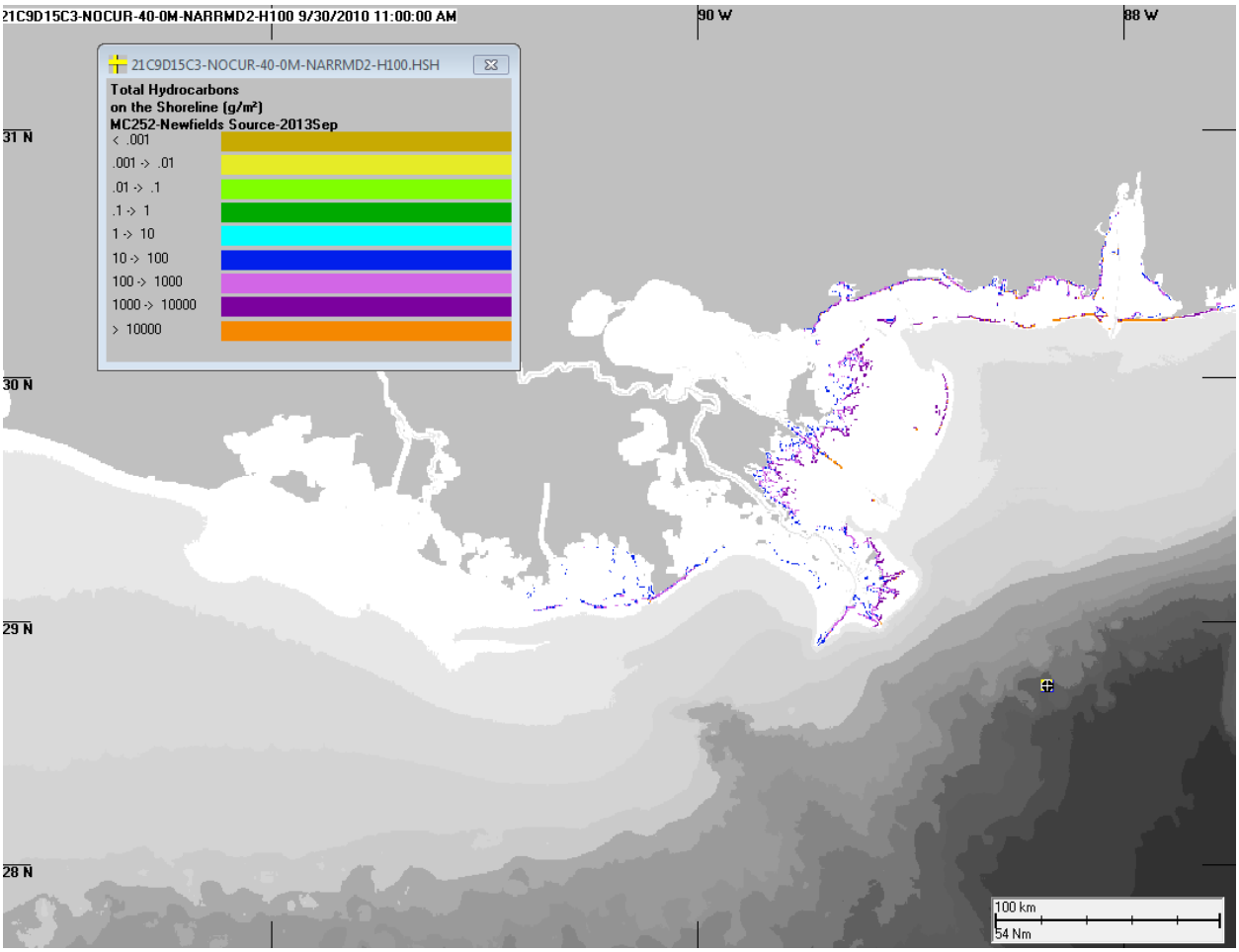

Figure D.1-25 Amount of oil accumulated on shorelines for the simulation using no currents and NARR winds (central).

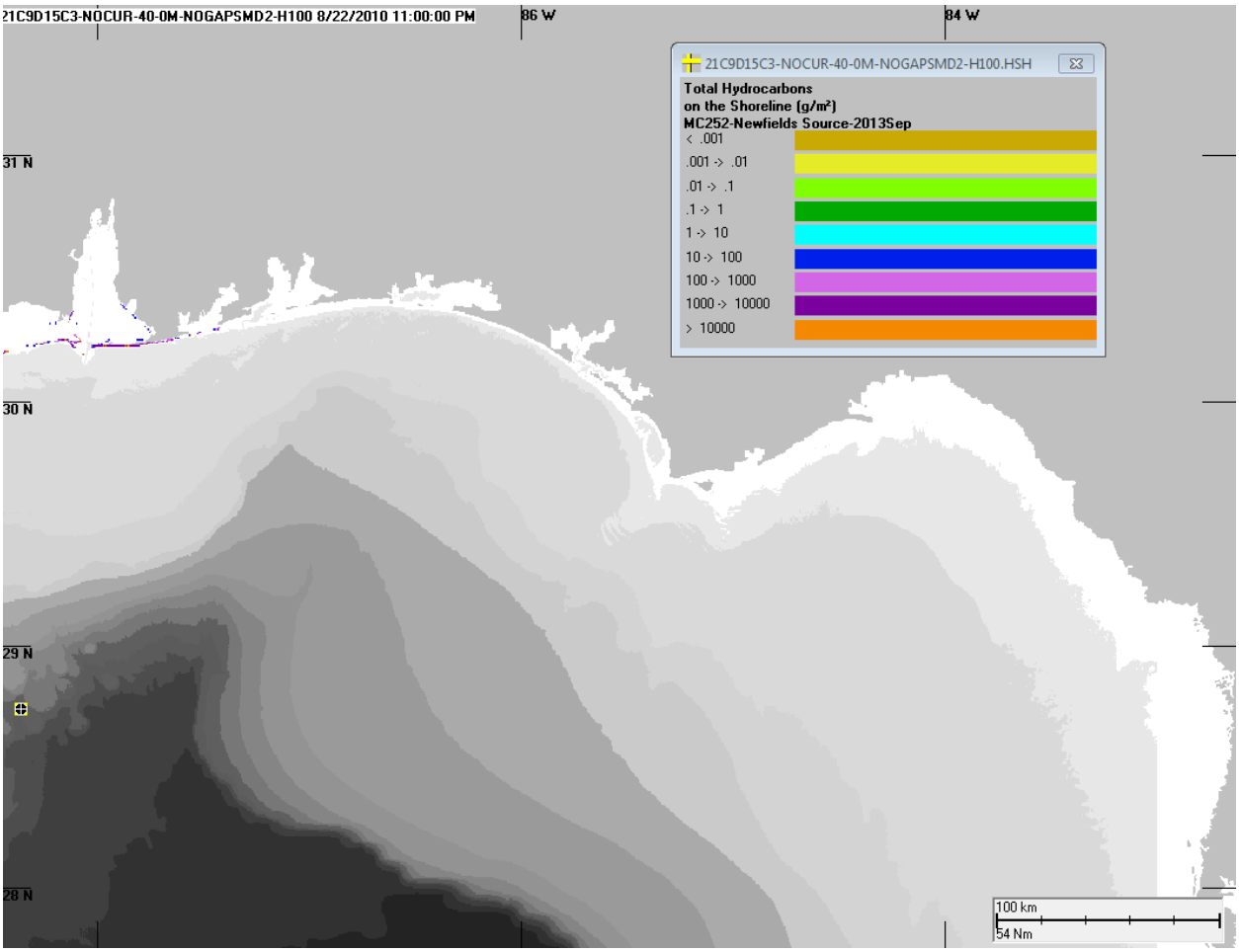

Figure D.1-26 Amount of oil accumulated on shorelines for the simulation using no currents and NOGAPS winds (east extent).

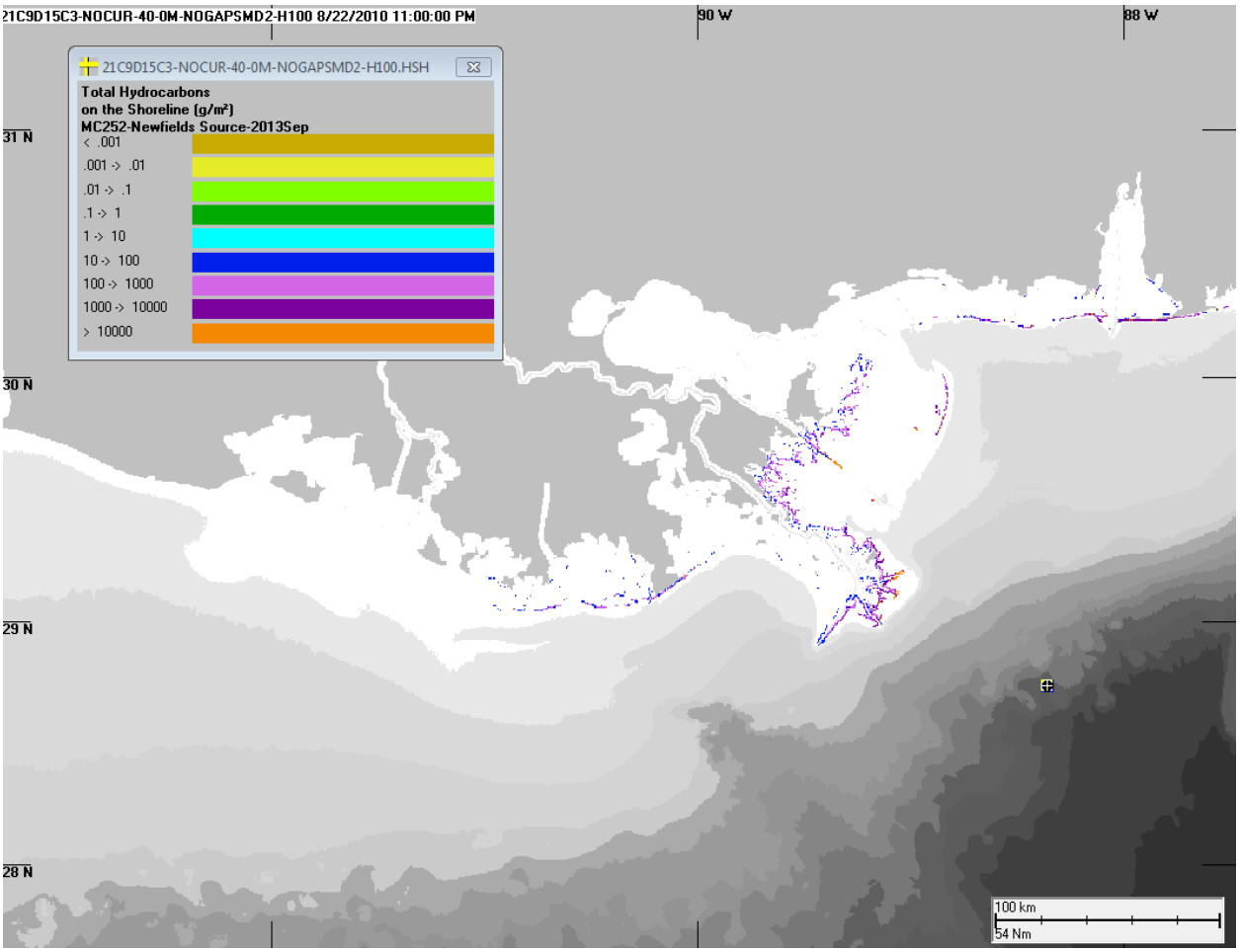

Figure D.1-27 Amount of oil accumulated on shorelines for the simulation using no currents and NOGAPS winds (central).

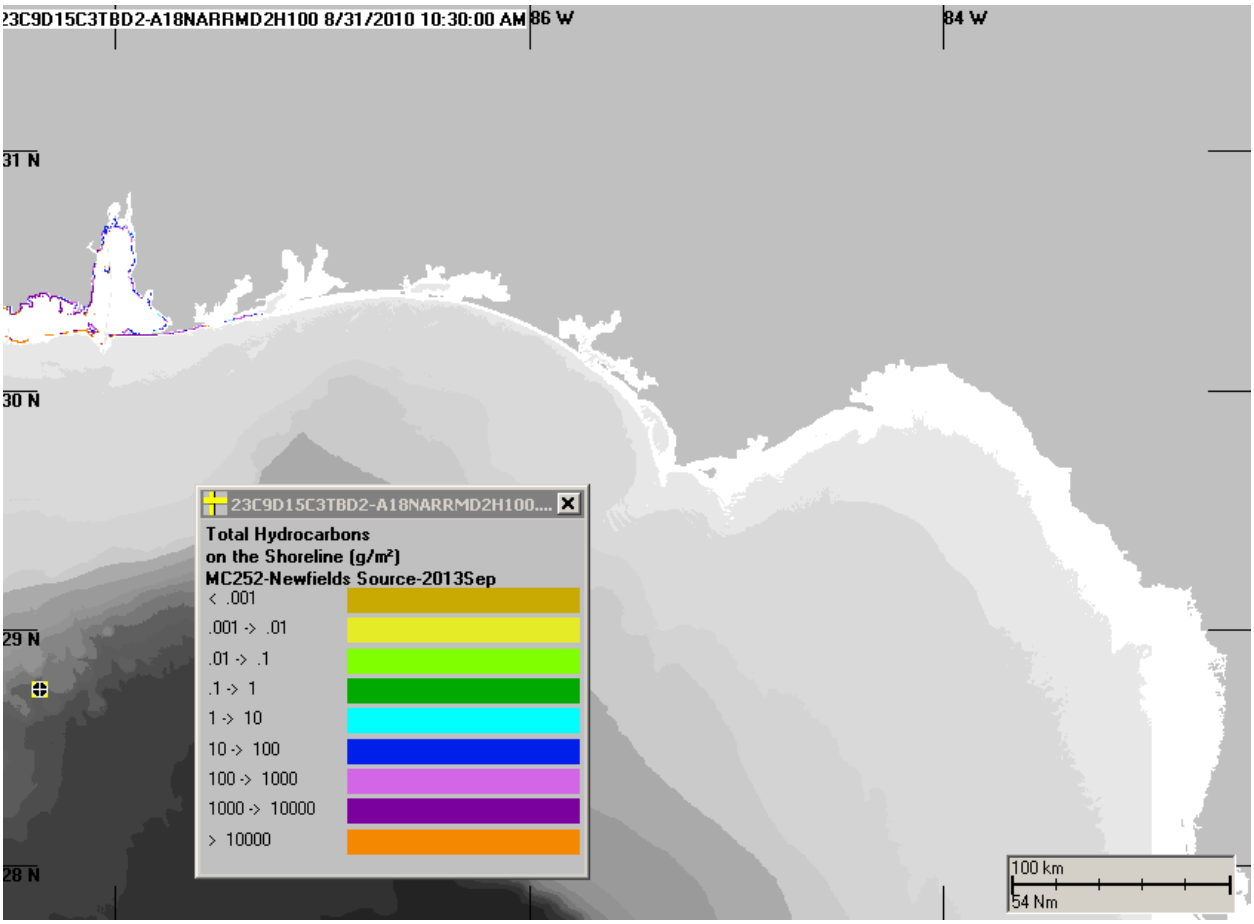

Figure D.1-28. Amount of oil accumulated on shorelines for the simulation using ADCP currents and NARR winds (east extent).

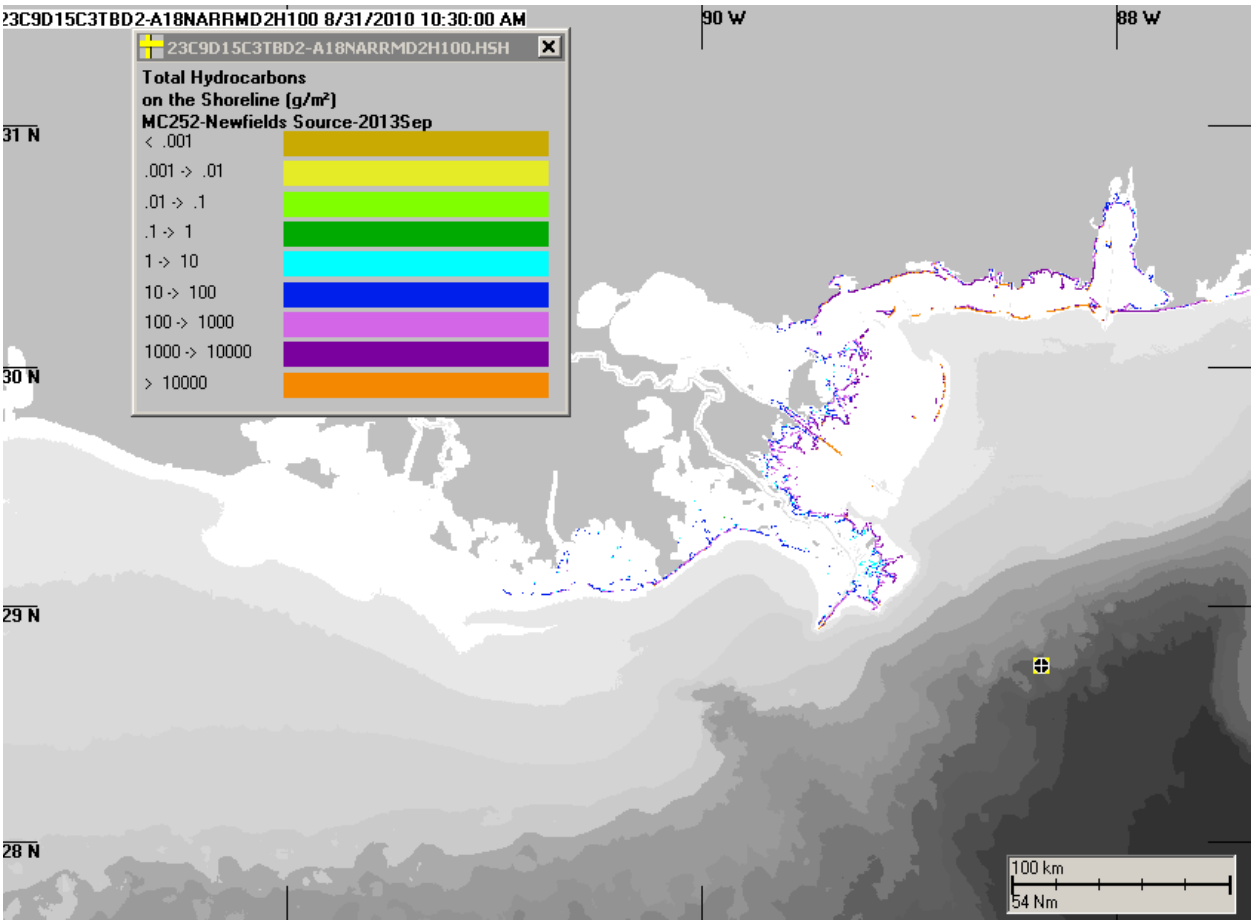

Figure D.1-29. Amount of oil accumulated on shorelines for the simulation using ADCP currents and NARR winds (central).

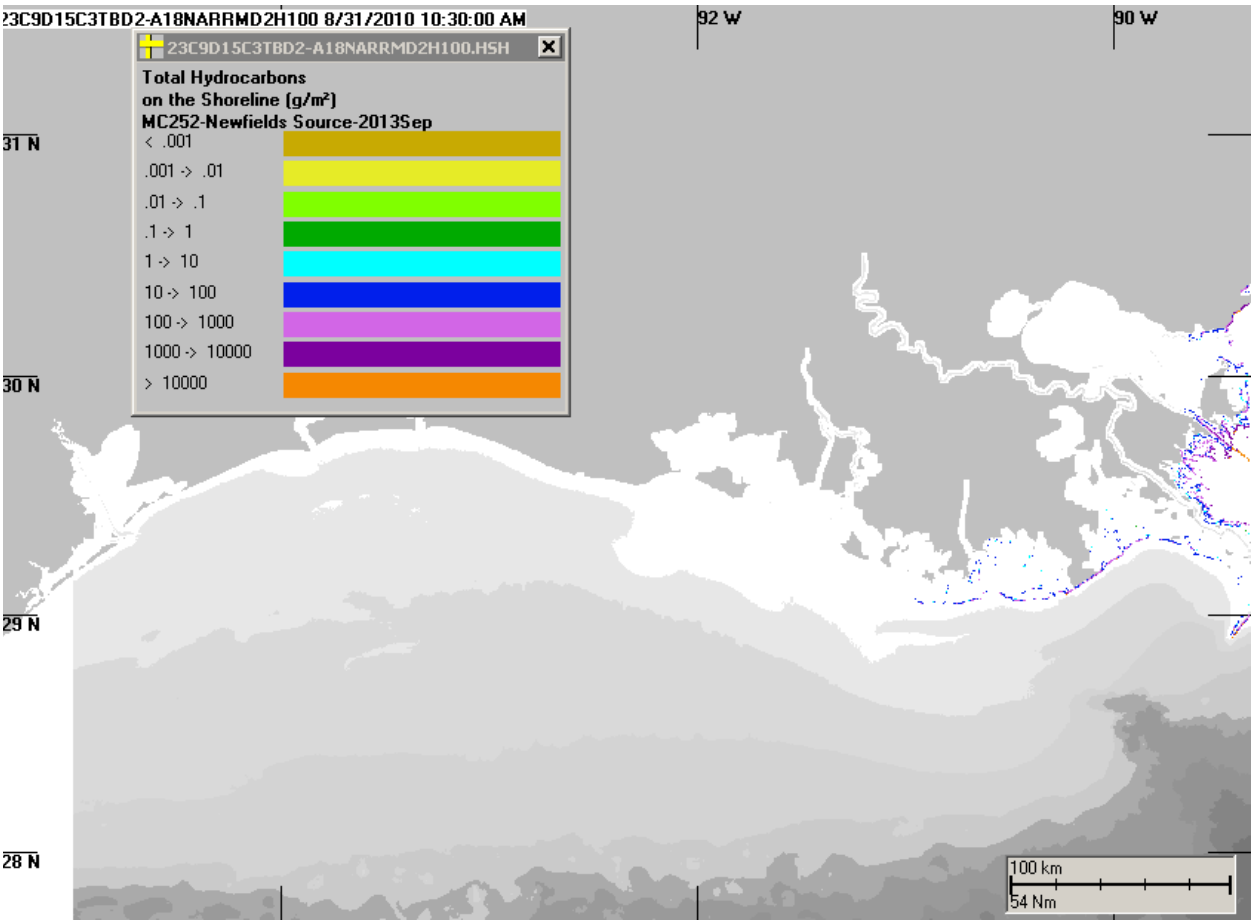

Figure D.1-30. Amount of oil accumulated on shorelines for the simulation using ADCP currents and NARR winds (west extent).

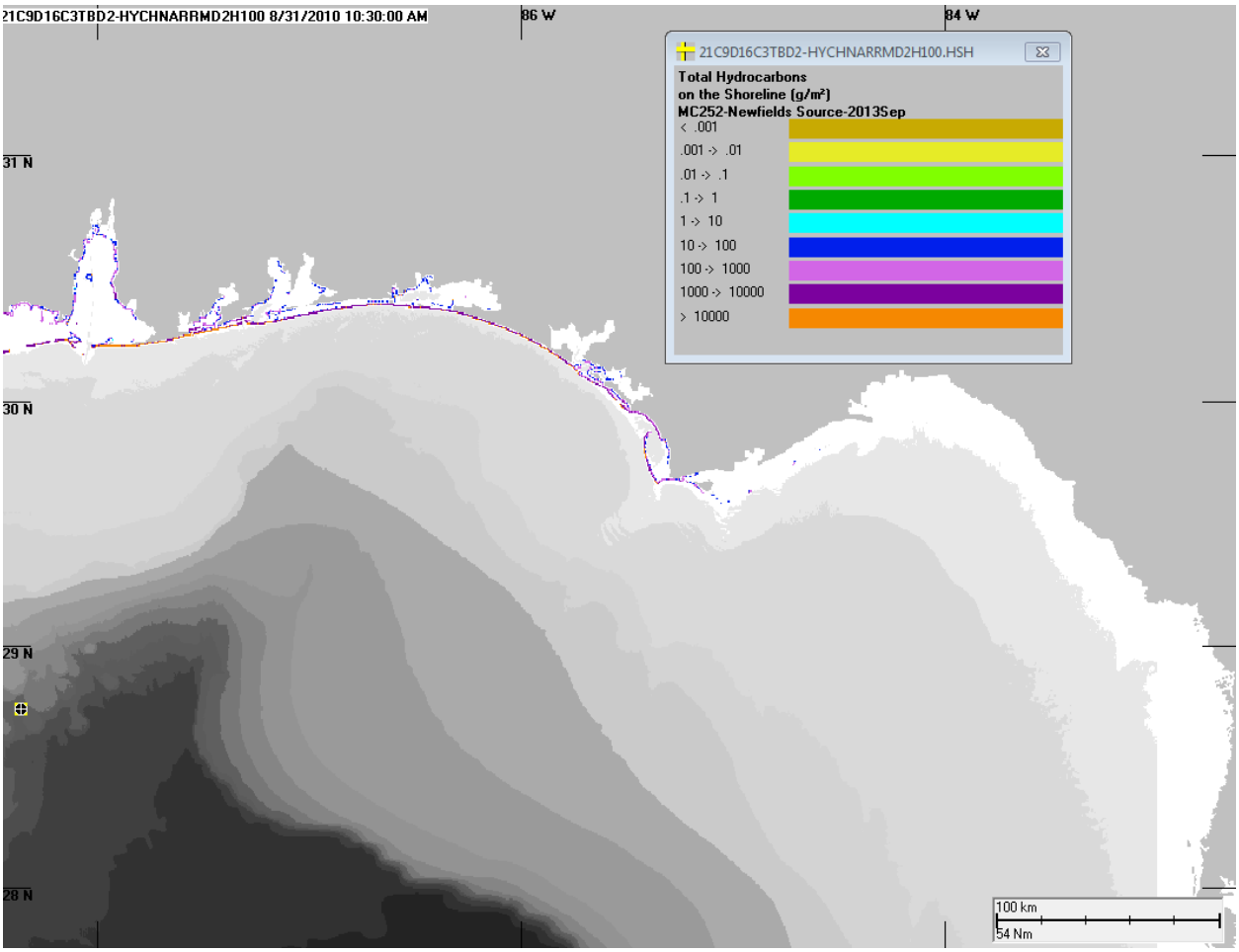

Figure D.1-31. Amount of oil accumulated on shorelines for the simulation without SSDI and using HYCOM-FSU currents and NARR winds (east extent).

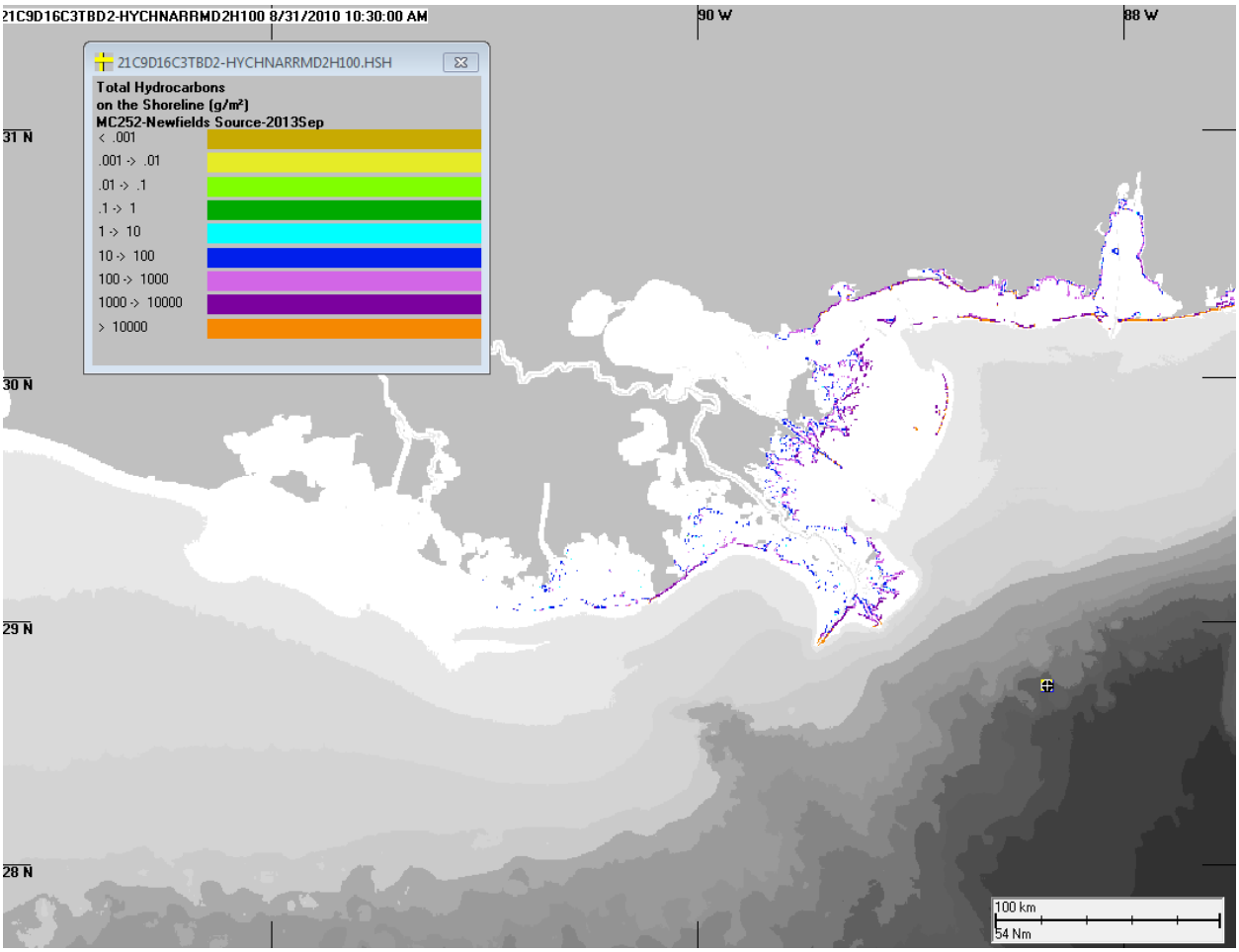

Figure D.1-32. Amount of oil accumulated on shorelines for the simulation without SSDI and using HYCOM-FSU currents and NARR winds (central).

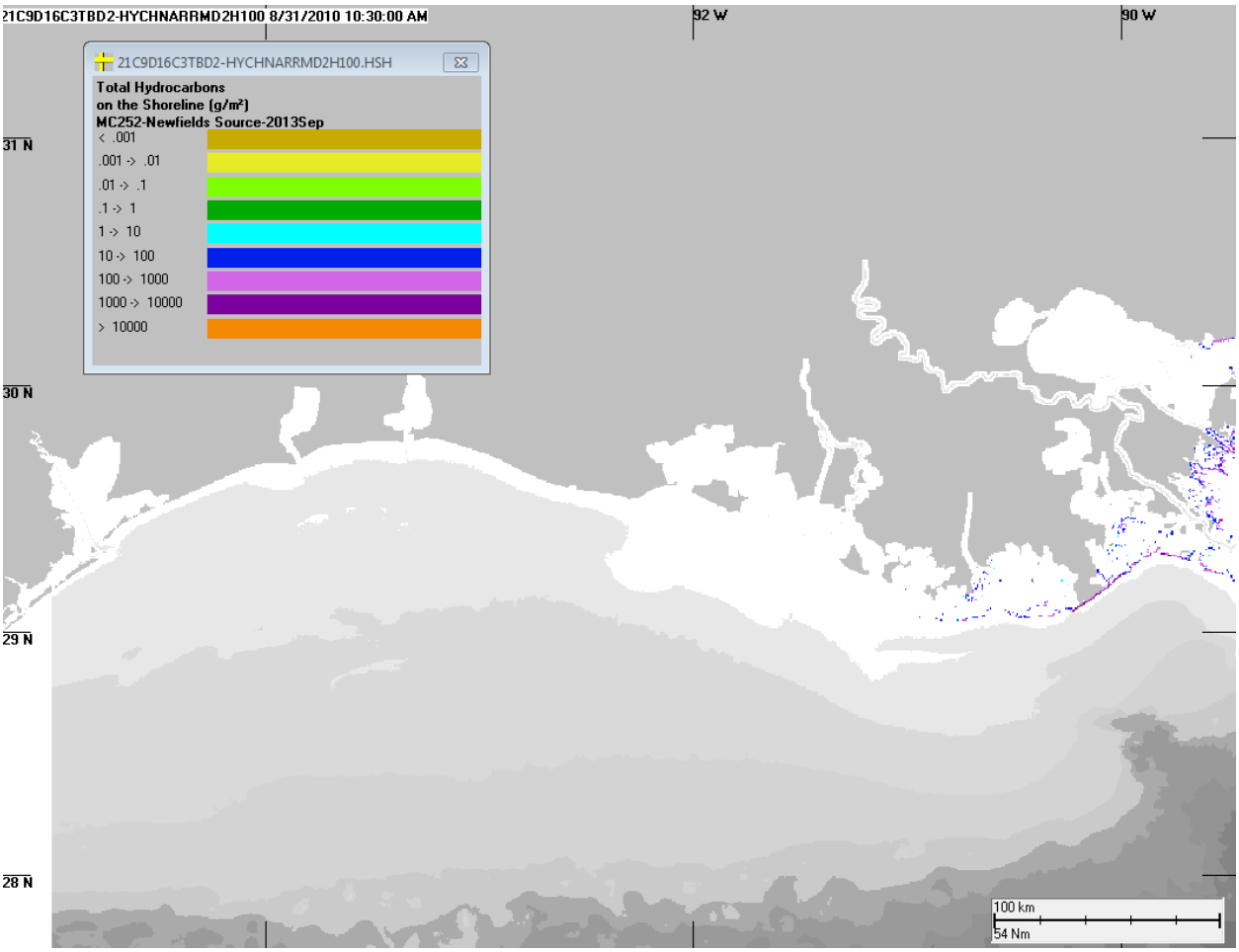

Figure D.1-33. Amount of oil accumulated on shorelines for the simulation without SSDI and using HYCOM-FSU currents and NARR winds (west extent).

D.2. Matching of Distribution of Oil on Shore

Figures in this section summarize the degree to which model predictions match the observed shore oiling. Each map shows a model results compared to SCAT-based observations of cumulative amount of oil coming ashore by September 30, 2010.

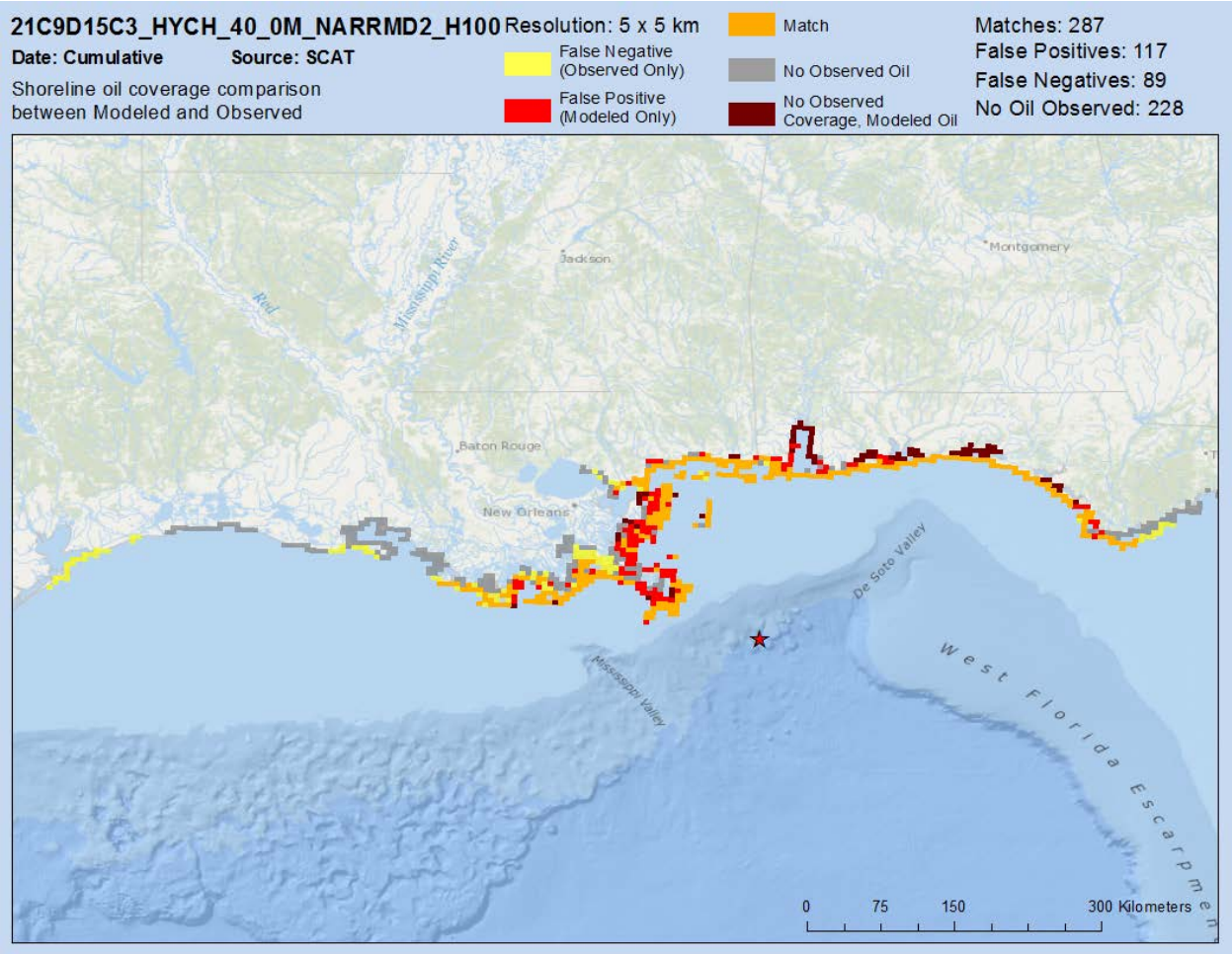

Figure D.2-1. Comparison of model predictions, for the base case simulation using HYCOM-FSU Reanalysis currents and NARR winds.

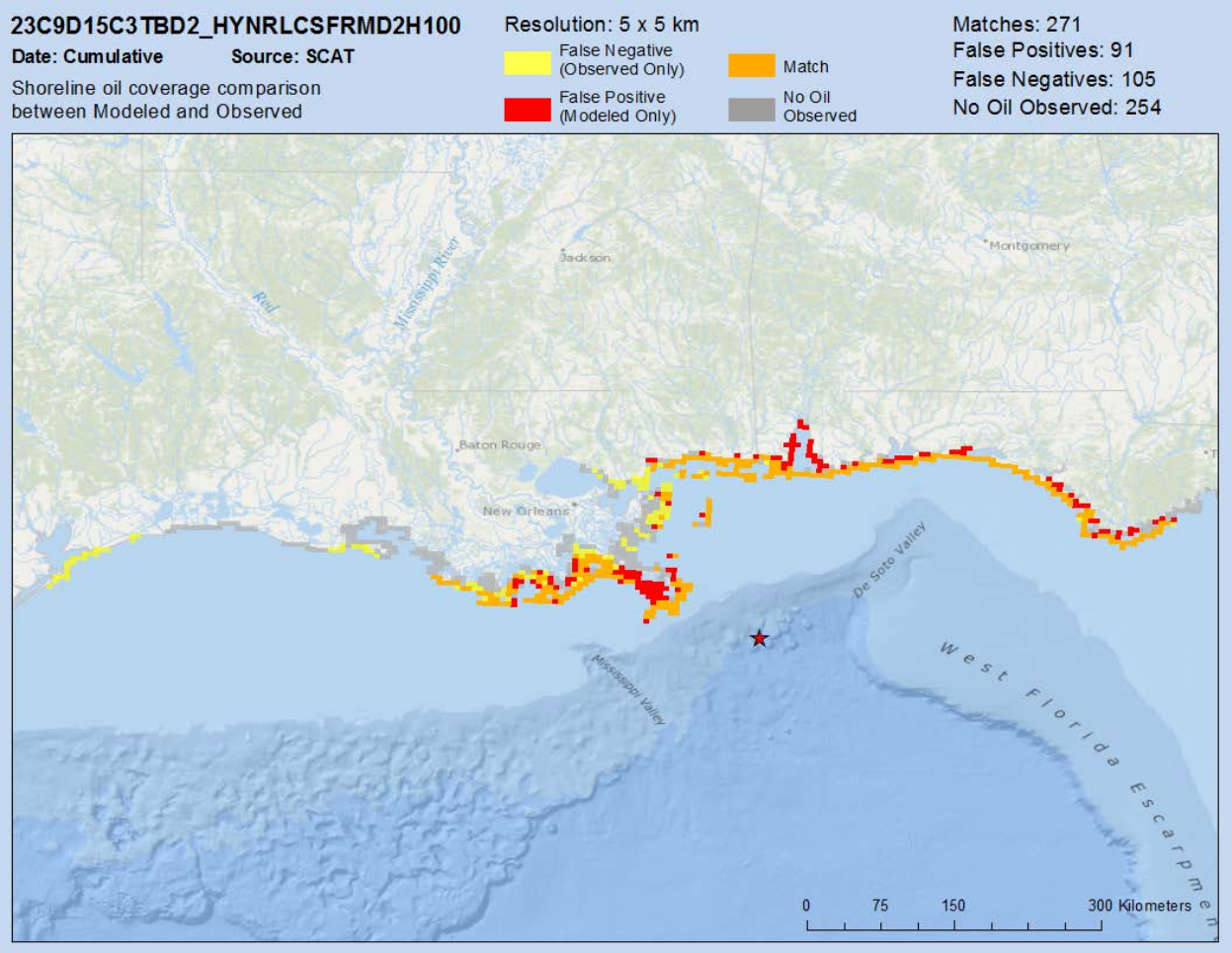

Figure D.2-2. Comparison of model predictions, for the simulation using HYCOM-NRL Reanalysis currents and CFSR winds.

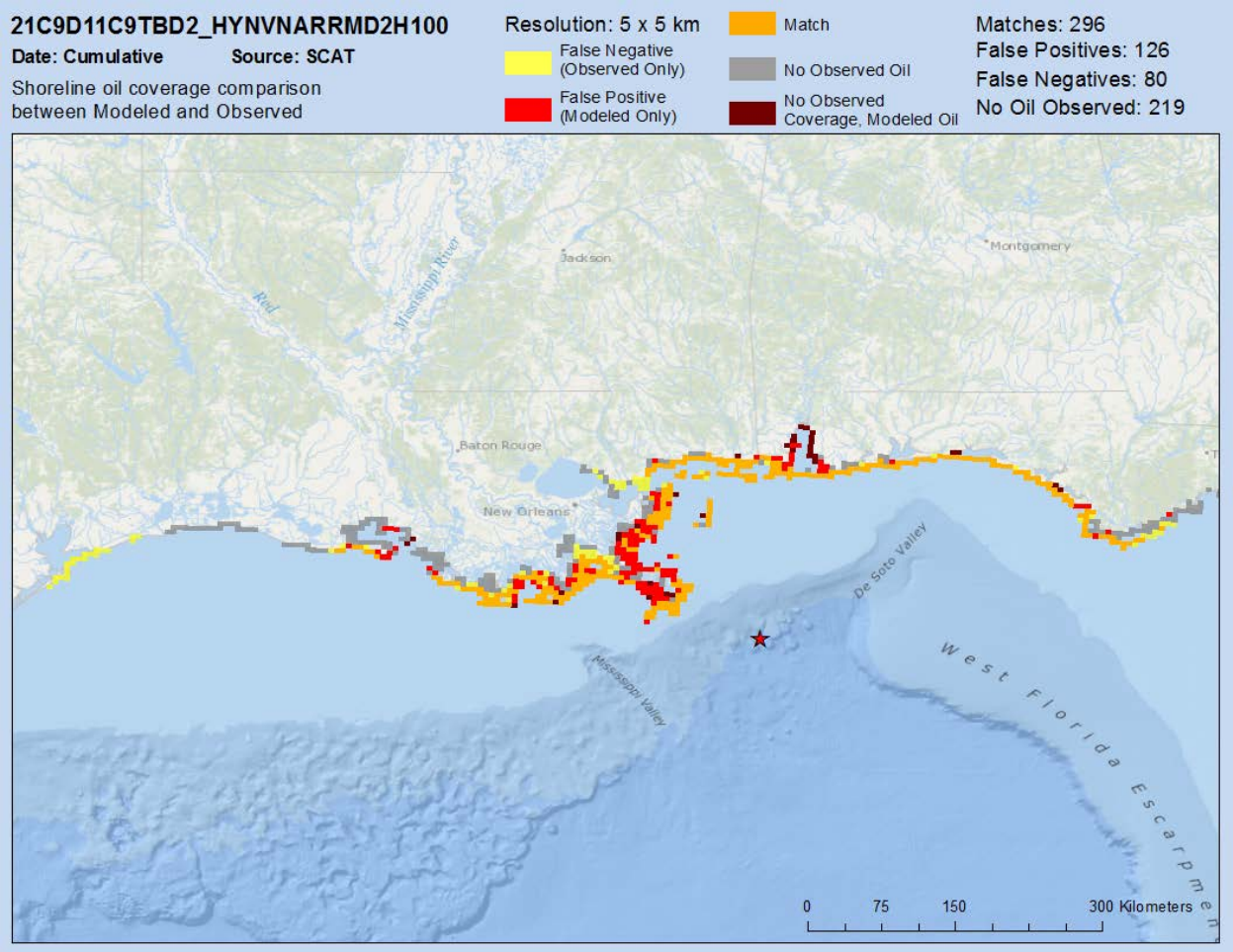

Figure D.2-3. Comparison of model predictions, for the simulation using HYCOM-NRL Real-time currents and NARR winds.

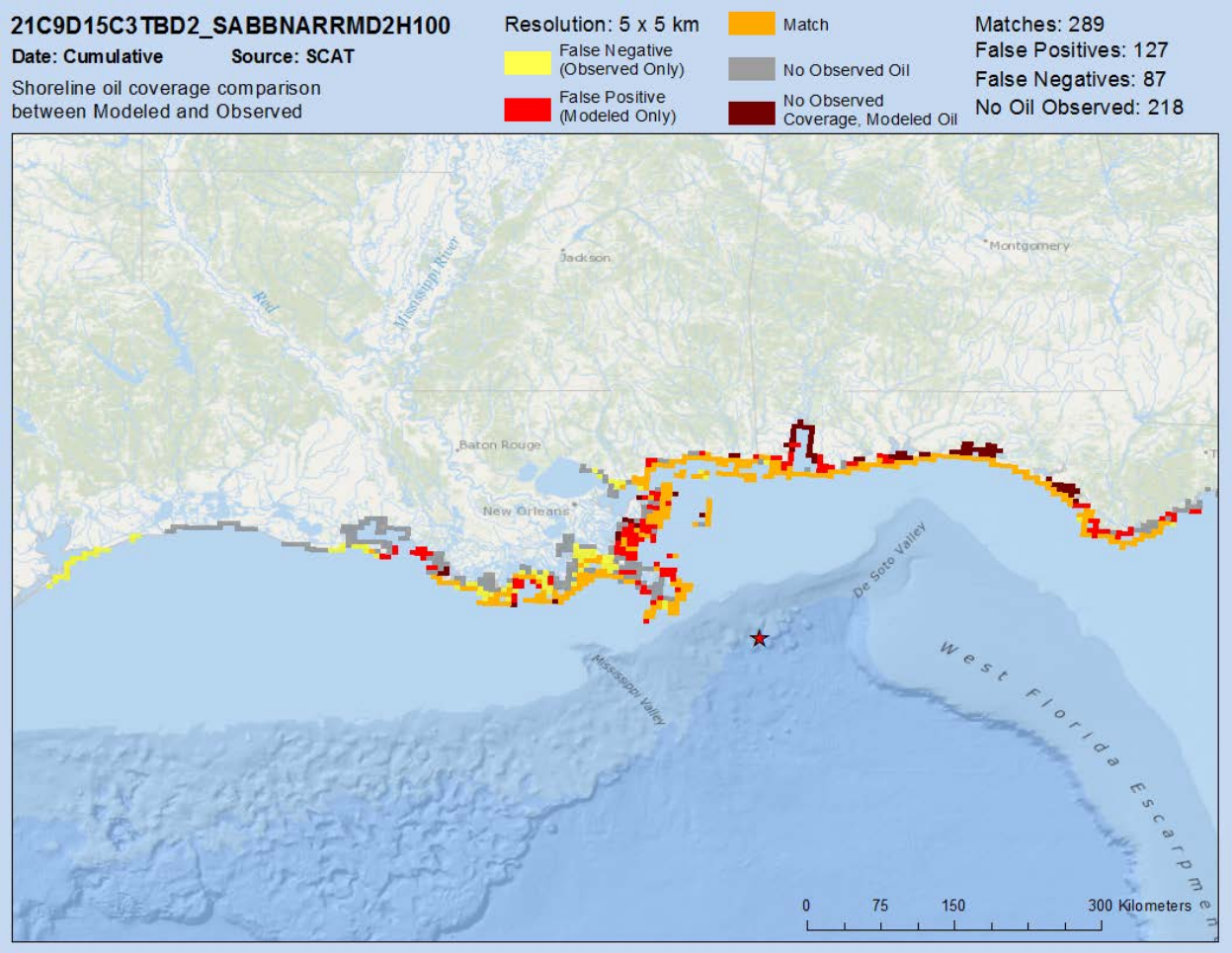

Figure D.2-4. Comparison of model predictions, for the base case simulation using SABGOM currents and NARR winds.

(False positives of modeled oil on shorelines to the east in the Big Bend of Florida are not shown.)

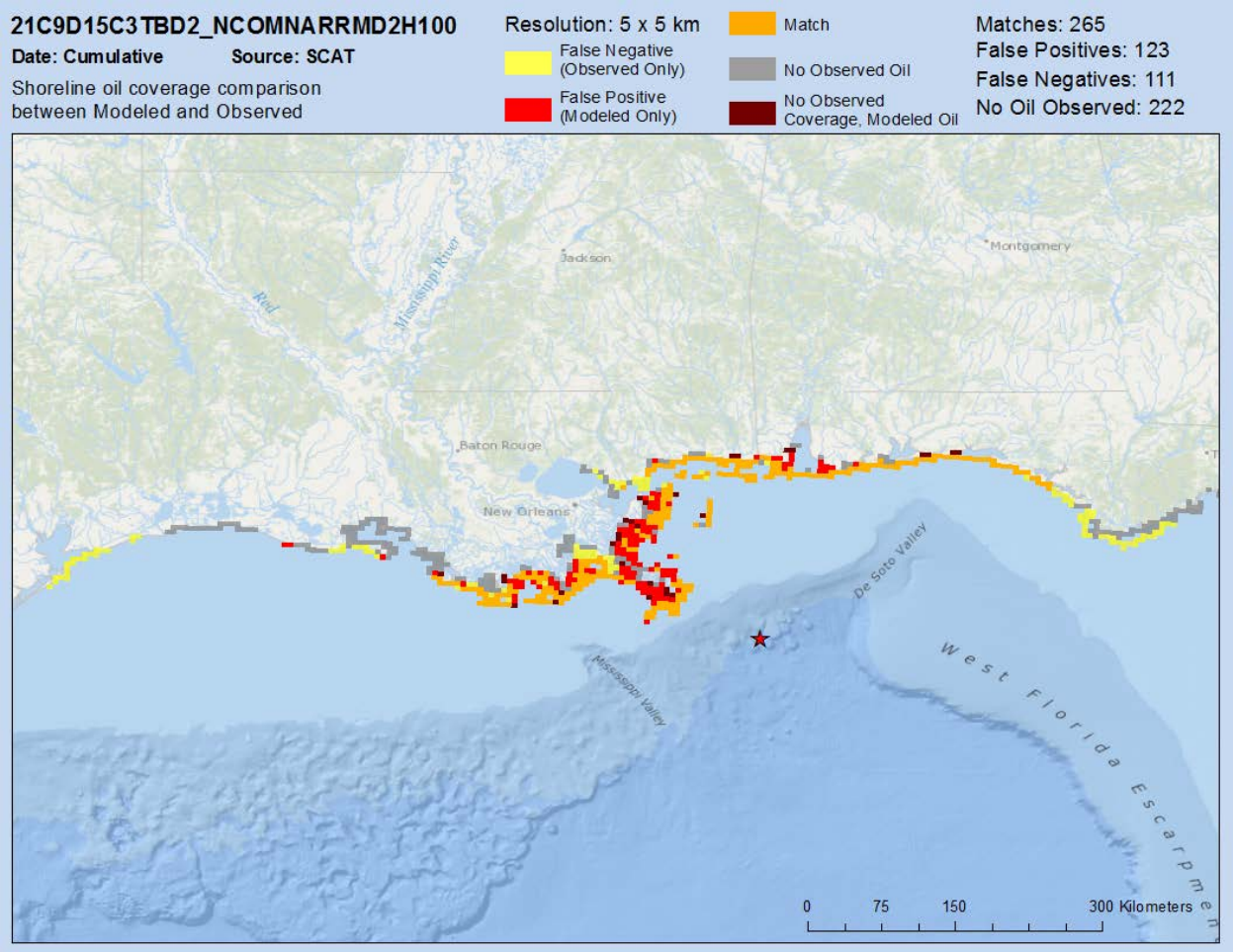

Figure D.2-5. Comparison of model predictions, for the simulation using NCOM Real-Time currents and NARR winds.

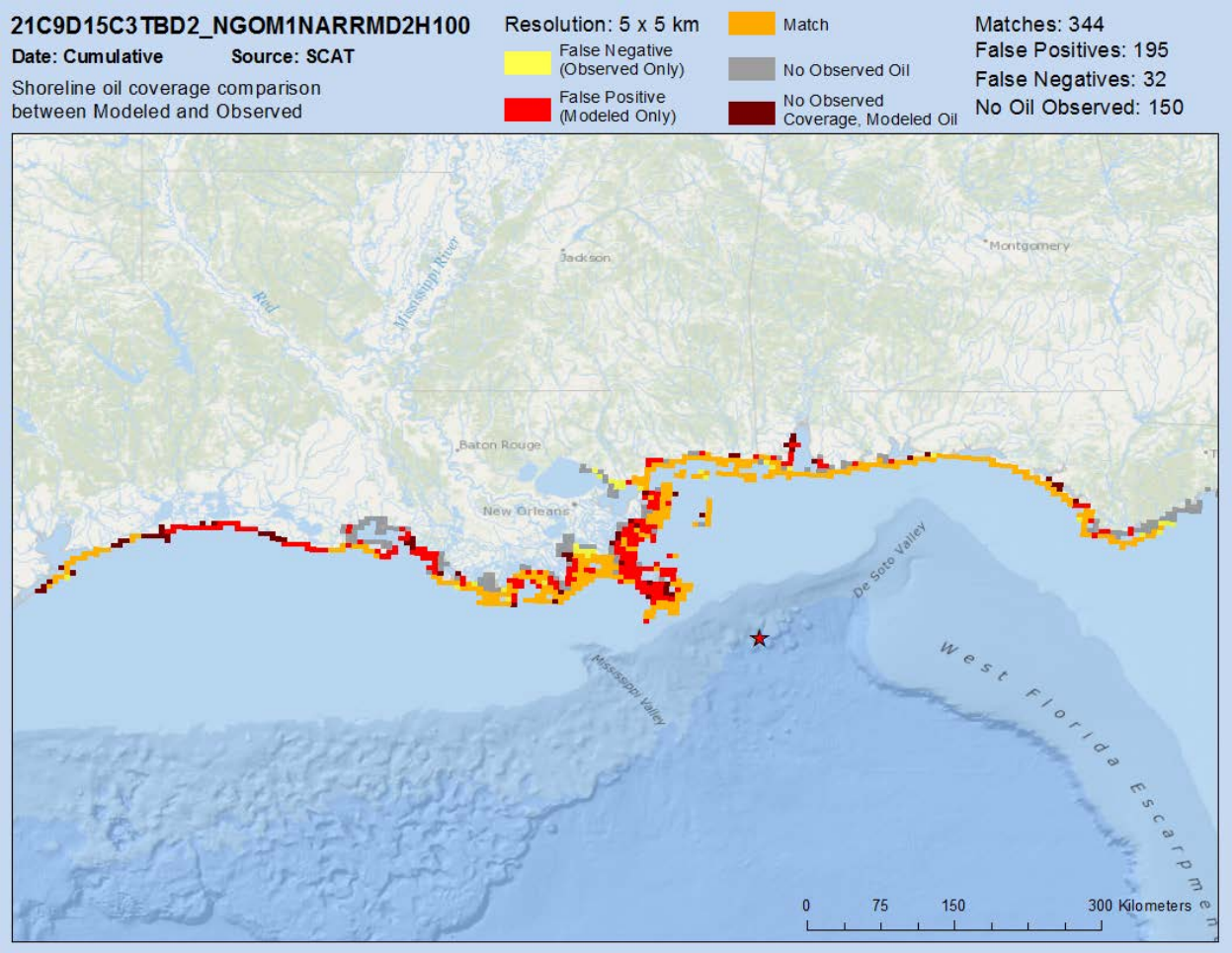

Figure D.2-6. Comparison of model predictions, for the simulation using NGOM-NOAA Real-Time currents and NARR winds.

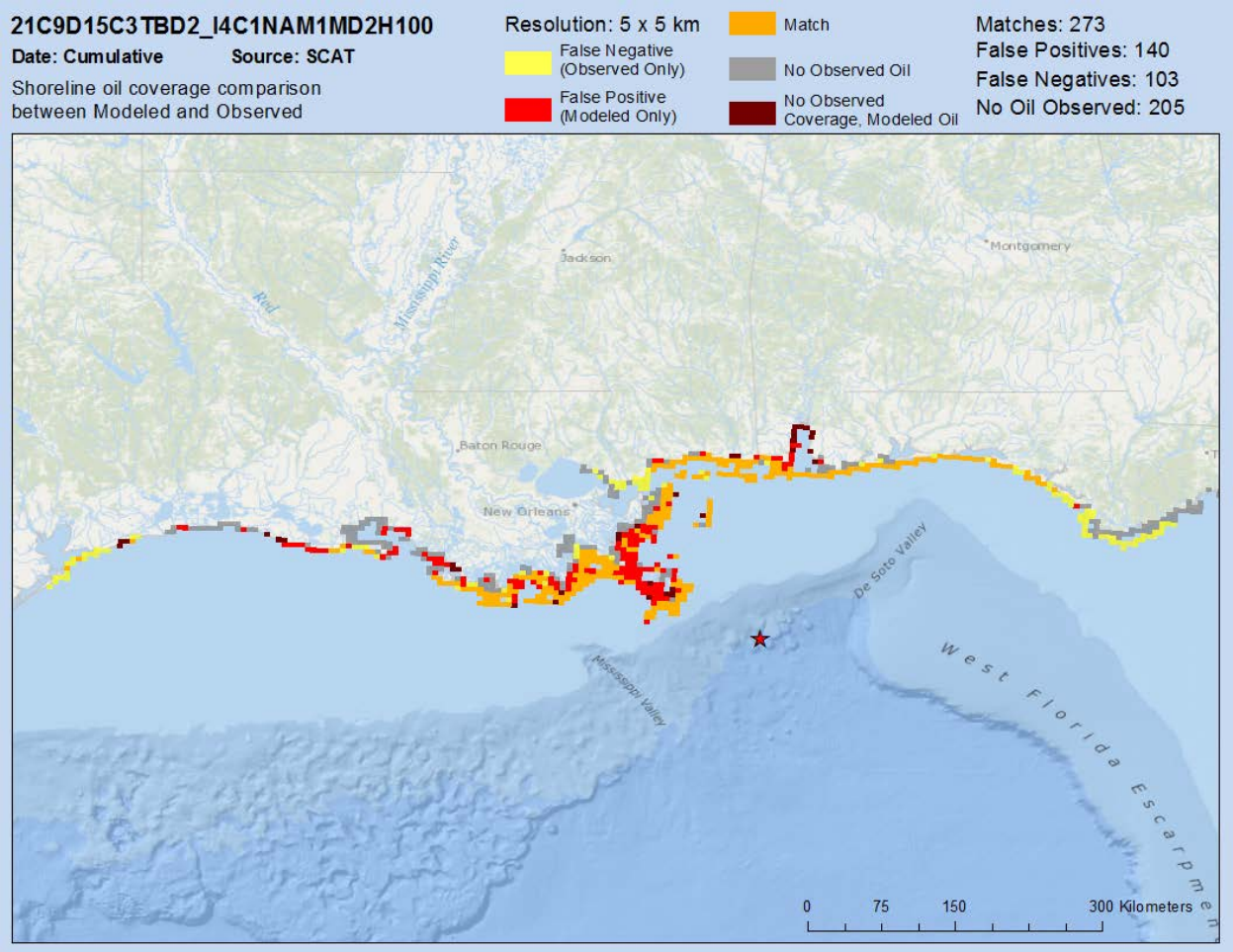

Figure D.2-7. Comparison of model predictions, for the simulation using IASROMS-hourly currents and NAM winds.

D.3. Timing and Distribution of Oil on Shore

Maps in this section show comparisons of model predictions to observed amount of oil coming ashore for the base case simulation using HYCOM-FSU currents and NARR winds.

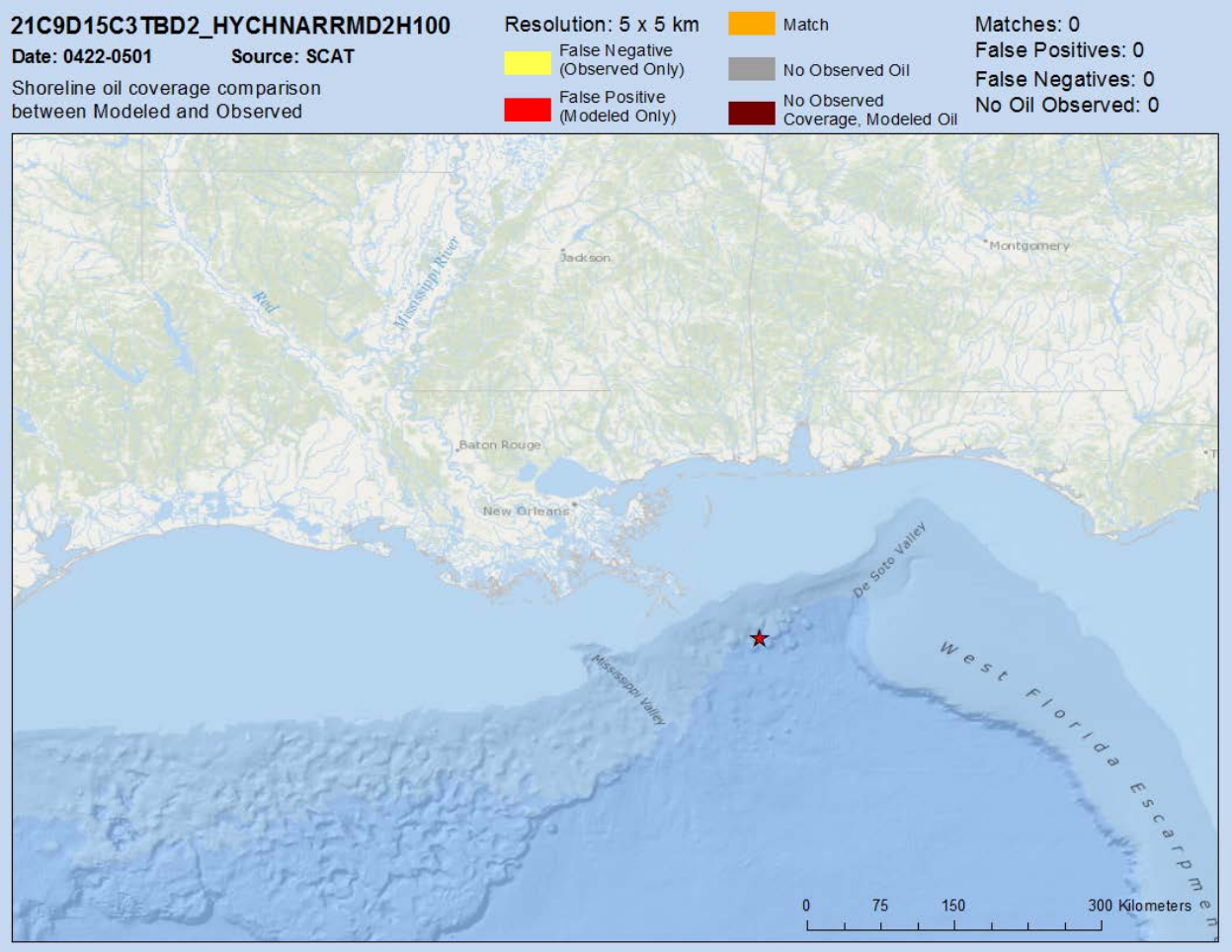

Figure D.3-1. Comparison of model to observed amount of oil coming ashore during 10-day interval 1, April 22 to May 1.

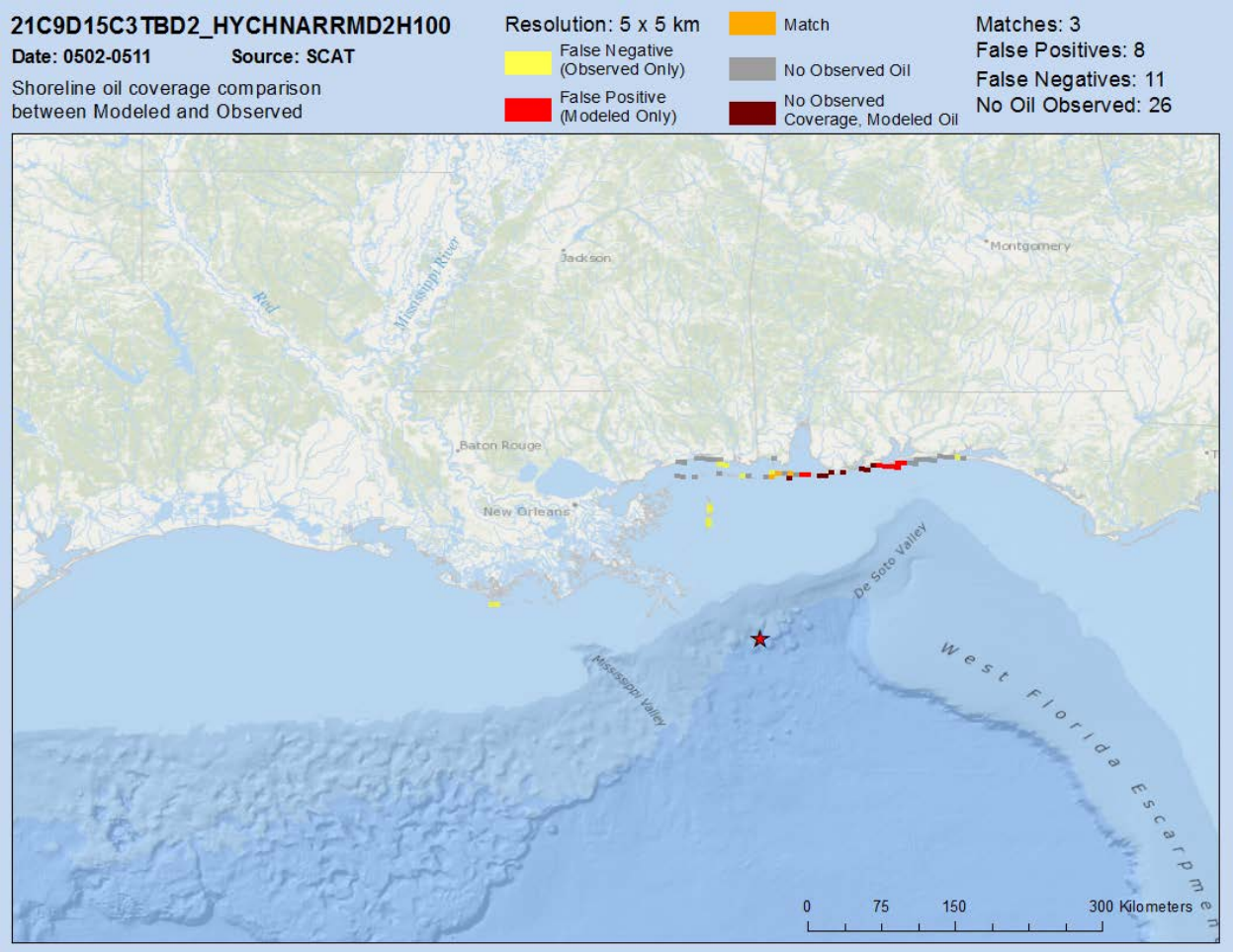

Figure D.3-2. Comparison of model to observed amount of oil coming ashore during 10-day interval 2, May 2 to May 11.

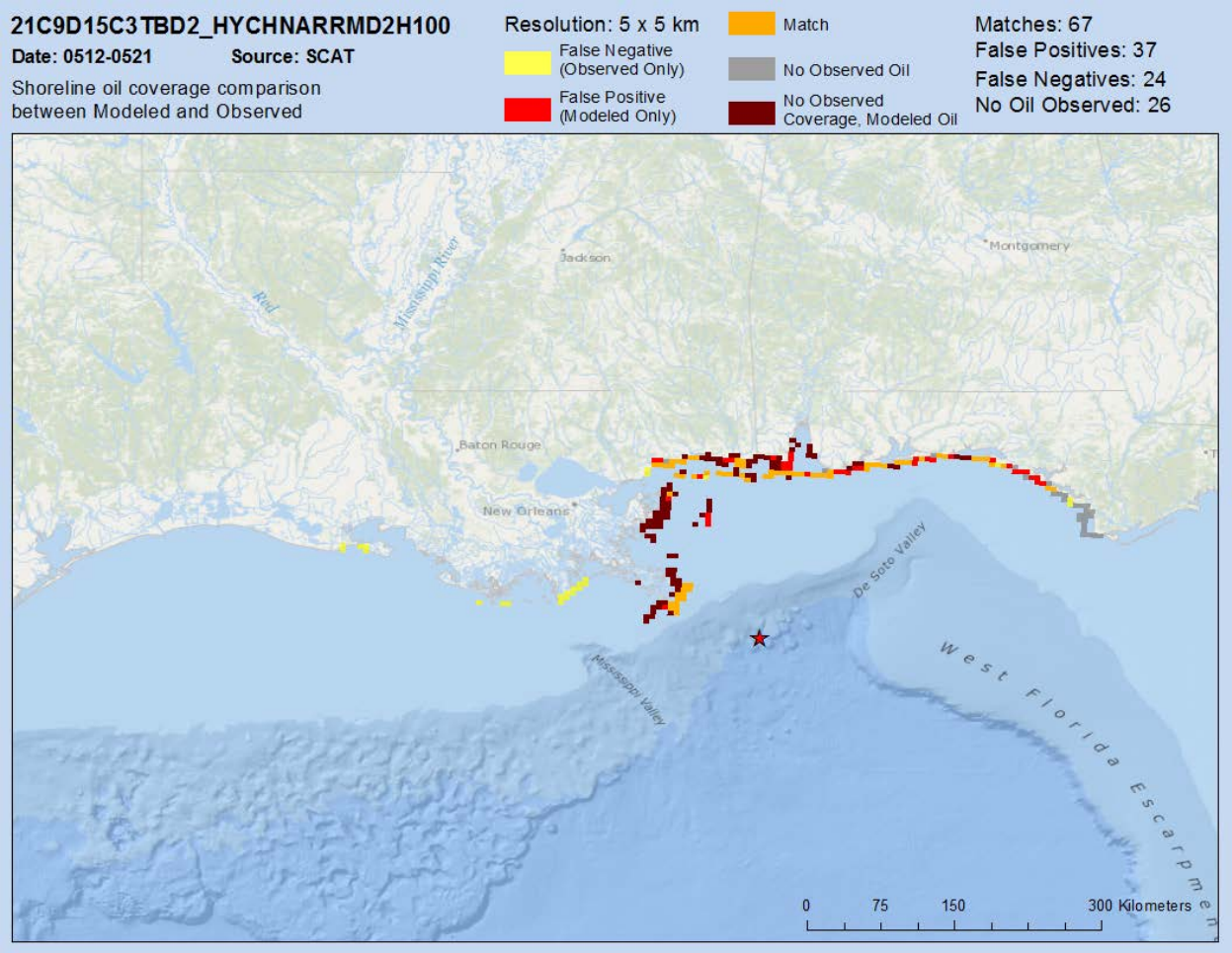

Figure D.3-3. Comparison of model to observed amount of oil coming ashore during 10-day interval 3, May 12 to May 21.

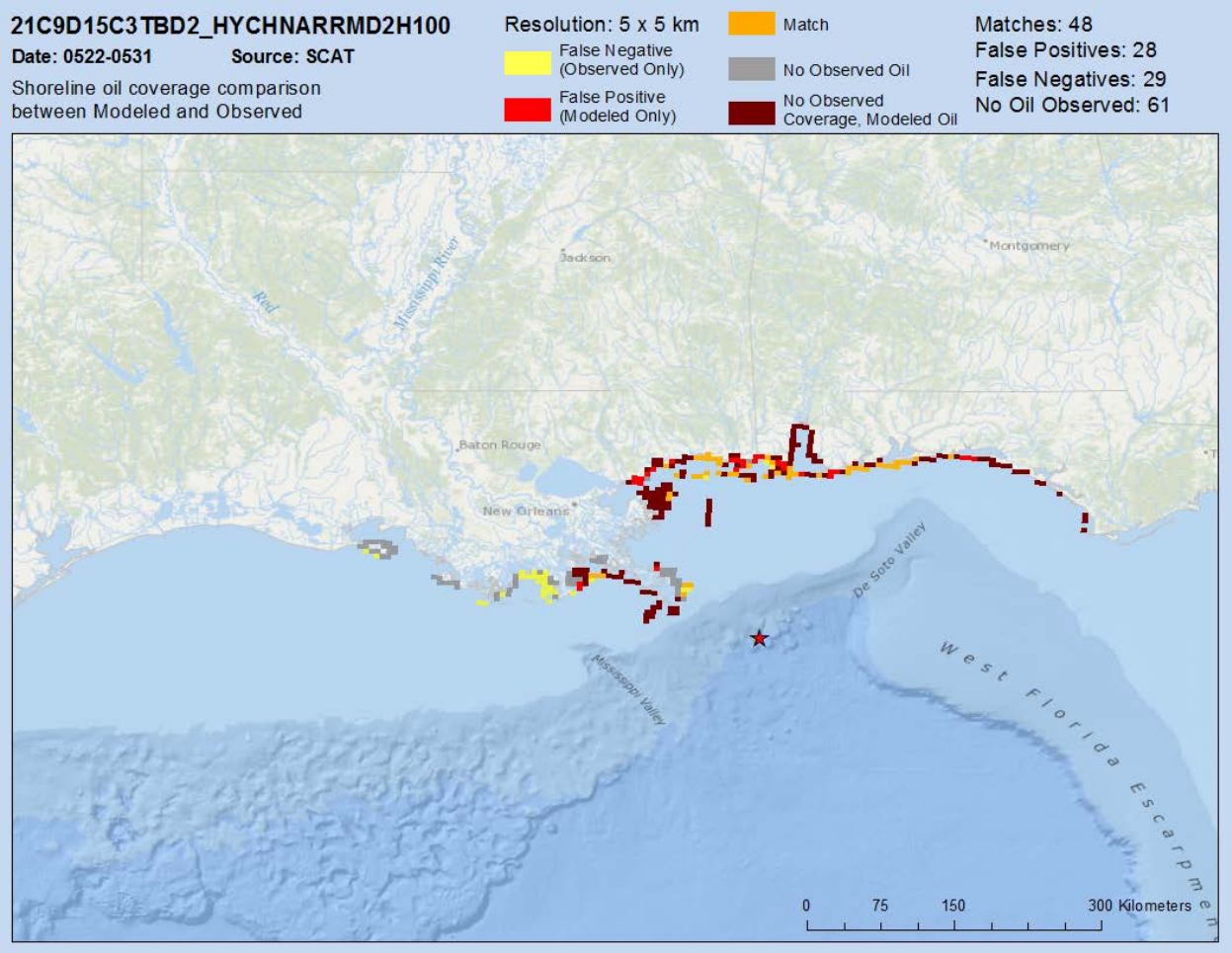

Figure D.3-4. Comparison of model to observed amount of oil coming ashore during 10-day interval 4, May 22 to May 31.

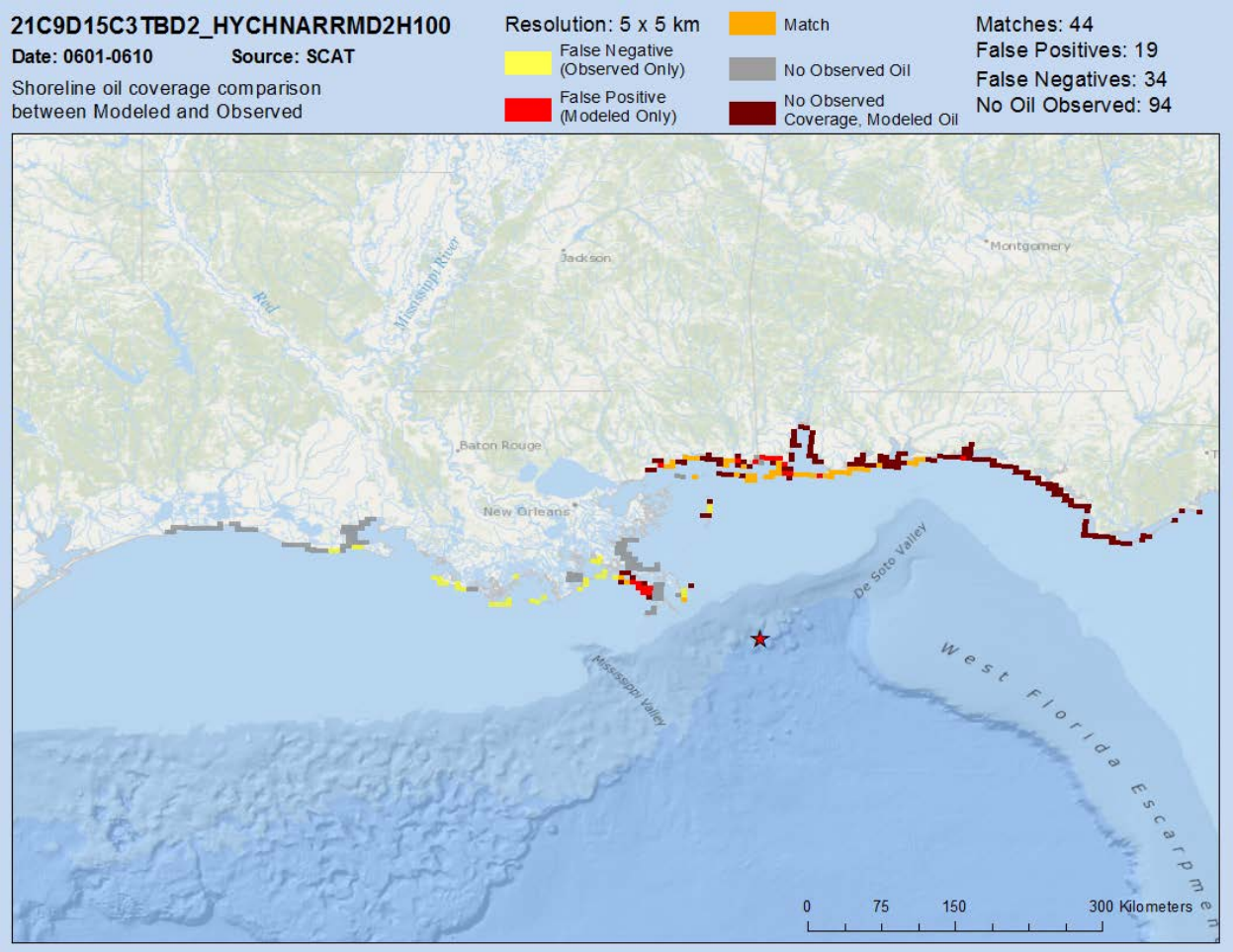

Figure D.3-5. Comparison of model to observed amount of oil coming ashore during 10-day interval 5, June 1–10.

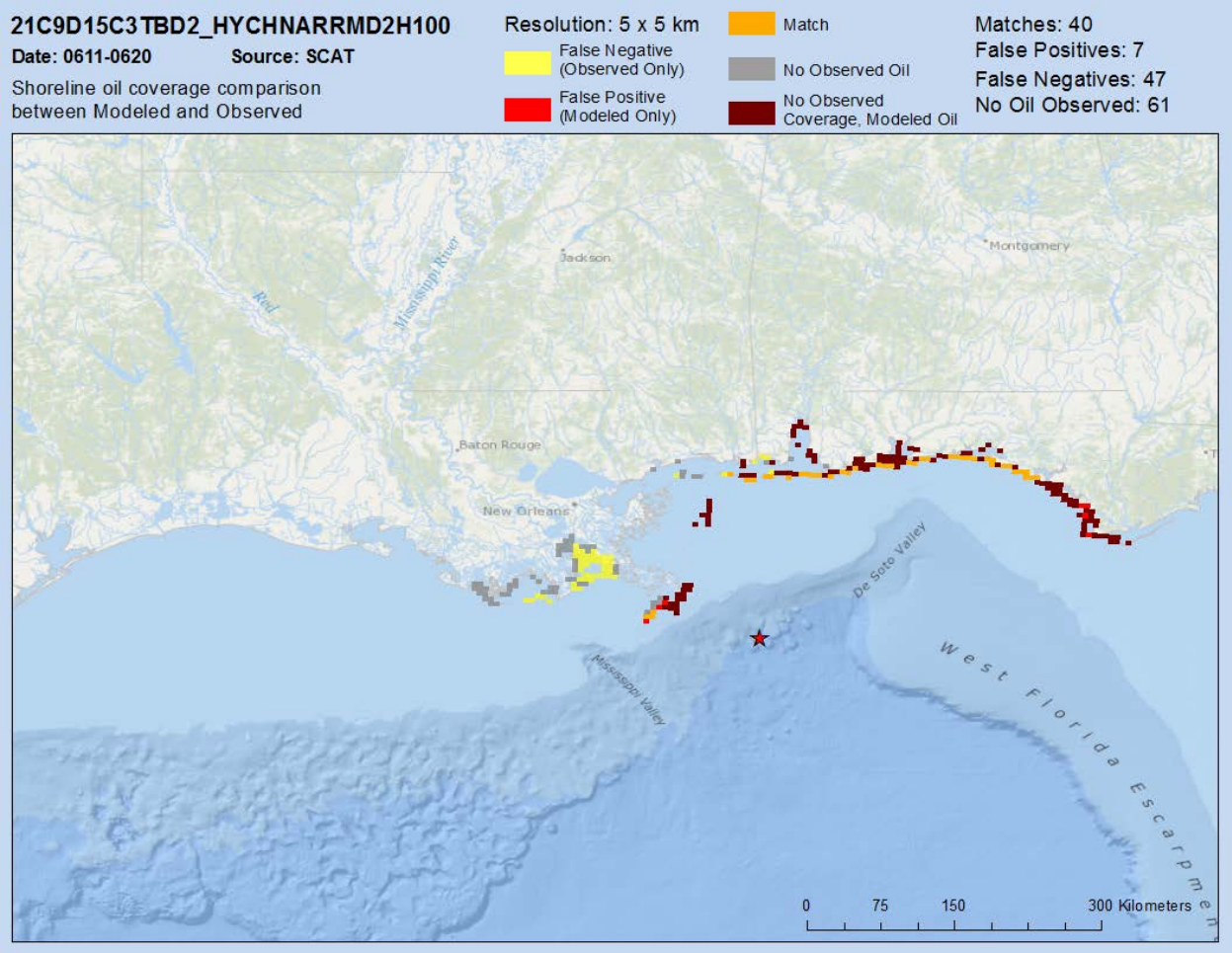

Figure D.3-6. Comparison of model to observed amount of oil coming ashore during 10-day interval 6, June 11–20.

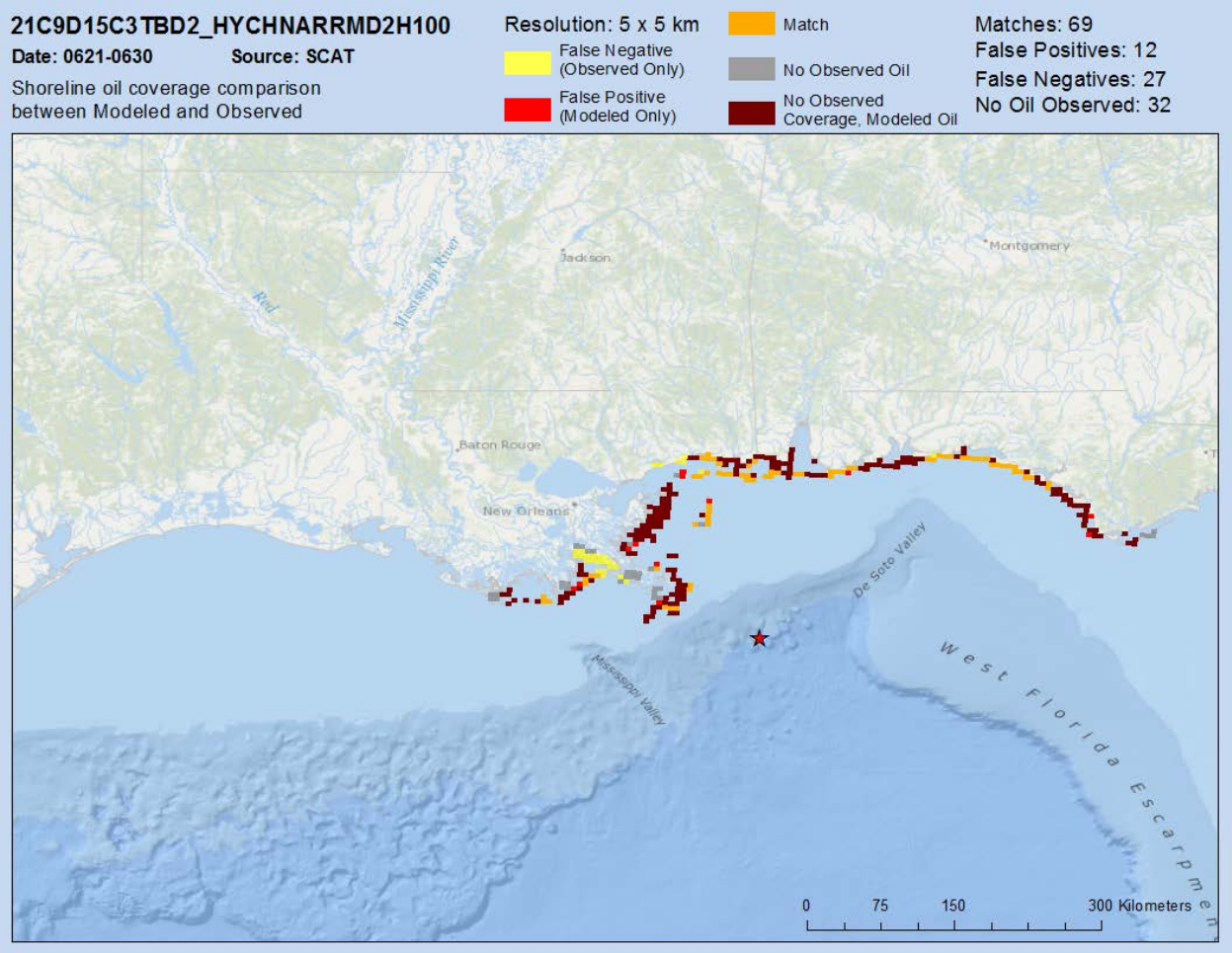

Figure D.3-7. Comparison of model to observed amount of oil coming ashore during 10-day interval 7, June 21–30.

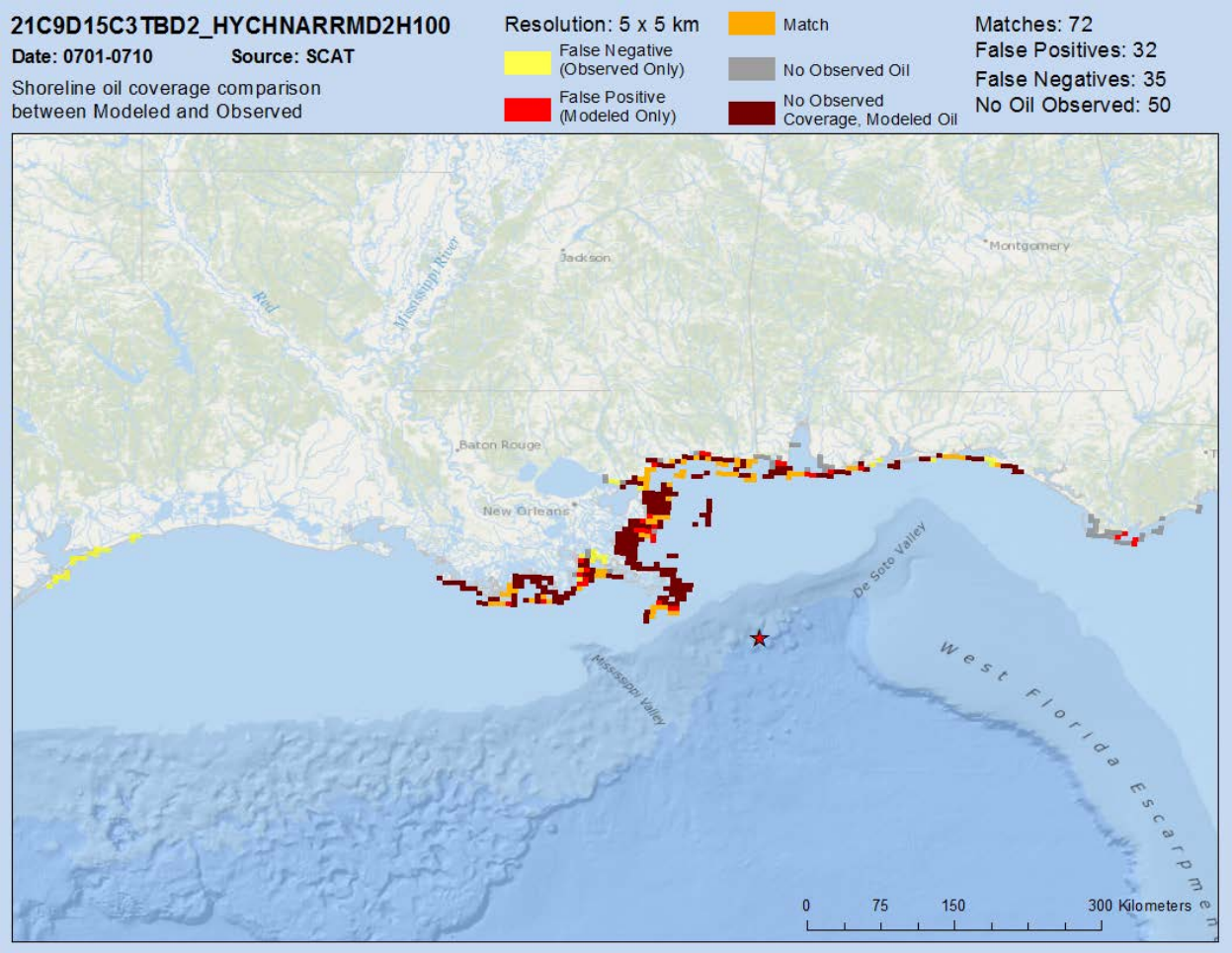

Figure D.3-8. Comparison of model to observed amount of oil coming ashore during 10-day interval 8, July 1–10.

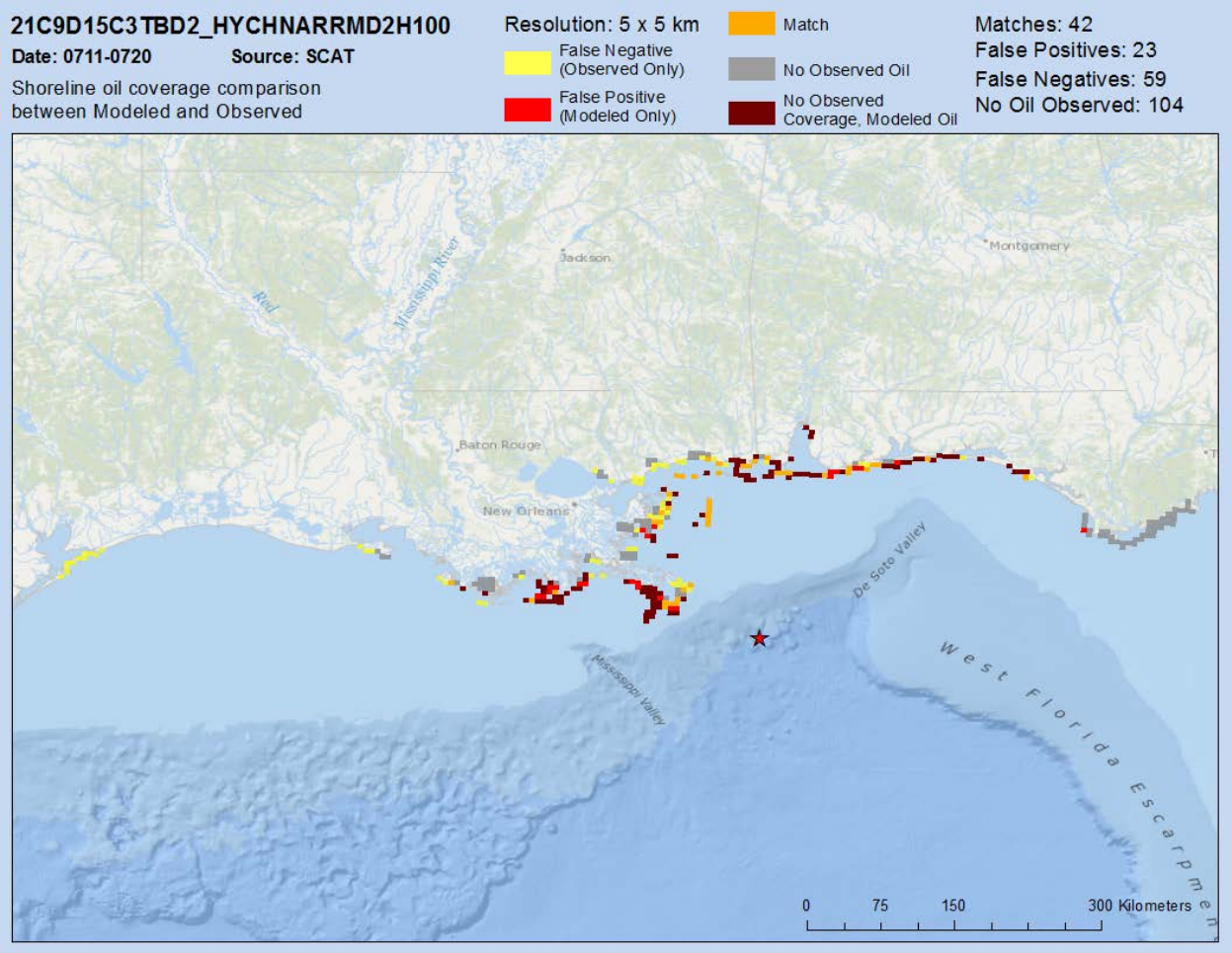

Figure D.3-9. Comparison of model to observed amount of oil coming ashore during 10-day interval 9, July 11-–20.

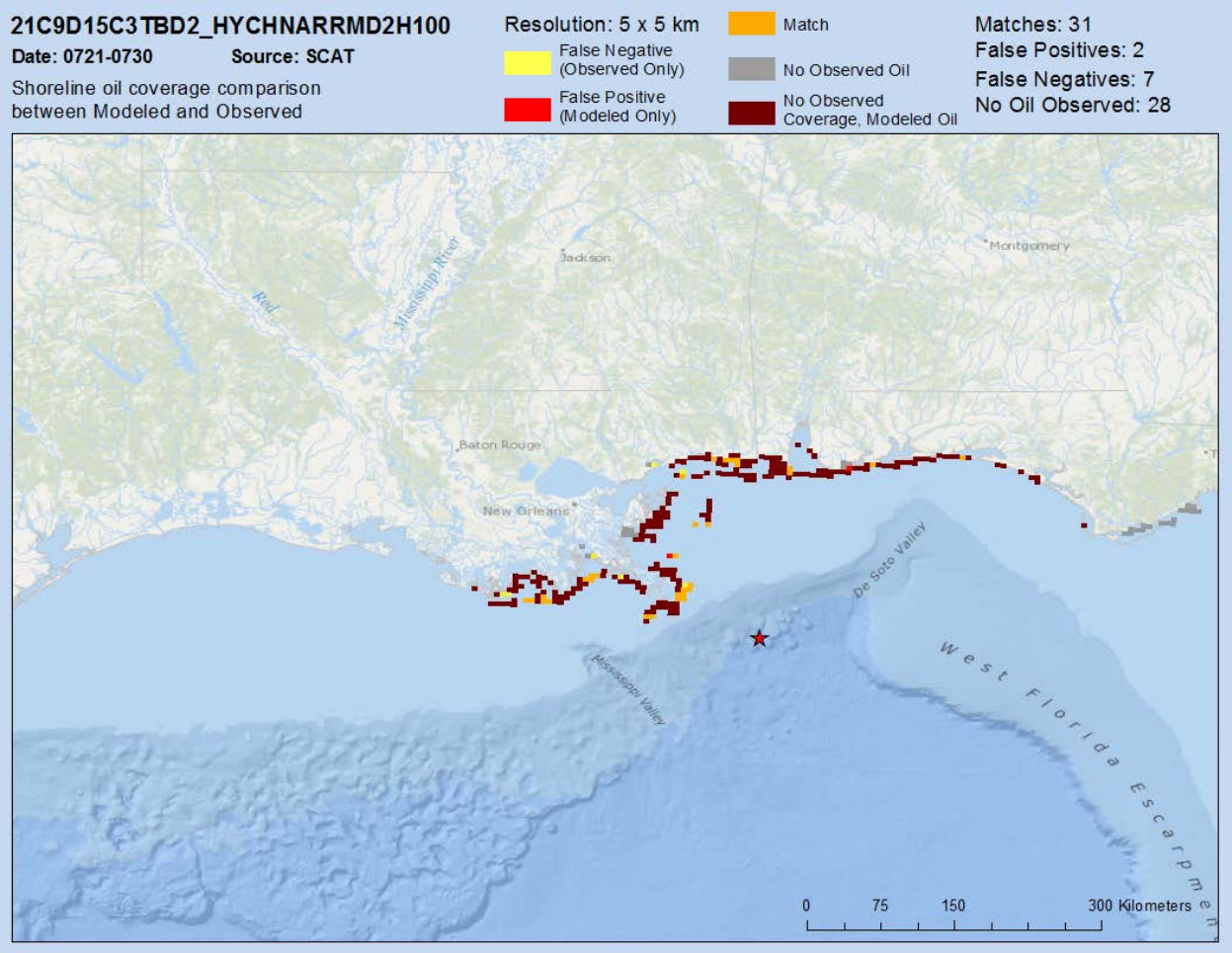

Figure D.3-10. Comparison of model to observed amount of oil coming ashore during 10-day interval 10, July 21–30.

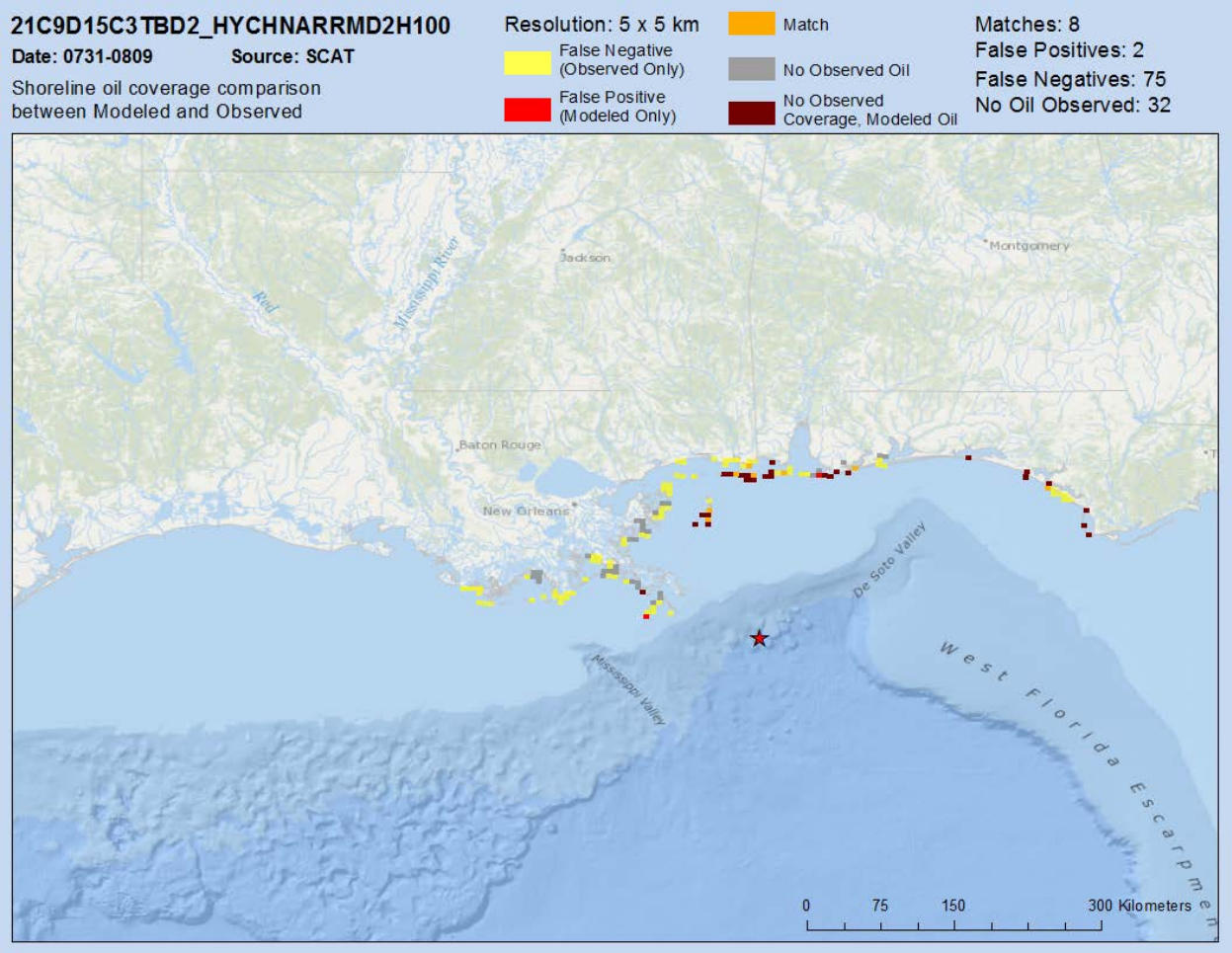

Figure D.3-11. Comparison of model to observed amount of oil coming ashore during 10-day interval 11 July 31–August 9.

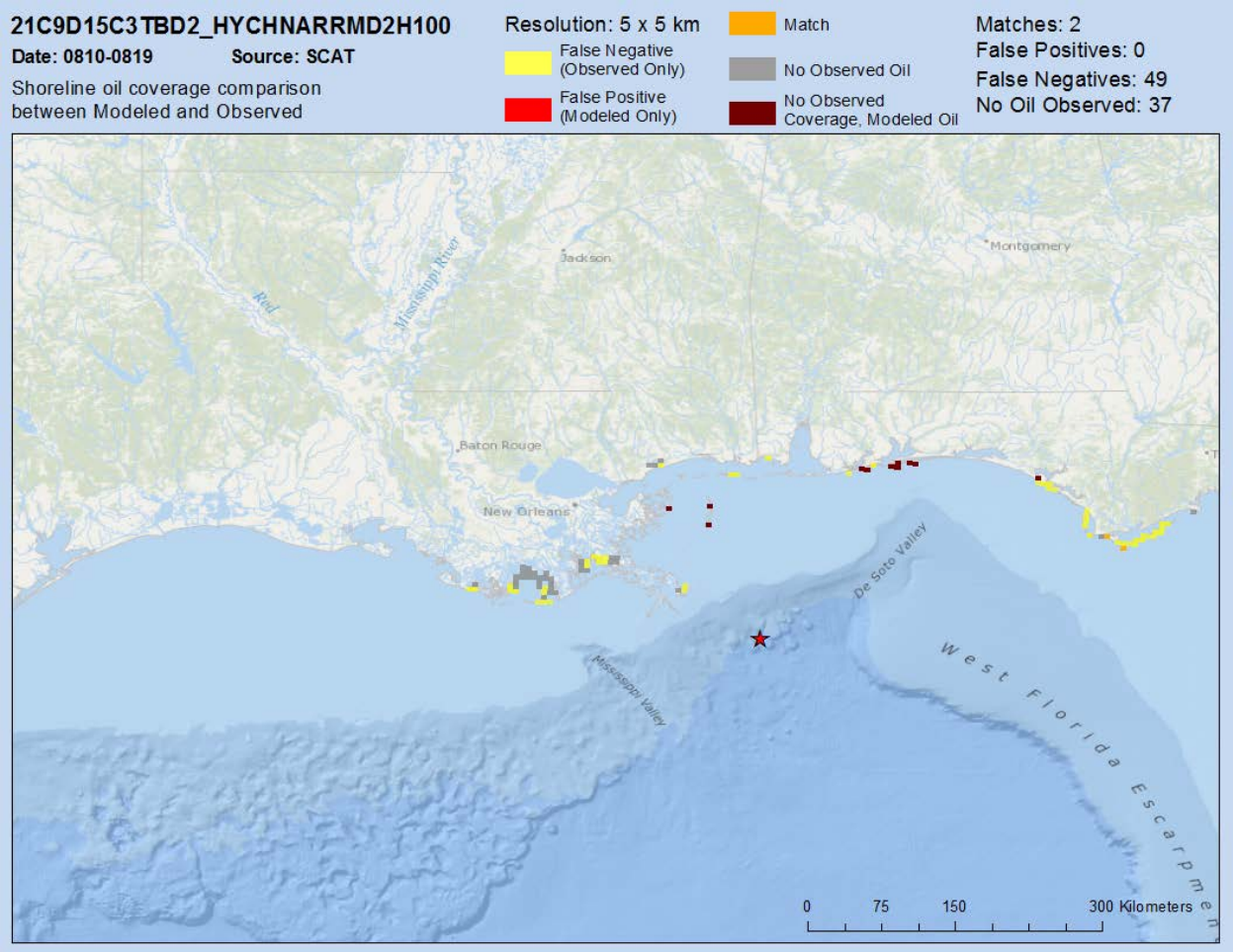

Figure D.3-12. Comparison of model to observed amount of oil coming ashore during 10-day interval 12, August 10–19.

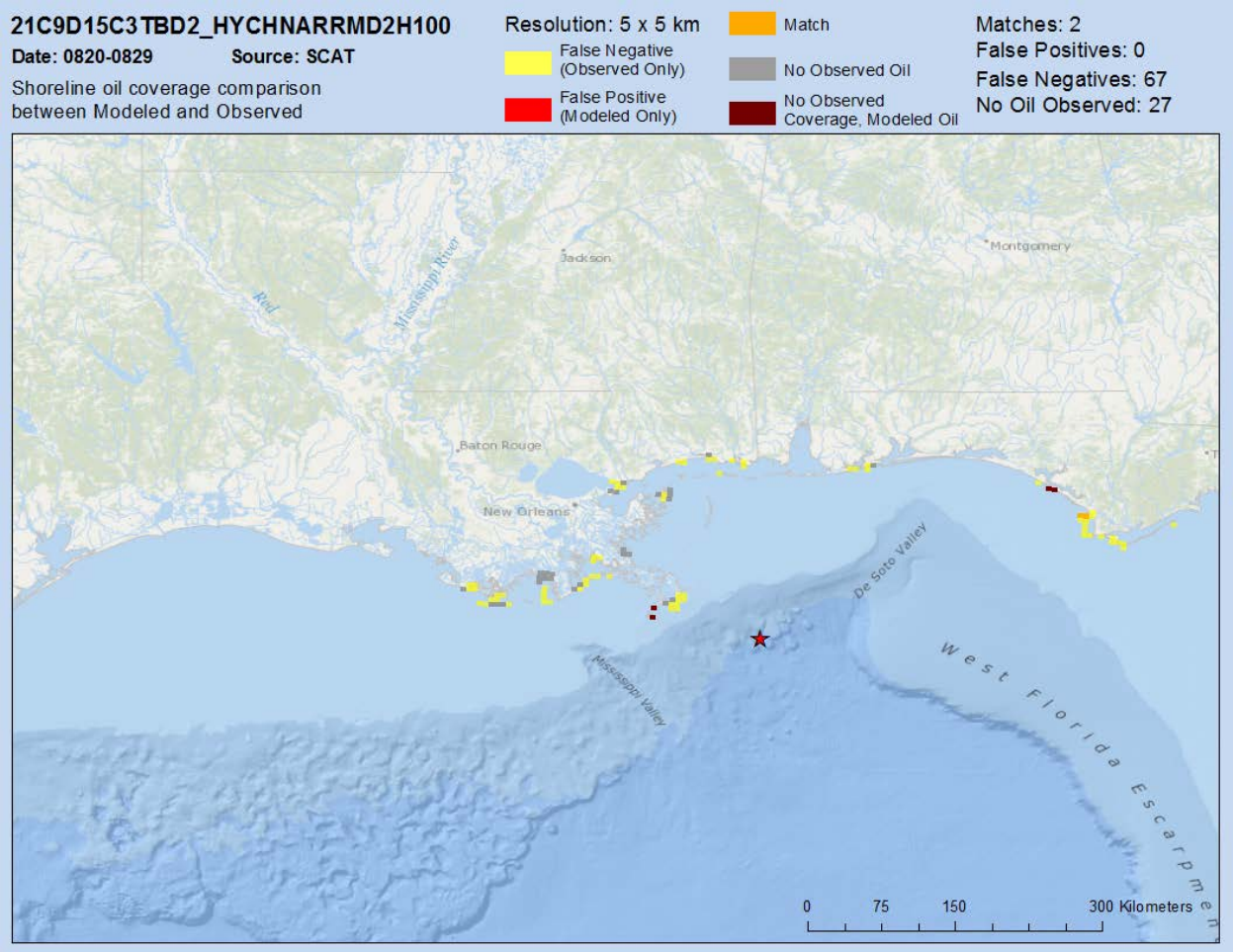

Figure D.3-13. Comparison of model to observed amount of oil coming ashore during 10-day interval 13, August 20–29.

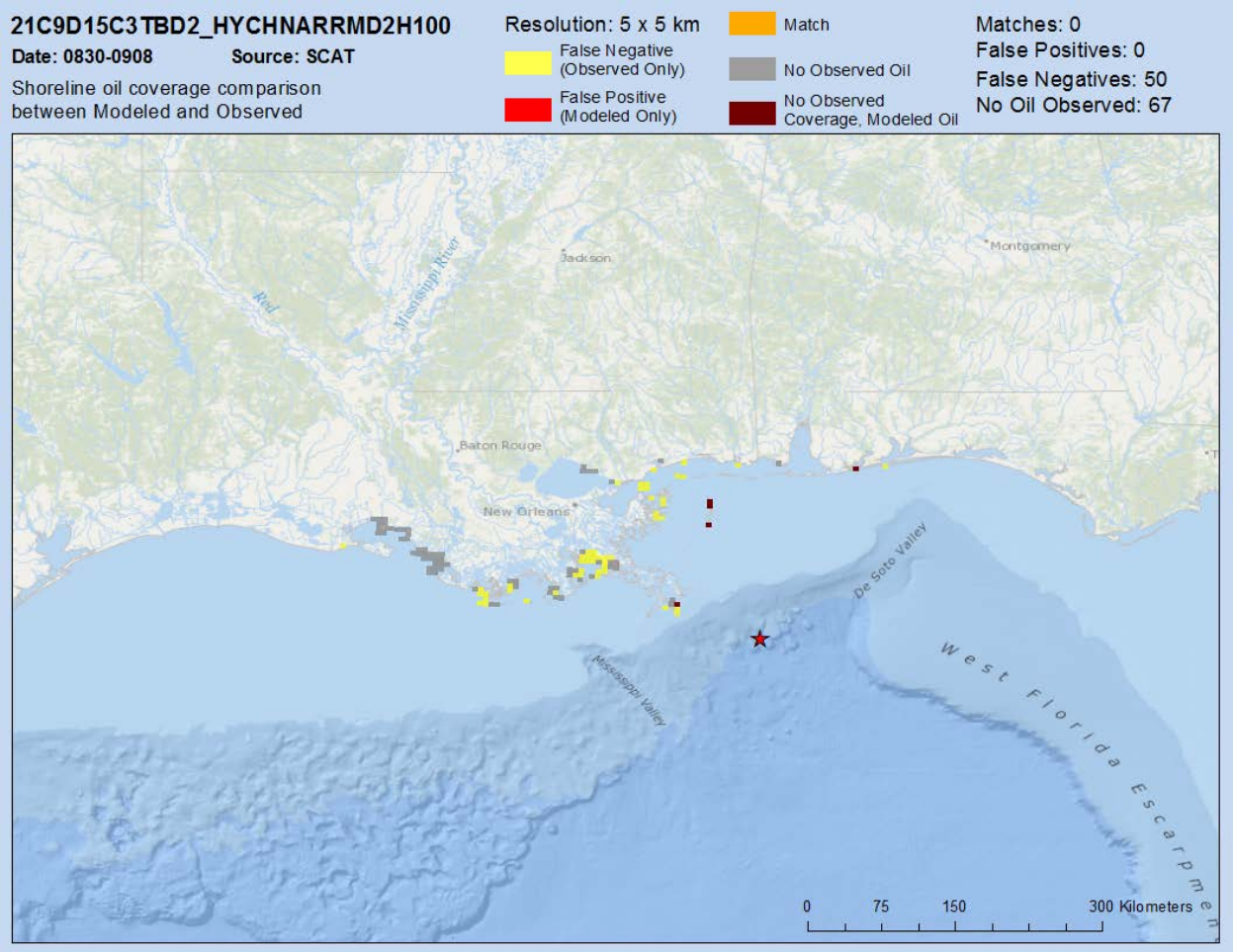

Figure D.3-14. Comparison of model to observed amount of oil coming ashore during 10-day interval 14, August 30–September 8.

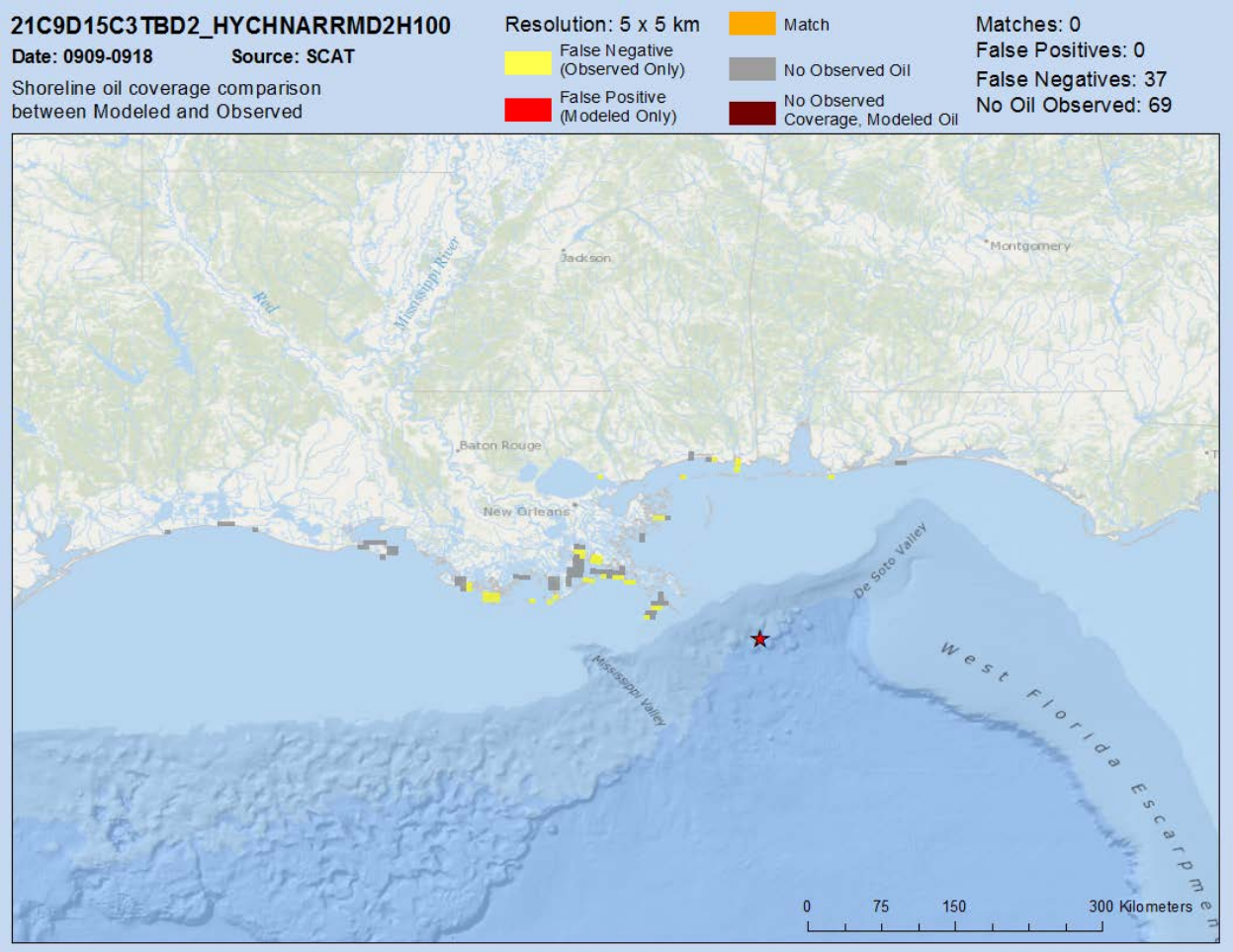

Figure D.3-15. Comparison of model to observed amount of oil coming ashore during 10-day interval 14, September 9–18.

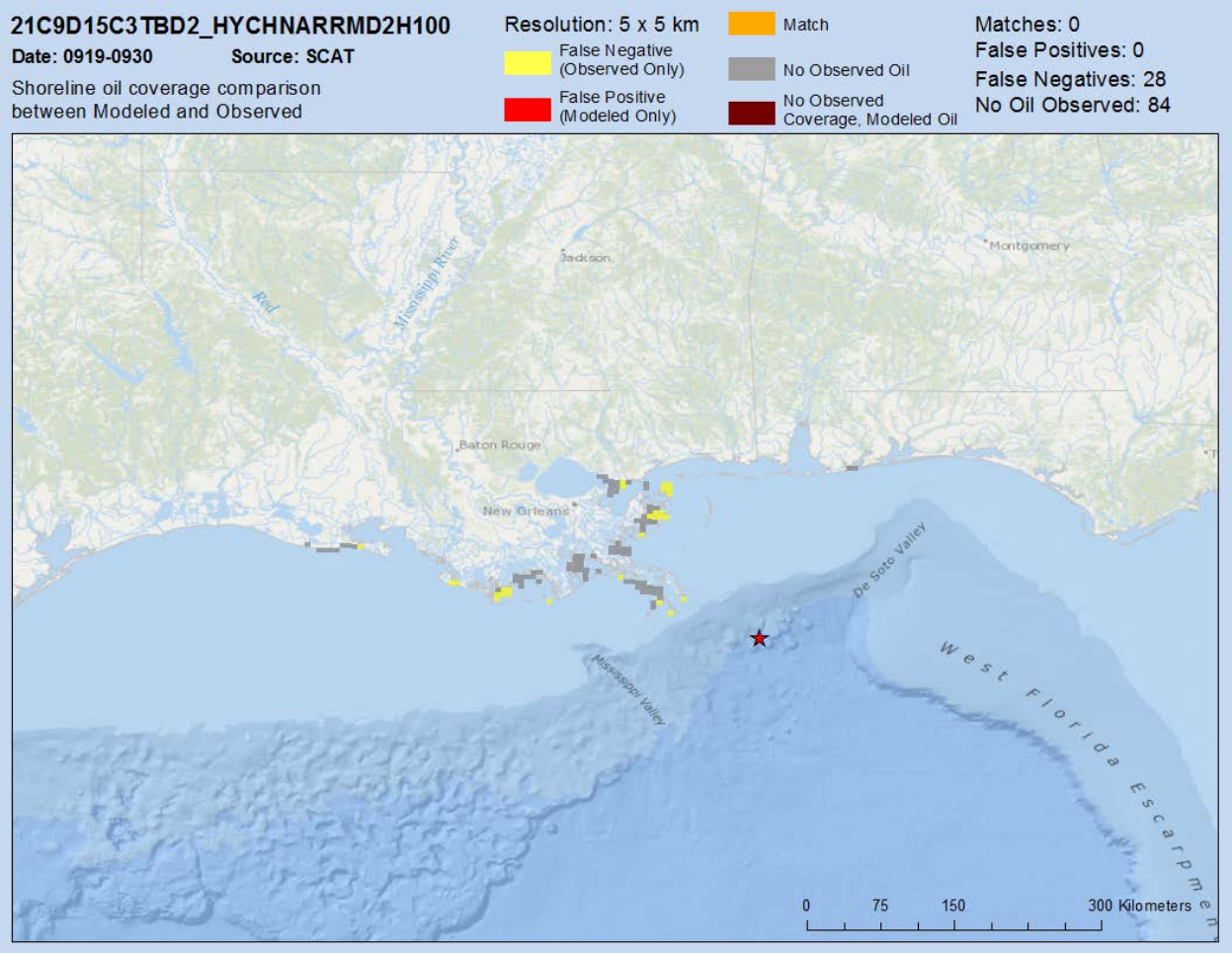

Figure D.3-16. Comparison of model to observed amount of oil coming ashore during 10-day interval 14, September 19–30.

Annex E: *Deepwater Horizon* Oil Spill Model Results: Subsurface Oil Concentrations

E.1. Trajectory of Oil Droplets

E.1.1 Spillet Age for HYCOM-FSU Simulation

Snapshots of the trajectory using HYCOM-FSU currents, integrating spillets over the water column and color-coded by the age of spillets, are provided in attachments to Annex E.1.1. The results are integrated and presented for three depth intervals:

- Annex E.1.1.1 HYCOM-FSU Trajectory Below 800m
- Annex E.1.1.2 HYCOM-FSU Trajectory 800–200m
- Annex E.1.1.3 HYCOM-FSU Trajectory 200–40m

E.1.2 Spillet Age for SABGOM Simulation

Snapshots of the trajectory using SABGOM currents, integrating spillets over the water column and color-coded by the age of spillets, are provided in attachments to Annex E.1.2. The results are integrated and presented for three depth intervals:

- Annex E.1.2.1 SABGOM Trajectory Below 800m
- Annex E.1.2.2 SABGOM Trajectory 800–200m
- Annex E.1.2.3 SABGOM Trajectory 200–40m

E.1.3 Spillet Age for ADCP Simulation

Snapshots of the trajectory using ADCP currents, integrating spillets over the water column and color-coded by the age of spillets, are provided in attachments to Annex E.1.3. The results are integrated and presented for three depth intervals:

- Annex E.1.3.1 ADCP Trajectory Below 800m
- Annex E.1.3.2 ADCP Trajectory 800–200m
- Annex E.1.3.3 ADCP Trajectory 200–40m

E.2. Total Hydrocarbons in Droplets

E.2.1 Total Hydrocarbon Concentrations for HYCOM-FSU Simulation

Snapshots of total hydrocarbon concentrations (THC) in oil droplets using HYCOM-FSU currents are provided in attachments to Annex E.2.1. The results are integrated and presented for three depth intervals:

- Annex E.2.1.1 HYCOM-FSU THC Below 800m
- Annex E.2.1.2 HYCOM-FSU THC 800–200m
- Annex E.2.1.3 HYCOM-FSU THC 200–40m

E.2.2 Total Hydrocarbon Concentrations for SABGOM Simulation

Snapshots of total hydrocarbon concentrations in oil droplets using SABGOM currents are provided in attachments to Annex E.2.2. The results are integrated and presented for three depth intervals:

- Annex E.2.2.1 SABGOM THC Below 800m
- Annex E.2.2.2 SABGOM THC 800–200m
- Annex E.2.2.3 SABGOM THC 200–40m

E.2.3Total Hydrocarbon Concentrations for ADCP Simulation

Snapshots of total hydrocarbon concentrations in oil droplets using ADCP currents are provided in attachments to Annex E.2.3. The results are integrated and presented for five depth intervals:

- Annex E.2.3.1 ADCP THC 1,400–1,200m
- Annex E.2.3.2 ADCP THC 1,200–1,000m
- Annex E.2.3.3 ADCP THC 1,000–800m
- Annex E.2.3.4 ADCP THC 800–200m
- Annex E.2.3.5 ADCP THC 200–40m

E.3. Total Dissolved Hydrocarbons below 40 m

E.3.1 Total Dissolved Hydrocarbon Concentrations for HYCOM-FSU Simulation

Snapshots of total dissolved hydrocarbon ("Dislv") concentrations using HYCOM-FSU currents are provided in attachments to Annex E.3.1. The results are integrated and presented for seven depth intervals:

- Annex E.3.1.1 HYCOM-FSU Dislv 1,400–1,200m
- Annex E.3.1.2 HYCOM-FSU Dislv 1,200–1,000m
- Annex E.3.1.3 HYCOM-FSU Dislv 1,00–800m
- Annex E.3.1.4 HYCOM-FSU Dislv 800–600m
- Annex E.3.1.5 HYCOM-FSU Dislv 600–400m
- Annex E.3.1.6 HYCOM-FSU Dislv 400–200m
- Annex E.3.1.7 HYCOM-FSU Dislv 200–40m

E.3.2 Total Dissolved Hydrocarbon Concentrations for SABGOM Simulation

Snapshots of total dissolved hydrocarbon concentrations using SABGOM currents are provided in attachments to Annex E.3.2. The results are integrated and presented for seven depth intervals:

- Annex E.3.2.1 SABGOM Dislv 1,400–1,200m
- Annex E.3.2.2 SABGOM Dislv 1,200–1,000m
- Annex E.3.2.3 SABGOM Dislv 1,000–800m
- Annex E.3.2.4 SABGOM Dislv 800–600m
- Annex E.3.2.5 SABGOM Dislv 600–400m
- Annex E.3.2.6 SABGOM Dislv 400–200m
- Annex E.3.2.7 SABGOM Dislv 200–40m

E.3.3 Total Dissolved Hydrocarbon Concentrations for ADCP Simulation

Snapshots of total dissolved hydrocarbon concentrations using ADCP currents are provided in attachments to Annex E.3.3. The results are integrated and presented for seven depth intervals:

- Annex E.3.3.1 ADCP Dislv 1,400–1,200m
- Annex E.3.3.2 ADCP Dislv 1,200–1,000m
- Annex E.3.3.3 ADCP Dislv 1,000–800m
- Annex E.3.3.4 ADCP Dislv 800–600m
- Annex E.3.3.5 ADCP Dislv 600–400m
- Annex E.3.3.6 ADCP Dislv 400–200m
- Annex E.3.3.7 ADCP Dislv 200–40m

E.4. Dissolved Component Concentrations for the ADCP Simulation below 40m

E.4.1 AR1

Snapshots of dissolved AR1 (BTEX) concentrations using ADCP currents are provided in attachments to Annex E.4.1. The results are integrated and presented for six depth intervals:

- Annex E.4.1.1 ADCP Dislv AR1 1,400–1,200m
- Annex E.4.1.2 ADCP Dislv AR1 1,200–1,000m
- Annex E.4.1.3 ADCP Dislv AR1 1,000–800m
- Annex E.4.1.4 ADCP Dislv AR1 800–600m
- Annex E.4.1.5 ADCP Dislv AR1 600–400m
- Annex E.4.1.6 ADCP Dislv AR1 400–200m

E.4.2 AR5

Snapshots of dissolved AR5 (C0-C2 naphthalenes) concentrations using ADCP currents are provided in attachments to Annex E.4.2. The results are integrated and presented for five depth intervals:

- Annex E.4.2.1 ADCP Dislv AR5 1,400–1,200m
- Annex E.4.2.2 ADCP Dislv AR5 1,200–1,000m
- Annex E.4.2.3 ADCP Dislv AR5 1,000–800m
- Annex E.4.2.4 ADCP Dislv AR5 800–600m
- Annex E.4.2.5 ADCP Dislv AR5 600–400m
- ADCP Dislv AR5 400–200m–There are no concentrations > 1 μg/L

E.4.3 AR7

Snapshots of dissolved AR7 (fluorenes and C0-C1 3-ring PAHs) concentrations using ADCP currents are provided in attachments to Annex E.4.4. The results are integrated and presented for five depth intervals:

- Annex E.4.3.1 ADCP Dislv AR7 1,400–1,200m
- Annex E.4.3.2 ADCP Dislv AR7 1,200–1,000m
- Annex E.4.3.3 ADCP Dislv AR7 1,000–800m
- Annex E.4.3.4 ADCP Dislv AR7 800–600m
- Annex E.4.3.5 ADCP Dislv AR7 600–400m
- ADCP Dislv AR7 400–200m–There are no concentrations > 1 μg/L

E.4.4 AR9

Snapshots of dissolved AR9 (soluble alkanes) concentrations using ADCP currents are provided in attachments to Annex E.4.6. The results are integrated and presented for six depth intervals:

- Annex E.4.4.1 ADCP Dislv AR9 1,400–1,200m
- Annex E.4.4.2 ADCP Dislv AR9 1,200–1,000m
- Annex E.4.4.3 ADCP Dislv AR9 1,000–800m
- Annex E.4.4.4 ADCP Dislv AR9 800–600m
- Annex E.4.4.5 ADCP Dislv AR9 600–400m
- Annex E.4.4.6 ADCP Dislv AR9 400–200m

E.5. Hydrocarbon Concentrations above 40 m

E.5.1 Total Hydrocarbon Concentrations in Droplets for HYCOM-FSU Simulation

Snapshots of total hydrocarbon concentrations in droplets in the upper 40 m using HYCOM-FSU currents are provided in attachment Annex E.5.1.

- Annex E.5.1 HYCOM-FSU THC 0–40m

E.5.2 Total Dissolved Hydrocarbon Concentrations for HYCOM-FSU Simulation

Snapshots of total dissolved hydrocarbon concentrations using HYCOM-FSU currents are provided in attachment Annex E.5.2. These concentrations are of PAHs (AR5 + AR6 + AR7 + AR8), as concentrations of AR1, AR2, AR3 and AR9 components are depleted immediately after oil surfaces by evaporation. The results are integrated and presented for the PAH pseudo-components:

- Annex E.5.2 HYCOM-FSU Dislv TPAH 0–40m

Annex F: *Deepwater Horizon* Oil Spill: Comparison of Modeled Subsurface Concentrations to Chemistry Data

F.1. HYCOM-FSU

Comparisons of model simulations using HYCOM-FSU currents and field-measured total particulate plus dissolved concentrations are provided in attachments to this Annex. The results are evaluated and presented for five depth intervals:

- Annex F.1.1 HYCOM-FSU MODEL-OBSERVED 1,400–1,100m
- Annex F.1.2 HYCOM-FSU MODEL-OBSERVED 1,100–800m
- Annex F.1.3 HYCOM-FSU MODEL-OBSERVED 800–500m
- Annex F.1.4 HYCOM-FSU MODEL-OBSERVED 500–200m
- Annex F.1.5 HYCOM-FSU MODEL-OBSERVED 200–40m

F.2. SABGOM

Comparisons of model simulations using SABGOM currents and field-measured total particulate plus dissolved concentrations are provided in attachments to this Annex. The results are evaluated and presented for five depth intervals:

- Annex F.2.1 SABGOM MODEL-OBSERVED 1,400–1,100m
- Annex F.2.2 SABGOM MODEL-OBSERVED 1,100–800m
- Annex F.2.3 SABGOM MODEL-OBSERVED 800–500m
- Annex F.2.4 SABGOM MODEL-OBSERVED 500–200m
- Annex F.2.5 SABGOM MODEL-OBSERVED 200–40m

F.3. ADCPS

Comparisons of model simulations using ADCP currents and field-measured total particulate plus dissolved concentrations are provided in attachments to this Annex. The results are evaluated and presented for five depth intervals:

- Annex F.3.1 ADCP MODEL-OBSERVED 1,400–1,100m
- Annex F.3.2 ADCP MODEL-OBSERVED 1,100–800m
- Annex F.3.3 ADCP MODEL-OBSERVED 800–500m
- Annex F.3.4 ADCP MODEL-OBSERVED 500–200m
- Annex F.3.5 ADCP MODEL-OBSERVED 200–40m

Department of the Interior (DOI)

The Department of the Interior protects and manages the Nation's natural resources and cultural heritage; provides scientific and other information about those resources; and honors the Nation's trust responsibilities or special commitments to American Indians, Alaska Natives, and affiliated island communities.

BOEM
Bureau of Ocean Energy Management

Bureau of Ocean Energy Management (BOEM)

The mission of the Bureau of Ocean Energy Management is to manage development of U.S. Outer Continental Shelf energy and mineral resources in an environmentally and economically responsible way.

BOEM Environmental Studies Program

The mission of the Environmental Studies Program is to provide the information needed to predict, assess, and manage impacts from offshore energy and marine mineral exploration, development, and production activities on human, marine, and coastal environments. The proposal, selection, research, review, collaboration, production, and dissemination of each of BOEM's Environmental Studies follows the DOI Code of Scientific and Scholarly Conduct, in support of a culture of scientific and professional integrity, as set out in the DOI Departmental Manual (305 DM 3).